infrastructures

Special Issue Reprint

Earthquake and Multi-Hazard Resilience

Community-Level Insights and AI/ML Applications

Edited by
Mojtaba Harati, John W. van de Lindt and Maria Koliou

mdpi.com/journal/infrastructures

MDPI

Earthquake and Multi-Hazard Resilience: Community-Level Insights and AI/ML Applications

Earthquake and Multi-Hazard Resilience: Community-Level Insights and AI/ML Applications

Guest Editors

Mojtaba Harati
John W. van de Lindt
Maria Koliou

MDPI

Basel • Beijing • Wuhan • Barcelona • Belgrade • Novi Sad • Cluj • Manchester

Guest Editors

Mojtaba Harati
Verisk Catastrophe and Risk Solutions
Boston
USA

John W. van de Lindt
Department of Civil and Environmental Engineering
Colorado State University
Fort Collins
USA

Maria Koliou
Zachry Department of Civil and Environmental Engineering
Texas A&M University
College Station
USA

Editorial Office
MDPI AG
Grosspeteranlage 5
4052 Basel, Switzerland

This is a reprint of the Special Issue, published open access by the journal *Infrastructures* (ISSN 2412-3811), freely accessible at: https://www.mdpi.com/journal/infrastructures/special_issues/4R6H5K58Z0.

For citation purposes, cite each article independently as indicated on the article page online and as indicated below:

Lastname, A.A.; Lastname, B.B. Article Title. *Journal Name* **Year**, *Volume Number*, Page Range.

ISBN 978-3-7258-8889-4 (Hbk)
ISBN 978-3-7258-8890-0 (PDF)
https://doi.org/10.3390/books978-3-7258-8890-0

© 2026 by the authors. Articles in this reprint are Open Access and distributed under the Creative Commons Attribution (CC BY) license. The reprint as a whole is distributed by MDPI under the terms and conditions of the Creative Commons Attribution-NonCommercial-NoDerivs (CC BY-NC-ND) license (https://creativecommons.org/licenses/by-nc-nd/4.0/).

Contents

About the Editors . . . . . **vii**

Preface . . . . . **ix**

Mojtaba Harati, John W. van de Lindt and Maria Koliou
Earthquake and Multi-Hazard Resilience: Community-Level Insights and AI/ML Applications
Reprinted from: *Infrastructures* **2026**, *11*, 273, https://doi.org/10.3390/infrastructures11080273 . **1**

Sarah Bashour, Bassam Hwaija, Fadwa Issa, Firas Al Mahmoud and George Wardeh
Wind-Induced Response of Coupled Shear Wall Systems Based on Wind Tunnel Testing
Reprinted from: *Infrastructures* **2026**, *11*, 236, https://doi.org/10.3390/infrastructures11070236 . **9**

Mojtaba Harati and John W. van de Lindt
Advancing Near-Field Tsunami Fragility Modeling Through Structural Simulation and Post-Event Damage Observations
Reprinted from: *Infrastructures* **2026**, *11*, 221, https://doi.org/10.3390/infrastructures11070221 . **31**

Mohsen Zaker Esteghamati and Shiva Baddipalli
An Ensemble Learning-Based Approach to Quantify Post-Earthquake Functional Recovery of a Steel Moment-Resisting Frame Inventory
Reprinted from: *Infrastructures* **2026**, *11*, 213, https://doi.org/10.3390/infrastructures11070213 . **59**

Mohamad Nassar, Fatiha Mouri and Ahmad Abo El Ezz
Assessment of Community Risk from Seismic-Induced Damage to Hazardous Materials Storage Tanks in Marine Ports
Reprinted from: *Infrastructures* **2026**, *11*, 49, https://doi.org/10.3390/infrastructures11020049 . . **73**

Qiuyan Gu and Jun Wang
Analyzing Natural Disaster Risk Factors in Engineering Projects: A Social Networks Analysis Approach
Reprinted from: *Infrastructures* **2025**, *10*, 352, https://doi.org/10.3390/infrastructures10120352 . **91**

Donata Carlucci, Donatello Cardone, Serena Parisi and Marco Vona
Artificial Intelligence Tools in the Management of Reinforced Concrete Structures: Potential, Critical Issues, and Preliminary Results on Structural Degradation
Reprinted from: *Infrastructures* **2025**, *10*, 306, https://doi.org/10.3390/infrastructures10110306 . **126**

Mojtaba Harati and John W. van de Lindt
Machine Learning Synthesis of Fire-Following-Earthquake Fragility Surfaces for Steel Moment-Resisting Frames
Reprinted from: *Infrastructures* **2025**, *10*, 280, https://doi.org/10.3390/infrastructures10110280 . **142**

Ehsan Harirchian and Viviana Iris Novelli
Leveraging Transformer Models for Seismic Fragility Assessment of Non-Engineered Masonry Structures in Malawi
Reprinted from: *Infrastructures* **2025**, *10*, 279, https://doi.org/10.3390/infrastructures10110279 . **163**

Yaser Hosseini, Reza Karami Mohammadi and Tony Y. Yang
Seismic Vulnerability Assessment and Prioritization of Masonry Railway Tunnels: A Case Study
Reprinted from: *Infrastructures* **2025**, *10*, 254, https://doi.org/10.3390/infrastructures10100254 . **194**

Giuseppe Brandonisio and Muhammad Tayyab Naqash
Community-Scale Seismic Vulnerability Assessment of RC Churches: A Simplified Approach for Cultural Infrastructure Resilience
Reprinted from: *Infrastructures* **2025**, *10*, 234, https://doi.org/10.3390/infrastructures10090234 . **219**

About the Editors

Mojtaba Harati

Mojtaba Harati is a research engineer at Verisk Catastrophe and Risk Solutions specializing in earthquake and multi-hazard resilience. He completed his postdoctoral research at the NIST Center for Risk-Based Community Resilience Planning at Colorado State University after earning a Ph.D. in Civil Engineering. His work develops simulation models spanning earthquake, tsunami, fire, flood, and tornado hazards, with an emphasis on multi-hazard fragility modeling, functional recovery, and economic loss estimation. A recurring theme is the integration of large-scale nonlinear simulation with machine learning to extend detailed structural analysis to asset inventories and communities while preserving physical meaning. He has contributed methods for earthquake–tsunami and fire-following-earthquake fragility surfaces, as well as data-driven recovery assessment, publishing in journals such as *Computer-Aided Civil and Infrastructure Engineering*, the *ASCE Journal of Structural Engineering*, and *Engineering Structures*. At Verisk, he applies this expertise as a research engineer at Verisk Catastrophe and Risk Solutions, where he contributes to catastrophe risk modeling, connecting resilience science to practical decision-making in infrastructure risk assessment and insurance analytics.

John W. van de Lindt

John W. van de Lindt is the Harold H. Short Endowed Chair Professor in the Department of Civil and Environmental Engineering at Colorado State University and Co-director of the National Institute of Standards and Technology-funded Center of Excellence for Risk-Based Community Resilience Planning. For more than two decades, his research has advanced performance-based engineering and test-bed applications of buildings and infrastructure systems subjected to earthquakes, hurricanes, tsunamis, tornadoes, and floods, and he has led numerous post-disaster field investigations. He is a principal contributor to IN-CORE, an open computational platform that enables communities to measure and plan for their resilience to natural hazards. He serves as Editor-in-Chief of the *ASCE Journal of Structural Engineering*, is a Fellow of the American Society of Civil Engineers, and has authored more than 450 technical articles and reports, including over 250 peer-reviewed journal papers. His honors include the ASCE Ernest E. Howard Award and multiple Raymond C. Reese Research Prizes for his work on the performance of structural systems under extreme hazards.

Maria Koliou

Maria Koliou is an Associate Professor and Zachry Career Development Professor in the Zachry Department of Civil and Environmental Engineering at Texas A&M University. She earned her diploma in civil engineering from the University of Patras, Greece, and her Ph.D. from the University at Buffalo, the State University of New York, in 2014, followed by a postdoctoral fellowship at the NIST-funded Center of Excellence for Risk-Based Community Resilience Planning at Colorado State University before joining Texas A&M in 2017. Her research spans structural dynamics, earthquake engineering, and multi-hazard performance-based design for system functionality and community resilience, with a focus on developing sustainable and hazard-resistant structural systems that account for economic and social dimensions. A recipient of the NSF CAREER Award, she has examined the seismic performance and functional recovery of wood-frame and other building systems and has contributed mathematical frameworks for assessing community resilience under multiple hazards. She is also a faculty fellow of the Hazard Reduction and Recovery Center at Texas A&M University.

Preface

The motivation for this Reprint is a simple observation with difficult consequences: earthquakes rarely act alone, and their effects rarely stop at a single structure. Ground shaking may be followed by fire, tsunami inundation, or technological accidents, and the failure of one building, storage tank, or lifeline can ripple outward into services, economic activity, and the daily lives of entire communities. Assessing resilience under these conditions demands more than predicting whether a component survives; it requires translating physical evidence into information that owners, engineers, and public agencies can act on, and doing so at a scale that exhaustive, high-fidelity analysis cannot reach.

We assembled this Reprint to gather complementary responses to that challenge. The collected studies move deliberately across scales, from component and building behavior to asset inventories, infrastructure portfolios, and community consequences, and they draw on nonlinear simulation, empirical observation, simplified mechanics, geospatial methods, and modern artificial intelligence and machine learning. Rather than advocating a single technique, the Reprint argues for matching model fidelity to the decision at hand, preserving the damaged state left by one hazard when analyzing the next, and keeping data-driven models traceable to physics and observation.

This Reprint is intended for researchers, practicing engineers, graduate students, and decision-makers concerned with seismic and multi-hazard risk. We hope it offers both concrete methods and a shared perspective: that resilience is advanced less by increasing complexity for its own sake than by connecting evidence across scales to the people and services that infrastructure is meant to protect.

Mojtaba Harati, John W. van de Lindt, and Maria Koliou
Guest Editors

infrastructures

MDPI

Editorial

Earthquake and Multi-Hazard Resilience: Community-Level Insights and AI/ML Applications

Mojtaba Harati [1,*], John W. van de Lindt [1] and Maria Koliou [2]

[1] Department of Civil and Environmental Engineering, Colorado State University, Fort Collins, CO 80523, USA; jwv@engr.colostate.edu
[2] Zachry Department of Civil and Environmental Engineering, Texas A&M University, College Station, TX 77843, USA; maria.koliou@tamu.edu
* Correspondence: m.harati@colostate.edu

1. Introduction

Earthquake resilience is increasingly a problem of interactions across hazards, assets, infrastructure systems, and recovery processes. Ground shaking can be followed by fire, tsunami inundation, or natural-hazard-triggered technological accidents; damage to a single building or storage tank can propagate through lifelines, emergency services, economic activity, and population exposure. At the same time, the scale of the built environment makes exhaustive high-fidelity analysis impractical for every asset. Resilience assessment, therefore, must do more than predict damage: it must translate physical evidence into transparent, scalable, and decision-ready information.

This Special Issue brings together ten contributions that address this translation challenge from complementary perspectives. The studies span component and building response, asset inventories, infrastructure portfolios, and community consequences. They combine nonlinear simulation, fragility and loss analysis, empirical observations, simplified mechanics, geospatial assessment, machine learning, computer vision, and network analysis. Not every paper operates directly at the community scale; rather, the collection shows how evidence at one scale can support decisions at another when fragility, functionality, exposure, recovery, and prioritization are explicitly connected.

Taken together, the central lesson is that model sophistication alone does not create resilience. High-fidelity analysis is valuable when it reveals governing mechanisms and produces reliable training or calibration data; reduced-order and machine-learning models are valuable when they preserve those insights while extending analysis to inventories; and screening tools are valuable when they identify where more detailed investigation is warranted. Figure 1 summarizes this progression. The following sections synthesize the contributions around sequential and cascading hazards, AI/ML-enabled scaling, and decision support under data constraints before identifying a shared research agenda.

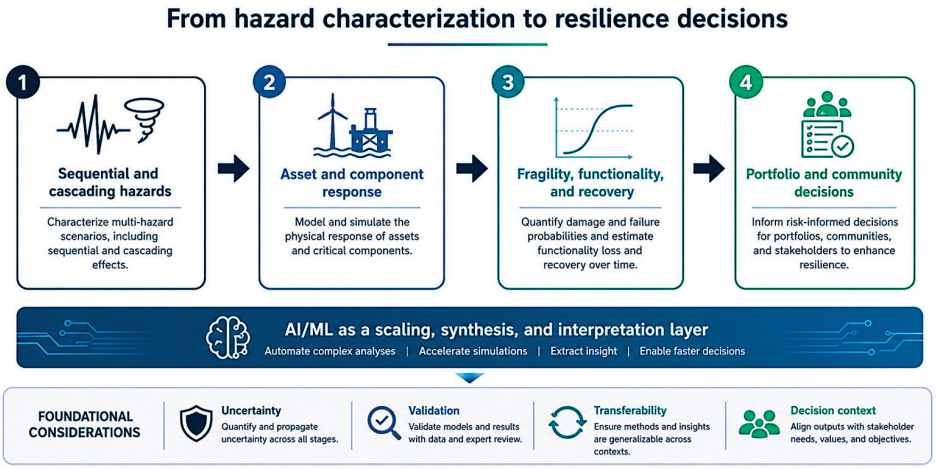

Figure 1. Integrative perspective emerging from the Special Issue: detailed hazard and structural evidence is translated into decision-ready resilience information through tiered models and explicit treatment of uncertainty and applicability.

2. Sequential and Cascading Hazards Across Scales

Nassar et al. 1 provide the clearest community-consequence pathway in this Special Issue. Their seismic Natech framework links scenario-based peak ground acceleration estimates for 12 earthquake scenarios to tank damage probabilities, hazardous-release likelihood, off-site consequence distances, population exposure, and potential domino effects among 49 port storage tanks. This chain makes explicit how moderate regional shaking can produce disproportionate consequences when hazardous inventories, spatial clustering, and urban exposure coincide. It also illustrates an important distinction: a community risk model is not simply an asset fragility model applied many times; it must represent release pathways, spatial overlap, and the people or functions located within the resulting consequence zones.

Harati and van de Lindt 2 address another state-dependent sequence: fire following earthquake in steel moment-resisting frames. Their framework transfers residual deformation and damage from nonlinear earthquake analysis into temperature-dependent fire simulations within a Monte Carlo environment, then represents the joint response as a fragility surface. The machine-learning synthesis closely reproduces the simulation-derived surfaces for the three-story case study ($R^2 > 0.95$ and RMSE < 0.02), demonstrating a practical route for retaining sequential hazard interactions without repeating the full simulation workflow for every application. The contribution is especially important because separate earthquake-only and fire-only checks cannot reproduce the interior of the joint hazard space, where prior seismic damage alters the subsequent fire capacity.

The near-field tsunami contribution extends the same state-transfer principle to earthquake–tsunami sequences (Contribution 3). It combines successive structural simulation, post-earthquake residual-state transfer, and tsunami loading with empirical damage observations from the 2011 Great East Japan tsunami. A distance-dependent intensity-shifting approach adapts baseline fragility relationships for near-coast conditions, while feature-importance analysis identifies momentum flux as the highest-ranked composite predictor within the evaluated empirical models and coastal proximity as an additional contributor. Importantly, the simulation demonstration uses a U.S. reinforced-concrete moment-frame archetype, whereas the empirical analysis uses Japanese wood-frame observations; the proposed bridge between physics and data is transferable, but quantitative fragility parameters remain typology- and site-specific.

https://doi.org/10.3390/infrastructures11080273

Together, Contribution 2 and 3 show why hazard sequence must be modeled as a change in structural state rather than as a simple combination of independent probabilities. Residual drift, accumulated plasticity, degradation, and the time between events influence the second-hazard response. This principle applies more broadly to aftershocks, flood–scour sequences, wind–rain interactions, and infrastructure systems in which one event reduces the capacity or accessibility needed to manage the next.

Bashour et al. 4 provide a complementary performance-based wind perspective rather than a sequential hazard model. Using wind-tunnel-derived pressure histories and nonlinear analysis of a 20-story coupled-wall building, they show that global code checks can mask localized serviceability and component vulnerabilities. A targeted refinement of wall piers, coupling beams, and boundary reinforcement increased baseline concrete volume by 4.33% while reducing peak roof drift by 60% and preventing structural yielding in the investigated configuration. The result reinforces a broader message across this Special Issue: resilience-relevant assessment requires performance measures at the scale where failure initiates, not only global strength or drift compliance. Because the case study is specific to one structural and aerodynamic configuration, its quantitative gains should be treated as design evidence rather than as universally transferable values.

These four studies therefore occupy different positions along a common chain—from hazard interaction and component response to release, exposure, and system consequences. Their collective contribution is a more precise vocabulary for multi-hazard assessment: sequential hazards require state transfer; cascading effects require propagation pathways; and comparative performance-based studies reveal which hazard or response measure governs a given design.

3. AI/ML as a Scaling, Synthesis, and Interpretation Layer

Across this Special Issue, AI/ML is used in four distinct roles: emulating computationally expensive analyses, deriving fragility relationships from structured data, interpreting influential features, and automating visual inspection. Treating these roles separately is important. A surrogate model may be judged by predictive error and domain coverage; an inspection model also depends on image quality and annotation consistency; and an explainability method describes model behavior but does not by itself establish physical causation.

Harirchian and Novelli 5 apply transformer architectures to fragility estimation for non-engineered masonry construction in Malawi. The database includes 646 surveyed wall records with geometric, material, connection, roof, and configuration features, and the models predict fragility-related outputs for multiple damage states. The transformer achieved the lowest aggregate error among seven evaluated machine-learning methods, indicating that attention-based models can capture nonlinear interactions in heterogeneous field data. The study is also a reminder that predictive performance within one regional dataset is not equivalent to external validity: broader use will require additional regions, independent test sets, careful treatment of class and feature distributions, and explicit reporting of the model's domain of applicability.

Carlucci et al. 6 move from tabular data to computer vision for reinforced-concrete infrastructure management. Their YOLO-based workflow classifies visible reinforcement degradation using an expert-annotated image set, expanded from 234 original images to 588 through augmentation and organized into four degradation classes. The paper appropriately characterizes the results as preliminary. Its most consequential contribution may be the articulation of the data problem: reliable deployment depends on standardized image acquisition, traceable labeling criteria, balanced and representative classes, and

 https://doi.org/10.3390/infrastructures11080273

validation on structures, environments, and cameras not seen during training. In safety-critical inspection, automated detection should support—rather than silently replace—engineering judgment and targeted verification.

Zaker Esteghamati and Baddipalli 7 demonstrate how machine learning can bring a computationally intensive resilience metric into design exploration. They first quantify functional recovery for an inventory of 100 steel special moment-resisting frames by coupling FEMA P-58 damage and loss assessment with the ATC-138 recovery framework, then train a random-forest surrogate using geometric and design variables. Test-set R^2 values of 0.89 for design-basis earthquakes and 0.93 for maximum-considered earthquakes show that recovery time can be approximated efficiently within the studied inventory. SHAP analysis identifies building weight and the average strong-column–weak-beam ratio as influential predictors. These rankings are valuable for design inquiry, but they should be interpreted as model-dependent associations within a correlated design space, not as isolated causal laws.

The fire-following-earthquake and tsunami papers (Contribution 2 and 3) add a third pattern: machine learning as a synthesis layer around physics-based simulation and empirical observations. This hybrid approach is especially promising because it can preserve state-dependent mechanics, reduce repeated computation, and expose the relative influence of input variables. Its credibility, however, rests on the quality of the simulations or observations used for training and on validation at the boundaries of the hazard and structural domains.

Collectively, these studies suggest that the most useful engineering AI is neither purely data-driven nor simply appended to conventional analysis. It is embedded in a workflow with explicit inputs, physically meaningful outputs, uncertainty characterization, independent validation, and an escalation path to detailed analysis when predictions fall outside the training domain. Explainability can improve transparency, but it must be paired with sensitivity analysis, error diagnostics, and engineering constraints.

4. Screening, Prioritization, and Decision Support Under Data Constraints

Large infrastructure inventories rarely have complete drawings, material tests, or budgets for detailed nonlinear analysis. Three contributions therefore focus on how limited information can still support defensible triage.

Brandonisio and Naqash 8 develop a simplified mechanics-based procedure for reinforced-concrete churches with recurring cathedral-portal frames. Their inventory of 54 reinforced-concrete churches in Naples identified 20 examples with the frequent portal configuration; the method combines linear and nonlinear static analysis, plastic limit theory, and capacity-spectrum concepts, with calibration and application to representative churches. The contribution is strongest when viewed as a typology-specific screening framework: it converts sparse geometric and material information into comparable capacity and vulnerability indicators for cultural infrastructure that also serves social and post-disaster functions. The authors clearly define applicability boundaries, including regular portal repetition and limited plan irregularity, which is essential for responsible regional use.

Hosseini et al. 9 address a network of 103 aging masonry railway tunnels and galleries exposed to 12 fault sources in northwestern Iran. Peak ground acceleration and displacement are combined with HAZUS- and SYNER-G-based fragility relationships, visual-inspection information, a damage index, and a normalized prioritization index. The resulting four classes place 10% of assets in the highest priority group, followed by 33%,

 https://doi.org/10.3390/infrastructures11080273

40%, and 17% in the remaining classes. The value of the framework is operational: it makes constrained rehabilitation sequencing explicit. Its principal limitation is equally instructive—common fragility relationships are applied because tunnel-specific material and geotechnical data are unavailable. The ranking should therefore initiate targeted investigation, not substitute for it.

Gu and Wang 10 widen the lens from physical assets to the structure of disaster-risk knowledge. From 81 studies, they identify 48 natural-disaster risk factors and use co-occurrence networks and centrality measures to compare factors discussed theoretically with those incorporated into predictive models. Earthquakes and floods occupy central positions, while several climatic, hydrological, and geological factors are discussed more often than they are modeled. The analysis highlights fragmentation and the limited treatment of multi-hazard coupling. At the same time, a literature co-occurrence network is not a causal hazard network; its centrality metrics reveal research attention and association patterns, not physical trigger probabilities or consequence pathways. Its most productive use is to identify blind spots and guide the construction of integrated, physically grounded models.

These studies share a decision philosophy: the purpose of screening is to allocate scarce attention. A useful screening method must be transparent about data requirements, assumptions, uncertainty, and applicability; produce rankings or thresholds tied to a real management action; and specify when an asset should advance to inspection, testing, nonlinear analysis, or intervention design. Under these conditions, simplified models complement rather than compete with high-fidelity analysis.

5. Cross-Cutting Lessons and Research Agenda

5.1. Connect Asset Response to Community Outcomes

The papers span components, buildings, inventories, ports, transportation assets, and literature-level risk networks. The next step is to make transitions among these scales explicit. Component damage must be translated into building functionality; building damage into downtime and service disruption; asset failures into network performance; and network disruption into population exposure, economic loss, and unequal recovery. The port study (Contribution 1) and functional-recovery study (Contribution 7) demonstrate two pieces of this chain, but fully integrated applications will require infrastructure interdependencies, utility restoration, transportation accessibility, emergency-service capacity, and household or business recovery.

5.2. Represent State Dependence and Time

Sequential hazards are not merely two hazards in the same map. The first event changes stiffness, strength, geometry, fire protection, access, and response capacity before the second begins (Contribution 2 and 3). Future frameworks should carry these state variables—and their uncertainty—across hazard phases, while also representing event timing, repair progress, aftershock sequences, and degraded emergency systems. Similar logic is needed for aging and deterioration: the inspection study (Contribution 6) and tunnel assessment (Contribution 9)] indicate that pre-event condition can be as important as event intensity.

5.3. Match Model Fidelity to the Decision

A tiered workflow emerges in this Special Issue. High-fidelity simulations establish mechanisms and benchmark data; surrogate models enable rapid design-space exploration; simplified mechanics and index-based methods screen portfolios; and detailed investi-

 https://doi.org/10.3390/infrastructures11080273

gation is reserved for assets whose risk or uncertainty justifies it. Future work should formalize transitions between tiers using error bounds, uncertainty thresholds, and value-of-information criteria. A model should be no more complex than the decision requires, but no simpler than the failure mechanism permits.

5.4. Build Trustworthy and Transferable AI/ML

Five priorities are especially important: provenance and quality control for training data; external validation across regions and typologies; uncertainty calibration rather than point prediction alone; physical consistency and behavior outside the training range; and reproducible benchmarks. Data augmentation, cross-validation, and SHAP are useful tools, but they do not by themselves demonstrate field transferability. Benchmark datasets should include raw inputs, preprocessing decisions, uncertainty definitions, and common performance metrics so that models can be compared fairly. Where safety decisions are involved, prediction intervals and abstention or escalation rules should accompany model outputs.

5.5. Broaden the Definition of Community Resilience

Community resilience depends on more than structural fragility. Social vulnerability, accessibility, institutional capacity, risk communication, cultural value, and distributional equity influence both consequences and recovery. Cultural infrastructure (Contribution 8), transportation tunnels (Contribution 9), industrial ports (Contribution 1), and engineering projects (Contribution 10) each serve different populations and functions. Future analyses should identify who benefits from mitigation, who remains exposed, and how resource prioritization changes when life safety, continuity, cultural significance, economic function, and equity are considered together.

5.6. Translating Research into Practice

Translation into practice will require interoperable data structures, open and versioned analytical workflows, clearly defined decision metrics, and collaboration with infrastructure owners and public agencies. Promising outputs include fragility and recovery libraries that retain their domains of applicability; portfolio dashboards that connect uncertainty to inspection or retrofit actions; and multi-hazard platforms that allow users to compare mitigation, preparedness, and recovery alternatives. Prospective validation after future events—and systematic updating as new data arrive—should be treated as part of the model lifecycle, not as a final research step.

6. Concluding Remarks

Taken together, the ten contributions show that progress in earthquake and multi-hazard resilience depends less on increasing model complexity for its own sake than on translating knowledge across scales. Sequential hazard models must preserve the damaged state left by prior events; AI/ML models must remain traceable to data and mechanics; screening tools must be aligned with real resource constraints; and asset-level results must be connected to functionality, exposure, recovery, and community priorities. This Special Issue therefore points toward a tiered and integrated resilience workflow in which detailed simulation, empirical evidence, machine learning, and simplified decision tools reinforce one another. The field's next challenge is to make that workflow operational, transferable, uncertainty-aware, and attentive to the people and services infrastructure is intended to protect.

https://doi.org/10.3390/infrastructures11080273

Author Contributions: Conceptualization, M.H., J.W.v.d.L., and M.K.; methodology, M.H., J.W.v.d.L., and M.K.; formal analysis, M.H.; investigation, M.H.; writing—original draft preparation, M.H.; writing—review and editing, J.W.v.d.L. and M.K.; visualization, M.H.; supervision, J.W.v.d.L. and M.K.; project administration, J.W.v.d.L.; funding acquisition, J.W.v.d.L. All authors have read and agreed to the published version of the manuscript.

Funding: This research was funded by the U.S. National Institute of Standards and Technology (NIST) through the Center for Risk-Based Community Resilience Planning, a NIST-funded Center of Excellence, under cooperative agreements with Colorado State University (Financial Assistance Award Nos. 70NANB15H044 and 70NANB20H008).

Data Availability Statement: The data, models, and code that support the findings of this study are available from the corresponding author upon reasonable request.

Acknowledgments: The Center for Risk-Based Community Resilience Planning is an NIST-funded Center of Excellence; the Center is funded through a cooperative agreement between the U.S. National Institute of Standards and Technology and Colorado State University. The views expressed are those of the authors and may not represent the official position of the National Institute of Standards and Technology or the U.S. Department of Commerce.

Conflicts of Interest: Author Mojtaba Harati was employed by Verisk Catastrophe and Risk Solutions. The research presented in this study did not use any proprietary data, models, or knowledge from Verisk. The remaining authors declare that the research was conducted in the absence of any commercial or financial relationships that could be construed as a potential conflict of interest.

List of Contributions

1. Nassar, M.; Mouri, F.; Abo El Ezz, A. Assessment of Community Risk from Seismic-Induced Damage to Hazardous Materials Storage Tanks in Marine Ports. *Infrastructures* **2026**, *11*, 49. https://doi.org/10.3390/infrastructures11020049.
2. Harati, M.; van de Lindt, J.W. Machine Learning Synthesis of Fire-Following-Earthquake Fragility Surfaces for Steel Moment-Resisting Frames. *Infrastructures* **2025**, *10*, 280. https://doi.org/10.3390/infrastructures10110280.
3. Harati, M.; van de Lindt, J.W. Advancing Near-Field Tsunami Fragility Modeling Through Structural Simulation and Post-Event Damage Observations. *Infrastructures* **2026**, *11*, 221. https://doi.org/10.3390/infrastructures11070221.
4. Bashour, S.; Hwaija, B.; Issa, F.; Al Mahmoud, F.; Wardeh, G. Wind-Induced Response of Coupled Shear Wall Systems Based on Wind Tunnel Testing. *Infrastructures* **2026**, *11*, 236. https://doi.org/10.3390/infrastructures11070236.
5. Harirchian, E.; Novelli, V.I. Leveraging Transformer Models for Seismic Fragility Assessment of Non-Engineered Masonry Structures in Malawi. *Infrastructures* **2025**, *10*, 279. https://doi.org/10.3390/infrastructures10110279.
6. Carlucci, D.; Cardone, D.; Parisi, S.; Vona, M. Artificial Intelligence Tools in the Management of Reinforced Concrete Structures: Potential, Critical Issues, and Preliminary Results on Structural Degradation. *Infrastructures* **2025**, *10*, 306. https://doi.org/10.3390/infrastructures10110306.
7. Zaker Esteghamati, M.; Baddipalli, S. An Ensemble Learning-Based Approach to Quantify Post-Earthquake Functional Recovery of a Steel Moment-Resisting Frame Inventory. *Infrastructures* **2026**, *11*, 213. https://doi.org/10.3390/infrastructures11070213.
8. Brandonisio, G.; Naqash, M.T. Community-Scale Seismic Vulnerability Assessment of RC Churches: A Simplified Approach for Cultural Infrastructure Resilience. *Infrastructures* **2025**, *10*, 234. https://doi.org/10.3390/infrastructures10090234.

9. Hosseini, Y.; Karami Mohammadi, R.; Yang, T.Y. Seismic Vulnerability Assessment and Prioritization of Masonry Railway Tunnels: A Case Study. *Infrastructures* **2025**, *10*, 254. https://doi.org/10.3390/infrastructures10100254.
10. Gu, Q.; Wang, J. Analyzing Natural Disaster Risk Factors in Engineering Projects: A Social Networks Analysis Approach. *Infrastructures* **2025**, *10*, 352. https://doi.org/10.3390/infrastructures10120352.

Disclaimer/Publisher's Note: The statements, opinions and data contained in all publications are solely those of the individual author(s) and contributor(s) and not of MDPI and/or the editor(s). MDPI and/or the editor(s) disclaim responsibility for any injury to people or property resulting from any ideas, methods, instructions or products referred to in the content.

infrastructures

MDPI

Article

Wind-Induced Response of Coupled Shear Wall Systems Based on Wind Tunnel Testing

Sarah Bashour [1], Bassam Hwaija [1], Fadwa Issa [1], Firas Al Mahmoud [2] and George Wardeh [3,*]

[1] Department of Structural Engineering, Faculty of Civil Engineering, Latakia University, Lattakia P.O. Box 2230, Syria; sarah.bashour@latakia-univ.edu.sy (S.B.); h.bassam65@latakia-univ.edu.sy (B.H.); fadwa.issa1978@latakia-univ.edu.sy (F.I.)
[2] CNRS, IJL, Université de Lorraine, 54000 Nancy, France; firas.al-mahmoud@univ-lorraine.fr
[3] L2MGC—Laboratoire de Mécanique et Matériaux du Génie Civil, CY Cergy-Paris, 95000 Cergy, France
* Correspondence: george.wardeh@cyu.fr

Abstract

Coupled shear wall systems are widely used in tall buildings due to their high lateral stiffness and effectiveness in controlling wind-induced serviceability responses. Reliable assessment of their behavior under realistic wind loading requires accurate load representation and properly calibrated numerical modeling. This study investigates the performance of coupled shear wall systems under wind loads derived from wind tunnel testing, where surface pressure time histories were extracted from the TPU Aerodynamic Database and used to generate equivalent full-scale, time-varying wind loads. The preliminary design of a 20-story building was established in ETABS based on current design codes. Detailed nonlinear time-history analyses were subsequently performed in OpenSees to assess the performance under three different wind hazards for the original and refined design, where shear walls were modeled using the Multiple-Vertical-Line-Element Model (MVLEM). Several wind demand indicators, including drift ratios, floor accelerations, and component and cladding performance were evaluated. The results demonstrate that the performance-based design framework enables the identification of critical vulnerabilities that may not be fully captured by conventional code-based drift and strength checks, particularly regarding localized damage accumulation and serviceability-related demands. Additionally, the refined configuration, while requiring only a 4.33% increase in total baseline concrete volume, effectively reduced peak roof drift by 60%, allowing reliable control of dynamic behavior and prevention of structural yielding, as well as ensuring the maintenance of both structural integrity and operational serviceability for the investigated high-rise configuration during severe wind events. Nevertheless, the findings are limited to the investigated building configuration and aerodynamic conditions considered in this study.

Keywords: coupled shear wall systems; wind-induced response; serviceability performance; nonlinear analysis; OpenSees

1. Introduction

Wind engineering remains one of the most challenging frontiers in structural science, driven by the increasing height and slenderness of modern buildings. A defining historical milestone was the 1978 Citicorp Center crisis, which revealed the unexpected vulnerability

of unconventional structural systems to quartering winds. Although subsequent reassessments demonstrated that face winds may govern design loads in many cases [1], this event remains a benchmark in engineering awareness and design philosophy.

As buildings evolved, design strategies transitioned from simple resistance-based approaches toward integrated systems that combine redundancy, stiffness control, and energy dissipation. Taipei 101 illustrates this evolution through the use of mega-columns and a 660-ton tuned mass damper designed to mitigate both wind and seismic effects [2]. More recently, extreme wind events such as the 2024 Houston Derecho have highlighted critical vulnerabilities in façade systems, where localized amplification phenomena—particularly wind channeling between adjacent structures—can induce significant damage even when design-level wind speeds are not exceeded [3]. These observations indicate that, while global structural stability is generally ensured, localized and non-structural responses remain a major challenge in wind-resistant design.

In this context, Performance-Based Design (PBD) has emerged as a fundamental shift from prescriptive approaches toward methodologies that explicitly evaluate structural behavior under defined hazard levels. In wind engineering, this paradigm has evolved into Performance-Based Wind Design (PBWD), where structures are required to satisfy multiple performance objectives, including serviceability, operational functionality, and safety, under wind events associated with different return periods [4–6]. Unlike traditional design approaches based on simplified load factors, PBWD establishes a direct link between structural demand and wind hazard intensity, incorporating probabilistic methods and advanced numerical simulations to better account for uncertainties in both loading and structural response [7].

A major advancement in PBWD is the recognition that wind-induced structural response may involve nonlinear behavior. Iancovici et al. [8] demonstrated that long-duration wind excitation, when analyzed through nonlinear time-domain simulations, can induce cumulative damage and localized inelastic behavior. This finding challenges the traditional assumption of purely elastic response under wind loading and establishes wind as a potential damage-accumulating mechanism. These insights have motivated a broader reassessment of PBWD methodologies, particularly regarding the need to incorporate nonlinear structural behavior into design frameworks.

From a broader perspective, Abdelwahab et al. [9] provide a comprehensive review of PBWD, identifying it as a rapidly developing field that still lags behind seismic performance-based design in terms of maturity and standardization. Their work highlights several fundamental challenges inherent to wind loading, including long-duration excitation, strong dependence on wind directionality, and the complexity of turbulence and vortex shedding phenomena. Furthermore, they identify critical research gaps, such as the need for efficient nonlinear analysis tools, improved hazard representation, and better integration of non-structural damage and uncertainties. This study establishes a global conceptual framework for PBWD and clearly defines the barriers that currently limit its widespread implementation in engineering practice. Directly addressing these limitations, Saini et al. [10] propose an advanced PBWD framework based on Database-Assisted Design (DAD), integrating wind tunnel pressure data, nonlinear dynamic structural analysis, and site-specific climatological information. Their methodology explicitly incorporates wind directionality by generating response surfaces as functions of wind speed and direction, which are subsequently combined with probabilistic wind hazard models to evaluate performance at different mean recurrence intervals. The results of their case study show that, although the structure satisfies strength-based design criteria, it fails to meet serviceability requirements—particularly with respect to inter-story drift and cladding performance—highlighting the importance of comprehensive performance evaluation beyond traditional design checks.

 https://doi.org/10.3390/infrastructures11070236

Together, these contributions illustrate a critical transition in PBWD development, from the conceptual identification of challenges [9] to their implementation in advanced physics-based frameworks [10]. However, they also reveal a persistent limitation, namely the high computational cost associated with nonlinear time-history analysis and multidirectional wind simulations, which remains a major obstacle to practical adoption.

In parallel, PBWE research has progressed toward more design-oriented methodologies. Athanasiou et al. [11] introduced a multi-hazard approach integrating wind and seismic actions and proposed controlled inelasticity through wind reduction factors, while Alanani and Elshaer [12] further advanced PBWD by incorporating surrogate modeling and optimization techniques to improve computational efficiency during early design stages. More recently, Gora et al. [13] emphasized the importance of accounting for non-stationary wind hazards, demonstrating that climate change may significantly increase structural response levels and the probability of exceeding serviceability limits over the lifecycle of tall buildings.

Overall, the current state-of-the-art reflects a progressive evolution from probabilistic conceptual frameworks toward nonlinear analysis and practical design-oriented methodologies. Abdelwahab et al. [9] define the theoretical challenges and research directions, while Saini et al. [10] demonstrate one of the most advanced current implementations, integrating nonlinear behavior, wind directionality, and probabilistic hazard within a unified PBWD framework.

These developments highlight that modern wind design must simultaneously address nonlinear structural response, uncertainty quantification, computational efficiency, and evolving wind hazard conditions, paving the way toward robust, standardized, and future-adaptive performance-based wind design methodologies.

While these findings illustrate the development of performance-based wind design, its practical application to coupled wall systems remains underexplored. Nonlinear response, ductile behavior of coupling beams, and stiffness of wall piers play a critical role in energy dissipation, overstrength, and drift control. However, how these features collectively influence system performance under prolonged, cyclic wind loading remains unclear. To address these limitations, this study provides the following contributions to the field of high-rise wind engineering: (1) establishing a component-level performance framework by tracking the Deformation Damage Index (DDI) across structural panel zones under wind tunnel-derived time histories, and demonstrating that global drift metrics can mask severe local non-structural vulnerabilities; (2) characterizing the dynamic sensitivity and aerodynamic trade-offs that occur when localized structural modifications alter the building's natural period; and (3) presenting a component-level refinement strategy aimed at improving wind-induced serviceability performance while limiting additional material consumption.

2. Methodology

A preliminary design of a 20-story building consisting of reinforced concrete coupled walls was first conducted using the software ETABS 22 following current wind and seismic design codes, where initial cross sections were assigned. Subsequently, a nonlinear time history analysis was conducted in OpenSees [14], as it enables more realistic prediction of inelastic response, plastic hinge spread, and cyclic degradation through capturing distributed plasticity and axial–flexural interaction of wall piers as well as strength degradation, stiffness deterioration, and hysteretic behavior of coupling beams. The assessment was performed for different wind hazards according to the ASCE prestandard for performance-based wind design [15] using wind tunnel time history loads extracted from the TPU aerodynamic database [16] and processed afterwards. Based on the results of the assessment, an iterative design process was conducted, resulting in a modified design which incorporates increased

 https://doi.org/10.3390/infrastructures11070236

stiffness in the wall piers and coupling beams, as well as strengthened reinforcement in the boundary elements, and comparisons of the two designs were conducted.

Several wind demand characteristics were studied, including hysteretic behavior, roof drift, stiffness reduction, deformation damage index, and acceleration in order to enhance the current insights into inelastic behavior of tall buildings subjected to wind loads.

2.1. Building Description

The case study is a reinforced concrete (RC) residential building with a height of H = 60 m (consisting of 20 stories with each story height h_s = 3 m) and a square-shaped plan with a width of 20 m. The structural system consists of ordinary frames to resist gravity loads only, and two coupled walls in each direction connected by a conventionally reinforced coupling beam to resist the combinations of gravity and lateral loads, as shown in Figure 1. It is assumed that the compressive strength of the concrete f'_c is 30 MPa and its modulus of elasticity per the Syrian code is $E = 5700\sqrt{f'_c}$ = 31 GPa [17]. The modulus of elasticity and yield strength of the steel are assumed to be 210 GPa and 400 MPa, respectively. The section properties of structural elements are reported in Table 1.

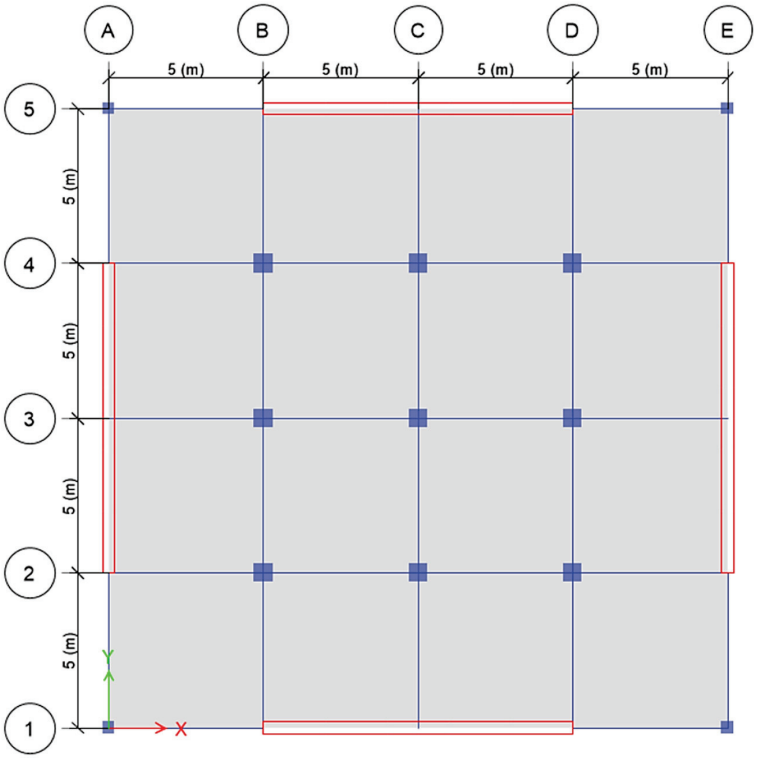

Figure 1. Structural plan.

Table 1. Section properties of structural elements.

Main Group	Structural Element	Stories	Section Dimensions	Flexural Stiffness Modifier	In-Plane Stiffness Modifier	Out-of-Plane Stiffness Modifier
Columns	Corner columns	All	40 × 40 cm	0.70 EIg	—	—
	Interior columns	1–5	70 × 70 cm	0.70 EIg	—	—
		6–10	60 × 60 cm	0.70 EIg	—	—
		11–15	50 × 50 cm	0.70 EIg	—	—
		16–20	40 × 40 cm	0.70 EIg	—	—

https://doi.org/10.3390/infrastructures11070236

Table 1. *Cont.*

Main Group	Structural Element	Stories	Section Dimensions	Flexural Stiffness Modifier	In-Plane Stiffness Modifier	Out-of-Plane Stiffness Modifier
Beams	Perimeter beams	All	30 × 55 cm	0.35 EIg	—	—
	Interior beams	All	25 × 40 cm	0.35 EIg	—	—
	Coupling beams	1–5	45 × 70 cm	0.35 EIg	—	—
		6–20	40 × 70 cm	0.35 EIg	—	—
Walls	Wall piers	1–5	45 cm thickness	—	0.35 EIg	0.10 EIg
		6–20	40 cm thickness	—	0.70 EIg	0.10 EIg
Slab	Floor slab	All	14 cm thickness	—	Rigid diaphragm	0.25 EIg

2.2. Preliminary Design

A preliminary design of the building was conducted considering gravity, seismic, and wind loads. In addition to the weight of the structural members, superimposed dead load of 2 kN/m^2 and live loads of 2 kN/m^2 were assigned as uniform loads for floors. Dead loads of 9.23 kN/m and 5.5 kN/m were assigned to the perimeter and interior frame beams, respectively. P-Delta effects were taken into account, and the natural period and frequency of the first mode were 2.585 s and 0.386 Hz, respectively. For seismic and wind design, the loads were taken per code UBC 97 [18] and ASCE 7-16 [19], respectively, which correspond to the Syrian design code. Load combinations for strength design are reported in Table 2.

Table 2. Syrian code design combinations.

Load Combination	Contents
Gravity loads	1.4D + 1.7L
Gravity and wind loads	1.2D + 0.5L + 1.6W and 0.99D + 1.6W
Gravity and seismic loads	1.4025D + 0.55L + 1.1E and 0.9075D + 1.1E

Note: D = dead and super dead load; L = reduced live load; W = wind load; and E = seismic load.

Design parameters for equivalent static seismic and wind loads are reported in Tables 3 and 4. As the main focus of this study is on wind loads, the site was deliberately chosen where wind loads govern the design over seismic loads.

Table 3. UBC 97 code design seismic parameters.

Parameter	Value
Soil profile type	S_B
Seismic zone factor	0.15
I, importance factor	1
T, natural period of structure	1.471 s
R, response modification factor	4.5

Table 4. ASCE 7-16 code design wind parameters.

Parameter	Symbol	Value
Basic wind speed (50-year MRI)	V	51 m/s
Exposure category	Exposure	C
Ground elevation factor	K_e	1.0
Topographic factor	K_{zt}	1.0

https://doi.org/10.3390/infrastructures11070236

Table 4. *Cont.*

Parameter	Symbol	Value
Gust effect factor	G	1.1
Directionality factor	K_d	0.85

2.3. Modified Design

Several enhancements were made based on the vulnerabilities detected in the original design following a judgment-driven and iterative design refinement approach. These modifications are summarized in Table 5, where the wall thickness was increased by 5 cm and the coupling beam depth was increased by 10 cm. Based on ETABS material takeoffs, the total baseline structural concrete volume is 2516 m^3. Thickening the designated shear walls and deepening the coupling beams adds 109 m^3. Therefore, the total volume of the modified building becomes 2625 m^3, confirming an overall structural material increase of just 4.33%, and verifying that the proposed structural enhancements are highly cost-effective. The reinforcement of boundary elements was also increased by 20%, while the other reinforcement ratios were kept the same.

Table 5. Modified design properties.

Structural Element	Section
Coupling beam (width × depth)	(50–45) cm × 80 cm
Walls	thickness
1st–5th stories	50 cm
6th–20th stories	45 cm

Table 6 reports boundary element lengths and the longitudinal and horizontal reinforcement of wall piers and coupling beams of the original design derived from the elastic strength design in ETABS, as well as the modified boundary element reinforcement.

Table 6. Boundary element length and reinforcement ratios.

Stories	Boundary Element Length (cm)	Uniform Wall Reinforcement Ratio (%)	Boundary Element Reinforcement Ratio (%) Original	Boundary Element Reinforcement Ratio (%) Modified	Wall Shear Reinforcement Ratio (%)	Coupling Beam Longitudinal Reinforcement (mm^2)	Coupling Beam Vertical Reinforcement (mm^2/m)
1–5	90	1.0	1.0	3.0	0.25	4729	3887
6–10	80	0.42	1.0	3.0	0.25	4140	3459
11–15	80	0.25	1.0	3.0	0.25	2409	1821
16–20	80	0.25	1.0	3.0	0.25	1027	1000

2.4. OpenSees Modeling Approach

The model used in OpenSees was developed by Kolozvari et al. and Tauberg [20,21]. Several assumptions were made in this model, such as considering the out-of-plane stiffness of the floor slab to be small, hence resulting in insignificant axial forces on walls via wall–wall or wall–column interaction. While this formulation represents a known limitation of the 2D modeling framework, the idealization is motivated by the immense stiffness mismatch between out-of-plane slab bending and in-plane wall rigidity, alongside expected severe slab cracking under lateral demands. Also, symmetry is used such that the model is two-dimensional and

 https://doi.org/10.3390/infrastructures11070236

consists of only two piers and one coupling beam connecting them. The analysis is performed for in-plane loads only, without considering the effect of out-of-plane deformation of the wall. Although a two-dimensional idealization was adopted to facilitate detailed tracking of local damage mechanisms, previous studies have shown that 2D coupled-wall models provide satisfactory predictions of global lateral response when torsional irregularities are limited and floor diaphragms behave approximately rigidly [20,21].

Figure 2 briefly illustrates the modeling approach. Tributary mass is assigned at the element nodes of each story, as well as the gravity loads based on corresponding tributary areas (Figure 2a). Half of the gravity loads are assigned to the P-delta column nodes of each floor, where an elastic element with a very large axial stiffness and negligible bending stiffness is assigned to the P-delta column (Figure 2b). Rigid links connect wall piers to the elastic coupling beam elements, which have a nonlinear shear hinge located at the beam midspan (Figure 2c).

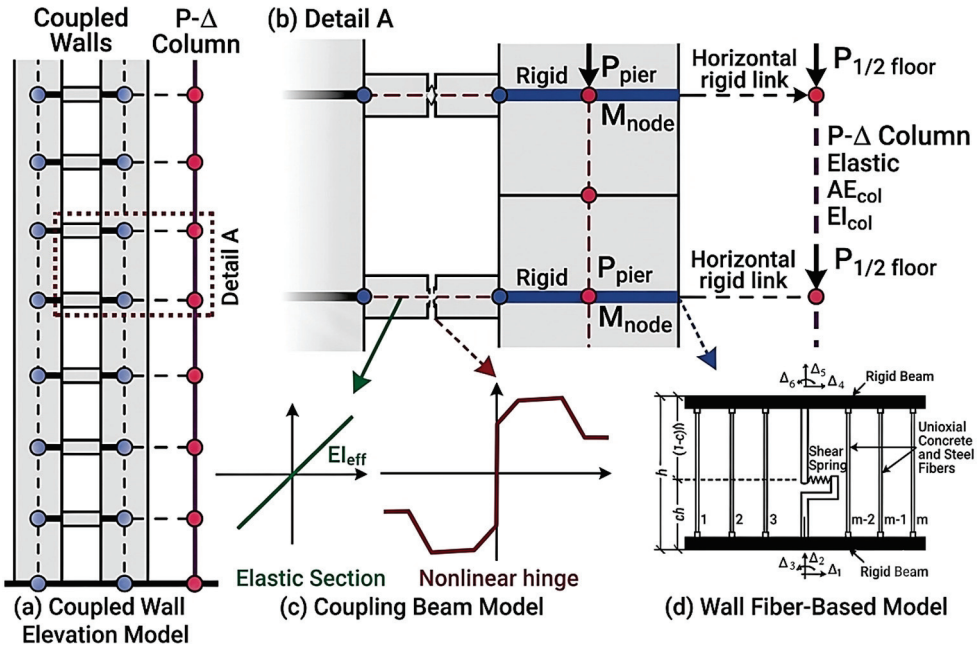

Figure 2. Modeling approach.

2.4.1. Modeling Walls

The Multiple-Vertical-Line-Element Model (MVLEM) [22] is used for modeling wall piers (Figure 2d). The fiber-based cross-sectional discretization of the MVLEM explicitly quantifies in-plane P-M coupling, directly capturing neutral axis shifts and dynamic axial force accumulation from the coupling beams. Two elements per story height for vertical discretization is deemed appropriate [20], and using a fiber size of 100 mm in the horizontal direction is also sufficient and more computationally efficient [21]. A mesh sensitivity assessment reported by Tauberg [21] demonstrated that two MVLEM elements per story provide a suitable balance between computational efficiency and numerical accuracy, with negligible variation in global response quantities compared with finer discretization. The material Concrete02 proposed by Yassin [23] is used in this study to simulate concrete behavior. Unconfined concrete behavior is based on Hognestad model [24], while the confined concrete relationship is based on the confinement model by Saatcioglu & Razvi [25]. Concrete tensile strength is estimated as $0.62\sqrt{f'_c}$ (MPa) [26], and tension softening stiffness value of $E_t = 0.05$E is used [23]. For the hysteretic behavior of reinforcing steel, the uniaxial hysteretic constitutive model SteelMPF [27] is used.

https://doi.org/10.3390/infrastructures11070236

The element's flexure and shear responses are uncoupled; therefore, the wall shear response is simulated using a linear elastic spring with a cracked effective shear stiffness of $0.5GA_w$ [28].

2.4.2. Modeling Coupling Beams

Coupling beams (Figure 3) are connected to the adjacent walls by rigid beam elements defined between the centerlines of the walls and the ends of the coupling beam element. An elastic beam element with an effective flexural stiffness of $0.07(l_n/h)I_g$ [28] is used to model deformation.

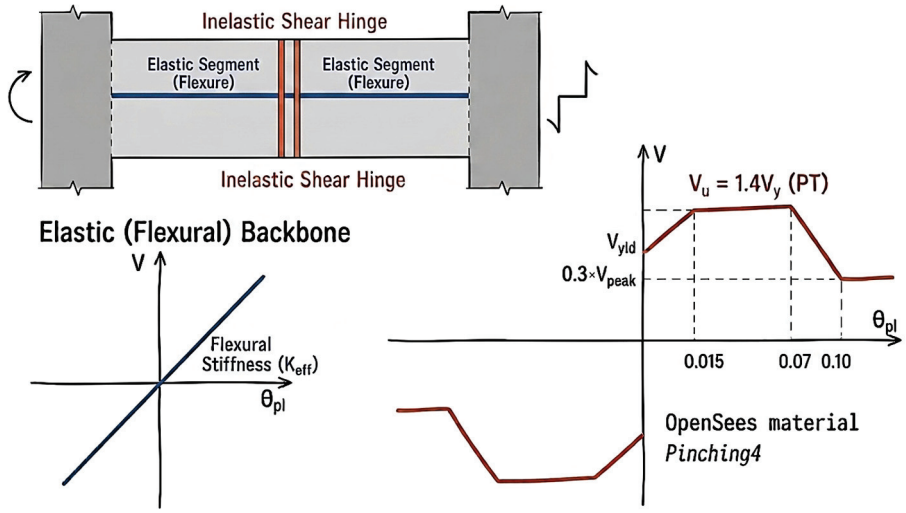

Figure 3. Coupling beam model.

For the hysteretic shear behavior, a nonlinear shear hinge located in the center of the beam is used with material Pinching4, available in OpenSees, consisting of four main points: Point1, the yield point; Point2, ultimate shear; Point3, the point at which the shear begins to degrade; and Point4, reaching the residual force.

The coupling beam hysteretic behavior was calibrated by Tauberg [21], and Table 7 illustrates the input values of material Pinching4 for FB33 (Conventional Reinforcement).

Table 7. Pinching4 input parameters [21].

Specimen	Yield Point (Point 1)	Peak Strength Point (Point 2)	Degradation Point (Point 3)	Residual Strength Point (Point 4)	FU/FY	rForceP
FB33 (Conventional reinforcement)	(0.001 L, FY)	(0.015 L, FU)	(0.045 L, 1.01 FU)	(0.07 L, 0.30 FU)	1.10	0.35

Note: OpenSees Pinching4 model (rDisP = 0.05; uForceP = 0.01; gK#: 0.5, 0.45, 0.4, 0.35, 1.0).

2.4.3. Damping

A Rayleigh damping ratio of 2% was adopted, consistent with commonly reported damping levels of reinforced concrete wall structures under serviceability-level wind excitation. The first and third vibration modes were selected to compute the mass- and stiffness-proportional damping coefficients [29].

2.4.4. Validation

A rigorous validation of this model was conducted by the authors in a previous work using Sugaya et al.'s experimental test of a 12-story coupled wall system [30]. Figures 4 and 5 illustrate the experimental setup and relationship of the base shear–12th floor drift

https://doi.org/10.3390/infrastructures11070236

ratio of the test vs. the analytical model. The numerical model reproduced the experimental hysteretic behavior, stiffness degradation pattern, and peak resistance with satisfactory agreement, supporting its application for subsequent wind-induced nonlinear analyses.

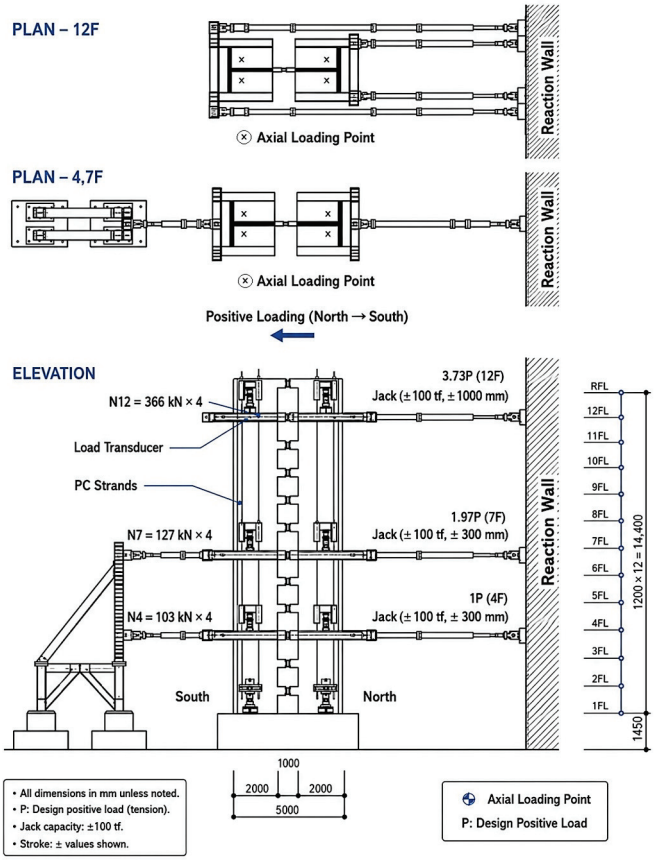

Figure 4. Test setup.

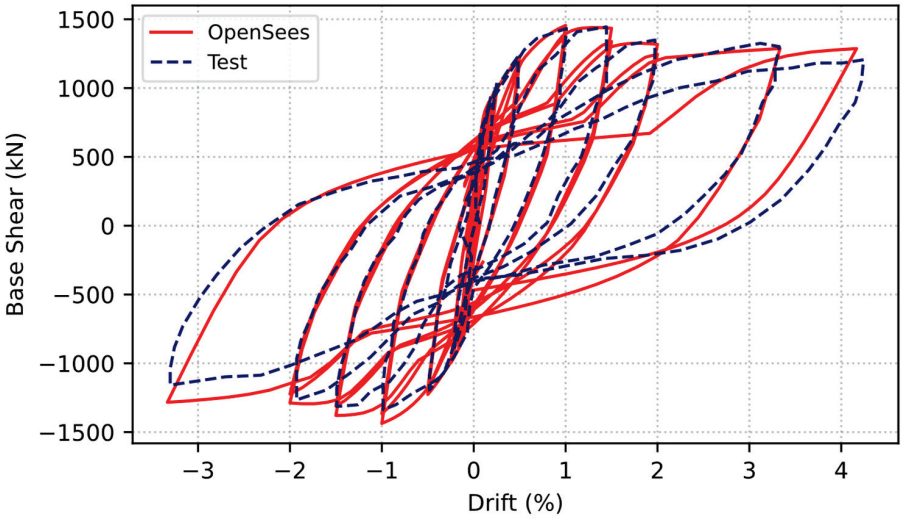

Figure 5. Experimental vs. analytical results of the 12-story coupled wall system.

While quasi-static cyclic testing differs from long-duration stochastic wind loading in frequency and load history, it serves as a validated baseline to capture material nonlinearities, stiffness degradation, and energy dissipation. Validating these fundamental structural mechanisms ensures that the numerical framework reliably predicts the hysteretic response

https://doi.org/10.3390/infrastructures11070236

under the alternating cyclic demands imposed by dynamic wind loading, consistent with established performance-based wind engineering methodologies [31,32].

2.5. Wind Loads for Performance Assessment

2.5.1. Wind Speeds

For a risk category II, the ASCE prestandard [15] identifies three wind hazards: 1 or 10 years MRI for the performance objective Occupant Comfort, 10 years MRI for Operational, and 700 years MRI for Continuous Occupancy (Limited Interruption). Equation (1) is used to obtain wind speed of different MRIs [33]:

$$V_T = [0.36 + 0.10 \ln(12T)] \times V_{50} \quad (1)$$

The wind speed calculated above should be converted to mean hourly wind speed at the site of the building and at the building roof level using Equation (2).

$$(V_{\text{hr}})_{\text{building}} = \frac{1}{1.525} \times (V_{3\,\text{sec}})_{\text{coastal}} \times \left(\frac{Z_{\text{ref, coastal}}}{Z_{\text{coastal}}} \right)^{\frac{1}{\alpha_C}} \times \left(\frac{Z_{\text{building}}}{Z_{\text{ref, building}}} \right)^{\frac{1}{\alpha_C}}, \quad (2)$$

where $Z_{\text{ref, coastal}}$, Z_{coastal}, and α_C are terrain exposure constants obtained from ASCE 7-16 [19], and 1.525 is the factor for conversion of 3 s averaged wind speed to hourly wind speed.

Table 8 presents basic wind speeds and the corresponding mean hourly wind speeds at the roof level for the hazard scenarios evaluated.

Table 8. Corresponding wind speed of each hazard.

MRI	Basic Wind Speed (m/s)	Mean Hourly Wind Speed at Roof Level (m/s)
10	43	37
700	64	56

2.5.2. Wind Load Calculation and Scaling Framework

Several analytical assumptions were enforced: (1) wind-induced torque is neglected due to the building's symmetrical plan, and a homogenous environment around the building with wind loading direction perpendicular to the face of the building along the line of symmetry is assumed [34]; (2) The correlation between the along- and cross-wind loading directions is negligible [35].

Based on this, the coupled wall system would be evaluated in two uncoupled orthogonal directions.

While this uncoupled 2D evaluation framework allows for a highly targeted tracking of localized damage, it represents an idealized boundary condition. In real-world multi-directional wind hazards, concurrent bi-axial demand states and complex wake interference from neighboring structures may induce coupled three-dimensional responses that fall outside the isolated scope of this study.

The wind loading histories are obtained from the wind pressure database for high-rise buildings (TPU) [16]. The database contains time series data of point wind pressure coefficients on the wall surfaces of different building models which were tested in wind tunnel tests. In this study, a Breadth:Depth:Height ratio of 1:1:3 was chosen for the building geometry of (20 m:20 m:60 m). This ratio was selected because it closely matches the geometric proportions of the investigated prototype structure and therefore minimizes

 https://doi.org/10.3390/infrastructures11070236

geometric scaling discrepancies. Also, a power law exponent factor of $\overline{\alpha} = 1/6$ was selected corresponding to exposure category C.

Because the TPU data represents rigid-model aerodynamic pressures governed solely by external geometry, the same pressure histories are applied to both configurations, since changing wall thickness or coupling beam depth does not alter the external geometry. The effects of altered structural stiffness and natural frequencies are natively captured through the dynamic response analysis in OpenSees.

To use the wind pressure coefficient loading histories in OpenSees, the coefficient values were converted to point load forces acting on the story levels. The pressure coefficients were used to obtain pressure values using the Bernoulli equation (Equation (3)).

$$P = \frac{1}{2} \times C_P \times \rho \times V_{hr,\ \text{building}}{}^2, \tag{3}$$

where ρ is the air density and Cp is the pressure coefficient obtained from the TPU database.

The transformation of pressure histories into floor-level time-history nodes follows a two-stage processing framework. First, the instantaneous full-scale wind force at a given elevation zone, $F_{\text{raw}}\ (z,t)$, is obtained by integrating the scaled model pressures across their respective tributary areas (Equation (4)). The pressure forces acting on opposite external faces of the building profile are summed concurrently.

$$F_{\text{raw}}\ (z,t) = \sum_{i=1}^{n_z} p_{\text{model}}\ (i,t) \times A_f\ (i), \tag{4}$$

where $p_{\text{model}}\ (i,t)$ is the pressure at tap i, and $A_{\text{f}}\ (i)$ is the corresponding tributary area at the full-scale structure. Because these elevation data lines do not line up with the story heights of the building, a linear interpolation function is enforced as formulated in Equation (5). The force vectors are mapped to the bounding structural floor diaphragms (j and j + 1) proportionally relative to their vertical proximity:

$$F_{\text{floor},j}(t) = \sum\nolimits_z \left(\frac{h_{j+1} - z}{h_{j+1} - h_j} \right) \times F_{\text{raw}}\ (z,t), \tag{5}$$

where h_j and h_{j+1} represent the absolute structural heights of the targeted floor diaphragms. Following this vertical interpolation, the total translational floor force is allocated equally to the parallel lateral-force-resisting lines due to structural symmetry. This linear allocation is standard practice in Database-Assisted Design (DAD) frameworks [10,16]. It functions as a direct static equivalence transformation that perfectly preserves the total integrated global story shears and overturning moments when mapping continuous aerodynamic pressure distributions to discrete floor levels, eliminating the risk of load amplification or the introduction of unphysical spatial eccentricities into the planar system. This process is carried out for the along-wind and cross-wind loading directions entirely independently, yielding uncoupled orthogonal loading files ready for multi-directional dynamic analysis.

The sampling time step of the TPU tests is 0.001 s, with 32,768 data points, which results in 32.77 s of total wind load duration. To go from the wind tunnel scale to the actual coupled wall system scale, the time step and total duration are multiplied by (length scale factor)/(velocity scale factor) [32]. For 10- and 700-year MRI wind loading histories, the total durations are 33.3 and 22.21 min, respectively. Lastly, a 20 s ramp is added to the beginning of the loading history in both directions, gradually increasing the forces to avoid the dynamic effect influencing the response of the building [31].

It should be noted that the wind pressure profiles utilized herein are based on an isolated, prismatic building model within the aerodynamic database. Consequently, the

 https://doi.org/10.3390/infrastructures11070236

presented results should be interpreted as representative of isolated-building behavior. Additional studies considering neighboring buildings, interference effects, shielding phenomena, and urban canyon effects are required before generalizing the conclusions to dense urban environments.

3. Results and Discussion

The results are presented in two sections. First, the verification of the original linear design against current code drift limits and comparison of design forces; and second, the application of nonlinear time-history analyses under wind loads to assess performance.

3.1. Linear Design Verification (ETABS)

As can be seen from Table 9, base shear and overturning moments are quite similar for wind and seismic loads, which can be expected for a building of this height; however, wind loads still governs the strength design for both the wall piers and coupling beams.

Table 9. Comparison of base shear and overturning moments of one coupled wall.

Force	Base Shear (kN)	Overturning Moment (kN.m)
wind	1491	50,174
seismic	1118	50,022

According to Figure 6, the lateral drift evaluations under wind and seismic actions demonstrate full compliance with governing building code requirements. Figure 6a illustrates that the maximum wind-induced elastic drift of 78 mm satisfies the serviceability limit of ASCE 7-16 (H/400), limiting facade and finish damage. As for the seismic load case, Figure 6b shows that the code-amplified inelastic drift ratio (0.00347) is much smaller than the allowable drift of 0.02, and the elastic serviceability drift (0.00077) is also much smaller than the acceptance criteria of $h_s/360 = 0.00278$.

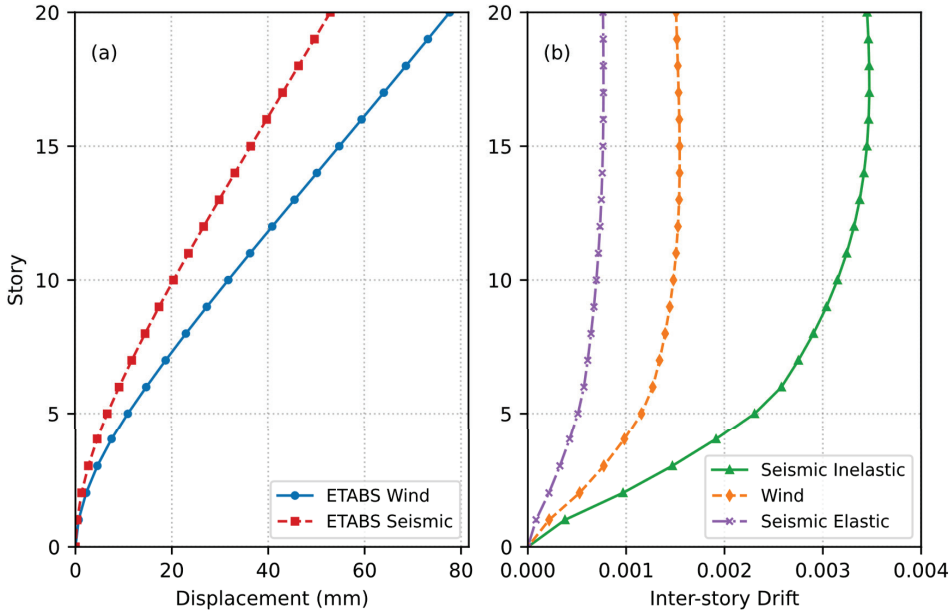

Figure 6. Drift and displacement comparisons: (**a**) Maximum displacement; (**b**) Maximum inter-story drift ratio.

https://doi.org/10.3390/infrastructures11070236

3.2. Performance Assessment of the Coupled Wall System (OpenSees)

3.2.1. Continuous Occupancy

To assess the performance for Continuous Occupancy, the coupled wall original design was first subjected to nonlinear time history analysis for the 700-year MRI wind speed for 11 different directions (0°, 5°, 10°, . . ., 50°). Figure 7 presents max base shear and maximum roof drift for all directions for along and cross wind. As can be observed, the maximum roof drift for both along and cross winds is at the 0° direction with governing along wind. For the majority of wind angles—particularly from 10° through 45°, the along wind governs over the cross wind. However, between 50° and 5°, the cross wind converges with the along wind, signaling areas where vortex shedding or cross-wind turbulence is playing a more significant role. For the purpose of this study, only the governing direction 0° will be focused on, as it is the governing direction. Although the 0° direction governed the global response indicators investigated herein, localized demands and component-level damage may differ under oblique wind directions and therefore deserve further investigation.

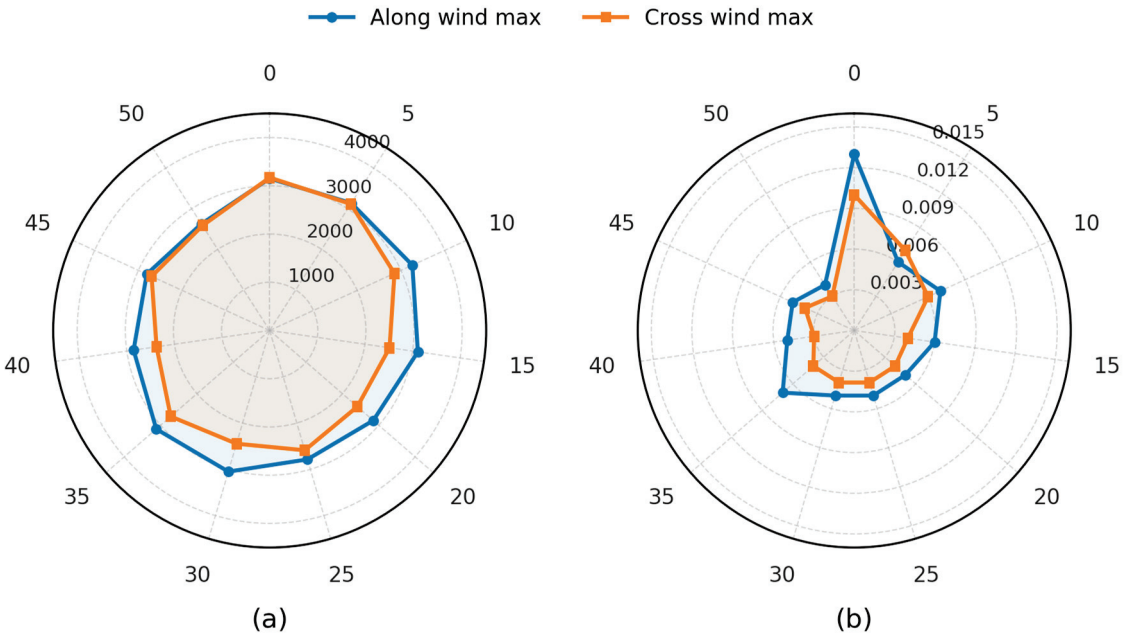

Figure 7. Maximum response for all wind loading directions of the original design: (**a**) Maximum base shear; (**b**) Maximum roof drift.

Figure 8 illustrates the global response difference between the two designs. The along wind governs the original design, which exhibits high nonlinear behavior with wide hysteretic loops, indicating significant cyclic energy dissipation. Conversely, the modified design collapses into tight, near-linear loops, storing and releasing energy elastically with minimal hysteretic damping, with a slight governing of the cross wind. In addition to that, the original design undergoes pronounced stiffness degradation and pinching behavior, which indicates cumulative concrete cracking and rebar slip as well as great damage in coupling beams. As for the modified design, the reinforcement of boundary elements succeeded in maintaining a uniform global stiffness throughout all cycles with very small degradation.

For drift demands, the modified design drastically improves serviceability by reducing peak roof drift by over 60% for along wind (from 0.013 to 0.005), which is the acceptance criteria for roof drift ratio (H/200) according to the ASCE prestandard [15]. Furthermore, while the original design accumulates substantial permanent residual drift, the modified

https://doi.org/10.3390/infrastructures11070236

design consistently passes through the origin or near it, achieving the acceptance criteria of H/1000 = 0.001 × H.

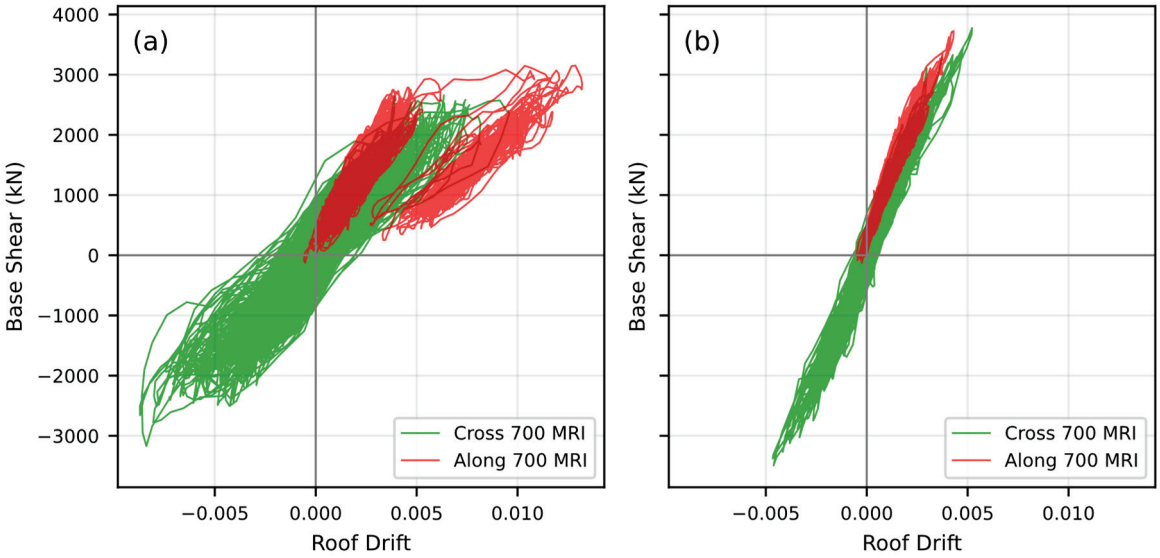

Figure 8. Base shear vs. roof drift hysteretic response: (**a**) Original design; (**b**) Modified design.

Due to enhanced stiffness, the modified design attracts a higher peak base shear of about 3700 kN versus approximately 3100 kN in the original design. However, the enhanced reinforcement of boundary elements and thickened piers successfully withstand this additional demand.

Table 10 tracks the sequencing of local limit states at the base of the wall piers against roof drift. Concrete cracking occurs at a slightly lower drift in the modified design compared to the original design as an effect of increased structural stiffness, which attracts higher flexural stresses at smaller global displacements. As for reinforcement yielding, in the original design it occurs at drifts of 0.0088 (along wind) and 0.0095 (cross wind), with concrete compression reaching its peak strength at 0.0125. This confirms that the wide hysteretic loops in the original configuration are driven by extensive cracking and severe material degradation at the pier base. Crucially, neither steel yielding nor concrete crushing is reached in the modified design, successfully confining the damage to initial micro-cracking and halting damage progression.

Table 10. Local limit states at the base of the wall piers.

State	Roof Drift			
	Original Design		Modified Design	
	Along	Cross	Along	Cross
first concrete cracking of the outer fibers in the walls	0.00125	0.0013	0.0011	0.0011
first yield of reinforcement	0.0088	0.0095	not reached	not reached
concrete reaching f_c'	0.0125	not reached	not reached	not reached

The coupling beam rotation across floors (Figure 9) reveals a significant reduction and redistribution of deformation demands due to the structural modifications. The original design experiences severe rotation demands in the upper floors, while the modified design reduces these peak demands to lower than 0.004 rad, significantly lowering plastic

https://doi.org/10.3390/infrastructures11070236

deformation. The localized deformation at Floor 2 is completely removed in the modified structure, and both along- and cross-wind rotations are tightly controlled below 0.0015 rad throughout the lower half of the building (Floors 1–11). While along-wind demands govern the upper floors of the original structure, the increased stiffness of the modified system shifts the governing demand to cross wind.

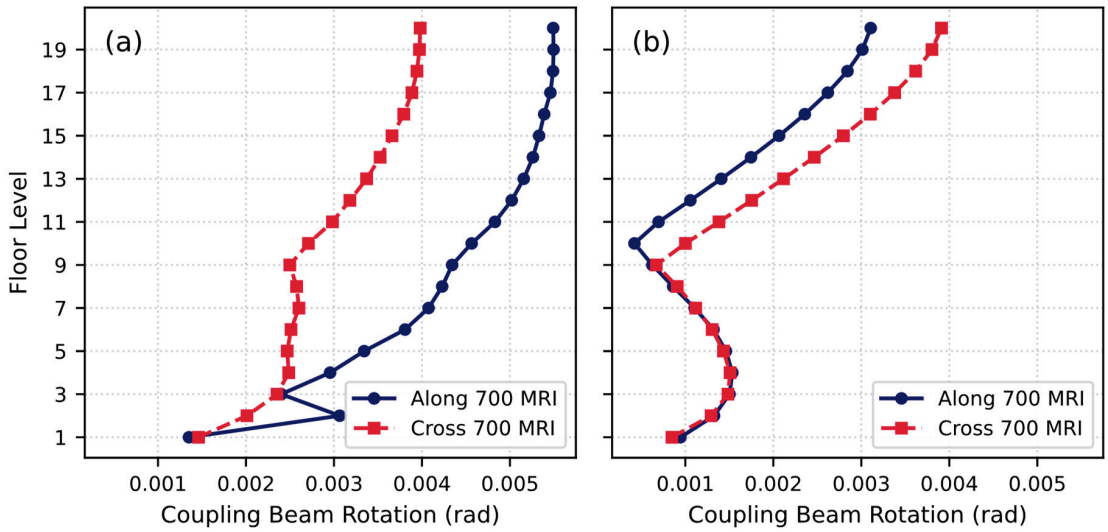

Figure 9. Coupling beam rotation across floors: (**a**) Original design; (**b**) Modified design.

To better understand the impact of the structural modifications, the shear force versus chord rotation response for the coupling beams at the maximum chord rotations are plotted in Figure 10. The original design highlights severe inelastic vulnerability, whereas the modified curves demonstrate an enhanced, high-stiffness response. For along wind, the original design experiences evident ratcheting progressing into the positive rotation region due to the strong mean wind component, and accumulating an unrecoverable residual rotation of about 0.0035 rad, indicating localized concrete crushing. As for the modified design, limited peak rotations of about 0.003 rad is reported, and a linear, steep response profile can be observed. It can be concluded that the thickened wall piers effectively suppressed global geometric drift, forcing the modified coupling beams to remain within a stable, near-elastic recovery mechanism.

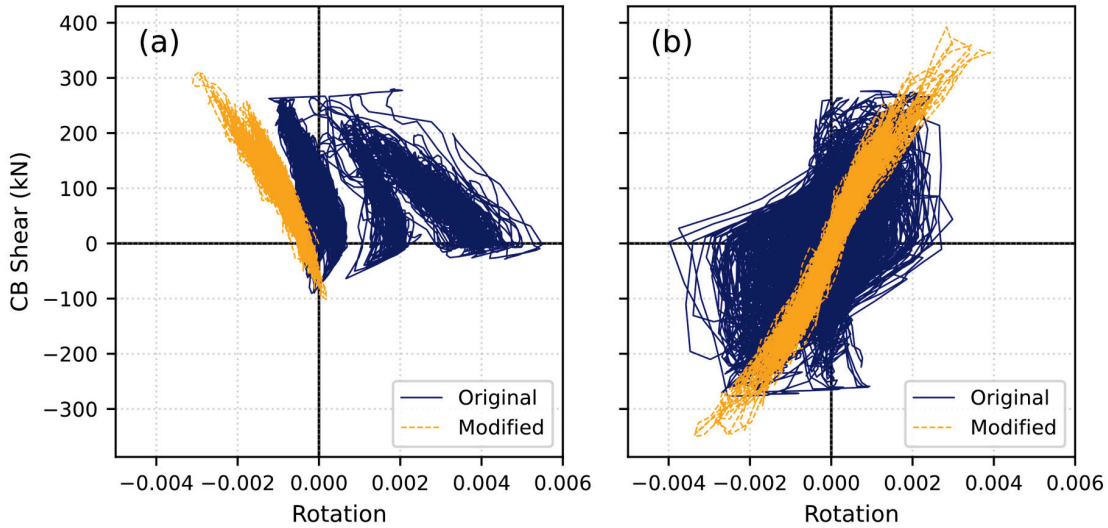

Figure 10. Coupling beam response at the critical maximum rotation: (**a**) Along; (**b**) Cross.

https://doi.org/10.3390/infrastructures11070236

Under cross wind, the original design undergoes extensive cyclic damage, severe concrete degradation, and diagonal shear cracking, as well as shear aggregate interlock, causing wide and highly pinched hysteretic loops with a flat zero-shear plateau. On the other hand, the modified design completely eliminates this pinching behavior, turning the response into tight, linear-elastic loops.

The results suggest that for this 20-story configuration, targeted strengthening of critical cyclic-demand regions such as coupling beams may represent a more material-efficient strategy than uniform global increases in wall dimensions, although additional case studies are required to confirm this observation.

To evaluate progressive structural damage and lateral stability under the 700-year MRI wind event, the global secant stiffness was tracked against the roof drift ratio (Δ) (Figure 11).

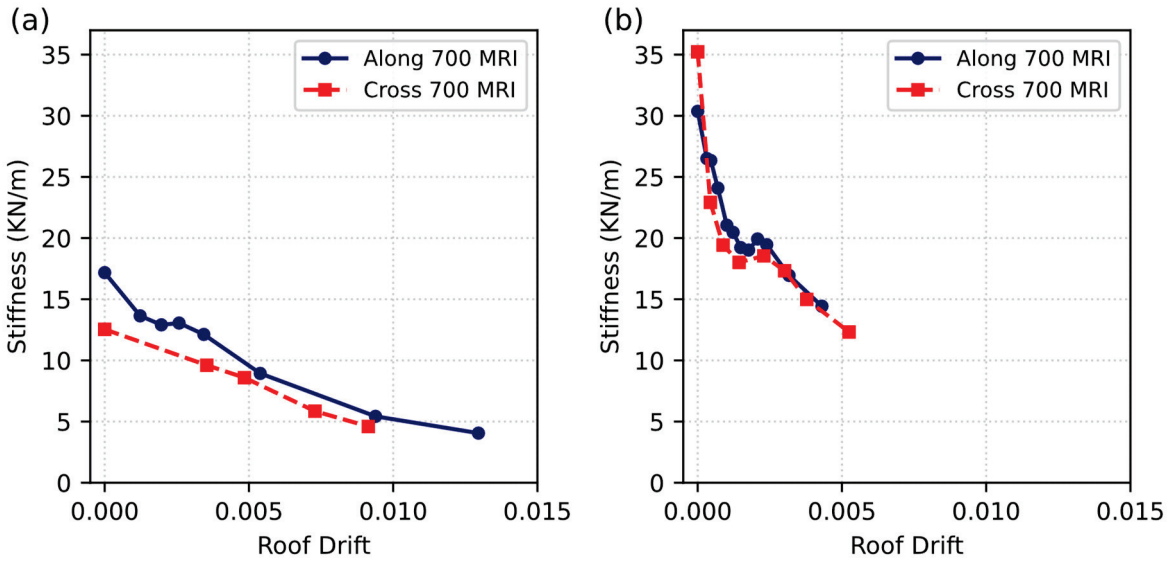

Figure 11. Secant stiffness degradation corresponding to roof drift: (**a**) Original design; (**b**) Modified design.

The structural modifications significantly increased the initial elastic stiffness of the system, as the initial stiffness of the original design went from 17.2 kN/mm (along-wind) and 12.5 kN/mm (cross-wind), to 30.5 kN/mm (along-wind) and 35.2 kN/mm (cross-wind) for the modified design. These represent 77.3% and 181.6% increases in initial stiffness, respectively. The reversal of the governing direction—where cross-wind stiffness exceeds along-wind stiffness in the modified structure—is due to the shortened fundamental period of the stiffer system (2.87 s for the original versus 2.47 s for the modified design, according to OpenSees analysis). This period shift alters the building's dynamic sensitivity, mobilizing higher stiffness to resist resonant vortex-shedding frequencies.

The progression of stiffness loss reveals fundamentally distinct mechanical behaviors between the two configurations: the original design suffers systemic degradation. As can be seen from following the concrete cracking at (Δ = 0.0013), the original structure exhibits severe continuous stiffness decay. Driven by boundary element reinforcement yielding (0.0088, 0.0095) and concrete crushing (Δ = 0.0125), the stiffness drops to a residual value of 4.0 kN/mm. This unmitigated degradation indicates a severe loss of coupling action and extensive plastic damage at the base of the pier walls.

As for the modified design, the stiffness stabilizes across the wind event, exhibiting an initial stiffness reduction up to a roof drift of 0.0015, corresponding to controlled outer-fiber

https://doi.org/10.3390/infrastructures11070236

concrete micro-cracking (Δ = 0.0011). However, the degradation curve stabilizes into a distinct stiffness plateau between Δ = 0.0015 and 0.0035, maintaining a stiffness of approximately 20 kN/mm before settling at a final residual value (between 11 and 14 kN/mm).

Ultimately, the modified design limits total stiffness loss, by preventing reinforcement yielding and concrete crushing, where the enhanced boundary elements and deeper coupling beams successfully constrained damage propagation.

3.2.2. Operational

Figure 12 compares the global hysteretic responses of the original and modified coupled wall systems under a 10-year MRI wind hazard. Both configurations satisfy the operational target drift limit of H/400 = 0.0025 × H, confirming elastic performance with negligible energy dissipation. In both designs, the along-wind response remains highly constrained, reaching maximum roof drifts of 0.0015. The cross-wind demands clearly dominate the lateral response due to dynamic excitation; however, the proposed structural modifications—increased wall thickness, deeper coupling beams, and enhanced boundary element reinforcement—significantly stiffen the system. This refinement successfully increases the serviceability safety margin against non-structural damage, and limits the peak cross-wind roof drift to approximately 0.0012 (a 40% reduction).

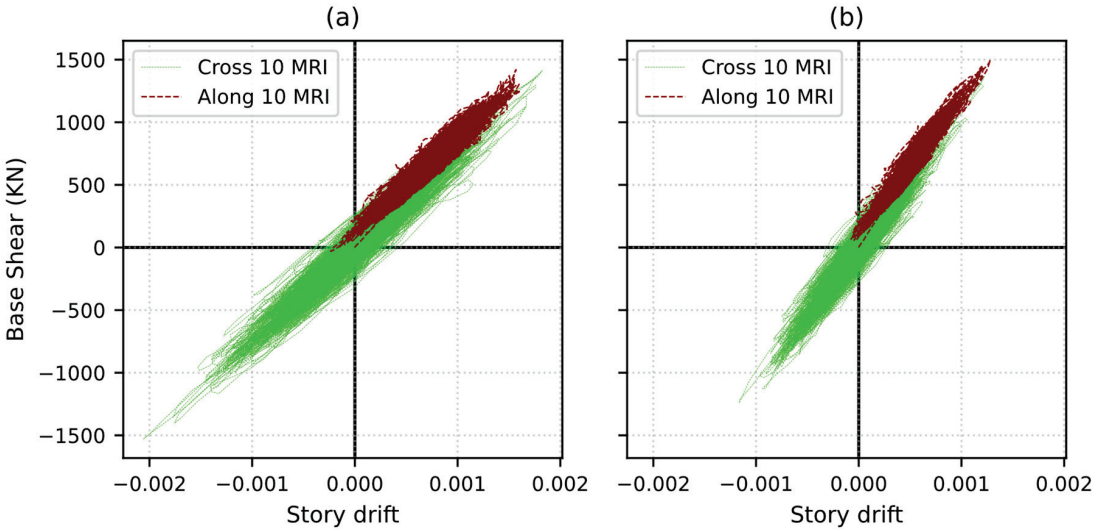

Figure 12. Global response for the Operational performance objective: (**a**) Original design; (**b**) Modified design.

To evaluate localized structural and non-structural vulnerability accurately, the Deformation Damage Index (DDI) was calculated for the panel zones (the zone enclosed by the wall piers and coupling beams) (Figure 13a). According to the ASCE prestandard [36], in high buildings the actual "racking" deformation experienced by infill panels and cladding due to significant dominance of axial deformations and global flexural rotation in vertical elements can be misrepresented by the traditional story drift ratios. Therefore, in order to isolate the actual in-plane shear strain responsible for structural damage, the DDI is computed based on the relative displacements of four nodal points, as expressed in Equation (6).

$$DDI = 0.5\left[\frac{X_A - X_C}{H_p} + \frac{X_B - X_D}{H_p} + \frac{Y_D - Y_C}{L_p} + \frac{Y_B - Y_A}{L_p}\right] \quad (6)$$

https://doi.org/10.3390/infrastructures11070236

where H_p and L_p represent the height and length of the panel element, respectively. By utilizing this damage index, the local performance assessment reveals a critical vulnerability in the original design. While global response showed acceptable roof drift for the original design, the local DDI captures severe localized shear strain concentrations exceeding the 0.0025 DDI limit between stories 4 and 14. Conversely, the increased stiffness and enhanced coupling efficiency of the modified system effectively suppress these localized shear strains, ensuring the entire height of the structure remains well within the allowable 0.0025 DDI limit. For practicing engineers, this confirms that relying on global building drift limits alone is insufficient; local indices like the DDI must be explicitly evaluated to safely protect non-structural facades and interior partitions from localized racking.

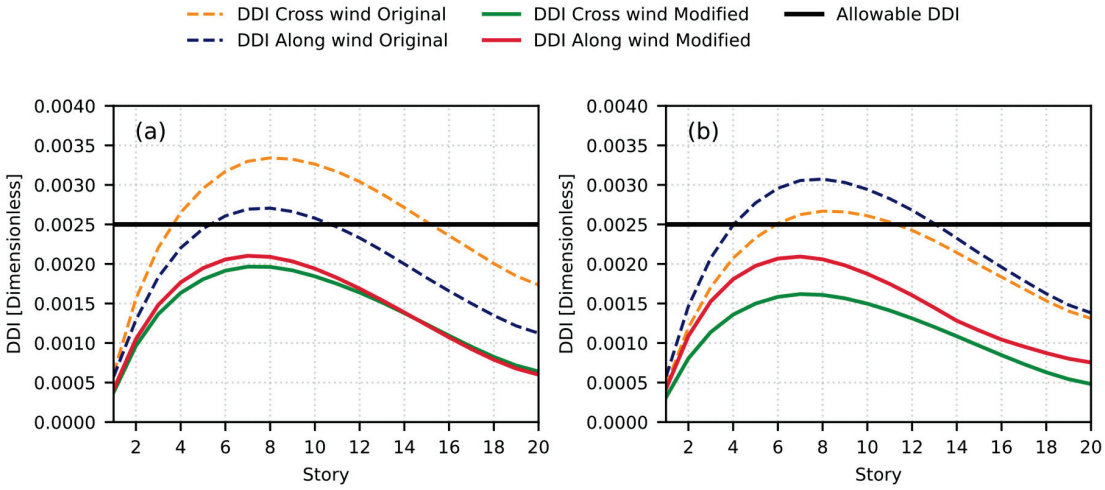

Figure 13. Deformation Damage Index (DDI) across floor levels for: (**a**) angle 0°, (**b**) angle 45°.

To verify localized performance under oblique wind conditions, a supplementary evaluation was conducted under a 45° wind direction (Figure 13b). The peak DDI values obtained under the 45° angle are lower in magnitude compared to the governing 0° direction. However, they exhibit similar performance characteristics; the original design results in a peak DDI of 0.0031, which exceeds the allowable damage threshold of 0.0025. In contrast, the modified design effectively controls the localized racking deformations under frequent wind events, reducing the peak DDI to 0.0021. This demonstrates that the proposed structural refinement provides consistent protection against localized non-structural damage across both 0° and 45° wind load cases.

3.2.3. Occupant Comfort

The motion comfort during more frequent but smaller wind intensities is of great importance in the design of wind-sensitive buildings; therefore, the motion comfort performance of the coupled wall in this study (both original and modified designs) is evaluated using the approach of perception ranges (Table 11) used in practice, as provided by Chang [36] using 10-year MRI wind speed. For the original design, the peak acceleration calculated according to Johann et al. [37] was equal to 21.1 mg and 25 mg for along and cross wind, respectively, corresponding to the annoying range of the comfort scale. For the modified design, peak accelerations reached 16 mg and 20.4 mg for along and cross wind, respectively, still in the annoying range but sitting nearly at the lower boundary of the threshold, which represents a marked improvement in serviceability performance of occupant comfort.

A similar behavioral trend was observed for motion comfort under the 10-year MRI wind hazard at a 45° angle. Although the absolute acceleration values are lower than those

https://doi.org/10.3390/infrastructures11070236

under the critical 0° wind vector, the original design still fails comfort thresholds in cross wind, with peak floor accelerations reaching 18.5 mg, along with an acceptable value of 12.36 mg for along wind. Implementing the modified structural layout successfully brings these demands down to 14.3 mg and 9.7 mg for along and cross wind, respectively, ensuring that acceptable occupant comfort is maintained across 0° and 45° wind orientations.

Table 11. Occupant comfort assessment based on peak floor acceleration criteria [36].

Peak Floor Acceleration (mg)	Comfort Limit
<5	Not perceptible
5–15	Threshold of perceptibility
15–50	Annoying
50–150	Very annoying
>150	Intolerable

4. Conclusions

This paper presents a performance-based wind evaluation of a 20-story RC coupled wall system, both an original code-compliant design and a modified configuration with increased wall thickness, deeper coupling beams, and enhanced boundary reinforcement. The following conclusions are drawn:

1. The original design satisfies the current linear code design methodologies in terms of serviceability and strength limits under wind loads.
2. Based on the response assessment, the 0° direction was found to govern both along- and cross-wind loads; it was therefore chosen as the focus of this study.
3. Under a 700-year MRI wind hazard, the original design exhibits severe degradation, with roof drifts up to 0.013. The modified design reduces peak roof drift by 60% (to 0.005) with only a 4.33% increase in concrete volume, meeting continuous occupancy criteria.
4. The original design experiences base pier yielding and concrete crushing under along-wind demands, while the modified design eliminates both, preserving sectional integrity.
5. Original coupling beams undergo severe plastic deformation and stiffness loss, while deeper beams in the modified design show stable hysteretic behavior, minimal damage, and preserved coupling action.
6. Stiffening the system shifts dominance to cross-wind response at upper floors due to resonant vortex shedding.
7. Global secant stiffness drops 76.7% in the original design, while the modified design maintains stable stiffness, indicating controlled micro-cracking.
8. Under a 10-year MRI wind hazard, both designs meet global drift limits, but localized evaluation (DDI) reveals severe vulnerabilities in the original (DDI = 0.0033 > 0.0025). The modified design reduces peak DDI to 0.0020, ensuring serviceability.
9. For occupant comfort under frequent winds, the modified design remains within the "annoying" threshold but near its lower bound, substantially improving serviceability.

This study supports the previous findings that while standard code compliance provides a baseline for design, it may not fully capture localized high-rise vulnerabilities under severe wind hazards. The performance-based approach—specifically, pairing minor increases in wall thickness with deeper coupling beams for this specific configuration of a single isolated building with a square plan, an aspect ratio of $H/D = 3$, and specific material properties—efficiently controls both global and local demands. This component-

https://doi.org/10.3390/infrastructures11070236

level refinement successfully prevents base pier yielding, suppresses localized shear strains (DDI), and limits floor drifts. These findings suggest that within the scope of this case study, targeted cross-sectional adjustments offer a reliable, material-efficient path to maintaining structural integrity and serviceability without massive structural over-sizing.

Future work should assess the effectiveness of these strategies in taller buildings—where higher-mode effects and aerodynamic damping prevail—and clarify the trade-off between enhanced coupling and cross-wind response. Consequently, the performance trends observed here should not be directly extended to different structural systems or aerodynamic configurations without re-examining the underlying variables, such as cross-wind vortex shedding frequencies and localized pressure distributions inherent to those alternative designs.

Author Contributions: Conceptualization, S.B., B.H. and F.I.; methodology, B.H., G.W. and F.A.M.; software, S.B.; validation, B.H. and F.I.; formal analysis, G.W. and F.A.M.; investigation, S.B.; resources, S.B.; data curation, S.B. and F.I.; writing—original draft preparation, S.B. and G.W.; writing—review and editing, B.H. and F.A.M.; visualization, G.W.; supervision, B.H. and F.I. All authors have read and agreed to the published version of the manuscript.

Funding: This research received no external funding.

Data Availability Statement: Data are available upon reasonable request from the corresponding author.

Conflicts of Interest: The authors declare no conflicts of interest.

Abbreviations

The following abbreviations are used in this manuscript:

A_w	Area of the wall pier web section
DAD	Database-Assisted Design
DDI	Deformation Damage Index
E	Concrete Young's modulus of elasticity
E_t	Tension softening stiffness
FU, V_u	Ultimate shear force
FY, V_y	Nominal shear capacity
f'_c	Concrete compressive strength
G	Shear modulus
H	Building height
h	Coupling beam depth
h_s	Story height
Ig	Gross sectional moment of inertia
l_n, L	Clear span of coupling beam
M_{node}	Mass corresponding to wall pier
MRI	Mean Recurrence Interval
PBD	Performance-Based Design
PBWD	Performance-Based Wind Design
$P_{1/2\ floor}$	Gravity load corresponding to one-half of the floor
P_{pier}	Gravity load corresponding to wall pier
RC	Reinforced Concrete
T	Return period in years
TPU	Tokyo Polytechnic University
$(V_{hr})_{building}$	Mean hourly wind speed at the building site and roof level
V_T	Wind speed of different MRIs
Δ	Roof drift ratio

https://doi.org/10.3390/infrastructures11070236

References

1. Duthinh, D. Blown Away: Citicorp Center Tower Repairs Revisited. *Eng. J.* **2019**. [PubMed]
2. Poon, D.C.K.; Shieh, S.; Joseph, L.M.; Chang, C.-C. Structural Design of Taipei 101, the World's Tallest Building. In Proceedings of the CTBUH 2004 Seoul Conference, Seoul, Republic of Korea, 10–13 October 2004.
3. Metwally, O.; Ibrahim, H.A.; Elawady, A.; Zisis, I.; Chowdhury, A.G. Wind Load Impact on Tall Building Facades: Damage Observations during Severe Wind Events and Wind Tunnel Testing. *Front. Built Environ.* **2025**, *10*, 1514523. [CrossRef]
4. Bezabeh, M.A.; Bitsuamlak, G.T.; Tesfamariam, S. Performance-Based Wind Design of Tall Buildings: Concepts, Frameworks, and Opportunities. *Wind Struct.* **2020**, *31*, 103–142.
5. Preetha Hareendran, S.; Alipour, A.; Shafei, B.; Sarkar, P. Performance-Based Wind Design of Tall Buildings Considering the Nonlinearity in Building Response. *J. Struct. Eng.* **2022**, *148*, 04022119. [CrossRef]
6. Kang, T.H.-K. Draft ISO Standard for Simplified Performance-Based Wind Design of Tall Concrete Buildings. *Adv. Wind Eng.* **2026**, *3*, 100121. [CrossRef]
7. Jain, A.; Srinivasan, M.; Hart, G.C. Performance Based Design Extreme Wind Loads on a Tall Building. *Struct. Des. Tall Build.* **2001**, *10*, 9–26. [CrossRef]
8. Iancovici, M.; Ionică, G.; Pavel, F.; Moța, F.; Nica, G.B. Nonlinear Dynamic Response Analysis of Buildings for Wind Loads. A New Frontier in the Structural Wind Engineering. *J. Build. Eng.* **2022**, *47*, 103708. [CrossRef]
9. Abdelwahab, M.; Ghazal, T.; Nadeem, K.; Aboshosha, H.; Elshaer, A. Performance-Based Wind Design for Tall Buildings: Review and Comparative Study. *J. Build. Eng.* **2023**, *68*, 106103. [CrossRef]
10. Saini, D.; Dokhaei, B.; Shafei, B.; Alipour, A. Performance Evaluation of High-Rise Buildings Using Database-Assisted Design Approach. *Struct. Saf.* **2024**, *109*, 102447. [CrossRef]
11. Athanasiou, A.; Tirca, L.; Stathopoulos, T. Performance-Based Wind and Earthquake Design Framework for Tall Steel Buildings with Ductile Detailing. *J. Wind Eng. Ind. Aerodyn.* **2023**, *240*, 105492. [CrossRef]
12. Alanani, M.; Elshaer, A. Performance-Based Layout Optimization Framework of Tall Buildings Subjected to Dynamic Wind Load. *Eng. Struct.* **2025**, *336*, 120333. [CrossRef]
13. Gora, A.; Huang, M.; Wang, C.; Zhang, R. Wind-Induced Dynamic Performance Evaluation of Tall Buildings Considering Future Wind Climate. *Appl. Sci.* **2025**, *15*, 5073. [CrossRef]
14. McKenna, F.; Fenves, G.L.; Scott, M.H. *Open System for Earthquake Engineering Simulation (OpenSees)*; University of California: Berkeley, CA, USA, 2000.
15. American Society of Civil Engineers; Scott, D. *Prestandard for Performance-Based Wind Design*; American Society of Civil Engineers: Reston, VA, USA, 2019.
16. TPU (Tokyo Polytechnic University). *Wind Pressure Database for High-Rise Building*; TPU: Tokyo, Japan, 2008.
17. Engineering Syndicate. *The Syrian Code for Concrete Structures*; Engineering Syndicate: Damascus, Syria, 2012.
18. International Conference of Building Officials. *Uniform Building Code, 1997*; 1997 Uniform Building Code; International Conference of Building Officials: Washington, DC, USA, 1997; ISBN 9781884590924.
19. American Society of Civil Engineers (ASCE). *Minimum Design Loads and Associated Criteria for Buildings and Other Structures*; American Society of Civil Engineers ASCE: Reston, VA, USA, 2017; ISBN 9780784414248.
20. Kolozvari, K.; Terzic, V.; Miller, R.; Saldana, D. Assessment of Dynamic Behavior and Seismic Performance of a High-Rise Rc Coupled Wall Building. *Eng. Struct.* **2018**, *176*, 606–620. [CrossRef]
21. Tauberg, N.A. Collapse Assessment of Reinforced Concrete Coupled Walls. Ph.D. Thesis, University of California, Los Angeles, CA, USA, 2019.
22. Orakcal, K.; Massone Sanchez, L.M.; Wallace, J.W.; Pacific Earthquake Engineering Research Center. *Analytical Modeling of Reinforced Concrete Walls for Predicting Flexural and Coupled—Shear-Flexural Responses*; PEER Report; Pacific Earthquake Engineering Research Center, College of Engineering, University of California: Berkeley, CA, USA, 2006.
23. Mohd Yassin, M.H. *Nonlinear Analysis of Prestressed Concrete Structures Under Monotonic and Cyclic Loads*; University of California: Berkeley, CA, USA, 1994.
24. Hognestad, E. *A Study of Combined Bending and Axial Load in Reinforced Concrete Members*; Bulletin (University of Illinois (Urbana-Champaign Campus). Engineering Experiment Station)); University of Illinois: Champaign, IL, USA, 1951.
25. Saatcioglu, M.; Razvi, S.R. Strength and Ductility of Confined Concrete. *J. Struct. Eng.* **1992**, *118*, 1590–1607. [CrossRef]
26. ACI Committee 318. *Building Code Requirements for Structural Concrete and Commentary (ACI 318-19)*; American Concrete Institute: Farmington Hills, MI, USA, 2019; ISBN 9781641950565.
27. Kolozvari, K.; Tran, T.A.; Orakcal, K.; Wallace, J.W. Modeling of Cyclic Shear-Flexure Interaction in Reinforced Concrete Structural Walls. II: Experimental Validation. *J. Struct. Eng.* **2015**, *141*, 04014136. [CrossRef]

https://doi.org/10.3390/infrastructures11070236

28. Los Angeles Tall Buildings Structural Design Council; Council on Tall Buildings and Urban Habitat. *An Alternative Procedure for Seismic Analysis and Design of Tall Buildings Located in the Los Angeles Region: A Consensus Document*; Los Angeles Tall Buildings Structural Design Council: Los Angeles, CA, USA; Council on Tall Buildings and Urban Habitat: Chicago, IL, USA, 2017.
29. Charney, F.A. Unintended Consequences of Modeling Damping in Structures. *J. Struct. Eng.* **2008**, *134*, 581–592. [CrossRef]
30. Teshigawara, M.; Sugaya, K.; Kato, M.; Nishiyama, I. Experimental Study on Overall Seismic Behavior of 12-Story Coupled Shear Wall: The U.S.-Japan Cooperative Earthquake Research Program on Composite and Hybrid Structures (HWS). *J. Struct. Constr. Eng.* **1997**, *62*, 149–156. [CrossRef] [PubMed]
31. Mohammadi, A. Wind Performance Based Design for High-Rise Buildings. Ph.D. Thesis, Florida International University, Miami, FL, USA, 2016.
32. Ghaffary, A.; Moustafa, M.A. Performance-Based Assessment and Structural Response of 20-Story SAC Building under Wind Hazards through Collapse. *J. Struct. Eng.* **2020**, *147*, 04020346. [CrossRef]
33. Peterka, J.A.; Shahid, S. Design Gust Wind Speeds in the United States. *J. Struct. Eng.* **1998**, *124*, 207–214. [CrossRef]
34. Isyumov, N.; Case, P.C. Wind-Induced Torsional Loads and Responses of Buildings. In *Proceedings of the Advanced Technology in Structural Engineering*; American Society of Civil Engineers: Reston, VA, USA, 2000; pp. 1–8.
35. Cui, W.; Caracoglia, L. Examination of Experimental Variability in HFFB Testing of a Tall Building under Multi-Directional Winds. *J. Wind Eng. Ind. Aerodyn.* **2017**, *171*, 34–49. [CrossRef]
36. Chang, F.K. Human Response to Motions in Tall Buildings. *J. Struct. Div.* **1973**, *99*, 1259–1272, Erratum in *J. Struct. Div.* **1974**, *100*, 1150–1150. [CrossRef]
37. Johann, F.A.; Carlos, M.E.N.; Ricardo, F.L.S. Wind-Induced Motion on Tall Buildings: A Comfort Criteria Overview. *J. Wind Eng. Ind. Aerodyn.* **2015**, *142*, 26–42. [CrossRef]

Disclaimer/Publisher's Note: The statements, opinions and data contained in all publications are solely those of the individual author(s) and contributor(s) and not of MDPI and/or the editor(s). MDPI and/or the editor(s) disclaim responsibility for any injury to people or property resulting from any ideas, methods, instructions or products referred to in the content.

 https://doi.org/10.3390/infrastructures11070236

infrastructures

MDPI

Article

Advancing Near-Field Tsunami Fragility Modeling Through Structural Simulation and Post-Event Damage Observations

Mojtaba Harati [1,2,*] and John W. van de Lindt [1]

[1] Department of Civil and Environmental Engineering, Colorado State University, Fort Collins, CO 80523, USA; jwv@engr.colostate.edu
[2] Verisk Catastrophe and Risk Solutions, Boston, MA 02111, USA
* Correspondence: m.harati@colostate.edu

Abstract

Tsunami fragility modeling plays a central role in probabilistic coastal risk assessment; however, representing structural vulnerability under near-field tsunami conditions remains challenging due to complex hydrodynamic loading, strong spatial variability, and the presence of pre-existing earthquake damage. This paper advances near-field tsunami fragility modeling through three specific contributions, each bridging simulation-based methods and empirical damage survey observations. First, it demonstrates how a successive earthquake–tsunami simulation framework can generate conditional fragility surfaces that explicitly account for pre-existing seismic damage without relying on statistically intractable probabilistic decompositions. Second, it develops and validates a distance-dependent intensity-shifting approach—derived from analysis of the 2011 Great East Japan tsunami survey dataset—that adapts baseline fragility curves to near-field and near-coast conditions in a physically interpretable and practically deployable manner. Third, it establishes an explicit cross-validation pathway between simulation-derived fragility surfaces and empirical damage observations through machine-learning-assisted feature importance analysis, a connection largely absent from prior literature. Together, these contributions provide a physically consistent and data-informed foundation for near-field tsunami fragility modeling that is directly applicable—as a methodological framework—to loss and resilience estimation platforms such as IN-CORE and HAZUS and to risk-informed coastal infrastructure design in subduction-zone regions, subject to typology-specific calibration; the simulation results are demonstrated for a US Reinforced Concrete (RC) moment-frame archetype and the empirical results for Japanese wood-frame construction, so direct quantitative application to other structural typologies requires recalibration of the respective model components.

Keywords: near-field tsunami; fragility modeling; multi-hazard simulation; momentum flux; damage survey data

1. Introduction

Tsunamis are among the most devastating coastal hazards and have repeatedly demonstrated their impacts in causing catastrophic losses to coastal communities and infrastructure. Historical events such as the 2004 Indian Ocean tsunami and the 2011 Great East Japan tsunami revealed the enormous destructive potential of tsunami inundation and emphasized the need for systematic approaches to tsunami risk assessment and mitigation. Over

the past two decades, the scientific community has made significant progress in developing quantitative frameworks for evaluating tsunami hazards and their potential impacts on the built environment [1–4]. In particular, probabilistic approaches to tsunami hazard and risk assessment have gained increasing attention as they allow for the explicit treatment of uncertainties associated with tsunami generation, propagation, and impact processes [5,6]. These developments are consistent with broader advances in probabilistic risk assessment methods that have long been applied in seismic hazard analysis and performance-based earthquake engineering [7–9]. More recently, probabilistic tsunami hazard and risk analysis frameworks have been widely adopted to support coastal disaster risk management and resilience planning initiatives [10,11].

Tsunami risk assessment generally involves the integration of several interrelated components, including hazard characterization, exposure modeling, and vulnerability modeling. Within probabilistic tsunami hazard and risk frameworks, tsunami hazard is commonly described using intensity measures such as flow depth, flow velocity, run-up height, and momentum flux [12,13]. These intensity measures are typically obtained through numerical simulations that model tsunami generation, propagation across ocean basins, and subsequent inundation of coastal areas [6,11]. Compared with other natural hazards such as earthquakes, tsunami hazard assessment relies heavily on numerical simulations due to the limited availability of observational data and the strong influence of coastal bathymetry and topography on wave transformation and inundation patterns [5,10]. As emphasized in recent studies, modern tsunami hazard assessment workflows often involve simulation-based probabilistic frameworks that propagate uncertainties from the initial tsunami source characterization through hydrodynamic modeling and ultimately to impact estimation [11,14,15].

A critical component of tsunami risk assessment is vulnerability modeling, which establishes the relationship between tsunami hazard intensity measures and the expected consequences for exposed assets. In probabilistic tsunami risk frameworks, vulnerability is commonly represented through fragility relationships that quantify the probability of exceeding specified structural damage states as a function of tsunami intensity measures [16,17]. Fragility functions provide an essential link between the physical characteristics of tsunami waves and the resulting damage to buildings and infrastructure, allowing hazard information to be translated into estimates of structural damage, economic loss, or casualties [6,11]. In addition, vulnerability assessment is closely connected to broader concepts of risk governance and disaster risk reduction, as fragility models are frequently used to predict potential damage and thus inform land-use planning, building code development, evacuation planning, and other risk mitigation strategies for coastal communities [18,19].

Several methodological approaches have been proposed for developing tsunami fragility relationships. Empirical approaches derive fragility functions directly from post-event damage observations collected during field surveys following major tsunami events [20,21]. Analytical approaches, in contrast, use structural analysis and hydrodynamic loading models to estimate structural response under tsunami forces [1,22]. Indicator-based approaches take a broader perspective by evaluating vulnerability through composite indicators that capture multiple dimensions of risk, including physical, economic, and social vulnerability [23]. Previous research has shown that tsunami damage is strongly influenced by hydrodynamic parameters such as flow depth, velocity, and momentum flux, highlighting the importance of accurately characterizing tsunami intensity measures when developing fragility models [6,10,24]. In practice, the choice of vulnerability modeling

 https://doi.org/10.3390/infrastructures11070221

approach often depends on the availability of damage data, structural information, and computational resources available for the analysis [11].

Despite the considerable progress achieved in tsunami vulnerability assessment, several critical research gaps persist, particularly for near-field tsunami scenarios. First, most existing fragility relationships have been developed under the implicit assumption that earthquake and tsunami hazards act independently, yet near-field events produce rapid sequential loading in which pre-existing earthquake damage substantially reduces structural capacity before inundation begins. Conventional empirical approaches cannot isolate this coupled effect because post-event surveys inherently reflect combined damage, while simplified probabilistic formulations based on Bayes-type decompositions are not physically estimable for earthquake–tsunami sequences [25]. Second, the vast majority of fragility models treat structural vulnerability as spatially uniform, neglecting the systematic attenuation of tsunami intensity with increasing inland distance and the amplified impulsive forces experienced in the immediate coastal zone. This spatial non-stationarity has direct consequences for engineering practice: design provisions and loss estimation tools calibrated on spatially averaged fragility data may significantly misrepresent risk in near-coast zones, where hydrodynamic loading is most severe. Recent work on tsunami-induced forces on coastal structures and protection infrastructure further highlights that momentum flux, bathymetric geometry, and urban arrangement produce highly variable loading conditions that single-parameter fragility curves cannot adequately capture [26,27]. Third, the vulnerability of a wide range of coastal infrastructure types—including bridges, which are critical lifeline components—remains poorly characterized under extreme hydrodynamic and hydraulic loading; hydraulic failures of such infrastructure have been shown to account for a substantial fraction of disaster-induced losses [28–30]. Finally, there is no established framework for translating simulation-derived fragility surfaces into practically usable tools that can be calibrated against empirical survey data and adapted across different coastal site conditions. These gaps collectively limit the ability of engineers and planners to develop reliable, site-specific fragility models for near-field tsunami risk and resilience assessments [24,31]. Analytical fragility models, on the other hand, require detailed structural modeling and accurate representation of complex tsunami loading mechanisms, which may introduce additional uncertainties if structural properties or loading conditions are poorly constrained [32]. Furthermore, the stochastic nature of tsunami hazards and the complex interactions between tsunami waves and coastal infrastructure make it difficult to capture the full range of possible damage scenarios using a single modeling approach [5,6]. These challenges have motivated increasing interest in hybrid approaches that combine physics-based simulations with empirical damage observations in order to improve fragility model calibration and reduce epistemic uncertainty in tsunami vulnerability assessments [11,33–37].

Motivated by these gaps, this paper advances near-field tsunami fragility modeling through three specific contributions, structured around two complementary pillars: physics-based successive simulation and empirical post-event damage survey analysis. First, it provides a structured evaluation of how coupled earthquake–tsunami simulation frameworks can generate conditional fragility surfaces without relying on statistically intractable probabilistic decompositions, thus offering a physically consistent pathway for near-field risk assessment. Second, it demonstrates, through analysis of the 2011 Great East Japan tsunami survey dataset, that fragility behavior is inherently spatially non-stationary and proposes a distance-dependent intensity-shifting approach to adapt baseline fragility curves to near-field and near-coast conditions—a practically interpretable strategy that does not require complete model redevelopment. Third, it explicitly connects simulation-derived

 https://doi.org/10.3390/infrastructures11070221

fragility surfaces with empirical damage observations and machine-learning-assisted feature importance analysis, providing a cross-validation pathway that has been largely absent from prior literature. From an engineering practice standpoint, the methodological insights developed here are relevant to the design of tsunami-resilient coastal infrastructure, to the calibration of loss estimation platforms such as IN-CORE and HAZUS, and to the development of risk-informed land-use planning and building code provisions in subduction-zone regions. Particular emphasis is placed on near-field tsunami environments, where waves generated by nearby seismic sources may reach coastlines within minutes, leaving no time for evacuation and creating the most severe hydrodynamic and structural demands on the built environment.

2. Near-Field and Far-Field Tsunami Characteristics

Tsunamis are commonly classified into near-field and far-field events depending on the distance between the tsunami source and the impacted coastline and the corresponding travel time of the tsunami waves [38,39]. Near-field tsunamis occur when coastal regions are located close to the source of tsunami generation, typically associated with subduction zone earthquakes or submarine mass failures occurring near the coastline. In these cases, tsunami waves may reach coastal areas within minutes to tens of minutes after the triggering event [40]. In contrast, far-field tsunamis originate from distant sources and travel across ocean basins before reaching remote coastlines, often requiring several hours to arrive [13]. This classification is important because it directly influences warning times, hazard characteristics, and the spatial variability of tsunami inundation processes [5,10]. Near-field tsunami events, such as those observed during the 2011 Great East Japan earthquake, often produce the most severe impacts due to the limited time available for evacuation and the extreme hydrodynamic conditions that can develop near the source region [6,11].

The generation mechanisms and wave propagation characteristics of near-field and far-field tsunamis differ substantially due to variations in the physical processes controlling tsunami initiation and ocean-scale propagation. Most destructive tsunamis are generated by large subduction zone earthquakes that produce vertical displacement of the seafloor, resulting in the displacement of a large volume of water and the formation of long-wavelength tsunami waves [5,41]. However, tsunamis may also be generated by other mechanisms including submarine landslides, volcanic eruptions, and atmospheric disturbances. These different sources lead to distinct wave characteristics and spatial distributions of tsunami intensity [42,43]. In near-field settings, tsunami waves often retain stronger nonlinear characteristics and may exhibit highly variable wave heights and inundation patterns due to complex coastal bathymetry and local topographic effects [44]. In contrast, far-field tsunamis propagate across ocean basins as long waves whose characteristics are strongly influenced by basin geometry and wave dispersion effects before interacting with coastal environments [45,46]. The hydrodynamic characteristics of tsunami inundation play a critical role in determining structural damage and therefore must be carefully considered in fragility modeling. Key tsunami intensity measures commonly used in hazard and vulnerability analyses include flow depth, flow velocity, run-up height, and momentum flux, all of which influence the hydrodynamic forces acting on coastal structures [47]. High flow depths can generate large hydrostatic forces on building components, while high flow velocities contribute to significant hydrodynamic forces that may lead to structural failure or scour [48]. In addition, tsunami flows frequently transport debris such as vehicles, building fragments, and vegetation, which can generate impact forces that significantly amplify structural damage. Observations from major tsunami events have demonstrated

 https://doi.org/10.3390/infrastructures11070221

that debris impact and debris accumulation can play a major role in building damage and infrastructure failure during tsunami inundation [49,50]. As a result, accurate representation of these hydrodynamic parameters is essential for developing realistic fragility relationships for tsunami-induced structural damage.

Fragility relationships aim to quantify the probability that a structure will reach or exceed a specified damage state given a particular hazard intensity measure [51]. However, the variability of tsunami loading conditions can introduce significant uncertainty in fragility estimation. Near-field tsunamis often involve complex hydrodynamic conditions with rapid changes in flow depth and velocity, leading to highly variable damage patterns even within relatively small geographic areas [42,52]. Such variability complicates the development of consistent empirical fragility relationships derived from post-event damage surveys. Consequently, simulation-based approaches that combine hydrodynamic modeling with structural analysis have become increasingly important tools for improving fragility estimation in tsunami risk assessments [53,54].

3. Simulation-Based Tsunami Fragility Modeling for Near-Field Tsunamis

Simulation-based fragility modeling provides a systematic framework for evaluating the probability of structural damage under coupled earthquake–tsunami hazard scenarios [1,55–58]. In the context of near-field tsunami events, this approach becomes particularly important because structures may already experience significant damage from the preceding earthquake before the arrival of the tsunami wave [22,59]. Consequently, the fragility of structures exposed to tsunami loads cannot be assumed to be independent of the earthquake damage state. Traditional approaches may appear, at first glance, to allow estimation of conditional failure probabilities through Bayes-type formulations—*P(TS|EQ) = [P(EQ|TS) P(TS)]/P(EQ)*—that combine earthquake and tsunami fragility curves. However, terms such as $P(EQ \mid TS)$ are not practically estimable, as they imply a conditional dependence that is not physically or statistically observable in realistic earthquake–tsunami sequences. Consequently, rather than pursuing such formulations, conventional methodologies rely on simplified statistical relationships—often linear or empirically calibrated mappings—such as those adopted in FEMA (2019) [60], to approximate multi-hazard interactions in a tractable manner.

To address this difficulty, recent efforts have increasingly turned to direct numerical simulation frameworks in which conditional probabilities $P(TS|EQ)$ are obtained explicitly from large-scale successive vulnerability simulations, rather than through indirect probabilistic inference [1,22,55,59]. Among the most notable advances in this line of research are studies that derive fragility relationships directly from simulated structural responses under combined hazard loading scenarios—an approach that has gained particular traction in near-field tsunami modeling, where the coupling between ground shaking and inundation demands cannot be decoupled without significant loss of accuracy. While the broader literature on this topic is extensive, the discussion that follows focuses on the most recent and methodologically consequential contributions that have shaped how near-field tsunami structural response is currently understood and simulated.

3.1. Near-Field Tsunami Fragility Simulation

The simulation framework begins with the development of nonlinear structural models capable of representing the response of coastal buildings subjected to both seismic and hydrodynamic loading. It is important to note that the illustrative simulations presented in this section are based on a reinforced concrete (RC) special moment-resisting frame

 https://doi.org/10.3390/infrastructures11070221

archetype (Figure 1, T_1 = 0.94 s), which is representative of modern US code-conforming construction and is used here to demonstrate the successive simulation methodology (the empirical component in Section 4 uses Japanese wood-frame buildings as noted in the abstract; the two components are complementary methodological demonstrations). As can be seen from Figure 1, structural systems are typically modeled using finite-element formulations that capture the nonlinear behavior of beams, columns, and joints. Rotational spring models are commonly used to represent nonlinear plastic hinge behavior at beam-column connections, while additional springs can capture joint shear failure mechanisms [25,61]. These modeling approaches allow the simulation to represent key damage mechanisms that occur during earthquake excitation, including stiffness degradation, strength deterioration, and plastic rotation accumulation [62]. The structural discretization also enables the representation of hydrodynamic loads acting on seaward columns and structural frames when tsunami waves inundate the building. Such modeling strategies allow the structural model to capture the progressive transition from earthquake-induced damage to tsunami-induced structural failure [25].

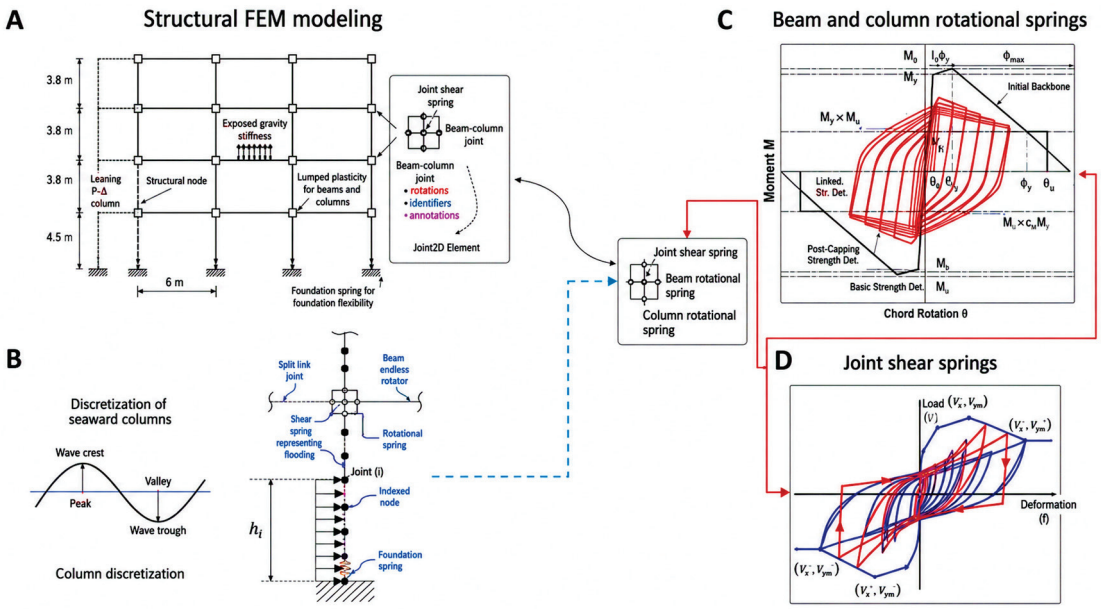

Figure 1. Schematic of nonlinear FEM model for typical RC frame in US with beam–column rotational springs and joint shear springs used to capture member and joint nonlinear behavior.

Once the structural model is established, the simulation procedure incorporates uncertainties associated with both hazard and structural parameters. As shown in Figure 2, ground motion records representing earthquake excitation are selected from standardized datasets such as the FEMA P-695 (regular-duration earthquakes) and M9 Project (long-duration earthquakes) record sets, which provide a suite of ground motions designed for collapse assessment studies of structural systems (see more details in [61]). The two sets differ substantially in their duration characteristics: FEMA P-695 records have a median significant duration ($D_{5–95}$, defined as the interval over which 5% to 95% of the total Arias intensity is accumulated) of approximately 15–25 s, while M9 Project records—representing Cascadia Subduction Zone scenarios—exhibit $D_{5–95}$ values exceeding 60 s, as illustrated in Figure 2. These records are scaled to represent a range of seismic intensity levels and applied to the structural model through nonlinear time-history analysis.

The resulting structural response captures the earthquake-induced damage state that forms the initial condition for the subsequent tsunami loading phase. For near-field

https://doi.org/10.3390/infrastructures11070221

tsunami scenarios as shown in Figure 3, the structural system may enter the tsunami loading phase with varying levels of residual damage, which significantly influences the structural capacity against hydrodynamic forces [22].

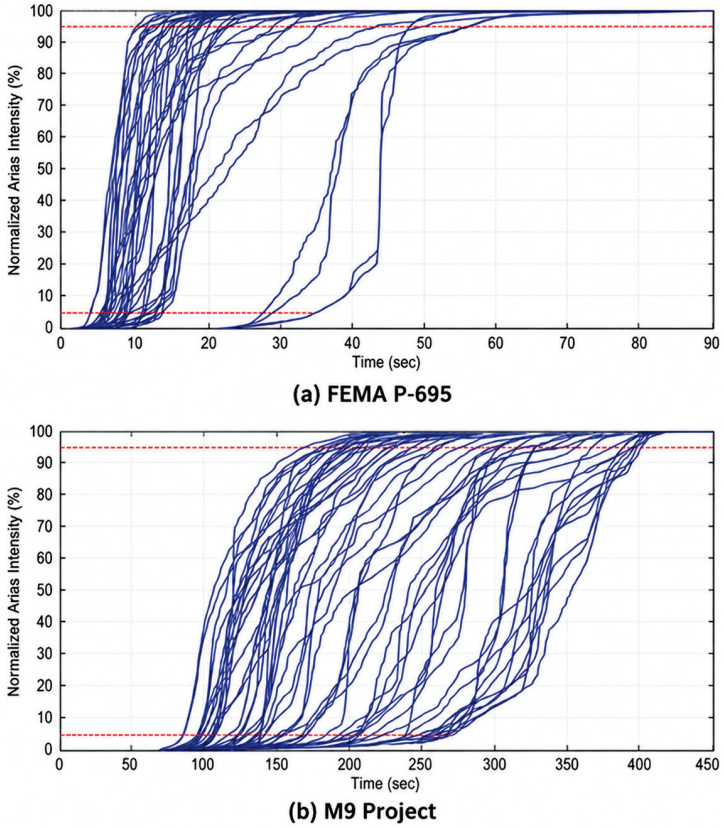

Figure 2. Comparison of regular- and long-duration earthquake records using cumulative energy distribution and motion duration ($D_{5–95}$) for the earthquake phase of the successive simulation.

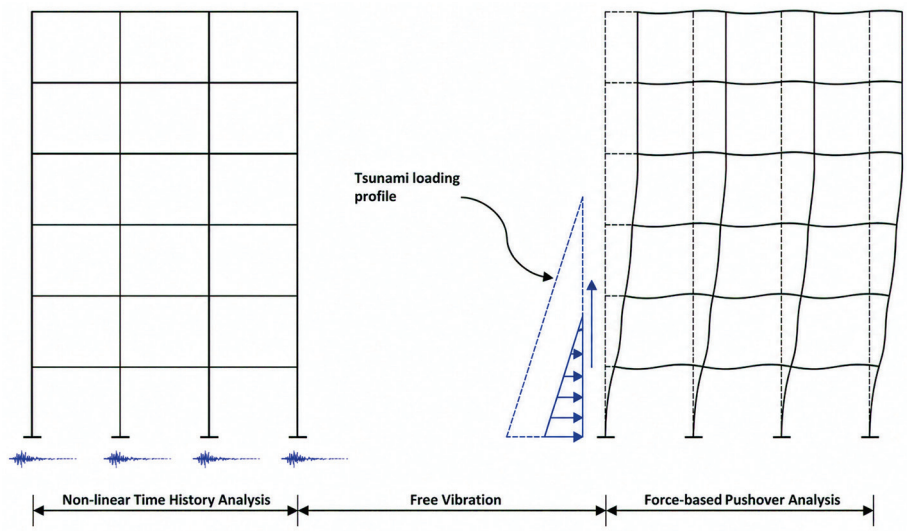

Figure 3. Analysis procedure: (1) nonlinear time-history analysis under earthquake loading; (2) post-earthquake free vibration to obtain residual deformation and damage states; and (3) pushover analysis of the damaged structure to assess residual lateral capacity under subsequent tsunami loading.

https://doi.org/10.3390/infrastructures11070221

The transfer of structural state from the earthquake phase to the tsunami loading phase follows explicit parameter-passing rules that govern the initial conditions of the second analysis stage. Specifically, at the conclusion of each nonlinear time-history analysis under earthquake excitation, three categories of state variables are extracted and carried forward: (i) residual nodal displacements and rotations, which define the deformed geometric configuration of the structure at the onset of tsunami loading; (ii) plastic hinge rotation demands accumulated at beam–column connections, which determine the remaining rotational capacity at each joint and therefore the effective lateral resistance of the degraded frame; and (iii) component-level stiffness and strength degradation parameters, updated through the hysteretic model during earthquake shaking, which reduce the backbone force–deformation relationship used in the subsequent pushover analysis. These extracted state variables collectively define the "damaged structural configuration" that serves as the starting point for the force-based pushover analysis conducted in the tsunami phase. Between the earthquake and tsunami phases, a free vibration step is introduced in which all external forcing is removed, and the structure is allowed to vibrate freely under its own inertia and restoring forces until kinetic energy dissipates and a stable static equilibrium is reached. This step serves two purposes: first, it eliminates transient velocity and inertia contributions that are present during shaking but physically absent at the onset of tsunami inundation—which arrives as a quasi-static rising flow rather than a dynamic impulse—ensuring that the extracted state variables reflect the true residual static condition of the damaged structure; second, it allows any remaining dynamic amplification in nodal displacements and plastic hinge rotations to settle, so that the three categories of state variables extracted for the pushover phase represent a physically consistent and statically admissible initial condition. No reinitialization of plastic hinge states or stiffness matrices is performed between the two main phases; the post-earthquake structural model is used directly, ensuring that the capacity reduction due to seismic damage is fully reflected in the tsunami demand-to-capacity comparisons. This one-way coupling approach—where earthquake damage governs the initial state of the tsunami analysis but tsunami loading does not retroactively influence the earthquake response—is physically appropriate given the rapid sequential nature of near-field events and is consistent with the successive analysis strategy described in detail in [25,63].

The tsunami loading, in the third phase of the simulation in Figure 3, is represented through hydrodynamic force components acting on the structural frame, typically including drag forces, hydrostatic pressures, and impulsive loads associated with bore impact or velocity contribution of tsunami waves. In the simulation framework, these loads are often represented using simplified hydrodynamic formulations in which the total lateral tsunami force depends on flow depth, flow velocity, and structural geometry. Because tsunami parameters exhibit significant variability, the simulation framework introduces these loads as random variables within a probabilistic modeling framework [25]. Multiple tsunami loading profiles with varying water depths and flow velocities are generated to represent different inundation scenarios (see [25] for more details). This probabilistic treatment allows the simulation to capture the wide range of tsunami forces that may occur during real coastal inundation events.

To evaluate structural performance under combined hazards, the structural demand is compared with the structural capacity for each pair of earthquake and tsunami intensity parameters to determine whether a specified damage state or collapse condition is reached [63]. Repeating this process across a large set of earthquake–tsunami intensity combinations produces a dataset of failure outcomes associated with different hazard intensities. This process produces a set of failure-probability points that describe the re-

 https://doi.org/10.3390/infrastructures11070221

lationship between earthquake intensity measures and tsunami intensity measures for different structural damage states.

3.2. Near-Field Tsunami Fragility Response

The results of the successive simulations using regular-duration earthquakes (FEMA P-695) can be visualized as a set of points representing the conditional failure probability $P(TS \mid EQ)$ across a two-dimensional hazard space. As shown in Figure 4, these points form the basis for constructing fragility surfaces that describe structural vulnerability of the RC frame archetype under combined earthquake–tsunami loading. Surface-fitting techniques can then be applied to the simulated failure probability points in order to obtain continuous fragility surfaces for different damage states [63]. These fragility surfaces provide a generalized representation of structural vulnerability across a wide range of earthquake and tsunami intensities, enabling probabilistic risk assessments that account for interacting hazards [64].

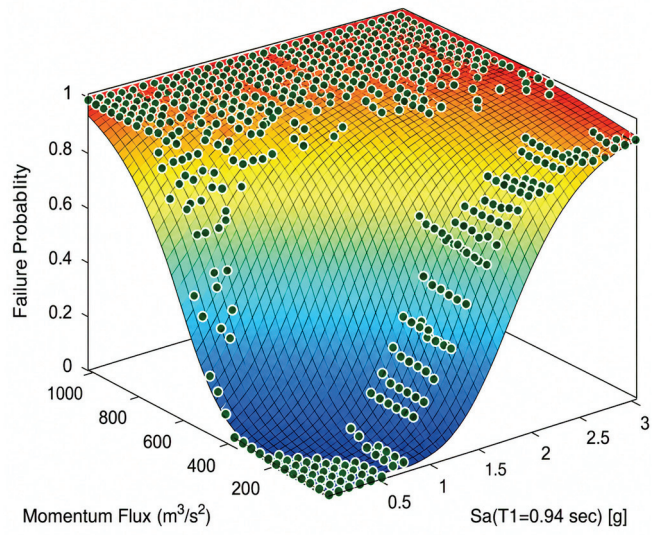

(**a**) Surface fitted to the points of failure probability

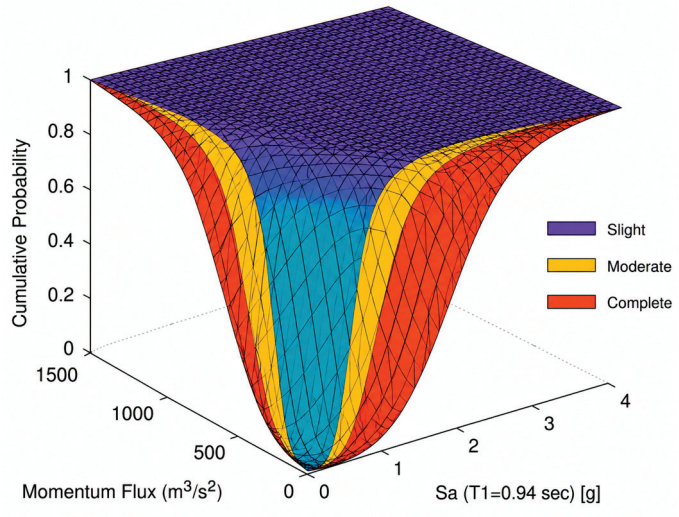

(**b**) Fragility surfaces on different damage states

Figure 4. Multi-hazard fragility surfaces relating spectral acceleration and tsunami momentum flux (MF) to structural damage probability for collapse and multiple damage states.

https://doi.org/10.3390/infrastructures11070221

Validation of the simulation framework is an essential component of the modeling process. For the earthquake component, the nonlinear structural model can be validated by comparing simulated structural responses—such as pushover curves and dynamic fragility curves (Figure 5)—with benchmark results reported in previous studies (e.g., [62]). For example, comparisons with established structural models can verify that the simulated building exhibits realistic stiffness, strength, and collapse behavior under seismic loading. Figure 5b presents the earthquake fragility curves for the RC frame archetype, showing the probability of exceeding on DS3/collapse damage state (as defined in Table 1) as a function of spectral acceleration at the fundamental period Sa(T_1 = 0.94 s). Each curve in the figure corresponds to the same structural limit state. Solid lines represent fragility curves derived from the present simulations; dashed lines represent benchmark fragility curves from [62] for the same archetype. The close agreement between these fragilities confirms that the simulated structural model reproduces the expected seismic fragility behavior of the archetype, providing confidence that the earthquake-induced damage states generated in the successive simulation (presented in Section 3.1) are physically consistent and suitable as initial conditions for the subsequent tsunami loading phase. The period of vibration and mode shapes have also been examined and found consistent with the benchmark values reported in [62].

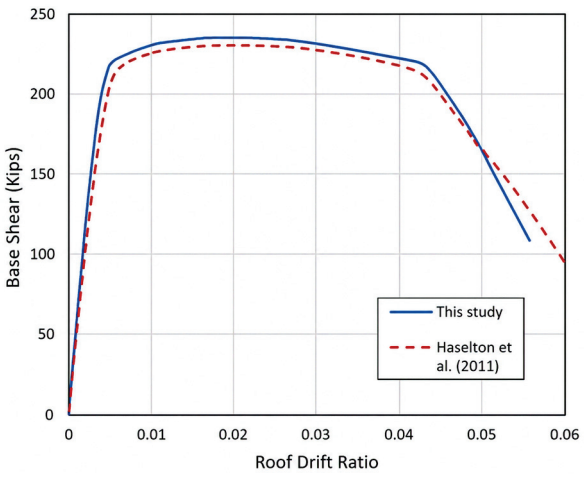

(**a**) Validation on Pushover response

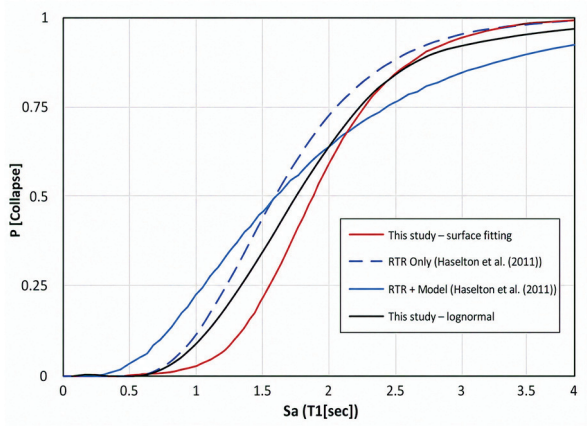

(**b**) Validation of earthquake fragility response

Figure 5. Validation of the RC special moment-resisting frame archetype: (**a**) simulated pushover response compared with benchmark results from [62]; (**b**) simulated earthquake fragility curves (on DS3/collapse) compared with benchmark models from [62].

https://doi.org/10.3390/infrastructures11070221

Table 1. Crosswalk between the seven-level MLIT damage scale (DS1–DS7) and the three-class IN-CORE damage taxonomy used in the machine-learning classification analysis (presented later in this paper).

IN-CORE Class	MLIT DS Levels Included	MLIT Damage Descriptions
Class 1	DS1, DS2, DS3	No damage; minor; slight
Class 2	DS4, DS5	Major; moderate
Class 3	DS6, DS7	Collapsed; washed away; complete

The close agreement between the simulated pushover response and the benchmark curve reported by Haselton et al. (2011) [62] provides confidence in the structural model and validates its suitability for the force-based pushover procedure used in the tsunami loading phase. The resulting fragility curves in Figure 6 can then be compared across earthquake intensity levels to examine how pre-existing seismic damage influences tsunami vulnerability. In near-field tsunami scenarios, structures subjected to strong ground shaking exhibit an increased baseline probability of failure before any tsunami loading is applied. Consequently, the tsunami fragility curves conditioned on earthquake intensity show a vertical shift relative to those derived for undamaged structures—manifesting as a non-zero failure probability at zero tsunami force, referred to here as the jump at the origin. This jump reflects the compounded damage state in which tsunami forces act on a structure whose capacity has already been reduced by seismic loading. As shown in Figure 7, this effect is further amplified when long-duration ground motion records (M9 Project) are used: the jump at the origin becomes more pronounced relative to results obtained with regular-duration records (FEMA P-695), consistent with the greater cumulative damage imposed by extended shaking—a pattern evident across all three intensity levels: higher Sa values (1.0 g and 1.5 g) produce both a larger jump at the origin and a leftward shift in the entire curve relative to the Sa = 0.5 g case, reflecting the greater reduction in structural capacity with increasing seismic demand (see [61] for details).

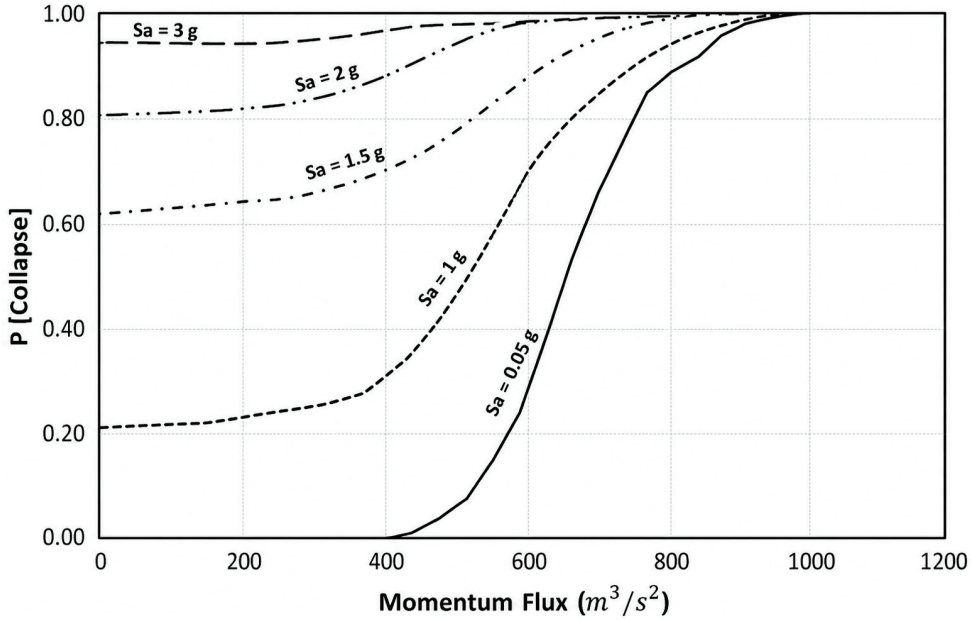

Figure 6. Tsunami fragility curves conditioned on prior earthquake intensity levels, illustrating increased initial failure probability for near-field tsunami scenarios compared to far-field conditions.

https://doi.org/10.3390/infrastructures11070221

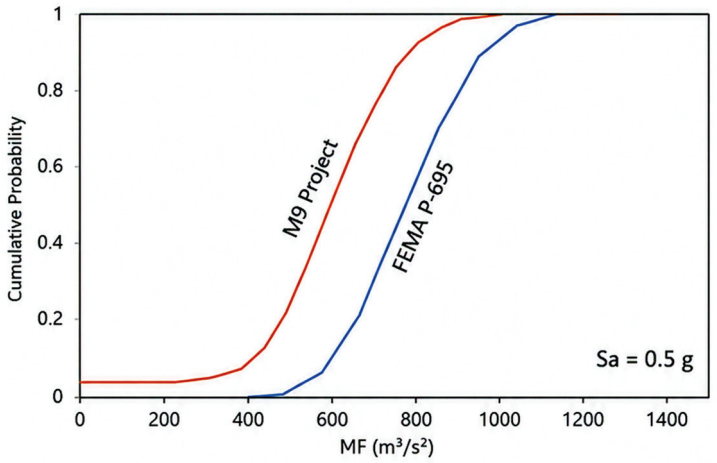

(**a**) Sa = 0.5 g

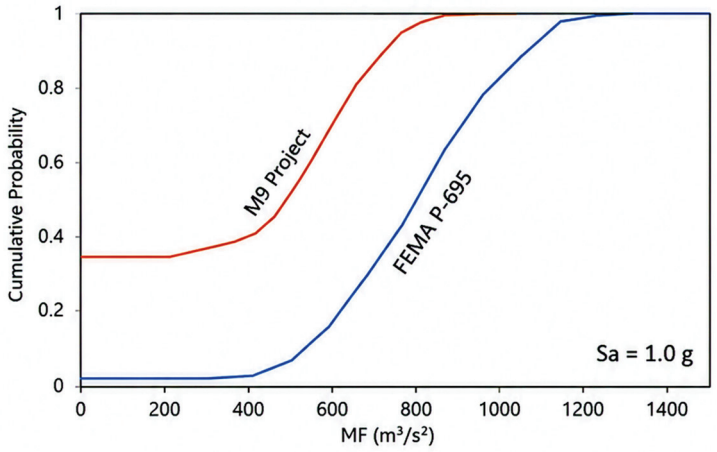

(**b**) Sa = 1.0 g

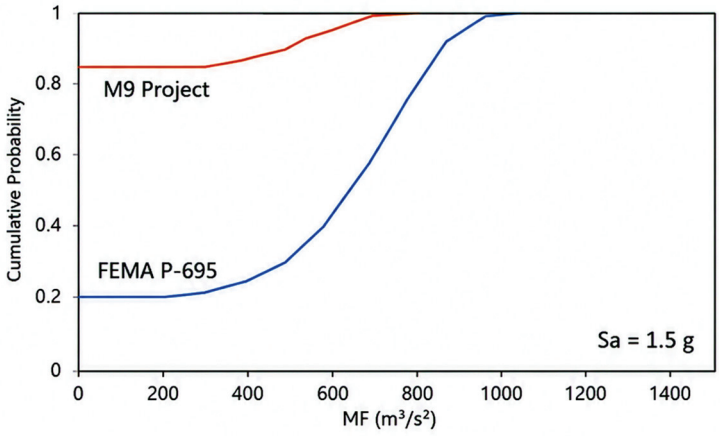

(**c**) Sa = 1.5 g

Figure 7. Comparison of tsunami fragility curves for different earthquake intensity levels (*Sa* = 0.5 g, 1.0 g, and 1.5 g) showing the vertical shift caused by pre-existing earthquake damage prior to tsunami loading.

4. Post-Tsunami Damage Survey

Post-tsunami damage survey datasets provide an essential empirical foundation for understanding how coastal buildings respond to tsunami inundation; in this study the empirical analysis is based on wood-frame building records from the 2011 Great East

https://doi.org/10.3390/infrastructures11070221

Japan survey, and the observations should be interpreted as typology-specific unless otherwise noted. While simulation-based fragility modeling enables controlled exploration of structural behavior under coupled earthquake–tsunami hazards, field observations provide direct evidence of real damage mechanisms and allow validation of the simulated fragility relationships [32,65,66]. In this study, post-tsunami survey data are analyzed to examine the relationship between structural damage, hydrodynamic intensity measures, and spatial characteristics such as distance from the coastline. These empirical observations allow the fragility models derived from numerical simulations to be interpreted within the context of actual tsunami damage patterns.

4.1. Damage Survey Data and Information

The damage data utilized in this study are based on the building-level survey dataset compiled by the Japanese Ministry of Land, Infrastructure, Transport and Tourism (MLIT) following the 2011 Great East Japan tsunami—a near-field event in which all surveyed structures were subjected to sequential earthquake and tsunami loading. The recorded damage states in the dataset therefore represent the outcome of coupled hazard exposure, not isolated tsunami response [67]. This dataset consists of detailed ex-post damage observations for a large number of structures across multiple affected coastal regions (Figure 8), including Miyako, Rikuzentakata, Minami-Sanriku, Kesennuma, Ishinomaki, Sendai Port, and Sendai Airport [68]. Each record in the dataset includes the observed damage state of individual buildings, categorized into seven discrete levels ranging from no damage (DS1) to washed away (DS7), along with key structural and site-related attributes such as construction type, number of floors, and inundation depth at the building location. The dataset therefore provides a comprehensive empirical basis for linking tsunami intensity measures to structural damage.

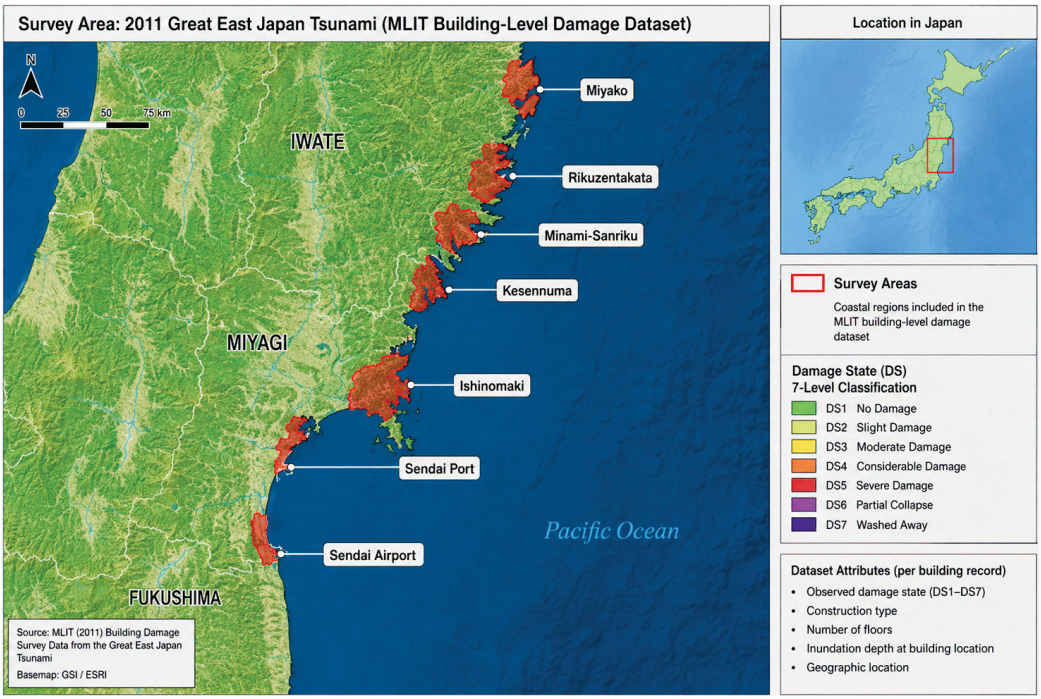

Figure 8. Survey areas covered by the MLIT building-level damage dataset following the 2011 Great East Japan tsunami, including seven coastal regions in Iwate and Miyagi Prefectures. Building damage was classified into seven states (DS1–DS7), with associated structural characteristics and inundation depths recorded for each surveyed structure.

https://doi.org/10.3390/infrastructures11070221

In addition to the original survey information, the dataset has been extended in previous studies to incorporate additional geospatial and proxy variables representing hydrodynamic effects, including shielding and debris interaction mechanisms [68]. These extensions introduce several hydraulic variables whose provenance and derivation differ importantly and are clarified here for transparency. The inundation depth h_MLIT is measured directly from post-event field survey records and represents the primary observed intensity measure. Flow velocity, however, was not directly recorded during the 2011 event owing to insufficient video documentation of the inundation; two distinct velocity estimates are therefore used in this study. The first, *v_c*, is an approximation derived from the survey data itself using a simplified analytical method (a depth-velocity proxy formula applied to the observed inundation depths); it is not a direct field measurement and carries the uncertainty inherent in any surrogate-based velocity estimate. The second pair of variables, *h_sim* and *v_sim*, are both outputs of a hydrodynamic simulation of the 2011 event calibrated against the field-observed inundation depths and spatial damage patterns; these variables provide physically consistent estimates of depth and velocity across the inundation zone but are model-derived rather than directly observed. The observed momentum flux *m_MLIT* is computed as $M = h_MLIT \cdot v_c^2$ (m^3/s^2) and therefore inherits the approximation uncertainty in *v_c*, while the simulated momentum flux *m_sim* is computed from *h_sim* and *v_sim*. Consequently, *h_MLIT* is the only hydraulic quantity with direct observational grounding; all velocity-dependent variables involve either approximation or simulation-based inference.

For the machine-learning classification analysis presented in the next section, the original seven-level MLIT damage scale (DS1–DS7) is aggregated into three ordered classes to align with the damage-state taxonomy used in the IN-CORE community resilience platform [69]. Class 1 (Minor/Slight Damage) includes DS1 (no damage), DS2 (minor damage), and DS3 (moderate damage); Class 2 (Moderate/Severe Damage) includes DS4 (major damage) and DS5 (complete damage); and Class 3 (Collapse/Complete Loss) includes DS6 (collapsed) and DS7 (washed away). This aggregation preserves the key engineering distinction between repairable damage, irreparable damage, and total loss while providing sufficient samples in each class for robust classifier training. The corresponding crosswalk is summarized in Table 1. Because both the original MLIT damage states and the aggregated IN-CORE classes are used throughout this section, their relationship is explicitly identified in the figures and discussion.

4.2. Observations on Near-Field Tsunamis from Damage Survey

A key insight obtained from the damage survey data is that structural damage exhibits a strong correlation with hydrodynamic intensity measures characterizing tsunami loading. Among these, momentum flux—defined in this study as $M = h \cdot v^2$ (m^3/s^2), where h is flow depth (m) and v is flow velocity (m/s), without inclusion of the fluid density ρ —emerges as one of the most informative parameters, as it captures the combined effect of hydrostatic and hydrodynamic forces acting on structures. Note that while ρ is excluded from the intensity measure definition (consistent with common practice in empirical fragility studies), it is retained when computing the hydrodynamic force component of the tsunami force for structural load calculations. The empirical results presented in this section and in Figures 9–13 are derived exclusively from wood-frame building records in the 2011 Great East Japan survey dataset. This typology is the most prevalent in the MLIT dataset and thus provides the largest sample for robust statistical analysis.

 https://doi.org/10.3390/infrastructures11070221

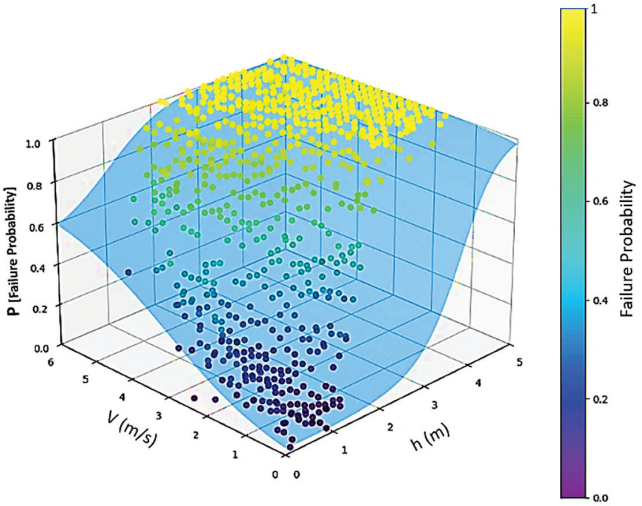

Figure 9. Failure probability surface as a function of inundation depth (h) and flow velocity (v), based on 2011 Great East Japan MLIT survey data. Points denote observed building outcomes, and the fitted surface represents the estimated probability of failure from binned empirical failure rates.

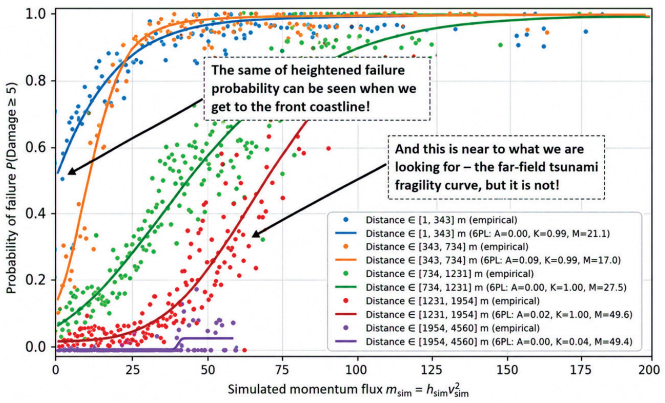

(**a**) Empirical fragility points grouped by distance from coastline

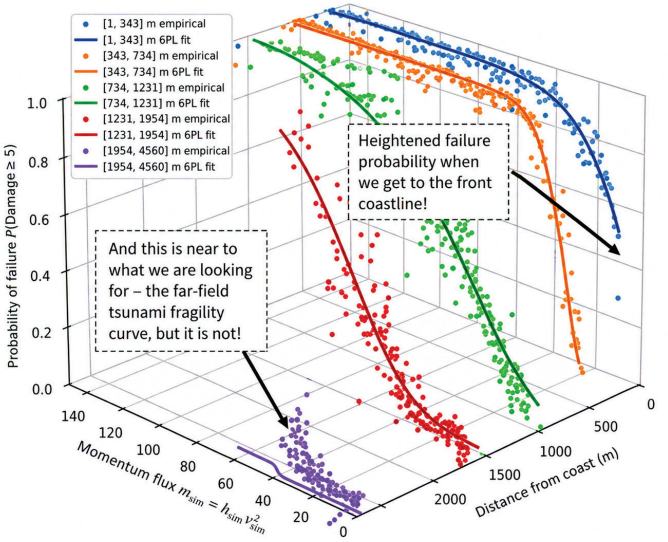

(**b**) 3D fragility for momentum flux versus the distance from coastline

Figure 10. (**a**) Empirical fragility data points for wood-frame buildings grouped by distance from coastline; (**b**) failure probability surface as a function of simulated momentum flux (m_{sim}) and distance from the coastline, illustrating the effects of tsunami intensity and coastal proximity on wood-frame building failure probability.

https://doi.org/10.3390/infrastructures11070221

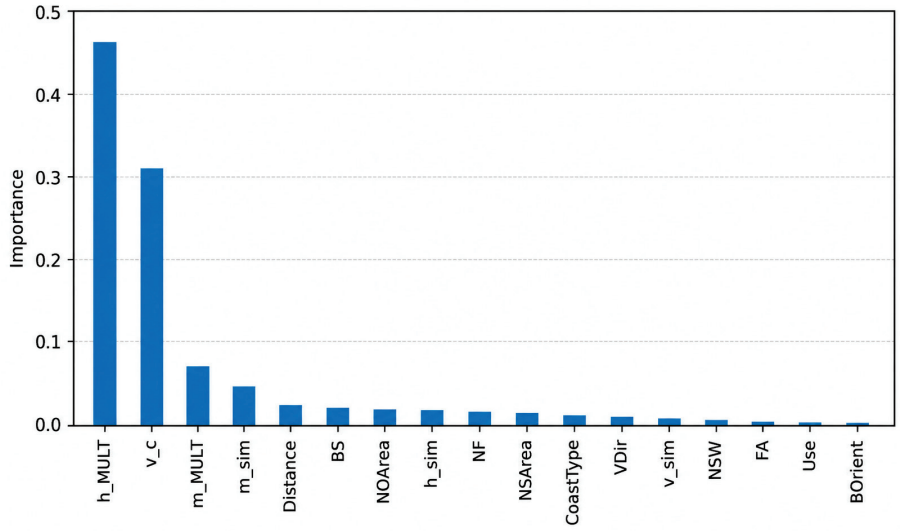

(**a**) Feature Importance Analysis of the variables invoved with the damage survey

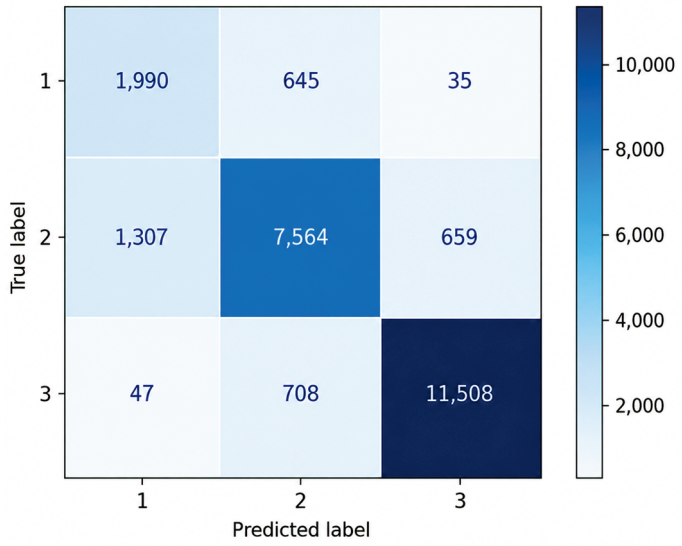

(**b**) Prediction matrix for different damage states

Figure 11. Machine-learning model evaluation for wood-frame buildings in the 2011 Great East Japan survey dataset: (**a**) XGBoost feature importance rankings for damage prediction; (**b**) confusion matrix for three-class damage classification on the test dataset, showing an overall accuracy of 87%.

Before presenting Figure 9, it is important to clarify how numerical failure probability values are generated from survey-based damage assessment. Each building record in the MLIT dataset carries an observed damage state (DS1–DS7) and associated hydraulic intensity values (inundation depth h and estimated flow velocity v). The binary failure criterion (DS $\geq$ DS4 = failure; DS < DS4 = non-failure) converts each record into a Bernoulli outcome [21]. To construct the 3D failure probability surface, the (h, v) domain is partitioned into a regular grid of bins; within each bin, the empirical failure probability is computed as the ratio of failed buildings to total buildings in that bin. These bin-level failure fractions constitute the data points visible in Figure 9. A smooth probabilistic surface is then fitted to these empirical data points using a parametric regression model, yielding a continuous failure probability function of h and v. This procedure is entirely empirical—no structural simulation is involved—and the resulting surface represents the observed conditional failure probability directly from the survey data. As illustrated in Figure 9, the probability

https://doi.org/10.3390/infrastructures11070221

of failure (DS $\geq$ DS4 of MLIT) for wood-frame buildings increases nonlinearly with both inundation depth (h) and flow velocity (v), highlighting their combined influence on structural damage. The resulting failure surface indicates that neither variable alone adequately characterizes structural response; rather, their interaction governs the transition to severe damage and collapse, supporting the use of composite intensity measures such as momentum flux in tsunami fragility modeling.

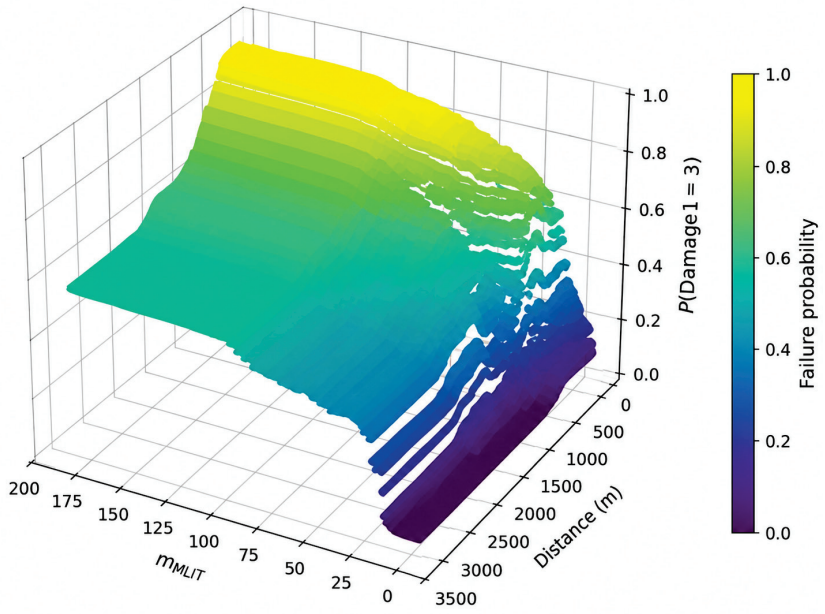

(**a**) Fragility surface of tsunami for momentum flux versus distance from the coastline

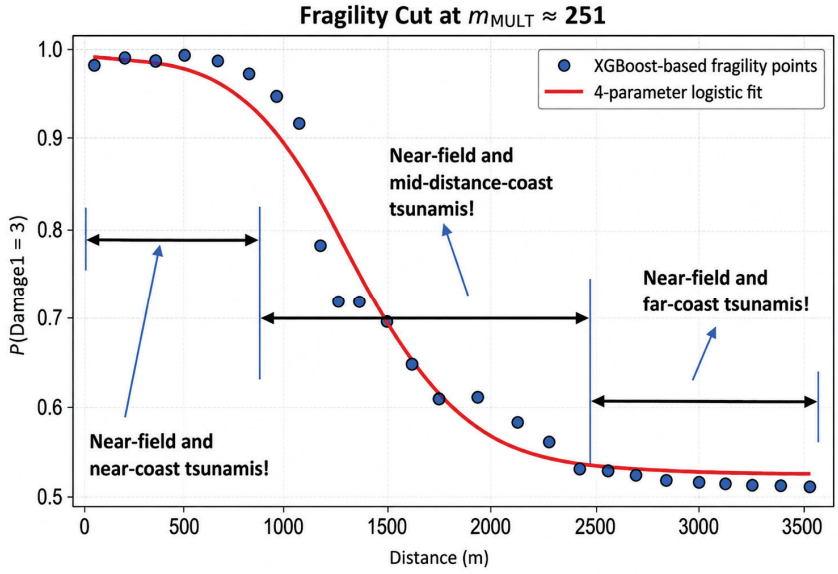

(**b**) Fragility attenuation curve as a function of distance from coastline

Figure 12. Failure probability as a function of tsunami intensity and coastal distance, illustrating coastal attenuation effects on wood-frame building vulnerability. $\text{Damage}_i = k$ denotes the predicted IN-CORE damage class for distance bin i.

Figure 10 uses the simulated momentum flux *m_sim* as the intensity measure on the horizontal axis. As described in Section 4.1, both depth and velocity fields are simulation-

https://doi.org/10.3390/infrastructures11070221

derived (calibrated against field observations), ensuring physically consistent hydrodynamic inputs for the distance-dependent fragility analysis.

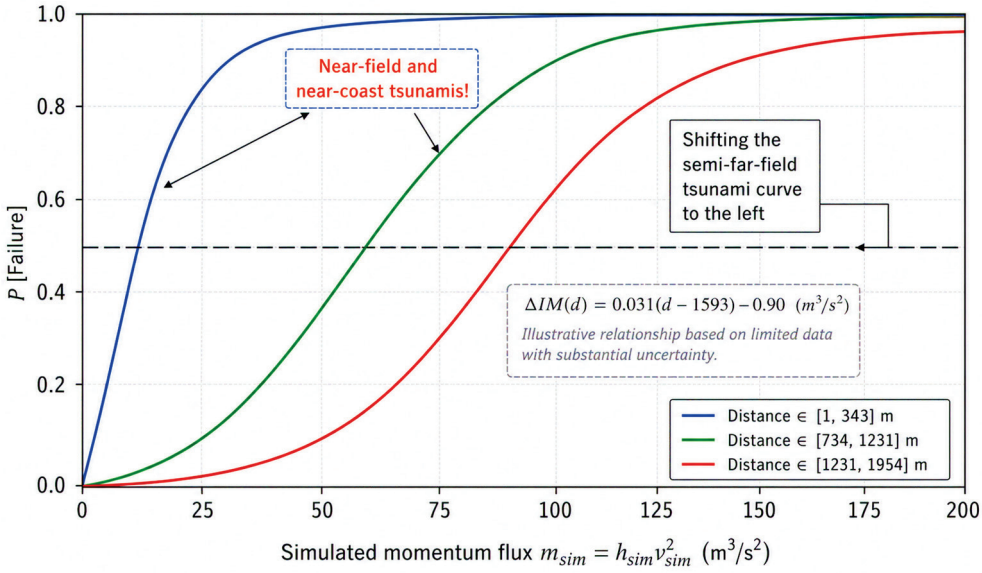

Figure 13. Influence of coastal distance on tsunami fragility curves for wood-frame buildings in the 2011 Great East Japan survey dataset, showing higher vulnerability under near-field, near-coast conditions. A distance-dependent intensity shift adapts a reference semi–far-field fragility curve to site-specific coastal locations.

This cross-validation between simulation-derived and empirical fragility behavior supports the physical realism of the successive earthquake–tsunami analysis framework. The results further indicate that hydrodynamic parameters, including inundation depth, flow velocity, and their combined momentum flux, are physically meaningful predictors of tsunami-induced structural damage, whereas the baseline failure probability at low tsunami intensities is influenced by pre-existing seismic damage. In Figures 9 and 10, structural failure is defined as the exceedance of DS4 (major damage), i.e., P(Damage $\geq$ DS4). This threshold was selected because DS4 marks the onset of irreparable structural damage and represents the engineering boundary beyond which a building is typically considered a total loss for recovery purposes. It also corresponds to the transition between IN-CORE Classes 1 and 2 in the adopted three-class damage taxonomy.

Another important observation emerging from the damage survey data is the significant influence of distance from the coastline on observed damage levels. Buildings located closer to the shoreline generally experience higher damage probabilities compared with buildings located further inland. When the dataset is stratified into distance bins measured from the coastline, the resulting fragility curves reveal systematic variations in failure probability with distance. Structures located in the near-coast region tend to exhibit a higher baseline probability of severe damage even at relatively moderate hydrodynamic intensities. In contrast, buildings located farther inland show a lower probability of failure for the same intensity levels. This trend suggests that coastal proximity plays a critical role in tsunami damage processes and should be considered explicitly in fragility modeling frameworks.

The influence of coastal distance on damage patterns also reveals important differences between near-coast, mid-coast, and far-coast tsunami effects. In the immediate coastal zone, buildings are exposed to highly energetic tsunami flows characterized by strong impulsive forces, debris impact, and rapid hydrodynamic loading. These mechanisms contribute to

https://doi.org/10.3390/infrastructures11070221

elevated damage probabilities in the near-coast region and can produce structural failures even when hydrodynamic intensity measures appear moderate. In addition, structures in this zone may experience stronger earthquake shaking prior to tsunami arrival, particularly in near-field tsunami events where the earthquake source is located close to the affected coastline. The combined effects of intense tsunami forces and potential earthquake damage lead to elevated fragility levels for buildings located near the shoreline.

At intermediate distances from the coastline, the tsunami flow tends to transition from highly impulsive conditions toward more stable hydrodynamic inundation behavior. In this region, damage patterns are influenced by both the residual energy of the incoming tsunami flow and the attenuation of impulsive forces with distance. As a result, fragility curves derived from damage observations in this region often exhibit intermediate characteristics between near-coast and far-coast behaviors. This transition zone is particularly important for fragility modeling because it captures the gradual attenuation of tsunami forces as the wave propagates inland.

For buildings located further inland, tsunami damage appears to be dominated primarily by hydrodynamic inundation rather than impulsive coastal forces. In these far-coast locations, debris impacts and bore-like forces become less dominant, and the structural response tends to be controlled primarily by sustained hydrodynamic loads. Consequently, the observed damage patterns in this region resemble what is typically described as far-field tsunami fragility behavior, in which structural vulnerability depends mainly on hydrodynamic flow parameters such as water depth and velocity. These conditions align closely with simplified engineering design approaches in which tsunami loads are represented through hydrodynamic pressure formulations, such as those incorporated into design guidance documents and coastal hazard engineering methodologies.

The inherently coupled nature of the 2011 dataset—in which earthquake and tsunami effects cannot be separated—deserves to be understood not only as a limitation for validation purposes but also as a feature that connects the empirical analysis directly to the near-field scenario motivating Section 3. The survey data capture exactly the conditions the successive simulation framework is designed to represent: structures whose seismic capacity had been partially consumed before tsunami loading commenced. In this sense, the empirical fragility curves in Figures 9, 10, 12 and 13 are the real-world analog of the simulation-derived conditional fragility surfaces in Figures 4–7, both reflecting the compounded vulnerability of structures under coupled earthquake–tsunami loading. It should nevertheless be noted that, for validation of the pure tsunami edge of the fragility surfaces, far-field tsunami fragility data would ideally be required, since none of the empirical curves represent pure far-field tsunami response—even for structures located relatively far from the coastline, the prior seismic event means that some degree of earthquake conditioning is present in all survey records.

Machine-learning-based (ML) analysis—using an XGBoost classifier—of the survey dataset further confirms the relative importance of key variables influencing tsunami damage. The wood-frame subset of the MLIT dataset used in the classification analysis comprises 97,852 records after cleaning (held-out test set: 24,463; training set: 73,389). The dataset was divided into a stratified 75/25 training/test split (random state = 42), preserving the IN-CORE class distribution in both partitions. Class imbalance was not explicitly corrected (no oversampling or class weighting was applied); the class distribution across the three IN-CORE classes is: Class 1 (minor/slight) 10.9% (n = 10,680), Class 2 (major/moderate) 39.0% (n = 38,120), and Class 3 (collapse/complete) 50.1% (n = 49,052). The classifier is an XGBoost multi-class model (objective: multi:softprob, eval_metric: mlogloss) with the following hyperparameters: n_estimators = 600, max_depth = 4,

 https://doi.org/10.3390/infrastructures11070221

learning_rate = 0.05, subsample = 0.8, colsample_bytree = 0.8. The input feature set comprises seven core MLIT variables: building structure type (BS), number of floors (NF), coast type (CoastType), floor area (FA), distance from coastline (Distance), building use (Use), and observed momentum flux (m_MLIT).

The confusion matrix in Figure 11b and all performance metrics reported below reflect predictions on the held-out test set only. Note that Figure 11a (feature importance) is derived from a separate XGBoost regressor trained on the continuous seven-level damage scale using an extended 17-variable feature set including simulated hydraulic variables (*h_sim*, *v_sim*, *m_sim*) and additional site attributes; this distinction is important because the feature ranking reflects the regressor's response surface rather than the classifier's decision boundaries.

Feature-importance evaluations presented in Figure 11a show that flow depth and flow velocity are the two dominant predictors of structural damage states, with momentum flux ranking as a more distant third predictor—nearly an order of magnitude lower in importance than depth—followed by distance from the coastline and other environmental variables. Notably, since momentum flux is itself a function of both flow depth and velocity, the strong individual importance of these two components is consistent with momentum flux acting as the underlying controlling parameter; the XGBoost model effectively decomposes its influence into its constituent variables, which together account for the combined hydrodynamic loading captured by momentum flux. This result supports the physical interpretation that tsunami forces are primarily governed by hydrodynamic loading mechanisms, while spatial characteristics influence how those forces are transmitted to the built environment.

The classification analysis presented in Figure 11b, based on the three-class IN-CORE damage taxonomy described in Table 1 (Class 1: minor/slight; Class 2: major/moderate; Class 3: collapse/complete) [69], demonstrates the following out-of-sample classification performance on the held-out test set. Overall weighted accuracy is 87%. Per-class metrics are as follows: Class 1 (minor/slight)—precision 78%, recall 49%, F1 = 0.60; Class 2 (major/moderate)—precision 81%, recall 88%, F1 = 0.84; Class 3 (collapse/complete)—precision 93%, recall 95%, F1 = 0.94; weighted macro-F1 = 0.86. The comparatively low recall for Class 1 (49%) is consistent with both the class imbalance ($\sim$11% of records) and the physical difficulty of distinguishing minor from moderate damage at low hydrodynamic intensities; because no class weighting or oversampling was applied, the model optimizes toward the majority classes. Despite this, the classifier achieves high performance on the two most consequential damage states—Classes 2 and 3 account for 89% of records and are identified with F1 scores of 0.84 and 0.94, respectively—confirming strong statistical relationships between damage patterns and hazard intensity measures.

An additional insight from the ML analysis over damage survey data is the identification of coastal attenuation effects in tsunami fragility behavior. As tsunami waves propagate inland, the energy of the flow gradually dissipates due to surface friction, topographic effects, and flow spreading. This attenuation process leads to systematic reductions in tsunami dominant forces with increasing distance from the coastline. When ML-assisted fragility curves derived for different coastal distance ranges are compared, as shown in Figure 12a, they exhibit systematic shifts toward lower failure probabilities with increasing distance from the coastline. This trend highlights that tsunami fragility relationships are not spatially uniform and must account for the attenuation of hazard intensity across the inundation zone, as illustrated in Figure 12b. The subscript notation used in Figure 12 (e.g., $\text{Damage}_1 = 3$) follows the same convention: the subscript identifies the distance bin

 https://doi.org/10.3390/infrastructures11070221

index and the integer value indicates the predicted IN-CORE damage class (1, 2, or 3) for that bin.

The observed spatial variation in fragility behavior seen from Figure 12b also suggests that fragility curves derived from damage survey data may represent different effective hazard regimes depending on the coastal distance of the surveyed structures. In particular, fragility relationships derived from buildings located far from the shoreline may resemble traditional far-field tsunami fragility curves, while buildings located near the coast may exhibit fragility characteristics influenced by both earthquake damage and intense impulsive tsunami forces. Understanding this distinction is critical when interpreting empirical fragility datasets because the observed damage patterns may reflect a mixture of near-field and far-field tsunami processes.

Figure 13 illustrates the systematic variation in tsunami fragility curves with coastal distance, highlighting the pronounced influence of near-field and near-coast effects on structural vulnerability. It is important to understand Figure 13 as the engineering operationalization of Figure 10a: the two figures represent the same underlying phenomenon at two levels of abstraction. Figure 10a presents the raw empirical observation—a three-dimensional failure probability surface in which damage probability varies jointly with momentum flux and coastal distance, with the surface shifting upward (higher failure probability at the same intensity) as distance from the coast decreases. Figure 13 then decomposes this 3D surface into a tractable engineering tool by expressing the distance-dependent behavior as a horizontal shift in a single reference fragility curve: instead of requiring a new fragility curve for every distance, the 3D variation in Figure 10a is captured by a single baseline curve plus the scalar function $\Delta\mathrm{IM}(d)$, which quantifies how far the fragility curve must be shifted leftward (toward lower intensity) to represent conditions at distance d from the coast. In other words, Figure 10a establishes that coastal distance is a significant determinant of tsunami vulnerability, and Figure 13 translates that observation into a practical parameterization: each fragility curve in Figure 13 corresponds to a horizontal cross-section of the 3D surface in Figure 10a at a fixed distance bin, and the horizontal separation between those curves is precisely what $\Delta\mathrm{IM}(d)$ quantifies.

As observed in this paper, structures located closer to the coastline exhibit significantly higher failure probabilities at lower intensity levels, effectively resulting in a leftward shift in the fragility curve relative to those representing semi–far-field conditions. It should be noted that the fragility curve for the far-distance bin [1954, 4560] m in Figure 13 is truncated at approximately $m_{sim} \approx 100\ \mathrm{m}^3/\mathrm{s}^2$. This truncation is entirely data-driven: the MLIT survey contains no records from this distance range with simulated momentum flux values exceeding this threshold, which is physically consistent with the strong attenuation of tsunami hydrodynamic intensity at large distances from the coastline. The fitted 6PL curve is therefore shown only over the range of observed data, and extrapolation beyond $m_{sim} \approx 100\ \mathrm{m}^3/\mathrm{s}^2$ for this distance bin is not supported. This constraint does not affect the derivation of $\Delta\mathrm{IM}(d)$, which depends only on the fitted median IM parameter $MF = 49.4\ \mathrm{m}^3/\mathrm{s}^2$ for this bin—a value that falls well within the observed data range and is therefore reliably estimated. The proposed shift, expressed as a function of distance, provides a practical mechanism to incorporate near-coast effects without redefining the entire fragility model, offering both computational efficiency and physical interpretability in multi-scale tsunami vulnerability assessments.

The distance-dependent intensity shift $\Delta\mathrm{IM}(d)$ shown in Figure 13 is a contribution of this work, derived as follows. For each coastal distance bin, the 6-parameter logistic (6PL) fragility curve was fitted to the empirical damage survey data, yielding a median intensity measure MF (the momentum flux value at which failure probability equals 0.5) for each

 https://doi.org/10.3390/infrastructures11070221

bin. The shift for bin i is then defined as $\Delta\mathrm{IM}(d_i) = \mathrm{M}(d_i) - {M_r}^{ef}$, where ${M_r}^{ef} = 49.6\ \mathrm{m^3/s^2}$ is the median IM of the reference (semi-far-field) bin [1231, 1954] m, whose midpoint ${d_r}^{ef} = 1592.5$ m serves as the baseline. A negative ΔIM indicates a leftward shift in the fragility curve relative to the baseline, corresponding to higher vulnerability at the same hazard intensity. Three of the five distance bins were used for regression: [343, 734] m (midpoint 538.5 m, $MF = 17.0$, $\Delta\mathrm{IM} = -32.6$), [734, 1231] m (midpoint 982.5 m, $MF = 27.5$, $\Delta\mathrm{IM} = -22.1$), and [1231, 1954] m (midpoint 1592.5 m, $MF = 49.6$, $\Delta\mathrm{IM} = 0.0$). The nearest-coast bin [1, 343] m (midpoint 172 m, $MF = 21.1$) was deliberately excluded from the regression because its fitted median $MF = 21.1\ \mathrm{m^3/s^2}$ is higher than that of the adjacent [343, 734] m bin ($MF = 17.0\ \mathrm{m^3/s^2}$), producing a non-monotonic pattern inconsistent with the expected inland attenuation trend. This non-monotonicity in the immediate coastal zone is physically attributable to the dominance of impulsive bore forces, debris impact, and wave breaking in the first 343 m from the shoreline—loading mechanisms that are not adequately captured by the simulated momentum flux m_{sim} alone and that can produce severe damage even at moderate depth-velocity combinations. As a result, the median IM derived from 6PL fitting in this zone reflects a mixture of hydrodynamic and impulsive damage mechanisms, rather than the quasi-steady inundation loading that the momentum flux intensity measure is designed to represent. Forcing this bin into a monotonic linear model would therefore introduce a physically unjustified constraint. The far-field bin [1954, 4560] m ($MF = 49.4$, $\Delta\mathrm{IM} \approx 0.2$) was also excluded because its ΔIM is negligibly different from zero and would add no meaningful information to the regression slope.

Ordinary least-squares regression of ΔIM on $(d - {d_r}^{ef})$ across the three selected bins, with a free intercept, yields: $\Delta\mathrm{IM}(d) = 0.031(d - 1593) - 0.90\ (\mathrm{m^3/s^2})$, where d is the coastal distance in meters. The regression statistics are: slope $a = 0.031\ \mathrm{m^3 s^{-2}/m}$ ($SE = 0.004$, 95% CI [−0.013, 0.076]), intercept $b = -0.90\ \mathrm{m^3/s^2}$, $R^2 = 98.75\%$, $p = 0.071$, and RMSE = $1.52\ \mathrm{m^3/s^2}$. The near-zero intercept ($b = -0.90$) confirms that the fitted line passes close to the origin of the $(d - {d_r}^{ef}, \Delta\mathrm{IM})$ space, consistent with the definition that ΔIM = 0 at the reference distance. The p-value of 0.071 reflects the small sample size ($n = 3$ bins) rather than a weak physical relationship; the high R^2 and low RMSE confirm that a linear model captures the trend well within the available data. Leave-one-out (LOO) cross-validation across the three bins yields a LOO-RMSE of $5.79\ \mathrm{m^3/s^2}$, which represents the expected prediction error when the equation is applied to a bin not used in fitting; this provides an honest estimate of out-of-sample uncertainty given the limited number of calibration points.

The domain of applicability of this equation is $d \in [343, 1593]$ m from the coastline, corresponding to the range spanned by the three regression bins. Within this range the equation predicts ΔIM values between $-39.95\ \mathrm{m^3/s^2}$ (at $d = 343$ m) and $0\ \mathrm{m^3/s^2}$ (at $d = {d_r}^{ef}$). Extrapolation below 343 m is not supported by the regression, and the non-monotonic behavior of the nearest-coast bin suggests that a different physical model may be needed in that zone. Extrapolation beyond 1593 m is similarly unsupported, as the far-field bin indicates $\Delta\mathrm{IM} \approx 0$ for all distances greater than the reference. This equation should be understood as an illustration of the methodological concept calibrated to the 2011 Great East Japan dataset for wood-frame buildings; practitioners are encouraged to apply the same regression procedure to their own site-specific survey data to derive locally calibrated shift functions. Finally, it should be noted that the reference baseline corresponds to the semi-far-field bin of this dataset, not a pure far-field fragility curve, since all surveyed structures experienced coupled earthquake–tsunami loading to some degree. The shift coefficients are therefore calibrated against this semi-far-field reference, and their applicability to a genuine far-field baseline remains subject to further validation.

 https://doi.org/10.3390/infrastructures11070221

5. Calibration Challenges for Near-Field Tsunami Fragility

This section identifies the specific limitations and calibration uncertainties arising from the two study components presented in Sections 3 and 4. The successive simulation framework is demonstrated for a single US RC special moment-resisting frame archetype (T_1 = 0.94 s). While this archetype is well-characterized and consistent with prior work, the resulting fragility surfaces (Figures 4–7) cannot be generalized to other structural typologies without recalibration. The tsunami loading phase uses a quasi-static force-based pushover rather than a fully dynamic representation; this one-way coupling approach is physically appropriate for the rapid sequential loading of near-field events but does not capture potential dynamic amplification from the tsunami itself. Sensitivity to earthquake record characteristics is also a recognized limitation: as shown in Figure 7, long-duration ground motions (M9 Project records) produce more pronounced jumps at the fragility curve origin than regular-duration records (FEMA P-695), indicating that the choice of ground motion set affects the magnitude of pre-existing damage and therefore the conditional tsunami fragility surface. Expanding the framework to multiple archetypes and earthquake record sets remains a priority for future work. Empirical intensity measure uncertainty (Section 4) arises from a physically based output of a calibrated hydrodynamic simulation. As detailed in Section 4.1, the 2011 event lacked direct velocity measurements; the two velocity estimates used (*v_c*, a depth-velocity proxy, and *v_sim*, a hydrodynamic simulation output) each carry uncertainty as described therein. The simulated momentum flux *m_sim* used in Figures 10–13 is therefore model-derived rather than directly observed, and its accuracy is bounded by the fidelity of the hydrodynamic simulation and the quality of the bathymetric and topographic inputs used in calibration. Users of *m_sim*-based fragility relationships should be aware that the intensity measure inherits epistemic uncertainty from the simulation chain, not only from the survey data itself.

The distance-dependent intensity shift $\Delta\mathrm{IM}(d)$ is derived from only three distance bins with sufficient data coverage for reliable 6PL fitting. The leave-one-out cross-validation yields a LOO-RMSE of 5.79 $\mathrm{m}^3/\mathrm{s}^2$, reflecting the limited number of calibration points. The regression p-value of 0.071 is attributable to this small sample size rather than a weak physical relationship, but users should treat the specific coefficient (a = 0.031 $\mathrm{m}^3\mathrm{s}^{-2}/\mathrm{m}$) as an illustrative estimate rather than a precisely determined universal constant. The nearest-coast bin, [1, 343] m, was excluded from the regression due to a non-monotonic pattern driven by impulsive bore and debris loading mechanisms not captured by *m_sim*; a separate model may be required for this zone. The far-distance fragility curve is truncated at *m_sim* $\approx$ 100 $\mathrm{m}^3/\mathrm{s}^2$ due to data sparsity at high intensities for that distance bin, reflecting real attenuation of tsunami forcing at large inland distances but also limiting the curve's upper range.

The $\Delta\mathrm{IM}(d)$ framework and the ML feature importance analysis are specific to this typology and this event; direct application to RC frames, masonry, or steel buildings, or to different tsunami events and coastal geographies, requires recalibration. The survey data reflect coupled earthquake–tsunami loading for all records—the M_3 9.0 Tōhoku earthquake preceded inundation for every surveyed structure—meaning that the empirical fragility curves are conditioned on the prior seismic event and do not represent pure tsunami vulnerability. Validation against a true far-field baseline (distant-source event, no earthquake pre-conditioning) has not been performed and remains a key gap. The XGBoost classifier achieves a recall of only 49% for Class 1 (minor/slight damage, ~11% of records) because no class weighting or oversampling was applied; practitioners using the classifier for operational damage prediction should be aware that minor damage is systematically under-predicted relative to the majority classes, and should consider

https://doi.org/10.3390/infrastructures11070221

applying class-balancing strategies for applications where minor damage identification is critical.

6. Summary and Conclusions

This paper advanced near-field tsunami fragility modeling through three specific contributions that bridge physics-based simulation and empirical damage survey analysis. First, a successive earthquake–tsunami simulation framework was applied to a US RC special moment-resisting frame archetype to generate conditional fragility surfaces that explicitly account for pre-existing seismic damage without relying on Bayes-type probabilistic decompositions that are not practically estimable for near-field sequences. The resulting surfaces reveal a characteristic jump at the origin—a non-zero baseline failure probability at zero tsunami force—that grows with increasing earthquake intensity and is further amplified by long-duration ground motions, confirming that pre-existing seismic damage is a physically meaningful and non-negligible determinant of tsunami vulnerability under near-field conditions. Second, analysis of the 2011 Great East Japan MLIT damage survey dataset demonstrated that tsunami fragility behavior is inherently spatially non-stationary: failure probabilities for wood-frame buildings increase systematically as coastal distance decreases, consistent with the amplified impulsive and hydrodynamic forces experienced in the immediate coastal zone. A distance-dependent intensity-shift function was derived through regression across three distance bins, providing a practical mechanism to adapt a single reference fragility curve to site-specific coastal locations without redefining the entire model. Third, machine-learning-assisted feature importance analysis using an XGBoost classifier confirmed that flow depth and velocity are the dominant predictors of structural damage, with momentum flux acting as the controlling composite parameter, and that distance from the coastline constitutes a significant secondary determinant—a finding that aligns with both the simulation results and the physical attenuation behavior observed in the survey data.

Several important calibration uncertainties and scope limitations should be recognized when interpreting these results. The simulation component is demonstrated for a single archetype and cannot be generalized to other structural typologies without recalibration; the one-way coupling approach, while physically appropriate for the rapid sequential loading of near-field events, does not capture potential dynamic amplification from tsunami inundation itself. The empirical component relies on velocity estimates that carry inherent uncertainty (as detailed in Sections 4.1 and 5), meaning that momentum-flux-dependent fragility relationships inherit epistemic uncertainty from the estimation chain. The distance-dependent shift function is calibrated from only three distance bins, and the resulting leave-one-out cross-validation error should be treated as an illustrative estimate rather than a precisely determined universal constant; the nearest-coast zone was excluded due to non-monotonic behavior driven by impulsive bore and debris loading mechanisms not captured by the simulated momentum flux. Furthermore, all empirical fragility relationships are specific to wood-frame construction in the 2011 Tōhoku event, conditioned on the prior magnitude 9.0 earthquake, and have not been validated against a pure far-field tsunami baseline.

Despite these limitations, the methodological framework developed in this study offers a physically consistent and data-informed foundation for near-field tsunami fragility modeling that is directly applicable—subject to typology-specific recalibration—to loss and resilience estimation platforms such as IN-CORE and HAZUS, and to risk-informed coastal infrastructure design in subduction-zone regions. The convergence of three independent lines of evidence—simulation-derived fragility surfaces, empirical survey-based damage

 https://doi.org/10.3390/infrastructures11070221

patterns, and machine-learning feature rankings—around the same governing physical mechanisms provides confidence in the robustness of the core findings. Future work should prioritize extending the successive simulation framework to additional structural typologies including wood-frame and masonry archetypes, incorporating dynamic tsunami loading representations, obtaining direct velocity measurements through instrumented field campaigns or high-resolution video analysis, and validating the distance-dependent shift framework against far-field tsunami datasets and different coastal geographies to establish the boundary conditions of its applicability.

Author Contributions: Conceptualization, M.H. and J.W.v.d.L.; methodology, M.H. and J.W.v.d.L.; formal analysis, M.H.; investigation, M.H.; writing—original draft preparation, M.H.; writing—review and editing, J.W.v.d.L.; visualization, M.H.; supervision, J.W.v.d.L.; project administration, J.W.v.d.L.; funding acquisition, J.W.v.d.L. All authors have read and agreed to the published version of the manuscript.

Funding: This research was funded by the U.S. National Institute of Standards and Technology (NIST) through the Center for Risk-Based Community Resilience Planning, a NIST-funded Center of Excellence, under Cooperative Agreements with Colorado State University (Financial Assistance Award Nos. 70NANB15H044 and 70NANB20H008).

Data Availability Statement: The data, models, and code that support the findings of this study are available from the corresponding author upon reasonable request.

Acknowledgments: The Center for Risk-Based Community Resilience Planning is an NIST-funded Center of Excellence; the Center is funded through a cooperative agreement between the U.S. National Institute of Standards and Technology and Colorado State University.. The views expressed are those of the authors and may not represent the official position of the National Institute of Standards and Technology or the U.S. Department of Commerce.

Conflicts of Interest: Author Mojtaba Harati was employed by Verisk Catastrophe and Risk Solutions. The research presented in this study did not use any proprietary data, models, or knowledge from Verisk. The remaining authors declare that the research was conducted in the absence of any commercial or financial relationships that could be construed as a potential conflict of interest.

References

1. Alam, M.S.; Barbosa, A.R.; Scott, M.H.; Cox, D.T.; van de Lindt, J.W. Multi-hazard Earthquake-Tsunami Structural Fragility Assessment Framework. In *Proceedings of the 13th International Conference on Applications of Statistics and Probability in Civil Engineering (ICASP13)*; Korean Institute of Bridge and Structural Engineers: Seoul, Republic of Korea, 2019; Volume 1, pp. 1318–1325. [CrossRef]
2. Amini, M.; Sanderson, D.R.; Cox, D.T.; Barbosa, A.R.; Rosenheim, N. Methodology to incorporate seismic damage and debris to evaluate strategies to reduce life safety risk for multi-hazard earthquake and tsunami. *Nat. Hazards* **2023**, *120*, 9187–9222. [CrossRef]
3. Charvet, I.; Suppasri, A.; Kimura, H.; Sugawara, D.; Imamura, F. A multivariate generalized linear tsunami fragility model for Kesennuma City based on maximum flow depths, velocities and debris impact, with evaluation of predictive accuracy. *Nat. Hazards* **2015**, *79*, 2073–2099. [CrossRef]
4. Foytong, P.; Ruangrassamee, A.; Lukkunaprasit, P.; Thanasisathit, N. Behaviours of reinforced-concrete building under tsunami loading. *IES J. Part Civ. Struct. Eng.* **2015**, *8*, 101–110. [CrossRef]
5. Geist, E.L.; Parsons, T. Probabilistic Analysis of Tsunami Hazards*. *Nat. Hazards* **2006**, *37*, 277–314. [CrossRef]
6. Grezio, A.; Babeyko, A.; Baptista, M.A.; Behrens, J.; Costa, A.; Davies, G.; Geist, E.L.; Glimsdal, S.; González, F.I.; Griffin, J.; et al. Probabilistic Tsunami Hazard Analysis: Multiple Sources and Global Applications. *Rev. Geophys.* **2017**, *55*, 1158–1198. [CrossRef]
7. Cornell, C.A. Engineering seismic risk analysis. *Bull. Seismol. Soc. Am.* **1968**, *58*, 1583–1606. [CrossRef]
8. Vamvatsikos, D.; Cornell, C.A. Incremental dynamic analysis. *Earthq. Eng. Struct. Dyn.* **2002**, *31*, 491–514. [CrossRef]
9. Ibarra, L.F.; Krawinkler, H. *Global Collapse of Frame Structures Under Seismic Excitations*; University of California: Berkeley, CA, USA, 2005.

10. Mori, N.; Goda, K.; Cox, D. Recent Process in Probabilistic Tsunami Hazard Analysis (PTHA) for Mega Thrust Subduction Earthquakes. In *The 2011 Japan Earthquake and Tsunami: Reconstruction and Restoration: Insights and Assessment After 5 Years*; Santiago-Fandiño, V., Sato, S., Maki, N., Iuchi, K., Eds.; Springer International Publishing: Cham, Switzerland, 2018; pp. 469–485. [CrossRef]
11. Behrens, J.; Løvholt, F.; Jalayer, F.; Lorito, S.; Salgado-Gálvez, M.A.; Sørensen, M.; Abadie, S.; Aguirre-Ayerbe, I.; Aniel-Quiroga, I.; Babeyko, A.; et al. Probabilistic Tsunami Hazard and Risk Analysis: A Review of Research Gaps. *Front. Earth Sci.* **2021**, *9*, 628772. [CrossRef]
12. Reis, C.; Baptista, M.A.; Lopes, M.; Oliveira, C.S.; Clain, S. Cascade earthquake and tsunami hazard assessment: A deterministic perspective for engineering purposes. *Int. J. Disaster Risk Reduct.* **2022**, *75*, 102952. [CrossRef]
13. Ma, T.; Shen, L.; Chen, Z.; Liang, D. Review on tsunami research and risk mitigation: From prediction models to resilient coastal communities. *npj Nat. Hazards* **2026**, *3*, 34. [CrossRef]
14. Zamora, N.; Grezio, A.; Papathoma-Köhle, M.; Jalayer, F.; Salmanidou, D.; Parsons, T.; Geist, E.L.; Selva, J.; Sørensen, M.B.; Rafliana, I. Frameworks for Assessing Tsunami Hazard and Risk. In *Probabilistic Tsunami Hazard and Risk Analysis: A Cookbook*; Sørensen, M.B., Behrens, J., Jalayer, F., Løvholt, F., Lorito, S., Rafliana, I., Salgado-Gálvez, M.A., Selva, J., Eds.; Springer Nature: Cham, Switzerland, 2026; pp. 13–86. [CrossRef]
15. Gibbons, S.J.; Lorito, S.; Macías, J.; Løvholt, F.; Selva, J.; Volpe, M.; Sánchez-Linares, C.; Babeyko, A.; Brizuela, B.; Cirella, A.; et al. Probabilistic Tsunami Hazard Analysis: High Performance Computing for Massive Scale Inundation Simulations. *Front. Earth Sci.* **2020**, *8*, 591549. [CrossRef]
16. Gunawan, W.C.; Alhamid, A.K.; Akiyama, M.; Permana, M.F.; Farid, M.; Kurniawan, A.; Adityawan, M.B. Probabilistic tsunami risk assessment based on supervised learning considering nonstationary sea-level rise and multiple source rupture: Application to Denpasar City of Bali. *Prog. Disaster Sci.* **2026**, *29*, 100505. [CrossRef]
17. De Risi, R.; Goda, K. Probabilistic Earthquake-tsunami Hazard Assessment: The First Step Towards Resilient Coastal Communities. *Procedia Eng.* **2017**, *198*, 1058–1069. [CrossRef]
18. Renn, O. New challenges for risk analysis: Systemic risks. *J. Risk Res.* **2021**, *24*, 127–133.
19. Rafliana, I.; Jalayer, F.; Cerase, A.; Cugliari, L.; Baiguera, M.; Salmanidou, D.; Necmioğlu, Ö.; Ayerbe, I.A.; Lorito, S.; Fraser, S.; et al. Tsunami risk communication and management: Contemporary gaps and challenges. *Int. J. Disaster Risk Reduct.* **2022**, *70*, 102771. [CrossRef]
20. Jalayer, F.; Ebrahimian, H.; Trevlopoulos, K.; Bradley, B. Empirical tsunami fragility modelling for hierarchical damage levels. *Nat. Hazards Earth Syst. Sci.* **2023**, *23*, 909–931. [CrossRef]
21. Charvet, I.; Macabuag, J.; Rossetto, T. Estimating Tsunami-Induced Building Damage through Fragility Functions: Critical Review and Research Needs. *Front. Built Environ.* **2017**, *3*, 36. [CrossRef]
22. Attary, N.; Van De Lindt, J.W.; Barbosa, A.R.; Cox, D.T.; Unnikrishnan, V.U. Performance-Based Tsunami Engineering for Risk Assessment of Structures Subjected to Multi-Hazards: Tsunami following Earthquake. *J. Earthq. Eng.* **2021**, *25*, 2065–2084. [CrossRef]
23. O'Brien, K.; Eriksen, S.; Nygaard, L.P.; Schjolden, A. Why different interpretations of vulnerability matter in climate change discourses. *Clim. Policy* **2007**, *7*, 73–88. [CrossRef]
24. Xiong, Y.; Liang, Q.; Park, H.; Cox, D.; Wang, G. A deterministic approach for assessing tsunami-induced building damage through quantification of hydrodynamic forces. *Coast. Eng.* **2019**, *144*, 1–14. [CrossRef]
25. Harati, M.; van de Lindt, J.W. Methodology to generate earthquake-tsunami fragility surfaces for community resilience modeling. *Eng. Struct.* **2024**, *305*, 117700. [CrossRef]
26. Millar, O.; Ma, L.; Karmpadakis, I. Tsunami-induced loads on coastal structures: Experimental investigation and prediction. *Ocean Eng.* **2025**, *336*, 121762. [CrossRef]
27. Torabbeigi, M.; Amir Hosseini, M.; Abolfathi, S. Modelling Tsunami wave impacts on the resilience of critical coastal protection infrastructure. *Ocean Eng.* **2026**, *343*, 123140. [CrossRef]
28. Tang, C.; Jia, Y.; Fei, L.; Liu, P.; Zhang, C.; Fang, Q.; Guo, A. Numerical investigation of breaking wave impact on coastal bridge superstructures with box girder. *Ocean Eng.* **2026**, *344*, 123740. [CrossRef]
29. Xiong, W.; Cai, C.S.; Zhang, R.; Shi, H.; Xu, C. Review of Hydraulic Bridge Failures: Historical Statistic Analysis, Failure Modes, and Prediction Methods. *J. Bridge Eng.* **2023**, *28*, 03123001. [CrossRef]
30. Jia, Y.; Ruan, H.; Fei, L.; Li, J.; Liu, P.; Fang, Q.; Guo, A. Experimental investigation of wave forces on superstructures of coastal bridges with curved box–girders. *Ocean Eng.* **2026**, *357*, 125618. [CrossRef]
31. Rodwell, J.; Williams, J.H.; Paulik, R. Empirical Fragility Assessment of Three-Waters and Railway Infrastructure Damaged by the 2015 Illapel Tsunami, Chile. *J. Mar. Sci. Eng.* **2023**, *11*, 1991. [CrossRef]

 https://doi.org/10.3390/infrastructures11070221

32. Oddo, M.C.; Cavaleri, L. Earthquake-tsunami combined fragility curves for coastal masonry buildings: A numerical-analytical approach. *Bull. Earthq. Eng.* **2025**, *24*, 2709–2734. [CrossRef]
33. Habibnia, M.; van de Lindt, J.W. Enhanced risk mapping for hurricane surge losses using synthesized probabilistic and machine learning models. *Int. J. Disaster Risk Reduct.* **2025**, *123*, 105523. [CrossRef]
34. Habibnia, M.; van de Lindt, J.W. Physics-Informed Stochastic Modeling of Tornado-Induced Building Losses. *J. Struct. Eng.* **2026**, *152*, 04026096. [CrossRef]
35. Habibnia, M.; van de Lindt, J.W. An interpretable framework for tornado loss estimation using parametric surrogate models and dual-objective adaptive smart sampling. *Comput.-Aided Civ. Infrastruct. Eng.* **2026**, *45*, 100047. [CrossRef]
36. Habibnia, M. Generalized Probabilistic Loss Modeling and Adaptive Resilience Strategies for the Built Environment. Ph.D. Thesis, Colorado State University, Fort Collins, CO, USA, 2026.
37. Habibnia, M.; van de Lindt, J.W. Innovative risk assessment approach for storm surge losses using adaptive models and machine learning algorithms. In Proceedings of the 14th International Conference on Structural Safety and Reliability—ICOSSAR'25, Los Angeles, CA, USA, 1–6 June 2025.
38. Sannikova, N.K.; Segur, H.; Arcas, D. Influence of Tsunami Aspect Ratio on Near and Far-Field Tsunami Amplitude. *Geosciences* **2021**, *11*, 178. [CrossRef]
39. Sharrocks, P.D.; Peakall, J.; Hodgson, D.M.; Barlow, N.L.M. Tsunami versus storms: Diagnostic sedimentary criteria in coastal lakes, lagoons and sinkhole deposits. *Earth-Sci. Rev.* **2025**, *271*, 105277. [CrossRef]
40. Laksono, F.A.T.; Mishra, M.; Fadlin; Kovács, J. Exploring the tsunami generation potential of major faults in the sicilian channel using 3D numerical modeling. *Ocean Model.* **2026**, *199*, 102625. [CrossRef]
41. Tappin, D.R. The Generation of Tsunamis. In *Encyclopedia of Maritime and Offshore Engineering*; John Wiley & Sons, Ltd.: Hoboken, NJ, USA, 2017; pp. 1–10. [CrossRef]
42. Vilibić, I.; Zemunik Selak, P.; Šepić, J. Meteorological Tsunamis: From Local Hazard to Global Relevance. *Rev. Geophys.* **2025**, *63*, e2024RG000867. [CrossRef]
43. Schindelé, F.; Kong, L.; Lane, E.M.; Paris, R.; Ripepe, M.; Titov, V.; Bailey, R. A Review of Tsunamis Generated by Volcanoes (TGV) Source Mechanism, Modelling, Monitoring and Warning Systems. *Pure Appl. Geophys.* **2024**, *181*, 1745–1792. [CrossRef]
44. Abdelhafeez, M.; Park, H.; Sherif, M.; Ghanem, A.; Moon, D.-S. Effects of tsunami wave and bathymetric parameters on hydrodynamic forces and structural fragility. *J. Build. Eng.* **2026**, *118*, 115077. [CrossRef]
45. Kolukula, S.S.; Murty, P.L.N.; Kumar, T.S.; Ramarao, E.P.; M. V, R.M. Tsunami modelling over global oceans. *R. Soc. Open Sci.* **2025**, *12*, 241128. [CrossRef] [PubMed]
46. Tsunami Hazard Assessment Based on Wave Generation, Propagation, and Inundation Modeling for the U.S. East Coast (NUREG/CR-7222)|Nuclear Regulatory Commission. Available online: https://www.nrc.gov/reading-rm/doc-collections/nuregs/contract/cr7222/index (accessed on 22 March 2026).
47. Koshimura, S.; Oie, T.; Yanagisawa, H.; Imamura, F. Developing Fragility Functions for Tsunami Damage Estimation Using Numerical Model and Post-Tsunami Data from Banda Aceh, Indonesia. *Coast. Eng. J.* **2009**, *51*, 243–273. [CrossRef]
48. Sturm, M.; Gems, B.; Keller, F.; Mazzorana, B.; Fuchs, S.; Papathoma-Köhle, M.; Aufleger, M. Experimental analyses of impact forces on buildings exposed to fluvial hazards. *J. Hydrol.* **2018**, *565*, 1–13. [CrossRef]
49. Koh, M.J.; Park, H.; Kim, A.S. Tsunami-driven debris hazard assessment at a coastal community: Focusing on shipping container debris hazards at Honolulu Harbor, Hawaii. *Coast. Eng.* **2024**, *187*, 104408. [CrossRef]
50. Nistor, I.; Goseberg, N.; Stolle, J. Tsunami-Driven Debris Motion and Loads: A Critical Review. *Front. Built Environ.* **2017**, *3*, 2. [CrossRef]
51. De Risi, R.; Goda, K.; Yasuda, T.; Mori, N. Is flow velocity important in tsunami empirical fragility modeling? *Earth-Sci. Rev.* **2017**, *166*, 64–82. [CrossRef]
52. Park, H.; Cox, D.T. Probabilistic assessment of near-field tsunami hazards: Inundation depth, velocity, momentum flux, arrival time, and duration applied to Seaside, Oregon. *Coast. Eng.* **2016**, *117*, 79–96. [CrossRef]
53. Del Zoppo, M.; Di Ludovico, M.; Lignola, G.P.; Prota, A. Time-dependent tsunami fragility analysis for reinforced concrete building stock. *Eng. Struct.* **2025**, *330*, 119931. [CrossRef]
54. Harati, M.; van de Lindt, J.W. Data-driven machine learning for multi-hazard fragility surfaces in seismic resilience analysis. *Comput.-Aided Civ. Infrastruct. Eng.* **2024**, *40*, 698–720. [CrossRef]
55. Alam, M.S.; Barbosa, A.R.; Scott, M.H.; Cox, D.T.; van de Lindt, J.W. Development of Physics-Based Tsunami Fragility Functions Considering Structural Member Failures. *J. Struct. Eng.* **2018**, *144*, 04017221. [CrossRef]
56. Alam, M.S.; Winter, A.O.; Galant, G.; Shekhar, K.; Barbosa, A.R.; Motley, M.R.; Eberhard, M.O.; Cox, D.T.; Arduino, P.; Lomonaco, P. Tsunami-Like Wave-Induced Lateral and Uplift Pressures and Forces on an Elevated Coastal Structure. *J. Waterw. Port Coast. Ocean Eng.* **2020**, *146*, 04020008. [CrossRef]

57. Park, S.; van de Lindt, J.W.; Cox, D.; Gupta, R.; Aguiniga, F. Successive Earthquake-Tsunami Analysis to Develop Collapse Fragilities. *J. Earthq. Eng.* **2012**, *16*, 851–863. [CrossRef]
58. Belliazzi, S.; Lignola, G.P.; Palermo, D. Simplified structural analysis framework for buildings under combined earthquake and tsunami loads. *Structures* **2025**, *77*, 109206. [CrossRef]
59. Attary, N.; Unnikrishnan, V.U.; van de Lindt, J.W.; Cox, D.T.; Barbosa, A.R. Performance-Based Tsunami Engineering methodology for risk assessment of structures. *Eng. Struct.* **2017**, *141*, 676–686. [CrossRef]
60. FEMA P-646 Guidelines for Design of Structures for Vertical Evacuation from Tsunamis, 3rd Edition | WBDG—Whole Building Design Guide. 2019. Available online: https://www.wbdg.org/ffc/dhs/criteria/femap646 (accessed on 30 November 2022).
61. Harati, M.; van de Lindt, J.W. Impact of Long-duration Earthquakes on Successive Earthquake-tsunami Fragilities for Reinforced Concrete Frame Archetypes. *J. Struct. Eng.* **2024**, *150*, 04024126.
62. Haselton, C.B.; Liel, A.B.; Deierlein, G.G.; Dean, B.S.; Chou, J.H. Seismic Collapse Safety of Reinforced Concrete Buildings. I: Assessment of Ductile Moment Frames. *J. Struct. Eng.* **2011**, *137*, 481–491. [CrossRef]
63. Harati, M.; van de Lindt, J.W. Fragility Function Development of RC Building Portfolio for Use in Earthquake-Tsunami Community Resilience Studies. *J. Perform. Constr. Facil.* **2024**, *39*, 04025019.
64. Harati, M.; van de Lindt, J.W. Community-Level Resilience Analysis using Earthquake-Tsunami Fragility Surfaces. *Resilient Cities Struct.* **2024**, *3*, 101–115.
65. Dias, W.P.S.; Yapa, H.D.; Peiris, L.M.N. Tsunami vulnerability functions from field surveys and Monte Carlo simulation. *Civ. Eng. Environ. Syst.* **2009**, *26*, 181–194. [CrossRef]
66. Suppasri, A.; Mas, E.; Charvet, I.; Gunasekera, R.; Imai, K.; Fukutani, Y.; Abe, Y.; Imamura, F. Building damage characteristics based on surveyed data and fragility curves of the 2011 Great East Japan tsunami. *Nat. Hazards* **2013**, *66*, 319–341. [CrossRef]
67. Scorzini, A.R.; Di Bacco, M.; Sugawara, D.; Suppasri, A. Extended MLIT dataset for the 2011 Great East Japan tsunami with inclusion of velocity information. *Mendeley Data* **2024**, *1*. [CrossRef]
68. Scorzini, A.R.; Di Bacco, M.; Sugawara, D.; Suppasri, A. Machine learning and hydrodynamic proxies for enhanced rapid tsunami vulnerability assessment. *Commun. Earth Environ.* **2024**, *5*, 301. [CrossRef]
69. van de Lindt, J.W.; Kruse, J.; Cox, D.T.; Gardoni, P.; Lee, J.S.; Padgett, J.; McAllister, T.P.; Barbosa, A.; Cutler, H.; Van Zandt, S.; et al. The interdependent networked community resilience modeling environment (IN-CORE). *Resilient Cities Struct.* **2023**, *2*, 57–66. [CrossRef]

Disclaimer/Publisher's Note: The statements, opinions and data contained in all publications are solely those of the individual author(s) and contributor(s) and not of MDPI and/or the editor(s). MDPI and/or the editor(s) disclaim responsibility for any injury to people or property resulting from any ideas, methods, instructions or products referred to in the content.

infrastructures

MDPI

Article

An Ensemble Learning-Based Approach to Quantify Post-Earthquake Functional Recovery of a Steel Moment-Resisting Frame Inventory

Mohsen Zaker Esteghamati * and Shiva Baddipalli

Department of Civil and Environmental Engineering, Utah State University, Logan, UT 84322, USA; e-shiva.baddipalli@usu.edu
* Correspondence: mohsen.zaker@usu.edu

Abstract

The quest for seismic resiliency requires designing for performance objectives beyond life safety. Functional recovery is an emerging objective often defined as the time required to restore a building's basic functionality to the pre-event level. Nevertheless, quantifying functional recovery is a complex, computationally intensive process that is challenging to integrate into a standard design workflow. This study develops a machine learning (ML) model to map design and geometric features of steel special moment-resisting frames (SMRFs) to their functional recovery under two hazard levels: design-basis (DBE) and maximum considered (MCE) earthquakes. First, functional recovery time was quantified for an inventory of 100 steel SMRFs with varying heights by integrating FEMA P-58 loss-based methodology with the ATC-138 framework. The building information and calculated recovery times were then used in a standard ML pipeline including feature selection, hyperparameter tuning, cross-validation, model evaluation, and model explainability. The results suggest that the ML model can accurately estimate functional recovery using design and geometric features, achieving R^2 values of 89% and 93% on the test set for DBE and MCE levels, respectively. In addition, for the studied regular SMRF buildings, the results indicate that building weight and the average strong-column weak-beam ratio are influential design parameters that govern functional recovery time, suggesting that a recovery-oriented design of steel SMRFs may benefit from minimizing building weight and avoiding overt column upsizing.

Keywords: functional recovery; machine learning; steel moment-resisting frames; explainability; ensemble learners

1. Introduction

A consistent lesson from past earthquakes is that while modern building codes limit the probability of collapse and subsequent fatalities, they do not adequately account for buildings' recovery time, resulting in significant economic and societal impacts [1,2]. For example, the 1995 Kobe earthquake left approximately 15,000 households residing in temporary housing three years post-event, while the 2011 Christchurch earthquake resulted in two years of disruptions to central business operations and the permanent closure of 11% of businesses [3,4]. To address these challenges, there is a critical need for performance objectives that extend beyond preventing structural collapse toward

encompassing recovery-based goals [5–7]. An emerging recovery performance objective is "functional recovery", often defined as the ability of a building to regain its *intended* function within a target timeframe after a disruptive event [8]. The recent NEHRP-recommended provisions (FEMA P-2082 [9]) suggest that functional recovery should serve as the primary basis for seismic design by assigning target recovery times to new buildings based on their risk category.

To integrate functional recovery into design, computational methods are needed to quantify building functionality and the specific recovery time with limited information. Currently, various recovery assessment frameworks have been proposed, but technical nuances remain [10–12]. Often built on a performance-based earthquake engineering (PBEE) framework [13,14], several example frameworks include REDi [15], ATC-138 [16], TREADS [10], and F-rec [12]. These frameworks link seismic damage to downtime and recovery by accounting for possible trajectories to restore building functionality states. Nevertheless, they differ significantly in their assumptions and approaches, and it is expected that the estimated recovery time for a single building varies considerably across these methods [17,18]. In addition, all existing recovery assessment models are computationally intensive, requiring extensive simulations and large amounts of data, limiting their use for design-space exploration and parametric studies at the building inventory scale [19]. This computational bottleneck creates a critical barrier to integrating functional recovery into the design process, particularly when engineers need to rapidly evaluate multiple design alternatives.

Several studies aim to quantify the recovery of different building types using advanced computational approaches. For example, Molina-Hutt et al. showed that tall buildings designed to current codes may experience significant time delays and suggested that a stricter design drift limit may mitigate this issue [20]. Blowes et al. proposed a risk-based methodology to quantify functional recovery using downtime simulation outputs and demonstrated that modern RC shear wall buildings still exhibit substantial downtime, particularly under moderate events [21]. Echeverria et al. evaluated functional recovery for retrofitting of existing buildings, and highlighted the importance of owner priorities, long-term occupancy considerations, and community resilience objectives in motivating recovery-oriented retrofit strategies [22]. Nevertheless, these studies still develop or leverage labor-intensive and complex simulations and probabilistic frameworks that are often inaccessible to engineering practitioners in design offices.

Machine learning (ML)-based methods offer a promising approach to developing efficient surrogate models that map building properties to seismic performance, substantially reducing the computational and technical burdens of integrating them into a design workflow [23]. For example, Forooghi et al. used a multi-output neural network to predict elastic and collapse load multipliers as structural vulnerability indicators directly from structural parameters [24]. Esteghamati and Flint developed ML models to map a limited set of geometric and design features to expected annual loss for an inventory of 720 mid-rise concrete moment-resisting frames designed for Charleston, SC [25]. Later, Esteghamati and Baddipalli demonstrated that ML can similarly map design and geometric features of steel moment-resisting frames to seismic response, fragility, and loss [26]. Nevertheless, only limited work focused on mapping recovery-based metrics to building design. For example, Issa et al. developed an ML-based optimization framework to support recovery-based design and applied it to a single office building case study. They showed that increasing structural strength through the importance factor is detrimental, whereas nonstructural enhancements are needed [27]. Tang et al. developed an ML-based surrogate that maps primary design variables to a building resilience index to support resilience-oriented pre-

 https://doi.org/10.3390/infrastructures11070213

liminary design, and interpret the model using SHAP [28]. Similarly, Pham and Becker used Gaussian process surrogate modeling to explore the relationship between the design of seismically isolated steel buildings and functionality [29].

This study develops an ensemble-learning-based ML model to estimate post-earthquake functional recovery time for steel SMRF buildings, based on building geometry and design. Additionally, using a standard explainability technique [30], the impact of different parameters on functional recovery time is examined. In particular, the influence of key design parameters is measured at two hazard levels: the maximum considered earthquake (MCE) and the design-based earthquake (DBE). Therefore, this study presents two novel contributions. First, it evaluates whether ML models can accelerate recovery-based design as computationally efficient surrogate models for steel SMRFs. Second, using explainability, this study aims to investigate the key parameters a designer can control to improve post-earthquake recovery of steel SMRFs, laying the foundation for additional research and guidance on future recovery-based design methodologies for steel SMRFs.

2. Methodology

Figure 1 presents the overall methodology, which consists of two main workflows: (1) recovery-based assessment by combining the output from fragility and loss assessment of FEMA P-58 [31] with ATC-138 [16] recovery quantification; (2) training and validations of an ML model using design and geometric features as inputs and recovery times as targets. The first workflow calculates functional recovery time for a building inventory of steel SMRFs and passes the building information and recovery data to the second workflow as a database for training and validating the ML model. Details regarding each workflow will be presented next.

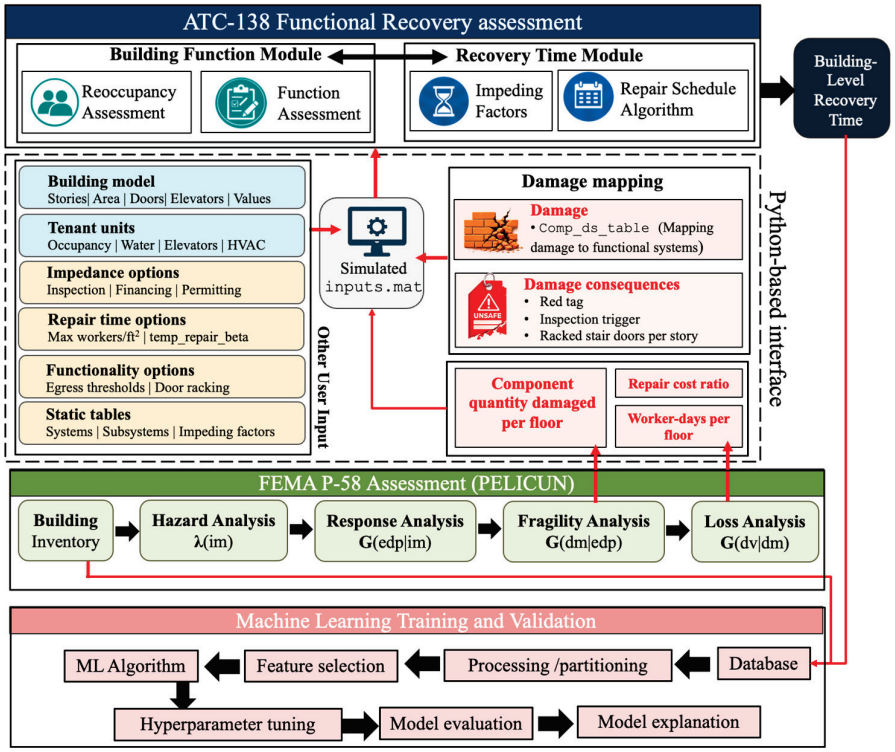

Figure 1. Schematics of the computational workflows used in this study.

https://doi.org/10.3390/infrastructures11070213

2.1. Building Inventory

This study leverages an inventory of 100 steel SMRFs from a database developed by Guan et al. [32]. The database comprises 1-, 5-, 9-, 14-, and 19-story buildings with typical story heights of 13 ft and first-story heights of 13 ft, 19.5 ft, and 26 ft. Each building consists of five bays in both longitudinal and transverse directions, with SMRFs located along the perimeter. The number of SMRF bays varies between 1, 3, and 5, with three bay widths of 20 ft, 30 ft, and 40 ft. All buildings were designed for a site in downtown Los Angeles, California, Site Class D with spectral accelerations of S_s = 2.25 g and S_1 = 0.6 g.

The database contains two-dimensional nonlinear models developed in OpenSees [33]. Since the buildings have regular, symmetric plans with perimeter lateral force-resisting systems resulting in minimal torsional and biaxial coupling, the two orthogonal directions are treated independently, and the two-dimensional models are analyzed separately. Nonlinear behavior of the frame member is represented using a concentrated plasticity formulation with plastic hinges at the member ends. The plastic hinges were defined using Ibarra–Medina–Krawinkler material model [34], which captures strength and stiffness deterioration under monotonic and cyclic loading. Second-order (P-Δ) effects of the tributary gravity loads are incorporated through a leaning column connected to the frame. Nonlinear time-history analyses were conducted using ground motions from 12 past California earthquakes. These GMs were scaled to three hazard levels: maximum considered earthquake (MCE), design-basis earthquake (DBE), and service-level earthquake (SLE) [32]. The results of the nonlinear time history analysis were post-processed, and three engineering demand parameters (EDPs) were obtained: peak inter-story drift ratio (PIDR), peak floor acceleration (PFA), and residual inter-story drift ratio (RIDR), which serve as inputs for subsequent recovery analyses. Additional information regarding the database can be found in [32].

2.2. Recovery Assessment

The methodology creates an interface to integrate PBEE loss assessment using open-source *Pelicun* (*ver 3.3*) [35] code with the implementation of the ATC-138 [11,16] functional recovery framework to generate building-level recovery time targets (Figure 1). To this end, the EDPs from nonlinear models were translated into seismic demand parameters at DBE and MCE hazard levels using a linear regression model in logarithmic space [36,37]. For each building, these demand models were then used to perform damage and loss assessment in Pelicun with 10,000 Monte Carlo realizations, generating quantities of damaged components at each damage state, repair times in worker-days, and building-level repair cost ratios. The EDPs were resolved at each floor and serve as the inputs to the component-level damage assessment, from which building-level recovery is obtained by propagating the story-resolved damage through the ATC-138 building-function fault tree and repair-scheduling algorithm. In this way, story access, tenant safety, tenant function, repair sequencing, and impediment factors were all evaluated based on the floor-level demands provided by the two-dimensional models. Damage consequences, including red-tag assignments and inspection triggers, were computed following the virtual inspection methodology of Cook et al. [38]. These data were then fed into two computational modules of the ATC-138 framework:

(1) The building function module determines the performance state through a hierarchical fault-tree architecture with four stages: (i) building safety, which evaluates building-wide safety issues, including unsafe placards, exterior falling hazards, and fire suppression failures; (ii) story access, which checks floor accessibility via stairs and doors; (iii) tenant safety, which identifies local safety hazards within individual

 https://doi.org/10.3390/infrastructures11070213

tenant spaces; and (iv) tenant function, which evaluates whether six key building systems (exterior envelope, interior condition, elevators, plumbing, electrical, and HVAC) support the tenant's intended use.

(2) The recovery time module estimates the time to restore each performance state through explicit modeling of (i) impeding factors such as inspection, temporary repairs, engineering mobilization, financing, permitting, contractor mobilization, and regional demand surges, and (ii) a repair scheduling algorithm that prioritizes repairs based on their impact on building functionality.

The median recovery times from Monte Carlo realizations for each building at each hazard level constitute the target variables for subsequent ML model development. In particular, two recovery-based metrics were defined as the median number of days to achieve functional recovery at DBE and MCE. Table 1 presents the assumptions used to estimate functional recovery. The resulting recovery times are most sensitive to the distributions of impeding factors in the ATC-138 recovery time module, which can exceed the active repair duration. Impeding factors, such as financing, permitting, engineering, contractor mobilization, and regional demand surges, are generally the largest contributors, with demand surges lengthening mobilization at higher hazard levels. The inspection and red-tag assumptions influence the onset of repairs, while the repair scheduling logic and the FEMA P-58 component consequence data influence the active repair duration. All buildings in the inventory were assessed under identical assumptions. Therefore, these choices primarily shift the absolute magnitudes of the recovery times rather than the relative differences among buildings, and the design–recovery relationships learned by the surrogate are expected to be more robust to these assumptions than the absolute recovery time values. Table 2 presents the distributional information on the estimated functional recovery times for different building classes at each hazard level. For each case, the median, 25th percentile (Q1), 75th percentile (Q3), minimum, and maximum values are reported. Overall, as building height increases, these values and ranges increase.

2.3. Machine Learning Model Training and Validation

An ensemble learner algorithm (Random Forest, RF) and a baseline multiple linear regression (MLR) model were used in this study to map building-level functional recovery at DBE and MCE to geometric and design features. The MLR model serves as a reference model to evaluate whether an ML model provides better mapping for this problem than a conventional statistical approach. RFs [39] extend the concept of decision trees and are a bagging-based ensemble learner. RFs aggregate the output from a large number of tree-based methods (simple decision trees) as follows:

$$\hat{y}_i = \frac{1}{K}\sum_{k=1}^{K} T_k(x_i) \tag{1}$$

where $\hat{y}_i$ is RF's prediction for the ith data instance, K shows the number of trees, x_i is the vector of input features for the ith instance, and T_k denotes the kth tree. RFs decorrelate the constituent stumps by allowing each model to be trained on a bootstrapped sample of training data and individual feature set [26,40]. RF demonstrated strong capability for modeling nonlinear relationships without requiring strong assumptions about data distributions [41]. In addition, previous studies have consistently demonstrated their ability to provide this mapping for other performance-based metrics, such as loss- or fragility-based parameters.

 https://doi.org/10.3390/infrastructures11070213

Table 1. Summary of the recovery-assessment assumptions.

Model Component	Basis/Tool	Key Assumptions
Component inventory	Building-specific structural & nonstructural inventory	Per-building quantities of structural and drift- and acceleration-sensitive nonstructural components, by story and direction, mapped to FEMA P-58 fragility groups
Damage & loss	FEMA P-58 (via Pelicun)	Component fragilities and consequence functions with repair time (worker-days for assigned per component and damage) and repair cost from the FEMA P-58 database; 10,000 Monte Carlo realizations per building
Inspection & red-tag	Virtual inspection (Cook et al. [38])	Unsafe-placard (red-tag) assignment from structural Safety Classes and extent of damage; inspection median 7 days (3 days essential, 1 day with BORP), triggered at 50% of the red-tag threshold
Residual drift	ATC-138 building-safety fault tree	Excessive residual drift contributes to unsafe-placard (red-tag) assignment; residual displacement that racks entry/exit doors compromises egress
Functionality criteria	ATC-138 building-function module	Four-stage fault tree (building safety, story access, tenant safety, tenant function); nine building systems, six of which govern tenant function; tenant-specific (occupancy-based) functional requirements; reoccupancy and functional-recovery states
Impeding factors	ATC-138 recovery-time module	Financing (60 days if repair cost exceeds cash-on-hand), engineering mobilization (1 day to 2 weeks), permitting (1 day over-the-counter/8 weeks full review), and contractor mobilization (system-dependent ranges); times modeled as truncated lognormal ($\beta = 0.6$), with contractor mobilization uniform
Regional demand surge	ATC-138 recovery-time module	Identified as a potential multiplier on inspection, financing, permitting, and mobilization times; not quantified in the base assessment
Repair sequencing & crew	ATC-138 repair-scheduling algorithm	Repairs prioritized by impact on functionality (structural repaired first if red-tagged); 1 worker per 1000 sq ft per story; 20–260 workers on site by building size; crew sizes after Yoo (2016) [42]
Nonstructural systems	FEMA P-58 fragilities; ATC-138 systems	Drift- and acceleration-sensitive nonstructural components included per the inventory and mapped to the ATC-138 tenant-function systems

https://doi.org/10.3390/infrastructures11070213

Table 2. Distribution of median functional recovery time (days) by hazard level and building class. For each building class, the median, the 25th–75th percentile interval (Q1–Q3), and the minimum–maximum interval of median realization from Monte Carlo realizations are reported. N = number of buildings in each category.

Building Class	N	DBE			MCE		
		Median	Q1–Q3	Min–Max	Median	Q1–Q3	Min–Max
Low-rise (1 story)	13	47	43–52	23–71	58	51–62	31–76
Mid-rise (5–9 stories)	52	138	112–153	91–190	160	135–188	117–216
High-rise (14–19 stories)	35	144	114–161	93–230	187	150–211	129–341
All buildings	100	127	101–152	23–230	158	134–195	31–341

The selected features include a large set of geometric and design parameters identified in several previous studies on steel SMRFs [19,26,43], including total building height (H), bay width (BW), number of stories (NS), first story height (h_1), and floor area (A_F). Beam design parameters included the average ($I_{b,avg}$), maximum ($I_{b,max}$), and minimum ($I_{b,min}$) moment of inertia, and the average flexural ($D/C_{b,flex}$) and shear ($D/C_{b,sh}$) demand-to-capacity ratios. Similarly, column design parameters covered average ($I_{c,i,avg}$), maximum ($I_{c,i,max}$) and minimum ($I_{ci,i,min}$) moment of inertia of internal columns, average ($I_{c,e,avg}$), maximum ($I_{c,e,max}$) and minimum ($I_{c,e,min}$) moment of inertia of external columns, average axial ($D/C_{c,ax}$), flexural ($D/C_{c,flex}$) and shear ($D/C_{c,sh}$) demand-to-capacity ratios. Building-level design parameters include average design drift (IDR_{Desgn}), the total weight of the building (W_T), the weight of lateral frames (W_L), the fundamental period (T_1), and average and design strong-column weak-beam ratios ($SCWB_{avg}$ and $SCWB_{Dsgn}$). Figure 2 provides the correlation matrix of several of these features. Several design variables, including W_T, NS, and SCWB, show strong correlations with other features, indicating that the building configuration strongly influences member sizing. In addition, A_F, BW, and IDR_{Dsgn} limits were mostly unrelated to other variables, as architectural needs and code requirements dictate them. Overall, Figure 2 indicates the presence of multicollinearity and partial correlations, underscoring the need for an ML model capable of addressing such issues.

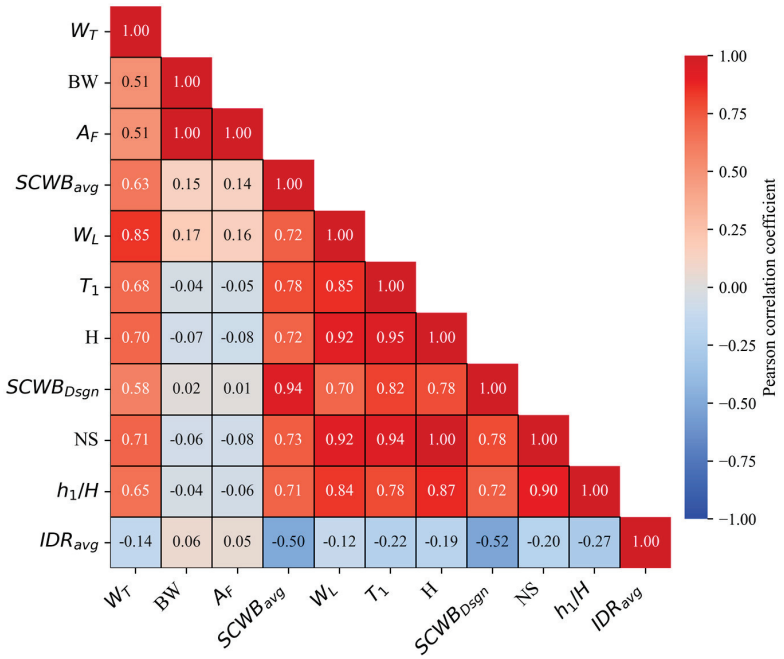

Figure 2. Correlation structure of several key design and geometry features. cell values are correlation coefficients.

https://doi.org/10.3390/infrastructures11070213

The training workflow (implemented in *Scikit-Learn* [44] *ver. 1.6*) used fixed train–test splitting, with 80% of the data reserved for training and 20% for testing. The ML pipeline included data preprocessing, feature selection, and model training and evaluation [45]. In this study, preprocessing, feature selection, and hyperparameter tuning were combined into a single pipeline, and each step was performed within a nested cross-validation loop. A fixed random seed was applied to the train–test split, the cross-validation folds, and all random forest components to ensure reproducibility. Feature selection used an embedded random forest-based approach in which, within the pipeline, an auxiliary random forest was fit, and the impurity-based importance score for each feature was computed. Subsequently, features whose importance exceeded a selection threshold were retained, while the remainder were discarded prior to fitting the primary random forest. Because the selector was part of the cross-validated pipeline, it was re-fit independently on the training partition of each fold rather than the full dataset, and consequently, the retained feature subset within any fold was determined using only that fold's training data, removing possible bias due to the influence of other folds or the held-out test. Hyperparameters were optimized using 5-fold cross-validation, in which the training data were randomly partitioned into 5 approximately equal folds; for each candidate configuration, the model was trained on 4 folds and evaluated on the 5th, repeating until each fold served once for validation. The feature-selection threshold was treated as a hyperparameter, allowing the retained features and model hyperparameters to be jointly optimized within a single cross-validated search. The hyperparameter tuning evaluated the impact of several key hyperparameters, including the number of trees, maximum tree depth, minimum samples required for node splitting, minimum samples required at leaf nodes, maximum number of features considered at each split, and feature selection threshold. A very broad range of trees was used to ensure model robustness. The maximum tree depth values control model flexibility with respect to overfitting. The number of samples requires node splitting, and terminal leaves aid in model generalization. The optimal hyperparameters were selected to achieve the highest "average" R^2 of cross-validation. The configuration yielding the highest average cross-validation R^2 was then re-fit on the entire training set and evaluated once on the held-out test set. Table 3 provides the search range and optimal values for the studied dataset.

Table 3. Hyperparameter search range and optimal values for the RF model.

Hyperparameter	Search Range	Optimal Values	
		DBE	**MCE**
n_estimators	{300, 500, 800, 1000, 1500}	1500	800
max_depth	{None, 5, 10, 15, 20, 30, 40}	None	10
min_samples_split	{2, 4, 6, 8, 10, 15}	4	4
min_samples_leaf	{1, 2, 3, 4, 5, 8}	1	1
max_features	{sqrt, log2, 0.3, 0.5, 0.7, 1.0}	log2	1.0
Feature-selection threshold	{mean, median, 0.005, 0.01, 0.02}	mean	median

Model performance was evaluated using three common statistical measures: (1) coefficient of determination (R^2), (2) mean absolute error (MAE), and (3) root mean square error (RMSE). Here, R^2 measures the proportion of variance in the observed recovery time (from simulation data) that the ML model explains. MAE quantifies the average absolute deviation between predicted and observed recovery times and represents typical prediction error. RMSE calculates the square root of the average squared prediction error, which penalizes the larger residuals. Therefore, while RMSE and MAE are both measures of error, RMSE is more sensitive to outliers, whereas MAE represents average model accuracy.

The trained model was explained using Shapley additive explanations (SHAP, ver. 0.45) [46]. In this game-theoretic approach, each feature is treated as a player in

 https://doi.org/10.3390/infrastructures11070213

a cooperative game, and the ML prediction is decomposed into an additive contribution for each feature relative to the baseline prediction [30]. As a result, SHAP quantifies the contribution of each input to the model prediction: positive SHAP values indicate that increasing the feature also increases recovery time, whereas negative values suggest a reduction in recovery time.

3. Results

3.1. Model Accuracy

Figure 3a–d compares the model performance for RF and a baseline MLR model for the two selected recovery-based outputs. Table 4 summarizes all the considered accuracy metrics. Overall, the RF model provides high accuracy metrics and consistently outperforms the baseline MLR model. On the Test set, the RF model achieves R^2 values of 89.3% and 93.6% for predicting functional recovery at the DBE and MCE levels, respectively, which are relatively 12% and 9% higher than those of the MLR model. In addition to the held-out test performance, the selected RF model attained 5-fold cross-validated R^2 values of 87.0% and 89.4% for the DBE and MCE levels, respectively, which are consistent with the held-out test values and indicate that the reported accuracy is not specific to the test partition. While R^2 values are similar between the two models, the actual prediction errors differ considerably. For example, considering RMSE, the RF model has 27% and 33% lower RMSE than the baseline MLR model when estimating functional recovery at the DBE and MCE levels, respectively. A similar observation can be made for MAE, where RF yields 16.4% and 25.6% lower values than the baseline model. The larger RMSE difference between the two models suggests that the RF model better predicts recovery times for cases with larger residuals. This observation is further reinforced in Figure 3, where the MLR model deviates notably at short recovery times, whereas the RF models capture that region more accurately.

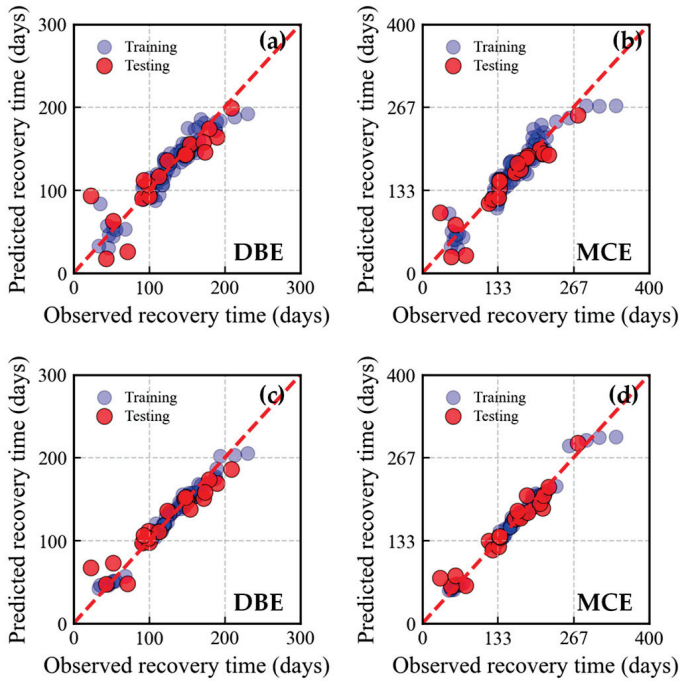

Figure 3. Predicted versus observed functional recovery time (days) for the random forest (RF) and baseline multiple linear regression (MLR) models: (**a**) RF, DBE; (**b**) RF, MCE; (**c**) MLR, DBE; (**d**) MLR, MCE; the solid diagonal denotes the perfect-prediction line.

https://doi.org/10.3390/infrastructures11070213

Table 4. Accuracy metrics for the RF and baseline MLR model.

Metrics	Hazard Level	Train		Test	
		MLR	**RF**	**MLR**	**RF**
R^2 (%)	DBE	90.8	97.8	79.8	89.3
	MCE	90.3	98.0	85.9	93.6
RMSE (day)	DBE	12.0	5.9	22.6	16.5
	MCE	17.0	7.7	23.1	15.5
MAE (day)	DBE	8.8	4.3	15.2	12.7
	MCE	12.6	4.9	16.4	12.2

3.2. Model Explanation

Figure 4a–d provides SHAP plots and their corresponding mean absolute values (bar plots) for the RF model. The plots include all features selected by the RF model for each recovery metric. Overall, the influential parameters and their contributions vary across hazard levels, though several parameters impact functional recovery at both levels.

Under DBE hazard level (Figure 4a,c), bay width, floor area, average strong-column weak-beam ratio, and total building weight are the most influential parameters. As shown in Figure 4a, a building with a higher floor area, bay width, and seismic weight may experience a longer recovery time to achieve functional recovery at the DBE, which matches engineering intuition. In addition, the RF model suggests that buildings with larger average strong-column weak-beam (SCWB) ratios tend to exhibit longer recovery times. However, this association should be interpreted as a model-based observation for the studied inventory rather than an isolated causal effect. This observation suggests that while maintaining SCWB is necessary for life safety, using a large value that further weakens beams will result in a higher recovery time, highlighting that a resilient design for special steel SMRFs may treat SCWB as an optimization problem to identify values that balance recovery and collapse probability for the building. Nevertheless, isolating the effect of SCWB from other correlated building-size parameters would require future controlled parametric studies.

Under the MCE hazard level (Figure 4b,d), most parameters show a smaller impact, with building total weight as the dominant factor. This observation is expected, as buildings with greater weight experience substantially higher seismic demand, which, at higher hazard levels, results in significantly greater damage, longer impediment times, and a more complex repair schedule. Bay width, floor area, and the ratio of first-story height to building height also rank high in the SHAP analysis, indicating some level of contribution. Lastly, it should be noted that several parameters, including bay width, floor area, building weight, and average SCWB, remained important for both hazard levels. While bay width and floor area are often determined by architectural needs, building weight and average SCWB are parameters controlled by the structural designer, with pathways to optimize these values. In other words, the results suggest that a recovery-based design for steel MRFs may benefit from well-established seismic design principles to minimize building weight and to make beams and columns more uniform in size. It should be noted that since several inputs are strongly correlated (Figure 2), notably the building-scale descriptors (i.e., frame weight, height, period, number of stories, height ratio, and SCWB), with pairwise correlations exceeding 0.85, the SHAP explanations should be treated cautiously for correlated features. For example, SHAP explanations are better interpreted at the level of dominant features and the direction of their effects, rather than as exact feature-level importances, and small differences in rank within a correlated group should not be over-interpreted.

https://doi.org/10.3390/infrastructures11070213

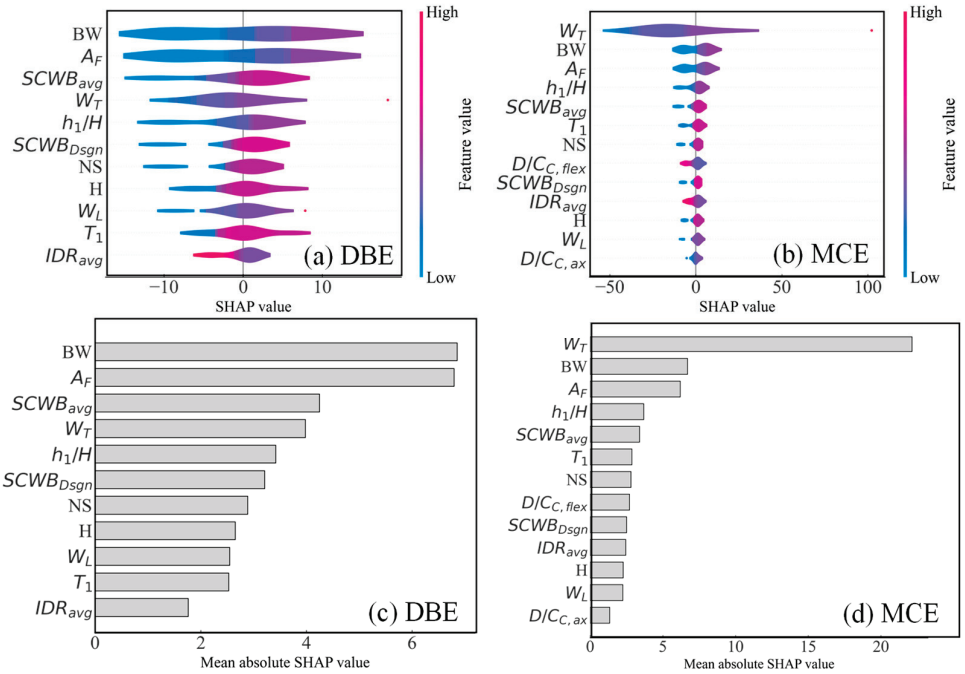

Figure 4. SHAP explanations of the RF model for functional recovery at the DBE (**a**,**c**) and MCE (**b**,**d**) hazard levels: (**a**,**b**) SHAP summary (beeswarm) plots and (**c**,**d**) mean absolute SHAP values (bar plots). In each summary plot, every point is a building; its horizontal position is the feature's SHAP contribution to the predicted recovery time (in days), and its color denotes the feature value from low (blue) to high (red), with features ordered top to bottom by overall importance. The bar plots report the mean absolute SHAP value (in days) of each feature, indicating its average contribution magnitude. The features are all the features retained by the RF model for each target recovery.

4. Conclusions

4.1. Summary of Findings

This study investigates the application of ML to predict the post-earthquake functional recovery time of steel SMRFs at two distinct hazard levels: DBE and MCE. An ensemble learner (i.e., RF) was trained and validated using a standard workflow comprising feature selection, hyperparameter tuning, and cross-validation. SHAP analysis was then performed to explain the RF model and evaluate the influential parameters that impact the functional recovery of steel SMRFs. The main results of this study are summarized as follows:

1. The RF model achieved R^2 values of 89.3% and 93.6% for predicting functional recovery at DBE and MCE hazard levels, respectively. In addition, the RF model achieved, on average, 30% lower RMSE and 21% lower MAE than the baseline regression model.
2. The SHAP analysis showed that the governing parameters and their impact vary across different hazard levels. Nevertheless, building weight, floor area, bay width, and average strong-column-to-weak-beam ratios remained influential across both hazard levels.
3. At the DBE hazard level, recovery was influenced by bay width, floor area, average strong-column-to-weak-beam ratio, and building weight, with buildings with larger values of these parameters exhibiting longer recovery times.
4. At the MCE level, building weight was the dominant factor with a notably higher impact than all other parameters.

https://doi.org/10.3390/infrastructures11070213

4.2. Limitation and Future Work

This study has several limitations that motivate further research. First, the building inventory is of moderate size, which, while adequate for training a classical ML model such as RF, lacks sufficient statistical power for rigorous feature importance analysis. In particular, because the held-out test set is small and a single fixed split was used, the reported metrics primarily reflect model performance within the sampled design space. As more comprehensive building inventories become available in the community, techniques such as repeated train/test resampling and grouped validation that hold out buildings by family (e.g., by height, bay width, or first-story height) would more rigorously quantify the variability in accuracy metrics and provide a better estimate of model generalizability. Such analyses are recommended for future work. In addition, the symmetric footprint, fixed location, and automated design further limit dataset variability. As such, the established relationship between design and recovery time requires further validation and evaluation with larger, more diverse datasets. Accordingly, the trained model should currently be interpreted as a design-support surrogate for the considered class of regular steel SMRFs (i.e., symmetric footprints designed for the studied site and hazard level), rather than a generalizable model for other structural systems, seismic regions, or irregular building configurations. In particular, the inventory does not sample alternative site or soil classes, different plan layouts and bay configurations, or alternative SMRF design practices. Therefore, the model is not expected to reflect their influence on recovery, and applying it under such conditions would constitute extrapolation beyond the sampled design space. The buildings were also represented with two-dimensional models. While such modeling is adequate for the regular, symmetric SMRFs considered here, this idealization may introduce inaccuracies in EDP estimates compared to a more detailed three-dimensional model needed for a realistic building inventory. However, the recovery assessments relied on several key assumptions due to limited information, including assumptions about the impeding factors, which require further assessment in future studies. Nevertheless, this preliminary study shows that developing ML-based surrogate models to treat recovery-based design as an inverse problem is feasible, and that there exist key seismic design parameters that can improve functional recovery of steel SMRFs. Such surrogate models can complement existing engineering design workflows by providing rapid estimates of performance metrics and facilitating the exploration of design alternatives. However, given their inherent limitations, including applicability primarily within the range of the training data, they should be viewed as decision-support tools rather than replacements for detailed engineering analyses, which remain essential for final assessment and design decisions.

Author Contributions: Conceptualization, M.Z.E.; methodology, M.Z.E. and S.B.; software, M.Z.E. and S.B.; validation, M.Z.E. and S.B.; formal analysis, M.Z.E. and S.B.; investigation, M.Z.E. and S.B.; resources, M.Z.E.; data curation, S.B.; writing—original draft preparation, M.Z.E. and S.B.; writing—review and editing, M.Z.E.; visualization, M.Z.E.; supervision, M.Z.E.; project administration, M.Z.E. All authors have read and agreed to the published version of the manuscript.

Funding: This research received no external funding.

Data Availability Statement: The data presented (trained model and codes) in this study are available on reasonable request from the corresponding author.

Acknowledgments: The first author was supported by the Utah Earthquake Engineering Research Center.

Conflicts of Interest: The authors declare no conflicts of interest.

References

1. Comerio, M.C. Estimating Downtime in Loss Modeling. *Earthq. Spectra* **2006**, *22*, 349–365. [CrossRef]
2. Esteghamati, M.Z.; Rodriguez-Marek, A.; Flint, M.M. A Reliability-Based Decision Support System for Resilient and Sustainable Early Design. In *Resilient and Sustainable Buildings*; American Society of Civil Engineers: Reston, VA, USA, 2023; pp. 177–228. [CrossRef]
3. Olshansky, R.B.; Johnson, L.A.; Topping, K.C. Rebuilding Communities Following Disaster: Lessons from Kobe and Los Angeles. *Built Environ.* **2006**, *32*, 354–374. [CrossRef]
4. Mieler, M.W.; Uma, S.R.; Mitrani-Reiser, J. Using Failure Analysis Tools to Establish Seismic Resilience Objectives for Building Components and Systems. *Bull. N. Z. Soc. Earthq. Eng.* **2016**, *49*, 86–97. [CrossRef]
5. Zaker Esteghamati, M. 2—Leveraging Machine Learning Techniques to Support a Holistic Performance-Based Seismic Design of Civil Structures. In *Interpretable Machine Learning for the Analysis, Design, Assessment, and Informed Decision Making for Civil Infrastructure*; Naser, M.Z., Ed.; Woodhead Publishing Series in Civil and Structural Engineering; Woodhead Publishing: Sawston, UK, 2024; pp. 25–49.
6. Joyner, M.D.; Kurth, M.H.; Pumo, I.; Linkov, I. Recovery-Based Design of Buildings for Seismic Resilience. *Int. J. Disaster Risk Reduct.* **2021**, *65*, 102556. [CrossRef]
7. Gentile, R.; Calvi, G.M. Direct Loss-Based Seismic Design of Reinforced Concrete Frame and Wall Structures. *Earthq. Eng. Struct. Dyn.* **2023**, *52*, 4395–4415. [CrossRef]
8. Earthquake Engineering Research Institute (EERI). *Functional Recovery: A Conceptual Framework with Policy Options*; Earthquake Engineering Research Institute: Oakland, CA, USA, 2019.
9. FEMA. *NEHRP Recommended Seismic Provisions for New Buildings and Other Structures*; FEMA: Washington, DC, USA, 2020.
10. Molina Hutt, C.; Vahanvaty, T.; Kourehpaz, P. An Analytical Framework to Assess Earthquake-Induced Downtime and Model Recovery of Buildings. *Earthq. Spectra* **2022**, *38*, 1283–1320. [CrossRef]
11. Cook, D.T.; Liel, A.B.; Haselton, C.B.; Koliou, M. A Framework for Operationalizing the Assessment of Post-Earthquake Functional Recovery of Buildings. *Earthq. Spectra* **2022**, *38*, 1972–2007. [CrossRef]
12. Terzic, V.; Villanueva, P.K.; Saldana, D.; Yoo, D.Y. Framework for Modelling Post-Earthquake Functional Recovery of Buildings. *Eng. Struct.* **2021**, *246*, 113074. [CrossRef]
13. Bertero, R.D.; Bertero, V.V. Performance-Based Seismic Engineering: The Need for a Reliable Conceptual Comprehensive Approach. *Earthq. Eng. Struct. Dyn.* **2002**, *31*, 627–652. [CrossRef]
14. Krawinkler, H.; Deierlein, G.G. Challenges Towards Achieving Earthquake Resilience Through Performance-Based Earthquake Engineering. In *Performance-Based Seismic Engineering: Vision for an Earthquake Resilient Society; Geotechnical, Geological and Earthquake Engineering*; Fischinger, M., Ed.; Springer: Dordrecht, The Netherlands, 2014; pp. 3–23.
15. Almufti, I.; Willford, M. *REDi^{TM} Rating System: Resilience-Based Earthquake Design Initiative for the Next Generation of Buildings*; Arup Co.: London, UK, 2013.
16. FEMA. *Seismic Performance Assessment of Buildings, Volume 8—Methodology for Assessment of Functional Recovery Time (ATC-138)*; FEMA: Washington, DC, USA, 2021.
17. Baddipalli, S.; Zaker Esteghamati, M. *Sensitivity of Post-Earthquake Functional Recovery to Modeling and Design Decisions in Steel Frame Buildings*; ASCE: San Antonio, TX, USA, 2026.
18. Baddipalli, S.; Gentile, R.; O'Reilly, G.; Shahnazaryan, D.; Zaker Esteghamati, M. Impact of Modeling Decisions on Seismic Loss and Fragility Assessment of Steel Buildings. *Earthq. Spectra* **2025**, *41*, 3858–3881. [CrossRef]
19. Zaker Esteghamati, M. Towards Using Explainable Data-Driven Surrogate Models for Treating Performance-Based Seismic Design as an Inverse Engineering Problem. *Philos. Trans. A Math. Phys. Eng. Sci.* **2025**, *383*, 20240050. [CrossRef] [PubMed]
20. Molina Hutt, C.; Hulsey, A.M.; Kakoty, P.; Deierlein, G.G.; Eksir Monfared, A.; Wen-Yi, Y.; Hooper, J.D. Toward Functional Recovery Performance in the Seismic Design of Modern Tall Buildings. *Earthq. Spectra* **2022**, *38*, 283–309. [CrossRef]
21. Blowes, K.; Kourehpaz, P.; Molina Hutt, C. Risk-Targeted Seismic Evaluation of Functional Recovery Performance in Buildings. *Earthq. Eng. Struct. Dyn.* **2023**, *52*, 4245–4264. [CrossRef]
22. Echeverria, M.J.; Mohammadgholibeyki, N.; Liel, A.B.; Koliou, M. Achieving Functional Recovery through Seismic Retrofit of Existing Buildings: Barriers and Opportunities. *J. Perform. Constr. Facil.* **2023**, *37*, 04023027. [CrossRef]
23. Hu, S.; Guo, T.; Alam, M.S.; Koetaka, Y.; Ghafoori, E.; Karavasilis, T.L. Machine Learning in Earthquake Engineering: A Review on Recent Progress and Future Trends in Seismic Performance Evaluation and Design. *Eng. Struct.* **2025**, *340*, 120721. [CrossRef]
24. Forooghi, A.; Imani, H.; Minutolo, V.; Zona, R. Multi-Output Neural Network for Elastic and Collapse Multipliers Prediction in Structural Vulnerability Assessment. *Int. J. Str. Stab. Dyn.* **2026**, *26*, 2750319. [CrossRef]
25. Zaker Esteghamati, M.; Flint, M.M. Developing Data-Driven Surrogate Models for Holistic Performance-Based Assessment of Mid-Rise RC Frame Buildings at Early Design. *Eng. Struct.* **2021**, *245*, 112971. [CrossRef]

 https://doi.org/10.3390/infrastructures11070213

26. Zaker Esteghamati, M.; Baddipalli, S. Efficiency and Explainability of Design-Oriented Machine Learning Models to Estimate Seismic Response, Fragility, and Loss of a Steel Building Inventory. *Earthq. Eng. Struct. Dyn.* **2024**, *54*, 618–647.
27. Issa, O.; Silva-Lopez, R.; Baker, J.W.; Burton, H.V. Machine-Learning-Based Optimization Framework to Support Recovery-Based Design. *Earthq. Eng. Struct. Dyn.* **2023**, *52*, 3256–3280. [CrossRef]
28. Tang, Q.; Cui, Y.; Jia, J. Machine Learning-Based Surrogate Resilience Modeling for Preliminary Seismic Design. *J. Build. Eng.* **2024**, *98*, 111226. [CrossRef]
29. Pham, H.G.; Becker, T.C. Achieving Functionality Targets for Seismically Isolated Steel Buildings Using Gaussian Process Modeling. *Earthq. Spectra* **2026**, *42*, e70050. [CrossRef]
30. Zaker Esteghamati, M.; Wang, J.; Wang, X.; Paal, S.G.; Murphy, J.; Namin, A.; Salman, A.; Sabari, A.A.; Ibrar, M.A.; Mazumder, R.; et al. Making the Black Box Transparent: State of the Art in Explainable Machine Learning for Structural Design and Assessment. *J. Struct. Eng.* **2026**, *152*, 03126002. [CrossRef]
31. FEMA. *Guidelines for Performance-Based Seismic Design of Buildings*; FEMA: Washington, DC, USA, 2018.
32. Guan, X.; Burton, H.; Shokrabadi, M.; Yi, Z. Seismic Drift Demand Estimation for Steel Moment Frame Buildings: From Mechanics-Based to Data-Driven Models. *J. Struct. Eng.* **2021**, *147*, 04021058. [CrossRef]
33. McKenna, F. OpenSees: A Framework for Earthquake Engineering Simulation. *Comput. Sci. Eng.* **2011**, *13*, 58–66. [CrossRef]
34. Ibarra, L.F.; Medina, R.A.; Krawinkler, H. Hysteretic Models That Incorporate Strength and Stiffness Deterioration. *Earthq. Eng. Struct. Dyn.* **2005**, *34*, 1489–1511. [CrossRef]
35. Zsarnoczay, A.; Manousakis, J.V.; Zhao, J. *NHERI-SimCenter/Pelicun*, version 3.3; NHERI SimCenter: Berkeley, CA, USA, 2024.
36. Zaker Esteghamati, M.; Huang, Q. An Efficient Stratified-Based Ground Motion Selection for Cloud Analysis. In Proceedings of the 13th International Conference on Applications of Statistics and Probability in Civil Engineering (ICASP13), Seoul, Republic of Korea, 26–30 May 2019.
37. Zaker Esteghamati, M. A Holistic Review of GM/IM Selection Methods from a Structural Performance-Based Perspective. *Sustainability* **2022**, *14*, 12994. [CrossRef]
38. Cook, D.T.; Liel, A.B.; DeBock, D.J.; Haselton, C.B. Benchmarking FEMA P-58 Repair Costs and Unsafe Placards for the Northridge Earthquake: Implications for Performance-Based Earthquake Engineering. *Int. J. Disaster Risk Reduct.* **2021**, *56*, 102117. [CrossRef]
39. Breiman, L. Random Forests. *Mach. Learn.* **2001**, *45*, 5–32. [CrossRef]
40. Hastie, T.; Tibshirani, R.; Friedman, J. *The Elements of Statistical Learning: Data Mining, Inference, and Prediction*, 2nd ed.; Springer: New York, NY, USA, 2016.
41. Zaker Esteghamati, M.; Gernay, T.; Banerji, S. Evaluating Fire Resistance of Timber Columns Using Explainable Machine Learning Models. *Eng. Struct.* **2023**, *296*, 116910. [CrossRef]
42. Yoo, D.Y. *Repair Time Model for Different Building Sizes Considering the Earthquake Hazard*; California State University: Long Beach, CA, USA, 2016.
43. Baddipalli, S.; Leavitt, N.; Zaker Esteghamati, M. Quantifying the Earthquake-Related Carbon Emissions of Steel Moment-Resisting Framed Buildings and Their Sensitivity to Modeling and Design Decisions. *J. Build. Eng.* **2026**, *125*, 116190. [CrossRef]
44. Pedregosa, F.; Varoquaux, G.; Gramfort, A.; Michel, V.; Thirion, B.; Grisel, O.; Blondel, M.; Prettenhofer, P.; Weiss, R.; Dubourg, V.; et al. Scikit-Learn: Machine Learning in Python. *J. Mach. Learn. Res.* **2011**, *12*, 2825–2830.
45. Zaker Esteghamati, M.; Kottke, A.R.; Rodriguez-Marek, A. A Data-Driven Approach to Evaluate Site Amplification of Ground-Motion Models Using Vector Proxies Derived from Horizontal-to-Vertical Spectral Ratios. *Bull. Seismol. Soc. Am.* **2022**, *112*, 3001–3015. [CrossRef]
46. Lundberg, S.M.; Erion, G.; Chen, H.; DeGrave, A.; Prutkin, J.M.; Nair, B.; Katz, R.; Himmelfarb, J.; Bansal, N.; Lee, S.-I. From Local Explanations to Global Understanding with Explainable AI for Trees. *Nat. Mach. Intell.* **2020**, *2*, 56–67. [CrossRef] [PubMed]

Disclaimer/Publisher's Note: The statements, opinions and data contained in all publications are solely those of the individual author(s) and contributor(s) and not of MDPI and/or the editor(s). MDPI and/or the editor(s) disclaim responsibility for any injury to people or property resulting from any ideas, methods, instructions or products referred to in the content.

infrastructures

MDPI

Article

Assessment of Community Risk from Seismic-Induced Damage to Hazardous Materials Storage Tanks in Marine Ports

Mohamad Nassar, Fatiha Mouri and Ahmad Abo El Ezz *

Construction Engineering Department, École de Technologie Supérieure, Université du Québec, Montreal, QC H3C 1K3, Canada; mohamad.nassar@etsmtl.ca (M.N.); fatiha.mouri.1@ens.etsmtl.ca (F.M.)
* Correspondence: ahmad.abo-el-ezz@etsmtl.ca

Abstract

Marine ports located in regions of moderate seismicity can face high Natech (natural hazard-triggered technological) risk because large inventories of hazardous materials are stored near dense urban populations. This study proposes and applies a Natech risk framework to a representative port on the Saint-Laurence River in Quebec, Canada. Site-specific peak ground accelerations (PGA) are first estimated for 12 earthquake scenarios using regional ground motion prediction equations adjusted for local site conditions. These hazard levels are combined with a damage probability matrix to estimate Hazardous Release Likelihood Index (HRLi) scores for atmospheric steel storage tanks. Offsite consequences are then evaluated to obtain Maximum Distances of Effect (MDEs) for different types of hazardous materials. MDE footprints are intersected with block-level demographic data and complemented by a domino-effect based on inter-tank spacing, yielding a tank-level Natech Risk Index $NRI_{i,s}$ for each storage tank (i) and seismic scenario (s). These values are then averaged over all tanks to obtain a scenario-level mean Natech Risk Index ($\overline{NRI}$) for each tank substance. Regression equations relating $\overline{NRI}$ to PGA are provided as a practical tool for defining critical intensity thresholds for seismic Natech risk management in marine ports.

Keywords: Natech risk assessment; marine ports; seismic risk; population exposure; storage tanks

1. Introduction

Marine ports support both global and regional energy supply chains by handling the import, export and storage of petroleum products, crude oil, liquefied petroleum gas (LPG) and other essential fuels. Situated along shorelines adjacent to major urban centers to allow efficient ship-to-shore transfers, these facilities bring high-hazard industrial installations into proximity with dense populations, creating the potential for Natech (natural hazards trigger technological accidents) events [1]. An important complementary perspective in the context of Natech risk is that of resilience, which emphasizes not only hazard assessment and vulnerability but also the capacity of infrastructure systems and communities to prepare for, withstand and recover from hazardous events. Recent work has highlighted the role of resilience frameworks in supporting risk-informed decision-making for critical infrastructure systems exposed to interacting natural and technological hazards [2]. Integrating resilience considerations with seismic Natech risk assessment can strengthen both mitigation prioritization and post-event planning by explicitly linking risk drivers to adaptive and recovery strategies.

Recent advances in Natech risk assessment have increasingly emphasized the need for integrated frameworks that explicitly link natural hazards, technological vulnerability, cascading effects and population exposure. Shafiei-Moghaddam et al. [3] developed a scenario-based seismic Natech framework for earthquake-induced chemical releases, demonstrating that risk escalation becomes pronounced once critical shaking thresholds are exceeded, particularly in regions where historical seismic data are limited. Their work highlights the importance of tracing the full pathway from ground motion to damage, release likelihood and off-site consequences rather than addressing these components in isolation.

Uncertainty-aware and system-level approaches have also gained prominence. For example, Kabir et al. [4] developed a Bayesian belief network-based Natech risk assessment model that explicitly propagates uncertainty across seismic hazard, equipment vulnerability and release pathways. While probabilistic methods offer valuable insights into uncertainty interactions, they often require extensive data and calibration, which may not be readily available for many port facilities. As a result, recent studies have emphasized the complementary role of scenario-based, deterministic approaches as effective screening tools for comparative risk evaluation and decision support in data-limited environments.

Earthquakes present a particular hazard in this context in two ways. The primary arises when seismic ground motions deform tank foundations, undermine anchorage systems and induce liquid sloshing and roof uplift in large storage vessels. Under earthquake shaking, storage tanks exhibit distinct failure mechanisms. Compressive hoop stresses at the shell base can trigger elephant-foot buckling once lateral displacements exceed critical levels [5]. Floating roofs face sloshing-induced uplift that can compromise roof seals and vents [6]. Tanks without anchorage may slide or overturn when inertial forces exceed frictional resistance. Furthermore, liquefaction-induced differential settlement can damage even anchored structures.

A secondary threat results from phenomena such as soil liquefaction, uneven ground settlement and surface cracking, all of which can amplify structural vulnerability. Should any containment fail under these stresses, flammable or toxic substances may escape, forming vapor clouds that can ignite, deflagrate or detonate and thus produce fires, explosions and widespread collateral damage.

Marine ports typically rest upon reclaimed sediments or alluvial deposits that often amplify seismic ground motions through complex site response. In regions of moderate seismicity, such as Eastern Canada, probabilistic seismic hazard assessments rely on regional ground motion prediction equations calibrated to local strong motion records. For example, Atkinson and Adams [7], Pezeshk et al. [8] and Pavel et al. [9] relate earthquake magnitude, source distance and average shear-wave velocity in the upper thirty m (V_{s30}) to peak ground acceleration (PGA) and spectral ordinates.

In parallel, resilience-oriented perspectives have been increasingly incorporated into Natech risk analysis. A systematic review by [10] synthesizes applications of Resilience Engineering principles to Natech accidents in the chemical and process industry, identifying key methods and gaps in how resilience is currently integrated into risk assessment frameworks. Similarly, Castro Rodríguez et al. [11] proposed a resilience-based framework for NaTech risk management in industrial critical infrastructures that emphasizes stages such as awareness, preparedness and recovery, highlighting the need to go beyond immediate consequence analysis to include adaptive and recovery capacities.

These resilience-oriented contributions underscore the value of identifying critical intensity thresholds and supporting more effective prioritization of mitigation and emergency-planning strategies tailored to complex multi-hazard environments.

In coastal regions of moderate seismicity, such as the eastern Canadian provinces, including Quebec [12], the historic earthquake record is sparse, leading to a systematic un-

 https://doi.org/10.3390/infrastructures11020049

derestimation of seismic risk [13]. Bridging this gap requires a quantitative framework that traces the entire sequence from seismic ground motion to community-level impacts. Existing assessments often address seismic hazard and technological vulnerability in isolation, rather than within an integrated, site-specific approach that explicitly captures the damage pathways linking ground shaking to hazardous-materials release and human exposure [3]. Cruz and Okada [14] established a Natech risk framework featuring a five-step workflow: geospatial inventory development, estimation of hazard release levels via damage analysis, domino effect scoring to account for cascading failures, mapping of population exposure using consequence analysis buffers and calculation of a NaTech Risk Index (NRI) by aggregating the product of release magnitude, effect distance and exposed population [15].

Subsequent studies have enhanced this workflow with high-resolution geographic information system inventories using unmanned aerial vehicle and LiDAR data, Bayesian networks to propagate uncertainty [4] and agent-based evacuation simulations to capture dynamic exposure patterns [16]. Offsite consequence analysis software such as RMP Comp [17] and ALOHA simulates vapor-cloud dispersion, pool fire thermal radiation and overpressure zones, delineating generated threat zone estimates.

The importance of cascading effects and industrial clustering has been clearly demonstrated in the recent literature. Zhou et al. [16] employed agent-based modeling to simulate Natech events in chemical clusters and showed that inter-facility interactions and escalation patterns significantly influence the timing and extent of facility failures, highlighting dynamic domino-type behaviors in complex systems [16]. Similarly, analyses of cascading scenarios in Natech risk assessment emphasize that densely packed installations such as tank farms and port facilities are especially vulnerable to domino effects due to short inter-unit distances and overlapping consequence footprints; these features can markedly amplify overall risk outcomes even when the initial triggering hazard is moderate [18,19]. These findings underscore that the spatial arrangement of storage tanks can be as influential as the intrinsic hazard of the stored substances.

In this study, a framework is developed that combines seismic hazard estimates, which are expressed in terms of peak ground acceleration, with a damage probability matrix for storage tanks in marine ports. Release footprints are then simulated and subsequently intersected with high-resolution demographic data to quantify potential exposure. Community risk is conceptualized as the expected number of individuals exposed to hazardous releases triggered by earthquake-induced damage to energy infrastructure. Critical shaking thresholds at which risk escalates sharply are identified, thereby highlighting conditions under which targeted mitigation and emergency-planning interventions would yield the greatest benefits.

The methodology is demonstrated using a case study of a typical port located on the Saint-Laurence River in the province of Quebec, Canada, located in a region of moderate seismicity in Eastern Canada, and offers the detailed data necessary to calibrate our seismic hazard, structural fragility and consequence models. The port covers approximately 12 square kilometers, bordering a metropolitan population, and contains 49 storage tanks that vary in shape and capacity.

In the present study, site-specific peak ground acceleration values were calculated for a set of earthquake scenarios with magnitudes ranging from 6.0 to 7.0 and epicentral distances between 5 km and 100 km. Fragility analysis is conducted using damage probability matrices calibrated to observed tank performance in moderate-to-strong earthquakes and is applied to derive Hazardous Release Likelihood Index (HRLi) scores at the tank scale, accounting for anchorage condition, geometry and local ground motion amplification.

Established consequence-analysis software is then employed to calculate the Maximum Distance of Effect (MDE) for releases of naphtha, LPG and methane. Finally, these

 https://doi.org/10.3390/infrastructures11020049

effect zones on block-level population data were overlayed to derive the NRI as a continuous function of PGA.

2. Materials and Methods

This study implements a comprehensive seismic risk assessment for storage tanks, which was inspired by the Natech risk framework of Cruz and Okada [14], while enriching it with an improved scoring method for population density and cascading effects due to tanks' proximity to site-specific geospatial, structural and demographic data. The methodology enables rapid evaluation of Natech risk by linking hazard identification, vulnerability analysis and risk index calculation (Figure 1). The methodology involves several steps, including seismic hazard characterization, inventory development, damage probability assessment and estimation of HRLi scores. As illustrated in Figure 1, the inventory and damage assessment steps are supported by a schematic representation of a representative aboveground atmospheric steel storage tank, highlighting the main geometric parameters (diameter D and height H) used to estimate storage volumes and characterize tank vulnerability. Finally, an NRI is calculated for each storage tank containing hazardous substances, enabling the identification of areas within the port where seismic Natech risk is highest.

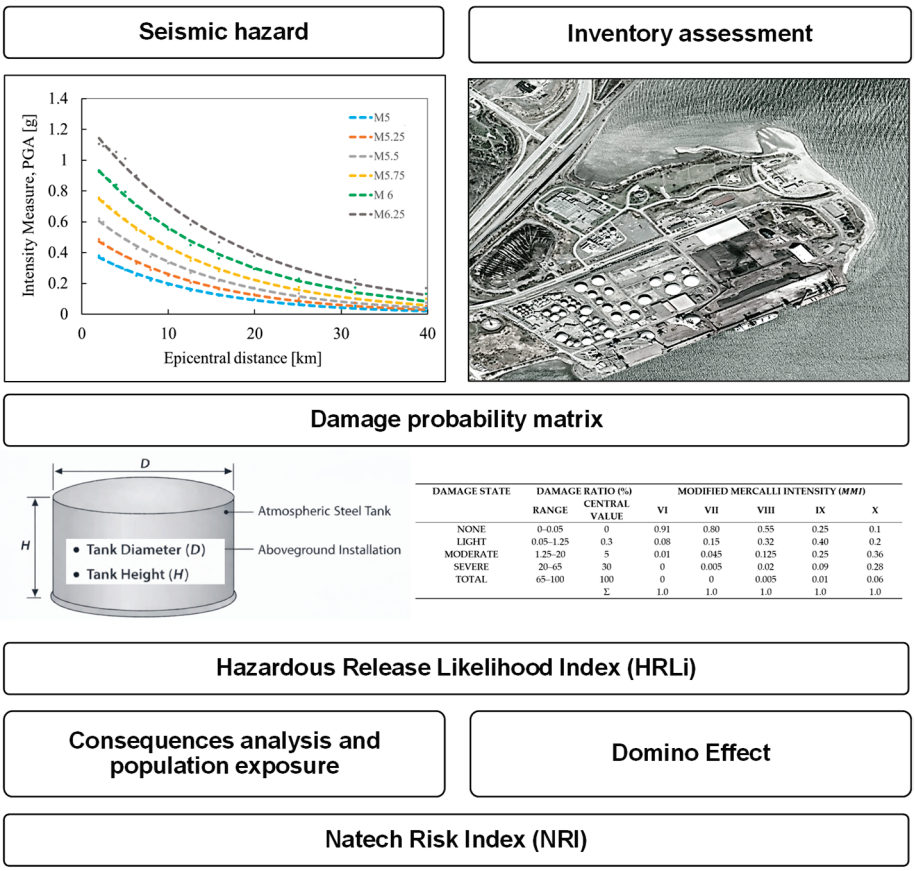

DAMAGE STATE	DAMAGE RATIO (%)		MODIFIED MERCALLI INTENSITY (*MMI*)				
	RANGE	CENTRAL VALUE	VI	VII	VIII	IX	X
NONE	0–0.05	0	0.91	0.80	0.55	0.25	0.1
LIGHT	0.05–1.25	0.3	0.08	0.15	0.32	0.40	0.2
MODERATE	1.25–20	5	0.01	0.045	0.125	0.25	0.36
SEVERE	20–65	30	0	0.005	0.02	0.09	0.28
TOTAL	65–100	100	0	0	0.005	0.01	0.06
		Σ	1.0	1.0	1.0	1.0	1.0

Figure 1. Framework for Natech risk assessment of storage tanks in port facilities.

This section describes the seismic Natech risk assessment methodology adopted in this study. The procedure integrates seismic hazard characterization, inventory development, damage-based hazardous release likelihood estimation, off-site consequence analysis, population exposure assessment and domino-effect modeling.

https://doi.org/10.3390/infrastructures11020049

2.1. Seismic Hazard Modeling

For the seismic hazard modeling in this study, the Ground Motion Prediction Equations (GMPE) equations of Atkinson and Adams [7] are used. For each site, the epicentral distance is calculated from the earthquake location to the asset coordinates and the rock-based IM values are corrected for local site effects using amplitude and frequency-dependent site amplification factors derived from the average shear wave Vs_{30}, in accordance with the Canadian Highway Bridge Design Code (CAN/CSA S6-14 [17]).

The seismic hazard modeling in this study is based on the GMPEs developed by Atkinson and Adams [7] for Eastern Canada. These GMPEs are originally provided as discrete lookup-table values for a reference site condition corresponding to $V_{s30} = 760$ m/s (B/C boundary) and form the basis of the Canadian National Seismic Hazard Model and the seismic design input adopted in the Canadian Highway Bridge Design Code [17]. To enable direct computation of PGA as a function of earthquake magnitude and source-to-site distance, the lookup-table values were converted into a closed-form regression model following the methodology proposed by Abo El Ezz et al. [20].

Local site effects were represented using Site Class C, consistent with the recommendations of CAN/CSA S6-14 [17], to provide a code-based and uniform representation of soil conditions for screening purposes. No sensitivity analysis with respect to alternative site classes or amplification uncertainty was performed.

Alternatively, in this study, median PGA values derived from the selected GMPE are propagated through the Natech risk framework. The analysis does not incorporate lower- or upper-bound ground-motion variability or probabilistic logic-tree formulations, as the objective is to develop a deterministic, scenario-based screening methodology suitable for comparative assessment of Natech risk.

This formulation covers median, lower-bound and upper-bound PGA predictions for Eastern Canada for M_w ranging from 5.0 to 7.25 and epicentral distances up to 40 km. In the present study, only median PGA values are considered.

Rather than reproducing detailed closed-form regression equations, the median PGA is expressed here in a generalized form as follows:

$$PGA_{median} = f\left(M_w; R_{epi}\right) \tag{1}$$

where M_w is the earthquake moment magnitude (dimensionless), R_{epi} is the epicentral distance (km) and f(·) denotes the regional GMPE calibrated for Eastern Canada.

The regression reformulation adopted in this study follows the methodology described by Abo El Ezz et al. [20], which provides explicit polynomial expressions for median PGA in Eastern Canada derived from the Atkinson and Adams [7] tables.

Information regarding the exact number of tanks, their structural types and the substances stored in each unit are not publicly available. To overcome this limitation, geospatial data from Google Earth Pro were used to identify and measure the tanks, which allowed the determination of their number, dimensions and general configuration.

Moreover, in the current study, twelve (12) earthquake scenarios' combined moment magnitudes $M_w \in \{5.5; 6.0; 6.5; 7.0\}$ and epicentral distances $R_{epi} \in \{10, 20, 30\}$ km (Table 1) are compiled for the assessment of seismic risk.

The selected magnitude and distance ranges are consistent with historical seismicity and regional hazard assessments for Eastern Canada and represent near-field to intermediate-field source conditions relevant to the Saint Lawrence River corridor. The scenarios are intended as a representative, screening-level set, rather than as a probabilistic

https://doi.org/10.3390/infrastructures11020049

hazard model, enabling systematic evaluation of intensity-dependent Natech risk and identification of critical PGA thresholds.

Table 1. Adopted earthquake scenarios and *PGA* values.

Scenario	M_w	R_{epi}(km)	*PGA*(g)
1	5.5	10	0.20
2	6.0	10	0.30
3	6.5	10	0.48
4	7.0	10	0.80
5	5.5	20	0.10
6	6.0	20	0.17
7	6.5	20	0.28
8	7.0	20	0.41
9	5.5	30	0.05
10	6.0	30	0.09
11	6.5	30	0.16
12	7.0	30	0.28

2.2. Inventory Assessment

Inventory assessment is a crucial step in the seismic risk assessment of storage tanks, as it requires identifying and characterizing all units in terms of their physical properties, stored substances and storage conditions. For the present study, an inventory of 49 tanks located at the studied port case was established using geospatial data from Google Earth Pro. Through these platforms, the tanks were visually identified; then, their external dimensions (diameter and height) were measured in order to estimate storage volumes.

Since information on the actual contents of the tanks was not publicly available, assumptions were made regarding the products stored. Three (3) representative hazardous substances were selected (naphtha, LPG and methane), which reflect common classes of flammable or toxic materials typically handled in port facilities.

All tanks were assumed to be constructed of steel, consistent with standard design practice for aboveground atmospheric storage tanks. These steps allowed us to generate a complete dataset of tank geometries, storage volumes and assumed contents (which formed the basis for the subsequent seismic risk analysis). For consistency and conservatism, storage tanks were assumed to be fully filled; the influence of partial filling or ullage conditions was not evaluated, as such operational variability was outside the scope of the present screening-level analysis.

2.3. Intensity Conversion and HLRi

For each scenario, the *PGA* was estimated at the tank sites considering site amplification factors. Since HRLi estimation requires both *PGA* and an intensity-based measure, the Modified Mercalli Intensity (*MMI*) was derived from *PGA* following the empirical relationship of [21]. Specifically, the *MMI* is computed as follows:

$$MMI = \frac{log(PGA) - 0.014}{0.3} \quad (2)$$

where *MMI* is dimensionless, *PGA* is expressed in cm/s^2, g is the gravitational acceleration (g = 9.81 m/s^2), used to convert *PGA* values originally expressed in units of g into cm/s^2.

This conversion enables the integration of PGA-based hazard scenarios into an intensity measure more directly correlated with observed structural damage. It should be noted that the PGA–MMI conversion adopted in this study follows a commonly used empirical relationship.

 https://doi.org/10.3390/infrastructures11020049

The obtained *MMI* values were then coupled with fragility functions to derive the HRLi for each tank and failure mode.

To further quantify the HRLi, a damage probability matrix proposed by Seligson et al. [22] is presented in Table 2 and employed and later recommended by Cruz et al. [14]. This approach assigns discrete scores to probability intervals, facilitating integration into the *NRI* framework (see Table 3). In fact, the HRLi is defined as a discrete score ranging from 1 to 5, derived from the probability of damage obtained from the damage probability matrix. Probability ranges are mapped to HRLi scores using the conversion scheme presented in Table 3. In the subsequent NRI calculation, HRLi is treated as a dimensionless index rather than a continuous probability.

Table 2. Damage probability matrix of tanks.

Damage State	Damage Ratio (%)		Modified Mercalli Intensity (*MMI*)				
	Range	Central Value	VI	VII	VIII	IX	X
None	0–0.05	0	0.91	0.80	0.55	0.25	0.1
Light	0.05–1.25	0.3	0.08	0.15	0.32	0.40	0.2
Moderate	1.25–20	5	0.01	0.045	0.125	0.25	0.36
Severe	20–65	30	0	0.005	0.02	0.09	0.28
Total	65–100	100	0	0	0.005	0.01	0.06
		Σ	1.0	1.0	1.0	1.0	1.0

Table 3. Probability-to-score conversion matrix for HRLi estimation.

Probability Range	Score
Less than 20%	1
20–40%	2
40–60%	3
60–80%	4
More than 80%	5

2.4. Consequence Analysis and Population Exposure

Once the HRLi is determined, the potential offsite consequences of each release scenario were assessed using the U.S. Environmental Protection Agency's RMP*Comp software: RMP*Comp [23]. This latter software simulates physical and toxicological hazard zones for flammable and hazardous materials. Inputs to this model included the stored substance type, estimated inventory volume, physical state and containment conditions.

RMP*Comp produced hazard footprint contours for three consequence types: (i) thermal radiation from pool fires, (ii) overpressure from vapor cloud explosions and (iii) toxic concentration thresholds for airborne releases. For each consequence category, the *MDE*, defined as the radial distance from the tank within which the threshold consequence level is exceeded, was recorded.

The present study does not consider alternative atmospheric stability classes or three-dimensional CFD-based dispersion modeling, as such analyses are outside the scope of the proposed scenario-based Natech risk screening framework.

Population exposure is estimated using a population-density-based approach, with population density expressed in inhabitants per square kilometer (inhabitants/km^2). The exposed population is calculated using the full MDE footprint, consistent with off-site consequence assessment practices.

Population density was computed as follows:

$$\text{Population Density} = \frac{\text{Total Number of Inhabitants}}{\text{Territorial Area}} \quad (3)$$

https://doi.org/10.3390/infrastructures11020049

The assumed population density is equal to 5673 inhabitants/km^2. The estimated exposed population within the impact zone was obtained using the following equation:

$$\text{Estimated exposed Population} = \text{Population Density} \times Area_{sci} \quad (4)$$

where Area_{sci} represents the area of the circular MDE footprint (in km^2).

The value of $Area_{sci}$ for each hazard zone is calculated using the polygon area measurement tool in Google Earth Pro. This methodology allows the estimation, for each storage tank, of the number of individuals potentially exposed in the event of hazardous-material release.

In this study, population exposure was estimated using a spatially averaged population density derived from dissemination-block census data for the surrounding urban area. Individual block-level population counts were not explicitly overlaid in the GIS analysis, as the objective was to provide a screening-level estimate of community exposure suitable for scenario comparison rather than a parcel-scale evacuation analysis.

Based on these population estimates, an $Area_{sci}$ score was assigned as follows:

- Score 1: 1–100 inhabitants;
- Score 2: 100–500 inhabitants;
- Score 3: 500–1000 inhabitants;
- Score 4: 1000–1500 inhabitants;
- Score 5: more than 1500 inhabitants.

2.5. Domino Effect and Mean Natech Risk Index

To account for the possibility of cascading accidents, a domino effect score $D_{i,s}$ was assigned to each tank. The principle is that when a hazardous release occurs, secondary accidents may be triggered in nearby tanks if they are located within the impact zone of the initial event. In this study, the impact zone was defined as a circular buffer with a radius equal to one-third of the Maximum Distance of effect MDE, consistent with recommendations in Cruz et al. [14].

Figure 2 illustrates the procedure used to assign domino effect scores ($D_{i,s}$) to storage tanks. The scoring is based on the number of neighboring tanks located within one-third of the MDE, which defines the critical zone for cascading accident potential.

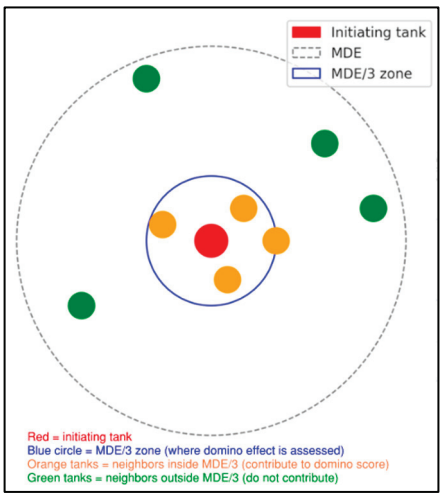

Figure 2. Illustration of the domino effect scoring method ($\text{D}_{\text{i,s}}$) applied to storage tanks.

The following scoring method was followed:

- Score 1: 1–5 tanks.

https://doi.org/10.3390/infrastructures11020049

- Score 2: 6–10 tanks.
- Score 3: 11–15 tanks.
- Score 4: 16–20 tanks.
- Score 5: more than 20 tanks.

As a result, the domino effect becomes a critical amplifying factor in overall Natech risk estimation. The $NRI_{i,s}$ for each individual tank and seismic scenario was computed as follows:

$$NRI_{i,s} = HRL_{i,s} \times \left(D_{i,s} + Area_{sci_{i,s}} \right) \tag{5}$$

where i denotes the tank and s the seismic scenario.

For each scenario s, the scenario-level mean NRI is obtained by averaging over the N_t tanks in the port:

$$\overline{NRI_s} = \frac{1}{N_t} \sum_{i=1}^{N_t} (NRI_{i,s}) \tag{6}$$

It should be noted that the arithmetic mean is used to represent the average port-level Natech risk, which is conditional on a given seismic scenario, consistent with the scenario-based objective of the proposed framework.

By examining the variation in $\overline{NRI_s}$ across the full range of modeled PGAs for median GMPE predictions, it is possible to identify critical intensity thresholds where the Natech risk escalates rapidly, guiding both mitigation prioritization and emergency preparedness planning.

It is acknowledged that different accident phenomena, such as pool-fire thermal radiation, BLEVE fireballs and vapor-cloud explosions, are governed by distinct physical damage mechanisms and threshold criteria, including heat-flux intensity, blast overpressure and impulse. Standard consequence-analysis references provide dedicated physical models for each phenomenon and clearly demonstrate that escalation potential strongly depends on the nature of the initiating event and the corresponding impact metrics [24]. Quantitative studies on domino effects further show that blast overpressure and thermal radiation can propagate damage to adjacent equipment when separation distances fall within critical impact zones, significantly increasing the likelihood of cascading failures [25,26].

Implementing consequence-specific interaction radii would therefore require explicit coupling between off-site consequence modeling outputs and structural vulnerability thresholds for neighboring tanks, which is beyond the scope of the present scenario-based framework. Accordingly, the adopted MDE/3 radius should be interpreted as a conservative, generalized interaction zone and the resulting domino scores $D_{(i,s)}$ represent relative escalation potential rather than precise physical damage probabilities.

3. Results

Table 4 summarizes the values of $\overline{D_{i,s}}$ and $\overline{Area_{sci}}$ for the three substances and all scenarios. Table 5 lists the adopted seismic scenarios, including earthquake magnitude, epicentral distance, PGA, MMI and the corresponding mean $\overline{NRI_s}$ values for the three studied substances, obtained by averaging tank-level values for all 49 tanks. The scenario risk assessments are conducted assuming the same type of substance for all 49 tanks. The analyses are then presented for each type of substance separately.

To illustrate how the $\overline{NRI_s}$ values in Table 5 were obtained, this subsection presents a complete intermediate calculation for Naphta's $\overline{NRI_s}$ value for the Scenario 6, corresponding to $M_w =$ 6.0 and $R_{epi} =$ 20 km.

https://doi.org/10.3390/infrastructures11020049

First, the PGA at the tank site is estimated using the regional GMPE of Atkinson and Adams [17]. For this magnitude–distance pair, the resulting ground motion is PGA = 0.17 g.

Next, the $HRL_{i,s}$ is obtained by combining the intensity level with the damage-probability matrix of Seligson et al. [22]. For a welded atmospheric tank subjected to MMI = VII, the expected mean value of $HRL_{i,s} = 0.15$ (score = 1) (see Table 3).

The domino effect score is then assigned using the approach of Cruz and Okada [14]. A circular buffer with a radius equal to one-third of MDE is drawn around each tank. The number of neighboring tanks within this buffer is counted. For this scenario, a mean domino score $\overline{D_{i,s}} = 4.95$ for 49 tanks is adopted, which represents a very low escalation potential (see Table 4).

Table 4. Mean $\overline{D_{i,s}}$ and $\overline{Area_{sci}}$ estimations for all substances and scenarios.

Substance	Scenario	$\overline{D_{i,s}}$	$\overline{Area_{sci}}$
Naphta	1	4.96	5
	2	4.95	5
	3	5	5
	4	5	5
	5	5	4.61
	6	5	4.61
	7	5	5
	8	5	4.61
	9	5	5
	10	5	5
	11	3	5
	12	3	5
LPG	1	3.33	2.33
	2	3.33	2.28
	3	3.33	2.33
	4	3.33	2.31
	5	3.33	2.31
	6	3.33	2.31
	7	3.33	2.31
	8	3.33	1.73
	9	3.33	2.31
	10	3.33	2.31
	11	3.33	2.31
	12	3.33	2.31
Methane	1	2	1.73
	2	2	1.73
	3	2	1.73
	4	2	1.73
	5	2	1.73
	6	2	1.73
	7	2	1.73
	8	2	1.73
	9	2	1.73
	10	2	1.73
	11	2	1.73
	12	2	1.73

Population exposure is then assessed by combining hazard footprint contours from RMP*Comp with local demographic data. For scenario 6, the estimated number of exposed individuals is approximately 15,480 inhabitants, corresponding to a mean exposure score $\overline{Area_{sci}} = 5$ for all 49 tanks (see Table 4).

https://doi.org/10.3390/infrastructures11020049

Table 4 reports scenario-averaged values of $\overline{D_{i,s}}$ and $\overline{Area_{sci}}$ obtained by averaging tank-level scores over all storage tanks.

This value represents the tank-level index $NRI_{i,6}$ for a given naphtha tank under Scenario 6. In practice, $NRI_{i,6}$ is computed for each of the 49 tanks, and the scenario-level mean index reported in Table 5 $\left(\overline{NRI_6} = 9.95\right)$ is obtained by averaging these 49 values according to Equation (6).

Table 5. Mean $\overline{NRI_s}$ estimation for all scenarios.

Scenario	M_w	R_{epi} (km)	*PGA* (g)	*MMI*	$HRL_{i,s}$ Probability (Score)	$\overline{NRI_s}$ Naphtha	$\overline{NRI_s}$ LPG	$\overline{NRI_s}$ Methane
1	5.5	10	0.2059	VIII	15% (1)	9.95	5.69	3.73
2	6.0	10	0.3099	VIII	15% (1)	9.95	5.69	3.73
3	6.5	10	0.4866	IX	34% (3)	19.91	11.30	7.47
4	7.0	10	0.8044	X	64% (4)	39.83	22.53	15.00
5	5.5	20	0.1049	VII	5% (1)	9.95	5.69	3.73
6	6.0	20	0.1725	VII	15% (1)	9.95	5.69	3.73
7	6.5	20	0.4192	VIII	15% (1)	9.95	5.69	3.73
8	7.0	20	0.2839	IX	24% (2)	19.91	11.3	7.47
9	5.5	30	0.0534	VI	1% (1)	9.95	5.69	3.73
10	6.0	30	0.0960	VII	5% (1)	9.95	5.69	3.73
11	6.5	30	0.1656	VII	5% (1)	9.95	5.69	3.73
12	7.0	30	0.2863	VII	5% (1)	9.95	5.69	3.73

To further explore the relationship between seismic intensity and Natech risk, Figure 3 illustrates the variation in the scenario-level mean $\overline{NRI_s}$ as a function of *PGA* for naphtha, LPG and methane. The plotted points represent the scenario-based results, while the dashed curves correspond to regression fits (see Equations (7)–(9) for regression fits).

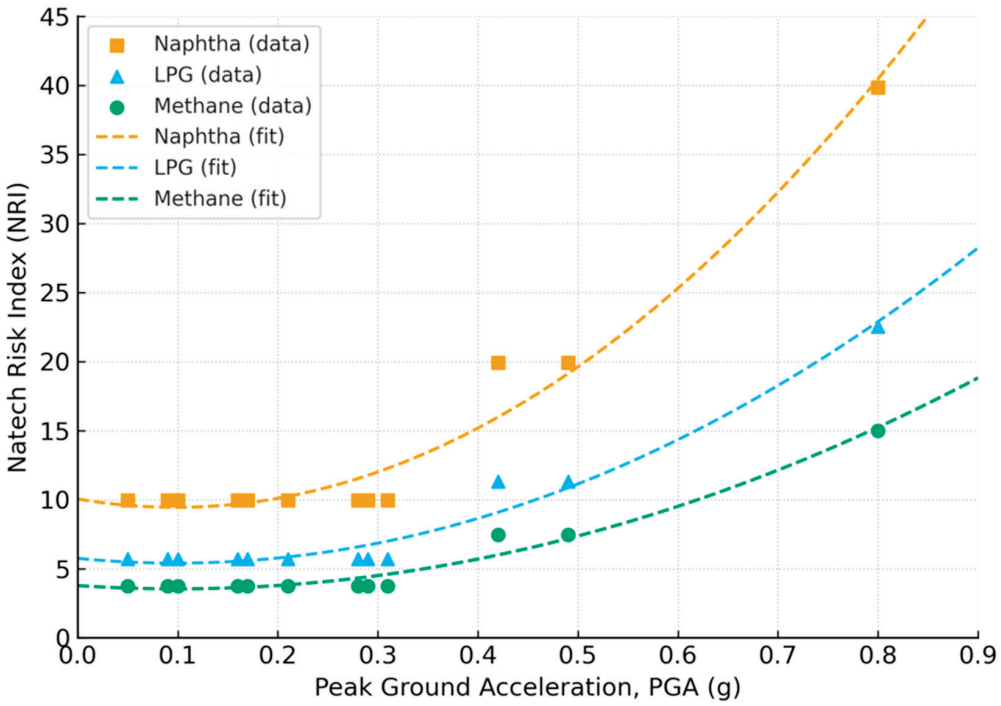

Figure 3. Variation in the $\overline{NRI_s}$ as a function of *PGA* for naphtha, LPG and methane (scenario-averaged over all 49 tanks and across 12 seismic scenarios).

https://doi.org/10.3390/infrastructures11020049

The following equations are the regression fits of mean $\overline{NRI_s}$ in function of PGA for naphtha, LPG and methane, respectively:

$$\overline{NRI}_{Naphta} = 62.96 \cdot PGA^2 - 12.35 \cdot PGA + 10.0 \ (R^2 = 0.968) \quad (7)$$

where $\overline{NRI}_{Naphta}$ denotes the mean NRI for naphta over all tanks for a given scenario.

$$\overline{NRI}_{LPG} = 35.49 \cdot PGA^2 - 6.97 \cdot PGA + 5.74 \ (R^2 = 0.967) \quad (8)$$

where $\overline{NRI}_{LPG}$ denotes the mean NRI for LPG over all tanks for a given scenario.

$$\overline{NRI}_{Methane} = 23.81 \cdot PGA^2 - 4.72 \cdot PGA + 3.77 \ (R^2 = 0.968) \quad (9)$$

where $\overline{NRI}_{Methane}$ denotes the mean NRI for methane over all tanks for a given scenario.

The quadratic regression relationships are derived from a limited number of high-PGA scenarios and are intended to illustrate the non-linear escalation of scenario-averaged Natech risk with increasing PGA. While the fitted curves capture the overall trend, the stability of the regression coefficients in the transition region would benefit from a denser sampling of earthquake scenarios at intermediate PGA levels. These relationships should therefore be interpreted as empirical, scenario-based trend representations rather than fully predictive models.

Figure 3 highlights how risk levels escalate nonlinearly with increasing PGA, particularly for naphtha, which exhibits higher sensitivity compared to LPG and methane. The regression curves are empirical, scenario-based fits illustrating non-linear risk escalation; additional earthquake scenarios would further refine coefficient stability in the transition region.

In addition, points represent scenario-averaged NRI values obtained by averaging across all tanks, as the figure focuses on inter-scenario risk escalation trends at the port scale.

4. Discussion

Based on Table 5., results of the NRI assessment across the twelve (12) seismic scenarios demonstrate that both the level of ground motion and the nature of the stored substances play critical roles in determining overall risk. A first observation is that moderate seismic scenarios (Scenarios 1, 2, 5, 6, 7, 9, 10, 11 and 12), corresponding to PGA values below 0.3 g and MMI of VII–VIII, generally yield stable and moderate $\overline{NRI_s}$ values. This behavior is consistent with recent scenario-based seismic Natech studies, which emphasize that risk escalation becomes pronounced after critical shaking thresholds because release likelihood increases non-linearly once damage states transition from light/moderate to severe. For example, Shafiei-Moghaddam et al. [3] used multiple earthquake hazard scenarios to assess chemical release risk and demonstrated how estimated risk levels vary strongly with scenario intensity. Similarly, Amaducci et al. [27] developed a quantitative risk assessment framework for earthquake-triggered Natech scenarios in pipeline systems, showing the relevance of integrated intensity–risk relationships for seismic risk management.

In these cases, naphtha consistently emerges as the most hazardous substances, with $\overline{NRI_s}$ scores close to 10, while LPG and methane remain in the lower-risk range.

The stability of NRI across different magnitudes but similar intensity classes (e.g., Scenarios 1 vs. 2, or Scenarios 5 vs. 6) highlights the dominant influence of MMI over earthquake magnitude alone in driving release probabilities and risk escalation.

In contrast, higher-intensity scenarios (Scenarios 3, 4 and 8), characterized by PGA values of 0.49 g and above and MMI levels of IX, show a sharp increase in $\overline{NRI_s}$ values.

 https://doi.org/10.3390/infrastructures11020049

Under these conditions, naphtha exhibits significantly higher risk values, reflecting their high volatility, flammability and potential to generate widespread impacts in the event of structural failure.

LPG also transitions from a low-to-moderate risk category (mean $\overline{NRI_s} \approx 11.3$–$22.5$), while methane, although still the lowest among the four, reaches values (mean $\overline{NRI_s} \approx 15$) that should not be overlooked. These findings indicate a nonlinear escalation of Natech risk once seismic intensity surpasses the VIII–IX threshold, consistent with fragility-based expectations of severe structural damage and increased release likelihood.

Another important finding is the role of tank clustering within the port. The short distances observed between several storage units substantially increase the probability of cascading accidents, meaning that even moderate release scenarios could lead to chain reactions involving multiple tanks. This configuration magnifies population exposure, particularly for naphtha tanks located near residential areas. Consequently, the proximity of tanks and their interaction through domino effects is as critical as the intrinsic hazard of the stored substances.

To quantify clustering, the inter-tank distances were measured by geospatial analysis. Table 6 summarizes representative distances between selected tanks across the port.

Table 6. Distances between representative tanks in the studied port.

Tanks	Distance (m)	Tanks	Distance (m)	Tanks	Distance (m)
1–2	35.14	16–18	25.86	32–34	24.03
1–3	32.71	17–19	21.17	33–34	32.25
2–4	52.30	18–19	31.61	33–35	20.80
3–4	40.18	17–20	29.18	34–36	17.58
3–5	25.70	19–21	35.62	35–36	18.77
4–5	45.34	20–21	16.45	37–38	187.03
5–6	24.50	21–22	19.74	37–16	124.84
6–7	36.74	22–23	25.17	39–40	11.07
6–8	37.53	23–28	20.62	40–42	9.39
8–9	42.92	20–23	44.37	39–41	9.50
7–9	31.69	23–28	19.77	41–42	10.71
7–10	53.20	23–32	28.61	41–43	12.28
9–10	71.33	18–24	33.57	41–44	12.23
10–11	82.99	24–25	25.19	42–44	16.00
10–12	81.78	25–26	21.10	42–45	11.88
12–14	50.69	26–27	35.91	43–44	9.91
11–12	45.42	28–29	14.22	44–45	8.10
11–14	37.61	28–32	14.62	46–47	9.26
12–13	41.38	29–30	14.53	46–49	8.12
13–14	50.16	29–31	18.38	47–48	7.51
13–15	24.01	30–31	20.72		
14–15	44.40	31–32	18.66		
16–17	16.88	31–33	51.32		

The results highlight several critical proximities well below 20 m, with some pairs separated by less than 10 m (e.g., tanks 44–45 at 8.1 m, tanks 47–48 at 7.5 m, tanks 41–42 at 10.7 m). These minimal separations fall within typical thermal radiation and overpressure footprints, confirming that the likelihood of cascading Natech events is high in the studied port.

These findings are consistent with a broad body of the Natech risk literature emphasizing the dominant influence of spatial configuration and inter-unit distances on escalation potential. Early foundational work by Cruz and Okada [14] demonstrated that closely

https://doi.org/10.3390/infrastructures11020049

spaced storage tanks substantially increase the likelihood of domino effects under both seismic and thermal loading, particularly when separation distances fall within characteristic thermal radiation or overpressure impact zones. Similarly, Necci et al. [28] showed that insufficient inter-tank spacing is one of the primary drivers of cascading accidents in Natech scenarios, often outweighing the contribution of the initial triggering hazard.

On the other hand, Figure 3 (see above) highlights several key observations, which are summarized as follows:

- For naphtha, a low-to-moderate risk is observed for PGA values greater than or equal to 0.31 g with mean $\overline{NRI_s} \approx 10$, followed by a significant to critical risk when PGA reaches or exceeds 0.42 g with $\overline{NRI_s} \approx 20$ and finally a catastrophic risk at $PGA = 0.8$ g with mean $\overline{NRI_s} \approx 40$. These products are highly flammable and in the event of rupture or leakage, they present a high risk of fire or explosion.
- For LPG, the risk remains low for $PGA \leq 0.31$ g with $\overline{NRI_s} \approx 5.69$, becomes significant at $PGA \geq 0.42$ g with mean $\overline{NRI_s} \approx 11.30$ and reaches a critical level at $PGA = 0.8$ g with mean $\overline{NRI_s} \approx 22.53$. In the event of a gaseous release, the consequences include a high risk of boiling liquid expanding vapor explosion and possible domino effects.
- For methane gas, the risk is low for $PGA \leq 0.31$ g with mean $\overline{NRI_s} \approx 3.73$, becomes moderate to significant at $PGA \geq 0.42$ g and finally reaches a critical level at $PGA = 0.8$ g with mean $\overline{NRI_s} \approx 15.00$. Methane is highly flammable and poses a significant risk of explosion.

The curves reveal three distinct phases: a nearly linear phase for PGA < 0.3 g, a critical transition phase for 0.3 g < PGA < 0.5 g and a nonlinear escalation for PGA > 0.5 g. As PGA increases, the mean $\overline{NRI_s}$ consistently rises for all products, with naphtha showing the highest sensitivity and the largest $\overline{NRI_s}$ values. LPG and methane also show increasing risk, but their mean $\overline{NRI_s}$ values remain lower for the same PGA. Data analysis shows that seismic risk increases sharply when PGA exceeds about 0.4 g. At this threshold, damage to energy infrastructures becomes much more severe, as confirmed in Scenarios 3, 4 and 8, where PGA $\geq$ 0.42 g. In these cases, the risk index for storage tanks reaches critical or even catastrophic levels, up to mean $\overline{NRI_s} \approx 40$.

Overall, the analysis highlights that naphtha represents the dominant contributor to Natech risk at the studied port, especially under high-intensity seismic shaking. LPG and methane, while comparatively less hazardous in moderate scenarios, still pose significant risks under strong ground motions due to their physical properties and storage conditions. These results underscore the importance of differentiated risk management strategies: reinforcing safety and containment measures for naphtha tanks, while ensuring adequate monitoring and contingency planning for LPG and methane installations.

Finally, the regression relationships between the mean Natech Risk Index $\overline{NRI_s}$ and PGA provide insight into how seismic Natech risk evolves as ground-motion intensity increases. The results indicate the existence of seismic intensity thresholds beyond which risk escalates nonlinearly, reflecting the transition from limited damage to widespread structural failure and cascading effects. This behavior is consistent with the established Natech literature, which shows that accident escalation becomes dominant once severe damage states are reached and domino mechanisms are activated in clustered industrial facilities. Krausmann et al. [29] highlighted the critical role of spatial configuration and escalation effects in governing Natech consequences and emphasized that scenario-based approaches are particularly well suited for capturing such nonlinear behaviors in complex industrial systems. In addition, official guidance by Necci and Krausmann [28] stresses that Natech risk assessment tools should be transparent, reproducible and operational,

 https://doi.org/10.3390/infrastructures11020049

especially in contexts where detailed facility data or fully probabilistic analyses are not feasible. Within this broader context, the proposed framework contributes a practical, scenario-based workflow that links seismic hazard intensity, release likelihood, off-site consequences, population exposure and escalation potential within a single screening indicator, supporting risk-informed decision-making for marine ports located in regions of moderate seismicity.

5. Conclusions

This study presented a framework to quantify seismic Natech risk in a representative port on the Saint-Laurence River in Quebec. By integrating regional seismic hazard estimates, damage-based Hazardous Release Likelihood Index HRLi scores, offsite consequence modeling and demographic exposure, the approach captures the full pathway from earthquake shaking to community-level impacts.

Results indicate that Natech risk remains moderate under shaking intensities of $PGA \leq 0.3$ g (MMI = VII–VIII) but escalates sharply once PGA exceeds 0.4 g (MMI = X). Naphtha was identified as the dominant risk drivers, with NRI values reaching catastrophic levels ($\overline{NRI_s} \approx 40$ at $PGA = 0.8$ g), while LPG and methane also showed significant escalation, including the potential for boiling liquid expanding vapor explosions. These findings underline the critical need for targeted risk reduction measures at marine ports located in regions of moderate seismicity.

A key outcome of this study is the establishment of regression relationships between NRI and PGA, which capture the nonlinear escalation of Natech risk with increasing seismic intensity. Notably, these equations can provide a quantitative foundation for future mitigation solutions, enabling researchers to predict how interventions such as anchorage retrofitting or soil densification may shift the risk curves and reduce vulnerabilities.

An important finding of this work is the critical role of tank clustering. The short distances observed between many tanks (often less than 20 m and in some cases below 10 m (e.g., tanks 44–45 separated by only 8.1 m, tanks 47–48 by 7.5 m and tanks 40–42 by 9.4 m)) significantly increase the probability of cascading accidents.

Under seismic-induced release, this proximity makes it highly likely that domino effects would trigger multiple tank failures, magnifying exposure for nearby communities. For example, clusters of naphtha tanks located near residential zones present particularly severe risks, as simultaneous releases could generate overlapping hazard zones. This configuration indicates that proximity and interaction between tanks are as critical as the intrinsic hazard of the stored substances and should therefore be explicitly integrated into site-specific Natech risk management strategies.

Overall, this proposed framework provides a tool to compare risk contributions and prioritize mitigation. Its adoption would strengthen seismic resilience in marine energy hubs while enhancing the safety of surrounding urban populations.

Future studies could refine population exposure estimates by explicitly overlaying dissemination-block population data from Statistics Canada within GIS environments, allowing tank-specific $Area_{sci}$ values to be computed. Such refinements would improve local resolution but are not expected to alter the scenario-averaged NRI trends identified in this study.

Additionally, future work should focus on expanding the set of earthquake scenarios, particularly at intermediate-to-high PGA levels, to further refine regression stability and enhance predictive robustness.

As future work, mitigation simulations could be performed to evaluate the effectiveness of various intervention strategies for reducing seismic Natech risk. Such analyses

 https://doi.org/10.3390/infrastructures11020049

would help identify how structural and geotechnical improvements can influence tank fragility and site-wide risk indices. For example, anchorage retrofit studies such as those by Phan et al. [30] demonstrate that anchored configurations perform substantially better than unanchored tanks under seismic loading, suggesting that similar simulations could quantify how increased anchorage capacity modifies local damage probabilities. Likewise, geotechnical investigations on soil densification and liquefaction resistance [31–33] provide a foundation for modeling how improvements in subgrade stiffness (e.g., higher Vs_{30} values) might mitigate foundation instability and reduce overall risk. Incorporating these types of mitigation scenarios into future numerical simulations would extend the present framework beyond risk quantification toward the development of actionable resilience and retrofit strategies for coastal ports. Additionally, probabilistic seismic reliability frameworks similar to those developed by Nassar et al. [34–36] for bridges could be extended to industrial port facilities for evaluating how mitigation measures (e.g., anchorage enhancement, base-isolation strategies and foundation improvement) influence overall Natech risk. Adapting such methodologies to storage-tank systems would allow for future research on designing resilience strategies for coastal ports.

Additionally, future extensions of the proposed framework could refine the domino-effect modeling by introducing consequence-specific interaction radii based on physical damage thresholds, such as thermal radiation levels for pool fires, overpressure criteria for vapor-cloud explosions or fireball radiation for BLEVE events. Incorporating heat-flux- or overpressure-based interaction distances would allow a more detailed representation of cascading failure mechanisms and could lead to substance- and release-type-dependent modifications of the domino-effect scores $D_{i,s}$.

While such refinements would increase model complexity and data requirements, they represent a natural progression toward higher-fidelity Natech risk assessments for port facilities, particularly when detailed consequence modeling and structural vulnerability data are available.

Limitations and Assumptions

The proposed seismic Natech risk assessment framework is intended as a screening-level, scenario-based methodology and several simplifying assumptions were adopted to ensure applicability in data-limited contexts. All storage tanks are assumed to be aboveground atmospheric steel tanks, consistent with common practice for large fuel and chemical storage facilities in marine ports. Detailed information on tank construction, anchorage systems, shell thickness and retrofitting history was not publicly available and therefore could not be explicitly modeled. While these factors influence seismic performance, their omission is consistent with the objective of comparative risk screening rather than detailed structural assessment.

Tank geometries and storage volumes were estimated using geospatial measurements from satellite imagery, which introduces uncertainty related to measurement resolution and the absence of detailed design drawings. The assumed tank characteristics are applied uniformly across scenarios to isolate the influence of seismic intensity, consequence magnitude and spatial configuration on Natech risk.

Consequently, the reported NRI values should be interpreted as relative indicators of risk escalation rather than absolute predictions of damage or release probability. These assumptions do not affect the identification of critical PGA thresholds but may influence the absolute magnitude of risk indices. Future studies could refine the analysis by incorporating tank-specific design and geotechnical data where available.

 https://doi.org/10.3390/infrastructures11020049

Author Contributions: M.N.: Methodology, result illustration, writing: original draft. F.M.: Methodology, formal analysis, writing: review and editing. A.A.E.E.: Conceptualization, methodology, supervision, writing: review and editing. All authors have read and agreed to the published version of the manuscript.

Funding: This study was supported through funding by École de Technologie Supérieure.

Data Availability Statement: All data generated or analyzed during this study are included in this article.

Conflicts of Interest: The authors declare no conflicts of interest.

Abbreviations

The following abbreviations are used in this manuscript:

NRI	Natech Risk Index
$NRI_{i,s}$	Natech Risk Index for tank i under seismic scenario s
$\overline{NRI_s}$	Mean Natech Risk Index for all tanks under seismic scenario s
PGA	Peak Ground Acceleration
GMPE	Ground Motion Prediction Equations
HRLi	Hazardous Release Likelihood Index
MDE	Maximum Distance of Effect
BLEVE	Boiling Liquid Expanding Vapor Explosion
CFD	Computational Fluid Dynamics
IM	Intensity Measure
LPG	Liquefied Petroleum Gas
MMI	Modified Mercalli Intensity
M_w	Moment Magnitude
R_{epi}	Epicentral Distance
V_{s30}	Average shear-wave velocity in the upper 30 m of soil

References

1. Cruz, A.M.; Krausmann, E. Vulnerability of the oil and gas sector to climate change and extreme weather events. *Clim. Change* **2013**, *121*, 41–53. [CrossRef]
2. Huang, Z.-K.; Zeng, N.-C.; Zhang, D.-M.; Argyroudis, S.; Mitoulis, S.-A. Resilience Models for Tunnels Recovery After Earthquakes. *Engineering* **2025**, *54*, 320–345. [CrossRef]
3. Shafiei-Moghaddam, P.; Jahangiri, K.; Hassani, N. Chemical release risk assessment in earthquake: Natech event scenario. *Heliyon* **2024**, *10*, e28797. [CrossRef]
4. Kabir, G.; Suda, H.; Cruz, A.M.; Giraldo, F.M.; Tesfamariam, S. Earthquake-related Natech risk assessment using a Bayesian belief network model. *Struct. Infrastruct. Eng.* **2019**, *15*, 725–739. [CrossRef]
5. Yazici, G.; Cili, F. Evaluation of the liquid storage tank failures in the 1999 Kocaeli Earthquake. In Proceedings of the 14th World Conference on Earthquake Engineering, Beijing, China, 12–17 October 2008.
6. Fabbrocino, G.; Iervolino, I.; Orlando, F.; Salzano, E. Quantitative risk analysis of oil storage facilities in seismic areas. *J. Hazard. Mater.* **2005**, *123*, 61–69. [CrossRef]
7. Atkinson, G.M.; Adams, J. Ground motion prediction equations for application to the 2015 Canadian national seismic hazard maps. *Can. J. Civ. Eng.* **2013**, *40*, 988–998. [CrossRef]
8. Pezeshk, S.; Zandieh, A.; Tavakoli, B. Hybrid empirical ground-motion prediction equations for eastern North America using NGA models and updated seismological parameters. *Bull. Seismol. Soc. Am.* **2011**, *101*, 1859–1870. [CrossRef]
9. Pavel, F.; Vacareanu, R.; Cioflan, C.; Iancovici, M. Spectral characteristics of strong ground motions from intermediate-depth Vrancea seismic source. *Bull. Seismol. Soc. Am.* **2014**, *104*, 2842–2850. [CrossRef]
10. Valente, M.; Ricci, F.; Cozzani, V. A systematic review of Resilience Engineering applications to Natech accidents in the chemical and process industry. *Reliab. Eng. Syst. Saf.* **2025**, *255*, 110670. [CrossRef]
11. Rodriguez, D.J.C.; Barresi, A.A.; Demichela, M. Critical infrastructure multi-risk deployment: An innovative framework to support NaTech preparedness in industrial facilities. *Process Saf. Environ. Prot.* **2025**, *202*, 107736. [CrossRef]

 https://doi.org/10.3390/infrastructures11020049

12. Lamontagne, M.; Halchuk, S.; Cassidy, J.F.; Rogers, G.C. *Significant Canadian Earthquakes 1600–2017*; Geological Survey of Canada: Ottawa, ON, Canada, 2018.
13. Franco, S.I.; Canet, C.; Iglesias, A.; González, C.V. Seismic activity in the Gulf of Mexico. A preliminary analysis. *Boletín Soc. Geol. Mex.* **2013**, *65*, 447–455. [CrossRef]
14. Cruz, A.M.; Okada, N. Methodology for preliminary assessment of Natech risk in urban areas. *Nat. Hazards* **2008**, *46*, 199–220. [CrossRef]
15. Showalter, P.S.; Myers, M.F. Natural Disasters in the United States as Release Agents of Oil, Chemicals, or Radiological Materials Between 1980–1989: Analysis and Recommendations. *Risk Anal.* **1994**, *14*, 169–182. [CrossRef]
16. Zhou, L.; Chen, G.; Zheng, M.; Gao, X.; Luo, C.; Rao, X. Agent-based modeling methodology and temporal simulation for Natech events in chemical clusters. *Reliab. Eng. Syst. Saf.* **2024**, *243*, 109888. [CrossRef]
17. *CAN/CSA-S6-14*; Canadian Highway Bridge Design Code. CSA Group: Mississauga, ON, Canada, 2014.
18. Ricci, F.; Yang, M.; Reniers, G.; Cozzani, V. Emergency response in cascading scenarios triggered by natural events. *Reliab. Eng. Syst. Saf.* **2024**, *243*, 109820. [CrossRef]
19. Misuri, A.; Cozzani, V. A paradigm shift in the assessment of Natech scenarios in chemical and process facilities. *Process Saf. Environ. Prot.* **2021**, *152*, 338–351. [CrossRef]
20. Abo-El-Ezz, A.; Farzam, A.; Fezai, H.; Nollet, M.-J. Scenario-based earthquake damage assessment of highway bridge networks. *Adv. Bridge Eng.* **2023**, *4*, 3. [CrossRef]
21. Abo-El-Ezz, A.; Houalard, C.; Nollet, M.-J.; Assi, R. Vulnerability assessment of seismic induced out-of-plane failure of unreinforced masonry wall buildings. *Can. J. Civ. Eng.* **2017**, *44*, 1045–1055. [CrossRef]
22. Seligson, H.A.; Eguchi, R.T.; Tierney, K.J.; Richmond, K. *Chemical Hazards, Mitigation and Preparedness in Areas of High Seismic Risk: A Methodology for Estimating the Risk of Post-Earthquake Hazardous Materials Release*; National Center for Earthquake Engineering Research: Taipei City, Taiwan, 1996.
23. RMP*Comp. Available online: https://cdxapps.epa.gov/olem-rmp-maintain/action/rmp-comp (accessed on 1 December 2025).
24. van den Bosch, C.J.H.; Weterings, R.A.P.M. *Methods for the Calculation of Physical Effects "Yellow Book"*; Committee for the Prevention of Disasters: The Hague, Denmark, 2005.
25. Cozzani, V.; Salzano, E. The quantitative assessment of domino effects caused by overpressure: Part I. Probit models. *J. Hazard. Mater.* **2004**, *107*, 67–80. [CrossRef]
26. Sun, D.; Jiang, J.; Zhang, M.; Wang, Z. Influence of the source size on domino effect risk caused by fragments. *J. Loss Prev. Process Ind.* **2015**, *35*, 211–223. [CrossRef]
27. Amaducci, F.; Misuri, A.; Bonvicini, S.; Salzano, E.; Cozzani, V. Quantitative risk assessment of Natech scenarios triggered by earthquakes involving pipelines. *Reliab. Eng. Syst. Saf.* **2024**, *245*, 109993. [CrossRef]
28. Necci, A.; Krausmann, E. *Natech Risk Management*; JRC Publications Repository: Brussels, Belgium, 2022; Volume 10, p. 666413.
29. Krausmann, E.; Cozzani, V.; Salzano, E.; Renni, E. Industrial accidents triggered by natural hazards: An emerging risk issue. *Nat. Hazards Earth Syst. Sci.* **2011**, *11*, 921–929. [CrossRef]
30. Phan, H.N.; Paolacci, F.; Di Filippo, R.; Bursi, O.S. Seismic vulnerability of above-ground storage tanks with unanchored support conditions for Na-tech risks based on Gaussian process regression. *Bull. Earthq. Eng.* **2020**, *18*, 6883–6906. [CrossRef]
31. Bao, X.; Jin, Z.; Cui, H.; Chen, X.; Xie, X. Soil liquefaction mitigation in geotechnical engineering: An overview of recently developed methods. *Soil Dyn. Earthq. Eng.* **2019**, *120*, 273–291. [CrossRef]
32. Bhanwar, P.; Dave, T. A review on soil liquefaction mitigation techniques and its preliminary selection. In Proceedings of the Indian Geotechnical Conference 2019: IGC-2019 Volume III, Surat, India, 19–21 December 2019; Springer: Singapore, 2019.
33. Idriss, I.M.; Boulanger, R.W. *Soil Liquefaction During Earthquakes*; Earthquake Engineering Research Institute: Oakland, CA, USA, 2008.
34. Nassar, M.; Guizani, L.; Nollet, M.J.; Tahan, A. A probabilistic approach to assess seismic base-isolated bridges reliability in cold climate. In Proceedings of the 11th National Conference in Earthquake Engineering, Los Angeles, CA, USA, 25–29 June 2018.
35. Nassar, M.; Guizani, L.; Nollet, M.-J.; Tahan, A. Seismic reliability assessment of base-isolated bridges in Quebec. *Can. J. Civ. Eng.* **2022**, *49*, 242–254. [CrossRef]
36. Nassar, M.; Guizani, L.; Nollet, M.-J.; Tahan, A. Effects of temperature, analysis and modelling uncertainties on the reliability of base-isolated bridges in Eastern Canada. *Structures* **2022**, *37*, 295–304. [CrossRef]

Disclaimer/Publisher's Note: The statements, opinions and data contained in all publications are solely those of the individual author(s) and contributor(s) and not of MDPI and/or the editor(s). MDPI and/or the editor(s) disclaim responsibility for any injury to people or property resulting from any ideas, methods, instructions or products referred to in the content.

infrastructures

MDPI

Article

Analyzing Natural Disaster Risk Factors in Engineering Projects: A Social Networks Analysis Approach

Qiuyan Gu and Jun Wang *

School of Management Engineering, Qingdao University of Technology, Qingdao 266520, China
* Correspondence: wangjun.gt@gmail.com

Abstract: Natural disasters pose significant risks to engineering projects, necessitating a systematic analysis of their risk factors. This study focuses on identifying and mapping these factors using a mixed-methods approach that integrates a qualitative literature review with scientometric analysis via Social Network Analysis (SNA). Through a meta-analysis of 81 peer-reviewed articles from Web of Science, Scopus, and ScienceDirect, the qualitative review establishes a comprehensive list and classification of 48 natural disaster risk factors, categorized into geological, climatic, hydrological, topographic, and biological groups, while providing a theoretical foundation. SNA complements this by quantifying co-occurrence frequencies, centrality metrics (degree, betweenness, and eigenvector), and network structures, revealing dynamic interactions, key influential factors, and research gaps—particularly in under-explored areas like hydrological hazards, extreme temperatures, lightning storms, and temperature variations—that qualitative methods alone might miss. This multi-perspective integration highlights discrepancies between theoretical discussions and practical applications, underscoring overlooked cascading effects. Findings emphasize the absence of an integrated model for all 48 factors, urging the development of a holistic predictive framework to bolster disaster resilience. Theoretically, the study offers a novel SNA-based quantification of factor importance and interrelations, addressing literature fragmentation. Practically, it guides project managers in prioritizing risks for optimized design, resource allocation, and prevention strategies. Future research should incorporate real-time data sources to refine this framework for enhanced risk management in engineering projects.

Keywords: engineering project; natural disaster; risk factors; risk management; social networks analysis

1. Introduction

Globally, the frequent occurrence of extreme weather events exacerbated by climate change, along with other natural disasters such as earthquakes, floods, mudslides, and hurricanes, poses significant risks and challenges to the development of the construction industry and engineering projects. Typically, natural disasters can cause large-scale damage to both ongoing and completed projects [1]. For instance, the 2023 earthquake in Turkey and Syria led to the collapse of thousands of buildings and caused severe damage to critical infrastructure [2]. According to data from the United Nations Office for Disaster Risk Reduction (UNDRR), approximately 350 to 500 natural disasters occur globally each year, and this number is on the rise. The sudden nature of natural disasters often results in varying degrees of damage to construction projects or completed infrastructure. Due

to their scale and unpredictability, natural disasters pose greater threats to engineering projects than other destructive forces [3].

Since the mid-20th century, the impact of natural disasters on engineering projects has attracted widespread attention, especially amid the large-scale construction of infrastructure projects. Natural disasters can cause severe damage to engineering projects, including structural damage, functional failure, and long-term safety concerns. The impact of natural disaster risks on engineering projects has long drawn extensive attention from academia and industry [4]. With the acceleration of global climate change and urbanization, the frequency and destructive power of natural disasters are increasing, introducing substantial uncertainty and risk to engineering projects. Considerable research has been devoted to assessing [5] and managing [6] the vulnerability and risk of engineering projects to natural disasters. As a result, research on the resilience of engineering projects has gained increasing focus, aiming to enhance their ability to withstand natural disasters. For example, Ouyang et al. proposed a resilience assessment framework for urban infrastructure systems [7].

Research on natural disasters affecting engineering projects is of significant importance [8]. In the past 30 years, with the implementation of the International Strategy and Action Plan for Disaster Reduction, disaster reduction science has become a global hotspot. By reviewing the knowledge system of natural disaster risk factors for engineering projects, it is evident that previous research mainly focused on a single natural disaster risk factor, such as floods [9], earthquakes [10], hurricanes [11], landslides [12], rockfalls [13], collapses [14]. In previous research, methods such as BP neural networks [15], disaster mapping and risk assessment [16], event maps [17], natural disaster knowledge map [18], multiple linear regression analysis [19], and others were used to conduct in-depth explorations of specific natural disasters in engineering projects, which have contributed to mitigating the impacts of natural disaster risks on engineering projects.

Overall, although existing studies have analyzed natural disaster risk factors affecting engineering projects through various methods, a comprehensive list of natural disaster factors for engineering projects has not been established [20]. While significant progress has been made in analyzing the risks of natural disasters for engineering projects, the frameworks used in practical applications remain insufficiently systematic and comprehensive. Most research focuses on one or a few specific natural disaster risk factors, conducting either risk assessments or analyses of natural disasters without specifying particular risk factors, which results in broad generalizations and a lack of systematic understanding of natural disaster risk factors within engineering projects. Furthermore, there may be linkage or superimposed effects among these natural disasters [21]. For instance, an earthquake may trigger flooding, especially when it causes dam failures or landslides [22]. The lack of an integrated framework means that some critical factors may be overlooked in the assessment process, or the interactions between disasters may not be systematically considered, which constitutes a critical knowledge gap and limits the forward-looking development of natural disaster risk prediction for engineering projects. Consequently, researchers and engineers have emphasized the need to establish an integrated framework. Such a comprehensive list would not only enhance the resilience of engineering projects, reducing disaster-related losses, but also promote more scientific resource allocation and emergency response. Moreover, clarifying the interactions among natural disasters could provide policymakers with a basis for optimizing disaster risk management and urban planning, ensuring sustainable development.

This study employs a mixed-methods approach, combining a qualitative literature review with scientometric analysis to achieve a comprehensive examination of natural disaster risk factors in engineering projects. The qualitative review systematically synthesizes existing literature to identify and classify 48 core risk factors, providing the theoretical foundation

and conceptual framework. However, traditional qualitative methods are often limited to descriptive analysis and are insufficient for capturing the dynamic interactions among factors. To address this limitation, we introduce Social Network Analysis (SNA) as a scientometric tool. Its relevance lies in its graph-theoretical basis, which enables the quantification of co-occurrence frequencies and centrality measures of risk factors, revealing research hotspots, gaps, and potential cascading effects. This quantitative supplement not only validates the reliability of the qualitative classification but also visualizes the overall structure of the risk network, offering multi-level insights and providing a research foundation for future disaster assessments in engineering projects. This paper analyzes 81 articles to examine the risk factors they address, systematically identifying natural disaster risk factors in engineering projects and constructing both the factor network and the factor model network. The study identifies key natural disaster risk factors as well as factors overlooked during the research process, revealing the complex relationships among these risk factors.

Compared with the existing literature, the primary contributions of this study are threefold:

1. Comprehensive identification and systematization of risk factors: This is the first study to systematically identify, classify, and compile a complete set of 48 natural disaster risk factors through rigorous comprehensive analysis. Building on this foundation, we construct a detailed factor network and corresponding model network, providing a structured and exhaustive reference framework that was previously lacking.
2. Novel integration of methodological approaches: We propose a unique hybrid framework that combines simplified analytical methods with SNA. This multi-level approach not only bridges the gap between theoretical risk discussions and practical modeling applications but also enables dynamic visualization of the interrelationships and structural evolution among risk factors. Compared with traditional linear or single-method analyses, our approach significantly enhances the reliability, depth, and interpretability of complex system evaluations.
3. New insights into overlooked hazards and practical implications: The study uncovers the low network connectivity and potential cascading effects of traditionally neglected risk factors, including hydrological hazards, extreme temperatures, lightning storms, and temperature variations. These findings highlight the urgent need for integrated, multi-hazard predictive models and offer actionable, evidence-based guidance for project managers to improve engineering design, optimize resource allocation, and strengthen disaster prevention and mitigation strategies.

The writing framework of this paper is as follows: The second part describes the literature review; the third part introduces the research methods, including simplified analysis and SNA; the fourth part discusses the results. The fifth part presents the final conclusion.

2. Literature Review

2.1. Natural Disaster Risk

Defining natural disasters in the context of engineering projects is complex, as highlighted by Lukic et al., who note the challenge of establishing a universally accepted definition, even when disasters are clearly identifiable [23]. A review of existing literature suggests a general definition of natural disasters in engineering projects as extreme environmental events caused by natural processes or phenomena, such as earthquakes, hurricanes, floods, and landslides [24]. These events can cause significant damage to civil engineering structures, disrupt social and economic systems, and impair infrastructure and essential services.

Natural disaster risk factors for engineering projects are typically categorized into five groups [25,26]: geological factors (e.g., earthquakes, geological structures, and conditions), climatic factors (e.g., storms, rainstorms, tornadoes, blizzards), hydrological factors (e.g., floods, tsunamis, sea-level rise), topographic factors (e.g., topography, elevation), and biological factors (e.g., fires, pests), or any combination thereof. To synthesize these classifications, recent reviews have mapped the evolution of risk frameworks, revealing a shift from isolated disaster assessments toward integrated resilience models that account for climate-amplified interactions [27]. For example, early studies emphasized probabilistic modeling of single events, such as earthquakes [28] or floods [29], whereas more recent integrated analyses highlight the need for holistic quantification of resilience, critiquing traditional metrics for underestimating the recovery dynamics of urban infrastructure [30]. This evolution underscores a critical gap: despite progress in earthquake risk factors, comprehensive lists remain fragmented and often overlook cascading effects, such as hydrological surges triggered by earthquakes.

Understanding the characteristics of natural disaster risks is critical for engineers and decision-makers in developing targeted preventive measures and ensuring effective disaster response [31]. Such understanding also facilitates the assessment of potential chain reactions triggered by natural disasters, enabling more comprehensive risk evaluations [32]. A literature review identifies the following characteristics of natural disaster risk factors [33]: (1) high unpredictability; (2) large-scale impact, often affecting multiple projects or entire regional infrastructures; (3) sudden onset, causing significant damage in a short time; (4) potential for chain reactions, such as earthquakes triggering landslides; and (5) long-term impacts. These characteristics underscore the need for comprehensive risk assessment and management to minimize the potential impacts of disasters on engineering projects.

In synthesizing previous work, studies have explored various natural disaster risk factors, including rapid assessment techniques for earthquake disaster losses [28], flood risk management [29], fuzzy comprehensive evaluation of collapse risks in mountain tunnel construction [34], comprehensive management of short-term extreme rainfall threats [35], deterministic modeling of dredging project durations [36], and a comprehensive index system for landslide susceptibility along highways [37]. However, as highlighted by reviews of construction disaster systems from 2010 to 2025 [38], these approaches often prioritize methodological trends at the expense of interdisciplinary integration, resulting in the neglect of socio-economic amplifiers within the civil engineering context [30]. This fragmentation limits holistic understanding and calls for the adoption of a unified framework aligned with global risk reporting.

Natural disasters pose significant risks to engineering projects, prompting extensive literature reviews to enhance understanding of these risks. Despite considerable progress, most studies focus on specific risks, assessing their magnitude, probability, and mitigation strategies, rather than providing a holistic understanding of the natural disaster risk system affecting engineering projects. Critically, this siloed approach—as evident in reviews of infrastructure projects identifying 128 cross-category risks [39]—fails to address interdependencies, such as how climatic factors may amplify geological vulnerabilities. Consequently, a comprehensive list of natural disaster risk factors for engineering projects has yet to be established. This paper employs SNA to identify these risks, create a comprehensive risk list, clarify the relationships among risk factors, and highlight the most critical factors.

2.2. Social Network Analysis

2.2.1. SNA Applications in Engineering Projects

In engineering projects, SNA is a method that examines networks composed of nodes and edges to study social structures, focusing on relationships among entities and their

formation into complex network structures for systematic analysis and visualization [40]. Over the past two decades, SNA has gained prominence in construction engineering and management (CEM) as projects are increasingly viewed as organizational networks [41]. For instance, Trach et al. applied SNA to evaluate communication quality among construction project participants, identifying key factors affecting communication and addressing low delivery efficiency [42]. He et al. employed Social Network Analysis to quantify the systemic risk and vulnerability of power grid disasters. They identified and analyzed the key risk factors of power grid disasters, constructed a power grid disaster system, and used the SNA framework to identify the core risk factors and critical combinations of risk factors in power grid disasters [43]. Similarly, Zheng et al. reviewed SNA applications in construction project management, addressing gaps through literature analysis, including applications in subway construction collapse accidents and freeway data decision networks [44]. Hazarika et al. explored SNA's application in natural disaster risk management for engineering projects [45]. They assessed the impact of natural disasters on project resilience and analyzed interrelationships among risk factors. Using SNA, researchers identified critical nodes and information flow paths essential in disaster scenarios, proposing strategies to enhance project resilience and demonstrating SNA's effectiveness in managing complex risk networks. Shan and Zhao [46] proposed a social network analysis (SNA) framework based on social media to assess disaster recovery and resilience in terms of infrastructure and psychological states. This framework aids disaster emergency management departments in formulating more precise and effective decisions for post-disaster reconstruction and psychological interventions, while providing references for enhancing urban disaster resilience. Wang et al. [47] applied SNA to HSE (Health, Safety, and Environment) risk network analysis, laying the foundation for disaster risk assessment and supporting multi-stakeholder coordination. They also proposed risk classification early warning and control strategies to rationally allocate emergency resources. Yang et al. [48] visualized flood risk networks using SNA, supporting the assessment and prediction of flash flood disasters. Shen et al. [49] applied SNA indicators to risk networks in large-scale programs, identifying cross-project dependencies and enhancing risk mitigation strategies.

2.2.2. Reasons for Selecting SNA

SNA is instrumental in revealing relationships between research literature [50–52]. SNA's utility in complex project management has been demonstrated by Lee et al., who highlighted its effectiveness in analyzing non-human resource networks, aiding strategic planning, and improving project delivery and interdisciplinary interactions [53]. Various methods have been used to analyze natural disaster risk factors, each with distinct benefits. For example, the Analytic Hierarchy Process (AHP) decomposes complex decision-making into hierarchical structures, determining factor weights through pairwise comparisons; Badea et al. used AHP to analyze supply chain collaboration barriers [54]. The Delphi method identifies and prioritizes risks through iterative expert consultations, as seen in Pratama et al.'s study of 28 toll road operation risks in Sumatra [55]. In another case, AHP was applied to assess flood risk in Malda, India, improving disaster map accuracy [56].

This paper adopts SNA for the following reasons: (1) SNA effectively captures the complex relationships and interactions among numerous natural disaster risk factors using graph theory and network structures, providing a global perspective; (2) it identifies key nodes and pathways; (3) it offers robust visualization tools; and (4) it integrates data from diverse sources to build comprehensive risk networks. Compared to other traditional methods, SNA exhibits significant advantages in capturing the dynamic correlations of risk factors and quantifying network structures. AHP determines factor weights through

pairwise comparisons and hierarchical decomposition, making it suitable for linear decision structures, but it struggles to handle nonlinear dynamic interactions between risk factors, such as the cascading effects of earthquakes inducing floods, leading to the neglect of potential bridging paths and amplification mechanisms in complex networks [54,57]. Similarly, the Delphi method relies on iterative expert consensus to prioritize risks, excelling in the subjective evaluation of single or few factors, but it is limited by expert biases and static feedback loops, and is unable to quantify global connectivity and evolutionary dynamics among multiple factors, such as topological changes in risk networks under climate change [55,58]. In contrast, SNA, based on a graph theory framework, can dynamically map multidimensional correlations between risk factors through co-occurrence frequency and centrality metrics (such as degree centrality), while visualizing network density and modular structures to reveal hidden cascading risk paths, thereby providing more comprehensive system-level insights [50–52]. This methodological innovation not only enhances the robustness and interpretability of risk assessment but also lays a quantitative foundation for constructing multi-hazard prediction models in engineering projects [57].

2.2.3. Integration with Factor Analysis and Literature Review

The integration of SNA with factor identification and analysis has been applied in previous studies on engineering project risks beyond natural disasters. Researchers have treated factors as nodes within SNA frameworks. For instance, Wang et al. used SNA to identify key safety risk factors in marine bridge construction [59], while Li et al. identified nine social risk factors and 12 stakeholders in infrastructure projects [60]. Aghililotf et al. applied SNA to analyze construction industry challenges, identifying key issues through network analysis [61]. In these studies, factors are represented as nodes connected to form a network. This paper adopts a similar logic, treating natural disaster risk factors as nodes in an SNA framework.

Literature reviews integrated with SNA have also been employed previously. For example, Assaad and El-adaway reviewed 43 journal articles to identify 20 factors contributing to the failure of design and construction companies, using SNA to highlight neglected factors [62]. Schreiber et al. conducted a systematic literature review on software development projects, emphasizing SNA's importance [63]. Tai et al. built an SNA model to analyze factors affecting BIM adoption in China's construction industry [64]. This paper similarly combines SNA with a literature review to identify natural disaster risk factors in engineering projects, building on existing research to analyze SNA's application.

2.2.4. Provided Benefits

Using SNA to analyze natural disaster risk factors in engineering projects leverages centrality indices to measure node importance or influence within a network. Key centrality measures include:

1 Degree Centrality: Reflects the number of connections a node has, indicating its direct influence. High degree centrality suggests a factor significantly impacts others, marking it as a key network member [65];
2 Betweenness Centrality: Measures how often a node lies on the shortest paths between other nodes, reflecting its role as a bridge or intermediary [66];
3 Eigenvector Centrality: Considers both the number and importance of a node's connections, with higher centrality indicating connections to other influential nodes [67].

These centrality measures provide a deeper understanding of network structures [68], aiding in the development of effective policies and decisions. In this paper, degree centrality, calculated from co-occurrence frequency matrices, ranks the importance of natural disaster

risk factors. This approach aligns with prior studies, such as Darko et al., who used degree centrality to analyze global green building research trends [69], and Yuan et al., who assessed key risk factors and stakeholders in high-density urban construction projects through co-occurrence and degree centrality analysis [70].

These centrality measures enable a deeper understanding of the network structure and provide hazard-specific insights into natural disaster risk networks, thereby supporting effective policy and decision-making. Degree centrality quantifies the direct exposure of each factor—analogous to assessing hazard frequency—and helps prioritize high-frequency risks (e.g., earthquakes). Betweenness centrality reveals the role of bridging nodes and maps potential cascading pathways (e.g., earthquakes triggering landslides), allowing interventions to target key intermediaries. Eigenvector centrality captures indirect amplification effects, reflecting system-level vulnerabilities (such as climatic factors amplifying hydrological risks through topographic conditions). This combination is well suited to the context of engineering projects, where disaster risks often manifest as asymmetric networks—dominated by a small number of highly influential factors—rather than evenly distributed interactions [69,70].

3. Research Methods

The authors conducted a meta-analysis of literature addressing natural disaster risk factors in engineering projects to achieve three objectives: (1) identify key natural disaster risk factors affecting engineering projects, (2) determine under-researched risk factors requiring further investigation, and (3) highlight the need for a holistic and comprehensive model to predict and mitigate natural disaster risks. The research framework is illustrated in Figure 1.

To ensure objectivity and reproducibility, this study predefined the parameters and criteria for identifying risk factors. First, based on predefined search terms, a systematic literature review was conducted using three databases: Web of Science, Scopus, and ScienceDirect (EI) [71]. A total of 130 articles were retrieved from Web of Science, 78 from Scopus, and 75 from ScienceDirect. After removing duplicates—15 overlapping articles between Web of Science and Scopus, and 1 between Scopus and ScienceDirect—283 articles were identified, and 16 duplicates were excluded, resulting in 267 articles. The complete list of all 283 articles is provided in Appendix A.1. These articles were screened based on three criteria: (1) relevance to natural disaster risk: ensuring that the articles explicitly address hazards such as earthquakes, floods, or storms, while excluding general climatic or anthropogenic risks that may dilute the focus on unpredictable, large-scale natural events relevant to engineering vulnerability; (2) pertinence to the construction industry: strictly limit the inclusion scope to the civil engineering context of the primary disaster-affected domains under discussion; and (3) focus on construction projects: focusing on project-specific analyses (e.g., risk assessment during the design or construction phases) rather than post-disaster recovery of completed structures. After screening, 44 articles were excluded for not addressing natural disaster risk, 120 for not pertaining to the construction industry, and 169 for not focusing on construction projects. Ultimately, 81 articles were selected for analysis of natural disaster risks in engineering projects. Finally, risk factors were extracted using content analysis, with co-occurrence frequency serving as the initial activation criterion. Following Newman's [72] network density principle to avoid noisy nodes, factors were included as network nodes only when they co-occurred in three or more articles. The classification of risk factors followed the five-category framework of Blaikie et al. [25], and the SNA parameters included degree centrality, betweenness centrality, and eigenvector centrality. These criteria ensured the transparency and objectivity of factor identification, avoiding potential biases.

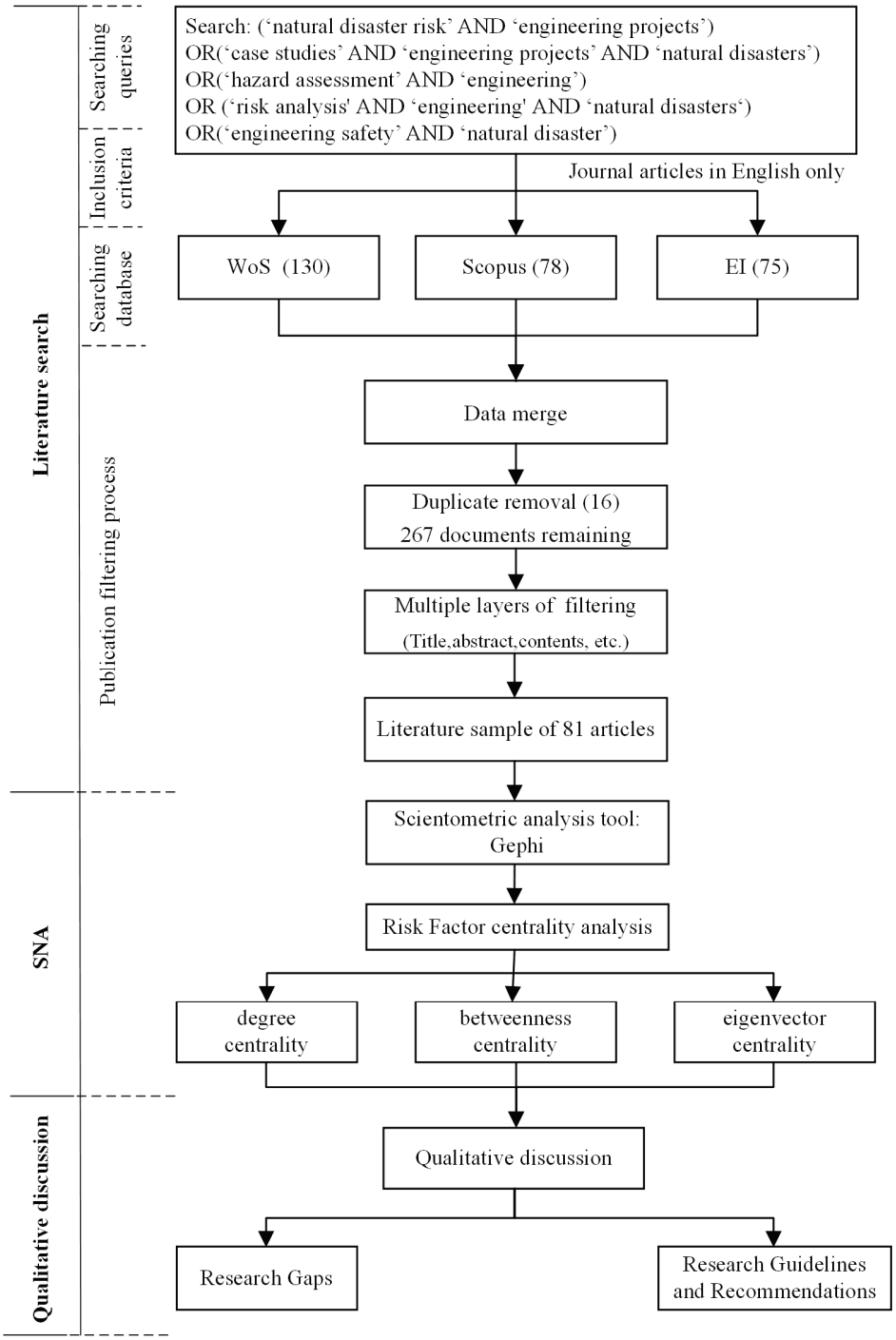

Figure 1. Research framework.

3.1. Meta-Analysis of the Literature

Following the approach of Ciurean et al. [73], which integrates theoretical discussion and modeling, the selected articles were categorized into two types: (1) studies focusing on theoretical aspects of natural disaster risk factors, and (2) studies combining theoretical and practical perspectives by examining the impacts of these risk factors.

Type 1: These articles provide theoretical discussions on natural disaster risk factors and their influence on engineering projects. Here, "theoretical discussion" refers to abstract or conceptual analyses without employing statistical, machine learning, or other mathemat-

ical/computational models. In this study, papers with theoretical discussions are denoted by the letter "M."

Type 2: These articles combine theoretical discussions (similar to Type 1) with predictive models based on selected natural disaster risk factors. Papers developing such models are denoted by the letter "S," indicating both theoretical mention (M) and model formulation (S).

A reference matrix was constructed, with natural disaster risk factors as rows and the 81 selected articles as columns. Each cell indicates whether a specific risk factor is mentioned or used in a given paper (1 for mentioned/used, 0 otherwise). A hypothetical diagram of the reference matrix, illustrating its transformation into an adjacency matrix, is shown in Figure 2.

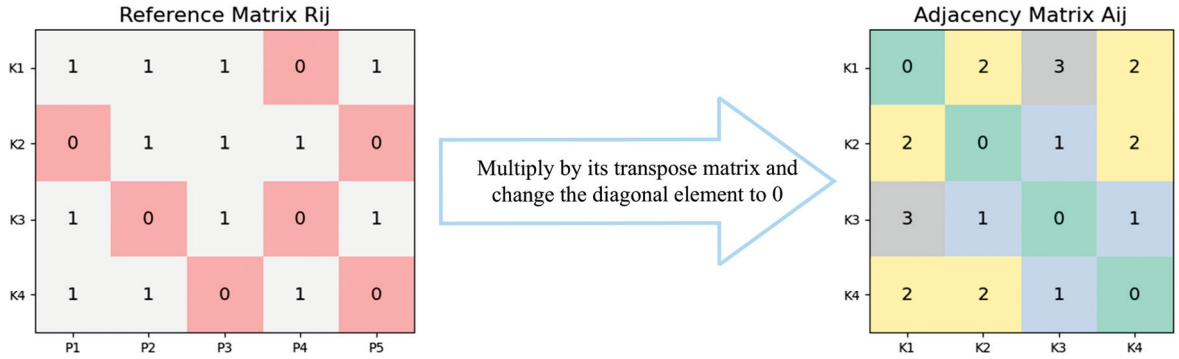

Figure 2. Adjacency matrix diagram.

The reference matrix "M" represents articles (Type 1) that provide theoretical discussions on natural disaster risk factors in engineering projects. Its purpose is to map the overall academic and professional discourse on these risk factors and identify those deemed most significant. The reference matrix "S" represents Category 2 literature, namely studies that construct predictive models based on specific natural disaster risk factors. Here, a "predictive model" refers to a quantitative or simulation-based framework used to estimate the potential impact of natural disaster risks on engineering projects. Such models typically employ mathematical, statistical, or computational methods to simulate scenarios and predict outcomes—for example, finite element analysis (FEA) models used to predict structural responses under earthquakes [10], or Monte Carlo simulation models used to assess flood inundation risks and the probabilistic failure rates of hydraulic infrastructure [9]. By incorporating empirical data and validation techniques, these models bridge the gap between theoretical risk discussions and engineering practice. The reference matrix "S" represents articles (Type 2) that develop predictive models based on specific natural disaster risk factors. Its purpose is to highlight the risk factors incorporated into existing models. By comparing matrices M and S, this study identifies discrepancies between risk factors discussed in theory and those applied in predictive models, addressing a key research question: which natural disaster risk factors are under-researched or overlooked in engineering projects, and which should be prioritized for future study?

Based on the reference matrices, two analytical approaches were employed: simplified analysis and SNA. In analyzing natural disaster risk factors for engineering projects, combining simplified analysis with SNA provides multi-level insights into the complex relationships and overall structure of these risk factors. This integrated approach not only underscores the importance of individual risk factors but also reveals their interactions and influence within disaster response or prediction frameworks [74].

SNA offers distinct advantages over simplified analysis, particularly in elucidating complex relational structures and dynamics. It enables a deeper examination of relational

networks within disaster management, identifying critical nodes with high centrality or connectivity. This method is particularly effective for capturing intricate interactions, such as multi-stakeholder collaboration and rapid response needs, which simplified analysis often fails to address [75]. When discrepancies arise between simplified analysis and SNA results, SNA is prioritized because it more comprehensively captures complex relational networks and their influence. By revealing key relationships and core nodes that simplified analysis may overlook, SNA provides a more accurate perspective on network dynamics, making it more reliable for analyzing complex systems [76].

3.2. Simplified Analysis

Simplified analysis involves reviewing the literature to identify future research needs by calculating the frequency of occurrence of natural disaster risk factors across previous studies. For this analysis, the reference matrix M is used to compute a score for each natural disaster risk factor by summing the values in each row, as shown in Equation (1). For example, a score of 16 for natural disaster risk factor F1 indicates that it was mentioned or discussed in 16 source papers. To enable comparison, the score for each factor is normalized by dividing it by the maximum score in the matrix, as shown in Equation (2). Thus, the normalized score for any natural disaster risk factor ranges from 0 to 1 (inclusive).

$$\text{Score}_i = \sum_{\text{x=first source in the matrix}}^{\text{last source in the matrix}} \text{W}_{i,x} \tag{1}$$

$$\text{Normalized Score}_i = \frac{\text{Score}_i}{\text{Maximum Score}_i \text{ in the Matrix}} \tag{2}$$

where Score_i is the total score for natural disaster risk factor i across all sources, and $\text{W}_{i,x}$ represents the value (1 or 0) of the cell corresponding to source x and risk factor i in the matrix.

3.3. Social Network Analysis

3.3.1. Adjacency Matrices Formation and Analysis

To perform SNA, the adjacency matrix A_{ij} is generated from the reference matrix R_{ij} (48 $\times$ 81), which indicates the presence of natural disaster risk factors in the literature. Specifically, the process is divided into two main steps: (1) constructing the reference matrix (literature-risk factor matrix), which records the occurrence of each risk factor in the 81 selected papers; and (2) deriving the adjacency matrix (risk factor-risk factor co-occurrence matrix) from the reference matrix, quantifying the interactions between factors. First, in the construction of the reference matrix, risk factors are extracted from the title, abstract, keywords, and body of each paper according to three predefined criteria, and classified using the five-category framework of Blaikie et al. (geological, climatic, hydrological, topographical, and biological). The matrix uses binary coding (1 for the presence of the factor, 0 for its absence) to avoid subjective weight bias. If risk factor i appears in paper j, then $R_{ij} = 1$; otherwise, $R_{ij} = 0$. By multiplying R_{ij} by its transpose and setting the diagonal elements to 0, the adjacency matrix A_{ij} (48 $\times$ 48) is generated, resulting in a symmetric matrix. In this matrix, both rows and columns represent natural disaster risk factors, and the cell values indicate the frequency of co-occurrence of risk factors in the source literature. The process of generating the adjacency matrix A_{ij} is illustrated in Figure 2.

The adjacency matrix A_{ij} is imported into Gephi software (version 0.9.1) for network visualization, enabling a graphical representation of the relationships among risk factors.

Degree centrality for each natural disaster risk factor is calculated using Equation (3), where D_i represents the degree centrality of risk factor i, and $y_{i,j}$ is the value in row i and column j of the adjacency matrix. To account for variations in network size, degree centrality is normalized by dividing it by the maximum degree centrality in the network, as shown in Equation (4). The normalized degree centrality for any risk factor ranges from 0 to 1.

$$D_i = \sum_{j:j \neq i} y_{i,j} \tag{3}$$

$$\text{Normalized } D_i = \frac{D_i}{\text{Maximum } D_i \text{ in the Matrix}} \tag{4}$$

3.3.2. Risk Factor Centrality Analysis

SNA indicators provide valuable insights into the distribution and relational patterns within the network of natural disaster risk factors. The key SNA indicators used are degree centrality, betweenness centrality, and eigenvector centrality:

1 Degree Centrality: Calculated using Equation (3), this measures the number of direct connections a risk factor has, indicating its influence within the network.

2 Betweenness Centrality: Calculated using Equation (5), this measures the extent to which a node lies on the shortest paths between other nodes, reflecting its role as an intermediary.

$$C_{bk} = \sum_{k \neq i \neq j \in G} \frac{g_{ij}(k)}{g_{ij}} \tag{5}$$

where C_{bk} is the betweenness centrality of node k, g_{ij} is the total number of shortest paths from node i to node j, and $g_{ij}(k)$ is the number of those paths passing through node k. A higher betweenness centrality indicates greater importance of the node in connecting other nodes within the network.

3 Eigenvector Centrality: Calculated using Equation (6), this considers both the number and importance of a node's connections.

$$\lambda x = Ax \tag{6}$$

where A is the adjacency matrix, x is the eigenvector centrality score vector for the risk factors, and λ is the eigenvalue. Eigenvector centrality is obtained by solving for the eigenvector and eigenvalue, reflecting the influence of a risk factor based on its connections to other influential factors.

4. Analysis and Results

Through analysis of the 81 selected articles, 48 natural disaster risk factors for engineering projects were identified, as listed in Table 1. Two matrices were constructed: the reference matrix M, capturing theoretical discussions of natural disaster risk factors and their sources (papers), and the model matrix S, representing risk factors used in predictive models. Of the 81 articles, 40 belong to Type 1 (theoretical discussions, forming matrix M), and 41 belong to Type 2 (theoretical discussions with predictive models, forming matrix S).

Table 1. Natural disaster risk factors of engineering projects.

Code	Factor	Category
F1	Hurricane	Climate factors
F2	Wind	Climate factors

Table 1. *Cont.*

Code	Factor	Category
F3	Wind speed	Climate factors
F4	Rainfall	Climate factors
F5	Flood	Hydrological factors
F6	Collapse	Geological factors
F7	Landslide	Geological factors
F8	Earthquake	Geological factors
F9	Typhoon	Climate factors
F10	Lightning storms	Climate factors
F11	Stormsurge	Hydrological factors
F12	Rockfall	Geological factors
F13	Fault displacement	Geological factors
F14	Rock avalanche	Geological factors
F15	Spalling	Geological factors
F16	High geothermal heat	Geological factors
F17	Debris flow	Geological factors
F18	Ice/Snow avalanches	Geological factors
F19	Extreme temperature	Climate factors
F20	Rainstorm	Climate factors
F21	Ice jam	Hydrological factors
F22	Drought	Climate factors
F23	Land subsidence	Geological factors
F24	Snowstorm	Climate factors
F25	Temperature variation	Climate factors
F26	Tornado	Climate factors
F27	Tsunami	Hydrological factors
F28	Meteorological hazard	Climate factors
F29	Geological hazard	Geological factors
F30	Fire	Climate factors
F31	Storm	Climate factors
F32	Coastal damage	Topographic factors
F33	Thunderstorm	Climate factors
F34	Downbursts	Climate factors
F35	Ground liquefaction	Geological factors
F36	Hydrological hazards	Hydrological factors
F37	River disaster	Hydrological factors
F38	Tree fall	Ecological factors
F39	Soil hazard	Geological factors
F40	Erosion	Hydrological factors
F41	Climate change	Climate factors
F42	The melting of ice	Climate factors
F43	High altitude	Topographic factors
F44	Lightning disaster	Climate factors
F45	Rain	Climate factors
F46	Severe environmental conditions	Ecological factors
F47	Karst	Geological factors
F48	Environmental corrosion	Hydrological factors

4.1. Simplified Analysis and Social Network Analysis

Both the reference matrix M and the model matrix S were analyzed using simplified analysis and SNA, with results presented in Figures 3 and 4, respectively. The scores for each factor from both simplified analysis and SNA are provided in Appendix A.2.

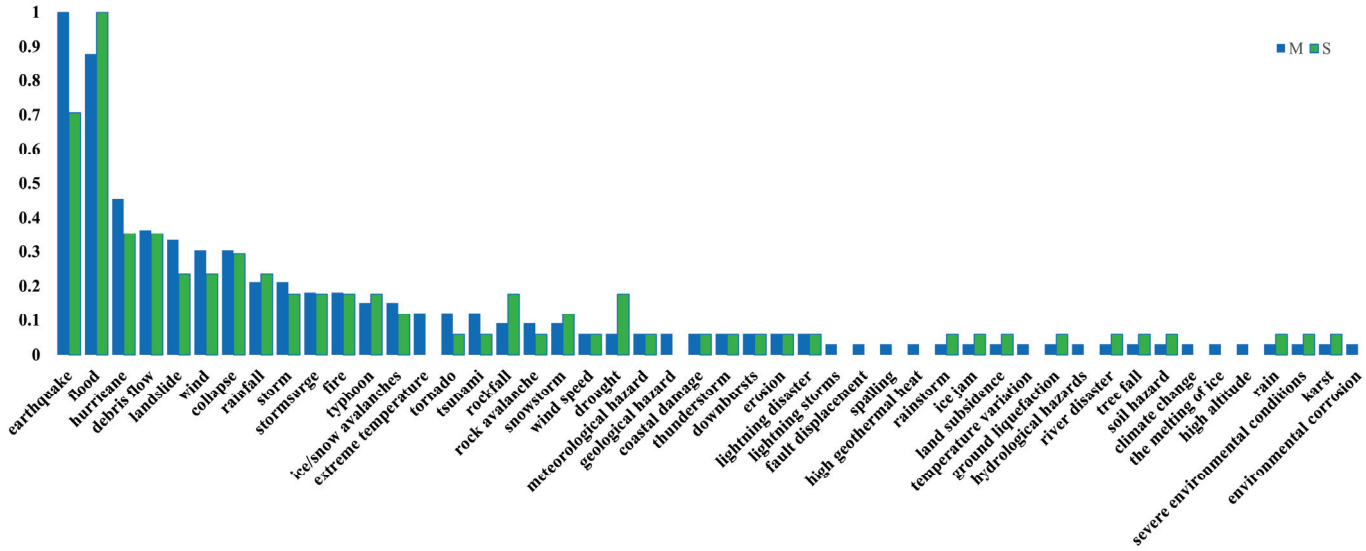

Figure 3. Obtained normalized scores for the simplified analysis.

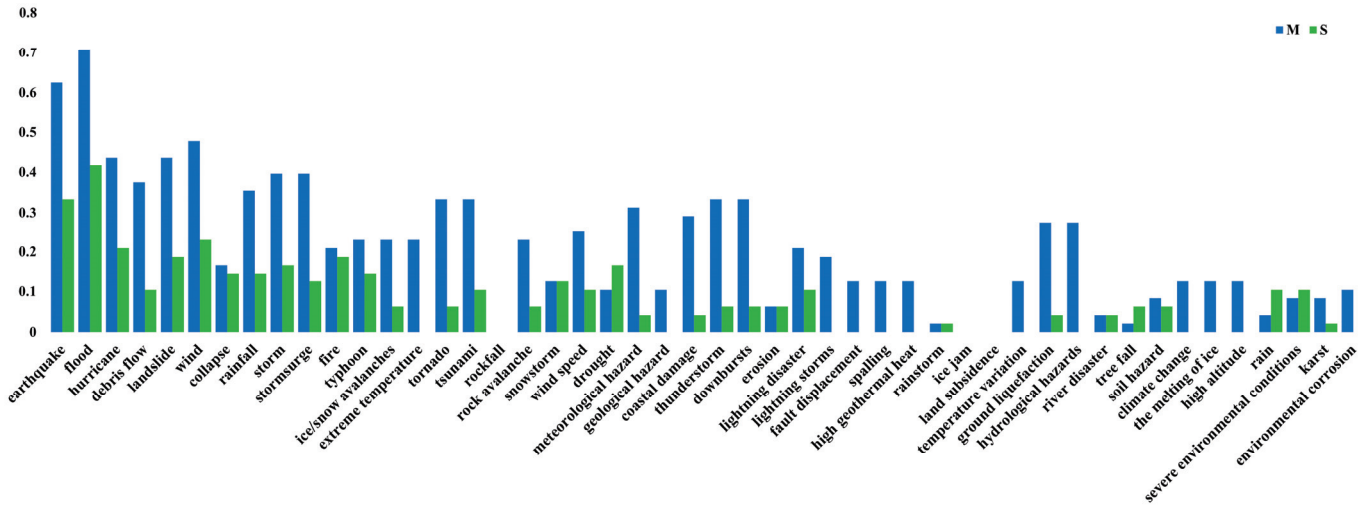

Figure 4. Obtained normalized scores for the SNA.

Figure 3 shows the occurrence frequency and normalized scores of natural disaster risk factors in the theoretical literature (matrix M). It can be seen that F8 (earthquake) and F5 (flood) have the highest scores, indicating that they receive the most attention in disaster research for engineering projects. In contrast, some factors, such as F36 (hydrological hazards) and F19 (extreme temperature), have lower scores, suggesting that although they are mentioned in some studies, they receive relatively little overall research attention. This trend reflects a bias in existing research toward high-impact but less diverse types of disasters.

Figure 4 shows the normalized degree centrality of nodes in the co-occurrence network constructed from matrix M. The results are highly consistent with Figure 3, with F8 (earthquake) and F5 (flood) remaining the most central nodes, having the highest number of connections. Notably, Figure 4 further reveals the relational structure among factors: for example, meteorological factors (such as F1, F2, and F20) form distinct highly connected clusters, while biological factors (such as F38, tree fall) exhibit significantly lower centrality. This indicates that the former are more likely to co-occur with other disasters, whereas the latter are often studied in isolation.

Figures 3 and 4 also reveal discrepancies between the theoretical discussions in matrix M and the risk factors incorporated into predictive models in matrix S. The simplified analysis highlights a significant gap for F8 (earthquake), which is even more pronounced in the SNA. This discrepancy suggests that the research attention devoted to certain risk factors, particularly earthquakes, does not align with their inclusion in predictive models, indicating under-exploration in practical applications. Additionally, risk factors such as F36 (hydrological hazards), F19 (extreme temperature), F10 (lightning storms), F25 (temperature variation), F41 (climate change), F42 (ice melting), F43 (high altitude), F13 (fault displacement), F15 (spalling), F16 (high geothermal heat), F48 (environmental corrosion), and F29 (geological hazards) are frequently mentioned in theoretical discussions (matrix M) but are absent from existing predictive models (matrix S), highlighting significant research gaps.

Figures 5–8 show the normalized degree centrality of natural disaster risk factors in engineering projects, calculated based on networks M and S. The depth of the color represents the strength of the factor's centrality and the intensity of its connections, with darker colors indicating greater strength. The size of the nodes is proportional to the normalized degree centrality of the risk factors, while the thickness of the links between nodes reflects the co-occurrence frequency in the matrices.

Figure 5 illustrates the co-occurrence network of natural disasters based on theoretical discussions (matrix M). In the figure, the size and color intensity of the nodes reflect the level of degree centrality, and the links represent the strength of co-occurrence. The network exhibits a clear "core–periphery" structure: F8 (earthquake) and F5 (flood) occupy the network center and frequently co-occur with multiple categories of risks, such as meteorological, geological, and hydrological factors, indicating strong systemic connectivity. In contrast, nodes such as F21 (ice jams) and F38 (tree fall) are located at the network periphery, suggesting that they are relatively isolated in existing theoretical research and lack systemic connections.

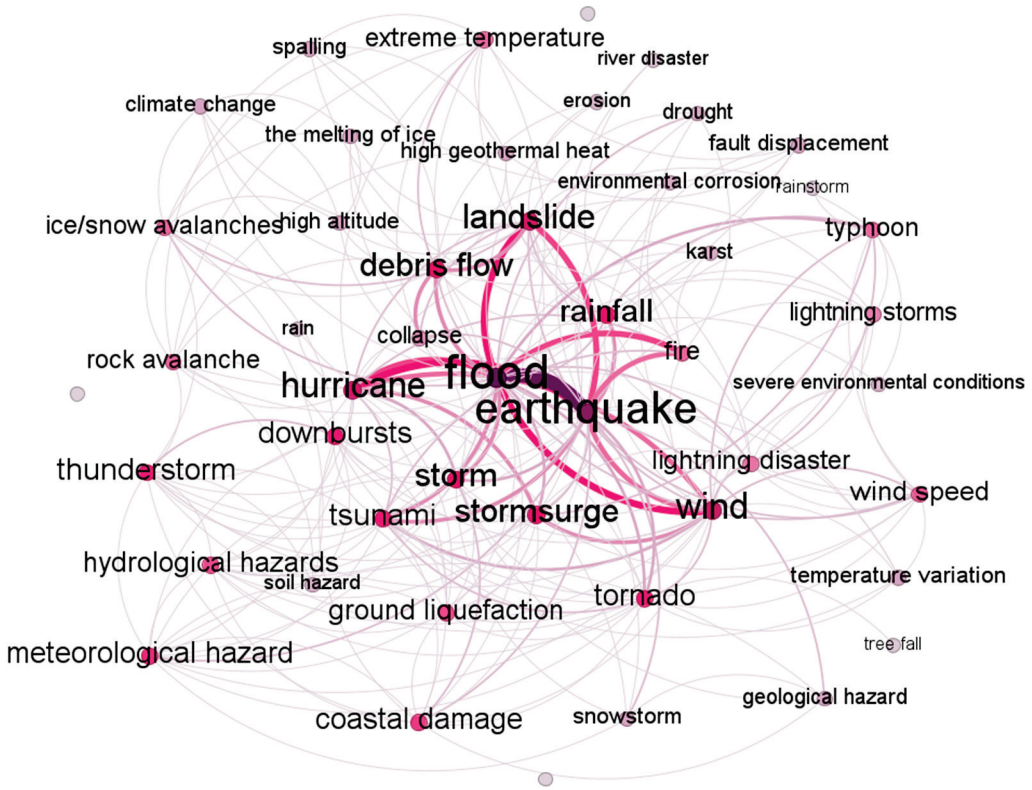

Figure 5. Co-occurrence map of natural disaster risk factors.

Figure 6 presents the strength of connections between factors in network M in a matrix format. The figure shows that disaster combinations such as earthquake–landslide, flood–storm, and storm–hydrological hazards exhibit the highest co-occurrence intensity, reflecting a strong focus in the literature on potential cascading disasters. In contrast, biological or ecological hazards generally show lower connectivity. These results support the structural features displayed in Figure 5, indicating that theoretical research tends to focus on typical disaster combinations.

Figures 7 and 8 illustrate the co-occurrence relationships of natural disaster risk factors in network S. These visualizations, based on simplified analysis, reveal the association patterns among the factors and their frequency of occurrence.



Figure 6. Connection strength diagram of different nodes in M matrix.

Figure 7 illustrates the co-occurrence network in predictive model-related literature (matrix S). Compared with Figure 5, network S is noticeably sparser, with a higher con-

centration of core nodes. F8 (earthquake) and F5 (flood) remain at the center, but the number of their connections with other factors is significantly lower than in matrix M, indicating that the risk factors included in actual predictive models are far fewer than those discussed theoretically. Many factors, such as F36 (hydrological hazards) and F19 (extreme temperature), are frequently discussed in the literature but rarely incorporated into models, highlighting a clear gap between theory and practice. Figures 5 and 7 reveal the implications of the core–periphery structure for the resilience framework: the high centrality of earthquakes and floods indicates their dominance in information flow, akin to hubs in disaster propagation. Within the framework of Ouyang et al. [7], this guides the prioritization of strengthening "bridging resilience"—for example, monitoring earthquake-induced hydrological pathways through sensor networks to reduce cascading failure rates. Although peripheral nodes have low visibility, they exhibit high radiative effects, exposing model blind spots and causing predictive bias.

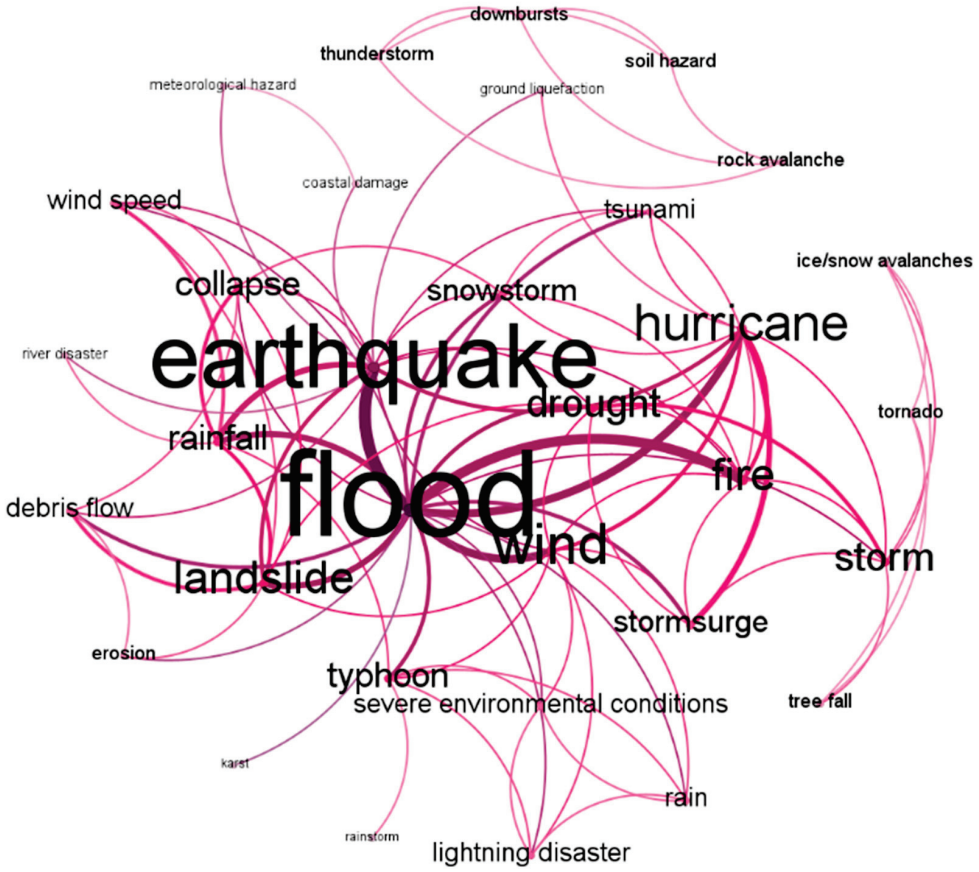

Figure 7. Co-occurrence diagram of natural disaster risk model.

Figure 8 further quantifies the co-occurrence strength of factors in network S. It can be observed that the combinations of factors considered in model-based studies are very limited, primarily focusing on small, classical combinations such as earthquake–landslide and flood–storm. Many cells in the matrix are zero, indicating that model-based studies make very limited use of multi-hazard coupling relationships. Notably, theoretically important climate-related factors (such as F19, F25, and F41) are almost entirely absent from the models, reflecting the structural limitations of current predictive models.

Figures 6 and 8 show that networks M and S exhibit similarities in normalized degree centrality. The matrices are color-coded, with cell colors representing the strength of connections between pairs of natural disaster risk factors. For instance, F8 (earthquake)

shows high normalized degree centrality in both networks, indicating that it is frequently mentioned in theoretical discussions and is also incorporated into predictive models. However, the co-occurrence heatmap highlights dense clustering in the geological–climate cluster, which goes beyond visual repetition and implies that the resilience framework needs to shift from static classification to modularization.



Figure 8. Connection strength diagram of different nodes in S matrix.

Figure 9 illustrates the score differences between the simplified analysis and SNA for matrices M and S. The results indicate a significant gap between theory and models: for example, F8 (earthquake) is highly prominent in the literature, but its centrality in models shows the most pronounced decline; meanwhile, some climate-related factors receive moderate scores in theory but are almost absent in models. This discrepancy suggests that future predictive models should more comprehensively consider factors frequently discussed in the literature but not yet incorporated, in order to enhance the completeness and effectiveness of the models. The difference between Matrix M and Matrix S reveals the gap between theoretical understanding and practical modeling: Network M has higher connectivity and density, indicating that the interconnections between risk factors are more thoroughly discussed in the theoretical literature, whereas Network S has lower density, with many widely discussed factors only frequently appearing in theory but rarely included in models.

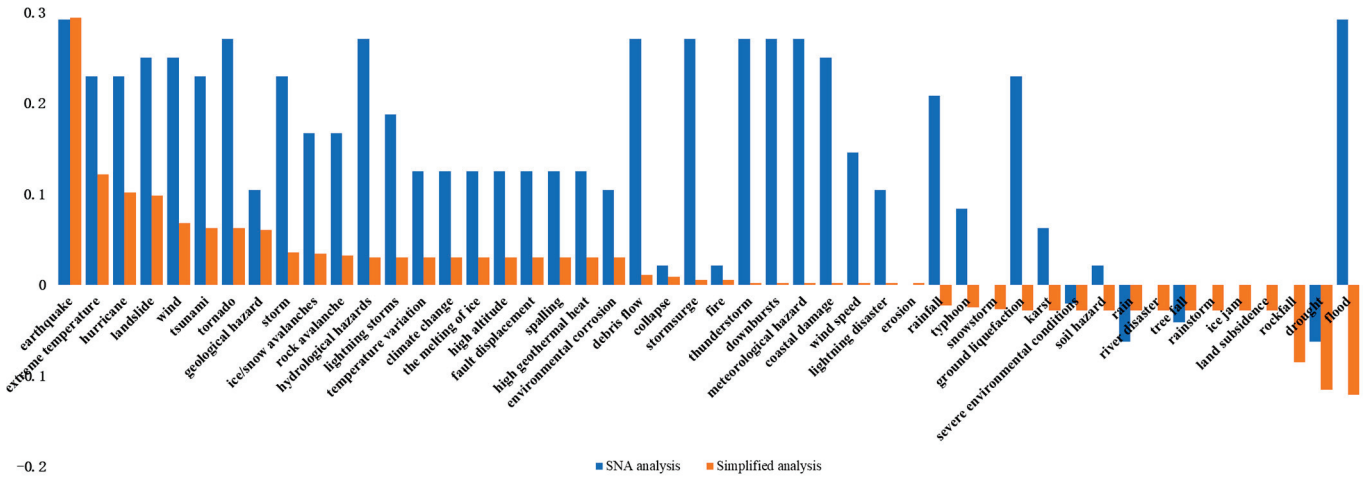

Figure 9. Obtained differences in M and S matrix scores using simplified analysis and SNA.

Although consensus factors such as earthquakes and floods occupy the core of the network, SNA reveals deeper amplification effects: these nodes do not dominate in isolation but amplify the influence of peripheral factors through high-betweenness bridging (e.g., earthquakes connecting geological and hydrological modules). For instance, extreme temperatures, though not high-frequency, act as amplifiers within the climate subnetwork. They are frequently discussed in theory but rarely incorporated into models, exposing a gap between practice and research. This gap points to cascading risk blind spots (e.g., temperature variability triggering increased flood intensity) and suggests new priorities for engineering design: not only reinforcing core hazards but also integrating the network resilience of peripheral factors. Furthermore, network module analysis shows asymmetric interactions among the five categories of factors (e.g., the biological factor module is isolated, with centrality <0.2), challenging the completeness of traditional classifications and calling for multi-hazard simulations.

4.2. Risk Factor Centrality Analysis

Centrality analysis was conducted on network M to assess the theoretical importance of natural disaster risk factors in academic discussions. Analyzing matrix M through SNA centrality measures reveals which risk factors are widely recognized as significant, forming the theoretical foundation for further research [65]. In contrast, centrality analysis of matrix S (practical application) may not fully capture the general importance of risk factors, as model development often depends on specific contexts and needs. Thus, other analytical methods, such as frequency statistics or context-specific matching analysis, may be more appropriate for matrix S to reflect the actual application of risk factors in predictive models [77]. The centrality measures applied to matrix M are detailed below. Using graph theory and statistical methods, three key centrality metrics were analyzed for network M.

Figure 10 shows that F5 (flood) and F8 (earthquake) have the highest degree centrality, indicating that projects affected by these disasters are highly likely to experience chain reactions with other disasters. This suggests that risk prevention and assessment efforts should prioritize factors with high centrality.

Figure 11 indicates that F5 (flood) and F8 (earthquake) also dominate in betweenness centrality, underscoring their critical role as intermediaries connecting other risk factors in the network.

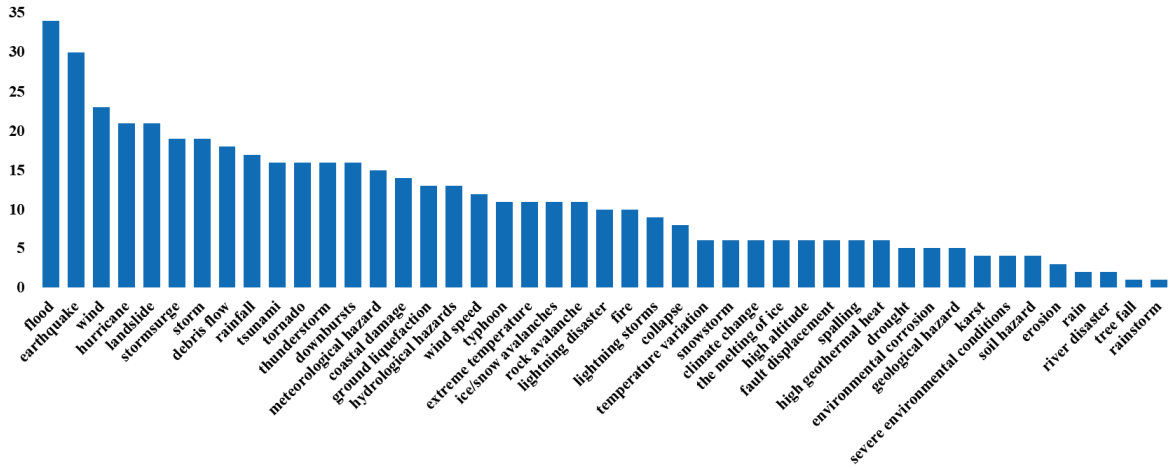

Figure 10. Degree centrality ranking of natural disaster risk factors.

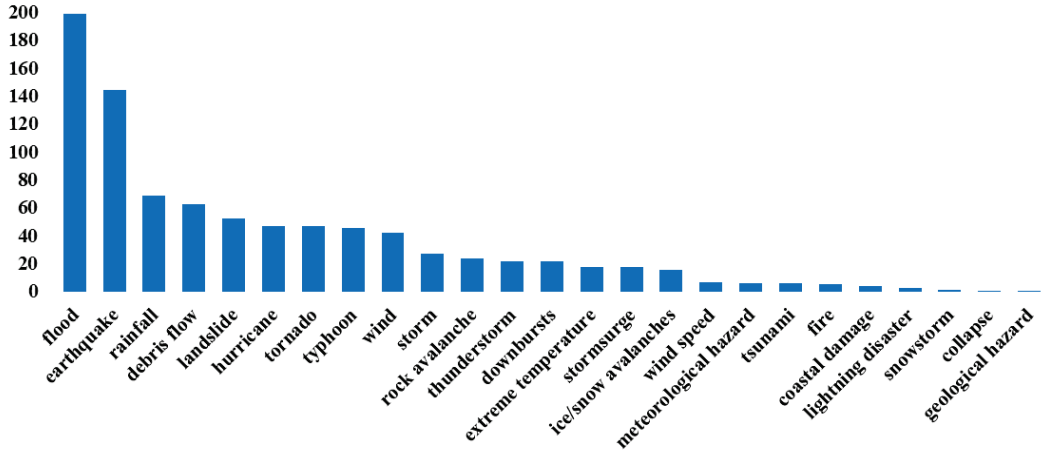

Figure 11. Betweenness centrality ordering.

Figure 12 reveals that F5 (flood) and F8 (earthquake) not only have numerous connections but are also linked to other influential risk factors, reinforcing their significance in the network. Additionally, the high betweenness centrality of hydrological factors suggests their role as cascade bridges. When combined with closeness centrality, it can further quantify the propagation speed and identify systemic risk hotspots. This omission highlights the static limitations of the current analysis but paves the way for the integration of a multi-hazard framework.

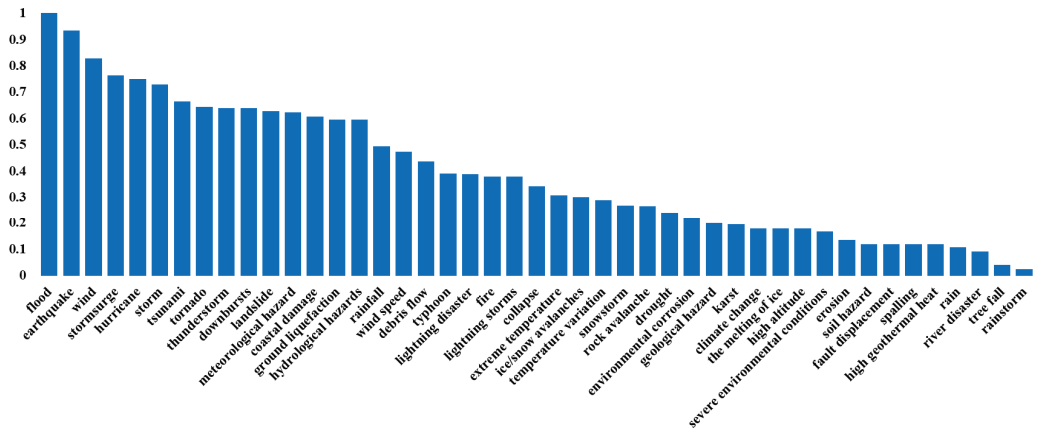

Figure 12. Eigenvector centrality ordering.

5. Discussion

This study synthesizes findings from prior research, identifying a comprehensive set of 48 natural disaster risk factors across five categories, providing a valuable resource for future researchers to assess the completeness of their risk assessment frameworks. Literature reviews that establish guidelines are a well-established practice in construction research. Such studies, both theoretically and practically, significantly contribute to the knowledge system by consolidating past work and laying a robust foundation for advancing research [78].

Through the literature review, this study identifies the following key findings and recommendations. These findings are directly derived from the SNA outputs (such as degree centrality, betweenness centrality, and eigenvector centrality) and bridge the gap between theoretical discussions (Network M) and predictive models (Network S), as illustrated in Figures 5 and 7. To enhance practical applicability, these findings have been translated into specific, actionable guidance, focusing on how SNA results can inform resource allocation and emergency planning.

1 Both F5 (flood) and F8 (earthquake) consistently rank highly in degree centrality, betweenness centrality, and eigenvector centrality, as well as in simplified analyses, reflecting their frequent discussion in theoretical and predictive models and their strong interconnections with other natural disaster risk factors. Previous studies have prioritized high-impact risks like F5 (flood) and F8 (earthquake), often neglecting other significant but less frequently studied risks, such as F12 (rockfalls), F23 (land subsidence), and F21 (ice jams).

2 Researchers are encouraged to incorporate critical natural disaster risk factors, such as F5 (flood), F8 (earthquake), F1 (hurricane), F2 (wind), and F26 (tornado), into their predictive models, as these consistently rank among the top 10 in degree centrality, betweenness centrality, and eigenvector centrality.

3 Future research should prioritize under-explored factors like F12 (rockfall), F21 (ice jam), and F23 (land subsidence), which were identified as isolated nodes in the SNA co-occurrence diagrams. This isolation indicates limited connections to other risk factors, potentially leading to their exclusion from predictive models and reducing model comprehensiveness. The project budget can be weighted according to centrality. For example, 40% of the total risk budget could be allocated to high-impact core nodes (such as F5 and F8, for deploying real-time monitoring sensors), while only 10% is allocated to low-connectivity nodes like F12 (rockfalls). By integrating the SNA map with GIS, resources can be prioritized to strengthen mountain slope stabilization, thereby optimizing resource utilization.

4 While many studies emphasize the need to explore diverse risk factors and their interrelationships, existing models predominantly focus on high-impact risks, overlooking others. The matrix in Figure 5 reveals that Network M exhibits stronger and denser connectivity than Network S, indicating greater interconnectivity among risk factors in theoretical discussions compared to predictive models. This gap suggests the need to develop a hierarchical response model: primary responses target core nodes, secondary responses address bridging nodes (e.g., F1, hurricane), and tertiary responses simulate cascading scenarios. For instance, in hurricane-prone areas, integrating threshold-based alert systems with drone inspections can reduce response time.

5 Earthquake risks (F8) warrant particular attention in future research, as both simplified analysis and SNA highlight their frequency and significance in engineering projects [79]. However, a notable gap exists between theoretical discussions and

applied models for F8 (earthquake), as evidenced by differences between matrices M and S in Figure 7.

6 Factors such as F36 (hydrological hazards), F19 (extreme temperature), F10 (lightning storms), F25 (temperature variation), F41 (climate change), F42 (the melting of ice), F43 (high altitude), F13 (fault displacement), F15 (spalling), F16 (high geothermal activity), F48 (environmental corrosion), and F29 (geological hazards) are marginalized in the network. This neglect stems from the literature's single-hazard focus and data scarcity, leading engineering assessments to bias toward high-frequency events. Future research should focus on risk factors that appear frequently in theoretical discussions but have not been incorporated into predictive models. This blind spot skews resources toward core hazards, amplifying cascading losses; project managers may overlook design buffers, increasing the risk of delays.

7 To enhance the prediction and mitigation of natural disaster impacts in engineering projects, future models—such as risk assessment frameworks, simulation tools, or predictive analytics systems—should selectively incorporate relevant subsets of the 48 risk factors identified in this study, tailored to the specific context of the project (e.g., regional hazard characteristics or project phases). Although developing a fully integrated model encompassing all factors may be challenging due to computational complexity and data requirements, creating modular or hierarchical models that allow these factors to be incorporated incrementally and in a scalable manner offers a more practical path toward comprehensive risk management. This approach can address the fragmentation observed in the current literature and support the implementation of adaptive risk management strategies across diverse engineering contexts.

The depth of this study lies in bridging known and unknown information: while confirming core factors, SNA quantifies the systemic role of overlooked factors, laying the foundation for a missing integrated model. In conclusion, this study aligns with existing scholarship and underscores the critical need for a comprehensive model to predict natural disaster risks in engineering projects, addressing a widely recognized gap in the literature. Furthermore, through the analysis of 81 articles and the comparison of SNA centrality results, we found that the failure of prediction models to incorporate risk factors widely discussed in the theoretical literature is primarily due to the mutually reinforcing effects of model complexity and disciplinary silos. Traditional methods (such as BP neural networks [15] and linear regression [19]) encounter the curse of dimensionality when expanded, leading to reduced accuracy, which makes engineering practice favor simpler models. Meanwhile, theoretical discussions are dominated by geology and climatology scholars, while civil engineering models tend to overlook cross-domain impacts. Due to budget or time constraints, these models prioritize "engineering-friendly" factors, creating a feedback loop.

Therefore, a modular prediction model is constructed based on 48 natural disaster risk factors to optimize disaster prevention and control strategies. Through a modular framework, geological, climatic, hydrological, topographic, and biological factors are integrated modularly, utilizing SNA centrality metrics (such as degree centrality and betweenness centrality) to prioritize high-influence factors and achieve targeted resource allocation. Here, the event of New York State coastal bridges affected by hurricane storm surges and waves is taken as an example [80], leveraging the interactions between prominent climatic and hydrological factors from the risk list in this study. The modular prediction model can be applied in layers: the climate module prioritizes the assessment of storm path probabilities, combined with SNA bridging path analysis to optimize pier reinforcement, such as elevating the deck clearance to 2–3 m; the hydrological module integrates

sea-level rise to design wave-dissipating structures, supplemented by biological factors for corrosion-resistant coatings. This scheme, in case simulations, will reduce the annual damage rate, providing actionable prevention strategies for coastal infrastructure.

6. Conclusions

This study reviews the existing literature on natural disaster risk factors, offering proactive guidance for future research to develop comprehensive and holistic models for assessing these risks in engineering projects. To achieve this, the authors (1) conducted a meta-analysis of prior research, (2) identified and categorized 48 natural disaster risk factors affecting engineering projects, and (3) employed SNA to quantitatively identify overlooked and under-researched factors in natural disaster risk assessments.

The study highlights both strengths and gaps in the current literature, providing a roadmap for areas requiring further investigation. For example, while theoretical discussions frequently address factors such as F36 (hydrological hazards), F19 (extreme temperatures), F10 (lightning storms), F25 (temperature variations), F41 (climate change), F42 (ice melting), F43 (high altitudes), F13 (fault displacement), F15 (spalling), F16 (high geothermal heat), F48 (environmental corrosion), and F29 (geological hazards), these factors are rarely incorporated into predictive risk models. This study underscores the need to prioritize these overlooked risk factors to enhance the understanding of their dynamics and improve risk assessment frameworks. To integrate these factors into predictive models, one can: (1) extend the framework to a dynamic Bayesian network, incorporating time-series data to simulate cascading probabilities; and (2) develop a hybrid framework that treats low-centrality factors as sensitivity parameters to enhance model robustness. This approach bridges the gap between theory and practice and advances an integrated resilience framework.

The recommendations proposed in this research advocate for a proactive approach to addressing complex natural disaster risks in engineering projects. Researchers are encouraged to focus on bridging the identified research gaps, particularly by integrating under-explored risk factors into predictive models to ensure more comprehensive risk management strategies.

However, this study has certain limitations. The literature search was restricted to articles from the Web of Science, Scopus, and ScienceDirect databases and included only English-language publications, potentially excluding valuable contributions from other databases or languages. Future research should broaden the scope by including additional databases and non-English sources to capture a wider range of risk factors, thereby enhancing the comprehensiveness of the analysis. In addition, the literature analysis in this study was limited to the selected search period, which may have overlooked emerging risk factors driven by recent extreme climate events. With the rapid development of natural disaster research, future findings may need to be validated and extended through regular updates of literature databases to ensure the timeliness and comprehensiveness of the framework. This approach would not only capture emerging interaction effects but also integrate real-time data sources, such as satellite monitoring, further enhancing the predictive accuracy of the models. Therefore, future work should extend to dynamic SNA metrics, such as closeness centrality or PageRank, to capture the dynamics of disaster propagation, and combine them with simulation tools to quantify cascading probabilities. Adopting this expanded approach will improve the management of engineering projects and enable relevant authorities to implement more effective disaster prevention measures.

By synthesizing findings from prior studies, this research establishes a robust foundation for studying natural disaster risk factors in engineering projects, significantly con-

tributing to the knowledge system. The results inform researchers about the current state of the field and highlight areas requiring further exploration, with the ultimate goal of minimizing the impacts of natural disasters on engineering projects.

Author Contributions: Conceptualization, Q.G. and J.W.; methodology, Q.G. and J.W.; validation, Q.G. and J.W.; formal analysis, Q.G. and J.W.; data curation, Q.G. and J.W.; writing—original draft preparation, Q.G.; writing—review and editing, J.W.; visualization, Q.G. and J.W.; supervision, J.W. All authors have read and agreed to the published version of the manuscript.

Funding: This research was funded by Shandong Province Natural Science Foundation, grant number ZR2023QG168.

Data Availability Statement: The data presented in this study are available on request from the corresponding author.

Conflicts of Interest: The authors declare no conflicts of interest.

Appendix A

Appendix A.1

The complete list of all 283 articles is provided here.

Table A1. The complete list of all 283 articles.

Index	Title	Year
1	AI-based risk assessment for construction site disaster preparedness through deep learning-based digital twinning	2022
2	Prioritizing Post-Disaster Reconstruction Projects Using an Integrated Multi-Criteria Decision-Making Approach: A Case Study	2022
3	Assessing the Risk of Natural Disaster-Induced Losses to Tunnel-Construction Projects Using Empirical Financial-Loss Data from South Korea	2020
4	Dynamic risk evaluation method for collapse disasters of drill-and-blast tunnels: a case study	2022
5	Risk-Informed Prediction of Dredging Project Duration Using Stochastic Machine Learning	2020
6	Geological Disaster Susceptibility Evaluation Using Machine Learning: A Case Study of the Atal Tunnel in Tibetan Plateau	2024
7	Exploring Cost Variability and Risk Management Optimization in Natural Disaster Prevention Projects	2024
8	Quantifying the Third-Party Loss in Building Construction Sites Utilizing Claims Payouts: A Case Study in South Korea	2020
9	Natural Assurance Schemes Canvas: A Framework to Develop Business Models for Nature-Based Solutions Aimed at Disaster Risk Reduction	2021
10	A Comprehensive Assessment Approach for Water-Soil Environmental Risk during Railway Construction in Ecological Fragile Region Based on AHP and MEA	2020
11	Risk Assessment of Rockfall Hazards in a Tunnel Portal Section Based on Normal Cloud Model	2017
12	Development of a Road Geohazard Risk Management Framework for Mainstreaming Disaster Risk Reduction in Developing Countries	2021
13	Scientific challenges in disaster risk reduction for the Sichuan-Tibet Railway	2022
14	Dynamic Evaluation Method of the EW-AHP Attribute Identification Model for the Tunnel Gushing Water Disaster under Interval Conditions and Applications	2021
15	Classification of Construction Hazards for a Universal Hazard Identification Methodology	2020
16	Combined System of Magnetic Resonance Sounding and Time-Domain Electromagnetic Method for Water-Induced Disaster Detection in Tunnels	2018
17	Effective Evaluation of Infiltration and Storage Measures in Sponge City Construction: A Case Study of Fenghuang City	2018
18	The cost of rapid and haphazard urbanization: lessons learned from the Freetown landslide disaster	2019
19	BIM-based Hazard Recognition and Evaluation Methodology for Automating Construction Site Risk Assessment	2020
20	Social Vulnerability Evaluation of Natural Disasters and Its Spatiotemporal Evolution in Zhejiang Province, China	2023

Table A1. *Cont.*

Index	Title	Year
21	Implications of building code enforcement and urban expansion on future earthquake loss in East Africa: case study-Blantyre, Malawi	2023
22	Workflows for Construction of Spatio-Temporal Probabilistic Maps for Volcanic Hazard Assessment	2022
23	Quantifying Hazard Exposure Using Real-Time Location Data of Construction Workforce and Equipment	2016
24	Risk assessment of debris flow disaster in mountainous area of northern Yunnan province based on FLO-2D under the influence of extreme rainfall	2023
25	Grain Risk Analysis of Meteorological Disasters in Gansu Province Using Probability Statistics and Index Approaches	2023
26	Dynamic Assessment of Drought Risk of Sugarcane in Guangxi, China Using Coupled Multi-Source Data	2023
27	Personality Assessment Based on Electroencephalography Signals during Hazard Recognition	2023
28	Hierarchical Structure Model of Safety Risk Factors in New Coastal Towns: A Systematic Analysis Using the DEMATEL-ISM-SNA Method	2022
29	Hazard function deployment: a QFD-based tool for the assessment of working tasks—a practical study in the construction industry	2020
30	Hazard Assessment for Biomass Gasification Station Using General Set Pair Analysis	2016
31	Integrating expert opinion with modelling for quantitative multi-hazard risk assessment in the Eastern Italian Alps	2016
32	Quantitative hazard assessment of rockfall and optimization strategy for protection systems of the Huashiya cliff, southwest China	2020
33	UAV Application for Typhoon Damage Assessment in Construction Sites	2022
34	Reliability and Robustness Assessment of Highway Networks under Multi-Hazard Scenarios: A Case Study in Xinjiang, China	2023
35	Probabilistic volcanic mass flow hazard assessment using statistical surrogates of deterministic simulations	2023
36	A Periodic Assessment System for Urban Safety and Security Considering Multiple Hazards Based on WebGIS	2021
37	A Building Classification System for Multi-hazard Risk Assessment	2022
38	Evaluating the impact of mental fatigue on construction equipment operators' ability to detect hazards using wearable eye-tracking technology	2019
39	A quantitative risk assessment development using risk indicators for predicting economic damages in construction sites of South Korea	2019
40	Validating ambulatory gait assessment technique for hazard sensing in construction environments	2019
41	Health Risk and Resilience Assessment with Respect to the Main Air Pollutants in Sichuan	2019
42	Evaluation of Thermal Hazard Properties of Low Temperature Active Azo Compound under Process Conditions for Polymer Resin in Construction Industries	2021
43	Controlling safety and health challenges intrinsic in exoskeleton use in construction	2023
44	Frazil ice jam risk assessment method for water transfer projects based on design scheme	2020
45	Scenario-based earthquake risk assessment for central-southern Malawi: The case of the Bilila-Mtakataka Fault	2022
46	Hazard Assessment of Rainfall-Induced Landslide Considering the Synergistic Effect of Natural Factors and Human Activities	2023
47	Multifactor Uncertainty Analysis of Construction Risk for Deep Foundation Pits	2022
48	Hazard and risk assessment for early phase road planning in Norway	2023
49	Quantifying workers' gait patterns to identify safety hazards in construction using a wearable insole pressure system	2020
50	Perceptions of disaster temporalities in two Indigenous societies from the Southwest Pacific	2021
51	Automated performance assessment of prevention through design and planning (PtD/P) strategies in construction	2024
52	Selection of Policies on Typhoon and Rainstorm Disasters in China: A Content Analysis Perspective	2018
53	Exploring construction workers' attention and awareness in diverse virtual hazard scenarios to prevent struck-by accidents	2024
54	Comprehensive assessment of geological hazard safety along railway engineering using a novel method: a case study of the Sichuan-Tibet railway, China	2020

Table A1. *Cont.*

Index	Title	Year
55	Quantitative Assessment of the State of Threat of Working on Construction Scaffolding	2020
56	Integration of InSAR and LiDAR Technologies for a Detailed Urban Subsidence and Hazard Assessment in Shenzhen, China	2021
57	Influence of Sociodemographic Factors on Construction Fieldworkers' Safety Risk Assessments	2022
58	Assessment of Health and Safety Solutions at a Construction Site	2013
59	Risk Assessment of Offshore Wind Turbines Suction Bucket Foundation Subject to Multi-Hazard Events	2023
60	Risk Analysis and Extension Assessment for the Stability of Surrounding Rock in Deep Coal Roadway	2019
61	Risk Assessment and Control of Geological Hazards in Towns of Complex Mountainous Areas Based on Remote Sensing and Geological Survey	2023
62	The 2013 European Seismic Hazard Model: key components and results	2015
63	Assessment of seismic hazard in the Erzincan (Turkey) region: construction of local velocity models and evaluation of potential ground motions	2015
64	Mechanism of water inrush in tunnel construction in karst area	2016
65	Safety Performance Assessment of Construction Sites under the Influence of Psychological Factors: An Analysis Based on the Extension Cloud Model	2022
66	An Improved Probabilistic Seismic Hazard Assessment of Tripura, India	2022
67	Probabilistic assessment of landslide tsunami hazard for the northern Gulf of Mexico	2016
68	Multi-Hazard Meteorological Disaster Risk Assessment for Agriculture Based on Historical Disaster Data in Jilin Province, China	2022
69	A Decision Support System for Organizing Quality Control of Buildings Construction during the Rebuilding of Destroyed Cities	2023
70	Hazard Assessment of Debris Flow: A Case Study of the Huiyazi Debris Flow	2024
71	Construction and Application of Safety Management Scenarios at Construction Sites	2024
72	Validity and reliability of a wearable insole pressure system for measuring gait parameters to identify safety hazards in construction	2021
73	Governing the Moral Hazard in China's Sponge City Projects: A Managerial Analysis of the Construction in the Non-Public Land	2018
74	Practice Framework for the Management of Post-Disaster Housing Reconstruction Programmes	2018
75	A spatiotemporal multi-hazard exposure assessment based on property data	2015
76	Use of Mamdani Fuzzy Algorithm for Multi-Hazard Susceptibility Assessment in a Developing Urban Settlement (Mamak, Ankara, Turkey)	2020
77	Occupational Risk Index for Assessment of Risk in Construction Work by Activity	2014
78	Stability of spatial dependence structure of extreme precipitation and the concurrent risk over a nested basin	2021
79	Assessment of check dams' role in flood hazard mapping in a semi-arid environment	2019
80	An Extension of the Failure Mode and Effect Analysis with Hesitant Fuzzy Sets to Assess the Occupational Hazards in the Construction Industry	2020
81	Hazard Zonation and Risk Assessment of a Debris Flow under Different Rainfall Condition in Wudu District, Gansu Province, Northwest China	2022
82	Developing a BIM and Simulation-Based Hazard Assessment and Visualization Framework for CLT Construction Design	2021
83	Risk Assessment for Hazard Exposure and Its Consequences on Housing Construction Sites in Lagos, Nigeria	2020
84	Enhancing Risk Assessment in Toll Road Operations: A Hybrid Rough Delphi-Rough DEMATEL Approach	2023
85	Risk-Informed Performance-Based Metrics for Evaluating the Structural Safety and Serviceability of Constructed Assets against Natural Disasters	2021
86	Dynamic Simulation of the Probable Propagation of a Disaster in an Engineering System Using a Scenario-Based Hybrid Network Model	2022
87	Predicting the resilience of transport infrastructure to a natural disaster using Cox's proportional hazards regression model	2017
88	Disaster Risk Management Through the DesignSafe Cyberinfrastructure	2020
89	Role of Predisaster Construction Market Conditions in Influencing Postdisaster Demand Surge	2018
90	Historic storms and the hidden value of coastal wetlands for nature-based flood defence	2020
91	A Decision Process for Optimizing Multi-Hazard Shelter Location Using Global Data	2020

Table A1. *Cont.*

Index	Title	Year
92	Study on the evolutionary mechanisms driving deformation damage of dry tailing stack earth-rock dam under short-term extreme rainfall conditions	2023
93	Essential Tools to Mitigate Vrancea Strong Earthquakes Effects on Moldavian Urban Environment	2013
94	Market-Implied Spread for Earthquake CAT Bonds: Financial Implications of Engineering Decisions	2010
95	Assessment of Damage Risks to Residential Buildings and Cost-Benefit of Mitigation Strategies Considering Hurricane and Earthquake Hazards	2012
96	Influence of rupture velocity on risk assessment of concrete moment frames: Supershear vs. subshear ruptures	2024
97	Loss Analysis for Combined Wind and Surge in Hurricanes	2012
98	Market Insurance and Self-Insurance through Retrofit: Analysis of Hurricane Risk in North Carolina	2017
99	Landslide susceptibility assessment using weights-of-evidence model and cluster analysis along the highways in the Hubei section of the Three Gorges Reservoir Area	2021
100	Ethical discounting for civil infrastructure decisions extending over multiple generations	2015
101	Discrete-Outcome Analysis of Tornado Damage Following the 2011 Tuscaloosa, Alabama, Tornado	2020
102	Framework for Earthquake Risk Assessment for Container Ports	2010
103	Research on real-time risk monitoring model along the water transfer project: a case study in China	2022
104	Failure analysis of the offshore process component considering causation dependence	2018
105	Risk-Based Design of Dike Elevation Employing Alternative Enumeration	2014
106	Seismic damage to pipelines in the framework of Na-Tech risk assessment	2015
107	Numerical and Physical Analysis on the Response of a Dam's Radial Gate to Extreme Loading Performance	2020
108	Flood susceptibility-based building risk under climate change, Hyderabad, India	2023
109	Machine learning network suitable for accurate rapid seismic risk estimation of masonry building stocks	2023
110	Dynamical process of the Hongshiyan landslide induced by the 2014 Ludian earthquake and stability evaluation of the back scarp of the remnant slope	2019
111	Probabilistic Flood Loss Assessment at the Community Scale: Case Study of 2016 Flooding in Lumberton, North Carolina	2020
112	Fragility assessment of traditional wooden houses in Madagascar subjected to extreme wind loads	2023
113	Insurance Pricing for Windstorm-Susceptible Developments: Bootstrapping Approach	2012
114	Flood characterization based on forensic analysis of bridge collapse using UAV reconnaissance and CFD simulations	2022
115	A Comparative Study of a Typical Glacial Lake in the Himalayas before and after Engineering Management	2023
116	An Integrated GIS-BBN Approach to Quantify Resilience of Roadways Network Infrastructure System against Flood Hazard	2020
117	Early warning method for overseas natural gas pipeline accidents based on FDOOBN under severe environmental conditions	2022
118	Framework for Multihazard Risk Assessment and Mitigation for Wood-Frame Residential Construction	2009
119	Attributes and metrics for comparative quantification of disaster resilience across diverse performance mandates and standards of building	2019
120	Risk Assessment of Shield Tunnel Construction in Karst Strata Based on Fuzzy Analytic Hierarchy Process and Cloud Model	2021
121	Fuzzy Comprehensive Evaluation of Collapse Risk in Mountain Tunnels Based on Game Theory	2024
122	The Practice of Forward Prospecting of Adverse Geology Applied to Hard Rock TBM Tunnel Construction: The Case of the Songhua River Water Conveyance Project in the Middle of Jilin Province	2018
123	Evolution Law and Grouting Treatment of Water Inrush in Hydraulic Tunnel Approaching Water-Rich Fault: A Case Study	2024
124	Dynamic Stability Analysis of Subsea Tunnel Crossing Active Fault Zone: A Case Study	2024
125	Flooded architecture as an adaptation tool for climate change impact-a case study of possible interpretation in Egypt	2024
126	Quantitative foundation stability evaluation of urban karst area: Case study of Tangshan, China	2015
127	Processes and techniques for rapid bridge replacement after extreme events	2007
128	Construction stability analysis of intersection tunnel in city under CRD method	2023
129	Public School Earthquake Safety Program in Nepal	2014
130	Research on the Resilience Evaluation of Rural Ecological Landscapes in the Context of Desertification Prevention and Control: a Case Study of Yueyaquan Village in Gansu Province	2024

Table A1. *Cont.*

Index	Title	Year
131	The Post-disaster House: Simple Instant House using Lightweight Steel Structure, Bracing, and Local Wood Wall	2021
132	Research on the Classification of Life-Cycle Safety Monitoring Levels of Subsea Tunnels	2017
133	Increasing vulnerability to floods in new development areas: evidence from Ho Chi Minh City	2018
134	Assessing the risk of natural disaster-induced losses to tunnel-construction projects using empirical financial-loss data from South Korea	2020
135	The centrality of engineering codes and risk-based design standards in climate adaptation strategies	2021
136	Fearing the knock on the door: Critical security studies insights into limited cooperation with disaster management regimes	2015
137	Risk assessment and management of vulnerable areas to flash flood hazards in arid regions using remote sensing and GIS-based knowledge-driven techniques	2023
138	Risk-informed prediction of dredging project duration using stochastic machine learning	2020
139	Considering Vulnerability in Disaster Risk Reduction Plans: From Policy to Practice in Ladakh, India	2015
140	Unnatural disaster: Human factors in the Mississippi floods	2008
141	Seismic performance evaluation and risk assessment of typical reinforced concrete frame buildings with masonry infill and conventional vertical extension in Nepal	2022
142	Delays in the road construction projects from risk management perspective	2021
143	Environmental vulnerability assessment of eco-development zone of Great Himalayan National Park, Himachal Pradesh, India	2015
144	A system for restoring production energy management after emergencies	2014
145	Scientific challenges in disaster risk reduction for the Sichuan–Tibet Railway	2022
146	Procedural effects of environment impact assessment on controlling natural disaster (landslides and flashflood) based on environmental degradation from development in Malaysia	2021
147	Existing power generation and network facilities improvement against seismic damage	2007
148	Urban planning challenges in the peripheral areas of Durres city (Porto Romano)	2013
149	Health impact assessments a tool for designing climate change resilience into green building and planning projects	2011
150	Novel AMI in Zigbee Satellite Network Based on Heterogeneous Wireless Sensor Network for Global Machine-to-Machine Connectivity	2024
151	Exploring Cost Variability and Risk Management Optimization in Natural Disaster Prevention Projects	2024
152	Study on the Factors Influencing and Mechanisms Shaping the Institutional Resilience of Mega Railway Construction Projects	2023
153	Development of model to predict natural disaster-induced financial losses for construction projects using deep learning techniques	2021
154	A Comprehensive Appraisal of the Factors Impacting Construction Project Delivery Method Selection: A Systematic Analysis	2023
155	Disaster risk reduction in developing countries: Costs, benefits and institutions	2012
156	Challenges and benefits of community-based safer school construction	2020
157	Categorizing sources of risk and the estimated magnitude of risk	2008
158	Prioritizing Post-Disaster Reconstruction Projects Using an Integrated Multi-Criteria Decision-Making Approach: A Case Study	2022
159	Flooded architecture as an adaptation tool for climate change impact—a case study of possible interpretation in Egypt	2024
160	The public-private partnership (PPP) disaster of a new hospital—expected political and existing business interaction patterns	2019
161	Quantifying the third-party loss in building construction sites utilizing claims payouts: A case study in south korea	2020
162	The Process and Challenges of Resident-Led Reconstruction in a Mountain Community Damaged by the Northern Kyushu Torrential Rain Disaster: A Case Study of the Hiraenoki Community, Asakura City, Fukuoka Prefecture, Japan	2023
163	Psychological symptoms and quality of life among the population of L'Aquila's "new towns" after the 2009 earthquake	2017
164	Riverbank settlement and humanitarian architecture, the case of mangunwijaya's dwellings and 25 years after, code river, Yogyakarta, Indonesia	2018
165	A Case Study on Performance of Jia Bharali River Bank Protection Measure Using Geotextile Bags	2016

Table A1. *Cont.*

Index	Title	Year
166	Research on the Resilience Evaluation of Rural Ecological Landscapes in the Context of Desertification Prevention and Control: a Case Study of Yueyaquan Village in Gansu Province	2024
167	Policies and architectures for the unthinkable era: New resilient landscapes in fragile areas of sardinia	2020
168	Lessons learned from an emergency bridge replacement project	2006
169	A Study of the Changing Process of the Conflict on a Large-Scale Regional Development Project	2000
170	Violations of Professional Technical Standards: Causes and Lessons Learned	2022
171	Study of Nonstationary Flood Frequency Analysis in Songhua River Basin	2023
172	Natural assurance schemes canvas: A framework to develop business models for nature-based solutions aimed at disaster risk reduction	2021
173	Prioritization of Strategic Initiatives in the Context of Natural Disaster Prevention	2019
174	Study of COVID-19 Health Protocol Standards in Construction Industry of Indonesia	2022
175	Geological Disaster Susceptibility Evaluation Using Machine Learning: A Case Study of the Atal Tunnel in Tibetan Plateau	2024
176	AI-based risk assessment for construction site disaster preparedness through deep learning-based digital twinning	2022
177	Systematic environmental impact assessment for non-natural reserve areas: A case study of the chaishitan water conservancy project on land use and plant diversity in Yunnan, China	2017
178	Post-earthquake highway reconstruction: Impacts and mitigation opportunities for New Zealand pinniped population	2023
179	Case Study of the Application of an Innovative Guide for the Seismic Vulnerability Evaluation of Schools Located in Sangolquí, Interandean Valley in Ecuador	2022
180	Mapping seismic risk awareness among construction stakeholders: The case of Iringa (Tanzania)	2022
181	Do Environmental Administrative Penalties Affect Audit Fees? Results from Multiple Econometric Models	2022
182	Heat Hazards in High-Temperature Tunnels: Influencing Factors, Disaster Forms, the Geogenetic Model and a Case Study of a Tunnel in Southwest China	2024
183	Analysis of the 2017 Knysna fires disaster with emphasis on fire spread, home losses and the influence of vegetation and weather conditions: A South African case study	2023
184	A Modified Mercalli Intensity map of Bangladesh: a proposal for zoning of earthquake hazard	2023
185	Ecological Risk Assessment of Land Use Change in the Tarim River Basin, Xinjiang, China	2024
186	Optimizing landslide susceptibility mapping using machine learning and geospatial techniques	2024
187	Urban Spatial Carrying Capacity and Sustainable Urbanization in the Middle-east Section of North Slope of Kunlun Mountains in Xinjiang, China	2023
188	The role of susceptibility, exposure and vulnerability as drivers of flood disaster risk at the parish level	2022
189	Snow avalanche susceptibility assessment based on ensemble machine learning model in the central Shaluli Mountain	2022
190	A Semi-Automated Two-Step Building Stock Monitoring Methodology for Supporting Immediate Solutions in Urban Issues	2023
191	A CAST-Based Analysis of the Metro Accident That Was Triggered by the Zhengzhou Heavy Rainstorm Disaster	2022
192	Research on the Interaction Mechanism between Landslide and Tunnel Engineering	2021
193	Design and Construction of a UAV for High Atmosphere Flight Powered by Hydrogen Fuel Cell	2023
194	Characteristics and Identification Method of Natural and Mine Earthquakes: A Case Study on the Hegang Mining Area	2022
195	Development of YOLOv8 and Segment Anything Model Algorithm-Based Hanok Object Detection Model for Sustainable Maintenance of Hanok Architecture	2024
196	A Study on the Propagation Trend of Underground Coal Fires Based on Night-Time Thermal Infrared Remote Sensing Technology	2022
197	Wide / narrow-area slope stability analysis considering infiltration and runoff during heavy precipitation	2023
198	Health and Safety Challenges Among Post-Disaster Reconstruction Workers	2023
199	Studying the Cable Loss Effect on the Seismic Behavior of Cable-Stayed Bridge	2023
200	Machine Learning-Based Prediction of Dynamic Responses of a Tower Crane under Strong Coastal Winds	2023
201	Potential flood hazard zonation and flood shelter suitability mapping for disaster risk mitigation in Bangladesh using geospatial technology	2021

Table A1. *Cont.*

Index	Title	Year
202	A Practical Swelling Constitutive Model of Anhydrite and Its Application on Tunnel Engineering	2024
203	Resilience assessment of tunnels: Framework and application for tunnels in alluvial deposits exposed to seismic hazard	2022
204	Seismic damage to pipelines in the framework of Na-Tech risk assessment	2015
205	Dynamical process of the Hongshiyan landslide induced by the 2014 Ludian earthquake and stability evaluation of the back scarp of the remnant slope	2019
206	A Comparative Study of a Typical Glacial Lake in the Himalayas before and after Engineering Management	2023
207	Framework for multihazard risk assessment and mitigation for wood-frame residential construction	2009
208	Loss analysis for combined wind and surge in hurricanes	2012
209	Socio-psychological factors explaining public engagement and support for drought disaster risk management	2024
210	A methodology for identifying, documenting and extrapolating potential good practices in disaster risk management	2024
211	Proposal of a comprehensive risk assessment model for cut slope considering long-term deterioration characteristics based on the concept of disaster immunity	2024
212	The urban political ecology of 'haphazard urbanisation' and disaster risk creation in the Kathmandu valley, Nepal	2023
213	Disaster risk management of debris flow based on time-series contribution mechanism (CRMCD): Nonnegligible ecological vulnerable multi-ethnic communities	2023
214	Reading indigenous signs: The wisdom of nagari communities toward natural disaster in Pasaman Barat	2024
215	Scientific challenges in disaster risk reduction for the Sichuan–Tibet Railway	2022
216	Natural disasters, stock price volatility in the property-liability insurance market and sustainability: An unexplored link	2024
217	Disaster risk management of cultural heritage: A global scale analysis of characteristics, multiple hazards, lessons learned from historical disasters, and issues in current DRR measures in world heritage sites	2024
218	An optimization-based risk management framework with risk interdependence for effective disaster risk reduction	2024
219	An Effective Disaster Recovery Model for Construction Projects	2024
220	Social construction of kentongan for disaster risk reduction in highland java and its potential for educational tool	2024
221	How a poverty alleviation policy affected comprehensive disaster risk reduction capacity: Evidence from China's great western development policy	2024
222	How to improve smart emergency preparedness for natural disasters? ---- Evidence from the experience of ten pilot provinces in China for smart emergency	2024
223	Risk management against indirect risks from disasters: A multi-model and participatory governance framework applied to flood risk in Austria	2024
224	Using traditional knowledge to reduce disaster risk—A case of Tibetans in Deqen County, Yunnan Province	2024
225	Application of African indigenous knowledge systems and practices for climate change and disaster risk management for policy formulation	2024
226	Exploring innovative techniques for damage control during natural disasters	2024
227	A systematic review of trustworthy artificial intelligence applications in natural disasters	2024
228	Social protection for climate-disasters: A case study of the program Keluarga Harapan cash transfer program for smallholder farm household in Indonesia	2023
229	Energy retrofitting of firms after a natural disaster: A 'build back better' strategy	2023
230	Quality of Life: Psychosocial Environment Factors (PEF) in the Event of Disasters to Private Construction Firms	2016
231	The catastrophic failure of the Jagersfontein tailings dam: An industrial disaster 150 years in the making	2024
232	Pro-poor change in the aftermath of disasters—Exploring possibilities at the intersection of disaster politics and land rights issues in Central Philippine	2023
233	Coupling coordination analysis of the economy-ecology-society complex systems in China's Wenchuan earthquake disaster area	2023
234	Natural disaster on Instagram: Examining representations of the 2018–2019 Tasmanian fires	2023

Table A1. *Cont.*

Index	Title	Year
235	Disaster-induced disruption of policies for informal urban settlements	2024
236	Assessing the economic loss due to natural disasters from outer space	2022
237	Analysis of factors influencing resource scheduling for emergency construction projects considering multiple spatial characteristics	2024
238	Using artificial intelligence to identify emergency messages on social media during a natural disaster: A deep learning approach	2023
239	High-resolution earthquake-induced landslide hazard assessment in Southwest China through frequency ratio analysis and LightGBM,	2024
240	Scoring, selecting, and developing physical impact models for multi-hazard risk assessment,	2022
241	Construction and evaluation of a polygenic hazard score for prognostic assessment in localized gastric cancer,	2022
242	Quantifying uncertainty and sensitivity in climate risk assessments: Varying hazard, exposure and vulnerability modelling choices,	2023
243	Objective-level resilience assessment of circular roadway tunnels with reinforced concrete liners for vehicle fire hazards,	2023
244	Comprehensive risk evaluation in Rapti Valley, Nepal: A multi-hazard approach,	2024
245	Climate Change monitoring with Art-Risk 5: New approach for environmental hazard assessment in Seville and Almería Historic Centres (Spain),	2024
246	A methodology for assessing wildfire hazard in Sweden—The first step towards a multi-hazard assessment method,	2022
247	Probabilistic seismic hazard and risk assessment of Mizoram, North East India,	2023
248	A general method for multi–hazard intensity assessment for cultural resources: Implementation in the region of Eastern Macedonia and Thrace, Greece	2024
249	Pre-earthquake fuzzy logic-based rapid hazard assessment of reinforced concrete buildings	2023
250	A new perspective in radon risk assessment: Mapping the geological hazard as a first step to define the collective radon risk exposure	2024
251	Meteorological hazard risk assessment of offshore wind power grids based on CVAR method,	2023
252	3D pose estimation dataset and deep learning-based ergonomic risk assessment in construction	2024
253	Geo-hazards assessment and land suitability estimation for spatial planning using multi-criteria analysis	2023
254	How long-term hazard assessment may help to anticipate volcanic eruptions: The case of La Palma eruption 2021 (Canary Islands)	2022
255	Analysis of debris flow control effect and hazard assessment in Xinqiao Gully, Wenchuan Ms 8.0 earthquake area based on numerical simulation	2024
256	Natural radioactivity, mineralogy and hazard assessment of syenogranites (ornamental stones) using a statistical approach	2024
257	"Natural" disasters and regional governance: Evidence from European NUTS-3 regions	2024
258	Developing a disaster risk index for coastal communities in southwest Bangladesh: Shifting from data-driven models to holistic approaches	2024
259	Who prioritizes safety from natural disasters in residential selection? Insights from a Japanese survey	2023
260	Determining geo-disaster chains probabilities and disaster mitigation mode: A meta-analytical perspective	2024
261	Integrated expression and analysis of urban flood disaster events from the perspective of multi-spatial semantic fusion	2024
262	Multiple resilience dividends at the community level: A comparative study of disaster risk reduction interventions in different countries	2023
263	Natural disaster shock, risk aversion and corn farmers' adoption of degradable mulch film: evidence from Zhangye, China	2021
264	Research on the layout of urban disaster-prevention and risk-avoidance green space under the improvement of supply and demand match: The case study of the main urban area of Nanjing, China	2023
265	Development and application of a model for assessing climate-related disaster risk	2022
266	Towards a procedure to manage safety on construction sites of rockfall protective measures	2023
267	Mining and analysis of public sentiment during disaster events: The extreme rainstorm disaster in megacities of China in 2021	2023
268	The imaginary and epistemology of disaster preparedness: The case of Japan's nuclear safety failure	2022
269	The important issue of awareness of disaster response to the COVID-19	2024
270	Safety map: Disaster management road network for urban resilience	2023

Table A1. *Cont.*

Index	Title	Year
271	Spatially non-stationarity relationships between high-density built environment and waterlogging disaster: Insights from xiamen island, china	2024
272	Fire safety behavior model for residential buildings: Implications for disaster risk reduction	2022
273	Home is restoration: Towards a health-based model of the importance of home for survivors of natural disasters	2022
274	Mitigating the flood disaster effects through the implementation of knowledge management: A systematic literature review	2024
275	To explore the optimal solution of different mapping units and classifiers and their application in the susceptibility evaluation of slope geological disasters,	2024
276	Budget allocation of food procurement for natural disaster response	2023
277	The influence of technical assistance and funding on perceptions of post-disaster housing safety after the 2015 Gorkha earthquakes in Nepal	2022
278	Rapid identification of damaged buildings using incremental learning with transferred data from historical natural disaster cases	2023
279	Mapping Construction Industry Roles to the Disaster Management Cycle	2014
280	A study on GIS-based spatial analysis of emergency response for disaster management: Focusing on Seoul	2024
281	Optimization-driven artificial intelligence-enhanced municipal waste classification system for disaster waste management	2024
282	Rebuilding historic urban neighborhoods after disasters: Balancing disaster risk reduction and heritage conservation after the 2015 earthquakes in Nepal	2023
283	Education for disaster resilience: Lessons from El Niño	2024

Appendix A.2

The scores for each factor from both simplified analysis and SNA are provided here.

Table A2. Comparison of normalized scores from simplified analysis and SNA.

Factor	Scores for the Simplified Analysis		Scores for the SNA	
Earthquake	1.0000	0.6250	0.3333	0.7059
Flood	0.8788	0.7083	0.4167	1.0000
Hurricane	0.4545	0.4375	0.2083	0.3529
debris flow	0.3636	0.3750	0.1042	0.3529
Landslide	0.3333	0.4375	0.1875	0.2353
Wind	0.3030	0.4792	0.2292	0.2353
Collapse	0.3030	0.1667	0.1458	0.2941
Rainfall	0.2121	0.3542	0.1458	0.2353
Storm	0.2121	0.3958	0.1667	0.1765
Stormsurge	0.1818	0.3958	0.1250	0.1765
Fire	0.1818	0.2083	0.1875	0.1765
Typhoon	0.1515	0.2292	0.1458	0.1765
Ice/Snow avalanches	0.1515	0.2292	0.0625	0.1176
Extreme temperature	0.1212	0.2292	0.0000	0.0000
Tornado	0.1212	0.3333	0.0625	0.0588
Tsunami	0.1212	0.3333	0.1042	0.0588
Rockfall	0.0909	0.0000	0.0000	0.1765
Rock avalanche	0.0909	0.2292	0.0625	0.0588
Snowstorm	0.0909	0.1250	0.1250	0.1176
Wind speed	0.0606	0.2500	0.1042	0.0588
Drought	0.0606	0.1042	0.1667	0.1765
Meteorological hazard	0.0606	0.3125	0.0417	0.0588
Geological hazard	0.0606	0.1042	0.0000	0.0000

Table A2. *Cont.*

Factor	Scores for the Simplified Analysis		Scores for the SNA	
Coastal damage	0.0606	0.2917	0.0417	0.0588
Thunderstorm	0.0606	0.3333	0.0625	0.0588
Downbursts	0.0606	0.3333	0.0625	0.0588
Erosion	0.0606	0.0625	0.0625	0.0588
Lightning disaster	0.0606	0.2083	0.1042	0.0588
Lightning storms	0.0303	0.1875	0.0000	0.0000
Fault displacement	0.0303	0.1250	0.0000	0.0000
Spalling	0.0303	0.1250	0.0000	0.0000
High geothermal heat	0.0303	0.1250	0.0000	0.0000
Rainstorm	0.0303	0.0208	0.0208	0.0588
Ice jam	0.0303	0.0000	0.0000	0.0588
Land subsidence	0.0303	0.0000	0.0000	0.0588
Temperature variation	0.0303	0.1250	0.0000	0.0000
Ground liquefaction	0.0303	0.2708	0.0417	0.0588
Hydrological hazards	0.0303	0.2708	0.0000	0.0000
River disaster	0.0303	0.0417	0.0417	0.0588
Tree fall	0.0303	0.0208	0.0625	0.0588
Soil hazard	0.0303	0.0833	0.0625	0.0588
Climate change	0.0303	0.1250	0.0000	0.0000
The melting of ice	0.0303	0.1250	0.0000	0.0000
High altitude	0.0303	0.1250	0.0000	0.0000
Rain	0.0303	0.0417	0.1042	0.0588
Severe environmental Conditions	0.0303	0.0833	0.1042	0.0588
Karst	0.0303	0.0833	0.0208	0.0588
Environmental corrosion	0.0303	0.1042	0.0000	0.0000

References

1. Bahmani, H.; Zhang, W. Application of System Thinking and Factors Interrelationship Analysis to Identify Primary Success Factors of Post-Natural Disaster Recovery Projects. *Sustainability* **2021**, *13*, 3392. [CrossRef]
2. China Daily. Devastating Earthquake Strikes Turkey and Syria, Thousands of Buildings Collapse. 2023. Available online: https://www.chinadaily.com.cn (accessed on 15 August 2024).
3. Cai, J.; Hao, H.; Ozbakkaloglu, T.; Zhang, Y.; Pan, J. Behavior of geopolymeric recycled aggregate concrete-filled FRP tube (GRACFFT) columns under lateral cyclic loading. *Eng. Struct.* **2020**, *222*, 111047. [CrossRef]
4. Ward, P.J.; Blauhut, V.; Bloemendaal, N.; Daniell, J.E.; de Ruiter, M.C.; Duncan, M.J.; Emberson, R.; Jenkins, S.F.; Kirschbaum, D.; Kunz, M.; et al. Natural hazard risk assessments at the global scale. *Nat. Hazards Earth Syst. Sci.* **2020**, *20*, 1069–1096. [CrossRef]
5. Godfrey, A.; Ciurean, R.L.; Van Westen, C.J.; Kingma, N.C.; Glade, T. Assessing vulnerability of buildings to hydro-meteorological hazards using an expert based approach–An application in Nehoiu Valley, Romania. *Int. J. Disaster Risk Reduct.* **2015**, *13*, 229–241. [CrossRef]
6. Horita, F.E.; de Albuquerque, J.P.; Marchezini, V.; Mendiondo, E.M. Bridging the gap between decision-making and emerging big data sources: An application of a model-based framework to disaster management in Brazil. *Decis. Support Syst.* **2017**, *97*, 12–22. [CrossRef]
7. Ouyang, M.; Dueñas-Osorio, L. Time-dependent resilience assessment and improvement of urban infrastructure systems. *Chaos* **2012**, *22*, 033122. [CrossRef]
8. El-Masri, S.; Tipple, G. Natural Disaster, Mitigation and Sustainability: The Case of Developing Countries. *Int. Plan. Stud.* **2002**, *7*, 157–175. [CrossRef]
9. Madhuri, R.; Raju, K.S.; Vasan, A. Flood susceptibility-based building risk under climate change, Hyderabad, India. *J. Water Clim. Change* **2023**, *14*, 2150–2163. [CrossRef]
10. Huang, Z.; Zhang, D.; Pitilakis, K.; Tsinidis, G.; Huang, H.; Zhang, D.; Argyroudis, S. Resilience assessment of tunnels: Framework and application for tunnels in alluvial deposits exposed to seismic hazard. *Soil Dyn. Earthq. Eng.* **2022**, *162*, 107456. [CrossRef]

11. Li, Y.; van de Lindt, J.W.; Dao, T.; Bjarnadottir, S.; Ahuja, A. Loss analysis for combined wind and surge in hurricanes. *Nat. Hazards Rev.* **2012**, *13*, 1–10. [CrossRef]
12. Deng, J. Research on the risk early warning of construction engineering under the coupling disaster of typhoons and rainstorms in coastal areas based on BP neural network. *J. Coast. Res.* **2020**, *105*, 151–154. [CrossRef]
13. Marchelli, M.; Coltrinari, G.; Degan, G.A.; Peila, D. Towards a procedure to manage safety on construction sites of rockfall protective measures. *Saf. Sci.* **2023**, *168*, 106307. [CrossRef]
14. Wu, B.; Qiu, W.; Huang, W.; Meng, G.; Huang, J.; Xu, S. Dynamic risk evaluation method for collapse disasters of drill-and-blast tunnels: A case study. *Math. Biosci. Eng.* **2022**, *19*, 309–330. [CrossRef]
15. Zhang, Y.; Li, J.; Liu, H.; Li, W.; Li, J.; Hou, L. Research on the interaction mechanism between landslide and tunnel engineering. *Adv. Mater. Sci. Eng.* **2021**, *2021*, 2265459. [CrossRef]
16. Essenfelder, A.H.; Bagli, S.; Mysiak, J.; Pal, J.S.; Mercogliano, P.; Reder, A.; Rianna, G.; Mazzoli, P.; Broccoli, D.; Luzzi, V. Probabilistic assessment of pluvial flood risk across 20 European cities: A demonstrator of the Copernicus disaster risk reduction service for pluvial flood risk in urban areas. *Water Econ. Policy* **2022**, *8*, 2240007. [CrossRef]
17. Liu, K.; Yin, C.; Sun, Y.; Du, M. Event Graph Construction Method on Natural Disaster Research. *ISPRS Ann. Photogramm. Remote Sens. Spat. Inf. Sci.* **2022**, *10*, 125–131. [CrossRef]
18. Zhang, B.; Yin, C.; Liu, K.; Zhai, X.; Sun, Y.; Du, M. Research on the construction of geographic knowledge graph integrating natural disaster information. *ISPRS Ann. Photogramm. Remote Sens. Spat. Inf. Sci.* **2022**, *10*, 79–85. [CrossRef]
19. Yum, S.G.; Ahn, S.; Bae, J.; Kim, J.M. Assessing the risk of natural disaster-induced losses to tunnel-construction projects using empirical financial-loss data from South Korea. *Sustainability* **2020**, *12*, 8026. [CrossRef]
20. Mileti, D. *Disasters by Design: A Reassessment of Natural Hazards in the United States*; National Academies Press: Washington, DC, USA, 1999.
21. Juarez Garcia, H. Multi-Hazard Risk Assessment: An Interdependency Approach. Ph.D. Thesis, University of British Columbia, Vancouver, BC, Canada, 2010. Available online: https://open.library.ubc.ca/collections/ubctheses/24/items/1.0062902 (accessed on 14 September 2024).
22. Fan, X.; Scaringi, G.; Korup, O.; West, A.J.; van Westen, C.J.; Tanyas, H.; Hovius, N.; Hales, T.C.; Jibson, R.W.; Allstadt, K.E.; et al. Earthquake-induced chains of geologic hazards: Patterns, mechanisms, and impacts. *Rev. Geophys.* **2019**, *57*, 421–503. [CrossRef]
23. Lukić, T.; Gavrilov, M.B.; Marković, S.B.; Komac, B.; Zorn, M.; Mlađan, D.; Đorđević, J.; Milanović, M.; Vasiljević, D.A.; Vujičić, M.D.; et al. Classification of natural disasters between the legislation and application: Experience of the Republic of Serbia. *Acta Geogr. Slov. Geogr. Zb.* **2013**, *53*, 150–164. [CrossRef]
24. Smith, K. *Environmental Hazards: Assessing Risk and Reducing Disaster*, 6th ed.; Routledge: Milton Park, UK, 2013. [CrossRef]
25. Baecher, G.; Bensi, M.; Reilly, A.; Phillips, B.; Link, L.E.; Knight, S.; Galloway, G. Resiliently Engineered Flood and Hurricane Infrastructure: Principles to Guide the Next Generation of Engineers. *Bridge* **2019**, *49*, 25–33.
26. Blaikie, P.; Cannon, T.; Davis, I.; Wisner, B. *At Risk: Natural Hazards, People's Vulnerability and Disasters*; Routledge: Milton Park, UK, 2014.
27. David, B.; Liu, J.; Wang, Y.; Georges, I. Toward Identifying and Analyzing Key Risk Factors and Their Interrelationships in Post-Disaster Reconstruction: A Comprehensive Study of Project Challenges and Case Analysis. *Sustainability* **2025**, *17*, 3696. [CrossRef]
28. Tan, Q.; Zhao, Z.; Yu, J.; Liu, Q. Research on Rapid Assessment Technology of Earthquake Disaster Loss Based on GIS. In Proceedings of the 2019 IEEE 2nd International Conference on Computer and Communication Engineering Technology (CCET), Beijing, China, 16–18 August 2019; pp. 164–167. [CrossRef]
29. Gebbeken, N.; Videkhina, I.; Pfeiffer, E.; Garsch, M.; Rudiger, L. Risk assessment and protection of the built infrastructure for flood events. *Bautechnik* **2016**, *93*, 199–213. [CrossRef]
30. Okem, E.S.; Nwokediegwu, Z.Q.S.; Umoh, A.A.; Biu, P.W.; Obaedo, B.O.; Sibanda, M. Civil engineering and disaster resilience: A review of innovations in building safe and sustainable communities. *Int. J. Sci. Res. Arch.* **2024**, *11*, 639–650. [CrossRef]
31. Cutter, S.L.; Burton, C.G.; Emrich, C.T. Disaster resilience indicators for benchmarking baseline conditions. *J. Homel. Secur. Emerg. Manag.* **2010**, *7*, 51. [CrossRef]
32. Pescaroli, G.; Alexander, D. Critical infrastructure, panarchies and the vulnerability paths of cascading disasters. *Nat. Hazards* **2016**, *82*, 175–192. [CrossRef]
33. Gallina, V.; Torresan, S.; Critto, A.; Sperotto, A.; Glade, T.; Marcomini, A. A review of multi-risk methodologies for natural hazards: Consequences and challenges for a climate change impact assessment. *J. Environ. Manag.* **2016**, *168*, 123–132. [CrossRef]
34. Zheng, W.; Xu, S.; Wang, Z. Fuzzy comprehensive evaluation of collapse risk in mountain tunnels based on game theory. *Appl. Sci.* **2024**, *14*, 5163. [CrossRef]

35. Xie, C.; Chen, Z.; Xiong, G.; Yang, B.; Shen, J. Study on the evolutionary mechanisms driving deformation damage of dry tailing stack earth–rock dam under short-term extreme rainfall conditions. *Nat. Hazards* **2023**, *119*, 1913–1939. [CrossRef]
36. Chou, J.-S.; Lin, J.-W. Risk-Informed Prediction of Dredging Project Duration Using Stochastic Machine Learning. *Water* **2020**, *12*, 1643. [CrossRef]
37. Chen, L.; Guo, H.; Gong, P.; Yang, Y.; Zuo, Z.; Gu, M. Landslide susceptibility assessment using weights-of-evidence model and cluster analysis along the highways in the Hubei section of the Three Gorges Reservoir Area. *Comput. Geosci.* **2021**, *156*, 104899.
38. dos Santos, T.D.; Uchida, T. Analysis of sediment disaster risk assessment surveys in Brazil: A critical review and recommendations. *Nat. Hazards Earth Syst. Sci.* **2025**, *25*, 4153–4180. [CrossRef]
39. Mushtaha, A.W.; Alaloul, W.S. Sustainability Factors Influencing Post-Disaster Reconstruction Projects: Critical Review and Bibliometric Analysis. *Sustain. Futures* **2025**, *10*, 100930. [CrossRef]
40. Fu, C.; Wang, J.; Qu, Z.; Skitmore, M.; Yi, J.; Sun, Z.; Chen, J. Structural equation modeling in technology adoption and use in the construction industry: A scientometric analysis and qualitative review. *Sustainability* **2024**, *16*, 3824. [CrossRef]
41. Zheng, X.; Le, Y.; Chan, A.P.C.; Hu, Y. Overview of the Application of Social Network Analysis in Construction Engineering and Management Research. In *20th International Symposium on Advancement of Construction Management and Real Estate*; Springer: Singapore, 2015. [CrossRef]
42. Trach, R.; Khomenko, O.; Trach, Y.; Kulikov, O.; Druzhynin, M.; Kishchak, N.; Ryzhakova, G.; Petrenko, H.; Prykhodko, D.; Obodianska, O. Application of fuzzy logic and SNA tools to assessment of communication quality between construction project participants. *Sustainability* **2023**, *15*, 5653. [CrossRef]
43. He, F.; Ji, L.; Li, C. Grid disaster risk identification based on social network analysis. *Reliab. Eng. Syst. Saf.* **2025**, *256*, 110756. [CrossRef]
44. Zheng, X.; Le, Y.; Chan, A.P.; Hu, Y.; Li, Y. Review of the application of social network analysis (SNA) in construction project management research. *Int. J. Proj. Manag.* **2016**, *34*, 1214–1225. [CrossRef]
45. Hazarika, H.; Haigh, S.K.; Chaudhary, B.; Murai, M.; Manandhar, S. (Eds.) *Natural Geo-Disasters and Resiliency: Select Proceedings of CREST 2023*; Springer: Berlin/Heidelberg, Germany, 2024.
46. Shan, S.; Zhao, F. Social media-based urban disaster recovery and resilience analysis of the Henan deluge. *Nat. Hazards* **2023**, *118*, 377–405. [CrossRef]
47. Wang, M.; Zhang, H.; Luo, Y.; Xu, M. Comprehensive risk management of health, safety and environment for social emergency rescue organization. *Heliyon* **2024**, *10*, e23021.
48. Yang, P.; Xu, X.; Shao, M.; Liu, Y. Intelligent Prediction of Flood Disaster Risk Levels Based on Knowledge Graph and Graph Neural Networks. *IEEE Access* **2025**, *13*, 8416–8424. [CrossRef]
49. Shen, W.; Xue, J.; Xiong, J.; Zhai, X.; Lee, S.; Lu, J. A Social Network–Based Approach for Analyzing Interproject Risks in Large-Scale Programs. *J. Constr. Eng. Manag.* **2025**, *151*, 04025124. [CrossRef]
50. Wang, J.; Chen, J.; Hu, Y. A science mapping approach based review of model predictive control for smart building operation management. *J. Civ. Eng. Manag.* **2022**, *28*, 661–679. [CrossRef]
51. Zhang, J.; Wang, J.; Zang, H.; Ma, N.; Skitmore, M.; Qu, Z.; Skulmoski, G.; Chen, J. The application of machine learning and deep learning in intelligent transportation: A scientometric analysis and qualitative review of research trends. *Sustainability* **2024**, *16*, 5879. [CrossRef]
52. Cao, Y.; Wu, S.; Chen, Y.; Skitmore, M.; Ma, X.; Wang, J. Enhancing Knowledge of Construction Safety: A Semantic Network Analysis Approach. *Buildings* **2025**, *15*, 3036. [CrossRef]
53. Lee, C.Y.; Chong, H.Y.; Liao, P.C.; Wang, X. Critical review of social network analysis applications in complex project management. *J. Manag. Eng.* **2018**, *34*, 04017061. [CrossRef]
54. Badea, A.; Prostean, G.; Goncalves, G.; Allaoui, H. Assessing risk factors in collaborative supply chain with the analytic hierarchy process (AHP). *Procedia-Soc. Behav. Sci.* **2014**, *124*, 114–123. [CrossRef]
55. Pratama, G.A.; Latief, Y.; Trigunarsyah, B.; Riantini, L.S.; Sihombing, L.B. Enhancing Risk Assessment in Toll Road Operations: A Hybrid Rough Delphi-Rough DEMATEL Approach. *Civ. Eng. J.* **2023**, *9*, 2130–2144. [CrossRef]
56. Saha, A.; Villuri, V.G.K.; Bhardwaj, A. Development and assessment of GIS-based landslide susceptibility mapping models using ANN, Fuzzy-AHP, and MCDA in Darjeeling Himalayas, West Bengal, India. *Land* **2022**, *11*, 1711. [CrossRef]
57. Hontoria, E.; Munier, N. *Uses and Limitations of the AHP Method a Non-Mathematical and Rational Analysis*; Springer: Berlin/Heidelberg, Germany, 2021.
58. Bertolotti, F.; Mari, L. An LLM-based Delphi Study to Predict GenAI Evolution. *arXiv* **2025**, arXiv:2502.21092.
59. Wang, J.; Yin, Y.; Wu, H.; Yang, T. Critical safety risks identification of bridge construction projects in the marine environment based on HHM and SNA. *J. Coast. Res.* **2020**, *108*, 48–52. [CrossRef]

60. Li, W.; Yuan, J.; Ji, C.; Wei, S.; Li, Q. Agent-based simulation model for investigating the evolution of social risk in infrastructure projects in China: A social network perspective. *Sustain. Cities Soc.* **2021**, *73*, 103112. [CrossRef]
61. Aghililotf, M.; Ramezanianpour, A.M.; Arbabi, H.; Maghrebi, M. Identifying construction managers' challenges: A novel approach based on social network analysis. *J. Constr. Eng. Manag.* **2024**, *150*, 04023141. [CrossRef]
62. Assaad, R.; El-adaway, I.H. Enhancing the Knowledge of Construction Business Failure: A Social Network Analysis Approach. *J. Constr. Eng. Manag.* **2020**, *146*, 04020052. [CrossRef]
63. Schreiber, R.R.; Zylka, M.P. Social Network Analysis in Software Development Projects: A Systematic Literature Review. *Int. J. Softw. Eng. Knowl. Eng.* **2020**, *30*, 321–362. [CrossRef]
64. Tai, S.L.; Zhang, Y.; Li, T. Factors affecting BIM application in China: A social network model. *J. Eng. Des. Technol.* **2021**, *19*, 373–384. [CrossRef]
65. Freeman, L.C. Centrality in social networks: Conceptual clarification. *Soc. Netw.* **2002**, *1*, 215–239. [CrossRef]
66. Brandes, U. A faster algorithm for betweenness centrality. *J. Math. Sociol.* **2001**, *25*, 163–177. [CrossRef]
67. Bonacich, P. Factoring and weighting approaches to status scores and clique identification. *J. Math. Sociol.* **1972**, *2*, 113–120. [CrossRef]
68. Aldrich, D.P. *Building Resilience: Social Capital in Post-Disaster Recovery*; University of Chicago Press: Chicago, IL, USA, 2012.
69. Darko, A.; Chan, A.P.; Huo, X.; Owusu-Manu, D.G. A scientometric analysis and visualization of global green building research. *Build. Environ.* **2019**, *149*, 501–511. [CrossRef]
70. Yuan, J.; Chen, K.; Li, W.; Ji, C.; Wang, Z.; Skibniewski, M.J. Social network analysis for social risks of construction projects in high-density urban areas in China. *J. Clean. Prod.* **2018**, *198*, 940–961. [CrossRef]
71. Eger, S.; Cao, Y.; D'Souza, J.; Geiger, A.; Greisinger, C.; Gross, S.; Hou, Y.; Krenn, B.; Lauscher, A.; Li, Y.; et al. Transforming science with large language models: A survey on ai-assisted scientific discovery, experimentation, content generation, and evaluation. *arXiv* **2025**, arXiv:2502.05151. [CrossRef]
72. Newman, M.E. Modularity and community structure in networks. *Proc. Natl. Acad. Sci. USA* **2006**, *103*, 8577–8582. [CrossRef] [PubMed]
73. Ciurean, R.L.; Schröter, D.; Glade, T. Conceptual frameworks of vulnerability assessments for natural disasters reduction. In *Approaches to Disaster Management-Examining the Implications of Hazards, Emergencies and Disasters*; InTech: London, UK, 2013; Volume 1, pp. 1–32.
74. Jones, E.C.; Faas, A.J. (Eds.) *Social Network Analysis of Disaster Response, Recovery, and Adaptation*; Elsevier: Amsterdam, The Netherlands, 2016.
75. Helbing, D. Globally networked risks and how to respond. *Nature* **2013**, *497*, 51–59. [CrossRef] [PubMed]
76. Zhang, Q.; Liu, C.; Zhu, W.; Mei, S. Demystifying the influencing factors of Construction 4.0 technology implementation from a sustainability starting point: Current trends and future research roadmap. *Buildings* **2024**, *14*, 552. [CrossRef]
77. Vignery, K.; Laurier, W. A methodology and theoretical taxonomy for centrality measures: What are the best centrality indicators for student networks? *PLoS ONE* **2020**, *15*, e0243367. [CrossRef]
78. Webster, J.; Watson, R.T. Analyzing the past to prepare for the future: Writing a literature review. *MIS Q.* **2002**, *26*, xiii–xxiii.
79. Naeim, F. Dynamics of Structures—Theory and Applications to Earthquake Engineering, Third Edition. *Earthq. Spectra* **2007**, *23*, 491–492. [CrossRef]
80. Li, S.; Wu, T.; Sett, K. *Real-Time Prediction of Storm Surge and Wave Loading on Coastal Bridges*; No. CAIT-UTC-REG 33; Center for Advanced Infrastructure and Transportation: Piscataway, NJ, USA, 2021.

Disclaimer/Publisher's Note: The statements, opinions and data contained in all publications are solely those of the individual author(s) and contributor(s) and not of MDPI and/or the editor(s). MDPI and/or the editor(s) disclaim responsibility for any injury to people or property resulting from any ideas, methods, instructions or products referred to in the content.

infrastructures

MDPI

Article

Artificial Intelligence Tools in the Management of Reinforced Concrete Structures: Potential, Critical Issues, and Preliminary Results on Structural Degradation

Donata Carlucci [1], Donatello Cardone [1], Serena Parisi [2] and Marco Vona [1,*]

[1] Department of Engineering, University of Basilicata, 85100 Potenza, Italy; donata.carlucci001@studenti.unibas.it (D.C.); donatello.cardone@unibas.it (D.C.)
[2] Independent Researcher, 85100 Potenza, Italy; parisiserena80@yahoo.it
* Correspondence: marco.vona@unibas.it; Tel.: +39-0971-205063

Abstract: The durability and management of reinforced concrete structures and infrastructures are a central issue in contemporary civil engineering. Efficient structural maintenance has become strategically critical to sustainable land and community management due to aging infrastructure, increasing operational stress, and limited financial resources. This study focuses specifically on reinforced concrete bridge piers, whose fundamental structural role influences road infrastructure management strategies. The objective of this study is to develop and use a system based on convolutional neural networks to visually, rapidly, and automatically identify degraded portions of the reinforcement, based on images acquired on-site or from visual inspections, and classify their level of degradation. The topic addressed is highly innovative. The need to define and calibrate reliable degradation classification criteria, and the difficulty of obtaining images and classifying them correctly for database construction, have influenced the development of the study and make the results interesting and promising, but absolutely preliminary.

Keywords: reinforce concrete infrastructures; infrastructures management; artificial intelligence (AI); inspections procedures; classification of degradation

1. Introduction

The durability and management of reinforced concrete structures and infrastructures is a central issue in contemporary civil engineering, especially in relation to the existing built heritage [1]. With the progressive aging of the engineering works and the intensification of loads, usage and economic stresses, the efficient maintenance of the structures assumed a strategic role in the sustainable management of the territory and communities.

In particular, the degradation of existing structures and infrastructures, especially the older ones, represents one of the main causes of loss of performances and built heritage. This has the potential to result in repercussions on the safety and reliability of the system as a whole, with very high direct and indirect costs and losses.

In existing and older reinforced concrete structures, the degradation of the reinforcement represents an extremely important phenomenon [2–9].

The safety of bridges and viaducts in Italy has been a relevant issue for several years. It is strictly connected to the management and maintenance of existing structures. Much attention has been paid in the regulatory field to the assessment activities of networks and individual structures [10–13]. Currently, safety assessment activities are conducted

following guidelines [14] that provide different levels of detail, based on six levels (ranging from zero to five). For the lowest levels (levels 0 and 1) the proposed study could be of great help not only by helping to provide information on bridges and viaducts but also by limiting the costs related to accurate surveys that are in any case based on visual inspections, design documentation and, finally, assessments that are in any case conditioned by the subjectivity and experience of the operator. In this context, the evaluation of the attention class (based on the ageing and degradation of the materials) can be supported by the proposed methodology which is also useful for reducing and making periodic inspections more efficient, providing a valuable tool to the management body to evaluate any further investigations (levels 2–5) by guiding and limiting the costs of in situ experimentation [15–17]. Furthermore, correct knowledge of the state of degradation can correctly guide intervention strategies, in a multi-criteria and multidisciplinary process [18,19].

In the context of traditional inspection techniques, which are primarily visual and encompass a range of accuracy levels, significant limitations emerge. These limitations are associated with the subjective nature of assessments and the substantial financial costs of investigation campaigns. These costs are frequently deemed to be unsustainable, even at low levels, given the substantial number of extant structures and the difficulty of extending the surveys to their significant portions [20–25].

In this scenario, the utilisation of advanced methodologies and instruments grounded in artificial intelligence (AI) could be a potentially efficacious solution to address the problem in a systematic and automated manner. The most recent scientific literature highlights the strong interest in the application of artificial intelligence, in particular deep learning and image processing, to improve the efficiency, accuracy and automation of crack detection, measurement and assessment in concrete structures, thus contributing significantly to the field of structural health monitoring [26,27].

Several researchers have investigated the use of convolutional neural networks (CNNs) and deep learning architectures, such as Fully Convolutional Networks (FCNs), for the analysis of damage to RC structures in terms of crack detection [28–33].

The use of various network architectures and the effectiveness of transfer learning to improve the detection accuracy is mainly oriented to the identification and segmentation of cracks (at appropriate levels of quality and quantity [34–36]), through the application of FCN-based methods and evaluating the performance of different pre-trained network architectures [37], also on civil infrastructures, reusing knowledge accumulated from other contexts [22]. Some studies focus on the use of image processing techniques to measure crack characteristics, such as length and width. This includes the use of smartphones and dedicated applications to facilitate non-contact measurements [38].

The evolution of artificial neural networks, particularly convolutional neural networks (CNNs), has enabled the automatic analysis of images, with potentially significant implications for the field of visual recognition of degradation [39–41]. Nevertheless, the efficacy of these tools is contingent upon the availability of correctly structured and significant data, which can reflect the complexity of the phenomena involved and the considerable variability of situations, details and structures [42]. The limited availability of representative image datasets, combined with the absence of standardized protocols for the acquisition and characterization of images and associated information (such as construction period, materials used and their mechanical characteristics, exposure environment, level of actions and stresses, element function, etc.), continues to represent a significant limitation to the optimal use of these resources. This limitation mainly affects the reliability of predictions.

In this context, the present study aims to contribute to the development of tools for the automatic recognition of the degradation of the reinforcements in reinforced concrete bridge

and viaduct structures, focusing on the degradation manifested through the reduction in the diameter of the reinforcement bars and the degradation of the surrounding concrete. This degradation often represents both the initial cause of the start of the oxidation and then corrosion of the reinforcements and an effect (in terms of expulsion of significant portions of concrete) of the corrosion in an advanced stage.

The present study focuses in particular on the piers of reinforced concrete bridges, subjected to heterogeneous environmental conditions, including freeze–thaw cycles and alternating dry and wet periods. Such conditions result in the non-uniform diffusion of aggressive agents within the structure, leading to the formation of zones exhibiting varying levels of vulnerability to corrosion.

The objective of the present study is to develop and use a system based on convolutional neural networks to visually identify, in a rapid and automated manner, the degraded portions of the reinforcement, starting from images acquired on site or from visual inspections, and to classify the level of degradation.

2. Materials, Methods, and Analyses

The degradation process of reinforced concrete structures is affected by a multitude of physical-chemical, environmental, and structural variables, attributable to the design methodologies (with particular reference to the construction details), the construction itself, and the characteristics of the materials (particularly the concrete that should act as protection), as well as the management strategies and practices employed. Damage and consequent cracking are often due to corrosion. Such damage typically manifests itself with cracks in the concrete, which can lead to structures being out of service or disproportionate collapse, even in the absence of accidental or unforeseen events but only as a result of live loads (Figure 1).



Figure 1. Effects of degradation due to lack of maintenance: incipient collapse (on the (**left**)) and disastrous collapse (on the (**right**)).

However, it should be noted that, on the one hand, the concept of robust structures in structural design remains partially controversial. On the other hand, in more recent structural design codes and standards, the term "robustness" is used to indicate the ability of a system to resist damage under extreme loads and to prevent the progressive spread of

(local) failure that would lead to disproportionate collapse. As Figure 1 shows, even the application of robustness concepts could not have avoided the disastrous collapse which, evidently, is of a progressive type due to lack of maintenance.

The classification and cataloguing of degradation on individual portions of structures, on individual structural elements, on entire structures and infrastructures directly affects the possibility of supporting a correct, effective and efficient decision-making process for infrastructure management and intervention planning.

The methodology employed in this study involves the utilisation of machine learning (ML) tools to analyse images, with the aim of achieving spatial recognition and assessing the severity of the damage. This is achieved through the implementation of object detection techniques. In Figure 2, the flowchart is reported.

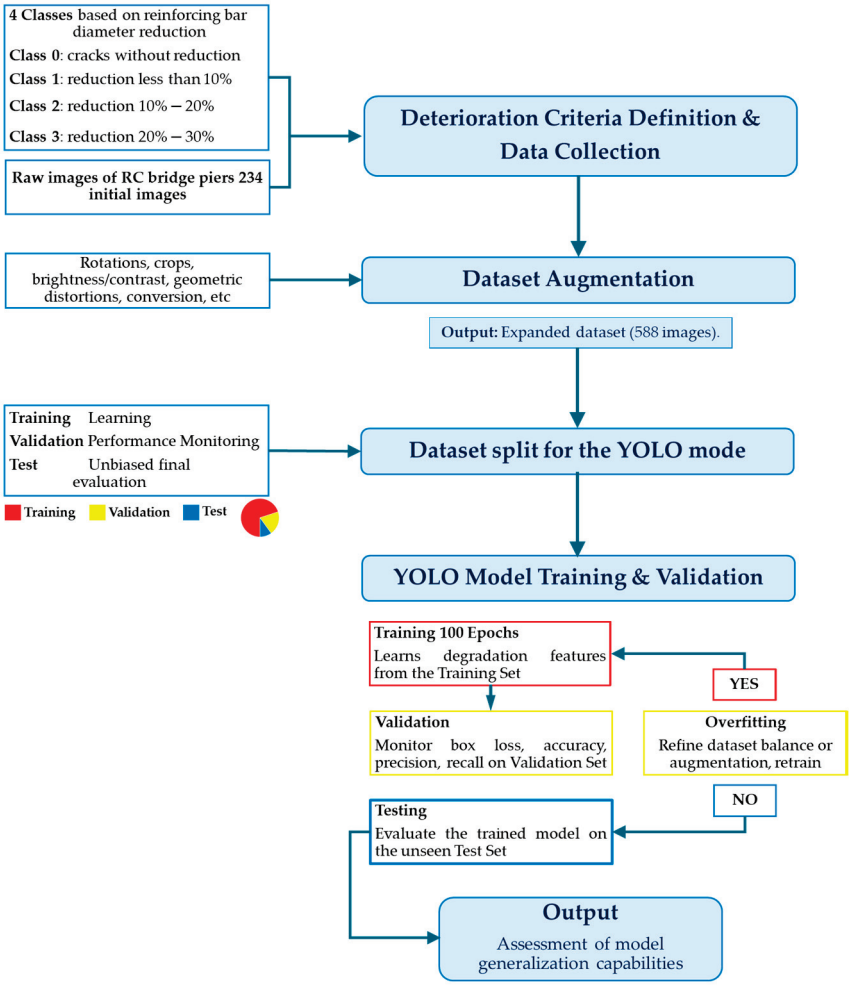

Figure 2. The flowchart of the used methodology.

The study identifies and addresses the main issues that are useful for a broad application of artificial intelligence tools in monitoring the degradation of structures and infrastructures:

- The construction of datasets representing real degradation images is achieved through collection, cataloguing and annotation based on specific skills and protocols.
- Procedures and methods of expansion of datasets also through the implementation of data augmentation techniques which is a promising avenue for enhancing the diversity and reliability of images.

The used procedure and training of the deep learning model are based on the YOLO (You Only Look Once) algorithm. YOLO-type algorithms are often used to improve damage detection in civil infrastructure [43]. The network was trained using a manually constructed dataset, in which each image was annotated with bounding boxes identifying the degraded regions of the armatures. Subsequently, data augmentation techniques (rotations, brightness variations, geometric distortions) were applied to virtually increase the size and variety of the dataset, simulating different operating conditions.

In accordance with the prevailing conventions for the implementation of AI-based recognition techniques, the dataset was segmented into three distinct subsets, designated for utilisation in the three fundamental phases of the research process: training, validation and testing. The model training was performed on the training subset, while the validation set enabled the monitoring of performance during the learning process. The final test enabled the evaluation of the effectiveness of the model on a set of images not previously used, thus verifying the ability to generalise the results obtained in variable conditions.

The model uses a deep convolutional network (CNN) that automatically learns the visual characteristics associated with each degradation class, performing successive iterations on the data until it optimises the ability to discriminate between the different conditions.

The computer vision employed in this application enables the system to interpret images autonomously, simulating the human observation and recognition process. The system has been developed to utilise deep learning in order to visually correlate the presence of specific defects with the degree of reduction in the metal section.

The following schematic illustrates the multi-layer architecture implemented in the neural network model used for processing. The architecture comprises a series of sequential layers, each with a specific computational function within the data flow.

The images employed for the training, validation and testing of the model were processed and annotated using the Roboflow tool, which facilitated the efficient creation and management of the dataset through object detection techniques.

The images selected for analysis span a range of deterioration conditions, influenced by various factors including the exhibition environment, design parameters, and construction variables. These variables encompass structural geometry, materials quality, concrete mix design, transport methods, installation processes, and management of routine maintenance.

The management and preparation of the dataset was conducted using the Roboflow platform, a specialized tool for workflows in artificial vision projects. Roboflow (https://roboflow.com/) facilitates the uploading of data in a variety of formats (images, videos, PDF), in addition to the possibility of accessing and integrating already annotated public datasets. In this phase, a proprietary dataset consisting of approximately 234 images was uploaded, with each image representing a different scenario of pathological degradation of the reinforcement.

2.1. Classification and Augmentation

The classification of degradation was determined by the intensity of the corrosive phenomenon, the percentage of reduction in the section of the reinforcement, the spread of cracks and the extent of detachment of the concrete cover. The classification of these classes was determined by the following intervals of reduction in thickness of the reinforcement (Figure 3):

- Class 0: cracks without any assessment of diameter reduction.
- Class 1: reduction in diameter less than 10%.
- Class 2: reduction in diameter ranging from 10% to 20%.
- Class 3: reduction in diameter ranging from 20% and 30%.

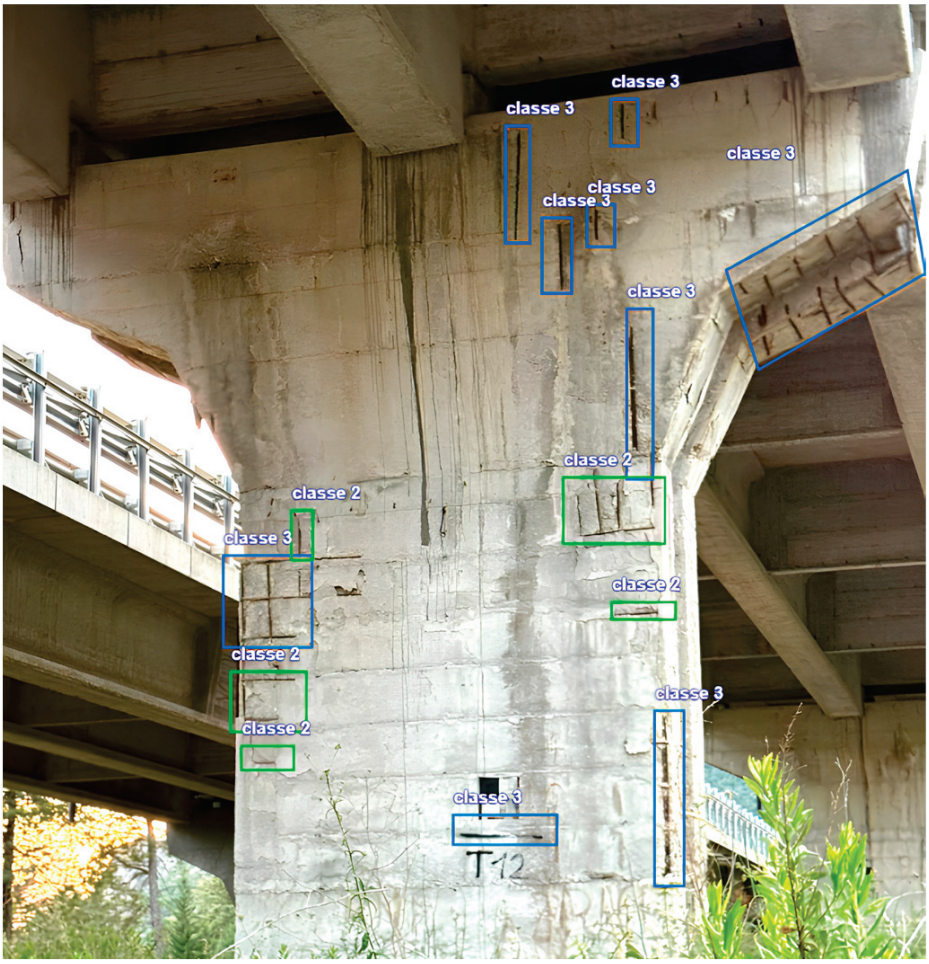

Figure 3. Example of the unique criterion for deterioration classification and bounding box for classifying the reduction in rebar diameter.

Each image was then assigned to a specific degradation class, representing the state of conservation of the visible reinforcement. The decision to incorporate a critical class is intended to facilitate the identification of the most compromised structural conditions, necessitating urgent interventions.

In many cases, the same pile exhibits different exposure conditions on its various faces, thereby determining a non-homogeneous behaviour in the degradation processes. This, in turn, necessitates a localized analysis. This approach therefore facilitates the evaluation of corrosion distribution with greater precision, thus supporting the planning of targeted interventions.

The following data sets were utilised for the training of the YOLO model, following standard convention:

- The training set, constituting 70% of the data, is utilised for the purpose of acquiring knowledge regarding the salient features of the data.
- The validation set (20%) was utilised for the purpose of conducting a comparison between the neural network predictions and the reference images. This process was undertaken with the objective of evaluating the reliability of the neural network in accurately classifying the degradation levels.
- The test set, constituting 10% of the dataset, is employed for the purpose of evaluating the generalisation capability of the model when confronted with unseen data.

In this particular instance, the restricted nature of the dataset necessitated meticulous attention during the training and validation phases, with the implementation of data augmentation techniques to enhance the diversity of the available sample sets.

This classified information formed the basis for the definition of the training set, acting as a reference tool for model training and ensuring that the network could learn to recognise, in a supervised manner, the visual patterns associated with the different stages of deterioration. Furthermore, some of the images from the aforementioned investigations were also utilised in the validation datasets. This was done in order to compare the model predictions with the diagnostic labels that had already been defined, and to evaluate the generalisation capacity on data that was known but not used in the training phase.

This approach enabled the integration of the diagnostic expertise acquired through engineering inspections with the capabilities of artificial intelligence technologies, thereby creating a system capable of automating the recognition of degradation phenomena. This system provides an objective and efficient means of supporting the evaluation process of the conservation conditions of reinforced concrete structures.

The input data underwent a preprocessing procedure to enhance the efficacy of model training and improve performance in the inference phase. This phase encompassed fundamental operations, including image normalization, resizing to standardized resolutions, and conversion to compatible formats.

Preprocessing was found to be of paramount importance in reducing the computational complexity of the model, thereby expediting the training process and enhancing the accuracy of predictions. This approach also contributed to enhancing the overall robustness of the neural network.

Subsequently, advanced data augmentation techniques were applied with the aim of artificially expanding the dataset and rendering the model more generalisable. The transformations performed include:

- Random angular rotations to simulate changes in structure orientation;
- Crops to focus on specific portions of the degradation zones;
- Proportional resizing to handle objects of different scales;
- Grayscale conversion, useful for testing the independence of the model from chromatic components;
- Brightness and contrast variations, to increase resilience to uncontrolled lighting conditions;
- Cuts and translations to simulate partial occlusions and camera movements.

These operations enabled the definition of an ordered sequence of transformations to be applied to the images, and to visualise their effects in real time. It is evident that the implementation of this structured procedure has enabled the creation of a more extensive, diverse and representative dataset, encompassing the various conditions observed within the structural field. This development has consequently led to an enhancement in the effectiveness of the training process and the model's capacity to accurately identify the diverse levels of reinforcement degradation.

Finally, a total of 588 output images were generated, encompassing both the original images and those obtained through data augmentation. This constituted a more robust and balanced dataset for training the neural network (Figure 4).

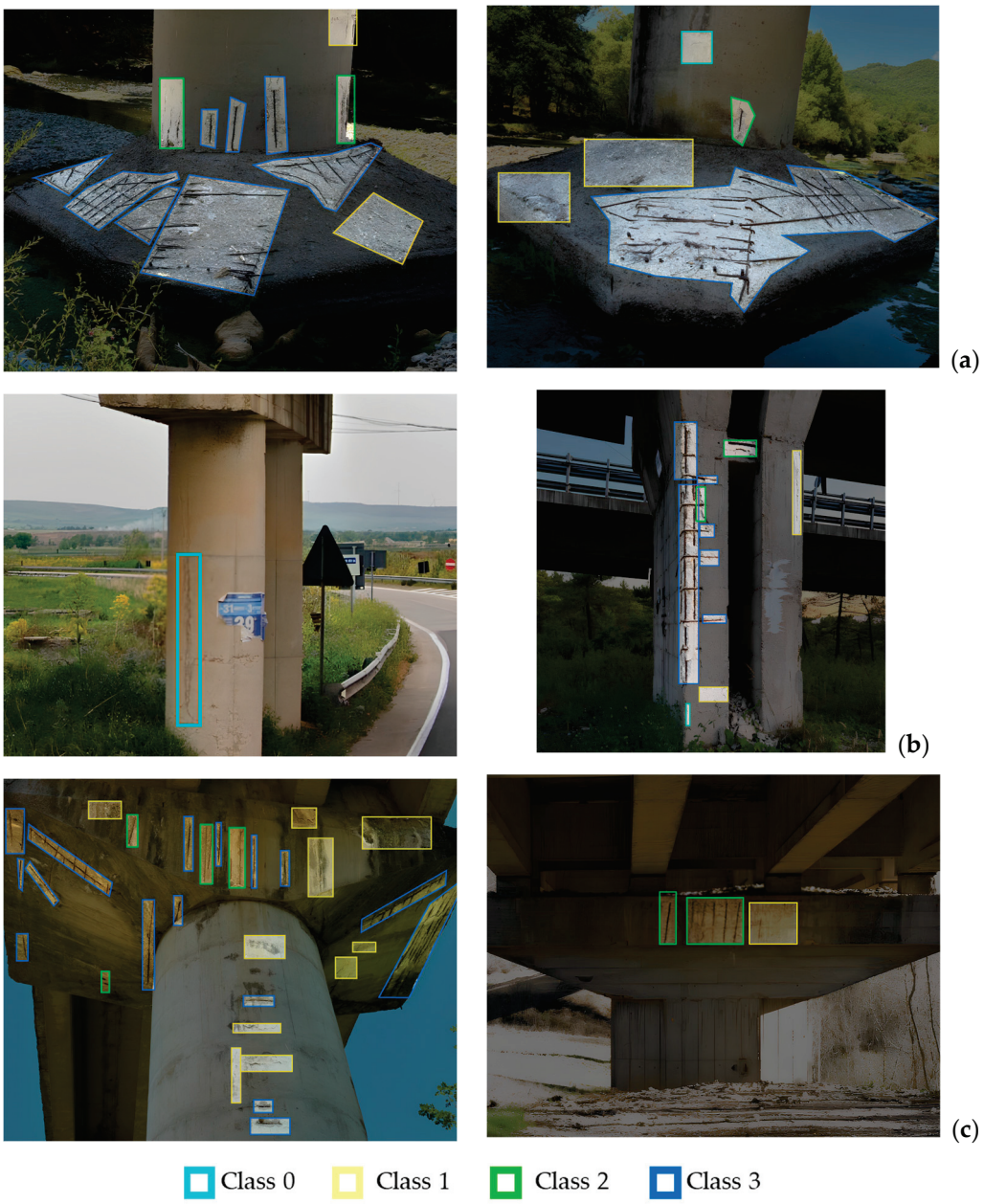

Figure 4. Sample of segmentation and augmentation of images of dataset for (**a**) Bridge Piers foundation, (**b**) Bridge Piers, (**c**) Pier Cap.

2.2. Training and Validation

Necessity for this operation arose from the requirement to automate and simplify the workflow between the two environments, whilst ensuring the protection of data. The YOLO model was trained for 100 epochs, at the conclusion of which graphical visualisations were produced that document the performance of the evaluation metrics, such as the loss function, precision, recall value and accuracy, monitored during the training process (see Figures 5 and 6). During the training phase of the object detection model, several performance metrics calculated on the validation set were monitored, in order to evaluate the generalisation capacity of the network. Figure 4 shows the evolution of the box loss, i.e., the error between the bounding boxes predicted by the model and the actual ones, during the training epochs. A progressive decrease in the loss is observed on the training data, a sign that the model is learning the relationships present in the data. However,

the loss on the validation data remains almost constant throughout the training period, suggesting overfitting.



Figure 5. The horizontal axis shows the epochs (from 0 to 100), while the vertical axis represents the loss value. The curves indicate the loss trend on the training set (in blue) and the validation set (in orange), respectively.

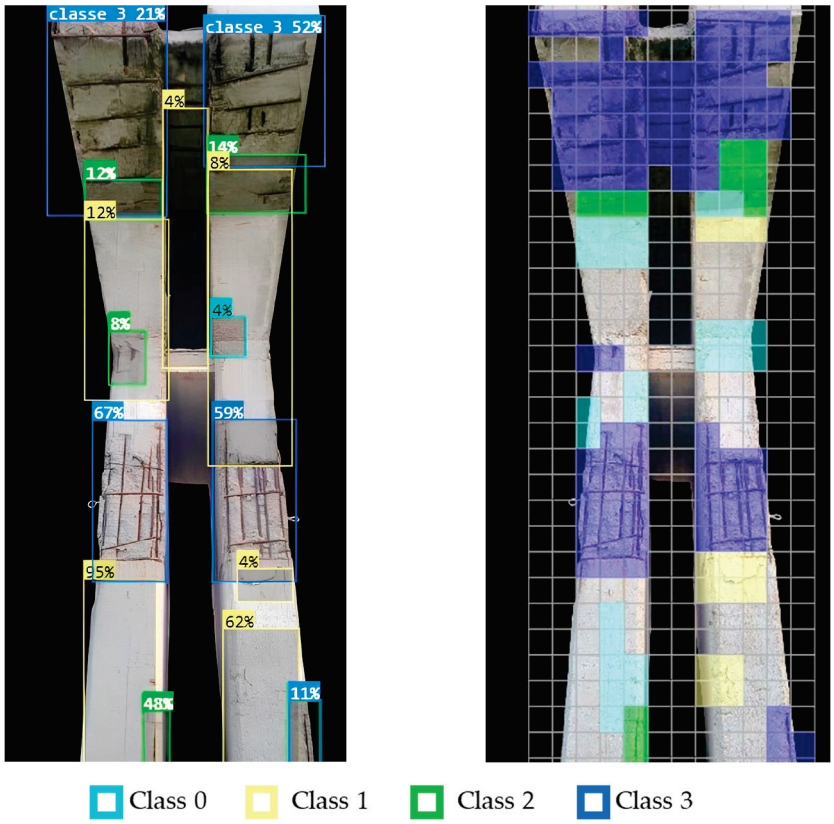

Figure 6. Comparison of results of the final test between final test (on the (left)) and direct investigations (on the (right)).

The x-axis shows the number of epochs, each of which represents a complete cycle of forward propagation and back propagation on the data of the entire dataset training. The y-axis shows the values of the accuracy metrics which constitute quantitative indicators of the model performance. The examination of the metrics reveals that the model's performance in terms of the classification and localisation of degradations in the reinforcements of reinforced concrete structures is not yet satisfactory.

Based on these considerations, the balance, quality and quantity of the dataset have been improved. Several training runs of the neural network were performed, varying the subdivisions between the training, validation and test sets, with the aim of improving the model's ability to generalize to previously unseen scenarios.

3. Results

The results of the study appear to be highly encouraging. The model demonstrated a high degree of accuracy in cases that were analogous to the images employed during the training process. However, it also exhibited a certain degree of difficulty in recognizing scenarios that diverged from those utilized during the learning process. The findings confirmed the necessity for datasets of greater size, as well as the importance of integrating visual data with contextual engineering information, such as the age of the structure, the structural typology, the materials used, and the environmental conditions.

Among the various iterations, the most significant learning curves were selected, which describe the trend of accuracy and loss during training and validation. The results show:

- A reduction in the distance between the training and validation curves, a sign that the model is tending to a better generalization;
- An improvement in the stability in the localization of the bounding boxes (box loss);
- A decrease in the classification error (class loss);
- An increase in the ability of the model to correctly detect objects (objectness loss), with less marked oscillations compared to the previous version.

A comparison of the curves reveals the presence of residual overfitting, as evidenced by discrepancies between the training and validation metrics. This finding underscores the necessity to augment the variability of the dataset through the incorporation of additional images, thereby enhancing the robustness of the model.

During the system's test phase, it demonstrated the capability to identify the degradation classes of the reinforcements, thereby achieving results that are in compliance with direct methodologies. Figure 6 depict some examples of processing produced by the model, with the predictions superimposed on the original images and direct comparison with the experimental data. In each case, the coordinates of the bounding boxes detected by the network and the degradation areas actually found on site will be compared. This will allow for the evaluation of spatial accuracy, the completeness of the detection and any discrepancies. This evaluation will guide subsequent activities of dataset extension and model calibration.

In order to enhance the efficacy of the inference phase, the threshold value of the confidence index in the predictions was appropriately reduced, thus increasing the sensitivity of the detection even in the presence of partial or small defects. This choice resulted in an enhancement of the capacity to discern potential instances of degradation, despite a marginal increase in the number of false positives, a phenomenon that can be effectively addressed through subsequent analyses. However, it should be noted that not all images in the dataset meet the necessary quality standards. In some cases, low resolution, the presence of visual noise or non-optimal lighting conditions have limited the reliability of the recognition process.

4. Discussion

The analysis of the model performance demonstrated a discrepancy between the accuracy achieved on the training set and that observed on the test set, thus indicating the

presence of overfitting. This behaviour can be attributed to the limited size of the dataset, which does not allow the model to effectively generalise on conditions not seen during the training phase. Consequently, the model acquired overly specific characteristics of the training data, failing to develop sufficiently robust and transferable representations to different or more complex conditions.

The neural network exhibited a commendable capacity to adapt and identify the degradation classes that were most prevalent in the dataset, which included bridge piers. However, the performance is less satisfactory in terms of the recognition of degradation on structural components with more complex geometries, inhomogeneous surfaces and variable shooting conditions. In such cases, the model is unable to accurately identify discontinuities, indicating a limited capacity to generalise beyond the predominant scenarios present in the training dataset.

In any case, the preliminary assessment of the severity of the damage related to the reduction in the resistant sections of the reinforcements is satisfactory. The results obtained confirm the potential of the method in supporting more efficient and adaptable evaluation and maintenance processes. The results obtained demonstrated a high degree of accuracy in cases that were most similar to the images used for training. However, the model exhibited difficulties in recognizing scenarios that differed from those present in the training dataset, indicating a limited capacity for generalization.

In such contexts, the effective organisation of data plays a fundamental role, since the dataset is the basis for the training and performance of the model. In the present study, this approach allowed the provision of structured information to the system on both the position of the degraded elements and the degree of degradation, significantly improving the ability of the object detection model to automatically recognise the different forms and levels of degradation.

In order to achieve this objective, an effort was made to define and apply a unique criterion for the restitution of the frames of the images used in the datasets and for the classification of the various types of degradation of the reinforcements. This was done to ensure coherence and uniformity in the management and representation of the data. This systematic methodology has been proven to be effective in supporting the model's ability to accurately identify deterioration phenomena in the analysed structures.

Existing structures frequently exhibit considerable heterogeneity in terms of structural and construction typology, maintenance status, conservation and operating conditions. This poses a significant challenge to the unification of methodologies and the direct utilisation of generalized models that lack sufficient validation. This variability is indicative of the inherent complexity of infrastructure projects yet concomitantly introduces inhomogeneities that impede the efficacy of artificial intelligence models. In this context, the employment of computer vision techniques, bolstered by deep learning models, has the potential to deliver solutions that are both faster and more efficient. Nevertheless, the full effectiveness of these measures is contingent upon the availability of a comprehensive database.

Another critical aspect pertains to the assessment of the state of degradation, which is often not directly and simply visible, particularly in the case of bridges and viaducts. While direct inspections remain a fundamental component of infrastructure management, they are inadequate to guarantee extensive and continuous control of the entire infrastructure heritage, especially considering the high number and morphological complexity of the elements to be monitored.

Despite significant advances in the field of automatic recognition of structural damage through the utilisation of deep learning-based models, the efficacy of these methodologies remains substantially constrained by the accessibility of training data. These data

are frequently not only deficient in terms of quality but also in absolute terms. This constraint is identified as a key challenge in the development of robust and generalizable predictive models.

The scarcity of available datasets has the effect of diminishing the capacity of models to recognise damage scenarios in a range of material and environmental conditions. It is evident that there is an absence of a univocal criterion for the restitution of the frames of the images utilised in the datasets. The heterogeneity of the visual acquisition conditions renders the classification of the various types of degradation of the reinforcement difficult.

The evaluation of the model's performance on unseen scenarios entails an examination of its generalisation capacity and its ability to avoid overfitting. The interpretation of the predictions made by artificial intelligence must be considered within a broader engineering context. This context encompasses the structural and environmental data of the analysed work. Improvement can be achieved through several factors, including:

- Increased dataset size (fewer parameterized images) and its potential imbalance compared to current degradation classes.
- Improved model architecture with better parameterization for the complexity of the civil engineering problem being investigated.
- Improved spatial and chromatic diversity of images in the dataset, increasing the model's ability to generalize results to extremely variable real conditions.

Finally, to broaden the research and its applications regarding the life cycle of structures, it is worth emphasizing that the study deals with existing reinforced concrete infrastructures, aged between approximately 40 and 60 years, for which the design did not consider the life cycle. For these types of structures, deterioration is undoubtedly increased by outdated design and construction procedures. Therefore, the use of appropriately validated artificial intelligence tools can be a key factor in defining management strategies and even in completely redefining the life cycle of the civil engineering works being studied. For newly designed and built structures, the life cycle is undoubtedly a fundamental element of design and management. For these types of civil engineering works, the use of artificial intelligence tools can provide important management support throughout the entire life cycle but must be specifically validated. New damage criteria and inspection methodologies will likely need to be defined.

5. Conclusions

In recent years, there has been growing interest in integrating AI-based tools into civil engineering, aiming to streamline the design, monitoring, maintenance, and management of structures and infrastructures. In particular, the automation of processes traditionally performed through manual activities (design, management, inspection, etc.) represents a concrete opportunity to reduce operating times and costs, while simultaneously improving the consistency, accuracy, and repeatability of technical assessments and the effectiveness and efficiency of procedures.

The adoption of AI is relatively easy and in its advanced stages for the design, construction, and management of new structures and infrastructures. This is thanks to the availability of consolidated procedures and experience, relatively clear regulations and guidelines, comprehensive design data, knowledge of the materials used, and the pursuit of structural and geometric regularity of structural elements. These factors favor the integration of AI models, coupled with the possibility of installing sensor devices from the initial stages for monitoring purposes.

The primary objective of this study is to develop a system based on intelligent algorithms to support the analysis of structural degradation, with reference to the reduction

in the thickness of metal reinforcement due to corrosion in existing reinforced concrete structures. The focus is on road infrastructures, such as bridges and viaducts, which are strategic elements for mobility. Given the large number of existing structures, it is essential to have objective, reliable, and replicable tools for rapid and/or more in-depth assessments.

The results of the study are to be considered absolutely preliminary but of considerable interest and very promising. The results obtained highlight the importance of having large, representative, and balanced datasets in terms of image distribution across the different types of degradation (carbonation, cracking, washout, etc.) and structural features, as well as with respect to environmental conditions, the geometric characteristics of the elements, and the image acquisition methods. Ensuring an adequate and uniform number of examples for each category allows the model to learn comprehensively and correctly generalize to different deterioration scenarios.

The need to integrate visual information with more complex and comprehensive models is clearly emerging, capable of adapting to different structural typologies, environmental conditions (humidity, temperature, exposure to atmospheric agents), the presence of carbonation, the mechanical function it performs within the construction system, the age of the structure, and the materials used. These are key factors that influence the progression of degradation and should be appropriately considered in the training phase of artificial neural networks to improve their predictive effectiveness and model robustness in real and complex scenarios.

Furthermore, a significant contribution could be made using synthetic data generation techniques, facilitated by three-dimensional graphic engines. The employment of three-dimensional graphic engines would indeed facilitate the regulated generation of realistic images, distinguished by elevated visual coherence and a substantial array of degradation scenarios, in conjunction with meticulously modelled environmental conditions. This approach would facilitate the large-scale production of synthetic datasets, which would in turn be capable of more accurately representing the complexity of existing infrastructure heritage.

The real problem, however, is acquiring a large enough number of images to make the results reliable. Currently, data is still scarce and perhaps insufficient for optimal training. To achieve effective improvements, it is necessary to increase the number of images. In this regard, it should be noted that several freely available datasets are available online (for example, https://universe.roboflow.com/sanacon/reinforcement-400-images/dataset/2, accessed on 1 September 2025, https://universe.roboflow.com/project-ida/structural-defects-cmies/, accessed on 1 September 2025); on the other hand, it should be emphasized that these datasets cannot be used for the objectives of this study. In fact, it is not possible to label the images since it is not possible to determine the physical quantities expected from the damage classes. Some images may be suitable for the purposes of this study (for example, for classes 0 and 1) but would not be usable to build a new training, which would be heavily unbalanced and strongly conditioned on the lower classes. Effective improvement is possible only through specifically detected images associated with the physical parameters needed to characterize the damage. Further improvements are possible through specific image processing from which some of the aforementioned information can be obtained (element dimension, diameter, etc.) but in this case the characterization and labelling process is still more lengthy and not free from possible and recurring evaluation errors. The complexity of the problem can be reduced by:

- Defining criteria for classifying degradation;
- Defining methods, procedures, and tools for assessing the damage caused by degradation;

- Defining image acquisition and classification procedures;
- Defining and classifying structures typologically, also based on their environmental context.

Author Contributions: Conceptualization, D.C. (Donata Carlucci), S.P. and M.V.; methodology, D.C. (Donata Carlucci) and M.V.; software, D.C. (Donata Carlucci) and M.V.; validation, D.C. (Donata Carlucci) and M.V.; formal analysis, D.C. and M.V.; investigation, D.C. (Donata Carlucci), D.C. (Donatello Cardone), S.P. and M.V.; resources, D.C. (Donata Carlucci), D.C. (Donatello Cardone), S.P. and M.V.; data curation, D.C. (Donata Carlucci), S.P. and M.V.; writing—original draft preparation, D.C. (Donata Carlucci) and M.V.; writing—review and editing, D.C. (Donata Carlucci), D.C. (Donatello Cardone), S.P. and M.V.; supervision, M.V. All authors have read and agreed to the published version of the manuscript.

Funding: This research was partially supported by 2020 MIUR PON R&I 2014–2020 Program (project MITIGO, ARS01_00964) and partially supported by P.R.I.N. Project 2022: "INSPIRE—Improving Nature-Smart Policies through Innovative Resilient Evaluations", Grant number: 2022J7RWNF.

Data Availability Statement: The original contributions presented in this study are included in the article. Further inquiries can be directed to the corresponding author.

Acknowledgments: The authors thank U. Erra and G. Manfredi (Department of Engineering, University of Basilicata, 85100 Potenza, Italy) for their valuable contributions.

Conflicts of Interest: The authors declare no conflicts of interest.

References

1. Vona, M.; Manganelli, B. The Historical and Cultural Value of RC Constructions and the Main Critical Issues for Rehabilitation. *Infrastructures* **2022**, *7*, 35. [CrossRef]
2. Cardone, D.; Possidente, V.; Perrone, G.; Spica, A.; Bernardini, D.; Ruta, D.; Paolone, A.; Braga, F.; Buttarazzi, F.; Rossi, A. Seismic performance of highway RC bridges with corroded piers. In *Bridge Maintenance Safety Management Digitalization and Sustainability, Proceedings of the 12th International Conference IABMAS, Copenhagen, Denmark, 24–27 June 2024*; CRC Press: Boca Raton, FL, USA, 2024; pp. 3889–3896.
3. Perrone, G.; Cardone, D.; Possidente, V. Influence of Structural Deterioration of RC Piers Due to Steel Corrosion on the Seismic Performance of Bridges. *J. Earthq. Eng.* **2025**, *29*, 2280–2302. [CrossRef]
4. Luchko, J.; Nazarevich, B.; Kovalchuk, V.V. Degradating concrete and reinforced concrete building structures and long-term structures. *Bull. Odessa State Acad. Civ. Eng. Archit.* **2022**, *86*, 35–46. [CrossRef]
5. Benítez, P.; Rocha, E.; Talukdar, S.; Varum, H.; Rodrigues, F. Efficiency analysis of optimal inspection management for reinforced concrete structures under carbonation-induced corrosion risk. *Constr. Build. Mater.* **2019**, *211*, 1000–1012. [CrossRef]
6. Bastidas-Arteaga, E.; Schoefs, F. Stochastic improvement of inspection and maintenance of corroding reinforced concrete structures placed in unsaturated environments. *Eng. Struct.* **2012**, *41*, 50–62. [CrossRef]
7. Zhao, Y.; Yu, J.; Hu, B.; Jin, W. Crack shape and rust distribution in corrosion-induced cracking concrete. *Corros. Sci.* **2012**, *55*, 385–393. [CrossRef]
8. Poonguzhali, A.; Shaikh, H.; Dayal, R.K.; Khatak, H.S. A Review on Degradation Mechanism and Life Estimation of Civil Structures. *Corros. Rev.* **2008**, *26*, 215–294. [CrossRef]
9. Medina, A.; González, L.J. Reinforced concrete long-term deterioration prediction for the implementation of a Bridge Management System. *Mater. Today: Proc.* **2022**, *58*, 1265–1271. [CrossRef]
10. ASCE/SEI-AASHTO Ad-Hoc Group on Bridge Inspection, Rating, Rehabilitation, and Replacement. White Paper on Bridge Inspection and Rating. *J. Bridge Eng.* **2009**, *14*, 1–5. [CrossRef]
11. Iacovino, C.; Turksezer, Z.I.; Giordano, P.F.; Limongelli, M.P. Comparison of Bridge Inspection Policies in terms of Data Quality. *J. Bridge Eng.* **2022**, *27*, 04021115. [CrossRef]
12. Riveiro, B.; Bouzas, Ó.; Barros, B.; Conde, B.; Cabaleiro, M.; Rodríguez, A.S.; Arias-Sánchez, P. Model updating of in-service bridges using multidisciplinary research —Case studies in Spain. *ce/papers* **2023**, *6*, 561–567. [CrossRef]
13. Meoni, A.; García-Macías, E.; Venanzi, I.; Ubertini, F. A procedure for bridge visual inspections prioritisation in the context of preliminary risk assessment with limited information. *Struct. Infrastruct. Eng.* **2023**, *21*, 1–27. [CrossRef]

14. Ministry of Infrastructure and Transportation. *DM 01/07/2022: Linee Guida per la Classificazione e Gestione del Rischio, la Valutazione della Sicurezza ed il Monitoraggio dei Ponti Esistenti*; Ministero delle Infrastrutture e dei Trasporti: Rome, Italy, 2022. (In Italian)
15. Vona, M. Characterization of In Situ Concrete of Existing RC Constructions. *Materials* **2022**, *15*, 5549. [CrossRef] [PubMed]
16. Malek, J.; Kaouther, M. Destructive and Non-destructive Testing of Concrete Structures. *Jordan J. Civ. Eng.* **2014**, *8*, 432–441.
17. Ivanchev, I. Investigation with Non-Destructive and Destructive Methods for Assessment of Concrete Compressive Strength. *Appl. Sci.* **2022**, *12*, 12172. [CrossRef]
18. Bošnjak, A.; Jajac, N. Determining Priorities in Infrastructure Management Using Multicriteria Decision Analysis. *Sustainability* **2023**, *15*, 14953. [CrossRef]
19. Anelli, A.; Vona, M.; Hidalgo, S.-C.S. Comparison of Different Intervention Options for Massive Seismic Upgrading of Essential Facilities. *Buildings* **2020**, *10*, 125. [CrossRef]
20. Rimkus, A.; Podviezko, A.; Gribniak, V. Processing digital images for crack localization in reinforced concrete members. *Procedia Eng.* **2015**, *122*, 239–243. [CrossRef]
21. Cardellicchio, A.; Ruggieri, S.; Nettis, A.; Renò, V.; Uva, G. Physical interpretation of machine learning-based recognition of defects for the risk management of existing bridge heritage. *Eng. Fail. Anal.* **2023**, *149*, 107237. [CrossRef]
22. Yang, Q.; Shi, W.; Chen, J.; Lin, W. Deep convolution neural network-based transfer learning method for civil infrastructure crack detection. *Autom. Constr.* **2020**, *116*, 103199. [CrossRef]
23. Fan, W.; Chen, Y.; Li, J.; Sun, Y.; Feng, J.; Hassanin, H.; Sareh, P. Machine learning applied to the design and inspection of reinforced concrete bridges: Resilient methods and emerging applications. *Structures* **2021**, *33*, 3954–3963. [CrossRef]
24. Li, T.; Liu, G.; Tan, S. Superficial Defect Detection for Concrete Bridges Using YOLOv8 with Attention Mechanism and Deformation Convolution. *Appl. Sci.* **2024**, *14*, 5497. [CrossRef]
25. Zhang, C.; Lei, X.; Xia, Y. Enhancing bridge inspection data quality using machine learning. *Autom. Constr.* **2025**, *175*, 106182. [CrossRef]
26. Spencer, B.F.; Hoskere, V.; Narazaki, Y. Advances in Computer Vision-Based Civil Infrastructure Inspection and Monitoring. *Engineering* **2019**, *5*, 199–222. [CrossRef]
27. Shen, W.; Tian, X.; Zeng, D.; Zhang, Y. Multi-scale image compression and reconstruction algorithm for structural health monitoring system. *Eng. Struct.* **2024**, *315*, 118516. [CrossRef]
28. Mundt, M.; Majumder, S.; Murali, S.; Panetsos, P.; Ramesh, V. Meta-learning convolutional neural architectures for multi-target concrete defect classification with the Concrete Defect Bridge Image Dataset. In Proceedings of the IEEE/CVF Conference on Computer Vision and Pattern Recognition (CVPR), Long Beach, CA, USA, 15–20 June 2019. [CrossRef]
29. Bhattacharya, G.; Puhan, N.B.; Mandal, B. Kernelized dynamic convolution routing in spatial and channel interaction for attentive concrete defect recognition. *Signal Process. Image Commun.* **2022**, *108*, 116818. [CrossRef]
30. Arbaoui, A.; Ouahabi, A.; Jacques, S.; Hamiane, M. Concrete cracks detection and monitoring using Deep Learning-based multiresolution analysis. *Electronics* **2021**, *10*, 1772. [CrossRef]
31. Zeeshan, M.; Adnan, S.M.; Ahmad, W.; Khan, F.Z. Structural crack detection and classification using deep convolutional neural network. *Pak. J. Eng. Technol.* **2021**, *4*, 50–56. [CrossRef]
32. Naji, K.; Gowid, S.; Ghani, S. AI and IoT-based concrete column base cover localization and degradation detection algorithm using deep learning techniques. *Ain Shams Eng. J.* **2023**, *14*, 102520. [CrossRef]
33. Xu, W.; Li, H.; Li, G.; Ji, Y.; Xu, J.; Zang, Z. Improved YOLOv8n-based bridge crack detection algorithm under complex background conditions. *Sci. Rep.* **2025**, *15*, 13074. [CrossRef] [PubMed]
34. Xu, G.; Yue, Q.; Liu, X.; Chen, H. Investigation on the effect of data quality and quantity of concrete cracks on the performance of deep learning-based image segmentation. *Expert Syst. Appl.* **2024**, *237*, 121686. [CrossRef]
35. Shim, S. Semantic segmentation for crack detection via generative knowledge distillation. *Autom. Constr.* **2025**, *175*, 106201. [CrossRef]
36. Tran, T.S.; Nguyen, S.D.; Lee, H.J.; Tran, V.P. Advanced crack detection and segmentation on bridge decks using deep learning. *Constr. Build. Mater.* **2023**, *400*, 132839. [CrossRef]
37. Dung, C.V.; Anh, L.D. Autonomous concrete crack detection using deep fully convolutional neural network. *Autom. Constr.* **2019**, *99*, 52–58. [CrossRef]
38. Ni, T.; Zhou, R.; Gu, C.; Yang, Y. Measurement of concrete crack feature with android smartphone APP based on digital image processing techniques. *Measurement* **2020**, *150*, 107093. [CrossRef]
39. Bayar, G.; Bilir, T. A novel study for the estimation of crack propagation in concrete using machine learning algorithms. *Constr. Build. Mater.* **2019**, *215*, 670–685. [CrossRef]
40. Ahila Priyadharshini, R.; Arivazhagan, S.; Arun, M. Crack recognition on concrete structures based on machine crafted and hand crafted features. *Expert Syst. Appl.* **2023**, *228*, 120447. [CrossRef]

41. Aung, P.P.W.; Sam, K.M.; Kulinan, A.S.; Cha, G.; Park, M.; Park, S. Enhancing deep learning in structural damage identification with 3D-engine synthetic data. *Autom. Constr.* **2025**, *175*, 106203. [CrossRef]
42. Zhou, Z.; Wang, C.; Han, X. Safety evaluation of cracked concrete structures with crack length index. *Theor. Appl. Fract. Mech.* **2022**, *122*, 103662. [CrossRef]
43. Su, P.; Han, H.; Liu, M.; Yang, T.; Liu, S. MOD-YOLO: Rethinking the YOLO architecture at the level of feature information and applying it to crack detection. *Expert Syst. Appl.* **2024**, *237*, 121346. [CrossRef]

Disclaimer/Publisher's Note: The statements, opinions and data contained in all publications are solely those of the individual author(s) and contributor(s) and not of MDPI and/or the editor(s). MDPI and/or the editor(s) disclaim responsibility for any injury to people or property resulting from any ideas, methods, instructions or products referred to in the content.

infrastructures

MDPI

Article

Machine Learning Synthesis of Fire-Following-Earthquake Fragility Surfaces for Steel Moment-Resisting Frames

Mojtaba Harati [1,2] and John W. van de Lindt [1,*]

[1] Department of Civil and Environmental Engineering, Colorado State University, Fort Collins, CO 80523, USA; m.harati@colostate.edu
[2] Verisk Exterem Event Solutions, Boston, MA 02111, USA
* Correspondence: jwv@engr.colostate.edu

Abstract: This paper presents a probabilistic methodology for generating fragility surfaces for low- to mid-rise steel moment-resisting frames (MRFs) under fire-following-earthquake (FFE). The framework integrates nonlinear dynamic seismic analysis, residual deformation transfer, and temperature-dependent fire simulations within a Monte Carlo environment, while explicitly accounting for uncertainties in structural properties, ground motions, and fire simulation. A fiber-based modeling strategy is employed, combining temperature-sensitive steel materials with fatigue and fracture wrappers to capture cyclic deterioration and abrupt failure. This formulation yields earthquake-only and fire-only fragility curves along the surface boundaries, while interior points quantify the joint fragility response under sequential hazards. The methodology is benchmarked against a machine learning (ML) synthesis framework originally developed for earthquake–tsunami applications and extended here to FFE. Numerical results for a three-story steel MRF show excellent agreement ($R^2 > 0.95$, RMSE < 0.02) between simulated and ML-generated surfaces, demonstrating both the efficiency and hazard-neutral adaptability of the ML framework for multi-hazard resilience assessment.

Keywords: fire-following-earthquake (FFE); multi-hazard fragility; steel moment-resisting frames; performance-based design; machine learning; structural resilience

1. Introduction

Historic events have shown that post-earthquake fires can be as devastating as the seismic shaking itself. The 1906 San Francisco earthquake triggered over 50 fires, with approximately 80% of the city's destruction attributed to these fires rather than the earthquake itself [1,2]. Similarly, the 1923 Great Kantō earthquake in Japan resulted in widespread conflagrations responsible for nearly 78% of the total damage and over 140,000 fatalities [1,3–5]. More recent disasters, such as the 1995 Kobe earthquake in Japan, which caused numerous urban fires [6], and the 2011 Christchurch earthquake in New Zealand, where fire outbreaks compounded seismic damage [7], underscore that fire-following-earthquake remains a persistent threat in modern cities. These events highlight the significant risk posed by fire-following-earthquake (FFE) scenarios, particularly in dense urban environments where earthquake-induced damage compromises both structural integrity and firefighting capabilities [8–10].

Earthquakes often rupture gas lines, damage electrical systems, and disable fire suppression mechanisms, creating conditions highly conducive to fire outbreaks [9]. Additionally, compromised water supply and obstructed transportation routes hinder emergency response efforts [11,12]. Despite this well-documented cascading hazard, current design

practices typically address seismic and fire risks independently. Building codes and standards such as ASCE 7-22 (2022) [13] and Eurocode 2 and Eurocode 8, 2nd Generation Drafts [14–16], prescribe separate criteria for seismic and fire loading, failing to account for their sequential or combined effects. Performance-based design (PBD) frameworks have advanced single-hazard risk assessment, particularly in seismic engineering through methodologies like FEMA P-58 (2012) [17] and FEMA P-695 (2009) [18]. However, these frameworks do not explicitly address cascading hazards such as FFE. While multi-hazard guidance exists for earthquake–tsunami scenarios, i.e., FEMA P-646 (2019) [19], there is a critical gap regarding sequential earthquake-fire risks [20,21]. This omission leaves structures potentially vulnerable to compounded damage when fire follows seismic events.

Steel moment-resisting frames (MRFs), widely used in seismic regions due to their ductility and energy dissipation capacity, face unique vulnerabilities under FFE conditions [22–25]. Research has shown that seismic damage degrades fire resistance by displacing fireproofing materials and compromising structural elements [26]. Full-scale experiments, such as those conducted at UC San Diego, have demonstrated how earthquake-induced residual drifts and breached compartmentation exacerbate fire spread and structural degradation [9,27–29]. To address these challenges, probabilistic methods and fragility analysis are increasingly being adopted for multi-hazard scenarios [30,31]. Fragility functions, which quantify the probability of exceeding damage states (DSs) given hazard intensities, are well-established in earthquake engineering [32,33]. Recent efforts have extended this concept to fire [34–36], and preliminary frameworks for FFE fragility modeling have emerged [21,37,38]. These studies emphasize the necessity of capturing uncertainties related to both hazards and the progressive degradation of structural capacity.

In dense urban areas surrounded by forests—particularly in dry climates such as Los Angeles—the ignition point of a mass fire may originate within the town itself rather than in the wildland perimeter [10,39]. Integrating performance-based earthquake and fire engineering into a unified FFE fragility framework provides a pathway to more resilient structural design [37]. By quantifying the probability of collapse or critical DSs under cascading hazards, such models can inform targeted risk mitigation strategies and guide updates to building codes [38]. Advancing this field is essential for safeguarding communities in seismically active regions where the threat of post-earthquake fires remains a persistent and under-addressed risk.

This paper introduces and validates a comprehensive methodology for generating fragility surfaces of steel moment-resisting frames under fire-following-earthquake. The framework integrates nonlinear dynamic earthquake analysis, residual deformation transfer, and probabilistic fire simulation within a Monte Carlo environment, while explicitly accounting for structural and hazard-related uncertainties. A fiber-based modeling strategy is employed to capture temperature-dependent degradation, cyclic deterioration, and ultimate fracture, ensuring realistic collapse representation. The methodology is further examined against a machine learning-based synthesis approach originally developed for earthquake–tsunami sequences, adapted here to earthquake–fire hazards. Through a case study on a three-story steel MRF, the study demonstrates how the proposed framework can be used to derive multi-dimensional fragility surfaces, evaluate the agreement between simulation- and ML-generated models, and provide probabilistically consistent insights into structural performance under cascading hazards.

2. Methodology to Generate Integrated FFE Fragility Surface

The proposed methodology follows a three-step sequential analysis framework to capture the cascading effects of earthquake and fire on steel MRFs. The framework inte-

grates nonlinear dynamic seismic response, residual deformation transfer, and subsequent fire exposure into a robust procedure for FFE fragility surface generation. Each successive simulation is performed within a Monte Carlo Simulation (MCS) environment, enabling uncertainty quantification and probabilistic estimation of collapse prevention or failure thresholds. The sequential procedure for generating FFE fragility surfaces is summarized in the flowchart shown in Figure 1.

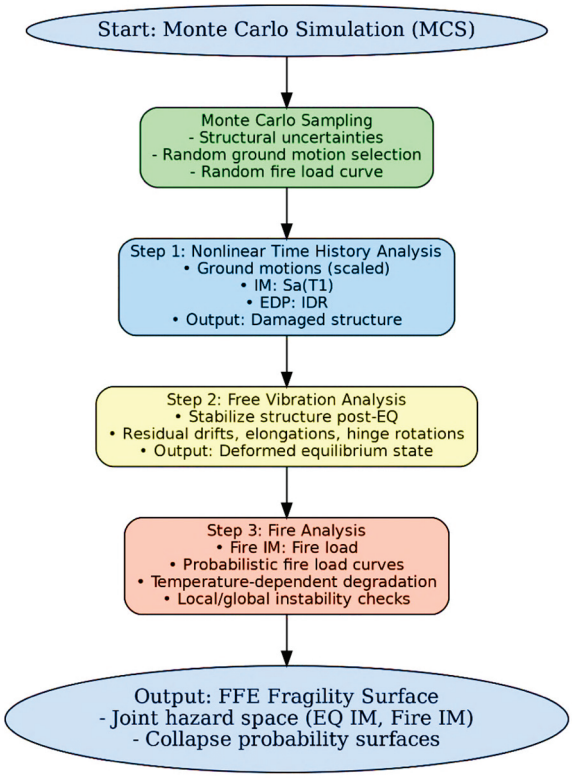

Figure 1. Framework for generating FFE fragility surfaces through sequential earthquake, residual deformation, and fire analyses within an MCS environment.

The first stage consists of nonlinear time history analysis under earthquake excitation, with the structural system initialized at ambient temperature equal to the surrounding environment. The finite element model (described in Section 3) is subjected to a suite of ground motions selected from predefined bins, with scaling applied using the point-scaling method. Spectral acceleration at the fundamental period, $Sa(T_1)$, is adopted as the earthquake intensity measure (IM), following common practice in multi-hazard fragility modeling [40,41]. For each ground motion, the structural model is sampled stochastically to reflect uncertainties in material properties, geometric imperfections, and damping characteristics. The engineering demand parameter (EDP) in this phase is the inter-story drift ratio (IDR) [40], with complete or collapse-prevention DSs adopted from HAZUS (2020) [42] thresholds. The outcome of this phase is a seismically damaged structure, including residual drifts and local deterioration, which is then carried forward into the next step. Similar to the hybrid OpenSees [43,44] modeling approach by Saed et al. (2025) [45], the model accounts for cyclic degradation mechanisms to ensure realistic representation of seismic damage.

To capture post-seismic permanent displacements, a free vibration analysis is performed immediately after the time history analysis under each ground motion record. This step allows the system to stabilize dynamically, converging toward its deformed equilibrium state [46,47]. The resulting configuration incorporates residual inter-story drifts, beam

elongations, and potential plastic hinge rotations, which represent the initial conditions for the subsequent fire analysis. This procedure is consistent with sequential frameworks used in prior studies of post-earthquake fire (PEF) modeling (e.g., Saed et al. (2025) [45]), where the deformed shape of the system directly influences thermal expansion demands, load redistribution, and local instabilities during fire.

The seismically damaged and deformed structural model is then subjected to a rising temperature profile defined through probabilistic fire load curves. While various fire IMs (e.g., duration, maximum temperature, area under temperature–time curve) exist in the literature [35,48], this study adopts fire load as the fire IM, as it provides a more direct quantification of thermal severity [49]. The thermal analysis applies time–temperature relationships to heated members, with fire-induced degradation in material stiffness and strength modeled using temperature-dependent constitutive laws [50–52]. Following practices demonstrated in recent OpenSees hybrid modeling efforts (e.g., Jiang et al. (2015) [51]), local stability is evaluated by tracking the reduction in beam and column strength to 80% of their maximum capacity [45], while global mechanisms are assessed through IDR thresholds similar to those defined in Step 1 [53]. Together, these limit states capture both localized instability (loss of load-carrying capacity in critical members) and global collapse-type responses.

The integrated procedure is executed probabilistically through MCS, where each simulation involves random generation of structural parameters through uncertainty sampling, selection of a ground motion from the earthquake bin scaled appropriately, nonlinear time history analysis under earthquake loading (Step 1), free vibration analysis to transfer residual deformation (Step 2), and sequential fire analysis under probabilistic fire loads (Step 3).

The binary outcome of each run (failure or survival at a given earthquake–fire IM pair) is accumulated across all simulations to calculate the conditional probability of exceeding specified limit states. These raw results are converted into multi-dimensional and multi-hazard FFE fragility surfaces, representing the joint hazard space of earthquake intensity and fire severity. The raw failure probability points can be fitted by a closed-form probabilistic surface function, originally adapted from Harati and van de Lindt (2024a) [46], which estimates the conditional exceedance probability for any earthquake–fire IM pair. The surface is expressed as:

$$P\left(IM_{EQ}, IM_{Fire}\right) = \frac{E(\frac{IM_{EQ}}{C_1} + \frac{IM_{Fire}}{C_2} + \alpha\left(\frac{IM_{EQ}}{C_1}\right)\left(\frac{IM_{Fire}}{C_2}\right))^n}{(\left(\frac{IM_{EQ}}{C_1} + \frac{IM_{Fire}}{C_2} + \alpha\left(\frac{IM_{EQ}}{C_1}\right)\left(\frac{IM_{Fire}}{C_2}\right)\right)^n + 1)} \quad (1)$$

where IM_{EQ} and IM_{Fire} denote the IMs for the earthquake (e.g., spectral acceleration at the fundamental period) and fire (e.g., equivalent temperature or fire load parameter), respectively. The parameters E, C_1, C_2, α, and n are fitting constants that control the scale, steepness, and interaction between the two hazards. Once the successive simulation model produces exceedance probabilities over a discretized (IM_{EQ}, IM_{Fire}) grid, a nonlinear regression algorithm (e.g., scipy.optimize.curve_fit) is used to calibrate the five parameters (see Harati and van de Lindt (2024a) [46] for details). This closed-form representation allows compact storage of fragility surfaces while providing sufficient flexibility to capture nonlinear damage accumulation and hazard interaction effects characteristic of earthquake–fire sequences.

3. Structural Modeling

The methodology developed in this study for structural modeling is designed for low- to mid-rise steel moment resisting frames subjected to PEF scenarios. While concentrated plastic hinge models (e.g., modified IMK hinges) [54,55] are often considered

superior for collapse simulations due to their ability to capture deterioration of stiffness and strength [56,57], the present framework adopts a fiber-based approach. This choice is essential because it allows the temperature–time history to be directly embedded in the element formulation [45,51], particularly in the third phase of analysis where fire governs structural performance. Computational demands, a common limitation of fiber approaches, are addressed by implementing the simulations within a multi-distributed MCS framework with parallel processing [58]. The stepwise framework for structural modeling is summarized in Figure 2, which illustrates the fiber-based methodology developed for steel MRFs under post-earthquake fire conditions.

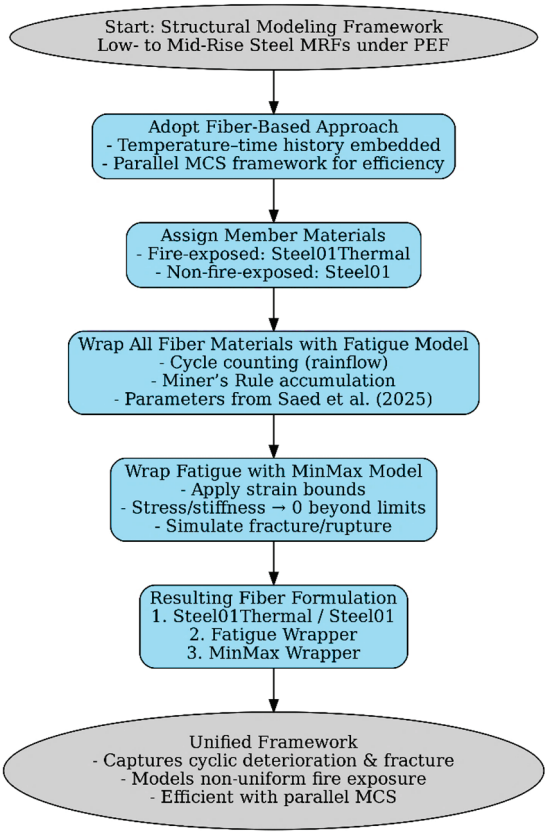

Figure 2. Flowchart of the fiber-based modeling methodology for steel MRFs under post-earthquake fire. The material parameters are based on Saed et al. (2025) [45].

In this approach, structural members are modeled using displacement-based beam-column elements with fiber sections. For elements directly exposed to fire, the Steel01Thermal material is assigned. This thermal extension of the widely used Steel01 model incorporates temperature sensitivity by requiring inputs of yield strength (F_y), elastic modulus (E_0), strain-hardening ratio (b), and optional isotropic hardening parameters (a_1–a_4). For non-fire-exposed members, the regular Steel01 formulation is used, reducing computational cost while preserving accuracy. By combining thermal and non-thermal fibers, the model captures the non-uniform thermal exposure expected in realistic fire scenarios.

To address cumulative cyclic deterioration, which is not inherently captured in fiber sections, each fiber section material is wrapped with the Fatigue material in OpenSees [43,44,59]. This model employs a modified rainflow cycle counting algorithm with Miner's Rule to track damage accumulation until fatigue life is exhausted [60]. Key parameters include E_0 (strain at which one cycle induces failure) and m (slope of the Coffin–Manson curve). As demonstrated by Saed et al. (2025) [45], calibrated parameter values effectively replicate experimentally

observed deterioration under combined seismic and thermal demands. This allows the fiber-based model to emulate the hysteretic degradation typically represented in modified IMK hinges [55], where low-cycle fatigue effects are embedded through experimental calibration. The fatigue and MinMax wrapper parameters were selected based on calibration to low-cycle fatigue test data and prior numerical studies [45,60], ensuring consistency with experimentally observed deterioration and fracture behavior in steel MRF components. The parameter values were verified to yield realistic hysteretic degradation and ultimate strain limits consistent with available experimental benchmarks.

To further control ultimate failure, the fatigue-wrapped material is then encapsulated with the MinMax material in OpenSees. The MinMax model applies lower and upper strain bounds to the parent material response [61]. When the fiber strain falls outside these thresholds, both stress and tangent stiffness drop to zero, simulating fracture or rupture at large elongations. In this layered configuration, the fatigue model governs cyclic deterioration, while MinMax governs final fracture behavior, thereby ensuring a comprehensive representation of material failure mechanisms.

The resulting fiber formulation can be described as a three-layered nesting scheme: (1) Steel01Thermal for temperature-sensitive stress–strain response in fire-exposed members and Steel01 for non-fire-exposed members; (2) a Fatigue wrapper applied to all fibers to capture low-cycle fatigue accumulation; and (3) a MinMax wrapper applied to all fibers to enforce large-strain fracture limits. While only fire-exposed elements incorporate temperature-dependent behavior through Steel01Thermal, every fiber section in the model—whether thermal or non-thermal—is wrapped with Fatigue and MinMax to ensure consistent representation of cyclic deterioration and ultimate fracture across the entire frame. This strategy maintains computational efficiency while providing a unified framework for simulating progressive collapse (i.e., a potential scenario in this fragility modeling) under combined seismic and fire demands. Overall, this methodology balances the fidelity of concentrated hinge models with the necessity of temperature-dependent fiber modeling in PEF studies. By embedding thermal degradation, cyclic fatigue, and fracture into a single fiber-based scheme, the framework provides a robust and computationally feasible platform for collapse and fragility assessment. The approach ensures that both strength and stiffness deterioration are realistically captured, while parallelized MCS implementation [46] makes the methodology suitable for large-scale resilience evaluations of steel MRFs under sequential earthquake–fire loading.

Earthquake and Fire Loadings

Gravity loads are modeled using probabilistic distributions to propagate uncertainties, which will be detailed in the following section (Section 4). For the seismic hazard, far-field ground motion records from FEMA P-695 (2009) [18] are employed as input. These records are scaled using the point scaling method across different seismic intensity levels, consistent with the multiple stripe analysis (MSA) framework [62] implemented within the proposed MCS procedure. This scaling approach aligns with common practices in MSA and incremental dynamic analysis (IDA) [63], ensuring that the treatment of earthquake loading is consistent with methodologies typically applied when seismic hazard is considered in isolation (e.g., see [33]). The seismic input used in this study is illustrated in Figure 3, which presents the response spectra of the selected FEMA P-695 far-field ground motion records. Each line corresponds to the spectral acceleration (Sa) of an individual record, while the thicker line denotes the median response spectrum across all records. The figure highlights the variability in spectral demand at short periods and the convergence toward lower values at longer periods. Using the median spectrum ensures that the seismic hazard representation is

consistent with standard practice for multiple-stripe or incremental dynamic analysis, while also capturing the dispersion of individual records needed for probabilistic assessment.

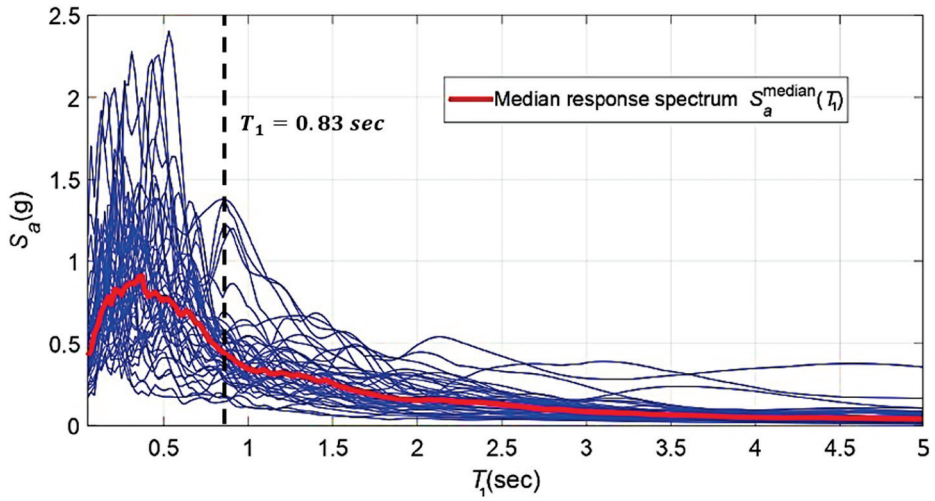

Figure 3. Response spectra of the selected FEMA P-695 [18] far-field ground motions (blue lines), with the corresponding median spectrum shown in red. The fundamental period of the case-study building ($T_1 = 0.83$ s) is marked to illustrate the point-scaling method used for spectral matching.

For the fire hazard, prior research has shown that the worst-case scenario occurs when fire engulfs the entire first story of the structure [21,23,45,64,65]. Accordingly, only the beams and columns of the first story are modeled with thermally sensitive fiber sections. To realistically simulate fire-induced deformations, equal degrees of freedom are disabled at the first floor, thereby permitting independent thermal elongation of members, especially beams, and allowing the model to capture violations of the rigid diaphragm assumption expected under severe fire exposure [45].

The model of the examined frame (discussed later) is built in OpenSees [43] using the dispBeamColumnThermal elements with Steel01Thermal material. The members are uniformly heated to more than 550 °C approximately, reaching a state of instability under the ISO-834 standard fire curve [15]. The temperature defined in this standard curve is applied as a boundary condition, with the expression later modified to enable uncertainty propagation:

$$T = 20 + 345\ log(8t + 1) \quad (2)$$

where t represents time in minutes. This choice reflects both the embedded functionality of Steel01Thermal and the widespread adoption of the ISO-834 curve in structural fire analysis [66]. While other time–temperature curves exist in the literature, the use of ISO-834 ensures direct compatibility with the OpenSees thermal module and facilitates a consistent representation of material degradation under elevated temperatures [67].

The maximum gas temperature in the compartment fire model was expressed as a function of both the fire load density and the ventilation opening factor, consistent with Eurocode parametric fire formulations [68,69]. In this study, a simplified surrogate relation was adopted to approximate the peak temperature:

$$T_{max} = 1325\ (1 - e^{-0.01qO}) \quad (3)$$

where q denotes the fire load density (MJ/m^2) and O is the opening factor. This expression reflects the asymptotic behavior of Eurocode parametric curves, which saturate toward approximately 1325 °C while accounting for increases in fire severity with greater com-

bustible energy and ventilation. The coefficient (0.01) serves as a calibration parameter to align the surrogate with Annex A of EN 1991-1-2 [16] over the practical range of q and O. While the canonical Eurocode model provides a time-temperature trajectory, the above formulation offers a computationally efficient representation of the expected peak, suitable for Monte Carlo-based fragility analyses where repeated evaluations are required.

The procedure begins by selecting a fire load value (q), from which the corresponding maximum temperature (T_{max}) is obtained using Equation (3). A randomly distributed fire duration (t) is then sampled (as discussed later) to ensure that the ISO-834 curve, expressed in Equation (2), reaches the same T_{max}. The variability of the resulting heating trajectories is illustrated in Figure 4, where the ISO-834 formulation is modified by introducing a lognormally distributed β factor multiplied to fire duration, t. This parameter governs the growth rate of the fire curve while preserving its asymptotic behavior. As shown in Figure 4, different realizations of β produce distinct heating curves within the first 25 min, all truncated at 500 °C. The reference ISO-834 curve ($\beta = 1$) is also plotted for comparison, demonstrating how the probabilistic treatment captures uncertainty in fire development while remaining consistent with the standardized model.

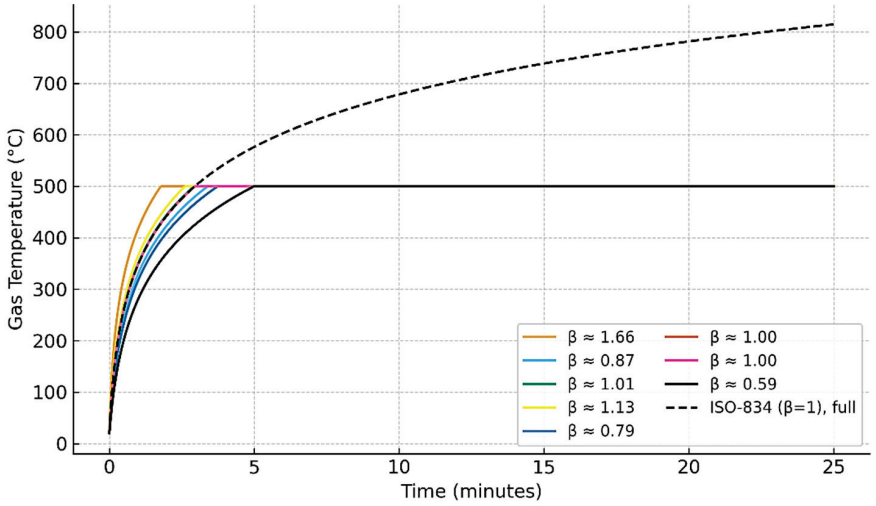

Figure 4. ISO-834 fire curves modified with a lognormally distributed β factor (median = 1.0, σ_{ln} = 0.3) and truncated at 500 °C, plotted for the first 25 min to illustrate variability in heating rates across different scenarios.

Through this combined loading protocol, the sequential effects of earthquake and fire are represented in a probabilistically consistent manner, ensuring that the interaction between seismic damage and subsequent thermal degradation is explicitly captured. The modeling strategy emphasizes the first-story members, which act as the critical components governing collapse potential, since both experimental and analytical studies have shown that failure is typically initiated at the base level where gravity demands are highest and fire exposure is most severe [23,45]. By embedding stochastic variability in both seismic input and fire development, the framework enables the generation of fragility functions that reflect not only mean performance but also the uncertainty associated with hazard intensity, damage accumulation, and structural deterioration.

4. Uncertainty Quantification

Uncertainty in the structural model is incorporated to capture variability in key parameters influencing dynamic and thermal response. Following established reliability studies [70,71], both dead load and seismic mass were modeled as lognormally distributed

with a mean of 1.05 multiplied by the computed value and a coefficient of variation (COV) of 0.10. For steel structures, the dominant source of material property uncertainty arises from variability in the yield strength (f_y) of steel fibers [70–72]. In this study, f_y was modeled as a lognormal random variable with a mean of 60 ksi (415 MPa) and a COV of 10% [71].

For the earthquake phase of the successive simulation, structural and input uncertainties were explicitly incorporated to capture the variability in seismic demand and response. The damping ratio was modeled as a lognormal variable with a mean of 0.065 and a COV of 0.60, consistent with the large scatter observed in experimental studies [71]. In addition, uncertainty in the seismic input motions was addressed by employing a bin of 44 far-field ground motion records recommended in FEMA P-695 [18]. These records were scaled across different intensity levels and used as input for the first phase of the simulation framework, thereby ensuring that both record-to-record variability and modeling uncertainties were propagated into the fragility analysis [73]. These probabilistic representations allow uncertainty in structural capacity and energy dissipation to be propagated consistently through the MCS procedures, ensuring that fragility estimates reflect both hazard and modeling variability. The Monte Carlo simulation framework was executed over thousands to millions of realizations, depending on the discretization of the joint intensity measure (IM) grid. Similar to the procedure established by Harati and van de Lindt (2025) [41], a pilot convergence analysis was first performed using $K_{initial} = 10$ samples to estimate the variance of failure probability at each IM pair. The required sample size was iteratively refined using $n_r = \left(Z^2\sigma^2 / E_r^2\right)$, targeting a 95% confidence level and an average error below 1%. The mean collapse probability stabilized at less than 1% variation across successive iterations, confirming convergence and statistical reliability of the final fragility surface. All uncertainty variables—including structural, seismic, and fire-related parameters—are jointly sampled in each Monte Carlo realization. To maintain statistical consistency across the sequential earthquake–fire phases, the random variables are generated simultaneously using Latin Hypercube Sampling (LHS), ensuring appropriate coverage of the joint parameter space and correlation among variables within each simulation.

Uncertainty in structural fire performance arises not only from variations in material properties and boundary conditions but also from the stochastic nature of fire development itself [74,75]. The thermal demand imposed on structural members depends on numerous uncertain parameters, including fire load density, compartment geometry, and ventilation conditions. To reflect this variability, a probabilistic framework was adopted in this study, where uncertainty in the fire curves is introduced through a lognormal distribution applied to the fire growth factor (β) [74]. The rationale for selecting a lognormal distribution is twofold. First, fire load and ventilation-related variables are inherently positive, making the lognormal a natural choice for representing skewed, non-negative random variables. Second, prior studies have shown that lognormal-type distributions provide a realistic statistical representation of fire load variability observed in experimental and field data [76,77]. By sampling β from a lognormal distribution centered around unity, the baseline ISO-834 curve can be stochastically perturbed, producing a family of fire curves that reflect uncertainty in the heating rate while preserving the standardized asymptotic shape.

In practice, the ISO-834 expression, $T = 20 + 345\ log(8\beta t + 1)$, was modified by introducing the random multiplier β into the time-scaling term. For each Monte Carlo sample, a β value is drawn from the lognormal distribution, generating a unique fire curve. This approach effectively models uncertainty in fire severity without requiring a departure from the widely recognized ISO-834 formulation, thereby ensuring compatibility with the thermal material models implemented in OpenSees.

Figure 5 illustrates the ensemble of probabilistic fire curves generated with this procedure. The dashed black line corresponds to the reference ISO-834 fire curve ($\beta = 1$), while the red lines represent curves generated using random samples of β from the lognormal distribution. As shown in this figure, the family of curves envelops the reference trajectory, capturing variability in early heating rates and peak temperatures. This representation propagates fire-demand uncertainty through the structural simulations, yielding fragility surfaces that reflect both hazard and structural variability.

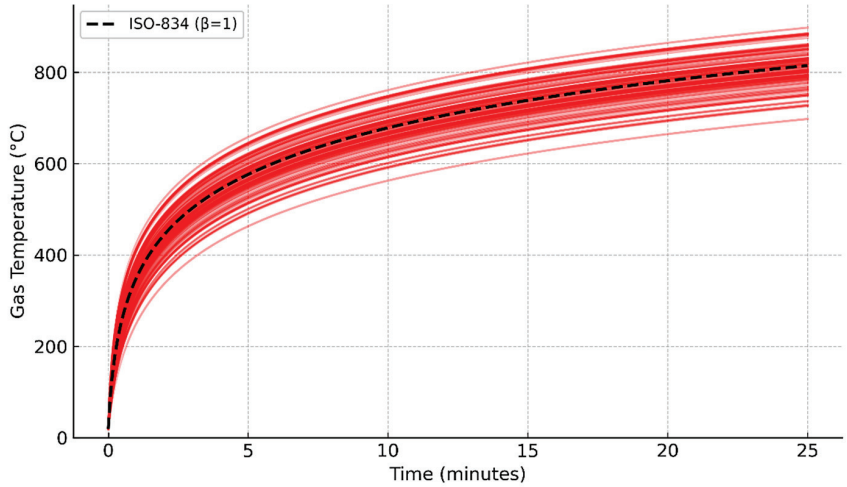

Figure 5. Ensemble of ISO-834 fire curves incorporating uncertainty through a lognormally distributed β factor (red lines). The reference ISO-834 curve ($\beta = 1$) is shown in black dashed.

5. Machine Learning-Based Fragility Surface Generation

In this study, the fragility surface mapping methodology selected to be examined against direct simulation builds upon the machine learning (ML) framework originally developed for earthquake–tsunami (EQ–TS) sequences [32]. In that work, an ensemble tree-based regression model—referred to as the g function—was trained to synthesize 2D fragility functions into a continuous three-dimensional (3D) fragility surface. The model operates on exceedance probabilities rather than raw IMs, enabling a hazard-neutral representation that generalizes across sequential hazard types [78].

As illustrated schematically in Figure 6, the framework requires two input fragility functions, each expressed as a 2D cumulative probability curve relating a scalar IM to the likelihood of exceeding a specific DS. For the FFE application, the first fragility function represents earthquake-induced collapse probabilities, while the second reflects fire-induced collapse probabilities. These boundary fragility curves are discretized and paired to span the joint hazard space, and their cumulative exceedance probabilities are provided as inputs to the ML model. The output is a synthesized fragility surface $P(DS \mid IM_{EQ}, IM_{Fire})$, which quantifies the conditional probability of DS exceedance as a function of both hazard intensities.

The central objective of this study is to assess whether fragility surfaces synthesized from the EQ–TS algorithm, when applied to earthquake and fire fragility functions, are consistent with those generated directly from FFE simulation data. Agreement between the synthesized and ML-generated surfaces would validate the EQ–TS methodology as a reliable surrogate for constructing fragility surfaces in new hazard pairings, bypassing the need for extensive sequential analyses. A key advantage of this approach lies in its adaptability: once trained on EQ–TS data, the model can be extended to FFE or other sequential hazards without retraining, provided that the input fragility curves exhibit smooth, monotonic, and bounded cumulative probability behavior [32,78]. This adaptability positions

the framework as a scalable tool for resilience assessment, where diverse multi-hazard scenarios can be represented efficiently within a unified fragility modeling architecture.

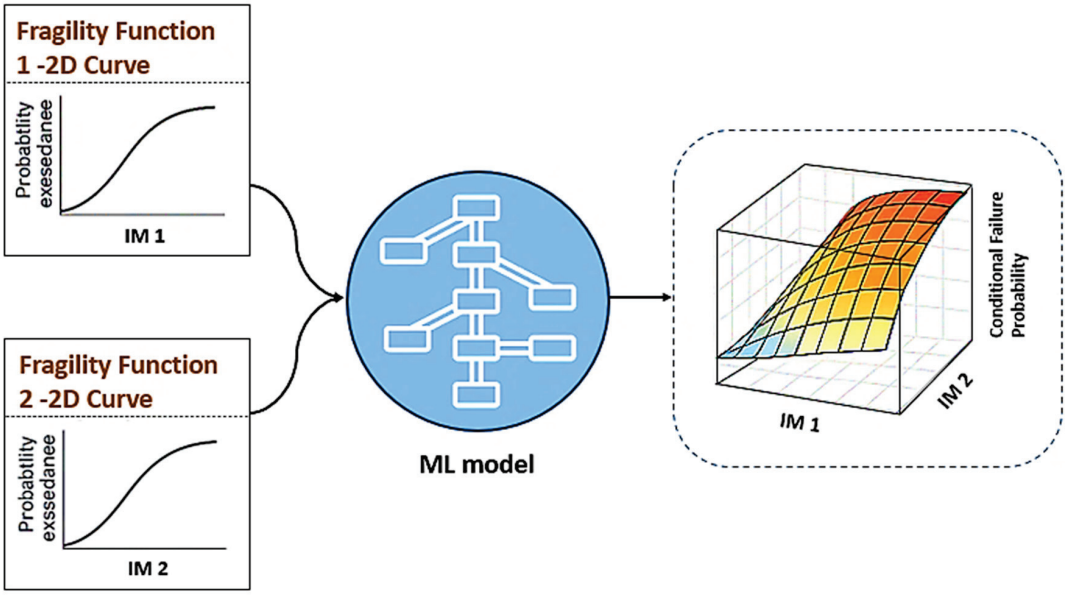

Figure 6. Schematic illustration of the EQ–TS-based ML framework for synthesizing two 2D fragility functions (earthquake and fire) into a multi-hazard fragility surface for fire-following-earthquake scenarios (after [78]).

6. Numerical Illustrations

The structure used as an illustrative example is a three-story steel moment-resisting frame representative of a generic office-type building located in a high seismic region of the western United States. The frame is modeled in a two-dimensional (2D) configuration and is adapted from the OpenSeesPy [79] example library. As shown in Figure 7, the frame consists of three bays in the horizontal direction, with each story height set at 3.05 m (10 ft). The bay widths vary along the transverse direction—5.3 m, 2.54 m, and 5.3 m—resulting in an overall building width of approximately 13.2 m (43.3 ft). The span length in the longitudinal direction is 4.9 m (16 ft). For stories not exposed to fire, rigid beam–column end connections are enforced using equal degrees-of-freedom constraints to realistically capture joint behavior. In this case study, only the first story is subjected to fire exposure, while the upper stories remain unheated, consistent with the worst-case fire scenario identified in prior studies [21,23,45,64,65]. However, this uniform heating assumption does not capture localized phenomena such as flame spread or ventilation-controlled burning. In realistic post-earthquake scenarios, partition wall damage can drastically alter ventilation conditions, potentially intensifying fire severity in certain compartments. Therefore, while the adopted modified ISO-834 curve provides computational efficiency and a consistent benchmark, it may underestimate localized thermal effects under realistic ventilation changes, which should be investigated in future studies.

Structural members are modeled using nonlinear displacement-based beam–column elements (described in Section 3) with fiber discretization of W-sections. Columns are modeled with W10 sections, while beams are modeled with W8 sections, with section properties (depth, flange, and web dimensions) corresponding to typical wide-flange members. The fiber-based formulation enables the model to capture both material inelasticity and geometric nonlinearity under combined seismic and fire demands.

This section presents the numerical results obtained by applying the developed framework to the illustrative example building. The simulations capture the interaction between earthquake-induced damage and subsequent fire demands in a probabilistic manner, yielding fire-following-earthquake fragility surfaces. These results provide a basis for evaluating the multi-hazard performance of low-rise MRF systems and serve as the benchmark for assessing the predictive capability of the machine learning framework.

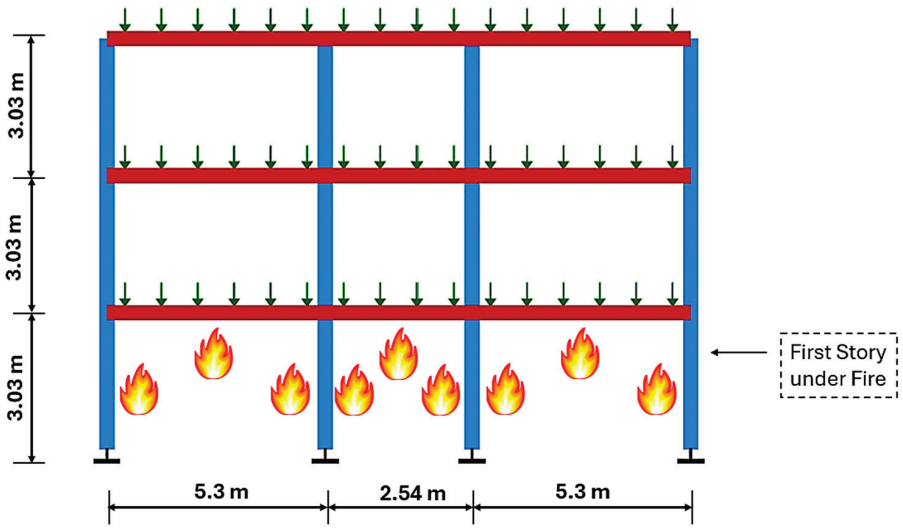

Figure 7. Schematic representation of the three-story steel moment-resisting frame used in the case study (sourced from OpenSeesPy (2025) [79] example library), showing beam–column configuration and applied gravity loads at each floor level.

Figure 8 shows the FFE fragility surface developed through the direct simulation methodology for the case study building. The black points represent simulated failure probabilities, while the fitted colored surface illustrates a continuous probabilistic representation of collapse likelihood as a function of earthquake intensity $Sa(T_1)$ and fire load. The agreement between the data points and the fitted surface demonstrates the ability of the successive nonlinear dynamic and thermal analyses to capture joint hazard effects and extend conventional single-hazard fragilities into a unified multi-hazard framework.

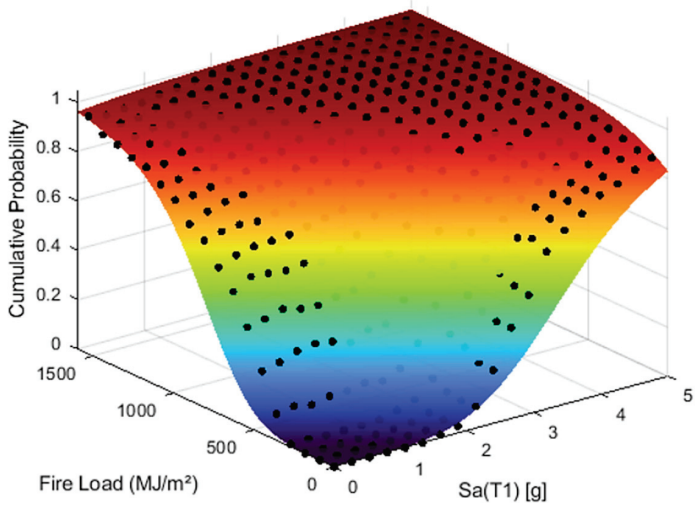

Figure 8. Fire-following-earthquake fragility surface showing cumulative collapse probability as a function of earthquake intensity and fire load; black dots denote simulation data points.

The boundaries of the surface yield conventional two-dimensional fragility curves for the earthquake-only and fire-only cases, demonstrating that the proposed sequential simulation framework naturally extends traditional single-hazard fragilities into a unified multi-hazard representation. These findings highlight the capability of the proposed approach to capture both single-hazard performance and the compounding effects of sequential earthquake–fire loading within a unified probabilistic framework. Importantly, the fragility functions and surfaces provide actionable insights for resilience planning and retrofitting strategies, enabling engineers and decision-makers to better evaluate building performance and prioritize mitigation under cascading hazards.

Figure 9 presents the results of the fragility analysis for the case study buildings under single- and multi-hazard conditions. The earthquake-only fragility curve in Figure 9a shows a median capacity of $\theta = 3.63$ g with $\beta = 0.344$, while the fire-only curve in Figure 9b yields a median capacity of $\theta = 861.2$ MJ/m^2 with $\beta = 0.350$. Both lognormal fits demonstrate excellent agreement with the simulation data, confirming the robustness of the direct analysis approach. Figure 9c illustrates the ML-generated FFE fragility surface, which transitions smoothly between the earthquake-only and fire-only boundaries and quantifies the probability of exceedance across the full range of joint hazard intensities. The two-dimensional fragility curves and their associated information were extracted from the boundaries of the directly simulated FFE fragility surface shown in Figure 8, and these serve as the input for the ML framework introduced earlier in this paper (Section 5). Using only these boundary fragilities, the ML methodology synthesizes the full FFE fragility surface shown in Figure 9c, which shows excellent consistency with the directly simulated surface.

Figure 10 compares the contour representations of the FFE fragility surface, $P(DS \mid IM_{EQ}, IM_{Fire})$ points, generated from direct successive simulations and the ML-based framework. Figure 10a shows the contour view of the surface obtained through direct analysis, where collapse probability increases smoothly with both earthquake intensity and fire load, and the white contour lines mark probability levels from 0.1 to 0.9. Figure 10b illustrates the contour view of the surface produced by the ML framework using only the boundary fragility curves as input.

As can be seen in Figure 10, the ML-generated surface replicates the key features of the directly simulated surface with high fidelity, including the slope of the probability gradients and the overall shape of the iso-probability contours. This close agreement confirms the capability of the ML approach to synthesize multi-hazard fragility surfaces without requiring extensive successive simulations and even a re-training process, offering substantial computational savings while maintaining accuracy. The ML method provides significant computational savings compared to direct numerical simulation, while maintaining strong agreement with the OpenSees-based reference surfaces. In quantitative terms, the ML-based synthesis required only a few seconds per fragility surface generation on a standard workstation, whereas the full OpenSees-based successive simulation demanded several days of high-performance computing, representing a computational reduction of roughly three orders of magnitude.

Figure 11 illustrates the difference surface between the ML-based and direct-simulation fragility surfaces, expressed in percentage terms. The contour lines at -1%, 0%, and +1% identify regions of underprediction (blue) and overprediction (red) by the ML framework relative to the benchmark direct-simulation surface. The results indicate that discrepancies remain small across the entire hazard space, generally within $\pm 1\%$. Localized areas of deviation appear at higher fire load levels combined with moderate seismic intensities, where the ML framework tends to slightly underpredict collapse probabilities. Conversely, minor overprediction is observed at lower fire loads and larger spectral accelerations. Despite these localized differences, the overall agreement is strong, demonstrating that the ML-based framework is

able to replicate the direct-simulation surface with high fidelity. Importantly, the ML model achieves this level of accuracy while reducing computational demands significantly, highlighting its suitability for large-scale community-level applications where thousands of hazard scenarios must be evaluated.

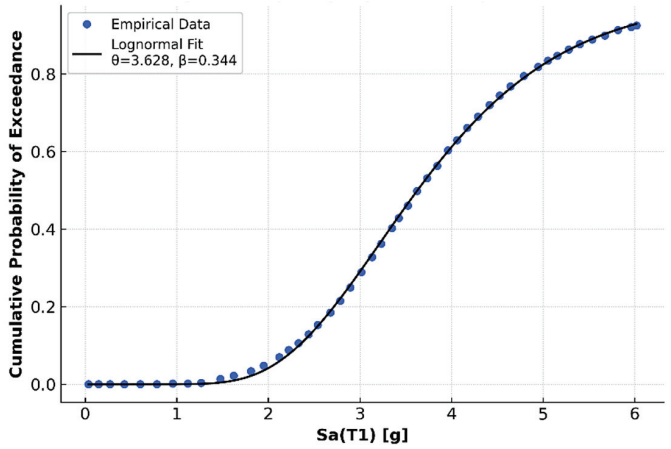

(**a**)

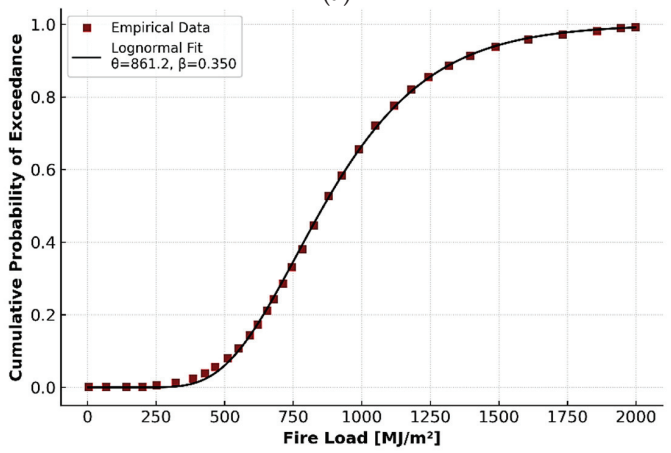

(**b**)

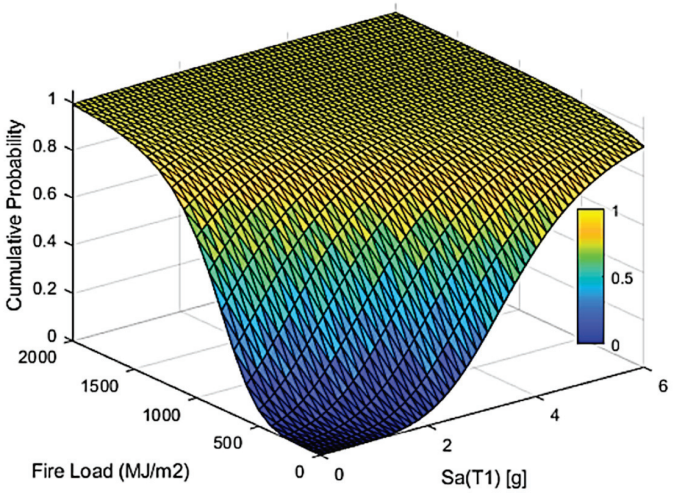

(**c**)

Figure 9. ML-based FFE surface development: (**a**) earthquake-only fragility curve, (**b**) fire-only fragility curve, and (**c**) ML-generated FFE fragility surface showing joint hazard effects.

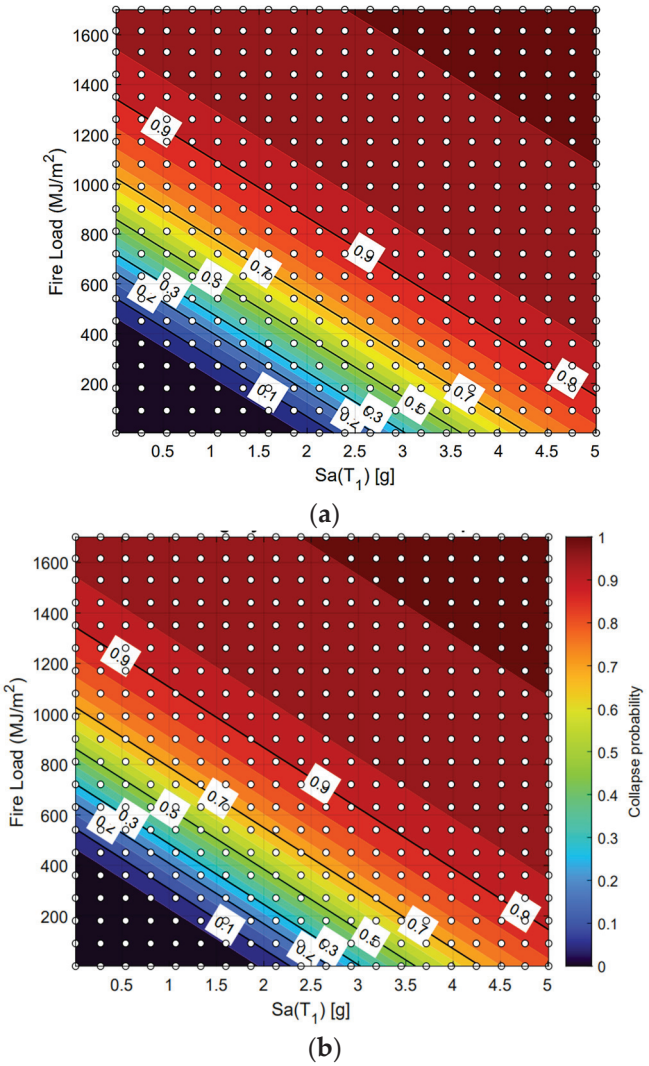

Figure 10. Contour representation of the FFE fragility surface based on different methods: (**a**) direct successive simulation; (**b**) ML-based framework.

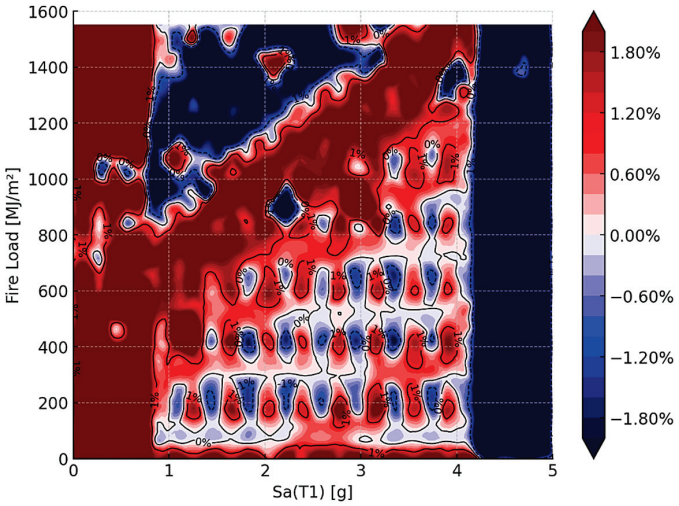

Figure 11. Difference surface between ML-based and direct-simulation fragility surfaces, shown as percentages with contours at −1%, 0%, and +1%.

Figure 12 presents a comparison between the ML-predicted fragility values and those obtained from direct simulations ($P(DS \mid IM_{EQ}, IM_{Fire})$ data points), based on 4000 points sampled from the fitted fragility surface. Each point represents a joint hazard intensity pair of earthquake and fire load, allowing evaluation of model performance across the full multi-hazard domain. The close alignment of the points with the fitted line indicates that the ML framework successfully captures the underlying simulation-based fragility relationships, providing an efficient surrogate for computationally intensive direct analyses. The results demonstrate consistently high predictive accuracy across all cases of joint hazard (IM) values, with R^2 values exceeding 0.959 and Root Mean Square Error (RMSE) values remaining below 0.018. Mean Absolute Error (MAE) values also remain low, typically within 0.007–0.011, indicating minimal average error across the fragility domain.

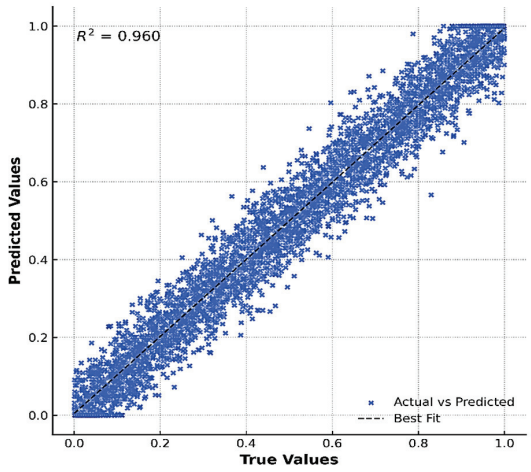

Figure 12. Predicted values from the ML model versus corresponding values from direct simulations for 4000 data points, showing strong agreement with the fitted line.

Numerical illustrations confirm that the developed framework reliably captures the cascading effects of earthquake and fire in a unified fragility representation for the case study building. The directly simulated FFE surfaces provide a robust benchmark for evaluating hazard interaction, while the machine learning framework demonstrates its ability to reproduce these results with high fidelity and significantly reduced computational demand. In this way, an FFE fragility surface can be constructed using available two-dimensional fragility curves for earthquake-only and fire-only hazards, enabling the use of the rich and well-established fragility or vulnerability functions already available for individual hazards in the literature. Together, the two approaches highlight a practical pathway for integrating simulation-based rigor with ML-driven efficiency, offering scalable, probabilistically consistent tools for structural performance assessment and resilience-oriented decision making under multi-hazard scenarios.

7. Summary and Conclusions

This study presented an integrated framework combining high-fidelity simulation and machine learning to generate fire-following-earthquake fragility surfaces for a steel moment-resisting frame. The proposed ML approach accurately reproduced the coupled hazard response predicted by nonlinear OpenSees analyses while reducing computational demand by several orders of magnitude. The framework demonstrates strong adaptability across multi-hazard sequences and provides a foundation for future extensions to other hazard pairings and structural systems.

The methodology was benchmarked against a machine learning synthesis framework originally developed for earthquake–tsunami sequences and extended here to earthquake–fire hazards. This framework, previously validated for mainshock–aftershock sequences, demonstrates robustness across different types of sequential hazards. Numerical results for a three-story steel MRF showed excellent agreement between simulated and ML-synthesized fragility surfaces, with a coefficient of determination (R^2) exceeding 0.95 and a root mean square error (RMSE) below 0.02 across all damage states. These results confirm not only the computational efficiency and predictive accuracy of the ML framework but also its apparent hazard-neutrality, as the same architecture can be effectively applied across diverse hazard pairings—earthquake–tsunami, mainshock–aftershock, and fire-following-earthquake—without retraining.

Beyond methodological development, the results of this study have direct implications for industry, federal agencies and research. For practicing engineers and consultants, the fragility surfaces generated through this framework can provide insights for performance-based design and retrofit decisions, especially for structures exposed to compound hazards. For policymakers and decision-makers, the ability to capture uncertainty and cascading effects within a unified fragility representation provides a powerful tool for risk assessment, emergency planning, and resilience-based policy development. In the research domain, the framework offers a benchmark for validating new modeling approaches and serves as a foundation for expanding fragility methodologies to community-scale resilience studies. The integration with ML further opens opportunities for rapid hazard assessment tools that can be embedded in next-generation catastrophe risk models and infrastructure digital twins like IN-CORE platform.

Despite its contributions, the methodology presented in this study is subject to several limitations that should be acknowledged and addressed in future work. First, the fire hazard was represented using the ISO-834 standard curve with stochastic modifications, which, while computationally efficient, may not capture localized or ventilation-controlled fire dynamics; future studies could incorporate more physically based fire models. Second, the case study was limited to a three-story steel MRF, and extension to taller buildings, different structural typologies, and irregular geometries is needed to evaluate broader applicability. Although the present investigation focused on a single structural configuration and a representative fire scenario, the findings consistently support the proposed methodology, and broader validation across diverse building types and fire conditions will strengthen its generality. Third, uncertainties in thermal–mechanical material properties were treated in a simplified manner, and temperature-dependent degradation models could be expanded using experimental calibration. Finally, while the ML framework demonstrated strong hazard-neutral adaptability, its extrapolation to hazard pairings with fundamentally different fragility curve characteristics (e.g., abrupt slope changes or discontinuities) remains untested, referring to both hazard pairings and structural behaviors that yield fragility curves with abrupt slope changes or discontinuities due to highly nonlinear or threshold-type responses. Additionally, the ML framework's performance has not yet been validated for other sequential hazard pairings (e.g., wind–surge and flood–earthquake) or for irregular and high-rise structural configurations, which may exhibit distinct interaction mechanisms. Future work should explore these extensions to assess the model's generalizability across a broader range of structural and hazard conditions. Future research should explore these extensions to enhance the robustness, generality, and practical deployment of the methodology.

Author Contributions: Conceptualization, M.H. and J.W.v.d.L.; methodology, M.H. and J.W.v.d.L.; formal analysis, M.H.; investigation, M.H.; writing—original draft preparation, M.H.; writing—review and editing, J.W.v.d.L.; visualization, M.H.; supervision, J.W.v.d.L.; project administration, J.W.v.d.L.; funding acquisition, J.W.v.d.L. All authors have read and agreed to the published version of the manuscript.

Funding: This research was funded by the U.S. National Institute of Standards and Technology (NIST) through the Center for Risk-Based Community Resilience Planning, a NIST-funded Center of Excellence, under cooperative agreements with Colorado State University (Financial Assistance Award Numbers: 70NANB15H044 and 70NANB20H008).

Data Availability Statement: Some or all data, models, or code that support the findings of this study are available from the corresponding author upon reasonable request.

Acknowledgments: The Center for Risk-Based Community Resilience Planning is a NIST-funded Center of Excellence; the Center is funded through a cooperative agreement between the U.S. National Institute of Standards and Technology and Colorado State University (NIST Financial Assistance Award Numbers: 70NANB15H044 and 70NANB20H008). The views expressed are those of the presenter and may not represent the official position of the National Institute of Standards and Technology or the U.S. Department of Commerce.

Conflicts of Interest: Author Mojtaba Harati was employed by the company Verisk Extreme Event Solutions. The research presented here did not use any proprietary data, models, or knowledge from Verisk. The remaining authors declare that the research was conducted in the absence of any commercial or financial relationships that could be construed as a potential conflict of interest.

References

1. Scawthorn, C. Fire Following Earthquake. *Fire Saf. Sci.* **1986**, *1*, 971–979. [CrossRef]
2. Scawthorn, C.; O'Rourke, T.D.; Blackburn, F.T. The 1906 San Francisco Earthquake and Fire—Enduring Lessons for Fire Protection and Water Supply. *Earthq. Spectra* **2006**, *22*, 135–158. [CrossRef]
3. Okazaki, T. *Impact of Natural Disasters on Industrial Agglomeration: The Case of the 1923 Great Kanto Earthquake*; Center for Research in Economics and Statistics (CIRJE): Tokyo, Japan, 2011.
4. Scawthorn, C.; Nishino, T.; Schencking, J.C.; Borland, J. Kantō Daikasai: The Great Kantō Fire Following the 1923 Earthquake. *Bull. Seism. Soc. Am.* **2023**, *113*, 1902–1923. [CrossRef]
5. Schencking, J.C. The Great Kanto Earthquake of 1923 and the Japanese Nation. *Educ. About Asia* **2007**, *12*, 14–22.
6. Namba, Y.; Yasuno, K.; Nishitani, T. Fire Spread Of Urban Area At The Kobe Earthquake. *Fire Saf. Sci.* **1997**, *5*, 959–970. [CrossRef]
7. Domingo, N.; Luo, H. Canterbury earthquake construction and demolition waste management: Issues and improvement suggestions. *Int. J. Disaster Risk Reduct.* **2017**, *22*, 130–138. [CrossRef]
8. Elhami Khorasani, N.; Garlock, M.E.M. Overview of fire following earthquake: Historical events and community responses. *Int. J. Disaster Resil. Built Environ.* **2017**, *8*, 158–174. [CrossRef]
9. Tian, Y.; Lu, M.; Xu, Z.; Ren, J. A fire following earthquake spread model considering building height and its application to real-world events. *Int. J. Disaster Risk Reduct.* **2025**, *118*, 105261. [CrossRef]
10. Zamanialaei, M.; Martin, D.S.; Theodori, M.; Purnomo, D.M.J.; Tohidi, A.; Lautenberger, C.; Qin, Y.; Trouvé, A.; Gollner, M. Fire risk to structures in California's Wildland-Urban Interface. *Nat. Commun.* **2025**, *16*, 8041. [CrossRef] [PubMed]
11. Smith, A.B. *U.S. Billion-Dollar Weather and Climate Disasters, 1980–Present (NCEI Accession 0209268)*; National Centers for Environmental Information (NCEI)/NOAA: Asheville, NC, USA, 2020; Available online: https://doi.org/10.25921/STKW-7W73 (accessed on 30 November 2022).
12. Suwondo, R.; Gillie, M.; Cunningham, L.; Bailey, C. Effect of earthquake damage on the behaviour of composite steel frames in fire. *Adv. Struct. Eng.* **2018**, *21*, 2589–2604. [CrossRef]
13. ASCE. *ASCE 7 Standard*; American Society of Civil Engineers: Reston, VA, USA, 2022; Available online: https://www.asce.org/publications-and-news/asce-7 (accessed on 30 November 2022).
14. CEN. *Eurocode 8: Design of Structures for Earthquake Resistance—Part 2: Bridges (prEN 1998-2:2023)*; European Committee for Standardization: Brussels, Belgium, 2023.
15. CEN. *BS EN 1993-1-2:2005—Eurocode 3: Design of Steel Structures. General Rules. Structural Fire Design (British Standard)*; British Standards Institution: London, UK, 2005; Available online: https://webstore.ansi.org/standards/bsi/bsen19932005-1326476?

gad_source=1&gad_campaignid=1041630452&gbraid=0AAAAAD_gXFWkPdY22xJDOBpmcERC6kHIe&gclid=Cj0KCQjwzt_FBhCEARIsAJGFWVkRQfjtL6ptSEPsSNdlWf3IWO0_NQ8fxkoBIKVaF-BxVgabJCHyKJAaAgpWEALw_wcB (accessed on 3 September 2025).
16. CEN. *Eurocode 1: Actions on Structures—Part 1–2: General Actions—Actions on Structures Exposed to Fire (EN 1991-1-2)*; European Committee for Standardization: Brussels, Belgium, 2002.
17. FEMA. *Seismic Performance Assessment of Buildings, Volume 1—Methodology (FEMA P-58)*; Federal Emergency Management Agency: Washington, DC, USA, 2012.
18. FEMA. *FEMA P-695: Quantification of Building Seismic Performance Factors*; Applied Technology Council: Redwood City, CA, USA, 2009; Available online: https://store.atcouncil.org/index.php?dispatch=products.view&product_id=210 (accessed on 30 November 2009).
19. FEMA. *FEMA P-646: Guidelines for Design of Structures for Vertical Evacuation from Tsunamis*, 3rd ed.; Whole Building Design Guide: Washington, DC, USA, 2019; Available online: https://www.wbdg.org/FFC/DHS/femap646.pdf (accessed on 30 November 2022).
20. Lou, T.; Wang, W.; Izzuddin, B.A. A framework for performance-based assessment in post-earthquake fire: Methodology and case study. *Eng. Struct.* **2023**, *294*, 116766. [CrossRef]
21. Memari, M.; Mahmoud, H. Framework for a performance-based analysis of fires following earthquakes. *Eng. Struct.* **2018**, *171*, 794–805. [CrossRef]
22. Covi, P.; Tondini, N.; Sarreshtehdari, A.; Elhami-Khorasani, N. Development of a novel fire following earthquake probabilistic framework applied to a steel braced frame. *Struct. Saf.* **2023**, *105*, 102377. [CrossRef]
23. Qin, C.; Mahmoud, H. Collapse performance of composite steel frames under fire. *Eng. Struct.* **2019**, *183*, 662–676. [CrossRef]
24. Quayyum, S.; Hassan, T. Seismic Performance of a Fire-Exposed Moment-Resisting Frame. *J. Struct. Eng.* **2018**, *144*, 04018206. [CrossRef]
25. Risco, G.V.; Zania, V.; Giuliani, L. Numerical assessment of post-earthquake fire response of steel buildings. *Saf. Sci.* **2023**, *157*, 105921. [CrossRef]
26. Yassin, M.H.; Bagchi, A.; Kodur, V.K.R. *Performance of Steel Moment Resisting Frame Buildings Subjected to Post-Earthquake Fire Exposure*; EERI: Oakland, CA, USA, 2010.
27. Covi, P.; Tondini, N.; Korzen, M.; Tsionis, G. Numerical-experimental analysis of a braced steel frame subjected to fire following earthquake. *Ce/Papers* **2021**, *4*, 1304–1310. [CrossRef]
28. Dwaikat, M.M.S.; Kodur, V.K.R.; Quiel, S.E.; Garlock, M.E.M. Experimental behavior of steel beam–columns subjected to fire-induced thermal gradients. *J. Constr. Steel Res.* **2011**, *67*, 30–38. [CrossRef]
29. Patringenaru. UC San Diego Conducts First-of-Its-Kind Seismic Testing on 6-Story Building | University of California. 2016. Available online: https://www.universityofcalifornia.edu/news/uc-san-diego-conducts-first-its-kind-seismic-testing-6-story-building (accessed on 3 September 2025).
30. Sherif, M.A. Multi-Hazard Fire Vulnerability Assessment and Resilience Quantification. Ph.D. Thesis, University of Hawai'i at Mānoa, Honolulu, HI, USA, 2025.
31. Tao, Y.; Xu, Z.D.; Dong, Y.R.; Dai, J.; Wei, Y.; Liu, X.Y.; Huang, X.H. Hybrid simulation testing and energy framework for performance-based assessment of structures under earthquake-fire sequential hazards. *J. Build. Eng.* **2025**, *106*, 112614. [CrossRef]
32. Harati, M.; van de Lindt, J.W. Data-driven machine learning for multi-hazard fragility surfaces in seismic resilience analysis. *Comput. Civ. Infrastruct. Eng.* **2024**, *40*, 698–720. [CrossRef]
33. Harati, M.; van de Lindt, J.W. Mainshock-aftershock building fragility methodology for community resilience modeling. *Structures* **2024**, *70*, 107742. [CrossRef]
34. Covi, P.; Tondini, N.; Sarreshtehdari, A.; Elhami-Khorasani, N. Fires Following Earthquake Fragility Functions for Protected Steel Braced Frames. *Fire Technol.* **2024**, *60*, 2815–2844. [CrossRef]
35. Gernay, T.; Khorasani, N.E.; Garlock, M. Fire Fragility Functions for Steel Frame Buildings: Sensitivity Analysis and Reliability Framework. *Fire Technol.* **2019**, *55*, 1175–1210. [CrossRef]
36. Gernay, T.; Elhami Khorasani, N.; Garlock, M. Fire fragility curves for steel buildings in a community context: A methodology. *Eng. Struct.* **2016**, *113*, 259–276. [CrossRef]
37. Carlton, A. Performance-Based Engineering Framework for Earthquake and Fire Following Earthquake. Master's Thesis, Michigan Technological University, Houghton, MI, USA, 2013. [CrossRef]
38. Lange, D.; Devaney, S.; Usmani, A. An application of the PEER performance based earthquake engineering framework to structures in fire. *Eng. Struct.* **2014**, *66*, 100–115. [CrossRef]
39. Mahmoud, H.; Chulahwat, A. Assessing wildland–urban interface fire risk. *R. Soc. Open Sci.* **2020**, *7*, 201183. [CrossRef]

40. Baker, J.W. Efficient Analytical Fragility Function Fitting Using Dynamic Structural Analysis. *Earthq. Spectra* **2015**, *31*, 579–599. [CrossRef]
41. Harati Mojtaba van de Lindt John, W. Fragility Function Development of RC Building Portfolio for Use in Earthquake-Tsunami Community Resilience Studies. *J. Perform. Constr. Facil.* **2024**, *39*, 04025019.
42. FEMA. *Hazus Earthquake Model Technical Manual*; Federal Emergency Management Agency: Washington, DC, USA, 2020.
43. McKenna, F. OpenSees: A Framework for Earthquake Engineering Simulation. *Comput. Sci. Eng.* **2011**, *13*, 58–66. [CrossRef]
44. Zhu, M. *OpenSeesPy Documentation, Version 3.5.1.3*; Software Documentation; Oregon State University: Corvallis, OR, USA, 2021.
45. Saed, G.; Tait, M.J.; Balomenos, G.P. Post-earthquake fire analysis of a low-rise steel frame in OpenSees using a hybrid model. *Structures* **2025**, *79*, 109658. [CrossRef]
46. Harati, M.; van de Lindt, J.W. Methodology to generate earthquake-tsunami fragility surfaces for community resilience modeling. *Eng. Struct.* **2024**, *305*, 117700. [CrossRef]
47. Mashayekhi, M.; Harati, M.; Estekanchi, H.E. Estimating the duration effects in structural responses by a new energy-cycle based parameter. *arXiv* **2019**, arXiv:1905.01737. International Institute of Earthquake Engineering and Seismology, Tehran, Iran.
48. Elhami Khorasani, N.; Gernay, T.; Garlock, M. Data-driven probabilistic post-earthquake fire ignition model for a community. *Fire Saf. J.* **2017**, *94*, 33–44. [CrossRef]
49. Razdolsky, L. *Probability-Based Structural Fire Load*; Cambridge University Press: Cambridge, UK, 2014. [CrossRef]
50. Choe, L.; Zhang, C.; Luecke, W.E.; Gross, J.L.; Varma, A.H. Influence of Material Models on Predicting the Fire Behavior of Steel Columns. *Fire Technol.* **2017**, *53*, 375–400. [CrossRef]
51. Jiang, J.; Jiang, L.; Kotsovinos, P.; Zhang, J.; Usmani, A.; McKenna, F.; Li, G.Q. OpenSees Software Architecture for the Analysis of Structures in Fire. *J. Comput. Civ. Eng.* **2015**, *29*, 04014030. [CrossRef]
52. Zhou, M.; Cardoso, R.P.R.; Bahai, H. A new material model for thermo-mechanical analysis of steels in fire. *Int. J. Mech. Sci.* **2019**, *159*, 467–486. [CrossRef]
53. Khorasani, N.E.; Gardoni, P.; Garlock, M. Probabilistic Fire Analysis: Material Models and Evaluation of Steel Structural Members. *J. Struct. Eng.* **2015**, *141*, 04015050. [CrossRef]
54. Ibarra, L.F.; Medina, R.A.; Krawinkler, H. Hysteretic models that incorporate strength and stiffness deterioration. *Earthq. Eng. Struct. Dyn.* **2005**, *34*, 1489–1511. [CrossRef]
55. Lignos, D.G.; Krawinkler, H. Deterioration Modeling of Steel Components in Support of Collapse Prediction of Steel Moment Frames under Earthquake Loading. *J. Struct. Eng.* **2011**, *137*, 1291–1302. [CrossRef]
56. Haselton, C.B. Assessing Seismic Collapse Safety of Modern Reinforced Concrete Moment Frame Buildings. Ph.D. Thesis, Stanford University, Stanford, CA, USA, 2006.
57. Haselton, C.B.; Liel, A.B.; Deierlein, G.G.; Dean, B.S.; Chou, J.H. Seismic Collapse Safety of Reinforced Concrete Buildings. I: Assessment of Ductile Moment Frames. *J. Struct. Eng.* **2011**, *137*, 481–491. [CrossRef]
58. van de Lindt, H. Impact of Long-duration Earthquakes on Successive Earthquake-tsunami Fragilities for Reinforced Concrete Frame Archetypes. *J. Struct. Eng.* **2024**, *150*, 1–19.
59. Zhou, Y.; Chen, P.; Gong, S. Mechanical Model of a Hybrid Non-linear Viscoelastic Material Damping Device With Its Verifications. *Front. Mater.* **2019**, *6*, 33. [CrossRef]
60. Shinde, V.; Jha, J.; Tewari, A.; Miashra, S. Modified Rainflow Counting Algorithm for Fatigue Life Calculation. In Proceedings of the Fatigue Durability Fracture Mechanics; Seetharamu, S., Rao, K.B.S., Khare, R.W., Eds.; Springer: Singapore, 2018; pp. 381–387. [CrossRef]
61. Ramirez, J.D.M.; Tirca, L. Numerical Simulation and Design of Friction-Damped Steel Frame Structures. In Proceedings of the 15th World Conference on Earthquake Engineering (WCEE 2012), Lisbon, Portugal, 24–28 September 2012.
62. Jalayer, F.; Cornell, C.A. Alternative non-linear demand estimation methods for probability-based seismic assessments. *Earthq. Eng. Struct. Dyn.* **2009**, *38*, 951–972. [CrossRef]
63. Vamvatsikos, D.; Cornell, C.A. Incremental dynamic analysis. *Earthq. Eng. Struct. Dyn.* **2002**, *31*, 491–514. [CrossRef]
64. Fischer, E.C.; Varma, A.H.; Gordon, J.A. Performance-Based Structural Fire Engineering of Steel Building Structures: Traveling Fires. *Front. Built Environ.* **2022**, *8*, 907237. [CrossRef]
65. Jiang, L.; Usmani, A. Computational performance of beam-column elements in modelling structural members subjected to localised fire. *Eng. Struct.* **2018**, *156*, 490–502. [CrossRef]
66. Maddalozzo, W.; Fischer, E.C. Post-Earthquake Fire Performance of Steel-Frame Buildings. In Proceedings of the 17th World Conference on Earthquake Engineering (WCEE 2021), Sendai, Japan, 13–18 September 2020.
67. Sourav, S.; Srivastava, A.; Yadav, H.; Murugesan, K. Using OpenSees Software Analysis of Structure in Fire. *YMER* **2023**, *22*, 1170–1175.

68. Franssen, J. Improvement Of The Parametric Fire Of Eurocode 1 Based On Experimental Test Results. *Fire Saf. Sci.* **2000**, *6*, 927–938. [CrossRef]
69. Wickstrom, U.; Byström, A. Compartment fire temperature – a new simple calculation method. *Fire Saf. Sci.* **2014**, *11*, 289–301. [CrossRef]
70. Ellingwood, B. *Development of a Probability-Based Load Criterion for American National Standard A58*; National Bureau of Standards: Gaithersburg, MD, USA, 1980.
71. Porter, K.A.; Beck, J.L.; Shaikhutdinov, R.V. Sensitivity of Building Loss Estimates to Major Uncertain Variables. *Earthq. Spectra* **2002**, *18*, 719–743. [CrossRef]
72. Attary, N.; Van De Lindt, J.W.; Barbosa, A.R.; Cox, D.T.; Unnikrishnan, V.U. Performance-Based Tsunami Engineering for Risk Assessment of Structures Subjected to Multi-Hazards: Tsunami following Earthquake. *J. Earthq. Eng.* **2021**, *25*, 2065–2084. [CrossRef]
73. Mashayekhi, M.; Harati, M.; Darzi, A.; Estekanchi, H.E. Incorporation of strong motion duration in incremental-based seismic assessments. *Eng. Struct.* **2020**, *223*, 111144. [CrossRef]
74. Franchini, A.; Galasso, C.; Torero, J.L. Consequence-Oriented Fire Intensity Optimization for Structural Design under Uncertainty. *J. Struct. Eng.* **2024**, *150*, 04024020. [CrossRef]
75. Guanquan, C.; Jinhui, W. Study on probability distribution of fire scenarios in risk assessment to emergency evacuation. *Reliab. Eng. Syst. Saf.* **2012**, *99*, 24–32. [CrossRef]
76. Melinek, S.J. The distribution of fire load. *Fire Saf. J.* **1993**, *20*, 83–88. [CrossRef]
77. Thauvoye, C.; Zhao, B.; Klein, J.; Fontana, M. Fire Load Survey and Statistical Analysis. *Fire Saf. Sci.* **2008**, *9*, 991–1002. [CrossRef]
78. Harati, M.; van de Lindt, J. Mainshock-Aftershock Fragility Surfaces: A Machine Learning Approach Using Direct Successive Simulation. 2025; *preprint*. [CrossRef]
79. OpenSeesPy. *The OpenSeesPy Library, Version 3.5.1.3*; Software Documentation; Oregon State University: Corvallis, OR, USA, 2025; Available online: https://openseespydoc.readthedocs.io/en/latest/ (accessed on 8 September 2025).

Disclaimer/Publisher's Note: The statements, opinions and data contained in all publications are solely those of the individual author(s) and contributor(s) and not of MDPI and/or the editor(s). MDPI and/or the editor(s) disclaim responsibility for any injury to people or property resulting from any ideas, methods, instructions or products referred to in the content.

infrastructures

MDPI

Article

Leveraging Transformer Models for Seismic Fragility Assessment of Non-Engineered Masonry Structures in Malawi

Ehsan Harirchian [1,*] and Viviana Iris Novelli [2]

[1] Institute of Structural Mechanics (ISM), Bauhaus-Universität Weimar, 99423 Weimar, Germany
[2] School of Engineering, Cardiff University, Cardiff CF24 3AA, UK; novelliv@cardiff.ac.uk
* Correspondence: ehsan.harirchian@uni-weimar.de

Abstract: Assessing seismic vulnerability is a critical step in evaluating the resilience of existing buildings, and fragility curves are widely used to quantify the probability of damage under varying levels of seismic intensity. However, traditional methods for generating these curves often rely on generalized assumptions that may not accurately capture the seismic behavior of diverse building types within a region. This limitation is particularly evident for non-engineered masonry buildings, which typically lack standardized designs. Their irregular and informal construction makes them difficult to assess using conventional approaches. Transformer-based models, a type of machine learning (ML) technique, offer a promising alternative. These models can identify patterns and relationships in available data, making them well suited for developing seismic fragility curves with improved efficiency and accuracy. While transformers are relatively new to civil engineering, their application to seismic fragility assessment has been largely unexplored. This study presents a pioneering effort to apply transformer models for deriving fragility curves for non-engineered masonry buildings. A comprehensive dataset of 646 masonry buildings observed in Malawi is used to train the models. The transformers are trained to predict the probability of four damage states: Light Damage, Severe Damage, Near Collapse, and Collapse based on Peak Ground Acceleration (PGA). The performance of the transformer-based approach is compared with other ML methods, demonstrating its strong potential for more efficient and accurate seismic fragility assessment. Future work could adopt the proposed methodology and extend the approach by incorporating larger datasets, additional regional contexts, and alternative ML techniques to further enhance predictive performance.

Keywords: transformer; machine learning; seismic vulnerability; fragility curves; masonry structures

1. Introduction

Evaluating seismic vulnerability in non-engineered buildings is not only essential, but also particularly challenging, especially in seismically active developing regions where such buildings are widespread. Such buildings often lack formal engineering design and exhibit irregular construction practices, making it difficult to reliably assess their seismic performance using conventional methods. Fragility curves are a key tool in seismic risk assessment, offering probabilistic estimates that quantify the likelihood that a structure exceeds specific damage thresholds due to seismic forces [1]. These curves are widely used

in the assessment of seismic risk, the estimation of loss, and the formulation of policies for the reduction and management of disaster risk.

Extensive efforts have been made to compile databases of fragility curves for infrastructure and buildings worldwide, providing critical tools to assess seismic risk. Nirandjan et al. [2] conducted a systematic review, creating a centralized database of more than 1510 vulnerability and fragility curves for critical infrastructure, including energy, transport, water, waste, telecommunications, health, and education systems exposed to natural hazards. Rota et al. [3] derived fragility curves from 30 years of Italian post-earthquake survey data, processing over 91,000 building inspection records across 23 typologies. The Global Earthquake Model, through the *OpenQuake* platform (https://www.globalquakemodel.org/ (accessed on 16 April 2025)), has developed an online vulnerability database that integrates fragility, vulnerability, and damage-to-loss functions with quality rating systems [4]. Di Ludovico et al. [5] specifically addressed the vulnerability of school buildings, developing fragility curves for Italian reinforced concrete and masonry schools using 2037 records from the 2009 L'Aquila earthquake.

Collectively, these studies demonstrate the importance of standardized fragility data for infrastructure resilience planning. However, applying these methods to developing countries and non-engineered constructions remains a significant challenge. Non-engineered buildings often exhibit irregular geometry, heterogeneous materials, and lack standardized design, while empirical data on seismic performance are scarce. Ahmad et al. [6] developed analytical frameworks for low-strength reinforced concrete structures commonly found in developing countries, incorporating realistic material models and stochastic capacity parameters. Khalfan et al. [7] highlighted the near absence of fragility curves for non-engineered residential buildings due to limited post-earthquake damage records and ground motion data. Novelli et al. [8] addressed this gap by deriving fragility curves for 646 non-engineered masonry buildings in Malawi through structural surveys and laboratory tests, revealing substantially higher vulnerability than previously estimated from international datasets. Khalfan [9] similarly emphasized the need for region-specific fragility assessments for non-engineered and unreinforced masonry houses in Indonesia. These studies underscore the difficulty of generating reliable fragility curves for non-engineered constructions in data-scarce, high-risk regions. Dai et al. [10] developed fragility functions for reinforced concrete columns with different levels of corrosion, finding that increased corrosion reduced fragility medians and substantially raised exceedance probabilities, supporting seismic loss and resilience assessments of aging structures. Yu et al. [11] conducted a time-dependent seismic fragility analysis of aging reinforced concrete structures in coastal areas, accounting for varying distances from the coastline, and showed that closer proximity to the coast accelerates corrosion and significantly increases seismic vulnerability.

Although there are numerous scientifically grounded methods for vulnerability assessment and fragility curve derivation, they often require intricate computations, detailed structural modeling, and extensive field and laboratory data collection [12–16]. As a result, the application of these methods, particularly in low-resource environments, poses significant challenges, mainly due to the lack of reliable data.

To overcome these obstacles, this study introduces the use of machine learning (ML) models, especially transformer architectures, as innovative tools to streamline and automate the development of fragility curves. Using comprehensive data sets and leveraging previous modeling efforts, the proposed ML models aim to directly predict the parameters of the fragility curve based on the characteristics of the building and the seismic input. These models will incorporate critical variables, including geometry, material properties, building

typology, and failure modes, and will output either damage state probabilities or fragility curve parameters.

The integration of ML into fragility assessment offers advantages: reduced reliance on detailed structural modeling, faster evaluation of large stocks, and applicability in data-scarce regions [17–20]. By identifying complex patterns in the available data, ML models can predict structural responses and damage probabilities without fully detailed physical models, streamlining the assessment process while maintaining reliability.

This study proposes a robust ML-based framework for deriving seismic fragility curves for non-engineered buildings. The framework enables the estimation of damage probabilities across a range of damage states, from light damage to collapse, under varying seismic intensities. This research builds on data collected during the *PREPARE* project in Malawi. Previous work by the authors primarily evaluated the probability of building collapse using ML, highlighting the high vulnerability of non-engineered masonry buildings in data-scarce, high-risk regions. However, that study did not address the full spectrum of seismic damage. The current research extends this approach by systematically incorporating structural parameters from detailed field surveys, including both material and geometric characteristics that influence seismic performance, to develop fragility curves for multiple damage states. Features are pre-processed, encoded, and filtered for relevance to damage probabilities at different Peak Ground Acceleration (PGA) levels. Predictive ML models are then trained and rigorously evaluated for accuracy. The ultimate goal is to apply these models to estimate building damage probabilities under unobserved or hypothetical seismic scenarios, providing a data-driven, scalable, and efficient methodology for comprehensive seismic vulnerability assessment. This approach addresses the limitations of the previous Malawi-focused study and the broader challenges posed by limited empirical data in regions dominated by non-engineered construction.

Ultimately, this study establishes a scalable ML-based framework for fragility estimation in non-engineered buildings, contributing to disaster preparedness and resilience in seismic regions. The key objectives are to (i) compare ML models across four damage states, (ii) derive fragility curves that integrate building characteristics and seismic intensity without detailed simulations, and (iii) introduce transformer-based models for the first time in this context. The main contributions include demonstrating transformers' potential, providing a scalable data-driven framework, and extending prior ML studies to cover the full spectrum of seismic damage.

2. Soft Computing Approaches for Seismic Vulnerability and Fragility Modeling

Evaluating and monitoring the seismic behavior of buildings is crucial to improve their structural resilience and developing effective mitigation strategies. Traditional analytical and numerical methods, while accurate, are often time-intensive and computationally demanding [21]. This has sparked the interest of researchers in proposing various approaches, particularly those utilizing soft computing techniques, to streamline seismic risk and vulnerability assessments. The application of ML models, as one of the soft computing techniques in this context, offers a promising pathway for identifying damage patterns and predicting seismic performance of existing reinforced concrete, as well as non-engineered structures that lack adequate engineering and seismic, or even basic structural considerations.

ML models learn from historical data to make predictions or classifications, making them suitable for seismic vulnerability assessment [22]. The effectiveness and performance of ML models are significantly dependent on the quality and completeness of the input data, typically structured as predictor and response variables [23].

In the context of seismic assessment, predictor variables often include key building characteristics such as structural typology, material properties, geometry, and construction quality that significantly affect a structure's response to ground motion. These characteristics determine how a building behaves under different levels of seismic intensity and, consequently, its probability of reaching various damage states. Due to the high cost and complexity of detailed numerical simulations and field assessments, ML models are a viable alternative for tasks such as identifying vulnerability through the development of fragility curves for different damage states, predicting structural response, and supporting seismic risk assessment [17,24].

There are many recent studies that have demonstrated the application of ML in predicting structural responses and classifying damage in buildings and infrastructures [25–27]. The application of ML models has been employed to assess the vulnerability of RC elements such as shear walls, infilled frames, and beam–column joints, but also to optimize and analyze the fragility of masonry-infilled RC and steel frames [28,29]. In the context of ML-based approaches for the evaluation of damage to unreinforced masonry and non-engineered buildings, Chomacki et al. [30] used Bayesian belief networks to assess damage to masonry buildings affected by mining environments. Rezaie et al. [31] employed K-Nearest Neighbors (KNN) for the evaluation of damage in rubble stone masonry piers, and Siam et al. [32] developed a framework for the prediction of performance and classification of damage in reinforced masonry shear walls. Harirchian et al. [33] applied multiple ML techniques to non-engineered masonry buildings, with Random Forest achieving low errors (MAPE 17.674%; RMSE 0.0617). Kazemi et al. [34] employed Artificial Neural Networks and Extreme Gradient Boosting to model reinforced concrete structures, reducing computational effort while maintaining accuracy. Zain & Dackermann [35] demonstrated the applicability of ML to school buildings in high-intensity seismic zones. Transformer-based models, a recent advancement in deep learning, offer additional advantages for seismic fragility assessment due to their ability to capture long-range dependencies and complex nonlinear relationships. Chen et al. [36] introduced DamFormer, a Transformer-based architecture for multitemporal remote sensing damage assessment, while Y. Chen et al. [37] applied Transformer and Informer networks for post-earthquake structural damage prediction, outperforming recurrent and convolutional networks. Soleimani-Babakamali & Esteghamati [38] utilized encoder–decoder models to estimate seismic demand from pushover analyses, achieving an 84% R^2 accuracy and facilitating the rapid derivation of fragility functions for building inventories.

In addition to ML approaches, other soft computing techniques have been explored to assess seismic vulnerability and fragility not only in terms of damage patterns or levels at the individual building level, but also across broader building typologies, supporting risk analysis at the neighborhood or city scale. Other techniques, such as fuzzy logic [39–42] and multi-criteria decision-making frameworks [43–45] have shown promising results in handling the inherent uncertainties and complexities of seismic performance evaluation. These techniques are particularly effective in scenarios where precise data is limited or expert judgment plays a significant role. Their ability to model nonlinear relationships and incorporate qualitative factors makes them valuable tools in the broader context of seismic risk analysis.

Comprehensive ML-based studies that address both seismic response and damage prediction, particularly in terms of estimating the probability of different damage levels, remain limited, especially for non-engineered buildings. Existing applications often focus primarily on collapse scenarios, without accounting for the full range of damage states that may occur across different building typologies at specific levels of ground shaking, such as PGA. This gap is largely due to the limited integration of field data and experimental data, as well as the resource-intensive nature of numerical simulations required to model structural

performance across multiple damage thresholds for the development of fragility curves. As a result, fragility curves are frequently derived using simplified assumptions, such as treating buildings of the same typology as having uniform material properties and construction quality, adopting generic capacity curves instead of detailed models, or neglecting secondary structural and non-structural components. These assumptions reduce computational demands and compensate for data scarcity, but they inevitably limit the precision of predicted damage states and may oversimplify the diversity of real-world structural behavior.

3. Methodology and Data

The fragility curves represent the probability of reaching different building damage states: Light Damage (LD), Severe Damage (SD), Near Collapse (NC), and Collapse (C). For probabilistic assessment, LD and SD are treated as distinct damage states, while exceedance probabilities are reported for NC and C at 16%, 50%, and 84%, reflecting varying confidence levels in the likelihood of reaching or exceeding these states. These curves were derived using ML following the procedure outlined below:

- Feature Selection: Structural parameters influencing seismic response were identified from field survey data, collected during the *PREPARE* project;
- Data Pre-processing: Categorical and ordinal structural parameters (variables) were encoded numerically for ML compatibility;
- Parameter Filtering: Among these features, those with high relevance to collapse probability under different PGA levels were retained;
- Dataset Splitting: The data was divided into training and test sets to build and evaluate predictive models;
- Model Training: Selected ML algorithms were trained on the prepared dataset;
- Performance Assessment: Model accuracy was evaluated using appropriate metrics;
- Application: Trained models were used to estimate collapse probabilities under unknown seismic scenarios.

Figure 1 presents a general flowchart illustrating the process from data collection to result interpretation and the prediction of fragility curves in this study. The selection of the most suitable ML algorithm was carried out by training and testing various ML techniques using all features from the input datasets. In this study, a single model with multiple inputs and multiple outputs was employed. Accordingly, each ML model used 21 input features and predicted 8 outputs.

3.1. Input Parameter

The dataset utilized in this research is taken from information gathered and analyzed over a three-year span within the framework of the *PREPARE* project (https://www.bristol.ac.uk/engineering/research/international-development/natural-disasters/prepare-africa/ (accessed on 1 January 2024)). The *PREPARE* initiative aims to enhance seismic risk preparedness and resilience in East African nations, with particular emphasis on tailoring strategies to local construction practices. The data collection comprises 323 residential buildings, with two walls evaluated in each, resulting in a total of 646 walls that were inspected and assessed on-site. These assessments were conducted in various locations throughout Malawi, including Salima, Blantyre, Lifidzi, and Golomoti. Detailed data and their distributions have been presented in previous studies [33,46,47]. The dataset contains 21 observed characteristics for each individual wall surveyed within the buildings. These variables, as presented in Table 1, capture essential structural characteristics relevant to assessing seismic vulnerability. The parameters include the fundamental period of vibration of the building,

which is crucial for dynamic analysis. Information on the quality of wall connections on both the right and left sides is also provided, as they play a significant role in influencing overall structural performance. Further geometric attributes, such as wall height, length, and thickness, are documented, along with the cumulative area of wall openings, including doors and windows. These contribute to understanding the wall's capacity and potential weaknesses. Details on the construction materials are also part of the dataset, including the masonry type (e.g., unfired or fired bricks), the dimensions of the bricks (height and length), and the degree of overlap (staggering) between them. The type of mortar, distinguishing between concrete and mud, was also recorded due to its impact on strength and durability. The configuration of the surrounding structure is captured through measurements such as the length of adjacent perpendicular walls and the number of internal walls, both parallel and perpendicular to the examined wall, as well as relative to the rear side. These features offer insight into the building's layout and connectivity.

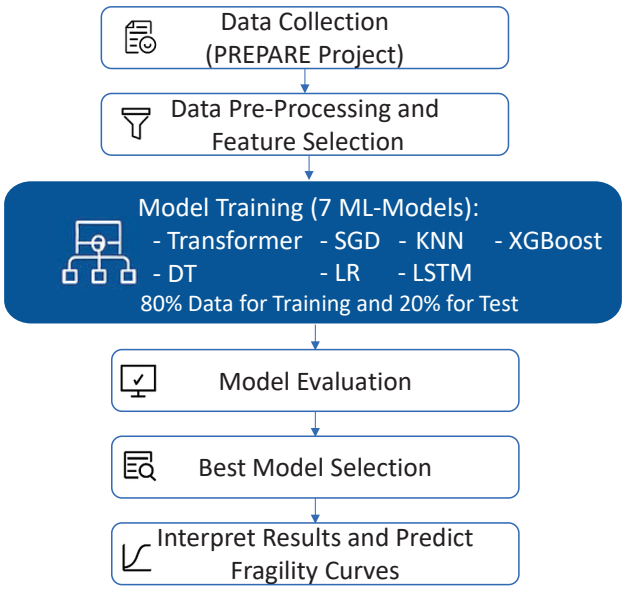

Figure 1. Overview of the workflow from data collection to fragility curve prediction.

Table 1. Feature descriptions with units or types.

No.	Description	Unit/Type
1	Structural fundamental period	s
2	Right wall connection quality	good/bad (categorical)
3	Left wall connection quality	good/bad (categorical)
4	Total area of openings (windows/doors)	m^2
5	Wall thickness	mm
6	Wall length	m
7	Wall height	m
8	Type of masonry used	fired/unfired (categorical)
9	Height of bricks	mm
10	Length of bricks	mm
11	Brick staggering (overlap)	mm
12	Type of mortar used	concrete/mud (categorical)
13	Length of wall perpendicular to inspected wall	m
14	No. of internal walls perpendicular to inspected wall	number
15	No. of internal walls parallel to inspected wall	number
16	No. of internal walls perpendicular to back & parallel to inspected wall	number
17	Type of roof	thatched/metallic (categorical)
18	Orientation of roof	parallel/orthogonal
19	Presence of gable	yes/no (binary)
20	Height of gable	m
21	Spandrel height	m

Roof characteristics were also surveyed, including the roofing material, orientation relative to the wall under investigation, and the presence and height of architectural elements like gables and spandrels. Together, these variables present a robust representation of the walls' material, geometric, and structural properties. The dataset serves as a foundation for applying data-driven approaches to model seismic fragility, using a methodology consistent with that established in previous studies [47].

In a previous study by Harirchian et al. [33], principal component analysis was applied to assess feature importance and ranking for the same dataset. In the current study, the focus is on comparing the predictive performance of different ML algorithms rather than feature selection. Additionally, the dataset has a moderate dimensionality and has been pre-processed well, which reduces multicollinearity and ensures that all features are informative. For these reasons, principal component analysis or other feature reduction techniques were not applied, as they fall beyond the scope of this study.

As part of a larger assessment of structural vulnerability, an experimental program was conducted to determine the mechanical characteristics of construction materials commonly used in the region, as documented in previous studies [48,49]. It includes collecting and testing representative samples from the buildings surveyed in the venue. By evaluating various properties of the material, including compressive strength and material consistency, the study aimed to gain a deeper understanding of how these materials impact the seismic performance of unreinforced structures.

3.2. Output Parameter

The information collected from field inspections and material testing formed the basis for generating static pushover (SPO) curves for a total of 646 individual walls. This approach extends the methodology originally introduced by D'Ayala [50], which models the structural response through simplified mechanical models. SPO analysis captures the inelastic behavior of each wall when subjected to increasing lateral loads, serving as a critical step in estimating the seismic demand and performance limits of buildings. These results led to the subsequent development of fragility curves that relate seismic intensity to the likelihood of damage in the observed buildings.

In this study, *SPO2IDA* [51] is used to transform SPO curves into Incremental Dynamic Analysis (IDA) curves. This transformation is based on a validated procedure in which the SPO curve, representing the structural capacity in terms of spectral acceleration versus displacement, is converted into an IDA backbone curve that reflects nonlinear response under a suite of ground motions. Specifically, three IDA curves are obtained, corresponding to the 16th, 50th, and 84th percentiles of the record-to-record variability, which captures the uncertainty in structural response (e.g., FEMA 1997). The spectral acceleration values derived for each limit state are subsequently converted to PGA using a scaling relationship based on the Boore et al. [52] ground motion prediction Equation. This approach ensures that PGA adequately captures the structural demand while remaining consistent with widely adopted practices for masonry buildings.

Novelli et al. [8,16] derived the fragility curves for Malawi that express the probability that a structure will reach or exceed specific damage states, such as light, severe, near collapse, and collapse, as a function of seismic intensity, typically measured in terms of PGA. In their study, they have proposed a structured, multi-step methodology to derive these curves, which serve as the outputs used in the present research:

1. Structural and Material Data Collection:
   Detailed surveys were conducted on 323 buildings (646 façades) to record their geometric characteristics, construction typologies, and other relevant structural attributes.

Simultaneously, laboratory tests were conducted to determine the mechanical properties of materials, including masonry units and mortar.

2. Failure Mode Identification: The Failure Mechanism Identification and Vulnerability Evaluation method (FaMIVE) [50,53] was employed to identify the governing failure modes for each façade. These included out-of-plane, in-plane, gable, and strip failures, determined based on the physical configuration and material characteristics of the structures.
3. Static Pushover (SPO) Modelling: Each façade was idealized as a single-degree-of-freedom (SDOF) system, and SPO curves were developed under three behavioral assumptions: (a) instability driven by geometry, (b) limited post-elastic deformation capacity, and (c) gradual strength degradation.
4. Incremental Dynamic Analysis (IDA): The SPO curves were transformed into IDA curves using the *SPO2IDA* method, allowing the modeling of dynamic structural response under increasing levels of seismic excitation.
5. PGA Derivation: Spectral acceleration values at various damage thresholds, obtained from IDA, were translated into corresponding PGA values using a suitable ground motion prediction equation.
6. Fragility Curve Construction: Finally, lognormal fragility functions were fitted to the PGA values associated with each damage state. For nonlinear behaviors (e.g., near collapse and collapse), variability due to different ground motion records was incorporated. In contrast, for more linear states (light and moderate damage), deterministic thresholds were applied across façades.

In this study, these fragility curves are leveraged as the basis for developing an ML-driven prediction framework. The proposed ML models aim to bypass the more complex intermediate steps, namely failure mode identification, SPO development, and IDA simulation, and instead learn direct relationships between input features (such as geometry, material strength, and building typology) and fragility parameters. The models are trained to estimate the median PGA (μ) and standard deviation (β) associated with each damage state, effectively condensing the conventional process into a more efficient pipeline that jumps from data collection (Step 1) directly to fragility estimation (Steps 5–6). This approach holds promise in significantly accelerating seismic risk assessments, particularly in regions where time, resources, and engineering expertise are limited.

3.3. Data Preparation

Effective data preparation is crucial for optimizing the performance of ML algorithms, as the quality and consistency of the data significantly impact the model's learning capabilities [54]. In this study, data pre-processing involved standardizing the features using the StandardScaler, which adjusts the data by centering it around the mean and scaling it to have unit variance. Subsequently, the data set was divided into two subsets: 80% of the data (516 samples) was used to train the model, while the remaining 20% (130 samples) were reserved for testing. The training data, which include known outputs, allows the model to learn patterns and fine-tune its parameters. The 20% test data are used to evaluate the performance of ML models on data that is new and unknown, which have not been seen during training.

4. Model Implementation and Validation

Seven ML models, including K-Nearest Neighbors (kNN), Linear Regression (LR), Stochastic Gradient Descent (SGD), Decision Tree (DT), Long Short-Term Memory (LSTM), Extreme Gradient Boosting (XGBoost), and Transformer architecture, have been employed in this study to predict fragility curves of buildings. The implementation was carried out

using Python 3.13.3, leveraging key libraries such as Scikit-learn 1.6.1, Pandas 2.3.1, NumPy 2.2.6, Matplotlib 3.10.3, Seaborn 0.13.2, and Torch 2.7 for data handling, visualization, and model development in a controlled virtual environment to ensure reproducibility. A concise introduction to each model is provided in the following section.

4.1. K-Nearest Neighbors (KNN)

KNN is a simple, instance-based learning algorithm that classifies data points based on the majority class of their nearest neighbors. It is non-parametric and effective for small datasets and can face difficulties with large datasets [55].

4.2. Linear Regression (LR)

LR is one of the simple yet powerful statistical methods for modeling the relationship between a dependent variable and one or more independent variables. It fits a straight line to the data by minimizing the difference between predicted and actual values. In addition to being easy to interpret and computationally efficient, LR only assumes a linear relationship and can struggle with complex, nonlinear patterns or outliers [56,57].

4.3. Stochastic Gradient Descent (SGD)

One of the efficient optimization algorithms used for large-scale linear classification and regression problems. It updates the model parameters iteratively based on a subset of the training data, offering fast convergence [58,59].

4.4. Decision Tree (DT)

A tree-structured model that splits data into subsets according to the feature values, making decisions through a series of if–else rules. It is intuitive, easy to interpret, and suitable for classification and regression tasks [60].

4.5. Long Short-Term Memory (LSTM)

A type of recurrent neural network designed to capture long-term dependencies in sequential data by using memory cells and gating mechanisms. It is widely applied in tasks such as time-series forecasting and natural language processing [61,62].

4.6. Extreme Gradient Boosting (XGBoost)

An efficient and scalable implementation of gradient boosting that builds an ensemble of decision trees. It is known for its high predictive accuracy, regularization techniques, and ability to handle large-scale structured data [63,64].

4.7. Transformer

The Transformer, well known for its significant impact in natural language processing, is applied in this study in a novel context to predict fragility curves of buildings. The significant ability of the Transformer to handle large and diverse input data makes it an ideal choice for this study, where traditional models may struggle to extract deep patterns from extensive structural parameters. Therefore, by implementing this powerful self-attention mechanism, the model effectively captures complex relationships in a multi-dimensional feature space and large-sized database [65,66].

It should be noted that the Transformer model is a high-capacity model and may overfit when trained on small datasets. To reduce the risk of overfitting in this context, the following measures were applied:

- Early Stopping: Training was monitored with patience of 10 epochs to prevent overtraining.

- Regularization: Weight decay (1×10^{-4}) was incorporated into the Adam optimizer to penalize large weights.
- Learning Curve Analysis: Training and validation losses were tracked across epochs, showing that the validation loss remained stable and did not diverge notably from the training loss.

4.8. Model Evaluation Metrics

It is vital to assess the performance of ML models in predicting fragility curves. Therefore, three commonly used regression metrics, including mean square error (MSE), root mean square error (RMSE), and mean absolute percentage error (MAPE) were employed.

- MSE: Measures the average of the squared differences between predicted and actual values; fewer values are better.
- RMSE: As the root of MSE, it gives an interpretable error metric in the same unit as the target variable.
- MAPE: Shows the prediction error as a percentage, making it easier to understand the accuracy of the model relative to the actual values.

These metrics offer a comprehensive view of each model's predictive accuracy and deviation from the true outcomes [67].

5. Results and Discussion

5.1. Correlation Between Input and Output Features

The correlation matrix, as shown in Figure 2, provides valuable and important information on the relationship between building features and the results of seismic fragility curves. It is worth noting that wall thickness and connection quality (Left Connection, Right Connection) exhibit strong positive correlations with most output variables, indicating their critical role in enhancing structural resistance during earthquakes. In contrast, the PGA exhibits a strong negative correlation with fragility thresholds, indicating that buildings with longer periods (typically more flexible) are more susceptible to seismic damage. Moderate correlations were observed for parameters such as the total opening area and the height of the story, suggesting that geometric characteristics also influence structural performance, albeit to a lesser extent. Features such as gable configuration and brick dimensions exhibit low or negligible correlations, suggesting a limited impact on fragility in this dataset. These findings help prioritize features for ML models and emphasize the importance of structural design and dynamic behavior in assessing seismic vulnerability.

Figure 3 shows the SHAP (SHapley Additive exPlanations) values, which illustrate the relative importance and directional impact of input features on the ML models used for predicting building fragility. The results indicate that the structural fundamental period is the most influential predictor, where higher values (shown in red) are associated with positive SHAP values, thus increasing the probability of higher damage states. Similarly, wall height, masonry type, and gable height contribute strongly to the model's output, confirming their critical role in seismic vulnerability. Features such as roof orientation, wall thickness, connection quality, and the total area of openings exhibit moderate influence, with their effects varying depending on whether the feature values are high or low. In contrast, brick dimensions, type of mortar, and roof type have minimal SHAP contributions, suggesting a limited role in driving fragility predictions. Overall, the analysis highlights that global structural and geometric parameters significantly influence the prediction process, while localized material properties have a secondary effect. This not only enhances the

interpretability of the ML model but also supports targeted seismic assessment and retrofitting strategies by identifying the features most responsible for shifts in fragility curves.

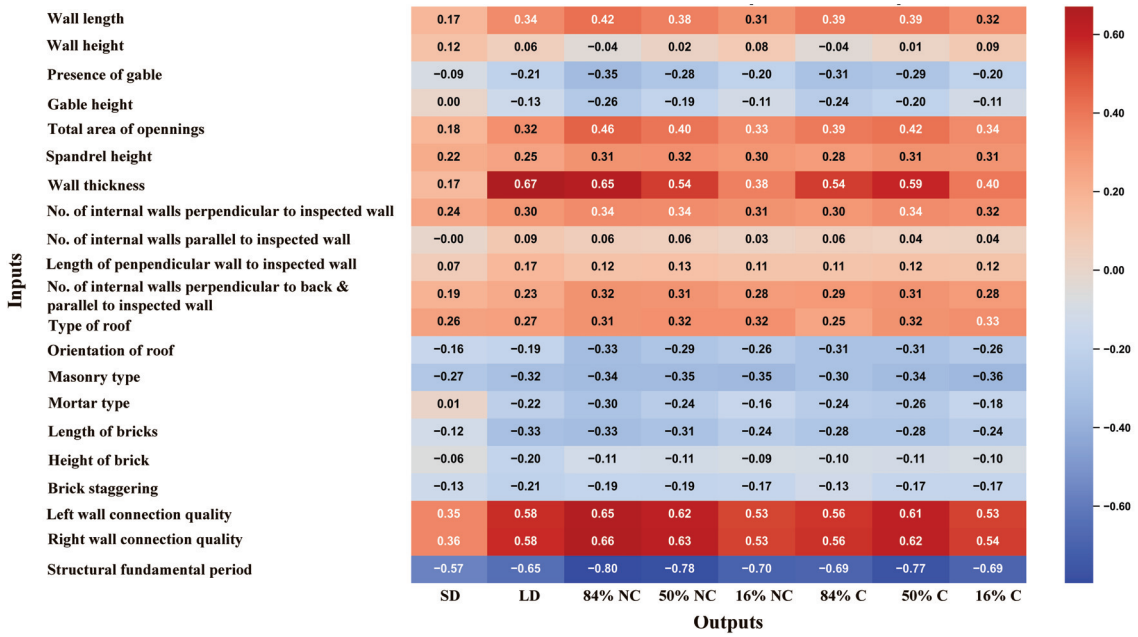

Figure 2. Correlation matrix of input features and output variables.

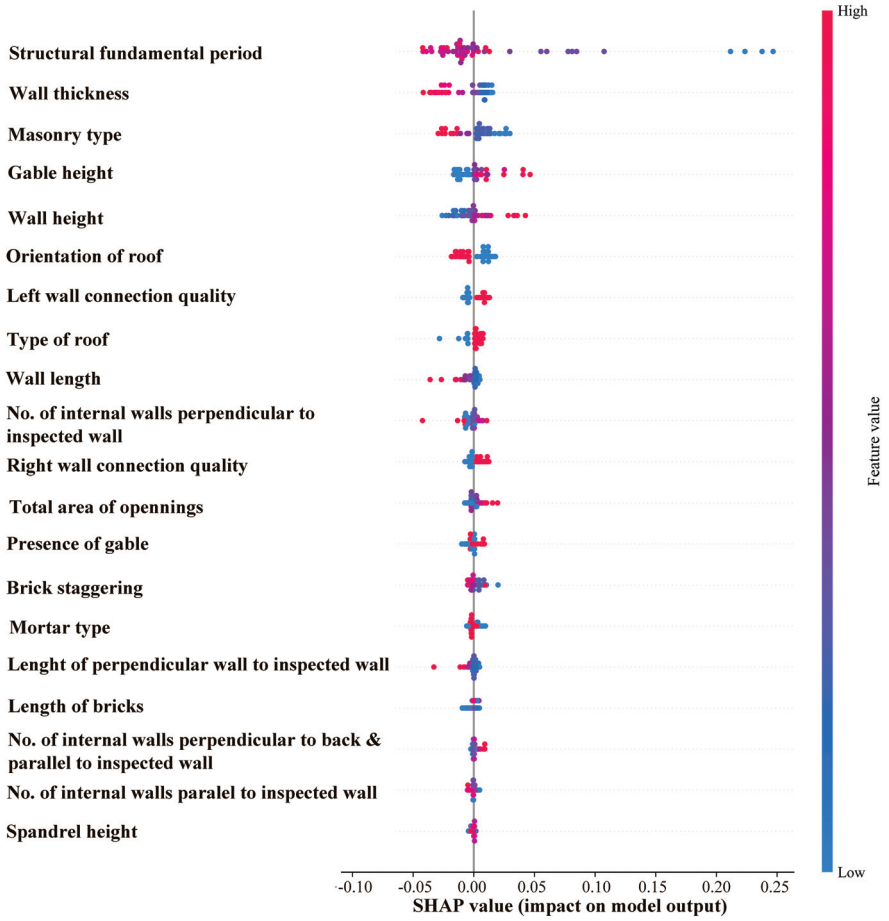

Figure 3. SHAP Analysis: Feature importance and directional impact on building fragility models.

5.2. Performance of ML Methods

The seven ML models, kNN, LR, SGD, DT, LSTM, XGBoost, and Transformer, were applied to the dataset, which includes field inspected buildings from Salima, Lifidzi, Golomoti, and Blantyre in Malawi.

Since the primary focus of this study is on the Transformer model, and to avoid excessive visual content, only the figures for its test data predictions are shown. However, model evaluation metrics for all ML models are presented and discussed to support the analysis. Figures 4–11 present the comparison between actual and predicted PGA (g) values in various damage states for test data using the Transformer model. The results indicate that all models demonstrated strong predictive performance, with predictions closely aligned with the observed values. To avoid an excessive number of figures for the training and testing results of different models across each damage state, the corresponding figures for each model are provided in Appendix A (Figures A1–A13).

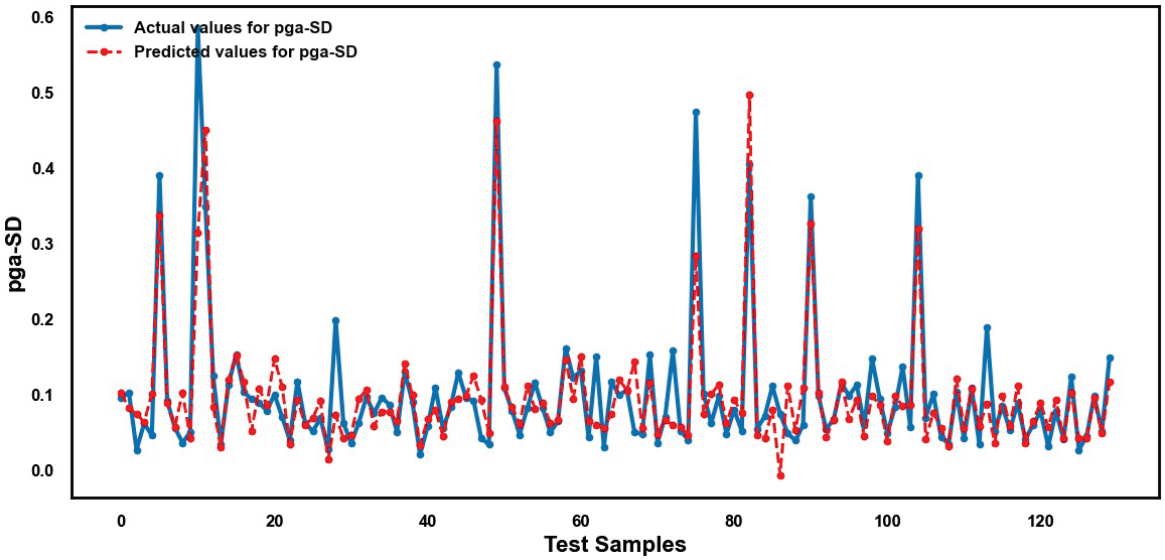

Figure 4. Actual and predicted values by Transformer for PGA-SD.

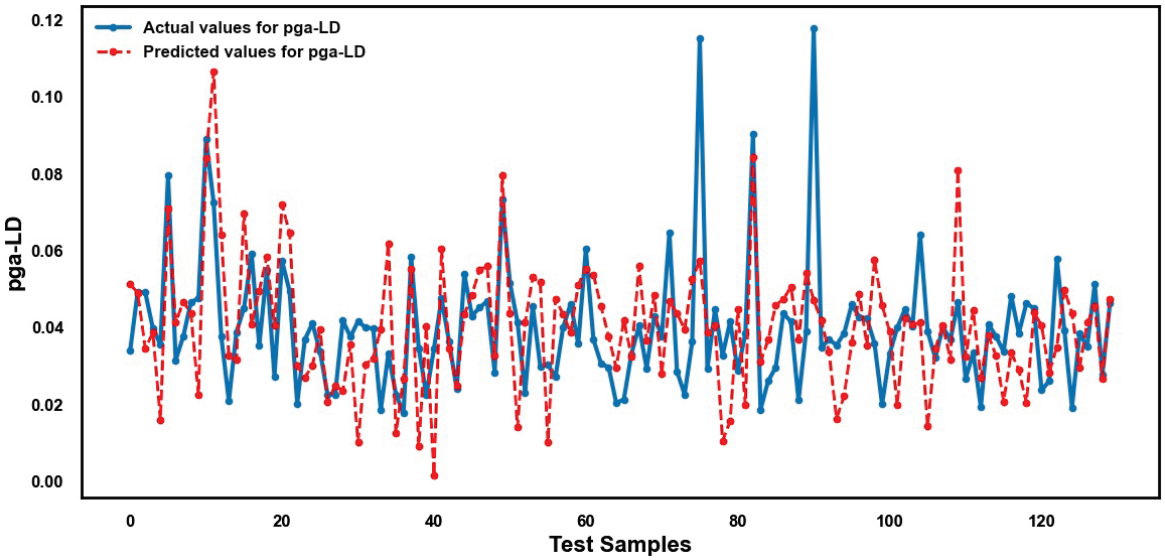

Figure 5. Actual and predicted values by Transformer for PGA-LD.

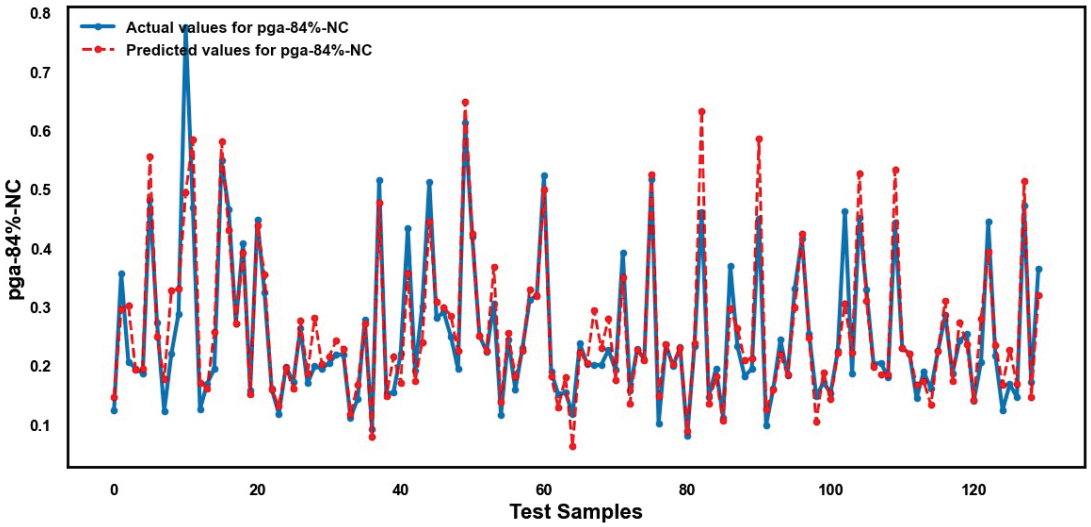

Figure 6. Actual and predicted values by Transformer for PGA-84% NC.

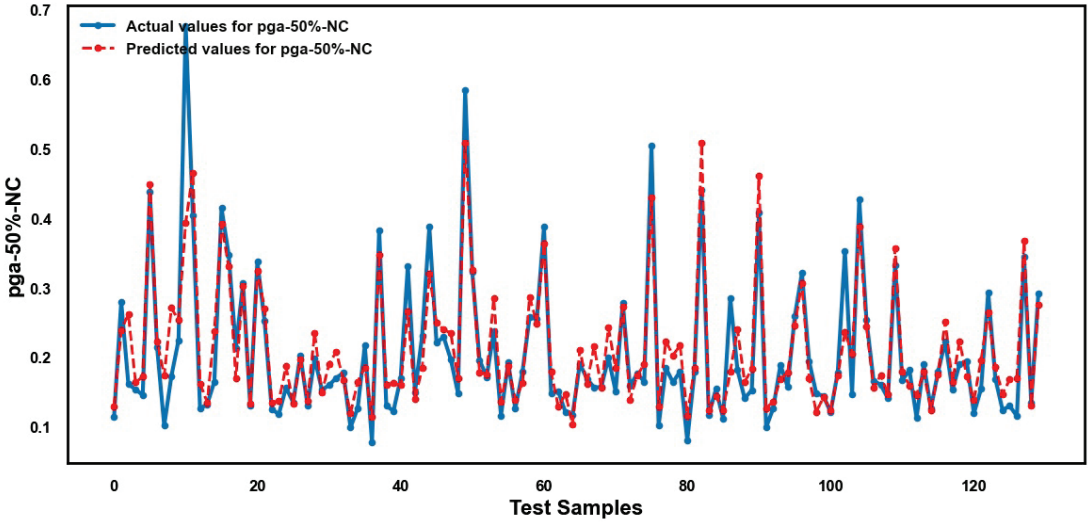

Figure 7. Actual and predicted values by Transformer for PGA-50% NC.

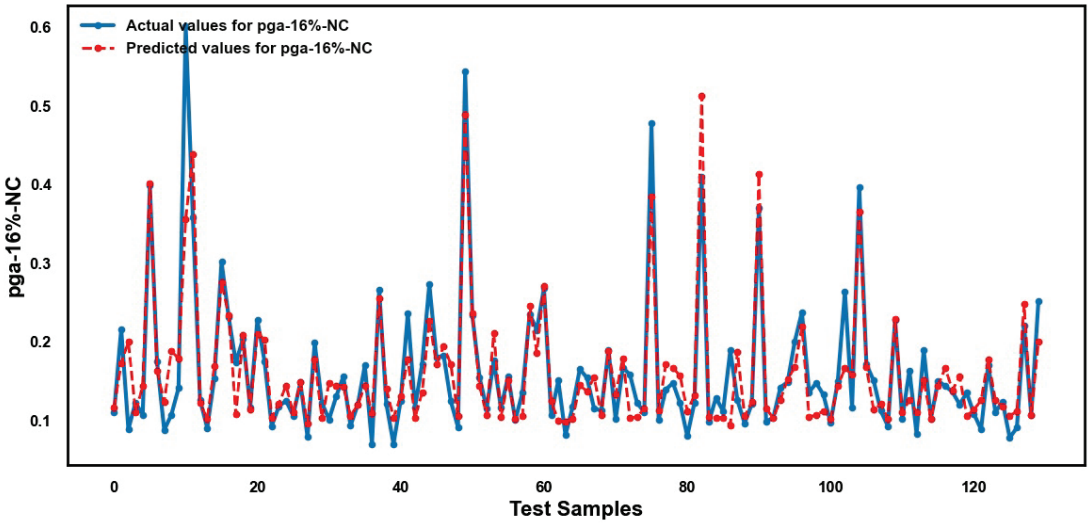

Figure 8. Actual and predicted values by Transformer for PGA-16% NC.

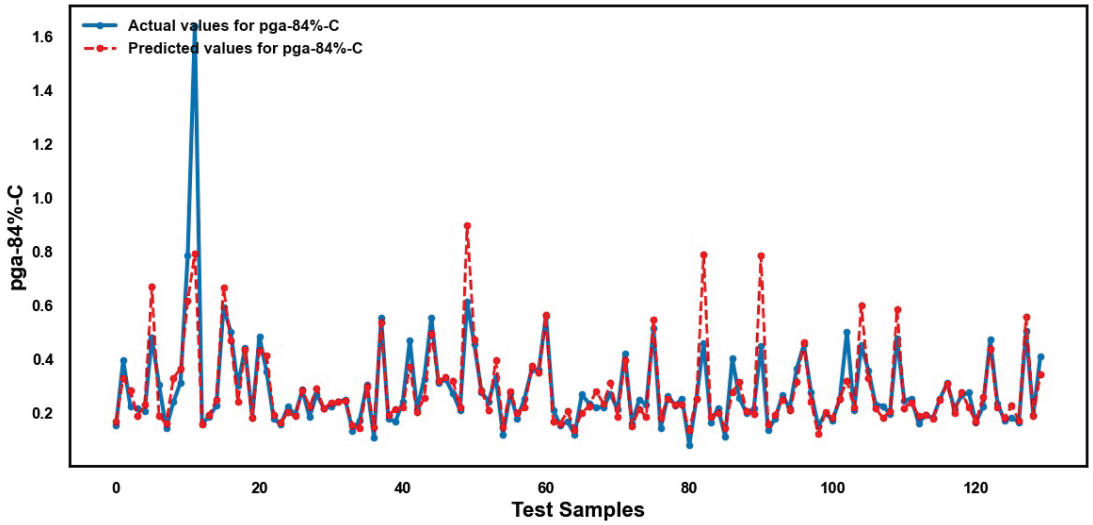

Figure 9. Actual and predicted values by Transformer for PGA-84% C.

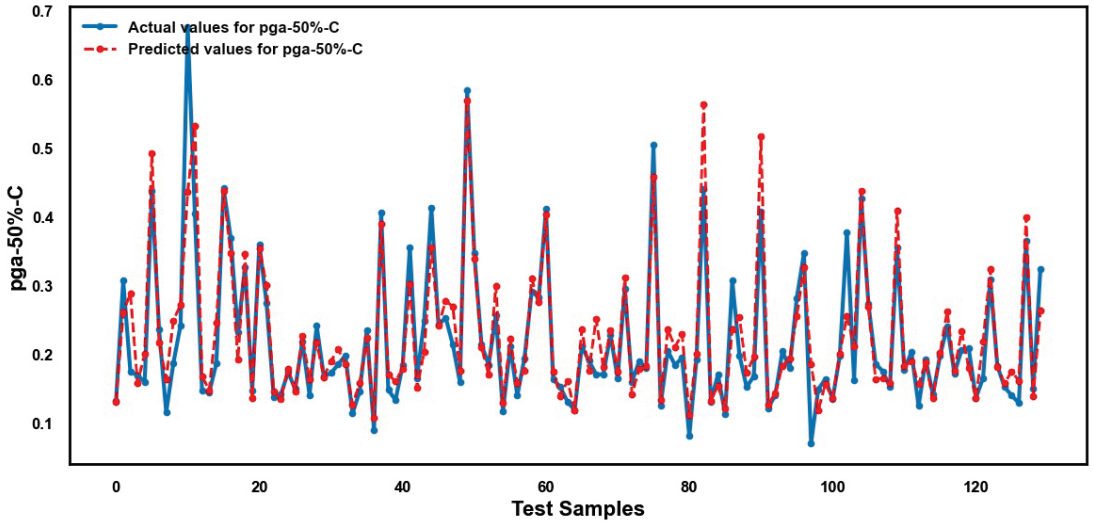

Figure 10. Actual and predicted values by Transformer for PGA-50% C.

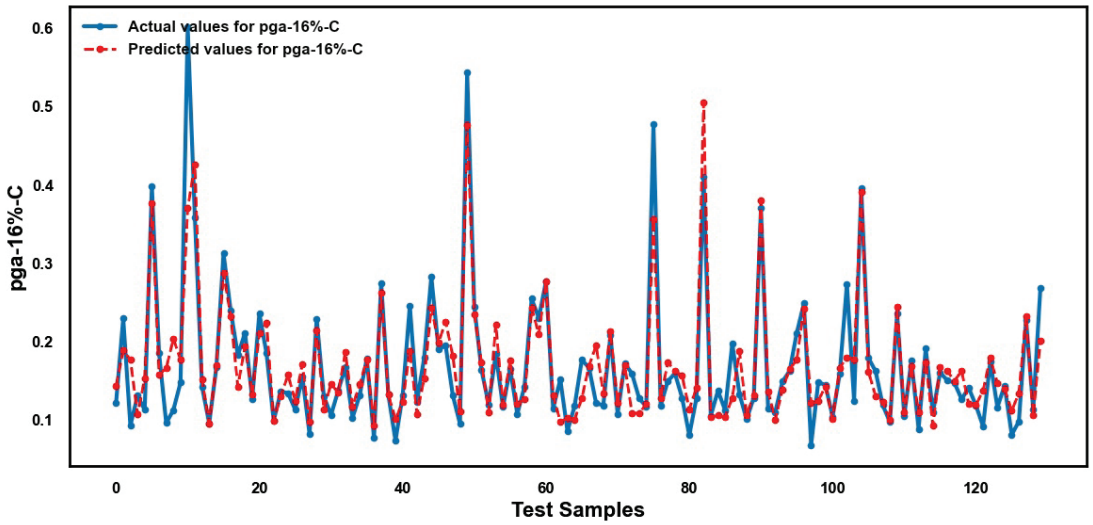

Figure 11. Actual and predicted values by Transformer for PGA-16% C.

Figure 12 shows the training and validation loss curves for the Transformer model over 300 Epochs, using MSE as the loss function. It can be seen that both training and validation losses decrease steadily and converge to low values. It indicates that the model effectively learned the underlying patterns in the data without overfitting. The very close alignment between the training and validation curves suggests a strong generalization to unseen data, which is essential for reliable predictions in practical applications. This kind of behavior confirms that the chosen Transformer architecture, along with the training configuration, is suitable for the regression task. Observing such a loss curve is a standard practice in model evaluation, as it provides direct insights into model performance and potential training issues such as underfitting or overfitting.

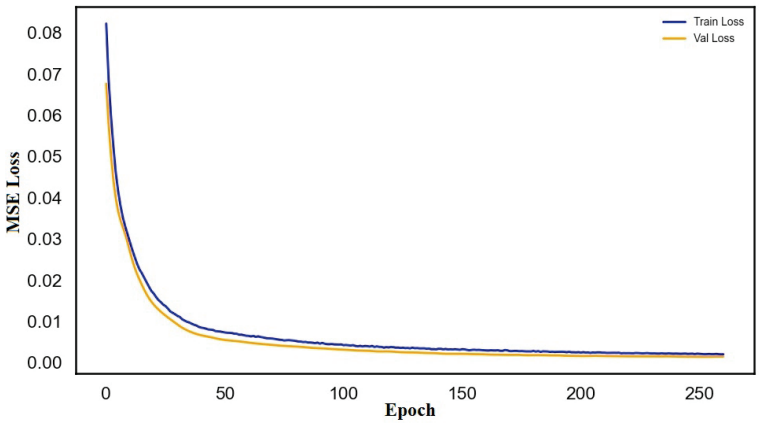

Figure 12. Training and validation loss curves of the Transformer model over 300 epochs using MSE loss.

Figure 13 presents the RMSE values for each ML model at different levels of the PGA. This allows for a detailed comparison and more granular assessment of how each model behaves under varying seismic intensities.

However, given the number of combinations and the potential for visual clutter, a summarized view of the results is also provided in Figure 14, which displays the mean values of the error metrics (MAPE, RMSE, and MSE) for each model. This summary helps prevent the need for multiple separate figures, improving visual clarity and making it easier to interpret the overall performance trends of the models.

As illustrated, the Transformer model consistently achieves the lowest error values in all three metrics, indicating superior predictive accuracy and generalizability. XGBoost follows as the next best performer, showing strong predictive capability. LSTM, LR, and DT exhibit similar intermediate performances, while SGD performs slightly worse than these models in terms of MAPE and RMSE. The KNN model performs the worst, with the highest error rates, suggesting a limited predictive capacity in this context. Compared to the previous study with similar data [33], the Transformer achieved better performance, reducing the MAPE from 17.674% to 14.325% and the RMSE from 0.0617 to 0.0384. Overall, the results indicate that the Transformer model surpasses traditional ML approaches in reliably predicting PGA. Although Transformers generally perform best with large datasets, this study successfully applied the model to a relatively small dataset, demonstrating its capability to derive fragility curves effectively. This novel application highlights the feasibility of the model and its potential for broader use in future seismic vulnerability assessments. Therefore, the use of the term Strong Potential in this study emphasizes the superior predictive performance of the Transformer, as evidenced by lower MAPE and RMSE values compared to other ML models. Furthermore, the model demonstrates robust generalization across multiple output variables and effectively

captures complex nonlinear relationships within seismic vulnerability data. Although training times are slightly longer and larger datasets are generally beneficial, the improved accuracy and ability of the model to model intricate interactions justify its designation as having a strong potential to derive reliable fragility curves.

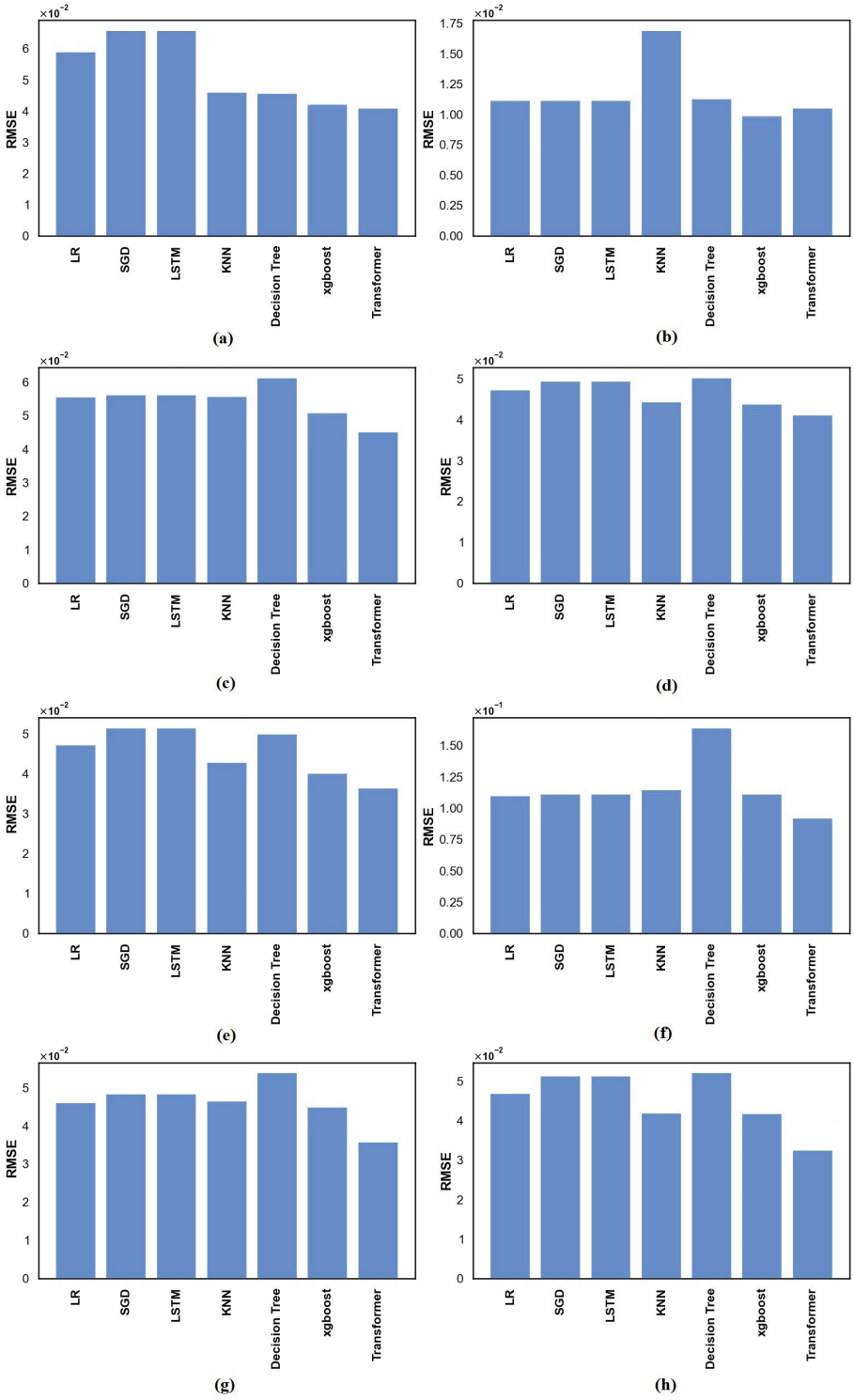

Figure 13. RMSE values for each ML model across different PGA levels (**a**) SD, (**b**) LD, (**c**) 84% NC, (**d**) 50% NC, (**e**) 16% NC, (**f**) 84% C, (**g**) 50% C, and (**h**) 16% C.

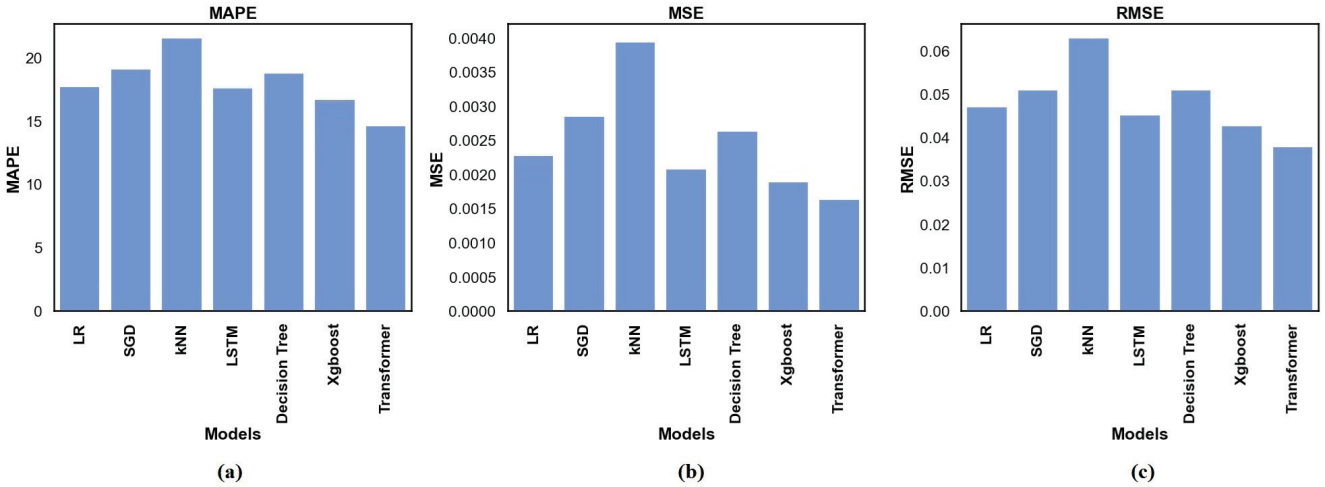

Figure 14. Mean values of error metrics (**a**) MAPE, (**b**) MSE, and (**c**) RMSE for different ML models.

Figure 15 illustrates the fragility curves corresponding to different levels of PGA and damage states predicted by the Transformer model using the dataset. As expected, the probability of collapse increases with higher levels of PGA. The steepness and position of each curve reflect the relative vulnerability of each type of building. Buildings labeled with "SD" and "LD" exhibit the most rapid increase in the probability of collapse at lower PGA values, indicating greater fragility. In contrast, buildings classified under "C" (presumably retrofitted or reinforced) exhibit high probabilities of collapse only at higher PGA levels, particularly the 84% C curve, which shows the highest resistance. The distinction between different percentiles (16%, 50%, and 84%) further demonstrates the variability in building performance due to uncertainties in construction quality, design, and materials. In general, the figure highlights that the characteristics of the building and the structural improvements have a significant impact on the risk of collapse under seismic load.

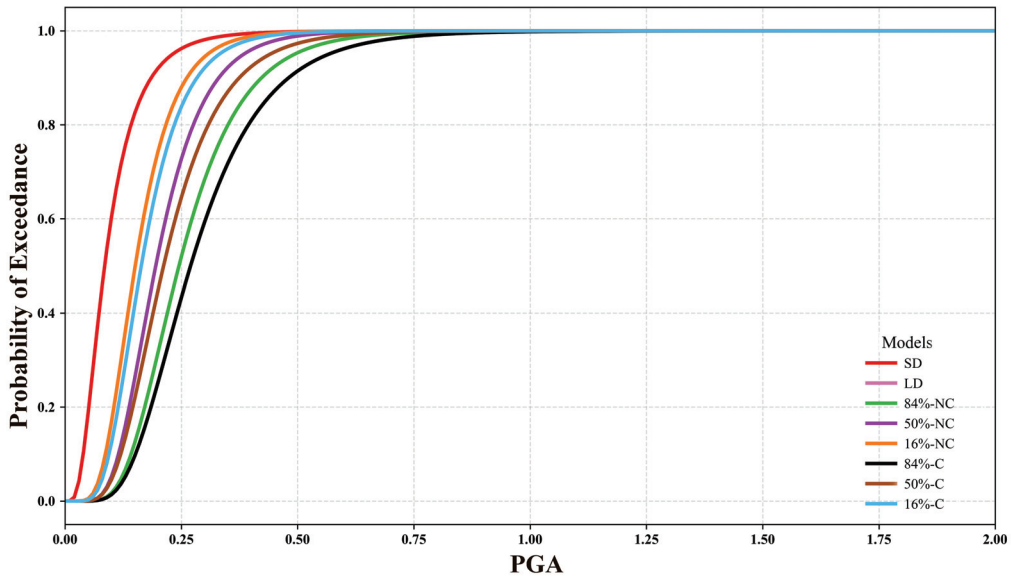

Figure 15. Fragility curves generated by the Transformer model corresponding to different predicted PGA levels based on the full dataset.

For better comparison and visual understanding of the Transformer model's predictions versus the actual PGA values, Figure 16 is presented. It displays the fragility curves

derived from the actual dataset alongside those predicted by the Transformer model using the full dataset. As observed, the predicted PGA values closely align with the actual data, showing only minor deviations, which are slightly higher in some cases and slightly lower in others. Overall, the predictions are highly consistent and fall within an acceptable range, demonstrating the model's reliability.

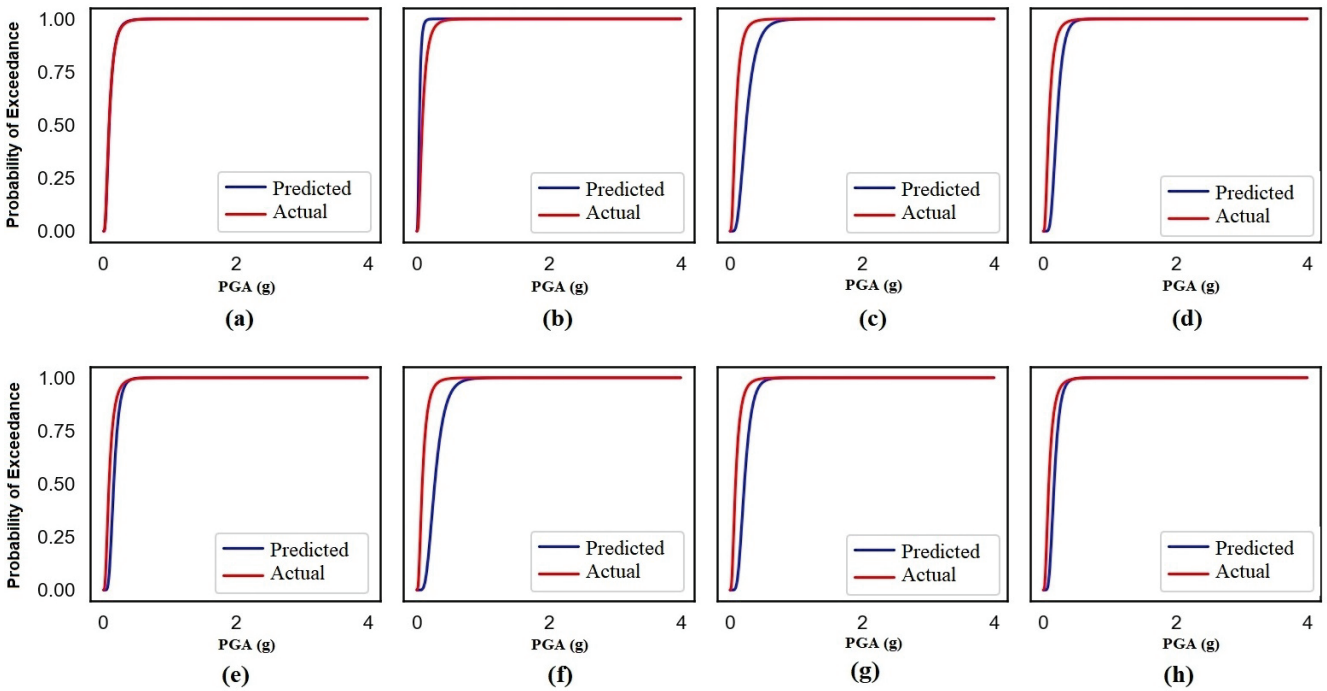

Figure 16. Fragility curves obtained using actual data set compared with predictions via Transformer based on all features and different PGA (**a**) SD, (**b**) LD, (**c**) 84% NC, (**d**) 50% NC, (**e**) 16% NC, (**f**) 84% C, (**g**) 50% C, and (**h**) 16% C.

6. Conclusions

Evaluating the seismic vulnerability of non-engineered masonry buildings in developing regions is crucial for minimizing risk to life and property in earthquake-prone areas. These buildings often lack structural resilience, making them especially susceptible to damage during seismic events. Given the extensive losses observed in past earthquakes, there is a growing need for data-driven strategies to support effective retrofitting and mitigation efforts. With the advancement of ML, new opportunities have emerged for seismic risk assessment. In this study, seven algorithms (kNN, LR, SGD, DT, LSTM, XGBoost, and Transformer) were trained on field-collected data from 646 masonry walls in Malawi to estimate collapse probabilities and derive fragility curves.

Among all models, the Transformer achieved the best performance, producing fragility curves that closely matched empirical data (Figure 16). Its capacity to capture complex nonlinear relationships distinguished it from the more conventional algorithms. Overall, the results demonstrate that Transformer-based models are a promising tool for assessing seismic fragility in non-engineered buildings. Their predictive accuracy and consistency with observed trends support their potential for real-world application and broader deployment.

Although the dataset was limited to Malawi, the findings are broadly representative of East African non-engineered masonry, where materials and construction practices are comparable. Laboratory testing of local materials increased confidence in the fragility curves, ensuring they capture regional structural behavior.

Future work could improve prediction performance by expanding datasets (more surveyed buildings and seismic records), testing alternative ML models, and integrating additional structural and environmental features relevant to target regions. These directions will strengthen model robustness and advance data-driven approaches for seismic vulnerability assessment.

Author Contributions: Conceptualization, E.H. and V.I.N.; methodology, E.H.; software, E.H.; validation, E.H. and V.I.N.; formal analysis, E.H.; investigation, E.H.; resources, V.I.N.; data curation, V.I.N.; writing—original draft preparation, E.H. and V.I.N.; writing—review and editing, E.H. and V.I.N.; visualization, E.H.; supervision, E.H.; project administration, E.H.; funding acquisition, E.H. All authors have read and agreed to the published version of the manuscript.

Funding: This research received no external funding.

Data Availability Statement: Data will be made available on request.

Conflicts of Interest: The authors declare no conflicts of interest.

Abbreviations

The following abbreviations are used in this manuscript:

ANN	Artificial Neural Network
C	Collapse
DT	Decision Tree
IDA	Incremental Dynamic Analysis
KNN	K-Nearest Neighbors
LD	Light Damage
LR	Linear Regression
LSTM	Long Short-Term Memory
MAPE	Mean Absolute Percentage Error
ML	Machine Learning
MSE	Mean Squared Error
NC	Near Collapse
PGA	Peak Ground Acceleration
RMSE	Root Mean Square Error
SD	Severe Damage
SGD	Stochastic Gradient Descent
SHAP	SHapley Additive exPlanations
SPO	Static Pushover
XGBoost	Extreme Gradient Boosting

Appendix A

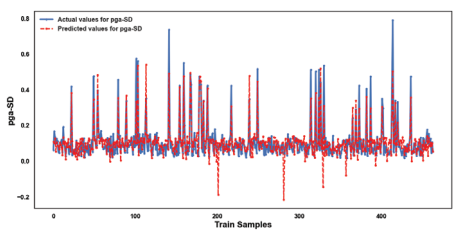

(**a**)

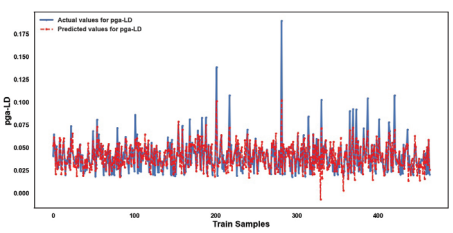

(**b**)

Figure A1. *Cont.*

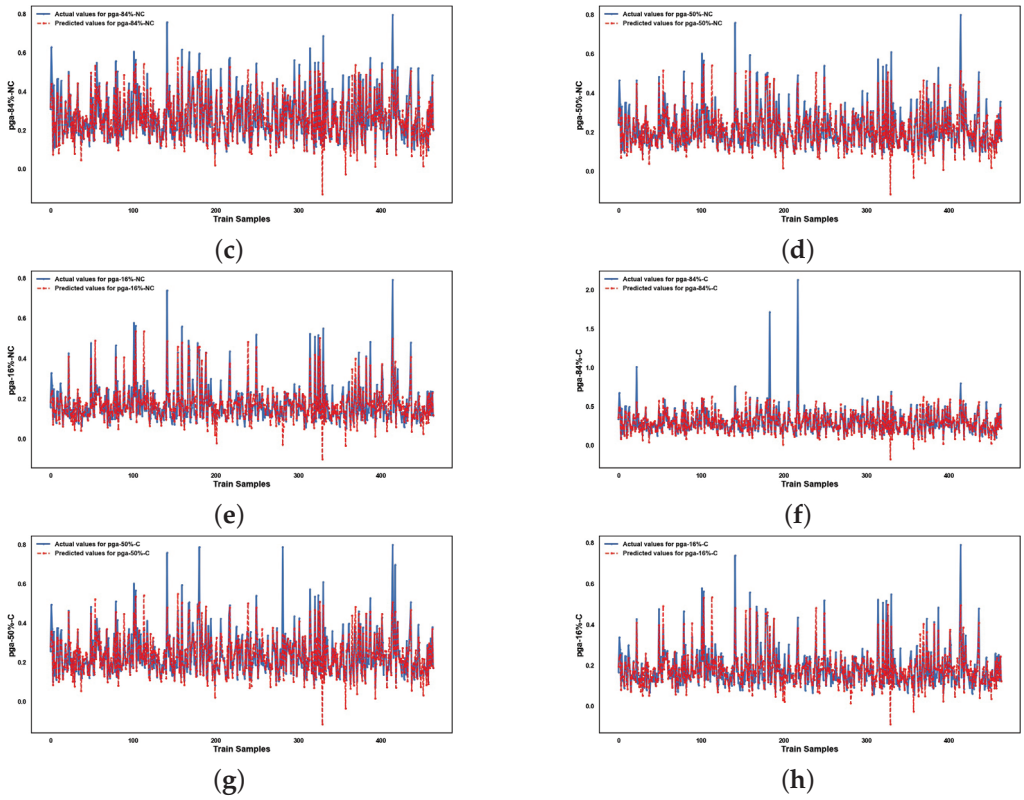

Figure A1. Actual and predicted values obtained from the LR model for the training dataset: (**a**) SD, (**b**) LD, (**c**) 84% NC, (**d**) 50% NC, (**e**) 16% NC, (**f**) 84% C, (**g**) 50% C, and (**h**) 16% C.

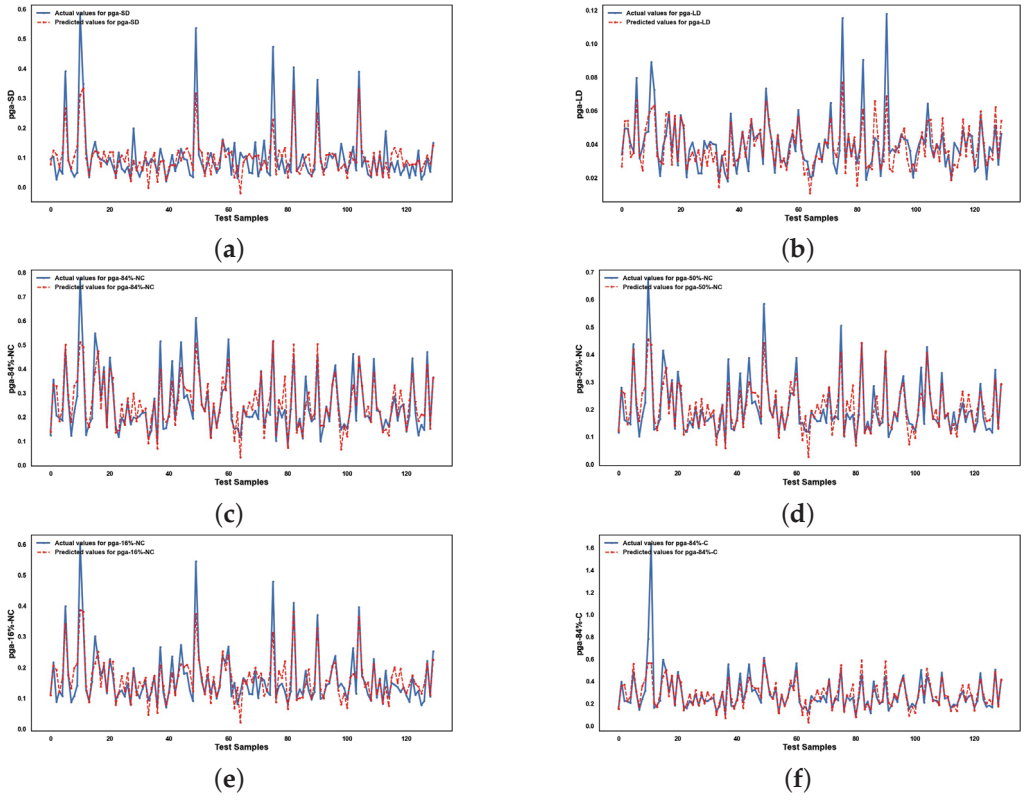

Figure A2. *Cont.*

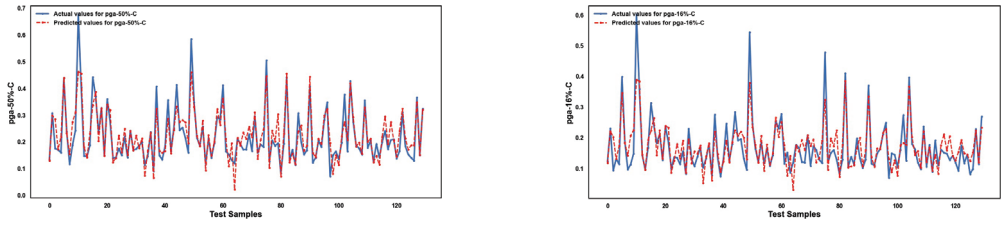

(**g**) (**h**)

Figure A2. Actual and predicted values obtained from the LR model for the test dataset: (**a**) SD, (**b**) LD, (**c**) 84% NC, (**d**) 50% NC, (**e**) 16% NC, (**f**) 84% C, (**g**) 50% C, and (**h**) 16% C.

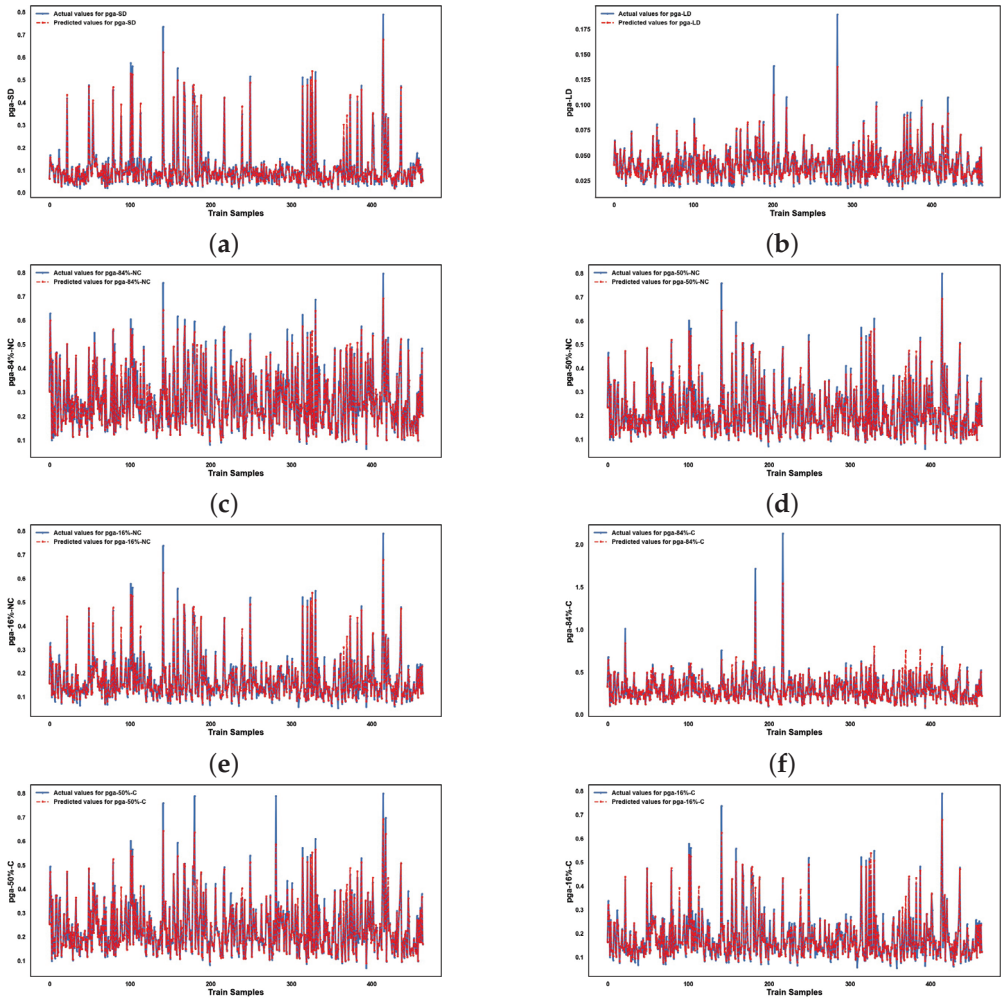

(**a**) (**b**)

(**c**) (**d**)

(**e**) (**f**)

(**g**) (**h**)

Figure A3. Actual and predicted values obtained from the RF model for the training dataset: (**a**) SD, (**b**) LD, (**c**) 84% NC, (**d**) 50% NC, (**e**) 16% NC, (**f**) 84% C, (**g**) 50% C, and (**h**) 16% C.

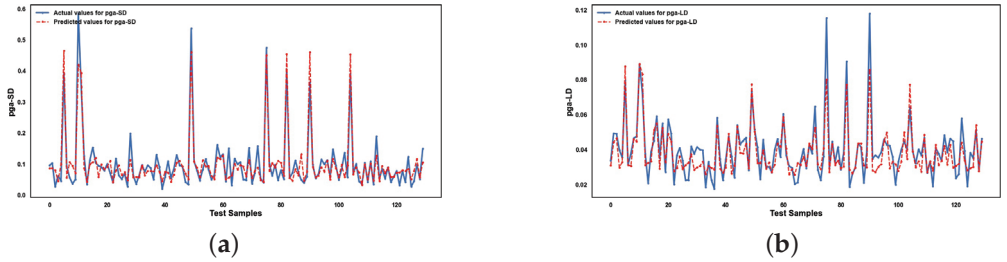

(**a**) (**b**)

Figure A4. *Cont.*

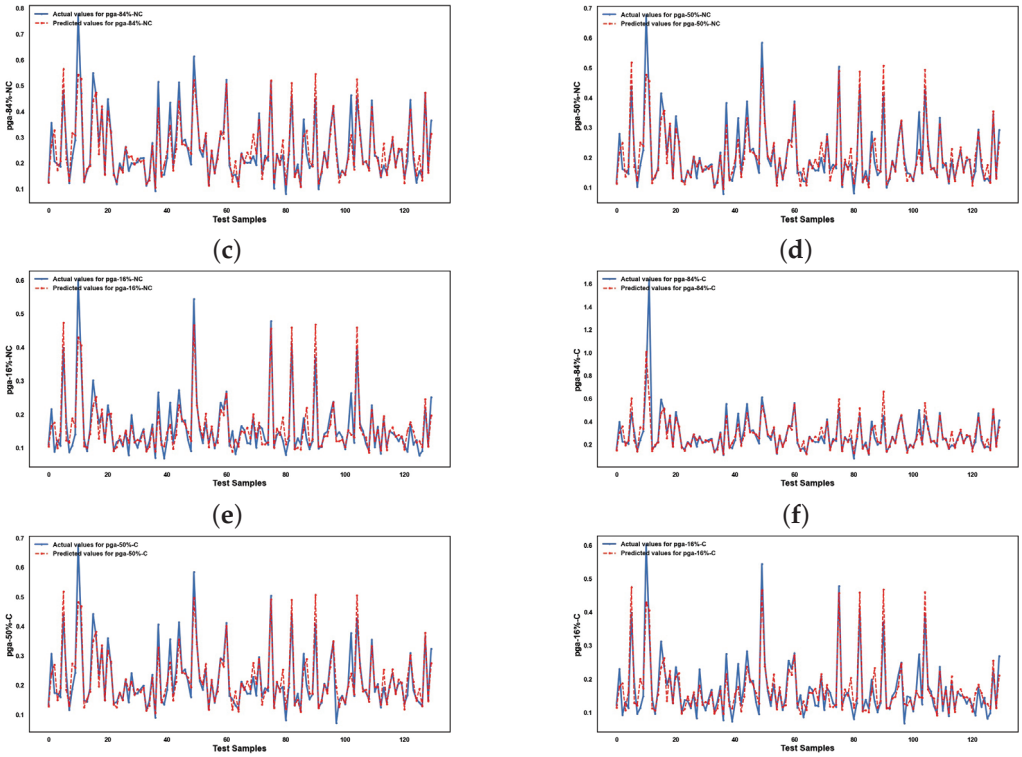

Figure A4. Actual and predicted values obtained from the RF model for the test dataset: (**a**) SD, (**b**) LD, (**c**) 84% NC, (**d**) 50% NC, (**e**) 16% NC, (**f**) 84% C, (**g**) 50% C, and (**h**) 16% C.

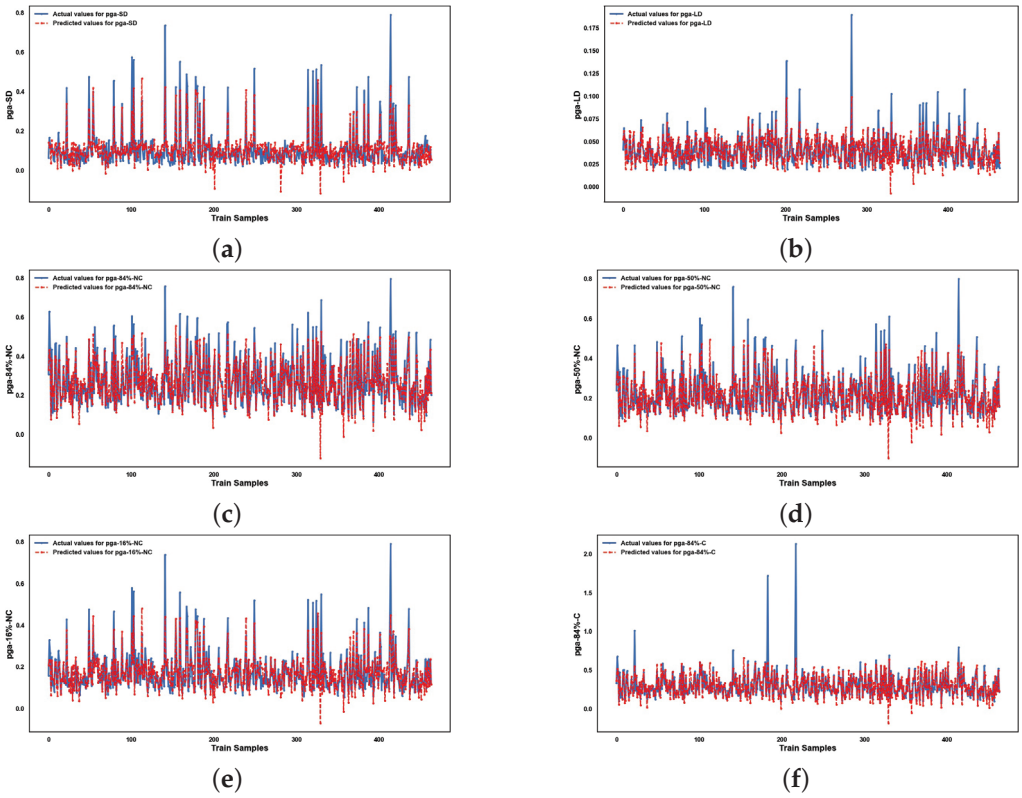

Figure A5. *Cont.*

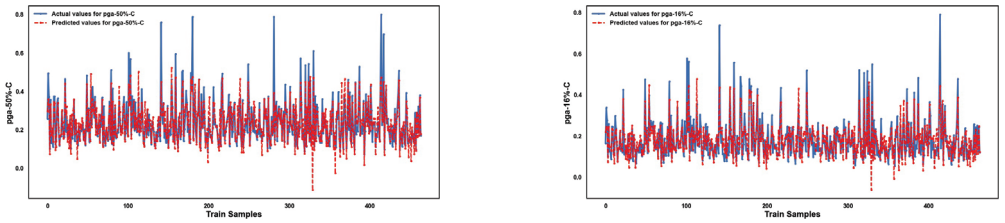

(**g**) (**h**)

Figure A5. Actual and predicted values obtained from the SGD model for the training dataset: (**a**) SD, (**b**) LD, (**c**) 84% NC, (**d**) 50% NC, (**e**) 16% NC, (**f**) 84% C, (**g**) 50% C, and (**h**) 16% C.

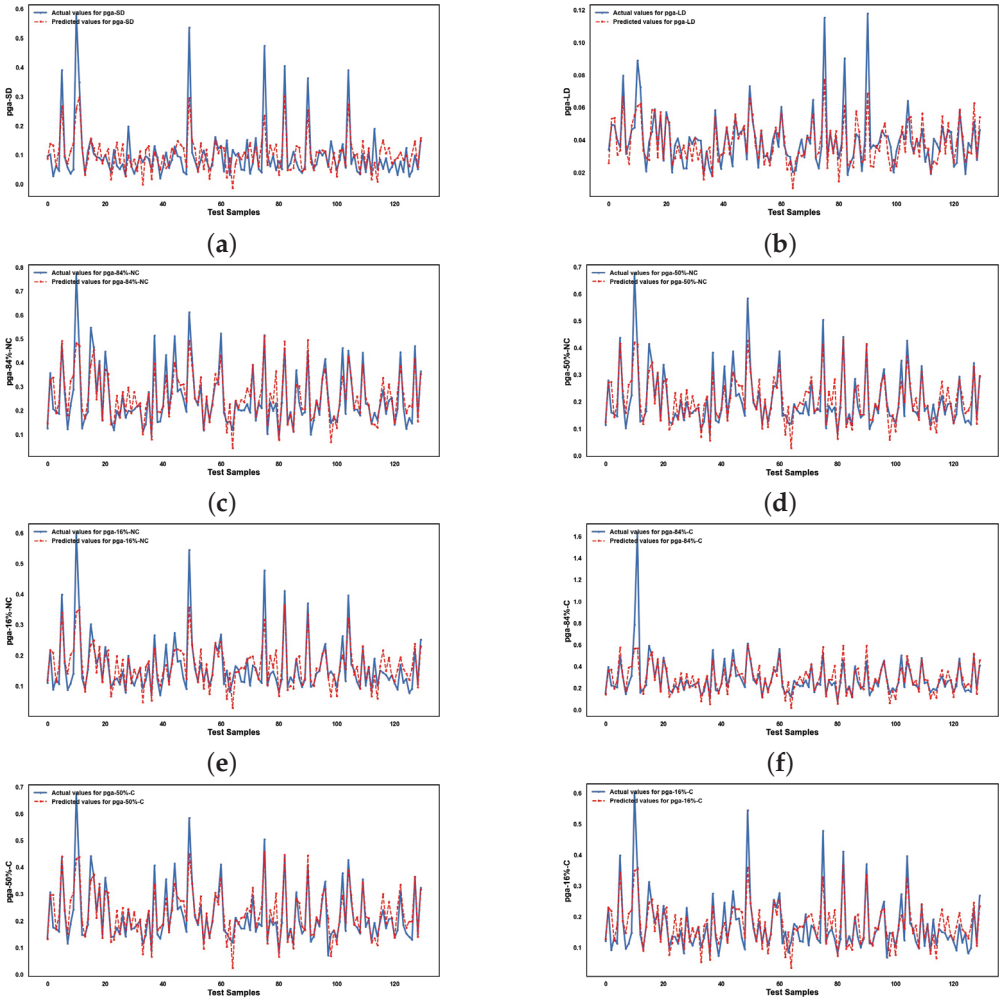

(**a**) (**b**)

(**c**) (**d**)

(**e**) (**f**)

(**g**) (**h**)

Figure A6. Actual and predicted values obtained from the SGD model for the test dataset: (**a**) SD, (**b**) LD, (**c**) 84% NC, (**d**) 50% NC, (**e**) 16% NC, (**f**) 84% C, (**g**) 50% C, and (**h**) 16% C.

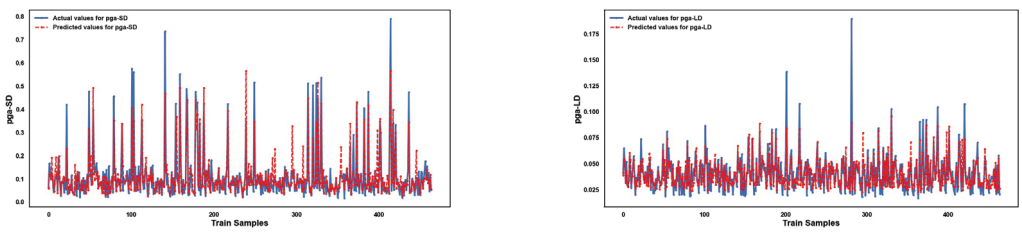

(**a**) (**b**)

Figure A7. *Cont.*

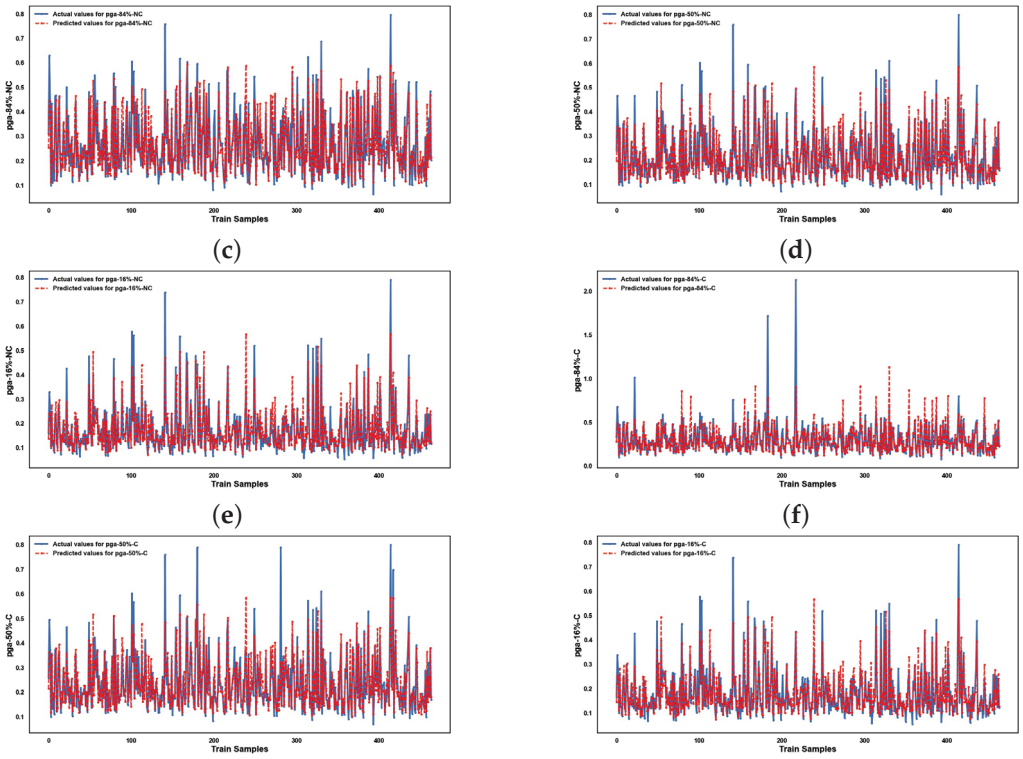

Figure A7. Actual and predicted values obtained from the KNN model for the training dataset: (**a**) SD, (**b**) LD, (**c**) 84% NC, (**d**) 50% NC, (**e**) 16% NC, (**f**) 84% C, (**g**) 50% C, and (**h**) 16% C.

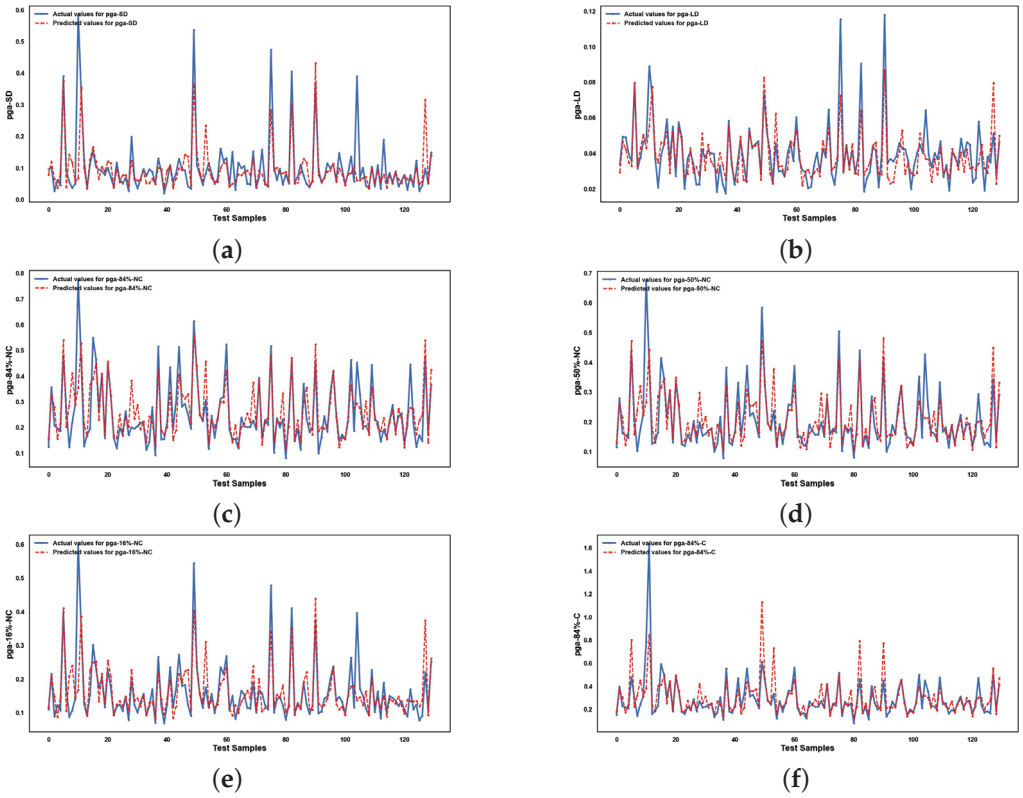

Figure A8. *Cont.*

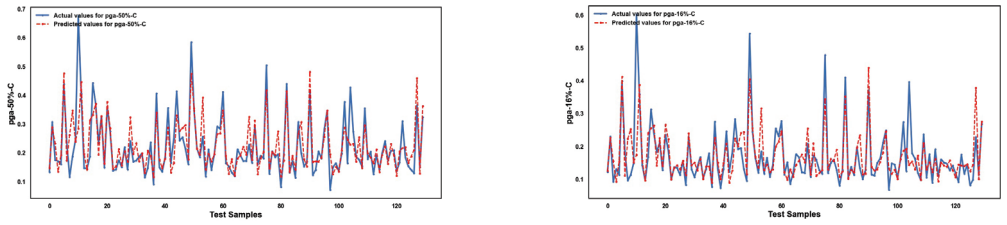

(**g**) (**h**)

Figure A8. Actual and predicted values obtained from the KNN model for the test dataset: (**a**) SD, (**b**) LD, (**c**) 84% NC, (**d**) 50% NC, (**e**) 16% NC, (**f**) 84% C, (**g**) 50% C, and (**h**) 16% C.

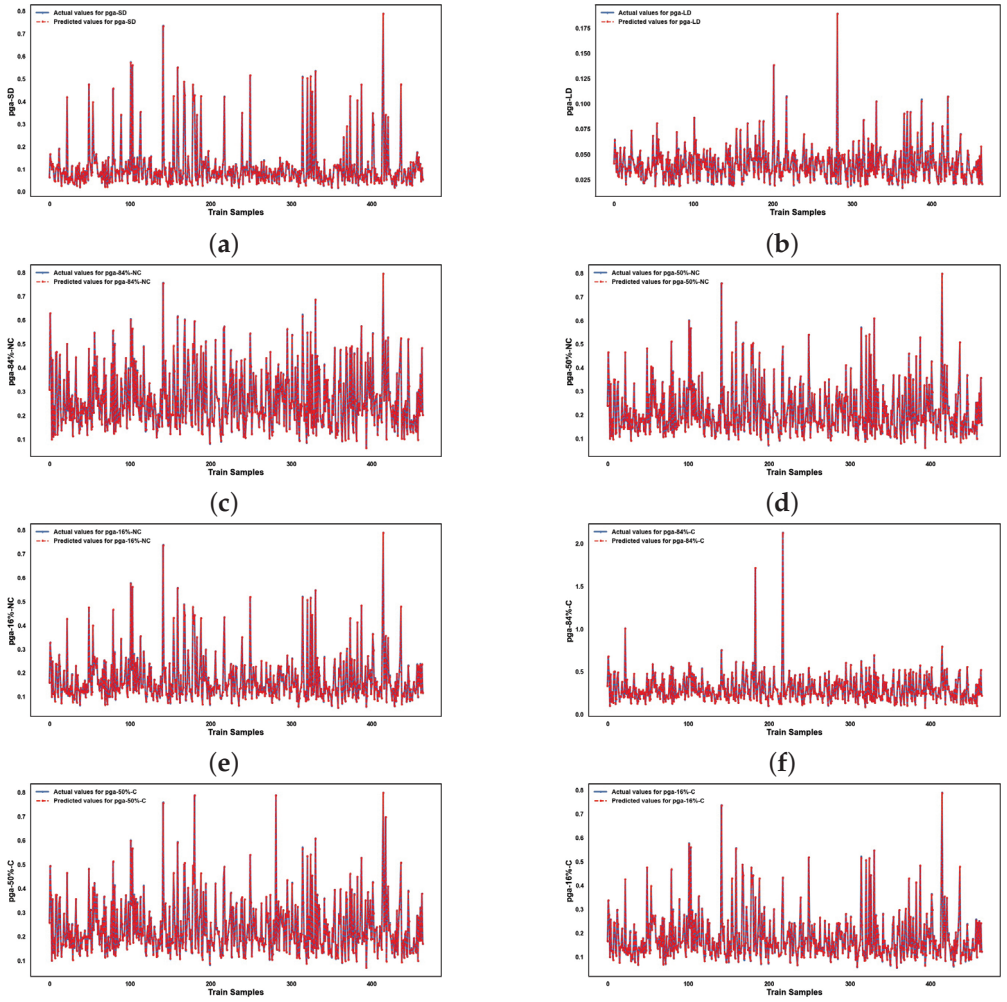

(**a**) (**b**)

(**c**) (**d**)

(**e**) (**f**)

(**g**) (**h**)

Figure A9. Actual and predicted values obtained from the XGBoost model for the training dataset: (**a**) SD, (**b**) LD, (**c**) 84% NC, (**d**) 50% NC, (**e**) 16% NC, (**f**) 84% C, (**g**) 50% C, and (**h**) 16% C.

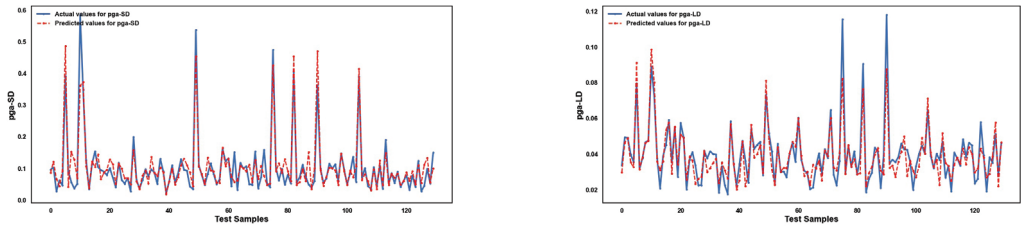

(**a**) (**b**)

Figure A10. *Cont*.

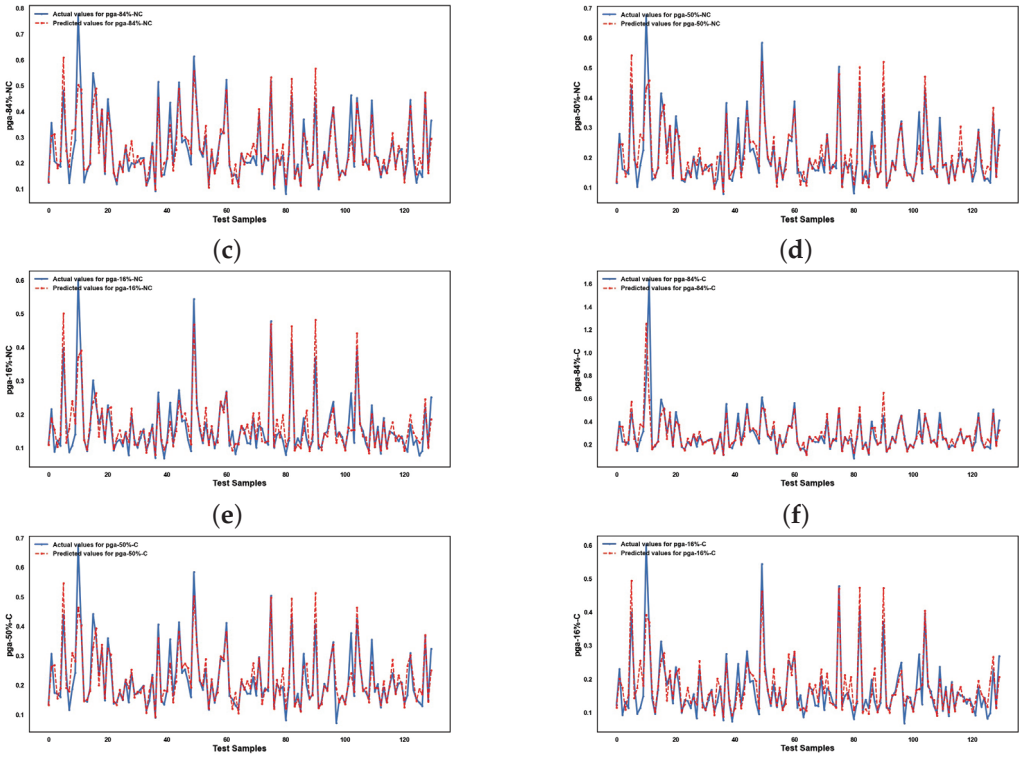

Figure A10. Actual and predicted values obtained from the XGBoost model for the test dataset: (**a**) SD, (**b**) LD, (**c**) 84% NC, (**d**) 50% NC, (**e**) 16% NC, (**f**) 84% C, (**g**) 50% C, and (**h**) 16% C.

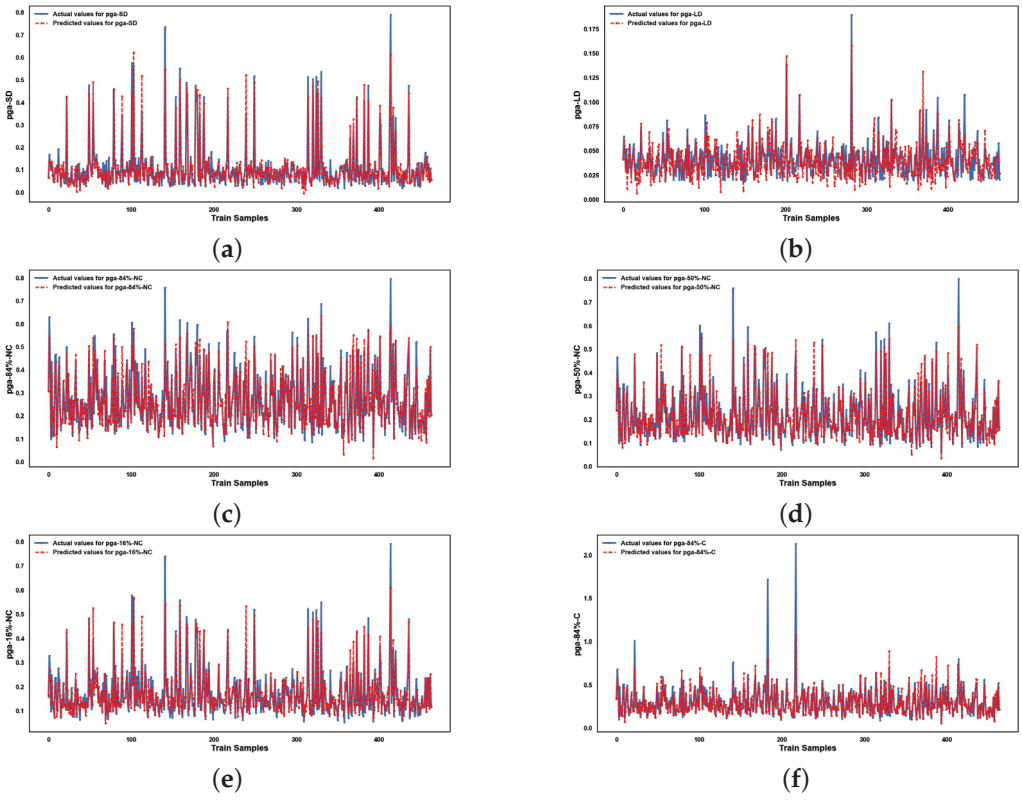

Figure A11. *Cont.*

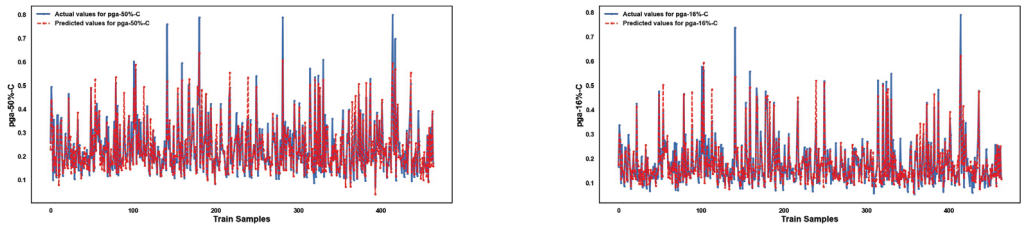

(**g**) (**h**)

Figure A11. Actual and predicted values obtained from the LSTM model for the training dataset: (**a**) SD, (**b**) LD, (**c**) 84% NC, (**d**) 50% NC, (**e**) 16% NC, (**f**) 84% C, (**g**) 50% C, and (**h**) 16% C.

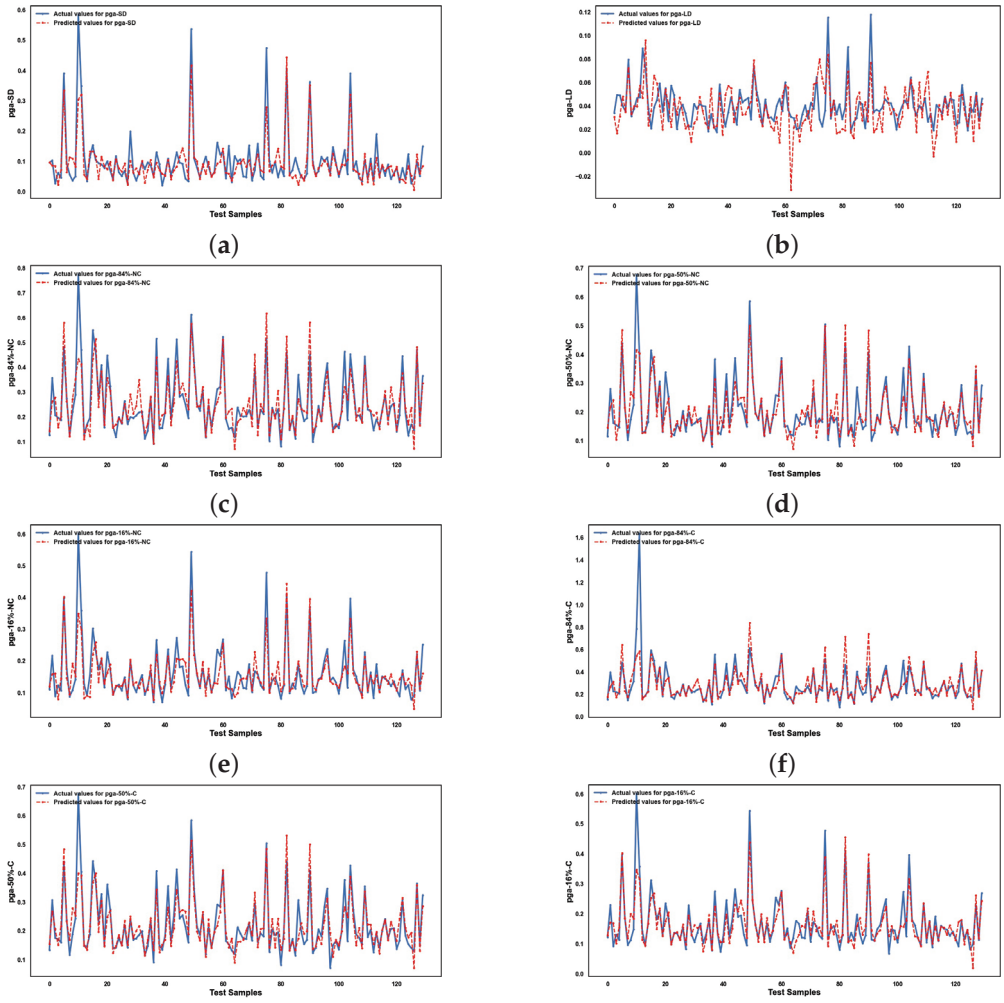

(**a**) (**b**)

(**c**) (**d**)

(**e**) (**f**)

(**g**) (**h**)

Figure A12. Actual and predicted values obtained from the LSTM model for the test dataset: (**a**) SD, (**b**) LD, (**c**) 84% NC, (**d**) 50% NC, (**e**) 16% NC, (**f**) 84% C, (**g**) 50% C, and (**h**) 16% C.

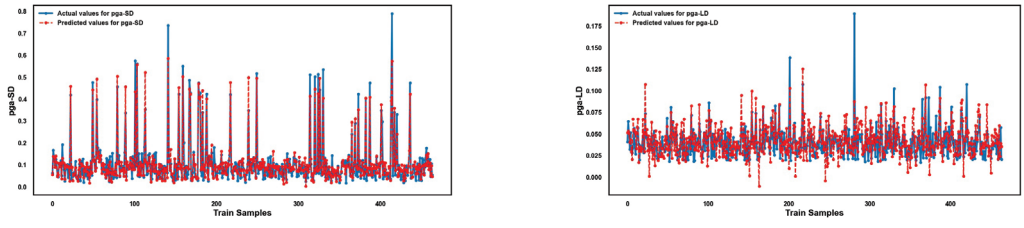

(**a**) (**b**)

Figure A13. *Cont*.

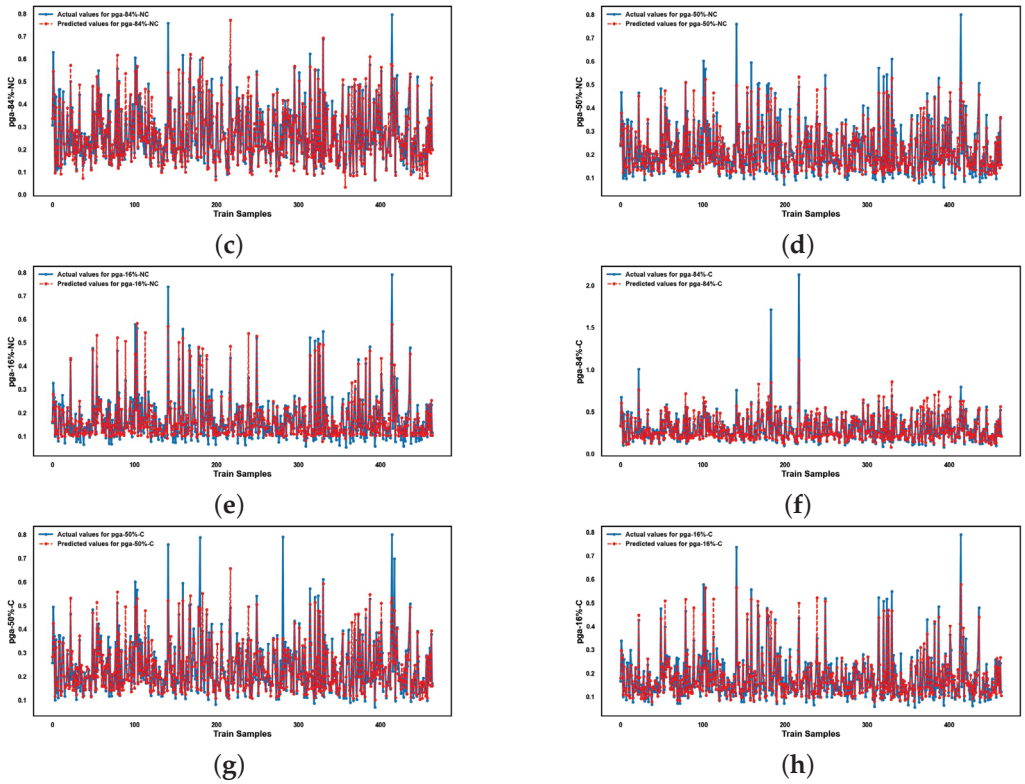

Figure A13. Actual and predicted values obtained from the Transformer model for the training dataset: (**a**) SD, (**b**) LD, (**c**) 84% NC, (**d**) 50% NC, (**e**) 16% NC, (**f**) 84% C, (**g**) 50% C, and (**h**) 16% C.

References

1. Bazzurro, P.; Cornell, C.; Menun, C.; Motahari, M. Guidelines for seismic assessment of damaged buildings. In Proceedings of the 13th World Conference on Earthquake Engineering, Vancouver, BC, Canada, 1–6 August 2004; Volume 1708.
2. Nirandjan, S.; Koks, E.E.; Ye, M.; Pant, R.; Van Ginkel, K.C.; Aerts, J.C.; Ward, P.J. Physical vulnerability database for critical infrastructure multi-hazard risk assessments–A systematic review and data collection. *Nat. Hazards Earth Syst. Sci. Discuss.* **2024**, *24*, 4341–4368. [CrossRef]
3. Rota, M.; Penna, A.; Strobbia, C. Processing Italian damage data to derive typological fragility curves. *Soil Dyn. Earthq. Eng.* **2008**, *28*, 933–947. [CrossRef]
4. Yepes-Estrada, C.; Silva, V.; Crowley, H. Gem vulnerability database for the openquake-platform. In Proceedings of the Second European Conference on Earthquake Engineering and Seismology, Istanbul, Turkey, 25–29 August 2014.
5. Di Ludovico, M.; De Martino, G.; Prota, A.; Manfredi, G.; Dolce, M. Relationships between empirical damage and direct/indirect costs for the assessment of seismic loss scenarios. *Bull. Earthq. Eng.* **2022**, *20*, 229–254. [CrossRef]
6. Ahmad, S.; Kyriakides, N.; Pilakoutas, K.; Neocleous, K.; Zaman, Q.U. Seismic fragility assessment of existing sub-standard low strength reinforced concrete structures. *Earthq. Eng. Eng. Vib.* **2015**, *14*, 439–452. [CrossRef]
7. Khalfan, M.; El-Dakhakhni, W.W.; Tait, M.J. Seismic risk assessment of nonengineered residential buildings in developing countries. *J. Perform. Constr. Facil.* **2016**, *30*, 4016013. [CrossRef]
8. Novelli, V.; Risi, R.; Ngoma, I.; Kafodya, I.; Kloukinas, P.; Macdonald, J.; Goda, K. Fragility curves for non-engineered masonry buildings in developing countries derived from real data based on structural surveys and laboratory tests. *Soft Comput.* **2021**, *25*, 6113–6138. [CrossRef]
9. Khalfan, M. Fragility Curves for Residential Buildings in Developing Countries: A Case Study on Non-Engineered Unreinforced Masonry Homes in Bantul, Indonesia. Master's Thesis, McMaster University, Hamilton, ON, Canada, 2013.
10. Dai, K.Y.; Yu, X.H.; Lu, D.G.; Qian, K. Fragility functions for corroded reinforced concrete columns. *J. Build. Eng.* **2024**, *82*, 108124. [CrossRef]
11. Yu, X.; Li, Z.; Yang, A.; Li, Y.; Lu, D.; Dai, K. Time-Dependent Seismic Fragility of Coastal RC Frames Considering Effect of Distance from Coastline. *Buildings* **2025**, *15*, 737. [CrossRef]

12. Sabetta, F.; Goretti, A.; Lucantoni, A. Empirical fragility curves from damage surveys and estimated strong ground motion. In Proceedings of the 11th European Conference on Earthquake Engineering, Paris, France, 6–11 September 1998; pp. 1–11.
13. Du, A.; Wang, X.; Xie, Y.; Dong, Y. Regional seismic risk and resilience assessment: Methodological development, applicability, and future research needs–An earthquake engineering perspective. *Reliab. Eng. Syst. Saf.* **2023**, *233*, 109104. [CrossRef]
14. Guo, J.; Zhang, P.; Wang, J.; Li, S.; Guan, Z. A novel framework for seismic fragility analysis with the combination of Box-Cox transformation and Bayesian inference. *Eng. Struct.* **2023**, *277*, 115436. [CrossRef]
15. Işık, E.; Bilgin, H.; Avcil, F.; İzol, R.; Arkan, E.; Büyüksaraç, A.; Harirchian, E.; Hysenlliu, M. Seismic performances of masonry educational buildings during the 2023 Türkiye (Kahramanmaraş) Earthquakes. *GeoHazards* **2024**, *5*, 700–731. [CrossRef]
16. Giordano, N.; De Risi, R.; Voyagaki, E.; Kloukinas, P.; Novelli, V.; Kafodya, I.; Ngoma, I.; Goda, K.; Macdonald, J. Seismic fragility models for typical non-engineered URM residential buildings in Malawi. *Structures* **2021**, *32*, 2266–2278. [CrossRef]
17. Harirchian, E.; Hosseini, S.E.A.; Jadhav, K.; Kumari, V.; Rasulzade, S.; Işık, E.; Wasif, M.; Lahmer, T. A review on application of soft computing techniques for the rapid visual safety evaluation and damage classification of existing buildings. *J. Build. Eng.* **2021**, *43*, 102536. [CrossRef]
18. Dabiri, H.; Faramarzi, A.; Dall'Asta, A.; Tondi, E.; Micozzi, F. A machine learning-based analysis for predicting fragility curve parameters of buildings. *J. Build. Eng.* **2022**, *62*, 105367. [CrossRef]
19. Thedy, J.; Liao, K.W. Machine Learning-Enhanced Fragility Curves: Advancing Reliability and Safety of Structures in Seismic Risk Assessment. *Reliab. Eng. Syst. Saf.* **2025**, *264* , 111361. [CrossRef]
20. Rajapaksha, R.; Siriwardana, C. A systematic review on different approaches used in the development of fragility curves for buildings. In Proceedings of the 12th International Conference on Structural Engineering and Construction Management, Kandy, Sri Lanka, 17–19 December 2021; Springer: Singapore, 2023; pp. 407–426.
21. Harirchian, E.; Lahmer, T.; Kumari, V.; Jadhav, K. Application of Support Vector Machine Modeling for the Rapid Seismic Hazard Safety Evaluation of Existing Buildings. *Energies* **2020**, *13*, 3340. [CrossRef]
22. Michalski, R.S.; Carbonell, J.G.; Mitchell, T.M. *Machine Learning: An Artificial Intelligence Approach*; Springer Science & Business Media: Berlin/Heidelberg, Germany, 2013.
23. Sun, H.; Burton, H.V.; Huang, H. Machine learning applications for building structural design and performance assessment: State-of-the-art review. *J. Build. Eng.* **2021**, *33*, 101816. [CrossRef]
24. Thai, H.T. Machine learning for structural engineering: A state-of-the-art review. *Structures* **2022**, *38*, 448–491. [CrossRef]
25. Harirchian, E.; Jadhav, K.; Kumari, V.; Lahmer, T. ML-EHSAPP: A prototype for machine learning-based earthquake hazard safety assessment of structures by using a smartphone app. *Eur. J. Environ. Civ. Eng.* **2022**, *26*, 5279–5299. [CrossRef]
26. Hwang, S.H.; Mangalathu, S.; Shin, J.; Jeon, J.S. Machine learning-based approaches for seismic demand and collapse of ductile reinforced concrete building frames. *J. Build. Eng.* **2021**, *34*, 101905. [CrossRef]
27. Mangalathu, S.; Jeon, J.S. Classification of failure mode and prediction of shear strength for reinforced concrete beam-column joints using machine learning techniques. *Eng. Struct.* **2018**, *160*, 85–94. [CrossRef]
28. Charalampakis, A.E.; Tsiatas, G.C.; Kotsiantis, S.B. Machine learning and nonlinear models for the estimation of fundamental period of vibration of masonry infilled RC frame structures. *Eng. Struct.* **2020**, *216*, 110765. [CrossRef]
29. Wu, J.R.; Di Sarno, L. A machine-learning method for deriving state-dependent fragility curves of existing steel moment frames with masonry infills. *Eng. Struct.* **2023**, *276*, 115345. [CrossRef]
30. Chomacki, L.; Rusek, J.; Słowik, L. Machine learning methods in damage prediction of masonry development exposed to the industrial environment of mines. *Energies* **2022**, *15*, 3958. [CrossRef]
31. Rezaie, A.; Godio, M.; Achanta, R.; Beyer, K. Machine-learning for damage assessment of rubble stone masonry piers based on crack patterns. *Autom. Constr.* **2022**, *140*, 104313. [CrossRef]
32. Siam, A.; Ezzeldin, M.; El-Dakhakhni, W. Machine learning algorithms for structural performance classifications and predictions: Application to reinforced masonry shear walls. *Structures* **2019**, *22*, 252–265. [CrossRef]
33. Harirchian, E.; Hosseini, S.E.A.; Novelli, V.; Lahmer, T.; Rasulzade, S. Utilizing advanced machine learning approaches to assess the seismic fragility of non-engineered masonry structures. *Results Eng.* **2024**, *21*, 101750. [CrossRef]
34. Kazemi, F.; Asgarkhani, N.; Jankowski, R. Machine learning-based seismic fragility and seismic vulnerability assessment of reinforced concrete structures. *Soil Dyn. Earthq. Eng.* **2023**, *166*, 107761. [CrossRef]
35. Zain, M.; Dackermann, U.; Prasittisopin, L. Machine learning (ML) algorithms for seismic vulnerability assessment of school buildings in high-intensity seismic zones. *Structures* **2024**, *70*, 107639. [CrossRef]
36. Chen, H.; Nemni, E.; Vallecorsa, S.; Li, X.; Wu, C.; Bromley, L. Dual-tasks siamese transformer framework for building damage assessment. In Proceedings of the IGARSS 2022—2022 IEEE International Geoscience and Remote Sensing Symposium, Kuala Lumpur, Malaysia, 17–22 July 2022; IEEE: Piscataway, NJ, USA, 2022; pp. 1600–1603.

37. Chen, Y.; Sun, Z.; Zhang, R.; Yao, L.; Wu, G. Attention mechanism based neural networks for structural post-earthquake damage state prediction and rapid fragility analysis. *Comput. Struct.* **2023**, *281*, 107038. [CrossRef]
38. Soleimani-Babakamali, M.H.; Esteghamati, M.Z. Estimating seismic demand models of a building inventory from nonlinear static analysis using deep learning methods. *Eng. Struct.* **2022**, *266*, 114576. [CrossRef]
39. Harirchian, E.; Lahmer, T. Developing a hierarchical type-2 fuzzy logic model to improve rapid evaluation of earthquake hazard safety of existing buildings. *Structures* **2020**, *28*, 1384–1399. [CrossRef]
40. Li, S.Q. A simplified prediction model of structural seismic vulnerability considering a multivariate fuzzy membership algorithm. *J. Earthq. Eng.* **2024**, *28*, 707–730. [CrossRef]
41. Lallam, M.; Djebli, A.; Mammeri, A. Fuzzy analytical hierarchy process for assessing damage in old masonry buildings: A case study. *Int. J. Archit. Herit.* **2025**, *19*, 408–427. [CrossRef]
42. Kiani, H.; Nasrollahzadeh, K. Fuzzy logic approach for seismic fragility analysis of RC frames with applications to earthquake-induced damage and construction quality. *Structures* **2023**, *55*, 1122–1143. [CrossRef]
43. Alizadeh, M.; Hashim, M.; Alizadeh, E.; Shahabi, H.; Karami, M.R.; Beiranvand Pour, A.; Pradhan, B.; Zabihi, H. Multi-criteria decision making (MCDM) model for seismic vulnerability assessment (SVA) of urban residential buildings. *ISPRS Int. J. Geo-Inf.* **2018**, *7*, 444. [CrossRef]
44. Alemdar, K.D. Seismic risk assessment of transportation networks for the impending Istanbul earthquake with GIS-based MCDM approach. *Nat. Hazards* **2025**, *121*, 10085–10123. [CrossRef]
45. Cruz, A.; Chieffo, N.; Karimzadeh, S.; Ortiz, A.; Sandoval, E.; Lourenço, P.B. Earthquake vulnerability assessment of non-engineered URM residential buildings. *Int. J. Disaster Risk Reduct.* **2025**, *122*, 105476. [CrossRef]
46. Kloukinas, P.; Novelli, V.; Kafodya, I.; Ngoma, I.; Macdonald, J.; Goda, K. A building classification scheme of housing stock in Malawi for earthquake risk assessment. *J. Hous. Built Environ.* **2020**, *35*, 507–537. [CrossRef]
47. Ngoma, I.; Kafodya, I.; Kloukinas, P.; Novelli, V.; Macdonald, J.; Goda, K. Building classification and seismic vulnerability of current housing construction in Malawi. *Malawi J. Sci. Technol.* **2019**, *11*, 57–72.
48. Voyagaki, E.; Kloukinas, P.; Novelli, V.; De Risi, R.; Kafodya, I.; Ngoma, I.; Goda, K.; Macdonald, J.H. Masonry panel testing in Malawi. In Proceedings of the 17th World Conference on Earthquake Engineering, Sendai, Japan, 27 September–2 October 2020.
49. Kloukinas, P.; Kafodya, I.; Ngoma, I.; Novelli, V.; Macdonald, J.; Goda, K. Strength of materials and masonry structures in Malawi. In *Advances in Engineering Materials, Structures and Systems: Innovations, Mechanics and Applications*; CRC Press: London, UK, 2019; pp. 1697–1702.
50. D'Ayala, D.F. Force and displacement based vulnerability assessment for traditional buildings. *Bull. Earthq. Eng.* **2005**, *3*, 235–265. [CrossRef]
51. Vamvatsikos, D.; Allin Cornell, C. Direct estimation of the seismic demand and capacity of oscillators with multi-linear static pushovers through IDA. *Earthq. Eng. Struct. Dyn.* **2006**, *35*, 1097–1117. [CrossRef]
52. Boore, D.M.; Stewart, J.P.; Seyhan, E.; Atkinson, G.M. NGA-West2 equations for predicting PGA, PGV, and 5% damped PSA for shallow crustal earthquakes. *Earthq. Spectra* **2014**, *30*, 1057–1085. [CrossRef]
53. D'Ayala, D.; Speranza, E. Definition of collapse mechanisms and seismic vulnerability of historic masonry buildings. *Earthq. Spectra* **2003**, *19*, 479–509. [CrossRef]
54. Zhang, S.; Zhang, C.; Yang, Q. Data preparation for data mining. *Appl. Artif. Intell.* **2003**, *17*, 375–381. [CrossRef]
55. Peterson, L.E. K-nearest neighbor. *Scholarpedia* **2009**, *4*, 1883. [CrossRef]
56. Montgomery, D.C.; Peck, E.A.; Vining, G.G. *Introduction to Linear Regression Analysis*; John Wiley & Sons: Hoboken, NJ, USA, 2021.
57. Weisberg, S. *Applied Linear Regression*; John Wiley & Sons: Hoboken, NJ, USA, 2005; Volume 528.
58. Tian, Y.; Zhang, Y.; Zhang, H. Recent advances in stochastic gradient descent in deep learning. *Mathematics* **2023**, *11*, 682. [CrossRef]
59. Amari, S.i. Backpropagation and stochastic gradient descent method. *Neurocomputing* **1993**, *5*, 185–196. [CrossRef]
60. Kingsford, C.; Salzberg, S.L. What are decision trees? *Nat. Biotechnol.* **2008**, *26*, 1011–1013. [CrossRef]
61. Sherstinsky, A. Fundamentals of recurrent neural network (RNN) and long short-term memory (LSTM) network. *Phys. D Nonlinear Phenom.* **2020**, *404*, 132306. [CrossRef]
62. Le, X.H.; Ho, H.V.; Lee, G.; Jung, S. Application of long short-term memory (LSTM) neural network for flood forecasting. *Water* **2019**, *11*, 1387. [CrossRef]
63. Cherif, I.L.; Kortebi, A. On using extreme gradient boosting (XGBoost) machine learning algorithm for home network traffic classification. In Proceedings of the 2019 Wireless Days (WD), Manchester, UK, 24–26 April 2019; IEEE: Piscataway, NJ, USA, 2019; pp. 1–6.
64. Kavzoglu, T.; Teke, A. Predictive performances of ensemble machine learning algorithms in landslide susceptibility mapping using random forest, extreme gradient boosting (XGBoost) and natural gradient boosting (NGBoost). *Arab. J. Sci. Eng.* **2022**, *47*, 7367–7385. [CrossRef]
65. Han, K.; Xiao, A.; Wu, E.; Guo, J.; Xu, C.; Wang, Y. Transformer in transformer. *Adv. Neural Inf. Process. Syst.* **2021**, *34*, 15908–15919.

66. Thoyyibah, T.; Haryono, W.; Zailani, A.U.; Djaksana, Y.M.; Rosmawarni, N.; Arianti, N.D. Transformers in machine learning: Literature review. *J. Penelit. Pendidik. IPA* **2023**, *9*, 604–610. [CrossRef]
67. Chicco, D.; Warrens, M.J.; Jurman, G. The coefficient of determination R-squared is more informative than SMAPE, MAE, MAPE, MSE and RMSE in regression analysis evaluation. *PeerJ Comput. Sci.* **2021**, *7*, e623. [CrossRef] [PubMed]

Disclaimer/Publisher's Note: The statements, opinions and data contained in all publications are solely those of the individual author(s) and contributor(s) and not of MDPI and/or the editor(s). MDPI and/or the editor(s) disclaim responsibility for any injury to people or property resulting from any ideas, methods, instructions or products referred to in the content.

infrastructures

MDPI

Article

Seismic Vulnerability Assessment and Prioritization of Masonry Railway Tunnels: A Case Study

Yaser Hosseini [1], Reza Karami Mohammadi [1,*] and Tony Y. Yang [2]

[1] Department of Civil Engineering, K. N. Toosi University of Technology, No. 1346, Vali Asr Street, Mirdamad Intersection, Tehran P.O. Box 15875-4416, Iran; hosseini@email.kntu.ac.ir
[2] Department of Civil Engineering, University of British Columbia, 6250, Applied Science Lane, Vancouver, BC V6T1Z4, Canada; yang@civil.ubc.ca
* Correspondence: rkarami@kntu.ac.ir

Abstract: Assessing seismic vulnerability and prioritizing railway tunnels for seismic rehabilitation are critical components of railway infrastructure management, especially in seismically active regions. This study focuses on a railway network in Northwest Iran, consisting of 103 old masonry rock tunnels. The vulnerability of these tunnels is evaluated under 12 active faults as seismic sources. Fragility curves derived from the HAZUS methodology estimate the probability of various damage states under seismic intensities, including peak ground acceleration (PGA) and peak ground displacement (PGD). The expected values of the damage states are computed as the damage index (DI) to measure the severity of damage. A normalized prioritization index (NPI) is proposed, considering seismic vulnerability and life cycle damages in tunnel prioritizing. Finally, a detailed prioritization is provided in four classes. The results indicate that 10% of the tunnels are classified as priority, 33% as second priority, 40% as third priority, and 17% as fourth priority. This prioritization is necessary when there are budget limitations and it is not possible to retrofit all tunnels simultaneously. The main contribution of this study is the development of an integrated, data-driven framework for prioritizing the seismic rehabilitation of aging masonry railway tunnels, combining fragility-based vulnerability assessment with life-cycle damage considerations in a high-risk and data-limited region. The framework outlined in this study enables decision-making organizations to efficiently prioritize the tunnels based on vulnerability, which helps to increase seismic resilience.

Keywords: seismic vulnerability; railway tunnel; rehabilitation prioritization; tunnel damage; old masonry tunnel; tunnels prioritization

1. Introduction

Railway tunnels are vital transportation infrastructure components, facilitating efficient and reliable transit. However, the structural integrity of these tunnels, particularly those constructed using traditional masonry techniques, has often been compromised by seismic activities. This study investigates a railway network in Northwest Iran, which includes 103 masonry tunnels, each over 50 years old and manually constructed. The Northwest of Iran is a seismic-prone area with several powerful active faults, and there is a lack of research on the integrated vulnerability assessment of railway tunnels in this region.

Past earthquakes have consistently demonstrated the vulnerability of tunnels to various types of damage, including cracking, spalling, and collapse [1–4]. For example, in the 1995 Kobe earthquake, more than 30 tunnels sustained minor damage, and 10 tunnels

needed significant repairs to ensure their safety [5]. During the 1999 Chichi earthquake in Taiwan, damage was reported in 50 tunnels, with 26 experiencing minor damage, 11 suffering moderate damage, and 13 being severely damaged [6]. In the 2008 Wenchuan earthquake with a moment magnitude of 7.8, inspections have revealed that 42 out of 52 tunnels have been damaged. Among these, 20 tunnels have experienced severe damage such as portal collapses, rock falls, and significant lining cracks, necessitating major repair [7]. The 2016 Kumamoto Earthquake in Japan, with a magnitude of 7.3, has caused various types of damage to the Tawarayama tunnel, including lining spalling and collapse, joint failures, groundwater leakage, and pavement deterioration [8]. However, there are numerous reports of tunnel damage caused by earthquakes [9–13], and it is vital to evaluate their seismic vulnerability and prioritize them for retrofitting, especially in old tunnels.

In recent years, there has been a growing body of research focusing on the seismic response of tunnels using a variety of experimental, numerical, and analytical approaches. Tsinidis et al. presented a comprehensive state-of-the-art review, including case studies of actual tunnel responses during earthquakes, shaking-table and centrifuge experiments, and modern numerical models, thereby highlighting current gaps and future research directions [14]. More recently, Wang et al. carried out shaking-table experiments and numerical analyses to investigate the seismic interaction mechanisms between adjacent horizontal parallel tunnels, revealing that tunnel spacing, burial depth, motion type, and soil characteristics significantly influence seismic behavior [15]. Zhao et al. developed three-dimensional numerical models to analyze the dynamic response of curved tunnels subjected to transverse SV-wave incidence, offering insights into deformation and internal force distributions under realistic conditions [16]. Complementing these studies, Lei et al. conducted shaking-table tests on overlapping tunnels simulating oblique intersecting configurations and evaluating structural responses under seismic loading. Collectively, these recent contributions underline the importance of accounting for complex tunnel geometries, soil–structure interactions, and multi-tunnel effects when assessing seismic vulnerability—strengthening the rationale for adopting an integrated prioritization framework as proposed in the present study [17]. In addition, recent studies have begun to address challenges unique to masonry structures. For instance, a study on the seismic retrofitting of a rubble masonry tunnel evaluated alternatives such as steel fiber shotcrete and inner concrete lining, offering insights into effective strengthening strategies for aging masonry tunnels. Meanwhile, post-earthquake investigations of tunnel performance during the February 2023 Kahramanmaraş earthquake sequence revealed that existing seismic risk models could be verified and refined based on real-world behavior, underscoring the need for reliable assessment frameworks, especially relevant to vulnerable or aged tunnels [18].

There are limited studies on old masonry tunnel modeling [19–21]. The existing technical literature is typically focused on modern reinforced concrete tunnel seismic vulnerability assessment [22–26]. Fragility curves serve as a main approach to represent the probability of a tunnel reaching or exceeding a specific damage state given a specific seismic intensity [27]. These curves have been developed using observational data from past earthquakes and analytical tunnel models [28]. Fragility curves provide a probabilistic assessment of tunnel performance under seismic loading and are widely used in vulnerability and risk assessment frameworks such as HAZUS [29]. Argyroudis and Pitilakis [30] proposed a numerical method for analyzing the seismic fragility of shallow tunnels located in alluvial deposits. Huang et al. [31] developed an analytical technique to create seismic fragility curves for rock tunnels by employing support vector machines (SVM), taking into account various uncertainties. Jamshidi Avanaki et al. [32] introduced a set of fragility curves for steel fiber-reinforced concrete used in segmental tunnels. Zhao et al. [33] developed fragility curves for circular tunnels by numerical modeling, taking

into account factors such as the properties of the concrete, the dimensions of the tunnel lining, and the reinforcement ratio. Ansari et al. [34] assess the seismic vulnerability of circular tunnels in Jammu and Kashmir (India), utilizing fragility functions and microzonation to evaluate damage probabilities across different hazard zones.

Other methods based on finite element analysis (FEA) provide a more detailed approach by simulating the seismic response of tunnels specifically [35]. FEA divides the tunnel structure and surrounding ground into small, discrete elements governed by mathematical equations, offering insights into stress distributions, deformation, and potential failure points in tunnel structures. Several studies have applied FEA to different tunnel types, including circular and rectangular tunnels, shallow and deep tunnels, as well as tunnels in soft and rock soils, highlighting tunnel-specific behavior under seismic loading [36–38]. The simplified method for seismic analysis of long tunnels is a practical approach widely used by practitioners. This method generally models the tunnel as a beam supported by mass-spring systems connected to the ground, enabling analytical solutions for seismic response while significantly reducing computational effort compared to FEA [39]. Tunnel-specific applications of simplified methods have been reported in recent studies, demonstrating their effectiveness in predicting tunnel deformation and potential damage during earthquakes [40]. Recent advancements in artificial intelligence (AI) have also introduced new dimensions to seismic vulnerability assessment. Machine learning techniques, including deep learning [41], random forest [42], artificial neural networks [43,44], fuzzy seismic fragility analysis [45], and fuzzy multi-criteria decision-making analysis [46], are used to analyze large and complex datasets for predicting tunnel performance and damage.

As mentioned, the majority of the existing research has concentrated on modern tunnels constructed with reinforced concrete or advanced linings, whereas masonry tunnels—widely used in historical railway networks and still in service in many countries—have received far less attention in terms of seismic vulnerability assessment. Their age, material degradation, and construction techniques make them substantially more fragile than modern counterparts. Furthermore, unlike concrete tunnels, masonry tunnels often exhibit irregular geometries, discontinuities, and weaker interfaces, which exacerbate their susceptibility to seismic damage. This knowledge gap underlines the necessity of studies dedicated to the seismic response and prioritization of masonry tunnels, particularly within critical transportation networks, as pursued in the present research.

However, the mentioned studies have been limited to the seismic vulnerability of one tunnel, and there is no study in the literature that prioritizes tunnels of a large network for seismic retrofitting, especially old railway tunnels. This study aims to address the gaps in existing research by providing an integrated vulnerability assessment of old railway tunnels under seismic excitation and establishing a systematic prioritization framework for their retrofitting. The present study investigates the seismic vulnerability of aging railway network tunnels in northwest Iran, which is a highly seismic-prone area. In this area, there are 103 tunnels, all over 50 years old. Five major active faults and seven micro faults are seismic sources threatening the tunnels. In this study, the term "micro faults" refers to smaller-scale faults that are typically less significant than major faults but can affect seismic activity. The seismic intensities, including peak ground acceleration (PGA) and peak ground displacement (PGD) at each tunnel location, have been calculated based on the seismic scenarios of each fault. The damage index (DI) of the tunnels has been obtained using the fragility curves provided in the HAZUS [29] methodology. Then, a normalized prioritization index (NPI) has been proposed to classify the tunnels for retrofitting. NPI not only takes into account seismic damage but also evaluates damage from the tunnel's lifecycle based on visual inspections. Finally, based on the NPI criteria, the tunnels are prioritized for seismic rehabilitation into

four categories. The findings of this study can significantly improve the safety of railway infrastructure in seismic regions when there are budget limitations for rehabilitation.

The study's remaining sections are organized as follows. Section 2 introduces the network topology of the study area and tunnel locations. Section 3 presents the topology of faults, seismicity characteristics of faults, and seismic intensity measures in the location of each tunnel. Section 4 describes the vulnerability analysis of tunnels. Section 5 develops the procedure for prioritizing tunnels, and Section 6 is the conclusion of this research.

2. Network Topology and Tunnel Location Identification

The railway network examined in this research, located in the northwest region of Iran, is marked on the Google Earth map and displayed in Figure 1. As shown in Figure 1, the railway network that is investigated in this research starts from Zanjan station and finally ends at Jolfa and Razi stations in East and West Azerbaijan provinces. Figure 2 provides a close-up view of tunnel locations and the railway line. Figure 3 provides examples of railway tunnels within the study area.

In the first step, the geographic coordinates (longitude and latitude) of the tunnels need to be extracted. These coordinates will then be used in the next steps to calculate the distance of each tunnel from the faults. The parameters of the tunnels in the network, including the number and type of tunnels, have been obtained from the Railway Organization of the Islamic Republic of Iran. The location of each tunnel has been manually extracted on the Google Earth map with high accuracy. The study area contains 83 tunnels and 20 galleries (in total 103 cases). In railways, galleries are used to prevent rocks and debris from falling onto the trains and tracks. These protective structures, often designed as semi-open tunnels or reinforced shelters, safeguard the railway infrastructure from natural hazards such as rockfalls and landslides. By providing a barrier between the mountain and the railway line, these galleries enhance safety for trains and passengers while also extending the lifespan of the railway tracks and related infrastructure.

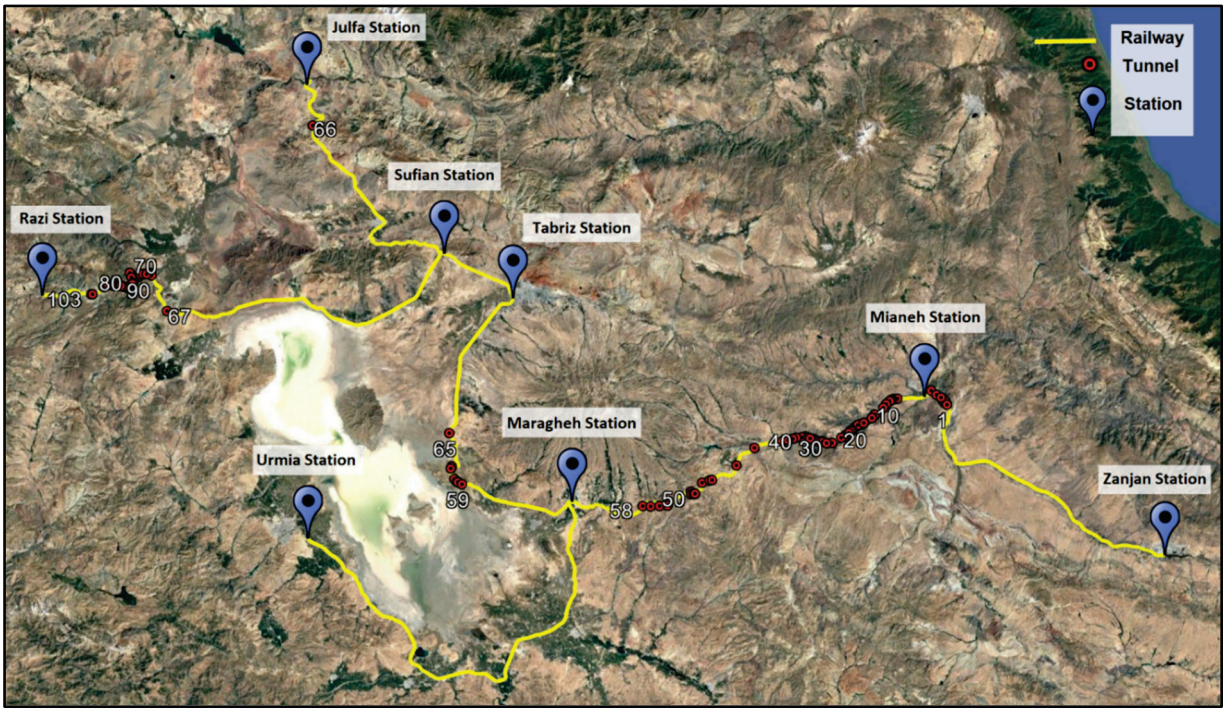

Figure 1. The railway network of the northwest of Iran (Study Area) ©2025 Google Earth.

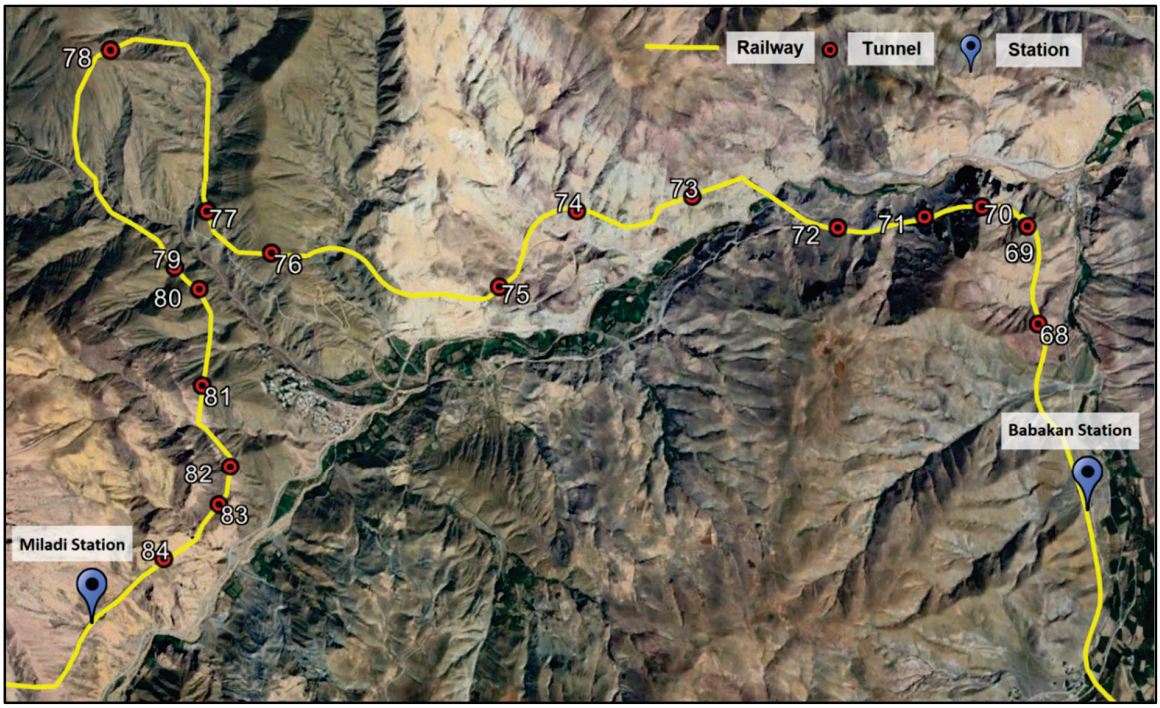

Figure 2. Tunnel locations between Babakan and Miladi stations in Razi axis (close-up view) ©2025 Google Earth.



Figure 3. Examples of railway tunnels in the study area.

3. Identification of Active Faults in the Region and Calculation of Intensity Measures

Earthquakes are primarily caused by the movement of faults in the Earth's crust. Faults are fractures or zones of weakness where blocks of rock can move relative to each other. Over time, tectonic forces accumulate tension along these faults. When this stress surpasses the rock's strength, the energy is released as seismic waves. This sudden release of energy causes the ground to shake, resulting in an earthquake. The location where the fault initially ruptures is known as the focal point, and the point on the Earth's surface directly above it is the epicenter. Faults are categorized into three main types based on geometry and displacement: normal faults (extension of the crust), reverse faults (compression of the crust), and strike-slip faults (lateral movement).

In this research, faults are modeled by multi-segment lines on the ground surface. The main active faults that affect the tunnels have been determined based on the studies of the Seismography Center of the Geophysics Institute of Tehran University. Five active faults, including Tabriz, Maku, Ahar, Bozqush, and Takhte Solaiman, are the main faults that will

affect the tunnels. Due to their significant length and potential to generate high-magnitude seismic events, the maximum ground acceleration (PGA) caused by these faults has been investigated in the vulnerability analysis of the tunnels. To consider the effects of micro-faults on the vulnerability of tunnels, the GIS layer of the fault map has been received from the Geological Organization of Iran, and seven effective micro-faults have been identified in the region. Due to their short length and limited seismic energy release, micro-faults may not generate significant ground acceleration at the regional scale. However, if these micro-faults are located in proximity to tunnels, the resulting ground displacement can pose a serious risk of structural damage [47,48]. For this reason, the maximum ground displacement (PGD) may be more important than acceleration in assessing tunnel damage influenced by micro-faults. Figure 4 shows the location of the tunnels, main faults, and micro-faults near the tunnels.

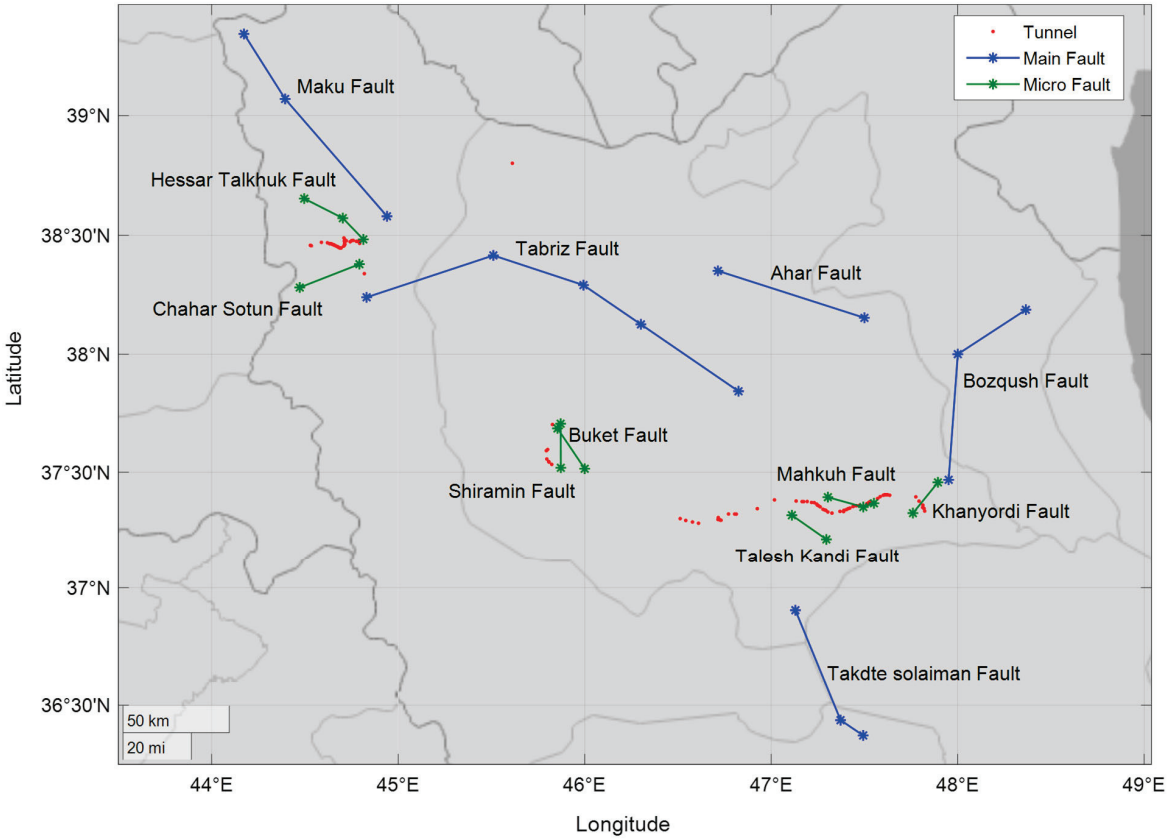

Figure 4. Location of tunnels, main faults, and micro faults.

3.1. Determining Seismicity Parameters of Faults

Determining the seismicity characteristics of faults in a region is an important parameter in estimating seismic vulnerability. To analyze the seismic vulnerability, it is necessary to collect the required data from the seismic sources. Seismicity parameters of faults, such as the geometry of faults, length of faults, faulting mechanism, maximum magnitude, etc., are crucial for understanding earthquake potential hazards and vulnerability assessments.

3.1.1. Determination of Fault Length and Faulting Mechanism

Fault length and faulting mechanism are the most important influencing parameters in predicting the seismic power of faults. In this section, the length of the faults and their mechanism of faulting are extracted from the data taken from the Geological Organization

of Iran and the Seismography Center of the Institute of Geophysics of Tehran University and are shown in Table 1.

Table 1. The length of the faults and their faulting mechanism.

Number	Fault Name	Length (km)	Faulting Mechanism
1	Tabriz	240	Strike-Slip (right-lateral)
2	Bozqush	102	Reverse
3	Maku	100	Strike-Slip (right-lateral)
4	Takhte Solaiman (Tekab)	70	Strike-Slip (right-lateral) and Thrust
5	Ahar	65	Strike-Slip (right-lateral)
6	Chahar Sotun	32	Reverse (thrust)
7	Buket	25	Reverse (thrust)
8	Hessar Talkhuk	23	Reverse (thrust)
9	Shiramin	21	Reverse (thrust)
10	Talesh Kandi	21	Reverse (thrust)
11	Khanyordi	19	Strike-Slip (left-lateral)
12	Mahkuh	17	Reverse

In Table 1, the faults are classified into strike-slip and reverse types. A fault that mostly moves horizontally along the fault line with little to no vertical displacement is known as a strike-slip fault. These faults are characterized by lateral motion, which can be either right-lateral or left-lateral. When compressional forces push the hanging wall upward to the footwall, typically at angles greater than 45 degrees, a reverse fault is formed. A specific type of reverse fault with a shallow dip of less than 45 degrees is called a thrust fault. Both types result from compressional stresses and are significant in mountain regions, capable of generating powerful earthquakes due to the substantial energy released when these faults slip.

3.1.2. Determination of the Maximum Magnitude of the Fault

In this research, the maximum magnitude that the fault has the potential to create has been used to evaluate the damage of tunnels because this is the worst-case seismic scenario in network vulnerability assessment. Several relations are provided to calculate the maximum magnitude of a fault [49]. In this study, four relationships are employed to determine the maximum moment magnitude of faults (M_{max}) according to Equations (1) to (4). These relationships have been respectively proposed by Wells and Coppersmith [50], Nowroozi [51], Ghassemi [52], and Thingbaijam et al. [53]. The detailed formulations are presented in the following.

$$\begin{array}{ll} \text{Strike} - \text{slip} & M_w = 1.21\ Log(L) + 5.16 \\ \text{Reverse} & M_w = 1.22\ Log(L) + 5 \\ \text{Normal} & M_w = 1.32\ Log(L) + 4.86 \end{array} \quad (1)$$

$$All \quad M_w = 0.86\ Log(L) + 5.36 \quad (2)$$

$$\begin{array}{ll} \text{Strike} - \text{slip} & M_w = 0.81\ Log(L) + 5.66 \\ \text{Thrust} & M_w = 0.97\ Log(L) + 5.29 \end{array} \quad (3)$$

$$\begin{array}{ll} \text{Strike} - \text{slip} & M_w = 1.47\ Log(L) + 4.32 \\ \text{Reverse} & M_w = 1.63\ Log(L) + 4.38 \\ \text{Normal} & M_w = 2.06\ Log(L) + 3.55 \end{array} \quad (4)$$

where (L) represents the fault length in kilometers. In this research, to reduce uncertainty, all the above 4 relationships have been used to calculate the maximum magnitude of faults, and their average is considered as the maximum possible magnitude of each fault listed in Table 2.

Table 2. The maximum magnitude of each fault.

Number	Fault Name	Maximum Magnitude of Faults (M_{max})
1	Tabriz	7.7
2	Bozqush	7.2
3	Maku	7.2
4	Takhte Solaiman (Tekab)	7
5	Ahar	7
6	Chahar Sotun	6.7
7	Buket	6.6
8	Hessar Talkhuk	6.6
9	Shiramin	6.5
10	Talesh Kandi	6.5
11	Khanyordi	6.5
12	Mahkuh	6.4

3.1.3. Calculation of the Peak Ground Acceleration and Peak Ground Displacement

Attenuation relationships are employed to calculate the seismic intensity measure, including PGA and PGD. In this research, the attenuation relationship developed by Darzi et al. [54] has been used to calculate the PGA at the location of each tunnel. This attenuation relationship, developed using seismic data from Iranian earthquakes, is highly accurate in determining seismic intensity. The general form of this attenuation relationship is presented in the following Equation (5):

$$Log_{10}(y) = f_M + f_R + f_{site} + f_{SoF} + \varepsilon \tag{5}$$

where

$$f_M = c_1 + m_1 M_w + m_2 M_w^2 \tag{5a}$$

$$f_R = r_1 Log_{10}\left(\sqrt{R^2 + h^2}\right) \tag{5b}$$

$$f_{site} = S_{II} II + S_{III} III \tag{5c}$$

$$f_{SoF} = f_{RV} RV + f_{SS} SS \tag{5d}$$

In Equation (5), y is the seismic intensity measure including PGA (cm/s^2), PGV (m/s), and spectral acceleration SA (cm/s^2) in different periods and f_M is magnitude function, f_R is distance function, f_{site} is a function of soil type and f_{SoF} is a function of the faulting mechanism of faults.

In Equation (5a), M_w is the moment magnitude, and c_1, m_1 and m_2 are regression coefficients. In Equation (5b), R is the closest distance of the structure (in this study, the tunnel) from the fault, r_1 and h are linear regression coefficients. In Equation (5c), II = 1, III = 0 for type soil II ($375 < V_{s30} < 750$) and III = 1, II = 0 for type soil III ($375 < V_{s30}$) which V_{s30} is the shear wave velocity in m/s and S_{II}, S_{III} are regression coefficients. In Equation (5d), parameters RV = 1 and SS = 0 for thrust-reverse fault and RV = 0 and SS = 1 for strike-slip fault, and for other faults, both parameters are equal to zero, also f_{RV} and f_{SS} are regression parameters. All the regression parameters in Equations (5a) to (5b) are provided in Darzi et al. [54].

To calculate the peak ground displacement (PGD) at each tunnel's location, the attenuation relationship developed by Alavi et al. [55] is used. This attenuation relationship is according to Equation (6):

$$Ln(PGD)(cm) = -8 + M_w + \frac{4M_w - 4Ln(R_{ClstD})}{6 + \frac{Ln(R_{ClstD})}{-8 + Ln(R_{ClstD}) + M_w^2 / Ln(R_{ClstD})} + \frac{M_w Ln(R_{ClstD})(M_w - 9)(2M_w - Ln(R_{ClstD}))}{3 - Ln(R_{ClstD})^2 - sin(\gamma) + V_{s30}\ M_w(3M_w - 15)}} \quad (6)$$

where M_w is the moment magnitude, R_{ClstD} is the closest distance from the structure to the fault, V_{s30} is the shear wave velocity at a depth of 30 (m) of the earth and $sin(\gamma)$ is the function of the faulting mechanism as follows:

$$sin(\gamma) = \begin{cases} 0.25 \text{ strike} - \text{slip} \\ -1 \ Normal \\ 1 \text{ Reverse} \end{cases}$$

Since this attenuation relationship is based on a comprehensive database of Iranian earthquakes and provides highly accurate ground displacement estimates, other attenuation relationships are not employed in this study.

4. Tunnel Vulnerability Assessment

Historical earthquakes have demonstrated that tunnels are vulnerable to seismic events. Significant damage can occur due to ground shaking, fault rupture, or soil-structure interaction. For instance, Figure 5 illustrates examples of tunnel damage from various past earthquakes, highlighting the range and severity of impacts that seismic events can have on tunnel structures.

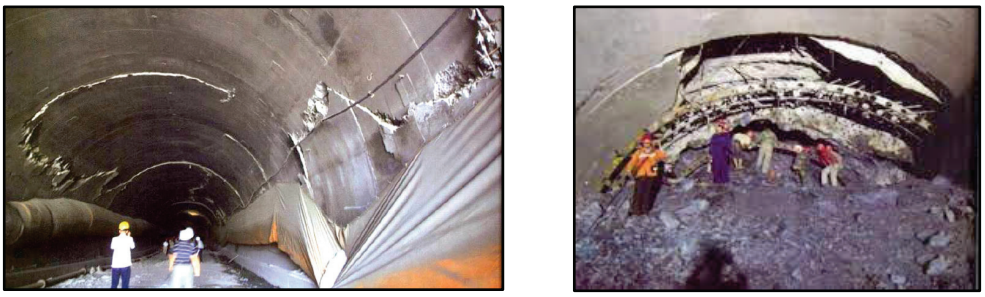

(**a**) (**b**)

Figure 5. Example of tunnel damage in the Wenchuan earthquake 2008 [3], (**a**) Cracking and spalling of the concrete liner near the portal, (**b**) Collapse of the tunnel.

The PGD and PGA at the location of each tunnel have been calculated based on Equations (5) and (6) for the earthquake caused by each of the 12 faults. As an example, Figures 6–11 show the PGD and PGA at the location of each tunnel under the Tabriz fault and Shiramin fault earthquake, respectively.

In this research, the approach for analyzing tunnel vulnerability is based on fragility curves. The fragility curve shows the probability of exceeding a damage state (DS) for various levels of seismic intensity. The fragility curve is usually expressed based on the lognormal distribution according to Equation (7):

$$P_{DS \geq DS_k | IM} = \Phi\left(\frac{ln(IM) - ln(\Theta_k)}{\beta_k}\right) \quad (7)$$

where $P_{DS \geq DS_k | IM}$ is the probability of exceeding the k-th damage state, Φ is the cumulative standard normal probability function, IM is the seismic intensity measure including PGA and PGD, Θ_k and β_k are the median and standard deviation of the k-th damage state. Considering that the tunnels in the study network are rock-type, the fragility parameters of

these tunnels should be extracted from the technical instructions. An identical fragility curve, which is derived from the HAZUS [29] and SYNER-G [56] methodologies, is used to analyze the vulnerability of all tunnels. Generating a specific fragility curve for each tunnel using analytical methods, such as incremental dynamic analysis (IDA), would be more beneficial. This process requires rock mechanics tests to determine the properties of the tunnel lining, such as compressive strength, modulus of elasticity, and other required parameters. However, due to the large number of old masonry tunnels (103 in total) and the limited availability of geotechnical data, tunnel-specific fragility development is out of the scope of this study.

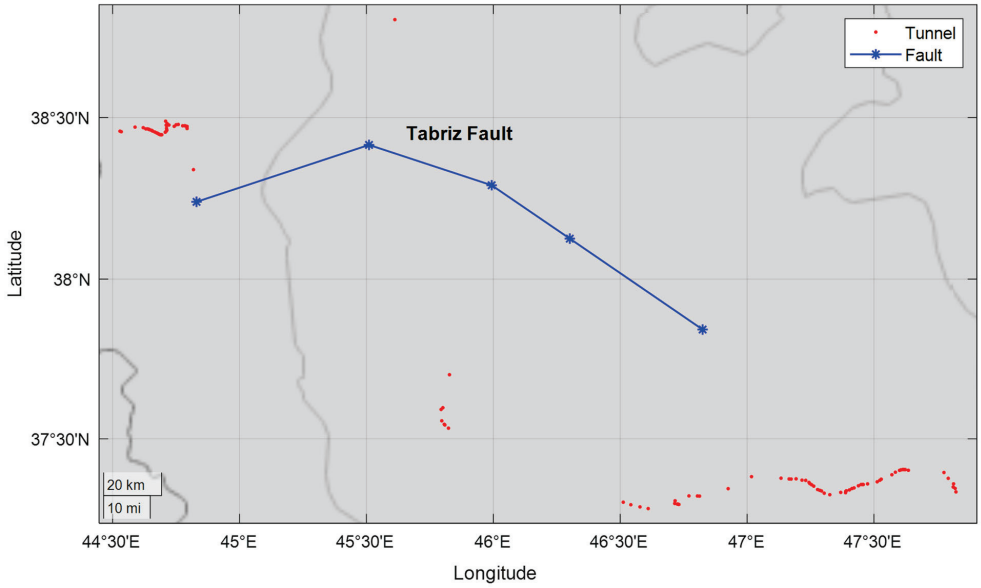

Figure 6. Locations of tunnels and the Tabriz fault.

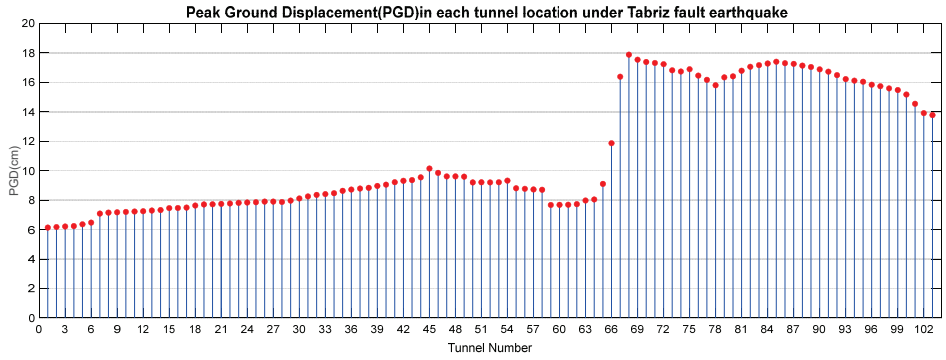

Figure 7. The PGD at the location of each tunnel was caused by the Tabriz fault Earthquake.

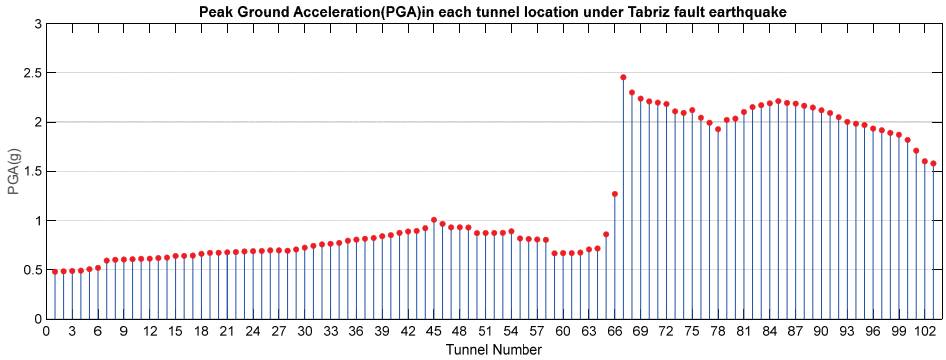

Figure 8. The PGA at the location of each tunnel caused by the Tabriz fault Earthquake.

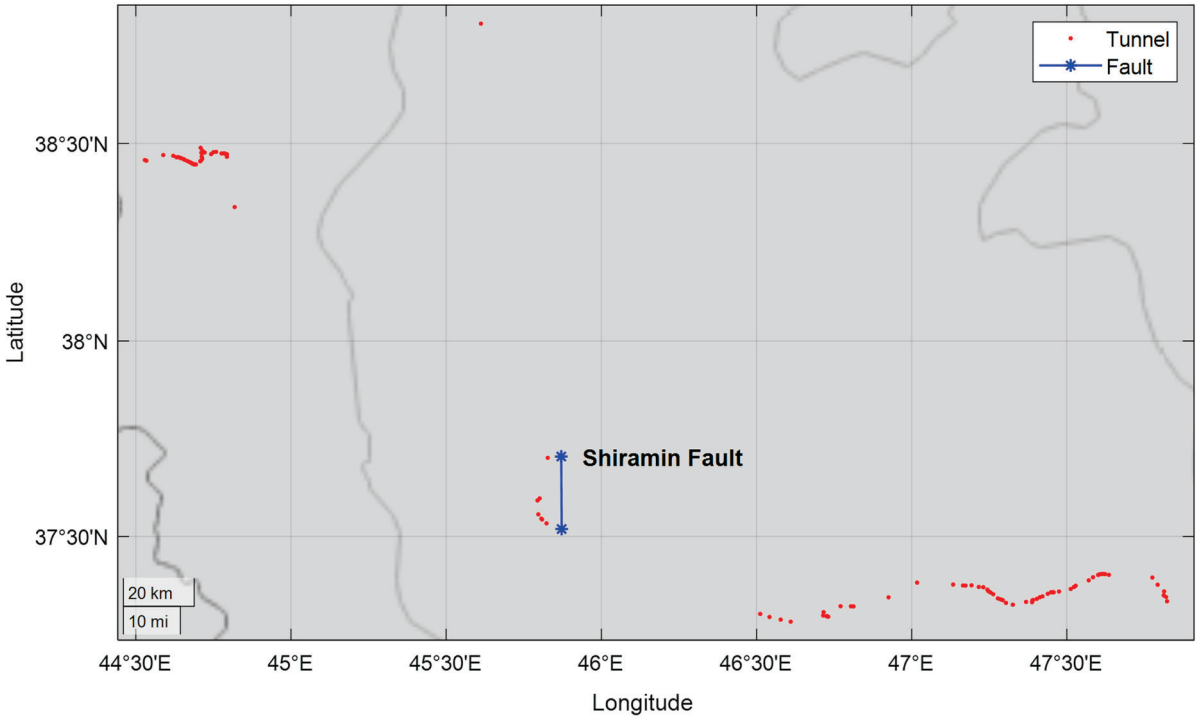

Figure 9. Location of tunnels and the Shiramin fault.

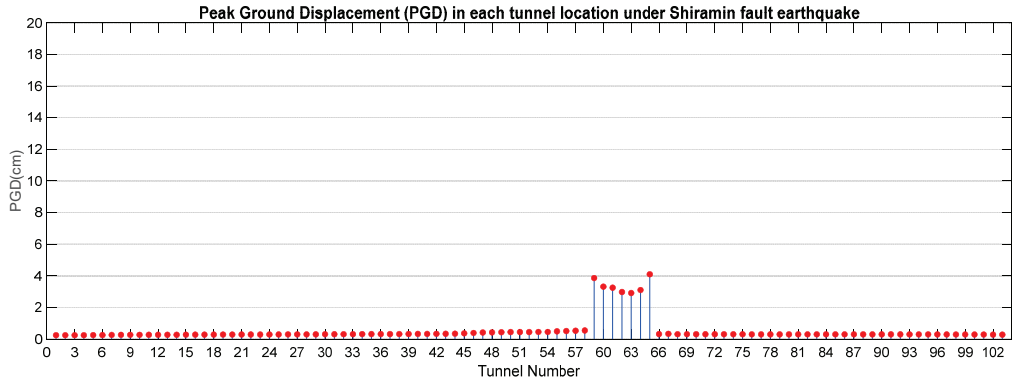

Figure 10. The PGD at the location of each tunnel caused by the Shiramin fault Earthquake.

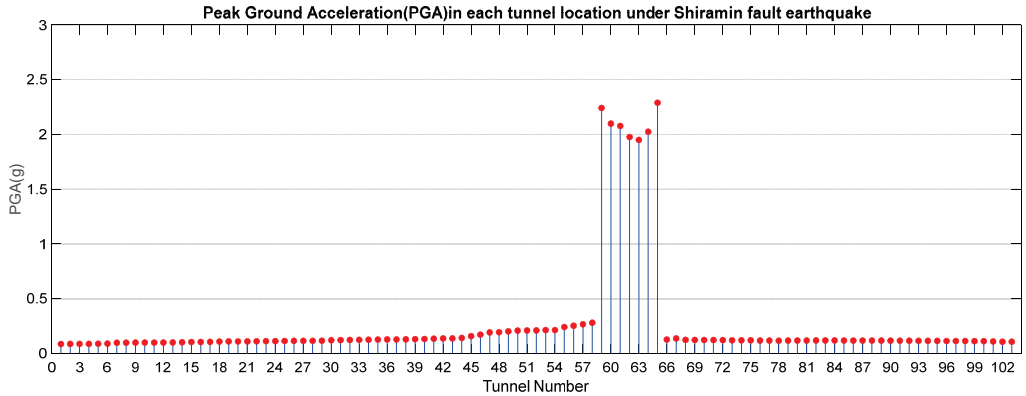

Figure 11. The PGA at the location of each tunnel caused by the Shiramin fault Earthquake.

In the HAZUS technical guide, rock railway tunnels are divided into two general categories: Bored/Drilled for tunnels and Cut/Cover for galleries, which are indicated by

the abbreviations HTU1 and HTU2, respectively. Table 3 shows the damage states defined in HAZUS for rock tunnels. Also, Table 4 shows the values of PGD fragility parameters, including median and standard deviation for rock railway tunnels, provided by HAZUS.

Table 3. Damage states of railway rock tunnels [29].

Damage State	Damage Description
None Damage (k = 0)	---
Slight/Minor (k = 1)	Minor cracking of the tunnel liner (damage requires no more than cosmetic repair) and some rock falling, or slight settlement of the ground at a tunnel portal
Moderate (k = 2)	Moderate cracking of the tunnel liner and rock falling
Extensive/Complete (k = 3)	Major ground settlement at a tunnel portal and extensive cracking of the tunnel liner/Major cracking of the tunnel liner, which may include possible collapse

Table 4. PGD fragility parameters for rock railway tunnels [29].

Classification	Damage State	Θ	β
Bored/Drilled (HTU1) & Cut/Cover (HTU2)	Slight/Minor	6.0	0.7
	Moderate	12.0	0.5
	Extensive/Complete	60.0	0.5

The European collaborative research project SYNER-G has provided PGA fragility parameters for rock railway tunnels. For PGA, SYNER-G is employed because it defines fragility for three damage states (slight, moderate, and extensive), whereas HAZUS provides only two (slight and moderate). This combined approach allows a more realistic evaluation of both displacement- and acceleration-induced vulnerabilities of rock tunnels. In addition, SYNER-G accounts for tunnel condition over its life cycle damage, considering both poor-to-average and good conditions. The damage states described in SYNER-G are similar to those presented in Table 3. Table 5 lists these parameters, including the standard deviation and median of the log-normal distribution, for rock railway tunnels. Given that the tunnels under study have a long lifespan (over 50 years), the SYNER-G fragility curves in poor condition have been used for the PGA parameter. Figures 12–14 show two cases of fragility curves of tunnels and galleries for PGA and PGD parameters.

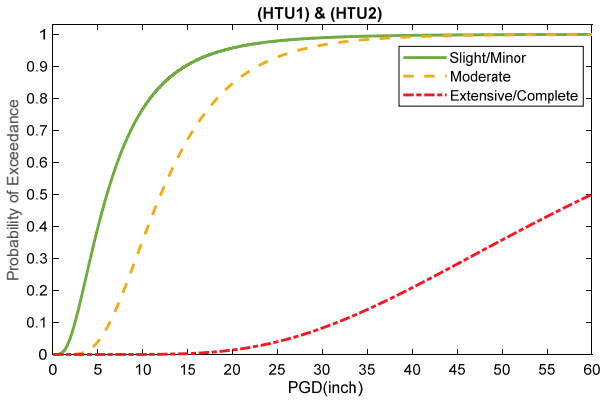

Figure 12. PGD fragility curves for rock tunnels and galleries [29].

Table 5. Fragility parameters for damage caused by PGA in railway rock tunnels [56].

Typology	Damage State	Θ (g)	β
Rock tunnels with poor-to-average conditions	Slight/Minor	0.35	0.4
	Moderate	0.55	0.4
	Extensive/Complete	1.1	0.5
Rock tunnels with good conditions	Slight/Minor	0.61	0.4
	Moderate	0.82	0.4
	Extensive/Complete	NA *	-
Alluvial (Soil) and Cut and Cover Tunnels with poor to average conditions	Slight/Minor	0.3	0.4
	Moderate	0.45	0.4
	Extensive/Complete	0.95	0.5
Alluvial (Soil) and Cut and Cover Tunnels with good conditions	Slight/Minor	0.5	0.4
	Moderate	0.7	0.4
	Extensive/Complete	NA *	-

* Not Available.

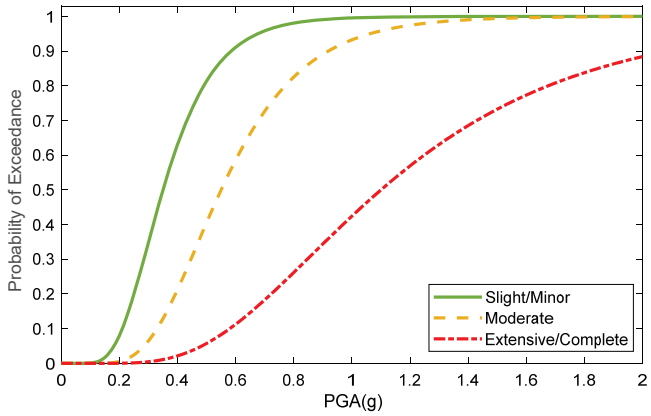

Figure 13. PGA fragility curves for rock tunnels, poor-to-average conditions [56].

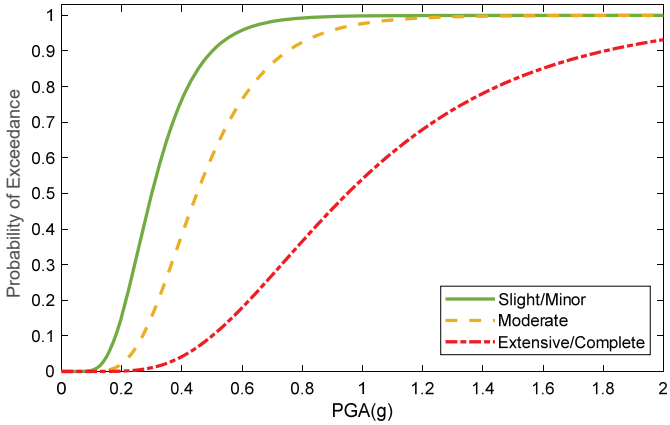

Figure 14. PGA fragility curves for galleries, poor-to-average conditions [56].

Damage Index and Vulnerability Curve

The probability that a tunnel will be in the k-th damage state (P_{DS_k}) is calculated based on the exceedance probability of the damage state obtained from Equation (7). Damage

state probability is computed in accordance with Equation (8), and Figure 15 shows the concept of damage state probability for a specific seismic intensity.

$$P_{DS_0|IM} = 1 - P_{DS \geq DS_1|IM}$$
$$P_{DS_k|IM} = P_{DS \geq DS_k|IM} - P_{DS \geq DS_{k+1}|IM}\ ,\ k = 1,\ 2 \tag{8}$$
$$P_{DS_3|IM} = P_{DS \geq DS_3|IM}$$

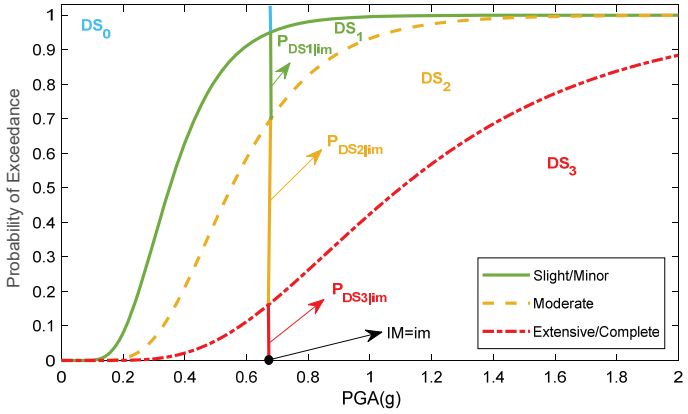

Figure 15. Schematic representation of the damage state probability $\left(P_{DS_k|IM}\right)$.

By mapping the damage states in the interval [0, 3], the expected values of the damage state are calculated as the damage index according to the following equation [25,57,58]:

$$DI = \sum_{k=0}^{3} k * P_{Ds_k|IM} \tag{9}$$

Table 6 shows the relation between the damage state (DS) and the damage index (DI). By calculating the DI for various values of seismic intensity, a diagram called the vulnerability curve is obtained, which is shown in Figures 16 and 17.

Table 6. Relationship between DS and DI.

PGD and PGA	
Damage State	**Damage Index**
Slight/Minor	$0 < DI < 1$
Moderate	$1 < DI < 2$
Extensive/Complete	$2 < DI < 3$

The damage index at the location of each tunnel caused by 12 faults is calculated separately for the seismic intensity measure parameters, i.e., PGD and PGA. As an example, Figures 18 and 19 show the damage index of tunnels for the earthquake resulting from the Tabriz fault. Also, Figures 20 and 21 illustrate the damage index of tunnels under the Shiramin fault earthquake. As shown in Figures 18–21, the Tabriz fault is large and affects almost all the tunnels in the region, while the Shiramin fault is small and affects only seven tunnels near it. According to Figures 18 and 20, the damage index of tunnels is generally less than one (i.e., 0 < DI < 1), indicating that with high probability they do not sustain severe damage under PGD and their performance will be preserved. However, due to the

uncertainties associated with fragility parameters and seismic input, this result should be considered as an expected result rather than an absolute outcome. Figures 19 and 21 show that PGA is the most important parameter in the vulnerability of tunnels, and the probability of severe damage under the PGA is very high in some tunnels. Therefore, the vulnerability of tunnels under PGA must be evaluated, and the tunnels with the higher probability of damage should be given higher priority for seismic rehabilitation.

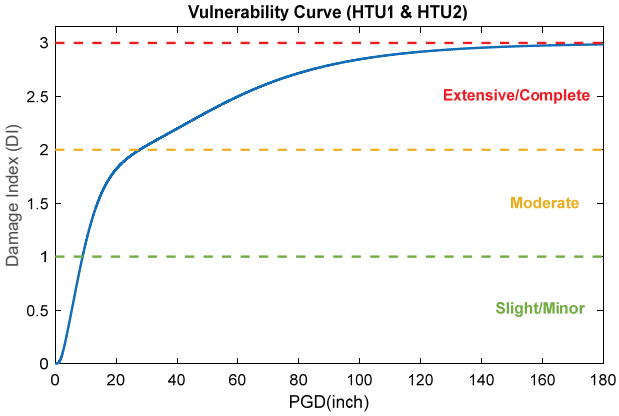

Figure 16. Vulnerability curve of railway rock tunnels under PGD.

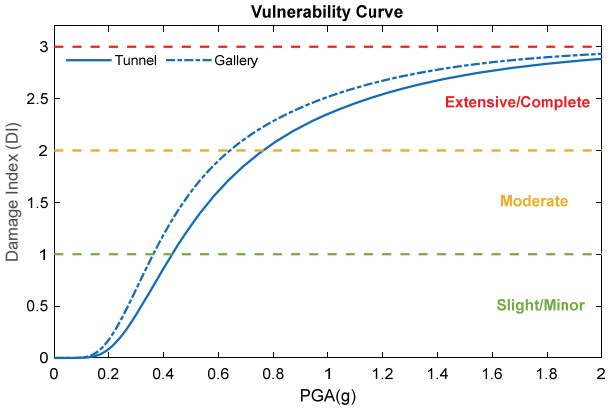

Figure 17. Vulnerability curve of railway rock tunnels under PGA.

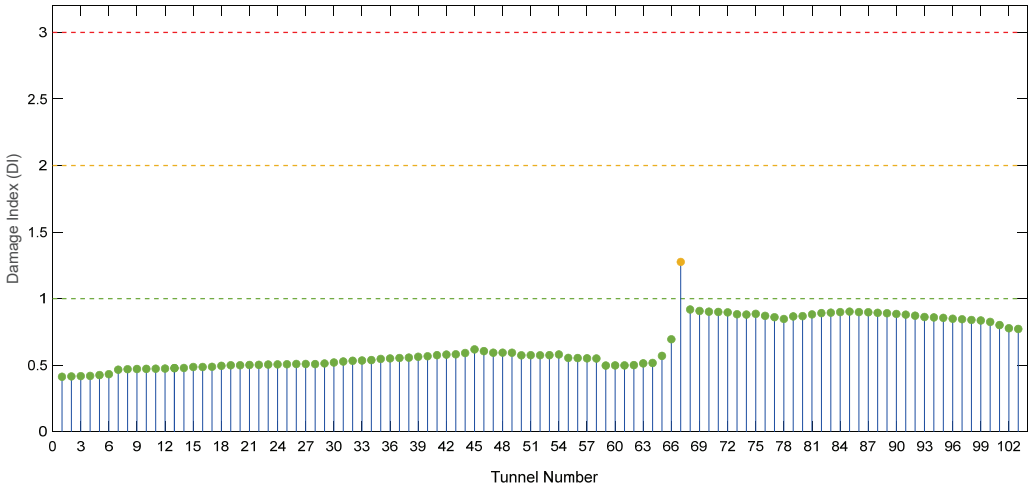

Figure 18. Damage index of tunnels under peak ground displacement (PGD)—earthquake caused by the Tabriz fault.

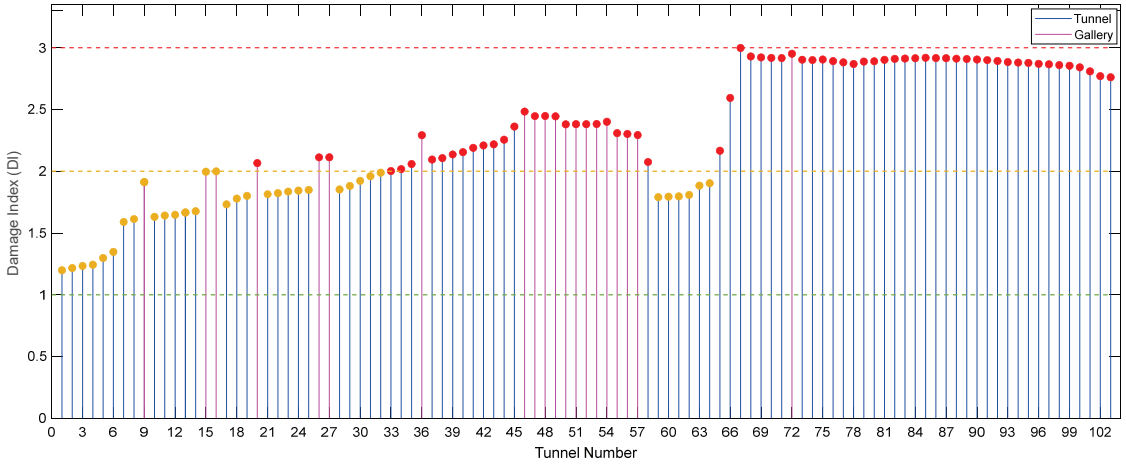

Figure 19. Damage index of tunnels under peak ground acceleration (PGA)—earthquake caused by the Tabriz fault.

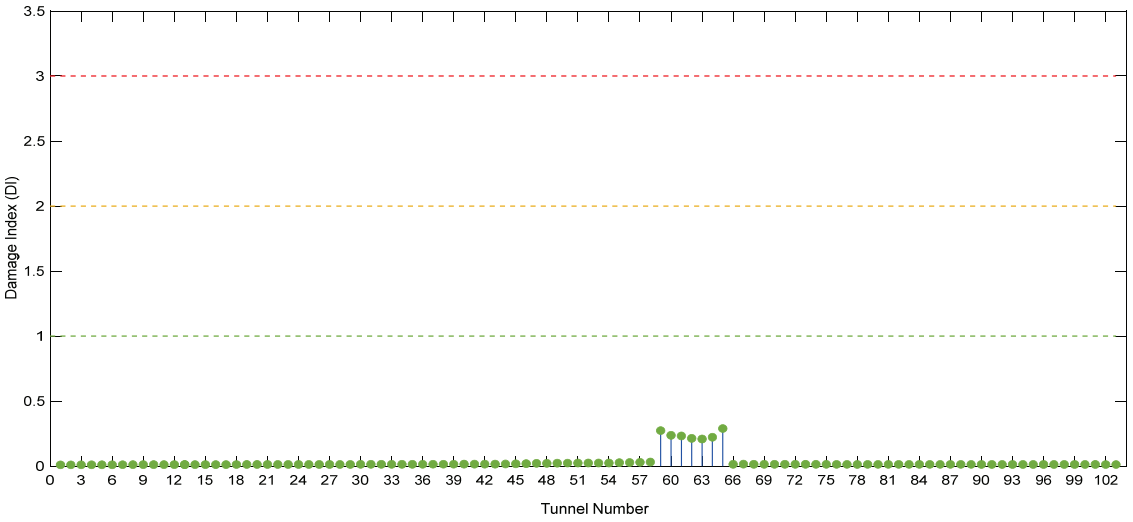

Figure 20. Damage index of tunnels under peak ground displacement (PGD)—earthquake caused by the Shiramin fault.

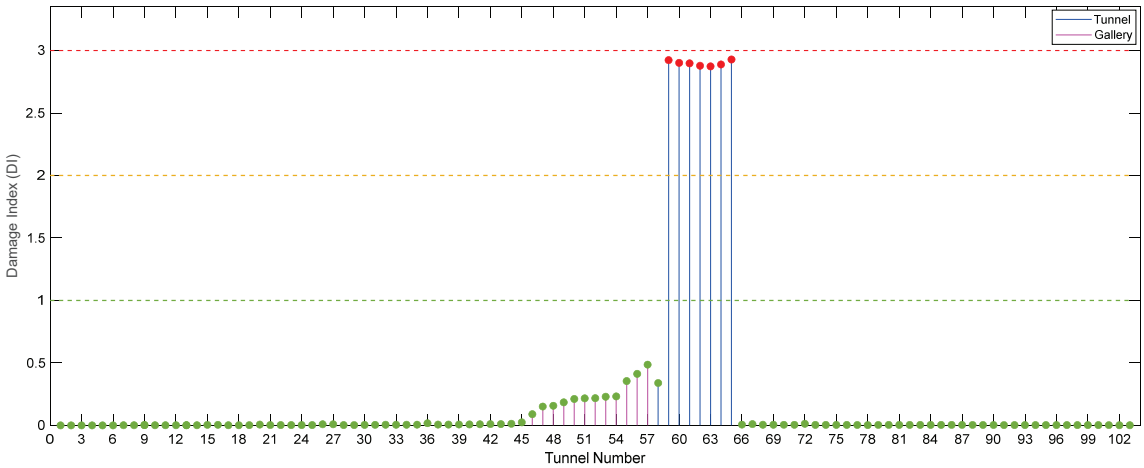

Figure 21. Damage index of tunnels under peak ground acceleration (PGA)—earthquake caused by the Shiramin fault.

5. Tunnels Prioritization

Due to budget limitations, it is not possible to rehabilitate all tunnels simultaneously. It is assumed that all tunnels have equal importance in terms of transportation, and prioritization is only based on their vulnerability, so that the tunnels with high vulnerability are given high priority for rehabilitation. An axis in the network may be more important in terms of transportation. Determining the network's importance weighting requires transportation data, such as the number of travels, and expert opinions, which necessitate further research. To prioritize tunnels, Equation (10) is proposed, which considers life cycle damages in addition to seismic vulnerability.

$$(\mathrm{NPI})_i = 100 \times \frac{(Seismic\ Vulnerability\ Index)_i + (Visual\ Inspection\ Weight)_i}{(Seismic\ Vulnerability\ Index)_{max} + (Visual\ Inspection\ Weight)_{max}} \quad (10)$$

where $(\mathrm{NPI})_i$ is the normalized prioritization index for the i-th tunnel, and the seismic vulnerability index (SVI) is the sum of the tunnel damage index caused by all faults, according to Equation (11):

$$(Seismic\ Vulnerability\ Index)_i = \sum_{j=1}^{N} (DI)_{ij} \quad (11)$$

where j denotes the fault counter and N represents the total number of faults (in this study, N = 12), and $(DI)_{ij}$ is determined according to Equation (9). Some tunnels have been damaged and cracked over time, so the impact of these damages is taken into account in terms of visual inspection weight (VIW) in Equation (10). Based on the visual inspection of the tunnels, the damages are categorized into three levels: high, medium, and low as defined in Table 7, according to engineering judgment. Figure 22 shows examples of tunnel lifetime damages in the study area. To quantify the damage, each damage level listed in Table 7 is given a corresponding weight as outlined in Table 8. In Equation (10), $(Seismic\ Vulnerability\ Index)_{max}$ is the maximum value of the damage index summation, which is equal to 14.127 for the tunnel $i = 16$ and $(Visual\ Inspection\ Weight)_{max}$ is the maximum weight obtained from visual inspection, which is equal to 3 (i.e., Equation (10) is normalized to 17.127). The prioritization criteria for classifying tunnels are defined based on the opinions of transportation managers, as shown in Table 9.

Table 7. Tunnel lifetime damages categorization.

Damage Level	Damage Description
High	Forming large gaps in the expansion joints, Significant ground settlement in the tunnel portal, High instability of the trench at the entrance-exit of the tunnel, Major horizontal cracks in the roof and sidewall of the tunnel, severe breakage and detachment of the lining, and water seepage from the crack, Falling rock cover of the tunnel
Medium	Minor vertical crack in the sidewall, Protrusion of the rock lining, defects of the drainage system, cracking of the tunnel portal and head-wall
Low	Slight cracks in the lining, Slight water leakage from the cover and floor, laxity of the rock lining

Table 8. Damage level weighing.

Damage level	Non	Low	Medium	High
Visual Inspection Weight (VIW)	0	1	2	3



(**a**) (**b**)

Figure 22. Examples of high damage levels: (**a**) severe water seepage, (**b**) a large gap in the expansion joint.

Table 9. Tunnel prioritization criteria based on NPI.

NPI	<60	60–70	70–80	80–100
Prioritization	Fourth Priority	Third Priority	Second Priority	First Priority

Finally, the tunnels are prioritized into four classes, which are shown in Table 10. The results reveal that 10 tunnels are assigned the first priority, 34 tunnels the second priority, 41 tunnels the third priority, and 18 tunnels the fourth priority. Therefore, most tunnels are classified as second and third priority. In Table 10, each of the four main classes is divided into subclasses that provide more precise prioritization. As mentioned, tunnel 16 has the maximum vulnerability index among all tunnels, but it is ranked in priority 1–5, which indicates the effect of visual inspection weight impacts on prioritization. However, Table 10 offers a detailed prioritization for the tunnels in the study area, considering both seismic vulnerability and lifetime damage. This enables decision-making organizations to effectively plan rehabilitation efforts, which play a crucial role in seismic risk reduction.

Table 10. Prioritization of tunnels.

Prioritization		Tunnel ID	Location		SVI	VIW	NPI
Main Class	Sub Class		Longitude	Latitude			
First Priority	1-1	27G *	47.3888725°	37.33695°	14.008	2	93.46
	1-2	33	47.2862134°	37.3399329°	12.067	3	87.97
	1-3	79	44.7109415°	38.4767273°	11.448	3	86.36
	1-4	92	44.6659554°	38.4556661°	11.224	3	83.05
	1-5	16G	47.5229574°	37.3712808°	14.127 **	0	82.48
	1-6	15G	47.5284559°	37.3745134°	14.117	0	82.42
	1-7	20G	47.455641°	37.3580349°	14.110	0	82.38
	1-8	97	44.6428761°	38.4640936°	11.085	3	82.23
	1-9	26G	47.3909989°	37.3383236°	14.012	0	81.81
	1-10	9G	47.6177549°	37.4046646°	13.858	0	80.91

Table 10. *Cont.*

Prioritization		Tunnel ID	Location		SVI	VIW	NPI
Main Class	Sub Class		Longitude	Latitude			
Second Priority	2-1	46G	46.925463°	37.3450689°	10.522	3	78.95
	2-2	36	47.2540745°	37.3573404°	13.519	0	78.92
	2-3	78	44.7087854°	38.4890092°	11.414	2	78.32
	2-4	103	44.5288089°	38.4581489°	10.326	3	77.80
	2-5	72G	44.7760481°	38.4747849°	11.885	1	75.23
	2-6	3	47.8121811°	37.3500978°	10.731	2	74.33
	2-7	69	44.7934602°	38.4728638°	11.717	1	74.25
	2-8	70	44.7871955°	38.4743938°	11.702	1	74.16
	2-9	74	44.7502806°	38.4781241°	11.598	1	73.57
	2-10	17	47.5125891°	37.3664136°	12.55	0	73.30
	2-11	1	47.8230224°	37.3349528°	10.547	2	73.26
	2-12	18	47.4747827°	37.359906°	12.534	0	73.18
	2-13	19	47.4575947°	37.3578464°	12.513	0	73.06
	2-14	21	47.4489004°	37.3579147°	12.495	0	72.95
	2-15	22	47.4385313°	37.3540995°	12.488	0	72.91
	2-16	14	47.570567°	37.3882992°	12.473	0	72.83
	2-17	23	47.4213621°	37.3474904°	12.469	0	72.80
	2-18	81	44.7122991°	38.4669846°	11.466	1	72.78
	2-19	24	47.4131818°	37.3454633°	12.453	0	72.71
	2-20	25	47.3687134°	37.3334281°	12.436	0	72.61
	2-21	13	47.5843369°	37.3962094°	12.409	0	72.45
	2-22	28	47.3880809°	37.3324979°	12.406	0	72.43
	2-23	29	47.3687134°	37.3334281°	12.343	0	72.07
	2-24	12	47.5843369°	37.3962094°	12.336	0	72.02
	2-25	11	47.6007783°	37.4020909°	12.311	0	71.88
	2-26	10	47.6127676°	37.4045944°	12.284	0	71.72
	2-27	8	47.6231588°	37.404382°	12.251	0	71.53
	2-28	67	44.8184487°	38.3393055°	11.228	1	71.39
	2-29	7	47.6354766°	37.4022436°	12.216	0	71.32
	2-30	30	47.3259049°	37.3262241°	12.201	0	71.24
	2-31	93	44.6576581°	38.4584875°	11.175	1	71.09
	2-32	31	47.3038634°	37.3308712°	12.125	0	70.79
	2-33	32	47.2932418°	37.3379031°	12.090	0	70.59
	2-34	34	47.2777637°	37.3423696°	12.037	0	70.28

Table 10. *Cont.*

Prioritization		Tunnel ID	Location		SVI	VIW	NPI
Main Class	Sub Class		Longitude	Latitude			
Third Priority	3-1	35	47.2627236°	37.3528734°	11.972	0	69.90
	3-2	37	47.2471531°	37.3607276°	11.894	0	69.44
	3-3	38	47.2440027°	37.3645507°	11.872	0	69.32
	3-4	39	47.230884°	37.3707979°	11.793	0	68.86
	3-5	68	44.7933504°	38.4663065°	11.732	0	68.50
	3-6	101	44.5882652°	38.4707001°	10.731	1	68.49
	3-7	40	47.216297°	37.3715659°	11.710	0	68.37
	3-8	71	44.7839813°	38.4750096°	11.694	0	68.28
	3-9	73	44.7585971°	38.4787578°	11.622	0	68.86
	3-10	75	44.742485°	38.4730574°	11.581	0	67.62
	3-11	41	47.1929316°	37.3756389°	11.555	0	67.46
	3-12	76	44.7218687°	38.4772168°	11.494	0	67.11
Third Priority	3-13	82	44.7137614°	38.4615824°	11.477	0	67.01
	3-14	83	44.7114959°	38.4584653°	11.467	0	66.95
	3-15	80	44.712759°	38.4756436°	11.458	0	66.90
	3-16	77	44.7145862°	38.4817574°	11.456	0	66.88
	3-17	84	44.7074516°	38.454875°	11.447	0	66.83
	3-18	42	47.1736966°	37.3749494°	11.422	0	66.69
	3-19	85	44.6935974°	38.4470138°	11.373	0	66.40
	3-20	43	47.1655401°	37.3752478°	11.362	0	66.34
	3-21	86	44.6887589°	38.4472039°	11.346	0	66.25
	3-22	87	44.6869354°	38.4473107°	11.337	0	66.19
	3-23	50G	46.7311721°	37.2957757°	8.327	3	66.13
	3-24	88	44.6833984°	38.4484213°	11.318	0	66.08
	3-25	89	44.6809867°	38.4495845°	11.306	0	66.01
	3-26	90	44.6773082°	38.4514458°	11.287	0	65.90
	3-27	91	44.6727701°	38.4531041°	11.262	0	65.76
	3-28	6	47.7756459°	37.3953886°	11.166	0	65.20
	3-29	94	44.6547987°	38.4598328°	11.159	0	65.15
	3-30	95	44.6528074°	38.4608566°	11.146	0	65.08
	3-31	44	47.1336416°	37.3776746°	11.101	0	64.82
	3-32	96	44.6453734°	38.4626368°	11.085	0	64.72
	3-33	98	44.6371453°	38.4653644°	11.048	0	64.51
	3-34	99	44.6307438°	38.4652606°	11.006	0	64.26

Table 10. *Cont.*

Prioritization		Tunnel ID	Location		SVI	VIW	NPI
Main Class	Sub Class		Longitude	Latitude			
Third Priority	3-35	5	47.7925656°	37.3771549°	10.988	0	64.20
	3-36	100	44.620597°	38.4688926°	10.937	0	63.86
	3-37	65	45.8272093°	37.702687°	8.754	2	62.74
	3-38	4	47.8135096°	37.3601098°	10.736	0	62.68
	3-39	2	47.8198049°	37.3458431°	10.625	0	62.04
	3-40	55G	46.6101971°	37.2829517°	7.368	3	60.54
	3-41	102	44.5339999°	38.4564628°	10.358	0	60.48
Fourth Priority	4-1	54G	46.7162409°	37.3073254°	8.237	2	59.77
	4-2	64	45.8012469°	37.5968033°	8.168	2	59.37
	4-3	63	45.7943015°	37.5915815°	8.097	2	58.96
	4-4	57G	46.5419076°	37.2948915°	7.083	3	58.87
	4-5	59	45.8233305°	37.5333576°	7.945	2	58.05
	4-6	60	45.8090345°	37.5431999°	7.914	2	57.89
	4-7	61	45.8067872°	37.5453676°	7.891	2	57.75
	4-8	62	45.7969424°	37.5562349°	7.862	2	57.58
	4-9	45	47.0175084°	37.3825017°	9.823	0	57.35
	4-10	49G	46.7708927°	37.3224207°	8.781	1	57.11
	4-11	51G	46.7270463°	37.2969702°	8.295	1	54.27
	4-12	52G	46.7255171°	37.2968576°	8.281	1	54.19
	4-13	47G	46.8126698°	37.3218622°	9.200	0	53.72
	4-14	48G	46.8041758	37.3222357°	9.113	0	53.21
	4-15	56G	46.5778717°	37.2882203°	7.214	1	47.96
	4-16	53G	46.7147613°	37.2988823°	8.195	0	47.85
	4-17	58	46.5119735°	37.3028089°	5.184	1	36.11
	4-18	66	45.6120502°	38.8015829°	4.781	0	27.91

* G denotes gallery, ** Maximum Seismic Vulnerability Index (SVI).

6. Conclusions

This study aims to assist railway network managers in prioritizing the rehabilitation of tunnels under budget constraints. This research provided an integrated assessment of the seismic vulnerability of masonry railway tunnels in Northwest Iran, highlighting the critical need for prioritization in rehabilitation efforts. The vulnerability of 103 old masonry rock tunnels was examined under the impact of 12 active faults using fragility curves derived from the HAZUS and SYNER-G methodologies. This approach enabled a systematic estimation of the probability of various damage states under different seismic intensities. The expected values of damage states were utilized as a damage index (DI), providing a measure of the severity of potential damage. It was found that tunnels under PGA are more vulnerable than PGD; therefore, the damage caused by PGA was taken into account. A normalized prioritization index (NPI) was proposed, integrating seismic

vulnerability and life cycle damages to effectively prioritize tunnels for rehabilitation. Four main classes were defined to prioritize. The results indicated that 10 tunnels were placed in the first class, 34 tunnels in the second class, 41 tunnels in the third class, and 18 tunnels in the last class. For each main class, a sub-classification was provided, which is essential for resource allocation in budget limitations.

It is hoped that this study will be useful in reducing seismic risk and helping railway transportation network managers. Future research can enhance the proposed framework by incorporating probabilistic seismic hazard models to account for the variability and uncertainties in seismic scenarios across different return periods and ground motion characteristics, such as magnitude. Moreover, developing tunnel-specific fragility curves using incremental dynamic analysis (IDA) can provide a more accurate representation of the seismic response of each tunnel, allowing for more precise damage estimation tailored to the structural and geotechnical characteristics of individual tunnels. Additionally, future studies could consider the effects of material degradation over time, inelastic behavior of lining shell elements, the influence of surrounding rock properties, and the presence of groundwater on the performance and vulnerability of each tunnel. Incorporating these parameters into the seismic assessment can improve the reliability of prioritization results. Expanding the framework to a multi-hazard context and integrating tunnel importance weighting in transportation networks or economic impact analysis would also make the rehabilitation strategy more comprehensive and practical for decision-makers. Furthermore, the methodology could be applied to other types of infrastructure, and the results could be validated using post-earthquake damage data to ensure robustness and generalizability.

Author Contributions: Conceptualization, Y.H. and T.Y.Y.; methodology, Y.H., T.Y.Y. and R.K.M.; software, Y.H.; validation, Y.H., T.Y.Y. and R.K.M.; formal analysis, Y.H.; investigation, Y.H.; resources, Y.H. and R.K.M.; data curation, Y.H.; writing—original draft preparation, Y.H. and R.K.M.; writing—review and editing, T.Y.Y. and R.K.M.; visualization, Y.H.; supervision, T.Y.Y. and R.K.M.; project administration, T.Y.Y.; funding acquisition, Y.H., T.Y.Y. and R.K.M. All authors have read and agreed to the published version of the manuscript.

Funding: This research received no external funding.

Data Availability Statement: Data will be provided upon request.

Acknowledgments: The authors wish to express sincere gratitude for the invaluable assistance and support received from the Islamic Republic of Iran's Railway Company (RAI) during this research.

Conflicts of Interest: The authors declare no conflicts of interest.

Abbreviations

The following abbreviations are used in this manuscript:

IM	Intensity measure
PGA	Peak ground acceleration
PGD	Peak ground displacement
DI	Damage index
DS	Damage state
HTU	HAZUS tunnel
SVI	Seismic vulnerability index
VIW	Visual inspection weight
NPI	Normalized prioritization index

References

1. Huang, S.; Xin, C.; Song, D.; Feng, W.; Liu, X.; Wang, E.; Xu, T.; Xiong, X. Resilience assessment of the seismic damage mechanism of the Daliang high-speed railway tunnel in the 2022 Menyuan earthquake (Mw 6.7) in China. *Transp. Geotech.* **2024**, *49*, 101417. [CrossRef]
2. Callisto, L.; Ricci, C. Interpretation and back-analysis of the damage observed in a deep tunnel after the 2016 Norcia earthquake in Italy. *Tunn. Undergr. Space Technol.* **2019**, *89*, 238–248. [CrossRef]
3. Yu, H.; Chen, J.; Bobet, A.; Yuan, Y. Damage observation and assessment of the Longxi tunnel during the Wenchuan earthquake. *Tunn. Undergr. Space Technol.* **2016**, *54*, 102–116. [CrossRef]
4. Wang, Z.Z.; Zhang, Z. Seismic damage classification and risk assessment of mountain tunnels with a validation for the 2008 Wenchuan earthquake. *Soil Dyn. Earthq. Eng.* **2013**, *45*, 45–55. [CrossRef]
5. Asakura, T.; Sato, Y. Damage to mountain tunnels in hazard area. *Soils Found.* **1996**, *36*, 301–310. [CrossRef] [PubMed]
6. Wang, W.; Wang, T.; Su, J.; Lin, C.; Seng, C.; Huang, T. Assessment of damage in mountain tunnels due to the Taiwan Chi-Chi Earthquake. *Tunn. Undergr. Space Technol.* **2001**, *16*, 133–150. [CrossRef]
7. Shen, Y.; Gao, B.; Yang, X.; Tao, S. Seismic damage mechanism and dynamic deformation characteristic analysis of mountain tunnel after Wenchuan earthquake. *Eng. Geol.* **2014**, *180*, 85–98. [CrossRef]
8. Zhang, X.; Jiang, Y.; Sugimoto, S. Seismic damage assessment of mountain tunnel: A case study on the Tawarayama tunnel due to the 2016 Kumamoto Earthquake. *Tunn. Undergr. Space Technol.* **2018**, *71*, 138–148. [CrossRef]
9. Yao, C.; He, C.; Wang, T.; Chen, C.; Geng, P.; Dong, W.; Yuan, F.; Xu, G. Damages of highway tunnels during 2022 Luding earthquake (Mw = 6.6). *Soil Dyn. Earthq. Eng.* **2024**, *177*, 108357. [CrossRef]
10. Chen, P.; Geng, P.; Chen, J.; Gu, W. The seismic damage mechanism of Daliang tunnel by fault dislocation during the 2022 Menyuan Ms6.9 earthquake based on unidirectional velocity pulse input. *Eng. Fail. Anal.* **2023**, *145*, 107047. [CrossRef]
11. Zhang, X.; Jiang, Y.; Maegawa, K. Mountain tunnel under earthquake force: A review of possible causes of damages and restoration methods. *J. Rock Mech. Geotech. Eng.* **2020**, *12*, 414–426. [CrossRef]
12. Roy, N.; Sarkar, R. A review of seismic damage of mountain tunnels and probable failure mechanisms. *Geotech. Geol. Eng.* **2017**, *35*, 1–28. [CrossRef]
13. Chen, Z.; Shi, C.; Li, T.; Yuan, Y. Damage characteristics and influence factors of mountain tunnels under strong earthquakes. *Nat. Hazards* **2012**, *61*, 387–401. [CrossRef]
14. Tsinidis, G.; de Silva, F.; Anastasopoulos, I.; Bilotta, E.; Bobet, A.; Hashash, Y.M.; He, C.; Kampas, G.; Knappett, J.; Madabhushi, G.; et al. Seismic behaviour of tunnels: From experiments to analysis. *Tunn. Undergr. Space Technol.* **2020**, *99*, 103334. [CrossRef]
15. Wang, G.; Shi, L.; Wang, J. Experimental and numerical studies on the seismic response of adjacent horizontal parallel tunnels. *Soil Dyn. Earthq. Eng.* **2023**, *172*, 107992. [CrossRef]
16. Zhao, H.; Ma, Y.; Yao, X. Dynamic Response of Curved Tunnels under Vertical Incidence of Transversal SV Waves. *Shock Vib.* **2023**, 8561647. [CrossRef]
17. Lei, H.; Wu, H.; Lai, T. Shaking Table Tests for Seismic Response of Oblique Overlapped Tunnel. *Shock Vib.* **2021**, 8816755. [CrossRef]
18. Daraei, A.; Ali, H.F.; Qader, D.N.; Zare, S. Seismic retrofitting of rubble masonry tunnel: Evaluation of steel fiber shotcrete or inner concrete lining alternatives. *Arab. J. Geosci.* **2022**, *15*, 1074. [CrossRef]
19. Chen, H.M.; Yu, H.S.; Smith, M.J. Physical model tests and numerical simulation for assessing the stability of brick-lined tunnels. *Tunn. Undergr. Space Technol.* **2016**, *53*, 109–119. [CrossRef]
20. Idris, J.; Al-Heib, M.; Verdel, T. Numerical modelling of masonry joints degradation in built tunnels. *Tunn. Undergr. Space Technol.* **2009**, *24*, 617–626. [CrossRef]
21. Idris, J.; Verdel, T.; Al-Heib, M. Numerical modelling and mechanical behaviour analysis of ancient tunnel masonry structures. *Tunn. Undergr. Space Technol.* **2008**, *23*, 251–263. [CrossRef]
22. Far, A.M.; Nejati, H.R.; Goshtasbi, K.; Khosrotash, M.; Moosavi, S.A. Seismic fragility analysis for probabilistic risk assessment of underground structures. *J. Earthq. Eng.* **2024**, *29*, 265–287. [CrossRef]
23. Liu, X.; Xu, Q.; Zhou, X.; Wang, J.; Xu, B.; Liu, B. Research on structural defect characteristics and influencing factors for high-fill cut-and-cover tunnels in mountainous areas. *Iran. J. Sci. Technol. Trans. Civ. Eng.* **2024**, *48*, 4409–4422. [CrossRef]
24. Antoniou, M.; Mantakas, A.; Nikitas, N.; Fuentes, R. A numerical case study on the long-term seismic assessment of reinforced concrete tunnels in corrosive environments. *J. Rock Mech. Geotech. Eng.* **2023**, *15*, 551–572. [CrossRef]
25. Tsinidis, G.; Karatzetzou, A.; Stefanidou, S.; Markogiannaki, O. Developments in seismic vulnerability assessment of tunnels and underground structures. *Geotechnics* **2022**, *2*, 209–249. [CrossRef]
26. Zou, Y.; Zhang, Y.; Liu, H.; Liu, H.; Miao, Y. Performance-based seismic assessment of shield tunnels by incorporating a nonlinear pseudostatic analysis approach for the soil-tunnel interaction. *Tunn. Undergr. Space Technol.* **2021**, *114*, 103981. [CrossRef]

27. Hu, X.; Zhou, Z.; Chen, H.; Ren, Y. Seismic fragility analysis of tunnels with different buried depths in a soft soil. *Sustainability* **2020**, *12*, 892. [CrossRef]
28. Andreotti, G.; Lai, C.G. Use of fragility curves to assess the seismic vulnerability in the risk analysis of mountain tunnels. *Tunn. Undergr. Space Technol.* **2019**, *91*, 103008. [CrossRef]
29. HAZUS. *Multi-Hazard Loss Estimation Methodology: Earthquake Model Hazus-MH 2.1 Technical Manual*; Federal Emergency Management Agency: Washington, DC, USA, 2013.
30. Argyroudis, S.A.; Pitilakis, K.D. Seismic fragility curves of shallow tunnels in alluvial deposits. *Soil Dyn. Earthq. Eng.* **2012**, *35*, 1–12. [CrossRef]
31. Huang, G.; Qiu, W.; Zhang, J. Modelling seismic fragility of a rock mountain tunnel based on support vector machine. *Soil Dyn. Earthq. Eng.* **2017**, *102*, 160–171. [CrossRef]
32. Avanaki, M.J.; Hoseini, A.; Vahdani, S.; de Santos, C.; de la Fuente, A. Seismic fragility curves for vulnerability assessment of steel fiber reinforced concrete segmental tunnel linings. *Tunn. Undergr. Space Technol.* **2018**, *78*, 259–274. [CrossRef]
33. Zhao, G.; Gardoni, P.; Xu, L.; Xie, L. Seismic probabilistic capacity models and fragility estimates for the transversal lining section of circular tunnels. *J. Earthq. Eng.* **2023**, *27*, 1281–1301. [CrossRef]
34. Ansari, A.; Rao, K.S.; Jain, A.K. Seismic vulnerability of tunnels in Jammu and Kashmir for post seismic functionality. *Geotech. Geol. Eng.* **2023**, *41*, 1371–1396. [CrossRef]
35. Saleh, A.M.; Rahgozar, M.A. Finite element seismic analysis of soil–tunnel interactions in clay soils. *Iran. J. Sci. Technol. Trans. Civ. Eng.* **2019**, *43*, 835–849. [CrossRef]
36. Luo, H.; Du, L.; Zheng, C.; Yang, X.; Wang, T.; Wang, Y. Study on the performance of mountain tunnel against mainshock–aftershock based on resilience evaluation framework. *Iran. J. Sci. Technol. Trans. Civ. Eng.* **2024**, *48*, 2215–2234. [CrossRef]
37. Junwei, Z.; Wan, Y.; Chenling, Z.; Tuo, C. Seismic stability of a mountain tunnel portal section lining. *Int. J. Geotech. Eng.* **2020**, *14*, 376–394. [CrossRef]
38. Ghadimi, C.A.; Tahghighi, H. Numerical finite element analysis of underground tunnel crossing an active reverse fault: A case study on the Sabzkouh segmental tunnel. *Geomech. Geoengin.* **2019**, *14*, 155–166. [CrossRef]
39. Yu, H.; Yuan, Y.; Bobet, A. Seismic analysis of long tunnels: A review of simplified and unified methods. *Undergr. Space* **2017**, *2*, 73–87. [CrossRef]
40. Reddy, A.D.; Singh, A. A simplistic method for assessing seismic damage in rock tunnels before earthquake: Part 1—Damage prediction and validation using seismic damage classification of tunnels. *Rock Mech. Rock Eng.* **2024**, *57*, 11001–11032. [CrossRef]
41. Ansari, A.; Rao, K.S.; Jain, A.K.; Ansari, A. Deep learning model for predicting tunnel damages and track serviceability under seismic environment. *Model. Earth Syst. Env.* **2023**, *9*, 1349–1368. [CrossRef]
42. Wang, L.; Geng, P.; Chen, J.; Wang, T. Machine learning-based fragility analysis of tunnel structure under different impulsive seismic actions. *Tunn. Undergr. Space Technol.* **2023**, *133*, 104953. [CrossRef]
43. Huang, Z.; Argyroudis, S.A.; Pitilakis, K.; Zhang, D.; Tsinidis, G. Fragility assessment of tunnels in soft soils using artificial neural networks. *Undergr. Space* **2022**, *7*, 242–253. [CrossRef]
44. Jafari, M. System identification of a soil tunnel based on a hybrid artificial neural network–numerical model approach. *Iran. J. Sci. Technol. Trans. Civ. Eng.* **2020**, *44*, 889–899. [CrossRef]
45. Xu, M.; Cui, C.; Zhao, J.; Xu, C.; Zhang, P.; Su, J. Fuzzy seismic fragility analysis of underground structures considering multiple failure criteria. *Tunn. Undergr. Space Technol.* **2024**, *145*, 105614. [CrossRef]
46. Jin, H.; Jin, X. Performance assessment framework and deterioration repairs design for highway tunnel using a combined weight-fuzzy theory: A case study. *Iran. J. Sci. Technol. Trans. Civ. Eng.* **2022**, *46*, 3259–3281. [CrossRef]
47. Trifunac, M.D.; Todorovska, M.I. Note on the useable dynamic range of accelerographs recording translation. *Soil Dyn. Earthq. Eng.* **2001**, *21*, 275–286. [CrossRef]
48. Talebian, M.; Jackson, J. A reappraisal of earthquake focal mechanisms and active shortening in the Zagros mountains of Iran. *Geophys. J. Int.* **2004**, *156*, 506–526. [CrossRef]
49. Kowsari, M.; Ghazi, H.; Kijko, A.; Javadi, H.R.; Shabani, E. Estimating the maximum earthquake magnitude in the Iranian Plateau. *J. Seismol.* **2021**, *25*, 845–862. [CrossRef]
50. Wells, D.L.; Coppersmith, K.J. New empirical relationships among magnitude, rupture length, rupture width, rupture area, and surface displacement. *Bull. Seismol. Soc. Am.* **1994**, *84*, 974–1002. [CrossRef]
51. Nowroozi, A.A. Probability of peak ground horizontal and peak ground vertical accelerations at tehran and surrounding areas. *Pure Appl. Geophys.* **2010**, *167*, 1459–1474. [CrossRef]
52. Ghassemi, M.R. Surface ruptures of the Iranian earthquakes 1900–2014: Insights for earthquake fault rupture hazards and empirical relationships. *Earth-Sci. Rev.* **2016**, *156*, 1–13. [CrossRef]

53. Thingbaijam, K.S.; Martin, M.P.; Goda, K. New empirical earthquake source-scaling laws. *Bull. Seismol. Soc. Am.* **2017**, *107*, 2225–2246. [CrossRef]
54. Darzi, A.; Zolfaghari, M.R.; Cauzzi, C.; Fäh, D. An empirical ground-motion model for horizontal PGV, PGA, and 5% damped elastic response spectra (0.01–10 s) in Iran. *Bull. Seismol. Soc. Am.* **2019**, *109*, 1041–1057. [CrossRef]
55. Alavi, A.H.; Gandomi, A.H.; Modaresnezhad, M.; Mousavi, M. New ground-motion prediction equations using multi expression programing. *J. Earthq. Eng.* **2011**, *15*, 511–536. [CrossRef]
56. SYNER-G. *Guidelines for Deriving Seismic Fragility Functions of Elements at Risk: Buildings, Lifelines, Transportation Networks and Critical Facilities*; Springer: Berlin/Heidelberg, Germany, 2013.
57. Hosseini, Y.; Mohammadi, R.K.; Yang, T.Y. A comprehensive approach in post-earthquake blockage prediction of urban road network and emergency resilience optimization. *Reliab. Eng. Syst. Saf.* **2024**, *244*, 109887. [CrossRef]
58. Hosseini, Y.; Mohammadi, R.K.; Yang, T.Y. Resource-based seismic resilience optimization of the blocked urban road network in emergency response phase considering uncertainties. *Int. J. Disaster Risk Reduct.* **2023**, *85*, 103496. [CrossRef]

Disclaimer/Publisher's Note: The statements, opinions and data contained in all publications are solely those of the individual author(s) and contributor(s) and not of MDPI and/or the editor(s). MDPI and/or the editor(s) disclaim responsibility for any injury to people or property resulting from any ideas, methods, instructions or products referred to in the content.

infrastructures

MDPI

Article

Community-Scale Seismic Vulnerability Assessment of RC Churches: A Simplified Approach for Cultural Infrastructure Resilience

Giuseppe Brandonisio [1] and Muhammad Tayyab Naqash [2,*]

[1] Department of Structures for Engineering and Architecture, University of Naples Federico II, P.le V. Tecchio, 80, 80125 Naples, Italy; giuseppe.brandonisio@unina.it
[2] Civil Engineering Department, Faculty of Engineering, Islamic University of Madinah, Prince Naif Ibn Abdulaziz, Al Jamiah, Medina 42351, Saudi Arabia
* Correspondence: mnaqash@iu.edu.sa or engr.tayyabnaqash@gmail.com

Abstract: This study proposes a simplified, mechanics-based methodology for assessing the seismic vulnerability of reinforced concrete (RC) churches, particularly those with basilica plans and cathedral portal frames such as a repetitive inclined-beam portal frame. The method integrates linear and nonlinear static analyses, plastic limit theory, and capacity spectrum methods to generate seismic risk indices using minimal input data, making it suitable for large-scale screening in low-data conditions. The model is calibrated using the Cathedral of Reggio Calabria and applied to the Church of San Giovanni Battista dei Fiorentini in Naples. Key outputs include simplified capacity curves and performance indicators. The methodology addresses current limitations in conventional approaches by offering an accessible tool for rapid assessment of cultural infrastructure. Future developments may incorporate AI and machine learning (AI/ML) techniques to improve typological classification and enable automated vulnerability screening at the regional scale.

Keywords: seismic vulnerability; reinforced concrete churches; cultural heritage resilience; simplified structural models; community-level assessment; pushover analysis; cathedral portal; earthquake engineering

1. Introduction

Reinforced concrete (RC) churches built in Italy throughout the 20th century represent a significant portion of the nation's cultural infrastructure. While these structures were initially conceived with modern materials and architectural ambitions, their seismic performance has become a growing concern due to aging, design irregularities, and lack of detailed structural documentation. Historically, churches also serve a dual function, not only as places of worship but also as community anchors during post-disaster recovery. This dual role underscores the necessity of ensuring seismic resilience, not just for structural preservation but for maintaining societal continuity.

While several studies have addressed the vulnerability of masonry churches, simplified evaluation frameworks for RC churches remain scarce. Conventional methods, such as nonlinear time-history analysis or finite element modeling, are often impractical due to missing construction data and computational demands. Recent literature [1–3] has highlighted the need for low-data assessment tools. This study addresses this gap by

adapting classical mechanics and limit state theory into a unified, simplified methodology tailored to RC churches with cathedral portal frames.

The innovation lies not only in the simplification of mechanics but also in its application at the community scale, where traditional tools are too resource-intensive. This dual-scale applicability both at building and community level, represents a key innovation of the proposed approach.

Italy's high seismicity, evidenced in regions such as Irpinia, L'Aquila, and Emilia Romagna, has highlighted the vulnerability of both masonry and RC churches) [4,5]. Unlike masonry structures, RC churches—especially those with basilica plans—often exhibit irregular geometries, tall naves, and non-ductile detailing. One recurring structural configuration is the "cathedral portal" frame, a simple yet widely used design consisting of inclined beams and repeated portal frames in the transverse direction. Despite its prevalence, this configuration introduces specific seismic vulnerabilities, particularly in the absence of rigid diaphragms and in the presence of high center-of-mass conditions. Masi [6] performed a seismic vulnerability assessment of gravity-load-designed RC frames typical of mid-20th century Italian buildings, highlighting the high risk associated with structures and the influence of infill configuration on overall seismic performance.

Conventional seismic assessment methods, such as Finite Element Modeling (FEM) or nonlinear time-history analysis, require extensive data and computational expertise, limiting their applicability for large-scale assessments. Several researchers have proposed performance-based methods and local failure mechanisms for masonry churches [1–3], but relatively fewer studies address RC churches with simplified, data-efficient models. This gap is particularly relevant for heritage inventories lacking structural drawings or material records.

To address this challenge, the present study proposes a simplified methodology for evaluating the seismic vulnerability of RC churches characterized by the cathedral portal frame. The approach combines linear and nonlinear static analysis, plastic limit theory, and capacity spectrum methods to generate a vulnerability index using minimal input data. The framework is calibrated with a real-world case study (Reggio Calabria Cathedral) and validated with an application to a typical church in Naples. Designed for rapid deployment, especially in data-scarce conditions, the model serves as a screening tool to prioritize retrofitting and risk mitigation efforts.

Beyond their architectural and historical significance, reinforced concrete churches also serve as critical community landmarks. In the aftermath of seismic events, these buildings often act as informal gathering spaces or aid distribution centers, further underscoring the need to assess their seismic safety not only as isolated structures but as essential components of community-level resilience [7,8].

In practice, churches are frequently used as emergency shelters and community hubs following seismic events. Therefore, their seismic resilience is closely tied to the strength of the surrounding population. This dual role, as cultural artifacts and functional infrastructure, requires a tailored approach to vulnerability assessment that goes beyond conventional engineering practices [9].

One of the central challenges in assessing seismic risk for heritage buildings lies in the lack of detailed structural documentation, particularly for older RC churches. This makes traditional FEM-based approaches resource-intensive and impractical for large-scale applications. The proposed methodology addresses this gap by offering a low-data, high-impact alternative for preliminary vulnerability screening. In doing so, it contributes to a broader urban resilience strategy, where safeguarding cultural infrastructure also means supporting social continuity during crises [10–12].

The PERPETUATE guidelines provide a performance-based framework for assessing seismic vulnerability of heritage masonry structures through displacement-based methods and appropriate modeling strategies for complex architectural forms [10].

This paper also discusses the potential integration of AI and machine learning techniques as a future development to extend the model's scalability and predictive power. By focusing on a typologically recurrent structural form, the methodology offers a replicable and practical solution for assessing the seismic safety of RC churches, an area where traditional analysis methods fall short due to resource and data constraints.

Recent studies on seismic assessment and retrofitting of cultural heritage structures, including masonry and reinforced concrete (RC) churches, have significantly contributed to advancing our understanding of their seismic behavior and vulnerability. Investigations such as those by Tzanakis et al. [13], Hadzima-Nyarko et al. [14], and Almassri and Safiyeh [15] have highlighted the critical role of numerical modeling in evaluating structural performance and retrofitting interventions. Research on seismic retrofitting techniques, including grout injection and RC jacketing, has proven effective in mitigating structural vulnerabilities while preserving architectural integrity.

Moreover, contributions like Sferrazza Papa et al. [16] focus on the role of roofing interventions in seismic performance, emphasizing the trade-offs between timber and reinforced concrete roofs. Davis et al. [17] provide practical insights into meso-scale seismic collapse analyses for historic masonry churches, addressing challenges posed by low-magnitude seismicity. Similarly, pragmatic approaches proposed by researchers like Amarantidou et al. [18] and Cianchino et al. [19] integrate soil–structure interaction (SSI) effects and address the complex interplay between original construction methods and modern retrofitting measures. These works collectively shed light on optimizing interventions for seismic safety and cultural preservation [20].

2. Reinforced Concrete Churches

2.1. General

Between the end of the nineteenth century and the first half of the twentieth century, the architecture of churches proposed new themes essentially linked to the innovations of building techniques and the use of modern construction materials (reinforced concrete, steel, glass, etc.) and in-depth study of technical solutions (visibility, lighting, acoustics, etc.). Even the construction of churches is in abundance in Italy; nevertheless, there is no specific style or configuration. Architects still lack nostalgic forms, uselessly pursued with simplifications, and the contributions of contemporary architecture. The first twenty years of the twentieth century saw the birth of modern architecture based on the explicit use of reinforced concrete structures. The expressive and technical significance of this material marked the most significant architectural achievements of the twentieth century. It allows you to create objects of any shape and size, allowing one to overcome nature's limits [21,22].

2.2. Classification Proposal

The first step in the present work is to identify a possible recurring structural pattern concerning reinforced concrete churches. Therefore, the churches located in Naples were first identified, considering both inside and outside in the historic center. About 534 churches have been identified, with 54 in reinforced concrete. It should be noted that the generic term "churches" includes major churches, small churches, and basilicas inside and outside the historic center. The reinforced concrete churches identified (Figure 1) were classified according to the type of plan (Figure 2) and the position of the bell tower (Figure 3). Classifying churches by structural typology and layout is useful for technical

modeling and provides a framework for prioritizing retrofitting efforts at the city or regional level. This approach enables stakeholders to evaluate vulnerability patterns and focus limited resources on the most at-risk structures, especially in urban centers with dense cultural heritage like Naples [23]. This typological mapping also facilitates comparative risk assessment across cities with similar architectural heritage.

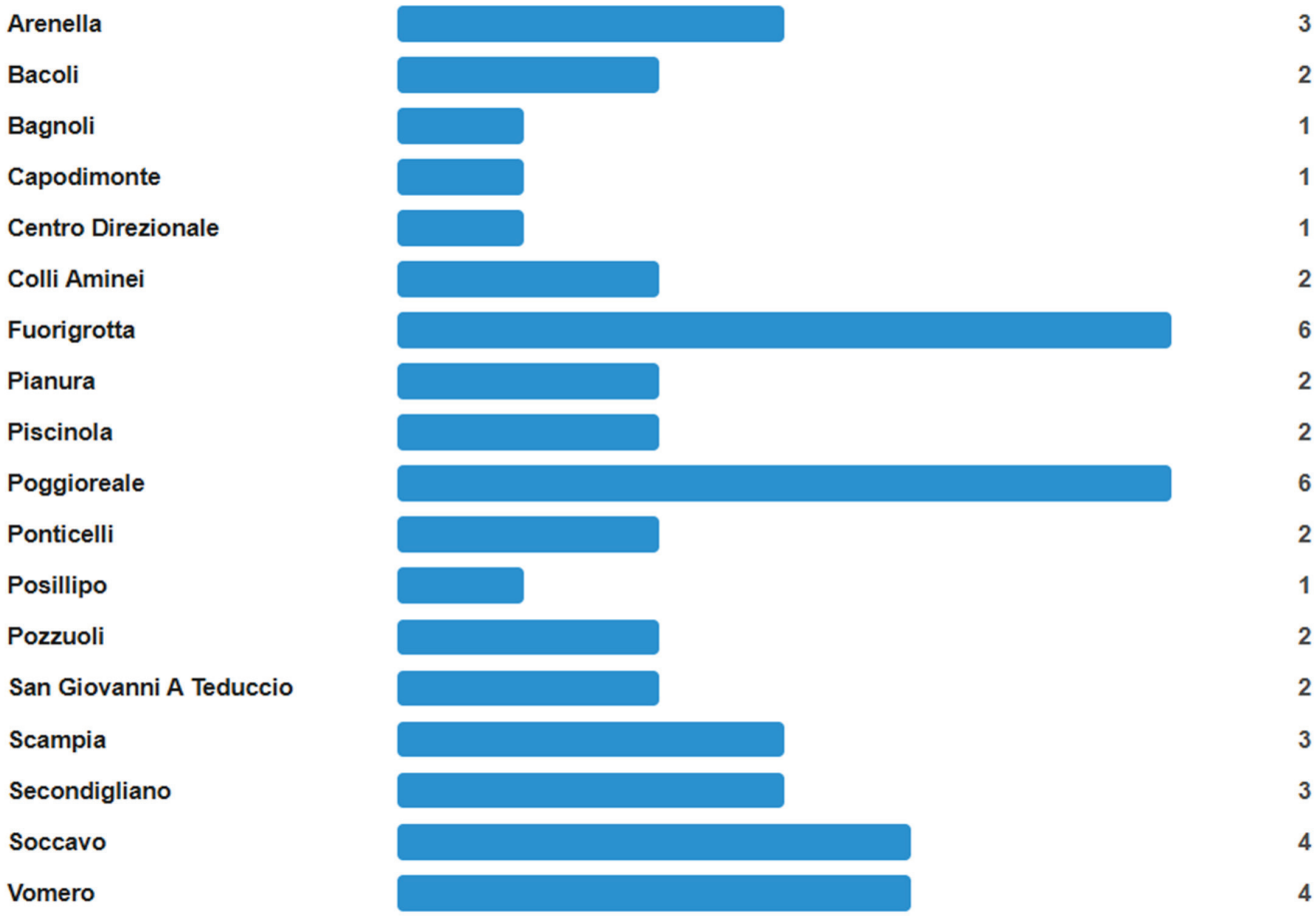

Figure 1. RC churches in Naples grouped according to their location.



Figure 2. Classification of RC churches in Naples based on the type of plan.



Figure 3. Classification of RC churches in Naples based on the position of the bell tower.

This classification provides the basis for modeling across multiple churches and supports the development of a regional vulnerability index.

A frequent approach immediately emerges from a preliminary analysis in 20 of the 54 churches studied. This simple portal pitch roof is known in the literature as the "cathedral portal," a simple scheme, but of great interest in the present work. Therefore, the frequent type of reinforced concrete church has a rectangular plan, a detached bell tower, and a structural calculation scheme of the cathedral portal type. In this work, bell tower-structure interaction is neglected as their analysis is considered beyond the scope of the current paper [24].

2.3. Typological Applicability and Boundaries

The proposed methodology is applicable primarily to RC churches that exhibit a repetitive transverse portal frame system commonly referred to as the "cathedral portal" configuration. These buildings typically possess a rectangular layout, lack rigid diaphragms, and were constructed between the 1930s and 1970s using early reinforced concrete technologies. The model assumes regular spacing of frames in the transverse direction and minimal plan irregularity. Table 1 summarizes the key typological features that define the domain of applicability. Structures falling outside of these boundaries such as those with complex plans, irregular diaphragms, or later construction detailing may require adaptation or alternative assessment methods.

Table 1. Summary of Typological Features and Applicability.

Feature	Applicable Range	Outside Scope
Structural System	Repetitive RC portal frames (cathedral type)	Shear wall systems, irregular hybrid systems
Plan Geometry	Rectangular or near-rectangular	Highly irregular or cruciform plans
Diaphragm Type	Flexible or partially rigid	Fully rigid slabs with modern detailing
Construction Era	~1930–1970	Post-1980 RC buildings with code-compliant details
Documentation Availability	Low to moderate	Fully documented structures (for FEM use)

The development of a structural typology for RC churches provides not only a basis for engineering analysis but also a replicable framework for other historic cities with dense church inventories, enabling comparative vulnerability assessments across regions.

2.4. The Cathedral Portal

The plane frame represents a particular structure consisting of elements loaded in a 2D plane. The members are commonly assembled in polygonal meshes with vertices representing the intersection of the members' axes that converge at the joints. The connection of the frames with the ground is realized with constraints in such a way that makes the system externally isostatic or hyperstatic. The nodes are rigid, and relative rotation at the ends of the members is not allowed. The load condition on a frame consists of several actions acting on the members and nodes. As a result of this load condition, a system of displacements (translations and rotations) is determined in the frame. The most important ones are at the nodes. From literature and in the hypothesis of linear behavior of structure and the possibility of using the principle of superposition, it is possible to calculate both stresses and deformations of all elements that constitute the frame. Figure 4 shows a simple portal frame fixed at the base at A and E with pitches inclined by an angle α. It is possible to calculate both stresses and deformations of all the members of the frame [24].

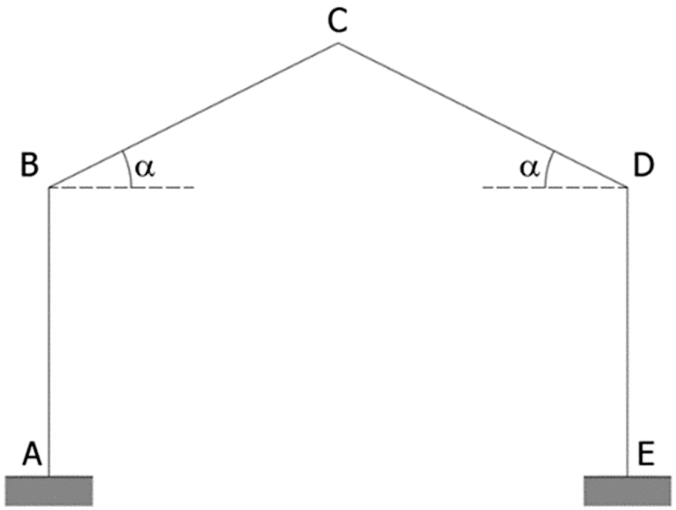

Figure 4. Cathedral schematized portal frame (A, B, C, D and E are nodes).

Since the end of each member has 3 degrees of freedom, the number of variables in such a scheme is given by the product of the number of nodes and the degrees of freedom. Therefore, in total, there are fifteen unknowns. The unknowns are reduced to nine by considering the external constraint conditions (fixed at nodes A and E). The axial stiffness of the members then provides four conditions. Two of these immediately turn into constraint conditions, canceling two other degrees of freedom for the embedded members ($v_A = v_B$; $v_E = v_D$). On the other hand, the other two conditions link the movements together. The seven remaining variables are divided into three rotational (φ_B; φ_C; φ_D) and four translational (u_B; u_C; v_C; u_D) unknowns. Internal relationships link translational unknowns; hence, two are dependent, and two are independent. Five unknowns are obtained by considering only the independent displacements: two translational and three rotational, translating into five additional constraints. The choice of the displacements is not unique. Still, the structure must have fixed nodes for the displacements to be considered independent (Figure 5).

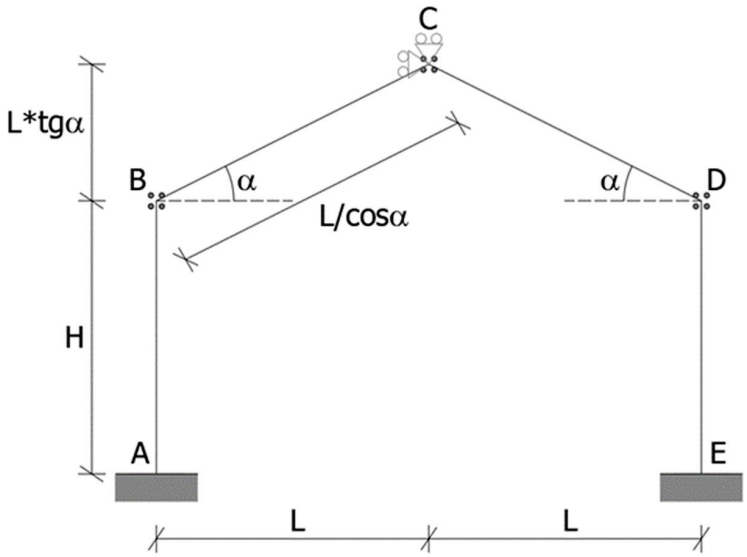

Figure 5. Portal frame with fixed nodes.

Once the stiffness matrix has been calculated and the force F is known, it is possible to calculate the displacement vector δ using Equation (1).

$$\delta_{5\times1} = K^{-1}{}_{5\times5} \times F_{5\times1} \quad (1)$$

Once the displacement vector has been defined, the actual stresses in the frame nodes are calculated. To quickly verify the results, refer to the Handbook of Reinforced Concrete (Santarella) [6], which provides the results in closed form for calculating the stresses of various types of frames.

This typological classification is not only a convenient structural modeling tool but also a practical tool for city authorities. By mapping churches with shared vulnerabilities, stakeholders can plan targeted retrofitting efforts and allocate limited resources more effectively, particularly in densely built historic urban centers like Naples.

3. Seismic Analysis

3.1. General

The Ministerial Decree of 17 January 2018 allows us to apply various analyses to evaluate the seismic capacity of RC buildings, such as (a) Linear static analysis, (b) Linear dynamic analysis, (c) Nonlinear static analysis, and (d) Nonlinear dynamic analysis. It is well known that modeling and verification requirements indicated for ordinary buildings cannot always be applied to structures with architectural heritage. However, it is necessary to evaluate the building's overall seismic behavior with appropriate models. This evaluation can be made by considering the entire church (global model) or limiting the analysis to the parts that constitute it (local model). In the study of seismic behavior of masonry churches, the use of local models appears to be the most appropriate. Hence, it is valuable to do member analysis or divide the church into portions characterized by a substantially independent seismic response and analyze them using local models. However, it is sometimes possible for churches in reinforced concrete to consider either or both global (full church) and local (frame only) models.

Furthermore, a fundamental problem distinguishing churches from other buildings is the absence of a rigid diaphragm, which leads to the difficult choice of the control point to consider. In general, for dissipative systems, the linear analysis methods are very restrictive, as they underestimate the resistance and deformation capacities of the materials. The most suitable methods of analysis are nonlinear ones. Plasticity in the linear elastic behavior approach has often been emphasized based on experimental investigations and surveys on actual structures [25]. It is well known that the elastic material is characterized by a natural state, such that under the action of external forces, it deforms and returns to its original position once the forces have been removed, regardless of the deformation it experienced. Therefore, the elastic material exhibits reversible deformations, accumulating the effort performed by external actions in the form of elastic potential energy, an energy that it returns ultimately during the unloading phase. However, it is well established that in a structure, loads induce local failures in various points (due to concentrated loads, residual stresses in steel profiles, eccentricity in assembly, local stresses, constraint failures in hyperstatic structures, thermal effects, shrinkage, manufacturing, and assembly imperfections) that exceed the permissible values. Although many of the causes listed above are not included in the structural analysis, there is no resulting failure [26].

The focus on transversal analysis is justified by the structural configuration of many RC churches, where portal frames are aligned in the transverse direction and often repeated. Past seismic events have shown that damage tends to concentrate along this axis due to geometric irregularities and lack of diaphragms. This transversal vulnerability is further exacerbated by the absence of rigid diaphragm, which reduces the structure's capacity to redistribute seismic forces in plan. Moreover, this directional focus aligns with observed damage patterns in recent Italian earthquakes, where lateral instability was often concentrated along the transverse axis due to repetitive portal frame configurations.

Unlike standard residential or office buildings, churches often lack rigid diaphragms and regular geometry, making traditional seismic analysis less directly applicable. These architectural idiosyncrasies underscore the need for simplified, yet robust, models that can be adapted to a wide variety of church typologies across Italy.

Given their irregular geometry, lack of diaphragms, and functionally critical role, churches require nonlinear assessment strategies that can capture failure mechanisms not evident in linear approximations [27].

3.2. Plastic Behavior and Theory of Plasticity

Thanks to numerous researchers due to their theoretical and experimental studies in the first half of the 20th century, the so-called theory of plasticity was developed (Heyman et al.) [9]. To easily understand the fundamental aspects of this theory, think of a simple single-axis load test. Considering a steel bar and carrying out a tensile test on it, it is possible to highlight some noticeable features:

Deformations result instantaneously upon application of the load.

The σ-ε plot is linear and reversible until a certain strain value ε_y is achieved, which corresponds to the yield stress σ_y.

For deformation values greater than ε_y, the material has a profoundly different behavior: a slight increase in stress is associated with a generic load increase, whereas high deformations are mostly permanent. Some of them are recovered with a small amount of unloading.

It is evident that, in general, the elastic behavior is characterized by a σ-ε curve that is not necessarily linear but reversible, where the deformations are recovered at unloading. The action depends only on the final value of the deformation. Several materials behave elastically, at least in the first phase of the loading process. Many of them exhibit behavior that can be considered linear with an excellent approximation. On the other hand, plastic behavior is characterized by permanent deformations that occur after the elastic phase. Upon unloading from a plastic phase, the material returns to behave elastically in a specific interval. From these reflections, it can be said that a deformable solid, when subjected to actions, exhibits elastic behavior if the stress is less than the yield stress. By increasing the forces, some parts of the member were plasticized. However, it might still be able to increase loads further in the presence of some portion that still behaves elastically and, therefore, supports the plasticized portion of the member. However, there is a limit to which the elastic part can no longer carry out this beneficial function; therefore, the body comes to "spread," and its deformation reaches the state of collapse [28,29].

3.3. Limit Analysis

The limit analysis, or collapse state, is that part of the plastic theory that allows for the direct evaluation of the collapse load (or limit load) of the structure, i.e., the value of the external load that leads to the loss of bearing capacity [16,30]. It is based on three fundamental assumptions: (a) perfectly plastic elastic material, (b) Small displacements until collapse, and (c) monotonously increasing loads.

This analysis is immediately interpretable and is substantially independent of the numerical parameters on which the calculation procedure depends. The general methods of finding the limit load are based on two fundamental theorems: the static theorem and the kinematic theorem. Based on these two theorems, it can be stated that the collapse multiplier represents the element of separation between two classes: the static ones and the kinematic ones. Therefore, in general, the limit analysis derives from the simple consideration that collapse occurs when the number of plastic hinges causes the structure

to fail. The plastic hinges appear during the progressive increase in loads and therefore fall into a kinematic collapse mechanism. Once the failure configuration with the relative set of plastic hinges has been identified, the structure's analysis is reduced to equilibrium conditions. However, this quick and straightforward way of proceeding requires the failure of some counterparts. The section does not collapse from the hypothesis where the first hinge is formed in a section, and the section does not collapse. Due to the increase in loads, subsequent hinges are formed, and the structure becomes a mechanism (any rotation at the plastic hinges is accepted). In this regard, consider the frame shown in Figure 6, loaded with an equal vertical and horizontal force. All the members are prismatic and have the same section; consequently, they have the exact plastic moment M_p. We can find the limit multiplier λL if the two loads increase proportionally. The system is three times hyperstatic. It follows that complete collapse requires the formation of 4 plastic hinges. The sections indicated that the shear stress is constant. At the same time, the bending moment varies linearly since the members are not loaded [31–34].

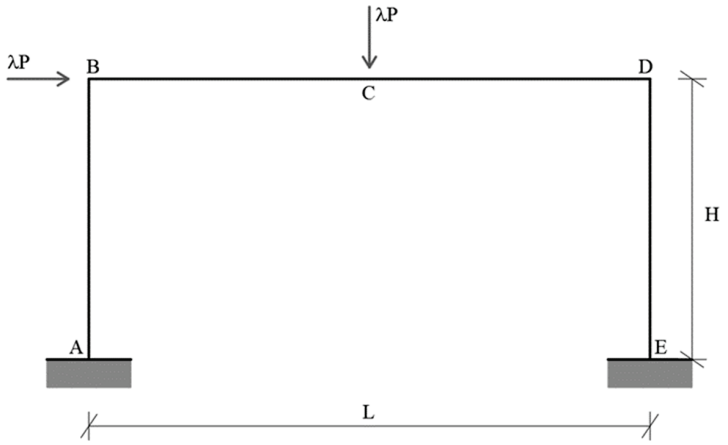

Figure 6. Simple frame encased at the base.

Plastic hinges can, therefore, only form in A, B, C, D, E. Specifically, a first possible mechanism is represented in Figure 7 and is called the "beam mechanism." This mechanism contains only three plastic hinges and is, therefore, a partial mechanism, as it leaves the columns of the portal undeformed. Instead, the mechanism that has the hinges in A, B, D, E (Figure 8) takes the name of the "Storey mechanism." Finally, the mechanism that presents the hinges in A, C, D, and E is represented in Figure 9 and is known as a "mixed mechanism." [6,35–37].

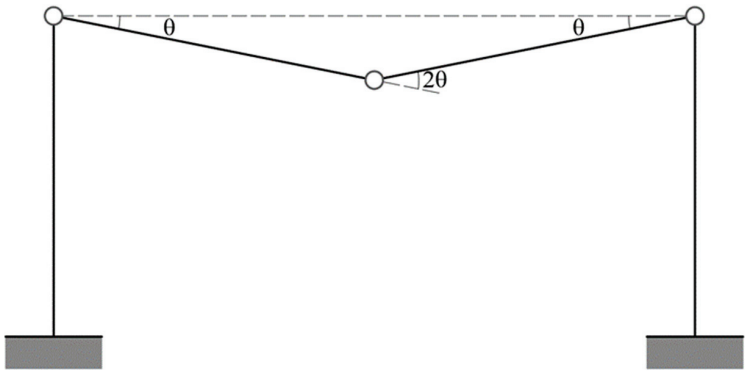

Figure 7. The beam failure mechanism of a plane frame.



Figure 8. Story failure mechanism.

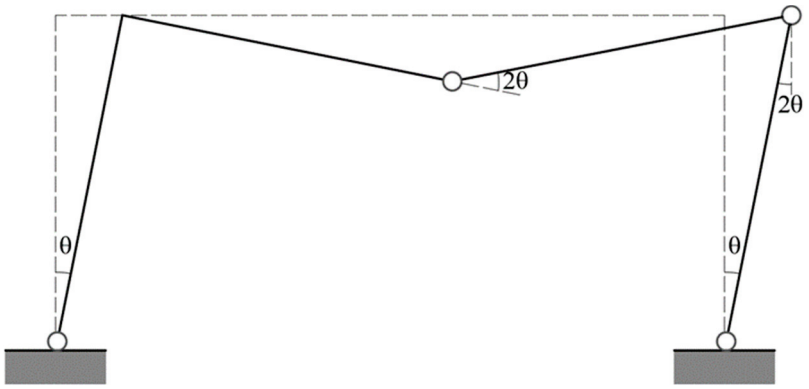

Figure 9. Hybrid failure mechanism.

From this, the kinematic theorem gives the following equations:
Beam Mechanism (Equation (2)).

$$\lambda * P * \frac{L}{2} * \theta = 4 * Mp * \theta \text{ from which } \lambda_{trave} = \frac{8 * Mp}{PL} \tag{2}$$

Soft Storey Mechanism Equation (3).

$$\lambda * P * H * \theta = 4 * Mp * \theta \text{ from which } \lambda_{piano} = \frac{4 * Mp}{PH} \tag{3}$$

Hybrid mechanism Equation (4).

$$\lambda * [(P * H * \theta) + \left(P * \frac{L}{2} * \theta\right)] = Mp * (\theta + +2\theta + 2\theta + \theta) \tag{4}$$

from which $\lambda_{misto} = \frac{6 * Mp}{P\left(H + \frac{L}{2}\right)}$.

If we report on a Cartesian diagram with L/H in the abscissa and $\frac{\lambda * P * L}{Mp}$ Ordinate, we obtain the graph in Figure 10 [25].

For a given L/H value, it is sufficient to estimate the vertical and determine the intersection points with the three curves represented. In this way, the portal collapses indifferently for L/H = 1 according to the Soft Storey and mixed mechanism. If L/H = 2, the collapse occurs according to the mixed mechanism. According to the beam and the mixed mechanism, the portal collapses indifferently if L/H = 4. Finally, if L/H > 4, the collapse occurs according to the beam mechanism (partial collapse). In this case, the determination of various rigid parts making up the rupture mechanism is immediate and

straightforward. In the case of pitched portals, such as those present in the church buildings under consideration, the kinematics of the collapse mechanism is more complex. It is often helpful to use mechanics techniques to find the center of rotation of different parts of the mechanism, which can be suitably combined. In the present paper, the rigorous procedure for calculating the collapse mechanisms of pitched portals is omitted since only the Soft Storey mechanism is considered in a simplified way (See Figure 11), which is identical to that analyzed for the simple frame fixed at the base.

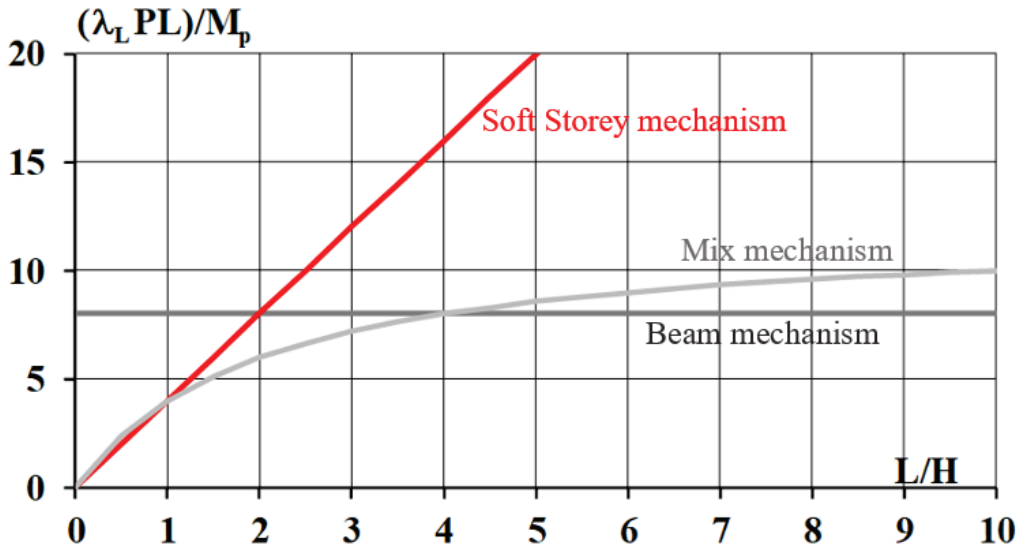

Figure 10. Collapse mechanisms as the L/H ratio varies.

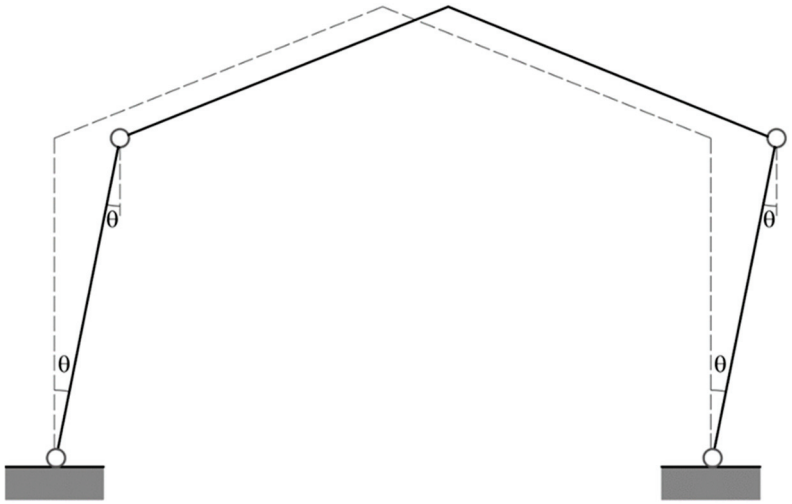

Figure 11. Story mechanism for the cathedral portal.

Building upon the theoretical framework and failure mechanisms discussed, the following section presents a simplified modeling approach tailored to the typological characteristics of RC churches.

4. Proposed Methodology

In this section, a simplified approach that allows the evaluation of the seismic vulnerability of reinforced concrete churches with the cathedral portal as a structural element by analyzing the geometry of the structural complexity is proposed and applied. This approach can be used for large-scale church vulnerability analysis or a general assessment of the seismic safety of the individual church after the evaluation of the Cathedral of Reggio

Calabria. It is ascertained that the critical element for certain types of church buildings is the transverse frame, which can be traced back with a good approximation to the cathedral portal analyzed in this work.

The proposed methodology is intended for preliminary screening purposes only and is not a substitute for code-compliant design or detailed assessment. The methodology is therefore aligned with the scope of preliminary screening assessments under NTC 2018, ensuring that safety margins are maintained while enabling evaluations.

In accordance with the Italian NTC 2018, the use of nonlinear analysis under low documentation conditions (FC = 1.35) is interpreted as acceptable only in the context of vulnerability ranking and prioritization, not for final retrofit design. The method is suitable for both pre-earthquake prevention planning and post-earthquake rapid condition screening of RC churches. Safety margins are preserved, and assumptions are clearly defined to avoid misuse.

The following section presents the simplified model in detail, emphasizing its applicability even with limited input data, making it ideal for rapid assessments at the community scale.

4.1. Description of the Proposed Model

One key advantage of this model is its applicability, even in the absence of detailed structural documentation, which is common in older churches. By relying on basic geometric and material properties, it offers a practical, alternative to full-scale FEM or nonlinear time-history analysis.

First, the frame's geometry is defined by entering its geometric dimensions and sections (Figure 12).

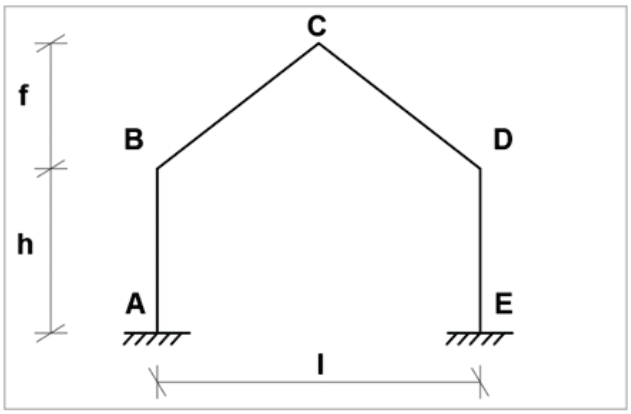

Data	
h [m]	5
l [m]	6
f [m]	2

Section AB		
b [m]	h [m]	E [MPa]
0.3	0.6	28,608

Section BC		
b [m]	h [m]	E [MPa]
0.3	0.5	28,608

Section CD		
b [m]	h [m]	E [MPa]
0.3	0.5	28,608

Section DE		
b [m]	h [m]	E [MPa]
0.3	0.6	28,608

Figure 12. Definition of geometric dimensions.

Then, the materials of the frame under consideration are defined (concrete and steel). Finally, the Confidence Factor is entered, which is based on the accuracy of the data available. Since this is a simplified analysis and does not have detailed information, FC = 1.35 is used, corresponding to a Knowledge Level equal to 1 (Figure 13).

Concrete				Steel			
C		16	20	Type	Aq42		
fcm [MPa]	28	γc	1.5	fyk [MPa]	230		
f_{LC1} [MPa]	11.85	εc [%]	3.5	ftk [MPa]	420	Confidence Factor	1.35
fctm [MPa]	1.90	fctk 95% [MPa]	2.48	f_{LC1} [MPa]	170.37		
fctk 5% [MPa]	1.33	fcfm [MPa]	2.29	Ecs [MPa]	210,000		
Ecm [MPa]	28,608	fctd [MPa]	0.89	εs=εyd [%]	1.86		

Figure 13. Definition of Materials and Confidence Factor.

The longitudinal reinforcements (the number of bars and their diameter in each section) and the stirrups (the diameter and pitch of bars) are incorporated. Finally, the concrete cover used in the calculations is specified (Figure 14).

Segment AB				Segment BC			
b [m]	h [m]	c [m]	d [m]	b [m]	h [m]	c [m]	d [m]
0.3	0.6	0.02	0.58	0.4	0.8	0.02	0.78
ϕ top [mm]	As [mm^2]	Number ϕ top	A's top[mm^2]	ϕ top [mm]	As [mm^2]	Number ϕ top	A's top[mm^2]
20	314	4	1256	18	254.34	3	763.02
ϕ bot [mm]	As [mm^2]	Number ϕ bot	As bot [mm^2]	ϕ bot [mm]	As [mm^2]	Number ϕ bot	As bot [mm^2]
20	314	4	1256	18	254.34	3	763.02
Asw ϕ8 a 2 legged [mm^2]		Spacing [cm]		Asw ϕ8 a 2 legged [mm^2]		Spacing [cm]	
100.52		20		100.52		20	
Segment CD				**Segment DE**			
b [m]	h [m]	c [m]	d [m]	b [m]	h [m]	c [m]	d [m]
0.4	0.8	0.02	0.78	0.5	0.8	0.02	0.78
ϕ top [mm]	As [mm^2]	Number ϕ top	A's top[mm^2]	ϕ top [mm]	As [mm^2]	Number ϕ top	A's top[mm^2]
18	254.34	3	763.02	20	314	4	1256
ϕ bot [mm]	As [mm^2]	Number ϕ bot	As bot [mm^2]	ϕ bot [mm]	As [mm^2]	Number ϕ bot	As bot [mm^2]
18	254.34	3	763.02	20	314	4	1256
Asw ϕ8 a 2 legged [mm^2]		Spacing [cm]		Asw ϕ8 a 2 legged [mm^2]		Spacing [cm]	
100.52		20		100.52		20	

Figure 14. Definition of longitudinal and transverse reinforcement.

Once the input data has been defined, it is possible to conduct linear analysis. Then, the load acting on the roof has been entered, and bending moment, shear, and normal stress diagrams are automatically drawn for the individual members and the overall structure (Figure 15a,b).

The simplified tool automatically generates a simplified resistance domain, as shown in Figure 16.

Finally, a fundamental pushover analysis is performed on the considered frame by referring to point C8.7.2.3 of the Circular of the new NTCs approved with DM 17/01/2018. In general, in the verification of a framed structure, it can be assumed that the collapse of a column occurs when the limit value θ_u (SLC) of the chord rotation is reached, which can be calculated with an analytical formulation provided by the standard. In the verifications of the Life Safety Limit State, the limit value of rotation at the chord θ_u (SLV) is obtained using Equation (5) equal to 75% of the collapse rotation is assumed:

$$\theta_{u(SLV)} = 0.75 * \theta_{u(SLC)} \quad (5)$$

At the Collapse Prevention Limit State, the capacity in terms of total rotation concerning the beam can be evaluated alternatively using numerical models that consider the contributions of concrete, steel, and steel-concrete interaction or employing proven formulas' validity (point C8.7.2.3.2). Multiplying this value by the column's height, it is possible to obtain approximately the final displacement δ_u of the element. For completion,

it is necessary to know the capacity θ_y in terms of total rotation concerning the chord when the yield stress is reached, which can be evaluated using the case of beams and columns C8.7.2.7a and C8.7.2.7b. By multiplying the value thus obtained by the height of the element, it is possible to obtain the displacement δ_y.

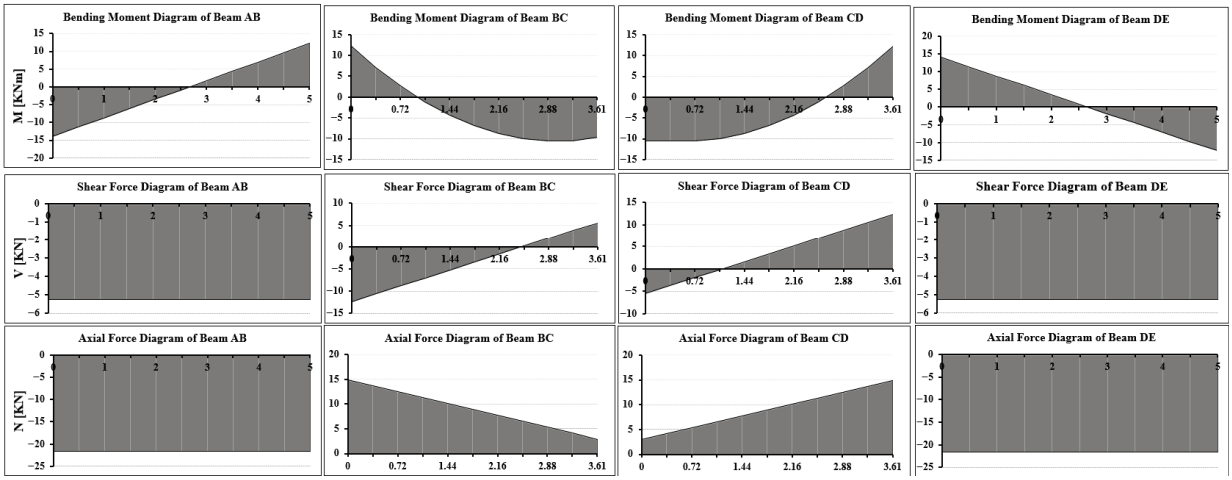

(**a**)

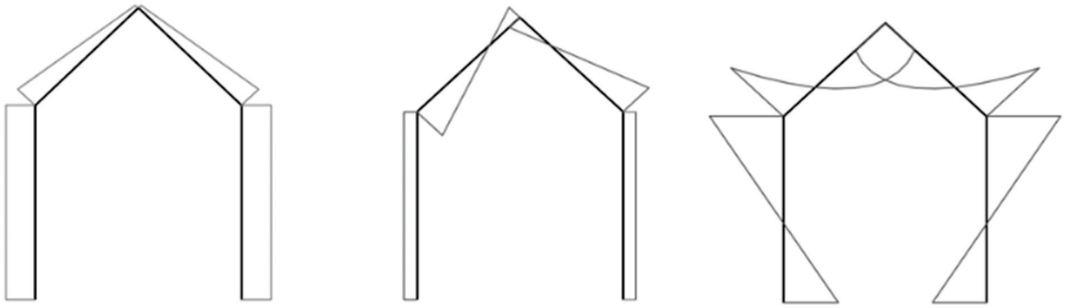

(**b**)

Figure 15. (**a**) Characteristic Stress diagrams of members. (**b**) Characteristic Stress diagrams of members in the frame.

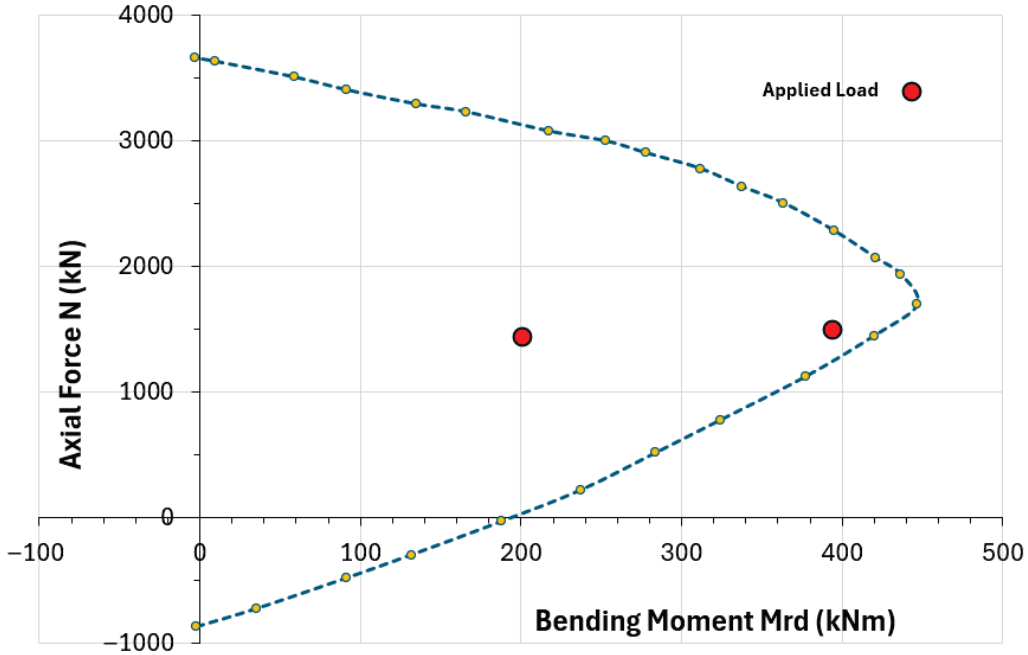

Figure 16. Simplified resistance domain (dotted line shows the envelope).

Assuming the activation of the soft story collapse mechanism, as seen in Figure 11, it is possible to obtain the value of F_u with the simplified formulas of the limit analysis. Finally, by dividing the value of F_u thus obtained by the frame's weight, it is possible to represent the in-plane $F/W - \delta$. The capacity curve can then be represented in the AD plane by modeling the cathedral frame as a one-degree-of-freedom system, compared with the Acceleration Displacement Response Spectrum of the location considered and the seismic risk index calculated (Figure 17) [13–15].

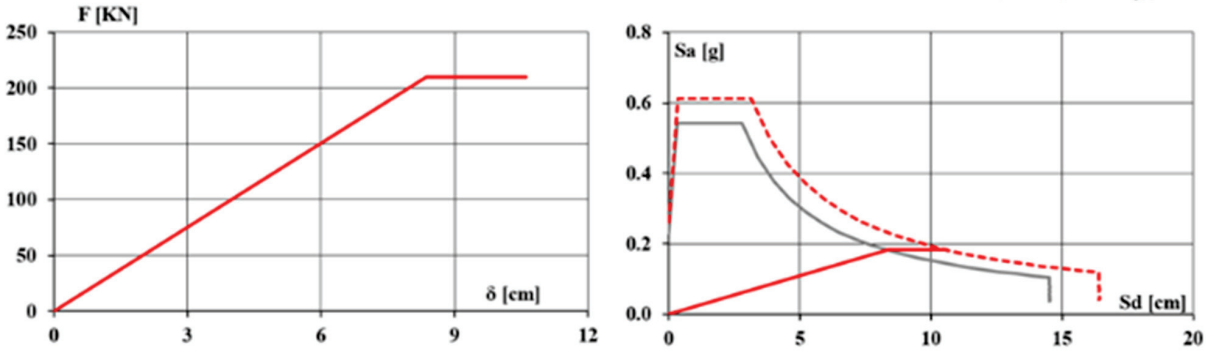

Figure 17. Simplified calculation of the seismic risk index.

4.2. Application of the Proposed Model

4.2.1. Case Study Overview

The proposed model is applied to the Church of San Giovanni Battista dei Fiorentini in Naples, a typical example of mid-20th century RC church architecture. The structure follows a basilical layout with a repetitive cathedral portal frame in the transverse direction. Given the absence of detailed design drawings, reinforcement and material values are estimated based on historical construction practices and regulatory provisions in place at the time.

4.2.2. Input Parameters and Assumptions

Table 2 summarizes the key input parameters used in the analysis. These reflect typical construction assumptions for RC churches built in the 1950s, including longitudinal reinforcement estimates and concrete class.

Table 2. Summary of Input Parameters and Output Results.

Parameter	Value/Assumption
Geometry	Portal height = 10.5 m; span = 12.0 m
Reinforcement (columns)	0.8% longitudinal (AQ42 steel), 2 cm cover
Concrete class	Assumed Rck = 20 MPa
Confidence Factor (FC)	1.35 (Knowledge Level 1, per NTC 2018)
Collapse mechanism	Soft storey (simplified plastic hinge model)
Capacity curve	Bilinear idealization from pushover analysis
ADRS spectrum	Based on Naples seismic zone parameters
Performance points	Life Safety (LS), Collapse Prevention (CP) from NTC 2018
Seismic Risk Index (ζE)	1.13
Displacement Ratio (δu/δmax)	1.37

4.2.3. Capacity Curve and Risk Index Derivation

The capacity curve is derived using a simplified pushover analysis of the cathedral portal frame, assuming a soft-storey failure mechanism. The bilinear curve captures both

elastic and plastic deformation stages. The ultimate displacement (δu) is estimated using chord rotation limits from NTC 2018 (θu), while the yield displacement (δy) is calculated using simplified formulations for RC columns.

The seismic risk index (ζE) is computed as the ratio of spectral capacity to demand at the Life Safety Limit State. A comparison with the ADRS spectrum is used to assess performance. The values obtained for the case study ζE = 1.13 and δu/δmax = 1.37 suggest that the structure meets minimum performance thresholds but may require further investigation for retrofit prioritization.

While tailored to a specific church, the process used here can be replicated across a broad inventory of similar structures, laying the groundwork for a city-wide vulnerability index that supports strategic retrofitting and emergency planning. This section is related to the proposed calculation model applied to the Church of San Giovanni Battista dei Fiorentini, as shown in Figure 18, built in 1952 in Piazza degli Artisti in Vomero, Naples.



Figure 18. Church of S. Giovanni Battista dei Fiorentini, Piazza degli Artisti, 1952.

For this purpose, a simplified analysis is carried out based on available information, assuming sections and reinforcements compatible with the state-of-the-art rules and the regulatory provisions at construction. The first step is to define the city of Naples's seismic hazard parameters. The elastic spectra are determined based on these parameters in terms of accelerations and displacements; therefore, the ADRS spectrum (Figure 19). The Comparison with ADRS is shown in Figure 20.

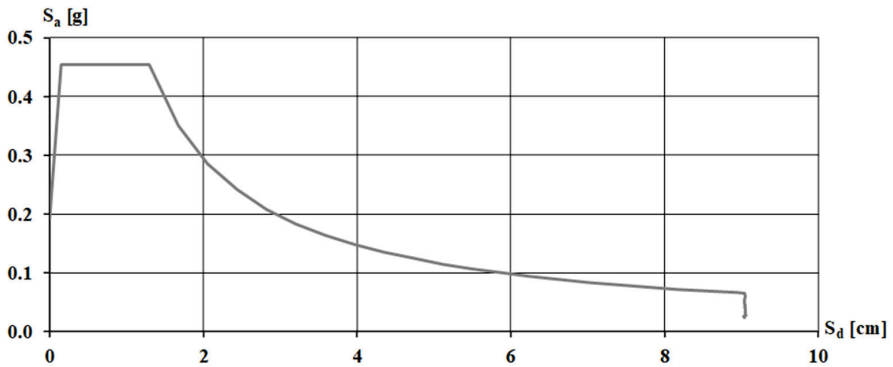

Figure 19. Acceleration Displacement Response Spectrum of the city of Naples.

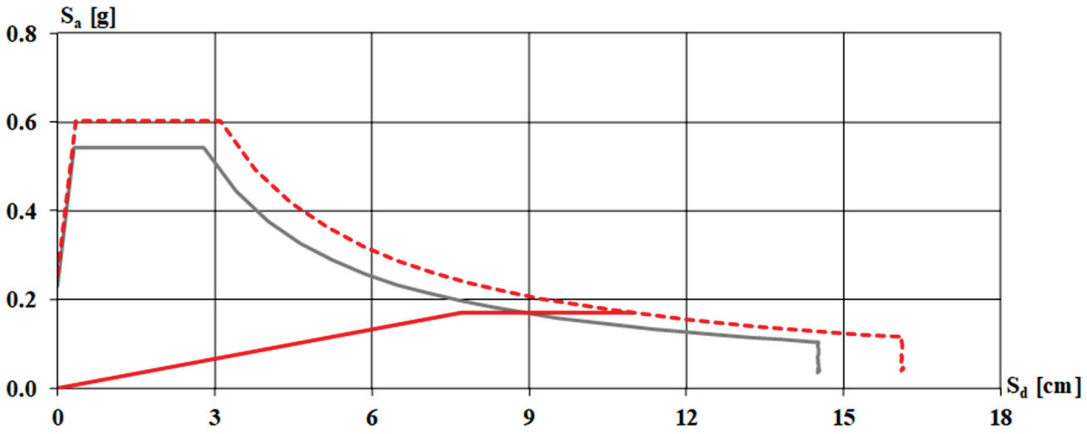

Figure 20. Comparison with ADRS.

Once the geometric dimensions have been entered, it is possible to note that at the time of construction, the RD 16/11/1939 was in force, which requires providing a minimum longitudinal reinforcement of 0.8% Ac (if Ac < 2000 cm^2) and 0.5 Ac (if Ac > 8000 cm^2) for the columns. The pitch had to be at least 1/2 of the column area, and the concrete cover was 2 cm. No specific information regarding the size and minimum reinforcement of the beams is reported. In the 1950s, the most widely used steel was AQ 42 type [16]. Inserting the above data results in the diagrams of the characteristics stress and the simplified resistance domain, which can be used for preliminary and quick verification.

Figure 21 presents an idealized force–displacement (F–δ) curve representing the lateral seismic response of a reinforced concrete (RC) cathedral portal frame. The bilinear shape captures both the initial elastic stiffness and the post-yield plastic behavior of the structure. Key performance points are identified: the Yield Point (red), where the frame transitions from elastic to inelastic behavior; Life Safety (LS) (orange), indicating the deformation level at which significant structural damage is expected but collapse is avoided; and Collapse Prevention (CP) (green), marking the ultimate deformation capacity before instability. These thresholds are crucial for nonlinear static (pushover) analysis and are used to derive the seismic risk index and performance level of RC churches. The diagram also delineates the Elastic and Plastic regions, providing a simplified but informative visualization of structural capacity under increasing seismic demand.

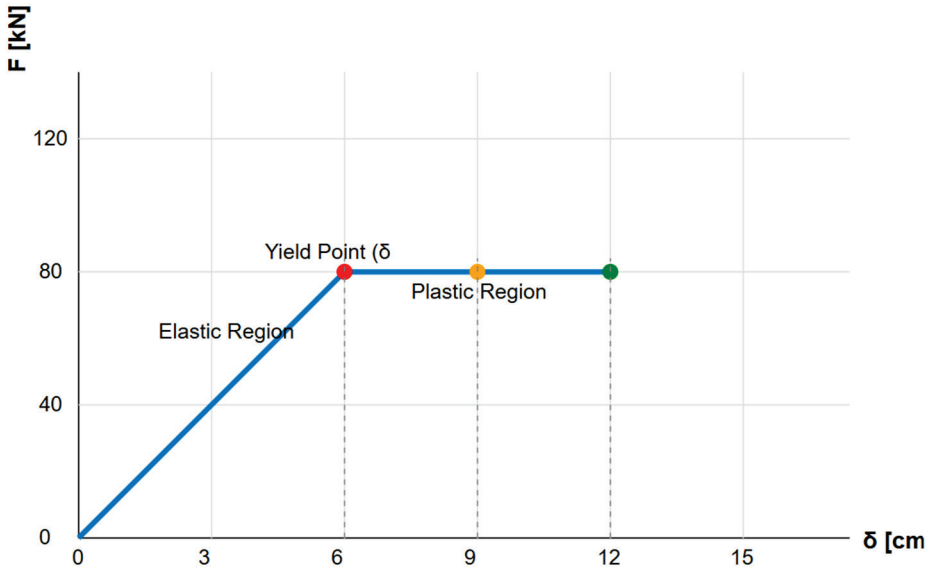

Figure 21. Simplified pushover curve of the Church of S. Giovanni Battista dei Fiorentini.

The results obtained provide the following values: u_{max}/d_{max} = 10.97/8.00 = 1.37, and ζE = 0.26/0.23 = 1.13

While this study focuses on a detailed case, the proposed framework can be extended to a larger inventory of RC churches to support urban-scale seismic risk mapping. By applying the model across a dataset of similar structures, local authorities could develop a city-wide vulnerability index, aiding emergency planning and heritage conservation strategies.

While based on a single structure, the methodology used here is transferable to a wide range of similar buildings. The ability to generate capacity curves and risk indices with minimal input makes this an ideal tool for regional-scale assessments.

4.3. Potential Integration with AI/ML Frameworks

Artificial Intelligence (AI) and Machine Learning (ML) are emerging as powerful tools in structural engineering and disaster risk reduction. While the present study focuses on a simplified, mechanics-based assessment model, future extensions could adopt AI/ML methods to enhance scalability and automate vulnerability classification.

A conceptual AI/ML workflow for seismic vulnerability assessment of reinforced concrete (RC) churches is presented in Figure 22. The process begins with the collection of structural and material data, such as geometric dimensions, reinforcement details, and construction age, followed by preprocessing steps like normalization and feature selection. These inputs can then be used to train supervised models (e.g., decision trees, regression algorithms) to predict a structure's seismic vulnerability index. Alternatively, unsupervised learning (e.g., clustering) could identify typological groups with similar vulnerability patterns.

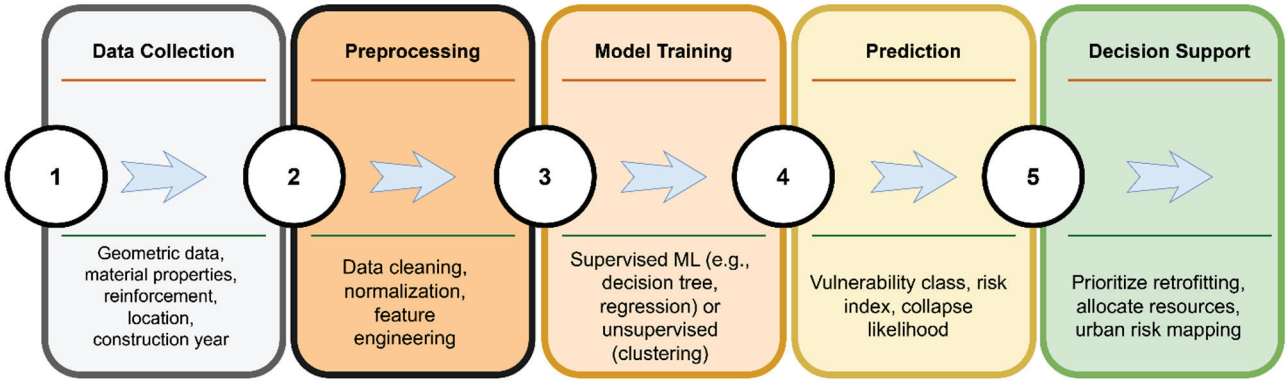

Figure 22. Conceptual AI/ML Workflow for Seismic Vulnerability Assessment of RC Churches.

The AI/ML-driven predictions could support decision-making by enabling rapid screening of extensive church inventories at the city or regional scale. This would be particularly valuable for local authorities or heritage conservation agencies that must prioritize retrofitting under limited resources. While this approach is not implemented in the current study, it represents a promising direction for future research integrating data science with structural safety and cultural resilience. By combining domain knowledge with data-driven pattern recognition, future systems could classify structural risk and recommend retrofit strategies based on typological and contextual similarities.

Future work could also explore integrating satellite data, GIS layers, or archival construction records to enrich AI/ML feature sets, potentially enabling vulnerability predictions even before on-site inspections.

The complete workflow of the proposed methodology is illustrated in Figure 23, where each stage from geometric input to risk index estimation is streamlined for rapid application in data-scarce environments.

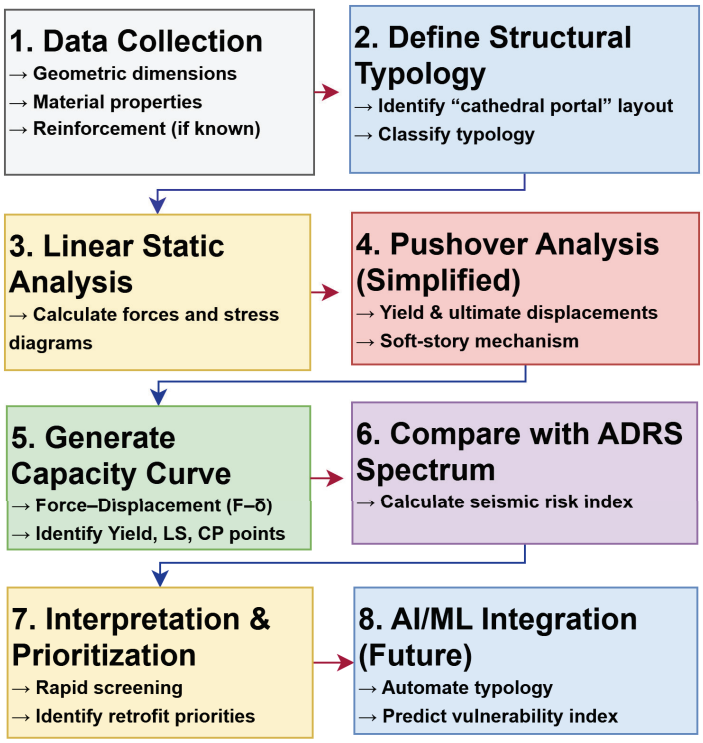

Figure 23. Simplified methodology for seismic vulnerability assessment of RC churches characterized by cathedral portal frames. The flowchart outlines all key steps, from data collection to performance evaluation and future AI/ML integration for scalability.

5. Discussion of Contributions and Limitations

The methodology presented in this study addresses a critical gap in seismic vulnerability assessment for RC churches, namely the lack of accessible tools that can be applied in the absence of detailed structural documentation. The proposed approach contributes to the field by introducing a framework based on simplified mechanics, which allows for rapid vulnerability screening at the community level. Its novelty lies in adapting classical limit analysis and pushover methods typically used in high-data contexts into a low-data, typology-driven model suitable for heritage infrastructure.

One of the key strengths of this method is its minimal input requirement, relying only on basic dimensions, reinforcement assumptions, and material properties. This makes it a viable tool for preliminary evaluations in regions where archival data are incomplete or missing. Additionally, the typological focus on the "cathedral portal" (refers to a repetitive inclined-beam portal frame) allows for replicability across a broad inventory of RC churches sharing similar structural characteristics. Moreover, the model's low computational demand makes it suitable for integration into mobile apps or web-based dashboards for use by non-experts in emergency situations.

However, the model also presents several limitations. The use of a high Confidence Factor (FC = 1.35) reflects the uncertainty in input data, and while the tool is useful for screening, it is not intended to replace detailed analysis for final design or retrofitting.

The method's flexibility also allows for potential integration with rapid post-earthquake assessment frameworks using mobile or web-based platforms in future implementations. Furthermore, the reliance on simplified collapse mechanisms does not capture

the full complexity of irregular geometries or dynamic interactions, such as tower-church interaction, which were excluded from this study.

Finally, the potential integration of AI/ML frameworks remains conceptual at this stage. Future work should focus on developing a data pipeline and training models capable of automatically classifying structural typologies and predicting seismic risk, especially when combined with GIS and remote sensing data.

Limitations of the Proposed Model

The proposed model is intended as a rapid, low-data screening tool and is not intended to replace detailed numerical simulations. A key limitation is the lack of validation against advanced Finite Element Method (FEM) models. This was not feasible due to insufficient structural documentation for the case studies, which reflects the real-world conditions the method is designed to address. However, this also limits the ability to quantify the model's accuracy compared to more detailed approaches.

Additionally, the simplified mechanics-based approach does not account for dynamic effects such as torsional response, soil-structure interaction, or the influence of bell towers. These simplifications are acceptable at the screening stage but must be addressed in detailed assessment phases.

The current model is calibrated and applied to a single case study, and while it is based on a recurrent structural typology, broader application requires careful typological matching. AI/ML integration remains a proposed direction and is not implemented in the current version.

Despite these limitations, the model provides a practical compromise between reliability and data availability, particularly for heritage inventories where detailed modeling is impractical.

6. Limitations and Future Directions

The simplified methodology presented in this study offers a reliable and accessible tool for preliminary screening of seismic vulnerability in reinforced concrete (RC) churches. However, its application is limited to initial assessments and does not replace detailed numerical simulations. The reliance on high confidence factors (e.g., FC = 1.35) reflects uncertainties in input data, and the exclusion of dynamic effects such as soil-structure interaction, torsional response, and tower-structure interaction constrains its scope. Additionally, the study's findings are based on a single case study, which necessitates broader validation across diverse typologies and geographic contexts to generalize its applicability.

Future research should focus on extending the methodology's scalability and precision through the integration of Artificial Intelligence (AI) and Machine Learning (ML). These technologies have the potential to automate typological classification and vulnerability prediction, enabling rapid assessments across large inventories of RC churches. A structured dataset comprising geometric dimensions, construction typologies, and historical performance data could serve as the foundation for supervised learning models, improving predictive accuracy. Furthermore, incorporating Geographic Information System (GIS) layers or satellite imagery into the framework may facilitate region-wide vulnerability screening without requiring extensive on-site surveys, making the methodology more accessible and practical for heritage conservation agencies.

By emphasizing specific quantitative findings, such as the seismic risk index (ζ_E = 1.13) and displacement ratio (δ_u/δ_{max} = 1.37), this study demonstrates the utility of simplified mechanics-based tools in identifying critical vulnerabilities and prioritizing retrofitting efforts. These results lay the groundwork for integrating advanced data-driven techniques

into the framework, supporting a more robust and scalable approach to cultural infrastructure resilience.

7. Outlook

The simplified, mechanics-based methodology developed in this study addresses a critical gap in seismic vulnerability assessment for RC churches in low-data scenarios. While effective for initial screening, future advancements should aim to enhance the model's scalability, accuracy, and automation. The integration of AI and ML techniques represents a promising direction, enabling rapid and automated vulnerability assessments across extensive inventories of heritage structures.

Developing structured datasets that include geometric attributes, construction typologies, and historical performance records will be essential for training supervised learning models capable of predicting seismic vulnerability indices with greater precision. Combining these datasets with GIS layers and remote sensing technologies could facilitate region-wide assessments, reducing reliance on resource-intensive on-site inspections.

Although AI integration remains conceptual in this study, it holds significant potential for complementing the mechanics-based framework. By automating typological classification and vulnerability estimation, future iterations of this methodology could support city-wide and regional-scale resilience strategies. These advancements would empower local authorities, civil protection agencies, and heritage conservation organizations to make informed decisions, prioritize interventions, and allocate resources effectively in seismically active regions.

8. Conclusions

This study presents a simplified methodology for assessing the seismic vulnerability of reinforced concrete (RC) churches characterized by cathedral portal frames. Designed for use in low-data scenarios, the proposed approach integrates classical mechanics, limit state theory, and pushover analysis to derive capacity curves and seismic risk indices for preliminary screening. The methodology was calibrated using the Cathedral of Reggio Calabria and validated on the Church of San Giovanni Battista dei Fiorentini in Naples, yielding specific quantitative findings that underscore its practical applicability.

Key findings from the analysis include the following quantitative results:

Seismic Risk Index (ζ_E): The computed seismic risk index for the case study was 1.13, indicating that the structure meets the minimum safety thresholds for the Life Safety Limit State (LS) but requires further investigation to confirm its performance under higher seismic demands.

Displacement Ratio (δ_u/δ_{max}): The ultimate displacement-to-demand ratio was found to be 1.37, demonstrating that the structure retains sufficient deformation capacity beyond the expected seismic demand.

Capacity Curve Performance: The simplified pushover analysis produced an idealized bilinear force–displacement curve, clearly delineating the elastic and plastic deformation regions. Critical performance points, such as the yield point, life safety limit, and collapse prevention limit, were identified and aligned with regulatory standards (NTC 2018).

Failure Mechanism: The soft-story collapse mechanism was identified as the dominant failure mode, confirming the vulnerability of the transverse cathedral portal frame configuration under seismic loading conditions.

These findings highlight the effectiveness of the proposed methodology in producing actionable insights with minimal input data. By focusing on geometric and material properties, as well as simplified structural mechanics, the approach enables rapid

assessments of seismic vulnerability, particularly for older RC churches with limited structural documentation.

The study's contributions extend beyond methodological innovation to practical implications for urban-scale applications. Specifically, the ability to generate capacity curves and risk indices with minimal computational resources supports city-wide vulnerability mapping, aiding stakeholders in prioritizing retrofitting efforts for heritage structures. The results for the Church of San Giovanni Battista dei Fiorentini demonstrate the scalability of the methodology to similar RC churches across Italy's seismic-prone regions.

Author Contributions: Conceptualization, G.B.; validation, G.B.; formal analysis, M.T.N.; investigation, M.T.N.; resources, G.B.; writing, original draft preparation, M.T.N.; writing, review and editing, G.B.; supervision, G.B. All authors have read and agreed to the published version of the manuscript.

Funding: This research received no external funding.

Institutional Review Board Statement: Not applicable.

Informed Consent Statement: Not applicable.

Data Availability Statement: The data presented in this study are available on request from the corresponding author.

Conflicts of Interest: The authors declare no conflicts of interest.

Abbreviations

Abbreviation	Definition
RC	Reinforced Concrete
CSM	Capacity Spectrum Method
ADRS	Acceleration–Displacement Response Spectrum
PGA	Peak Ground Acceleration
NTC	Norme Tecniche per le Costruzioni (Italian Building Code)
FEM	Finite Element Method
AI	Artificial Intelligence
ML	Machine Learning
SLV	Life Safety Limit State (Stato Limite di Vita)
SLC	Collapse Limit State (Stato Limite di Collasso)
θy	Yield Rotation
θu	Ultimate Rotation
δy	Yield Displacement
δu	Ultimate Displacement
MP	Plastic Moment
Sa	Spectral Acceleration
Sd	Spectral Displacement
FC	Confidence Factor
GIS	Geographic Information System

References

1. Brandonisio, G.; Lucibello, G.; Mele, E.; De Luca, A. Damage and performance evaluation of masonry churches in the 2009 L'Aquila earthquake. *Eng. Fail. Anal.* **2013**, *34*, 693–714. [CrossRef]
2. Lagomarsino, S.; Ottonelli, D.; Cattari, S. Performance-based assessment of masonry churches: Application to San Clemente Abbey in Castiglione a Casauria (Italy). In *Numerical Modeling of Masonry and Historical Structures: From Theory to Application*; Elsevier: Amsterdam, The Netherlands, 2019. [CrossRef]

3. Di Sabatino, U.; Gattulli, V.; Lepidi, M.; Potenza, F. New insights in the modal identification of a monumental structure from long-term seismic structural monitoring. In Proceedings of the 6th International Operational Modal Analysis Conference, IOMAC 2015, Gijon, Spain, 12–14 May 2015.
4. Rovida, A.; Locati, M.; Camassi, R.; Lolli, B.; Gasperini, P. The Italian earthquake catalogue CPTI15. *Bull. Earthq. Eng.* **2020**, *8*, 2953–2984. [CrossRef]
5. Akinci, A.; Moschetti, M.P.; Taroni, M. Ensemble smoothed seismicity models for the new Italian probabilistic seismic hazard map. *Seismol. Res. Lett.* **2018**, *89*, 1277–1287. [CrossRef]
6. Masi, A. Seismic vulnerability assessment of gravity load designed R/C frames. *Bull. Earthq. Eng.* **2003**, *1*, 371–395. [CrossRef]
7. Yüceer, H. Heritage and Resilience: Issues and Opportunities for Reducing Disaster Risks. In Proceedings of the 4th Session Global Platform Disaster Risk Reduction, Geneva, Switzerland, 19–23 May 2013.
8. Naqash, M.T.; De Matteis, G.; De Luca, A. Effects of Capacity Design Rules on Seismic Performance of Steel Moment Resisting Frames. In Proceedings of the 15th World Conference on Earthquake Engineering, Lisbon, Portugal, 24–28 September 2012.
9. Zizi, M.; Corlito, V.; Lourenço, P.B.; De Matteis, G. Seismic vulnerability of masonry churches in Abruzzi region, Italy. *Structures* **2021**, *32*, 662–680. [CrossRef]
10. Lagomarsino, S.; Cattari, S. PERPETUATE guidelines for seismic performance-based assessment of cultural heritage masonry structures. *Bull. Earthq. Eng.* **2015**, *13*, 13–47. [CrossRef]
11. Lagomarsino, S.; Modaressi, H.; Pitilakis, K.; Bosiljkov, V.; Calderini, C.; D'ayala, D.; Benouar, D.; Cattari, S. PERPETUATE Project: The proposal of a performance-based approach to earthquake protection of cultural heritage. In Proceedings of the Advanced Materials Research, Lijiang, China, 19–23 July 2010. [CrossRef]
12. Lourenço, P.B. Computations on historic masonry structures. *Prog. Struct. Eng. Mater.* **2002**, *4*, 301–319. [CrossRef]
13. Tzanakis, M.J.; Papagiannopoulos, G.A.; Hatzigeorgiou, G.D. Seismic response and retrofitting proposals of the St. Titus Chruch, Heraklion, Crete, Greece. *Earthq. Struct.* **2016**, *10*, 1347–1367. [CrossRef]
14. Hadzima-Nyarko, M.; Ademovic, N.; Pavic, G.; Kalman Šipoš, T. Strengthening techniques for masonry structures of cultural heritage according to recent Croatian provisions. *Earthq. Struct.* **2018**, *15*, 473–485. [CrossRef]
15. Almassri, B.M.; Safiyeh, A.A. Non-linear Pushover Analysis and simulation of progressive collapse mechanisms using FE Models for Nativity Church. *Earthq. Struct.* **2021**, *21*, 185–204. [CrossRef]
16. Sferrazza Papa, G.; Tateo, V.; Parisi, M.A.; Casolo, S. Seismic response of a masonry church in Central Italy: The role of interventions on the roof. *Bull. Earthq. Eng.* **2021**, *19*, 1151–1179. [CrossRef]
17. Davis, L.; Cogliano, M.; Casotto, C.; Grecchi, G.; Ozcebe, S.; Tsioli, C.; Malomo, D. Pragmatic seismic collapse meso-scale analysis of old Dutch masonry churches. *Earthq. Eng. Struct. Dyn.* **2024**, *53*, 622–645. [CrossRef]
18. Amarantidou, K.G.; Katsimpini, P.S.; Papagiannopoulos, G.; Hatzigeorgiou, G. Seismic Assessment and Strengthening of a Load-Bearing Masonry Structure Considering SSI Effects. *Appl. Sci.* **2025**, *15*, 8135. [CrossRef]
19. Cianchino, G.; Masciotta, M.G.; Verazzo, C.; Brando, G. An Overview of the Historical Retrofitting Interventions on Churches in Central Italy. *Appl. Sci.* **2023**, *13*, 40. [CrossRef]
20. Brandonisio, G.; Naqash, M.T. Validation of numerical results of complex seismic analysis through simple analytics. *J. Umm Al-Qura Univ. Eng. Archit.* **2024**, *15*, 93–111. [CrossRef]
21. Levin, R.; Jencks, C.A. The Language of Post-Modern Architecture. *J. Aesthet. Art Crit.* **1978**, *37*, 239. [CrossRef]
22. Porrini, D.; De Masi, F. Managing climate change risk: The case of the Italian Churches. *Nat. Hazards.* **2021**, *105*, 2619–2637. [CrossRef]
23. Caporali, D.; Moccia, F.D. *Napoliguida. Tra Luoghi e Monumenti della Città Storica*; Napoli e la Campania: Napoli, Italy, 2001.
24. Beninato, F.; Fori, D.; Vacca, V. *La Risoluzione dei Telai Piani: Analisi del Comportamento Statico-Deformativo e Calcolo delle Sollecitazioni*; Dario Flaccovio Editore: Palermo, Italy, 2014.
25. Massonnet, C.E. European Approaches to P -Δ Method of Design. *J. Struct. Div.* **1978**, *104*, 193–198. [CrossRef]
26. Nassar, M.; Abo El Ezz, A. Fragility-Based Seismic Risk Assessment of Reinforced Concrete Bridge Columns. *Infrastructures* **2025**, *10*, 123. [CrossRef]
27. Pardalopoulos, S.I.; Gkektsi, A.E.; Lekidis, V.A. Evaluation of an Approximate Seismic Assessment Procedure for Load-Bearing Masonry Buildings. *Infrastructures* **2025**, *10*, 118. [CrossRef]
28. Naqash, T. Pushover response of multi degree of freedom steel frames. *Civ. Eng. J.* **2020**, *6*, 86–97. [CrossRef]
29. Ali, S.S.A.; Waqas, A.; Shahzada, K.; Naqash, T.; Amjad, A.; Khan, S.N. Assessment of safety measures against seismic and fire hazards in the University of Buner. *Disaster Adv.* **2021**, *14*, 37–43. [CrossRef]
30. Massonnet, C.; Save, M. *Structures with a Single Parameter*, 3rd ed.; B. NELISSEN Publishers: Liège, Belgium, 1976; 637p.

31. Federal Emergency Management Agency (FEMA). *NEHRP Guidelines for the Seismic Rehabilitation of Buildings FEMA 273 and NEHER Commentary on the Guidelines for the Seismic Rehabilitation of Buildings FEMA 274*; Federal Emergency Management Agency Developed by Applied Technology Council: Washington, DC, USA, 1997.
32. Fajfar, P.; Dolšek, M. A practice-oriented estimation of the failure probability of building structures. *Earthq. Eng. Struct. Dyn.* **2012**, *41*, 531–547. [CrossRef]
33. Fajfar, P.; Kilar, V.; Marusic, D.; Perus, I.; Magliulo, G. The extension of the N2 method to asymmetric buildings. In Proceedings of the 4th European Workshop on the Seismic Behaviour of Irregular and Complex Structures, Thessaloniki, Greece, 26–27 August 2005.
34. Fajfar, P. A Nonlinear Analysis Method for Performance-Based Seismic Design. *Earthq. Spectra* **2000**, *16*, 573–592. [CrossRef]
35. Hopkins, D.C. Seismic design of reinforced concrete and masonry buildings. *Bull. N. Zeal. Soc. Earthq. Eng.* **1992**, *25*, 362. [CrossRef]
36. Yuen, Y.P.; Kuang, J.S. Nonlinear seismic responses and lateral force transfer mechanisms of RC frames with different infill configurations. *Eng. Struct.* **2015**, *91*, 125–140. [CrossRef]
37. Robazza, B.R.; Brzev, S.; Yang, T.Y.; Elwood, K.J.; Anderson, D.L.; McEwen, B. Seismic behaviour and design code provisions for predicting the capacity of ductile slender reinforced masonry shear walls. *Eng. Struct.* **2020**, *222*, 110992. [CrossRef]

Disclaimer/Publisher's Note: The statements, opinions and data contained in all publications are solely those of the individual author(s) and contributor(s) and not of MDPI and/or the editor(s). MDPI and/or the editor(s) disclaim responsibility for any injury to people or property resulting from any ideas, methods, instructions or products referred to in the content.

MDPI AG
Grosspeteranlage 5
4052 Basel
Switzerland
Tel.: +41 61 683 77 34

Infrastructures Editorial Office
E-mail: infrastructures@mdpi.com
www.mdpi.com/journal/infrastructures



Disclaimer/Publisher's Note: The title and front matter of this reprint are at the discretion of the Guest Editors. The publisher is not responsible for their content or any associated concerns. The statements, opinions and data contained in all individual articles are solely those of the individual Editors and contributors and not of MDPI. MDPI disclaims responsibility for any injury to people or property resulting from any ideas, methods, instructions or products referred to in the content.





Academic Open
Access Publishing

mdpi.com

ISBN 978-3-7258-8890-0